ISSN en trámite

instituto de astronomía

unam

revista mexicana de astronomía y astrofísica

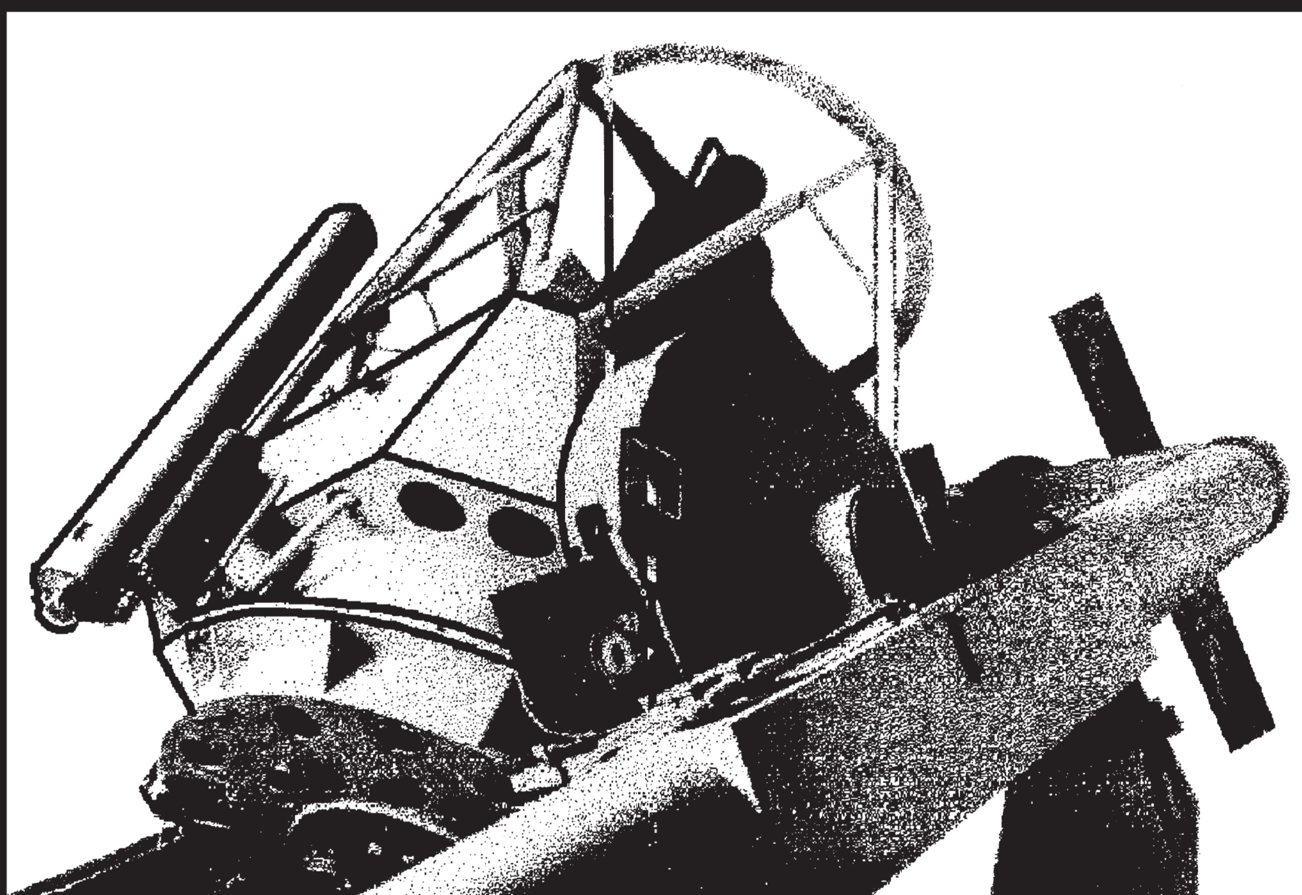

volumen 59
número 2
octubre 2023

volumen 59, número 2, octubre 2023

revista mexicana de astronomía y astrofísica

Instituto de Astronomía
Universidad Nacional Autónoma de México

revista
mexicana de
astronomía
y astrofísica

ISSN en trámite

URL de DOI: https://doi.org/10.22201/ia.01851101p.2023.59.02

rmaa@astro.unam.mx

http://www.astroscu.unam.mx/RMxAA/

La *RMxAA* aparece indexada en Current Contents, Science Citation Index, Astronomy and Astrophysics Abstracts, Physics Briefs, Publicaciones Científicas en América Latina, Astronomy and Astrophysics Monthly Index, PERIODICA, RedALyC, Latindex y SciELO.

Revista Mexicana de Astronomía y Astrofísica, volumen 59, número 2, octubre 2023, es una publicación semestral, editada y distribuida por el Instituto de Astronomía, UNAM, Circuito Exterior, Ciudad Universitaria, 04510, Alcaldía Coyoacán, Ciudad de México, Teléfono: 5556223906, Correo Electrónico: rmaa@astro.unam.mx, ISSN en trámite. Editora responsable: Christine Patricia Allen Armiño. Distribución: Bienes y Servicios del Instituto de Astronomía, UNAM. Impresa por Grupo Edición, S.A. de C.V., Xochicalco 619, Colonia Letrán Valle, 03650, Alcaldía Benito Juárez, Ciudad de México. Fecha de impresión: 27 de septiembre de 2023. Número de ejemplares impresos: 500 en papel Couché de 100 gramos los interiores y en cartulina Couché de 250 gramos los forros. Precio de la publicación: gratuito.

CONTENTS

Revista Mexicana de Astronomía y Astrofísica, **59**, 155–169 (2023)

https://doi.org/10.22201/ia.01851101p.2023.59.02.01

ASTROPHYSICAL STUDIES OF 9 UNSTUDIED OPEN STAR CLUSTERS USING *GAIA DR3*

W. A. Badawy[1], A. L. Tadross[1], Y. H. M. Hendy[1], M. N. Ismail[2], and A. Mouner[2]

Received November 21 2022; accepted March 8 2023

ABSTRACT

Using the Gaia DR3 data sets, this work gives an analysis of nine open clusters: Dolidze 25, Kronberger 13, Kronberger 18, Majaess 99, NGC 7795, Ruprecht 139, Teutsch 55, S1, and FSR 0596, which are close to the Galactic plane of the Milky Way. The number of probable cluster members is found to be 81, 77, 120, 155, 108, 110, 160, and 116 respectively. Radii are determined as 5.40, 5.25, 4.80, 4.20, 4.28, 3.70, 4.30, 4.30, and 3.53 arcmin, respectively. With solar metallicity isochrones log ages of 7.70, 9.00, 8.35, 7.50, 9.00, 8.00, 7.50, 8.50, and 9.5 yr are determined for these clusters. The best fitting of the isochrone produced distances of 2.6, 1.27, 1.16, 1.16, 3.10, 1.64, 2.50, 2.44, and 0.98 kpc that are similar to the distances calculated from inverting median parallaxes. The mass function slopes are in agreement with the Salpeter value. The results of the total masses are found to be 116.07, 79.33, 141.24, 147.34, 145.76, 491.01, 155, 212.46, and 82.79 $M_\odot$.

RESUMEN

En este trabajo estudiamos, con datos del GAIA DR3, nueve cúmulos abiertos: Dolidze 25, Kronberger 13, Kronberger 18, Majaess 99, NGC 7795, Ruprecht 139, Teutsch 55, S1, y FSR 0596, todos ellos cercanos al plano galáctico. Encontramos que el número de miembros probables es de 81, 77, 120, 155, 108, 110, 160, y 116, respectivamente. Los radios que determinamos son: 5.40, 5.25, 4.80, 4.20, 4.28, 3.70, 4.30, 4.30, y 3.53 arcmin, respectivamente. Si suponemos isocronas con metalicidades solares los logaritmos de las edades en años son: 7.70, 9.00, 8.35, 7.50, 9.00, 8.00, 7.50, 8.50, y 9.5. El mejor ajuste de las isocronas produjo distancias de 2.6, 1.27, 1.16, 1.16, 3.10, 1.64, 2.50, 2.44, y 0.98 kpc, similares a las obtenidas a partir de las paralajes medias. Las pendientes de las funciones de masa concuerdan con el valor de Salpeter. Encontramos valores para las masas totales de 116.07, 79.33, 141.24, 147.34, 145.76, 491.01, 155, 212.46, y 82.79 $M_\odot$, respectivamente.

Key Words: Hertzsprung-Russell and colour-magnitude diagrams — methods: data analysis — open clusters and associations: general — stars: luminosity function, mass function

1. INTRODUCTION

To better understand the structure and evolution of the Milky Way, open clusters (OCs) are helpful probes. OCs can be used to examine the history of star evolution because they are created by the collapse and fragmentation of massive molecular clouds (Bate et al. 2003; Harris and Pudritz 1994). For more than 1.3 billion sources, the third Gaia data release (Gaia DR3) offers precise five-parameter astrometric data (positions, proper motions, and parallaxes). Gaia DR3 demonstrates how well these data can be utilized to identify cluster members, particularly in high-density areas, and it is quite successful. Over the years, OCs have been the focus of numerous studies. They are crucial and frequently utilized to understand different aspects of the Galactic disc, such as the Milky Way's spiral arms (Bonatto et al. 2006).

2. DATA ANALYSIS AND PROCEDURE

In our previous research (Badawy et al. 2022), we studied the vector point diagrams of a large sample

[1]National Research Institute of Astronomy and Geophysics, Cairo, Egypt.
[2]Faculty of Science, Al-Azhar University, Cairo, Egypt.

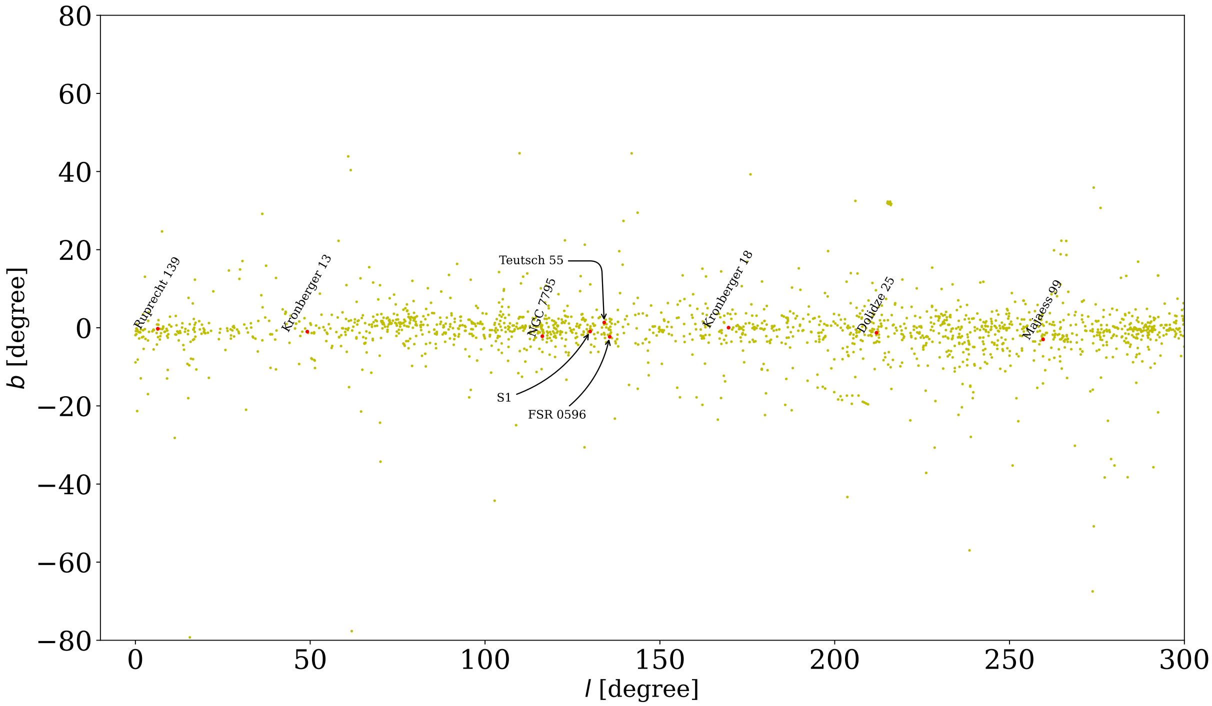

Fig. 1. The locations of the studied clusters (red dots). The yellow dots represent all the clusters obtained from Dias' catalog (Dias et al. 2014). The color figure can be viewed online.

of open stellar clusters selected from the Dais Catalog using the astrometric data of Gaia DR2. Here, we selected 9 objects that lie very close to the galactic plane and have not been studied astrometrically before using Gaia DR3 (Gaia Collaboration et al. 2022). There are full astrometric solution of positions on the sky (α, δ), parallax (ω), and proper motions (μ_α, μ_δ) for around 1.46 billion sources, with a limiting magnitude of about $G \approx 21$. We used the library Astroquery to obtain Gaia data. Astroquery is an Astropy-affiliated package that contains a collection of tools to access online astronomical data.The standard dataset of these clusters was downloaded from *Astroquery.gaia* package[3]. Using the library python package (`astroquery.simbad`)[4] we can get the central coordinates of our clusters. The source data were downloaded from the Gaia DR3 database service with radii of 0.2 degrees This package allows access to the European Space Agency Gaia Archive[5]. From the Dias catalog (Dias et al. 2014), the open clusters under study were selected and distributed according latitude and longitude, as shown in Figure (1), where the red dots represent the open clusters that are currently being studied, while the yellow dots represent all the open clusters in the catalog.

In order to select the membership, we follow the following steps. The vector point diagram (VPD) of proper motions is very useful in identifying field stars from the member stars of a cluster (Yadav et al. 2013; Straižys et al. 2019; Tadross and Hendy 2021, 2022). The vector point diagrams for all clusters are shown in Figure 2. The densest area of the cluster was placed in a sub-circle with a radius of 0.2 deg. Figure 3 shows those member stars that move at the same speed and direction in the sky (co-moving stars). The position uncertainties are $0.01 - 0.02$ mas for $G < 15$, 0.05 mas at $G = 17$, 0.4 mas at $G = 20$, and 1.0 mas at $G = 21$ mag. Due to the high accuracy of Gaia DR3, we use the sources that have $G \leq 20.5$ mag. The proper motion uncertainties are $0.02 - 0.03$ mas/yr for $G < 15$, 0.07 mas/yr at $G = 17$, 0.5 mas/yr at $G = 20$, and 1.4 mas/yr at $G = 21$ mag. The condition of 3σ for proper motions was applied to the member stars. The 3σ error in parallax was also calculated for the mean and median of the cluster. If a star of 3σ parallax error is found within the cluster mean parallax and lies inside the cluster's region, it is considered to be a member star. If we take 2σ parallax errors in-

[3]`https://astroquery.readthedocs.io/en/latest/gaia/gaia.html`

[4]`https://astroquery.readthedocs.io/en/latest/simbad/simbad.html`

[5]`http://gea.esac.esa.int/archive/`

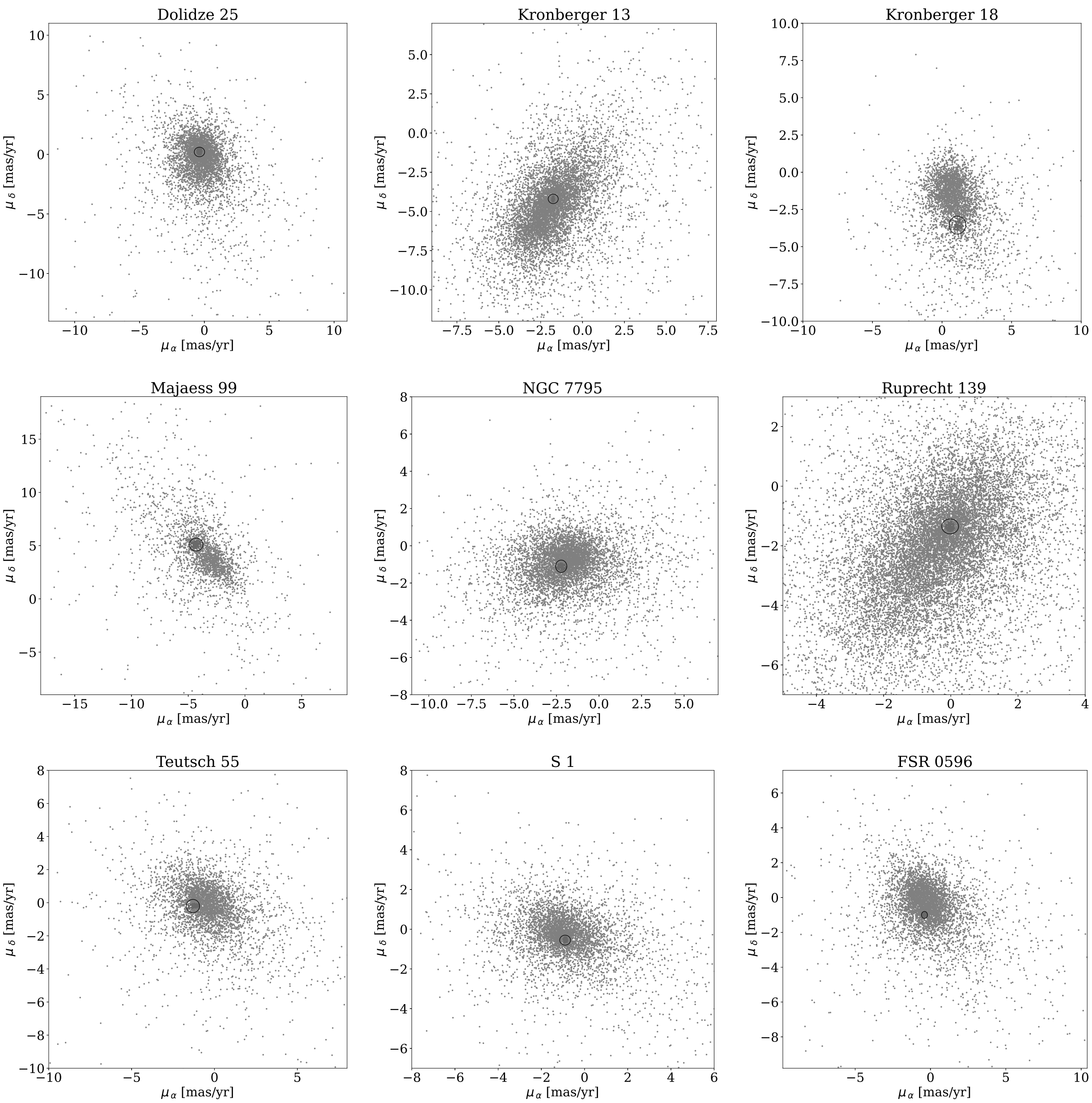

Fig. 2. The vector point diagrams (VPDs) of the studied clusters. The densest areas were placed in sub-circles with radii of 0.2 degrees.

stead of 3σ, some of the stars will be outside of the cluster's region and so they will not be considered member stars of the cluster. The parallax uncertainties are $0.02 - 0.03$ mas for $G < 15$, 0.07 mas at $G = 17$, 0.5 mas at $G = 20$, and 1.3 mas at G$= 21$ mag. We used only sources with parallaxes > 0. In their discussion of the conventional method of inverting parallaxes to determine distance, Luri et al. (2018) explain that the method is only accurate when there are no measurement uncertainties and when the distance is > 100 pc. It is not applicable for negative parallaxes arising from the survey's measurement process. The left hand side of Figure 4 shows the studied clusters' parallax range. Member stars are represented by blue dots, and background field stars are represented by yellow dots. The middle and right hand sides of Figure 4 show the stars' parallaxes in relation to their magnitudes and counts. Also, one of the parameters that must be taken into consideration is the value of the renor-

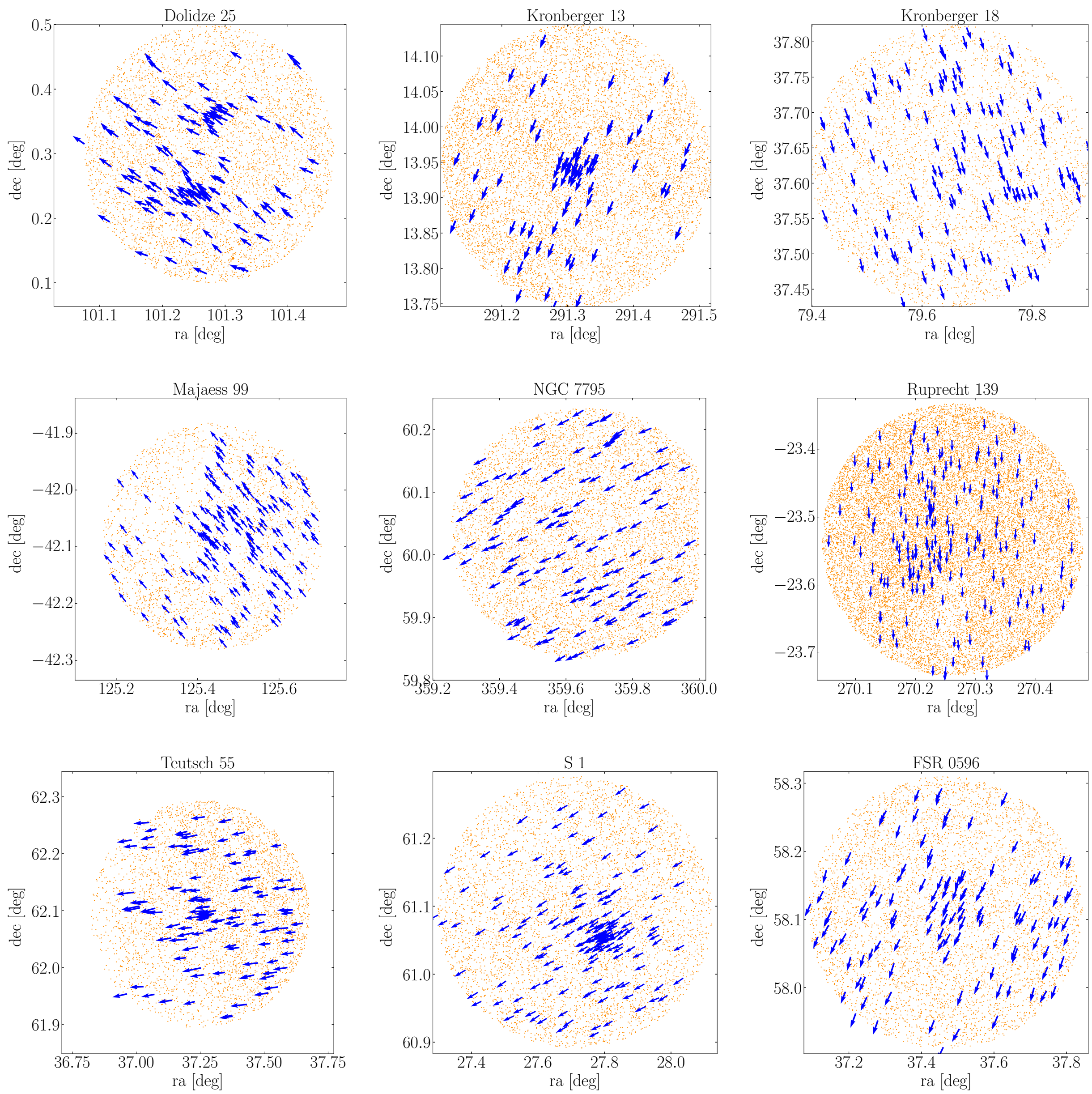

Fig. 3. Co-moving stars of the studied clusters. The blue arrows indicate the member stars as they move together in the same direction and speed, while the yellow dots show the background field stars. The color figure can be viewed online.

malized unit weight error, RUWE, which indicates that the single-star model provides a good fit to the astrometric observations, when it is ≤ 1.4 (Tadross and Elhosseiny 2022). As a result, these member stars form the usual shape for the color-magnitude diagram, CMD of the cluster, (Hendy and Tadross 2021). When the radius of the cluster is calculated (see § 3), all the stars that fall within this radius are regarded as member stars, and the stars outside this radius are regarded as background field stars.

3. OPEN CLUSTER SELECTION

Based on the Dias catalog (Dias et al. 2014), which has 2167 open clusters, we selected the current 9 open clusters that are close to the galactic plane and have members' proper motions separated from

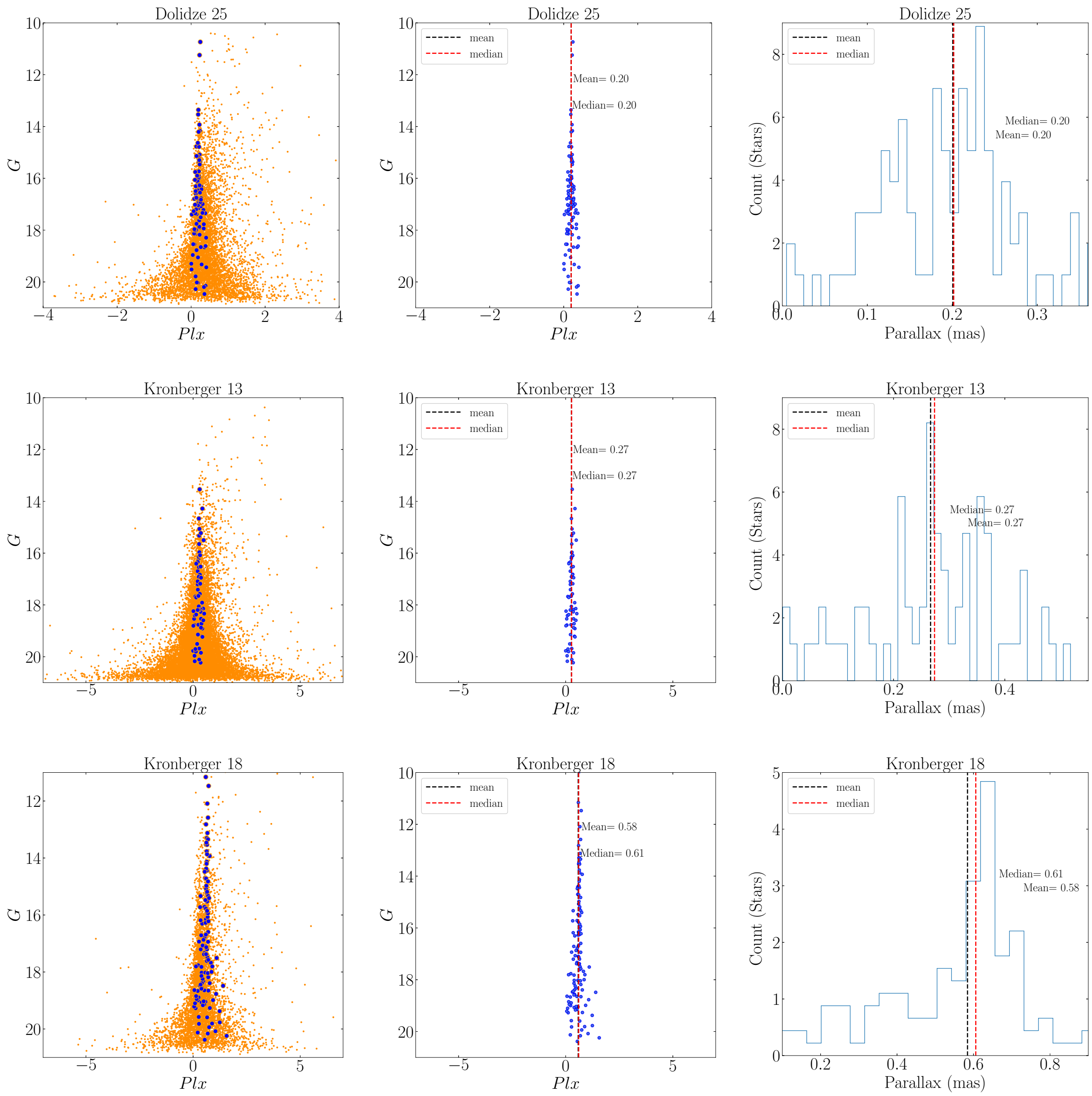

Fig. 4. The left-hand panels show the parallax range of studied clusters. The blue dots represent the member stars, while the yellow dots represent the background field stars. The middle and right hand panels show the parallax versus the magnitudes and the count numbers. The color figure can be viewed online.

the field stars. The quality of Gaia DR3 astrometry provides high accuracy proper motions in right ascension and declination (μ_α, μ_δ). Some OCs in Gaia, through, (Cantat-Gaudin et al. 2019) as well as OCs with unclear overdensities in VPDs, were excluded from our study. Kronberger13 and Ruprecht 139 are located in the first Galactic quadrant, and the rest of the clusters are located in the second Galactic quadrant.

The investigated nine open clusters, Dolidze 25 (Number=555 stars, Distance=6800 pc, E(B−V)=0.80 mag, log age=6.80 yr, Radius=10.50 arcmin). Kronberger 13 (Number=26 stars, Distance=1380 pc, E(B−V)= 1.13 mag, log age= 8.60 yr, Radius= 2.53 arcmin). Kronberger 18 (Number=40 stars, Distance= 3250 pc, E(B−V)=1.29 mag, log age= 8.00 yr, Radius=2.00 arcmin). Majaess 99 (Number=85 stars,

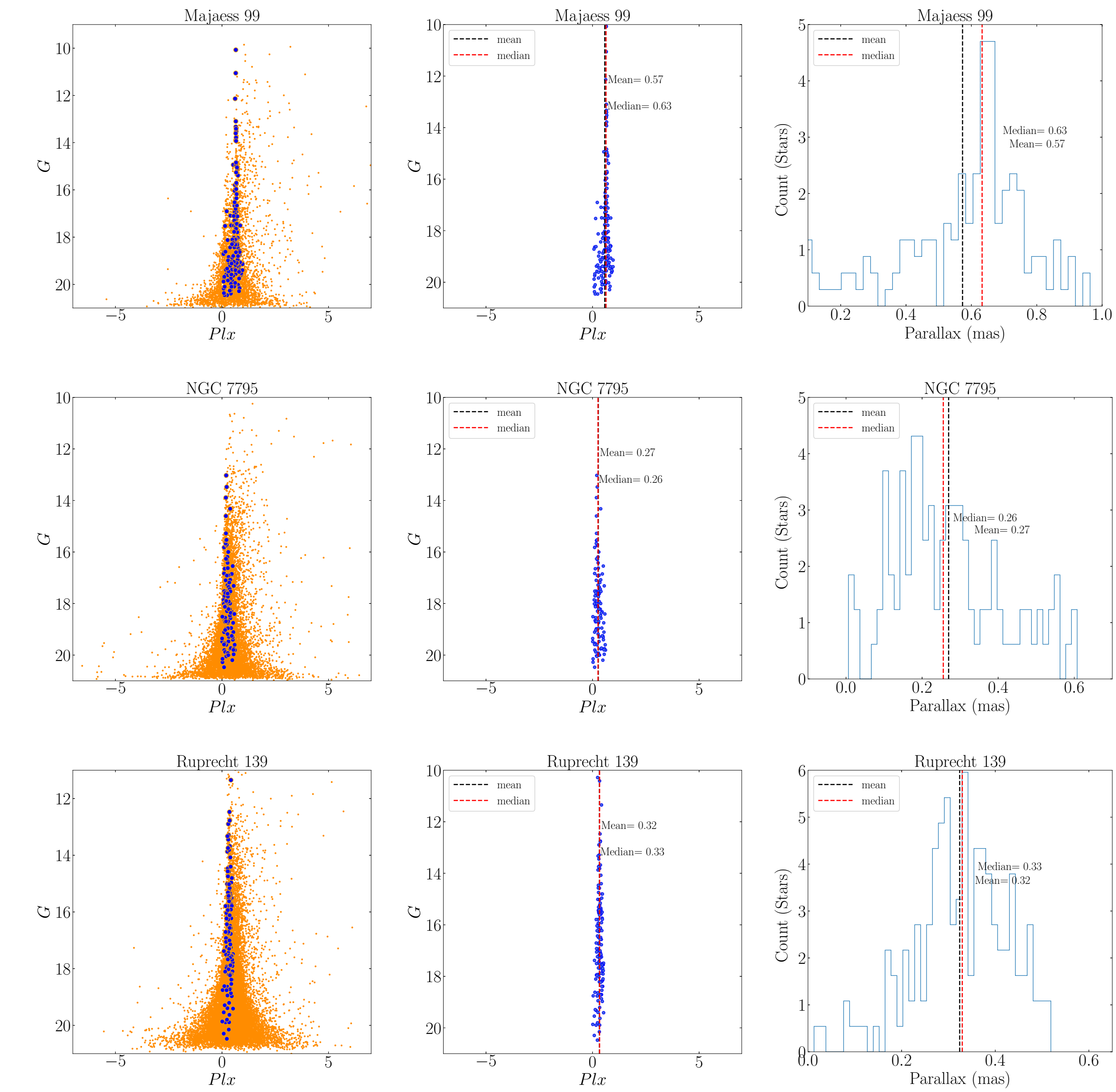

Fig. 4. Continued

Radius=5.50 arcmin). NGC 7795 (Number=806 stars, Distance=2105 pc, E(B−V)= 1.00 mag, log age=8.65 yr, Radius=11.00 arcmin). Ruprecht 139 (Number=1416 stars, Distance=550 pc, E(B−V)=0.15 mag, log age= 9.05 yr, Radius=11.58 arcmin). S1 (Number=101, Distance=2200 pc, E(B−V)=0.77 mag, log age= 7.40 yr, Radius=4.00 arcmin). Teutsch 55 (Number=80 stars, Distance=6020 pc, E(B−V)= 0.82 mag, log age=6.70 yr, Radius= 4.50 arcmin). FSR 0596 (Number=29 stars, Distance=1417 pc, E(B−V)=0.52 mag, log age=9.15 yr, Radius=2 arcmin). These OCs have been reported by Sampedro et al. (2017). A cluster may be difficult to find depending on a variety of parameters, including the density of the background, interstellar extinction, the population density, the age, and the proper motions of the field stars (Cantat-Gaudin et al. 2018).

4. SPATIAL STRUCTURE: CLUSTERS' SIZES, CENTERS, AND RICHNESS

Knowing cluster size is a substantial issue to investigate the cluster's dynamic evolution. It is hard

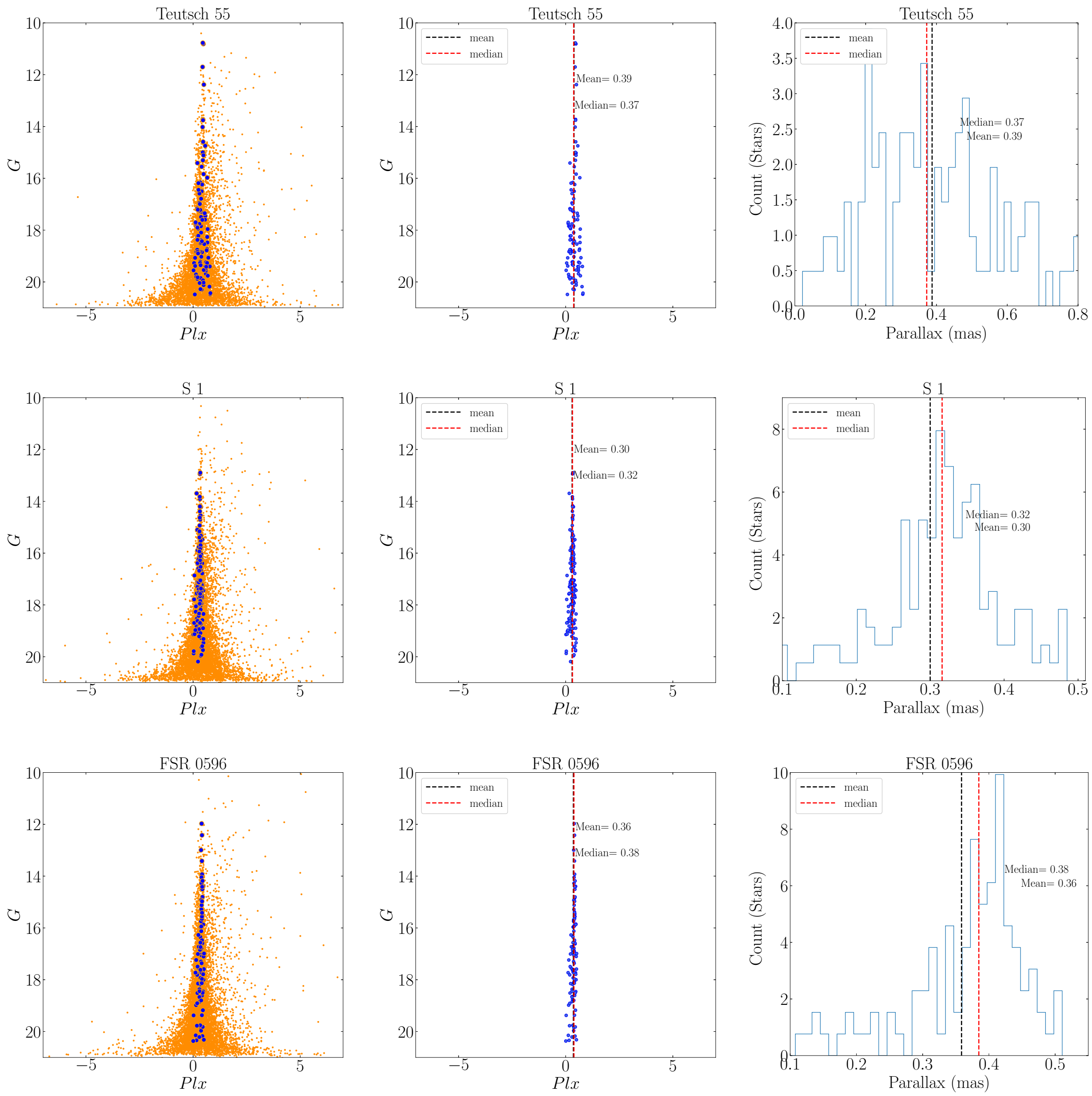

Fig. 4. Continued

to determine the precise cluster center and radial extent. Cluster radius estimation is one of the most significant basic parameters (Bisht et al. 2020). The cluster center is taken at the most over-condensation area of the cluster region taken from Dias' catalog. Subsequently, using Gaia DR3 data, we divided the area of the cluster into equal-sized bins in RA and Dec and counted the stars in each bin. The mean and median values have been applied to both RA and Dec. We estimated the radial stellar density profile (RDP) by estimating the stellar density in concentric circular rings centered at the cluster center. The number of stars in each annular region is counted (Joshi et al. 2012). The number density in the i zone is then $\rho_i = N_i/A_i$, where N_i and A_i are the star number and the area of the i zone, respectively. The error bars are derived supposing that the number of stars in an area follows the Poisson error. The limiting radius R_{lim} could be estimated to cover the entire cluster region and reached a sufficient stability, where the member stars merge with the field ones (Tadross and Hendy 2022). Therefore, R_{lim}

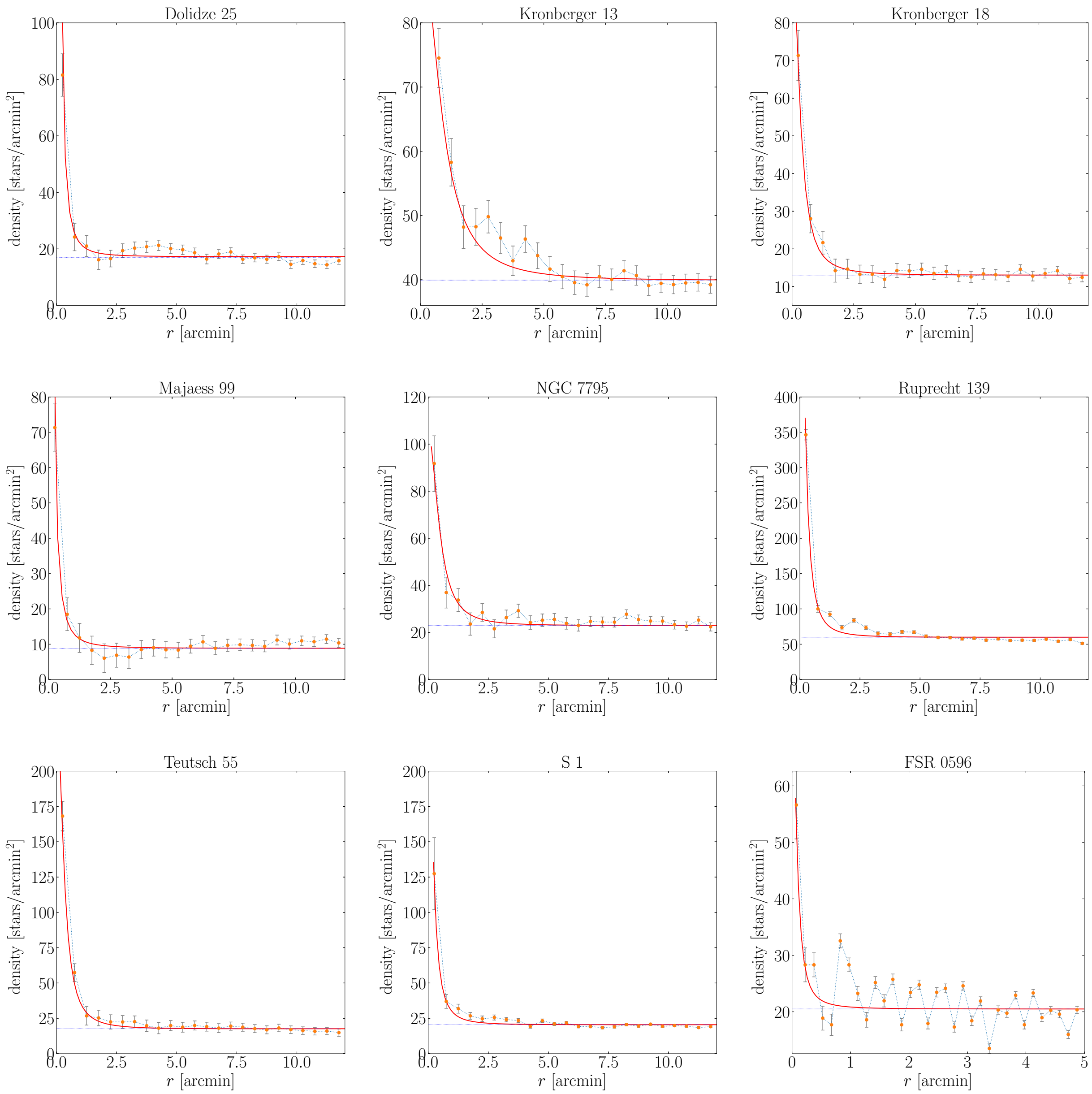

Fig. 5. The RDP curves of the studied clusters. Errors are determined by the relation $(1/\sqrt{N})$, where N is the number of cluster member stars in each radial bin. The King profile (1966) is represented by the red line, while the background density is represented by the blue line. The color figure can be viewed online.

was calculated according to the following formula of Bukowiecki et al. (2011); we can get the boundary radius by applying the equation as follows:

$$R_{lim} = R_c \sqrt{\frac{f_o}{3\sigma_{bg}} - 1}, \tag{1}$$

where σ_{bg} is the uncertainty of the f_b value. So, the estimated radius of such cluster is just a minimum radial range of the cluster (Maurya and Joshi 2020).

The spatial structure and radial density of the OCs were derived by fitting the RDP given by King (1966) as follows:

$$f(R) = f_b + \frac{f_o}{1 + (\frac{R}{R_c})^2}, \tag{2}$$

where f_b, f_o, and R_c are the background field density, central star density and the core radius of the cluster, which is defined as the radial distance from

TABLE 1

THE STRUCTURE PARAMETERS' VALUES OF THE STUDIED CLUSTERS

Cluster	f_o	f_b	R_{lim}	R_c	R_t	C
...	star/arcmin^2	star/arcmin^2	arcmin	arcmin	arcmin	...
Dolidze 25	81.75	4.27	5.40	0.12	7.12	1.65
Kronberger 13	85.24	39.93	5.25	0.89	6.27	0.77
Kronberger 18	89.74	13.04	4.80	0.34	7.60	1.15
Majaess 99	341.84	8.85	4.20	0.12	7.71	1.54
NGC 7795	3.83	1.81	4.28	0.50	6.33	0.32
Ruprecht 139	640.91	59.90	3.70	0.21	11.52	1.24
Teutsch 55	242.59	17.62	4.30	0.32	7.84	1.13
S 1	242.89	20.49	4.30	0.22	8.70	1.29
FSR 0596	55.00	20.49	3.53	0.09	6.36	1.59

TABLE 2

THE PASSBANDS FOR THE GAIA FILTER

Filter	G	G_{BP}	G_{RP}
A_λ/A_V	0.83627	1.08337	0.63439

the center where the stellar density $f(R)$ becomes half of its central value f_o. The estimated values of the structural parameters are reported in Table 1 for all the clusters. The stellar density distributions for the studied clusters are shown in Figure 5 where the solid red curves are the King profiles. Furthermore, the tidal radius of the cluster R_t is the distance from the core of the cluster, where the effect of gravity for the Galaxy is equal to that of the cluster. With the mass calculation of these clusters, the tidal radius can be estimated by using Jeffries et al. (2001) equation as follows:

$$R_t = 1.46 \times (M_c)^{\frac{1}{3}}, \tag{3}$$

where R_t and M_c are the tidal radius (in parsecs) and the total mass of the cluster (in solar masses). The concentration parameter C indicates how the member stars are prominent compared with the field stars; based on Peterson and King (1975), we can obtain the concentration parameter as follows:

$$C = \log\left(\frac{R_{lim}}{R_c}\right). \tag{4}$$

5. COLOR-MAGNITUDE DIAGRAM, AGE AND DISTANCE

The distances and ages of the Galactic OCs are important parameters when using them as tracers to investigate the structure and chemical evolution of the Galaxy. The analysis of the color-magnitude diagram (CMD) is a commonly used method for analyzing the observable main sequence of a cluster. Due to their sharing the same origin, the cluster members move through space in the same direction and at the same speed. It is necessary to identify which star evolutionary isochrones (from the COLIBRI tracks of Marigo et al. 2017) match well the cluster's main-sequence curve (CMD 3.6 input form)[6]. To lessen the impact of field stars contamination only the cluster members are used. By fitting the theoretical isochrones of solar metallicity $Z = 0.0152$ provided by Marigo et al. (2017) on the CMD of the clusters, the ages and distances of the clusters have been determined. The passbands of the Gaia filters are obtained from Riello et al. (2021), as listed in Table 2. To achieve the best fit while changing the isochrone of a given age for different distance-modulus, the reddening $E(G_{BP}-G_{RP})$ values established are employed as reported in Table 3. The presence of interstellar dust lying along the line of sight of the cluster reddens the observed magnitudes and colors due to the scattering of background star light by dust particles. The redding values are taken from the isochrones fitting to the CMD of the studied clusters. The red lines in Figure 6 show the best fitting isochrones to the CMDs of the studied clusters.

To calculate the true distance to the cluster, the apparent distance modulus must be corrected for the reddening parameter, which has a significant impact on the total absorption value, $(m-M)_o = (m-M) - A_G$, where $A_G = 1.86E(G_{BP}-G_{RP})$. By converting the current color excess to $E(B-V)$ and correcting the magnitudes for interstellar reddening, these ratios have been employed, with $A_V = R_V E(B-V)$, where $R_V = 3.1$.

[6] `http://stev.oapd.inaf.it/cgi-bin/cmd`

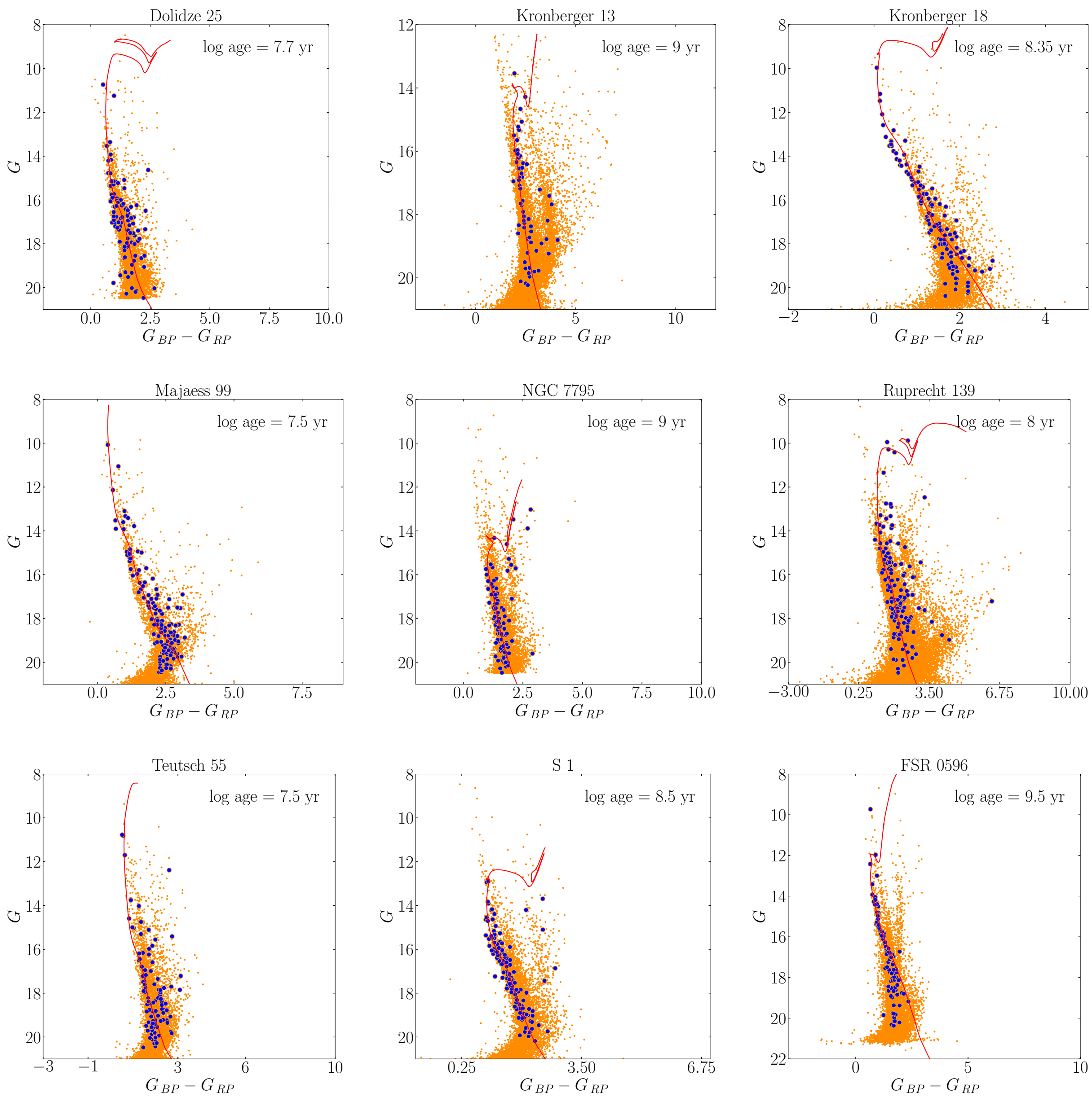

Fig. 6. The color-magnitude diagrams of the studied clusters. Probable cluster members are represented by blue dots which are obtained from the VPDs. The color figure can be viewed online.

As reported in Table 3, the estimated Cartesian Galactocentric coordinates ($X_\odot$, $Y_\odot$, $Z_\odot$) and distances from the Galactic center (R_{GC}) are provided. The calculation of cluster's geometric distances has been taken from Tadross (2011). The distance between the Sun and the Galactic core is $R_o = 8.20$ kpc (Bland-Hawthorn et al. 2019). The distance from the Sun, $R_\odot$, the axes of the projected rectangular distances on the Galactic plane, $X_\odot$ and $Y_\odot$, and the distance from the Galactic plane, $Z_\odot$, are known as the Galactic geometric distances. Such distances are significant for studying the Galaxy's structure or the traces left by the Milky Way arms.

6. LUMINOSITY FUNCTION

The total number of a cluster stars across all magnitude bins is known as the luminosity function (LF). Figure 7 provides the predicted LF for

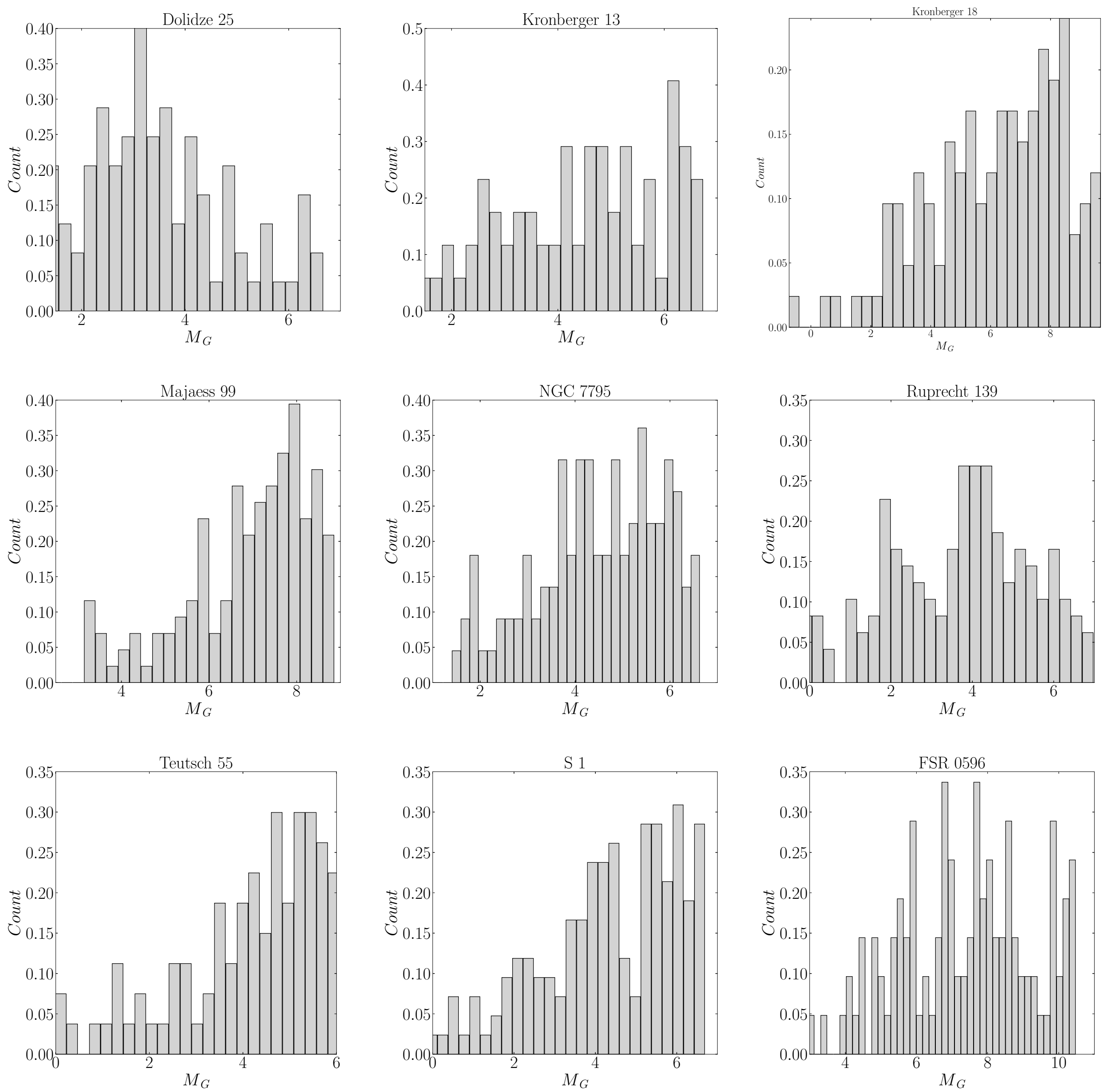

Fig. 7. The luminosity functions of the main-sequence stars of the studied clusters.

the studied clusters. The LF shows how the cluster members absolute magnitudes are distributed. The apparent G magnitudes of the cluster members were converted into absolute magnitudes using the distance moduli determined through isochrone fitting, $M_g = G - (m - M)$. By using the data from the isochrones of Marigo et al.(2017) at the cluster's age, it is possible to determine the luminosities and masses of the cluster members. For the most effective potential estimates of the LF and mass function (MF) which will be mentioned in the next section, the magnitude bin intervals are chosen to be suitable for stars in each bin. Table 3 shows the LF and MF derived for the studied clusters.

7. MASS FUNCTION

Understanding the process of star formation and the subsequent chemical and dynamical evolution of the star clusters depends heavily on the initial mass function (IMF) investigations Kroupa (2002). The

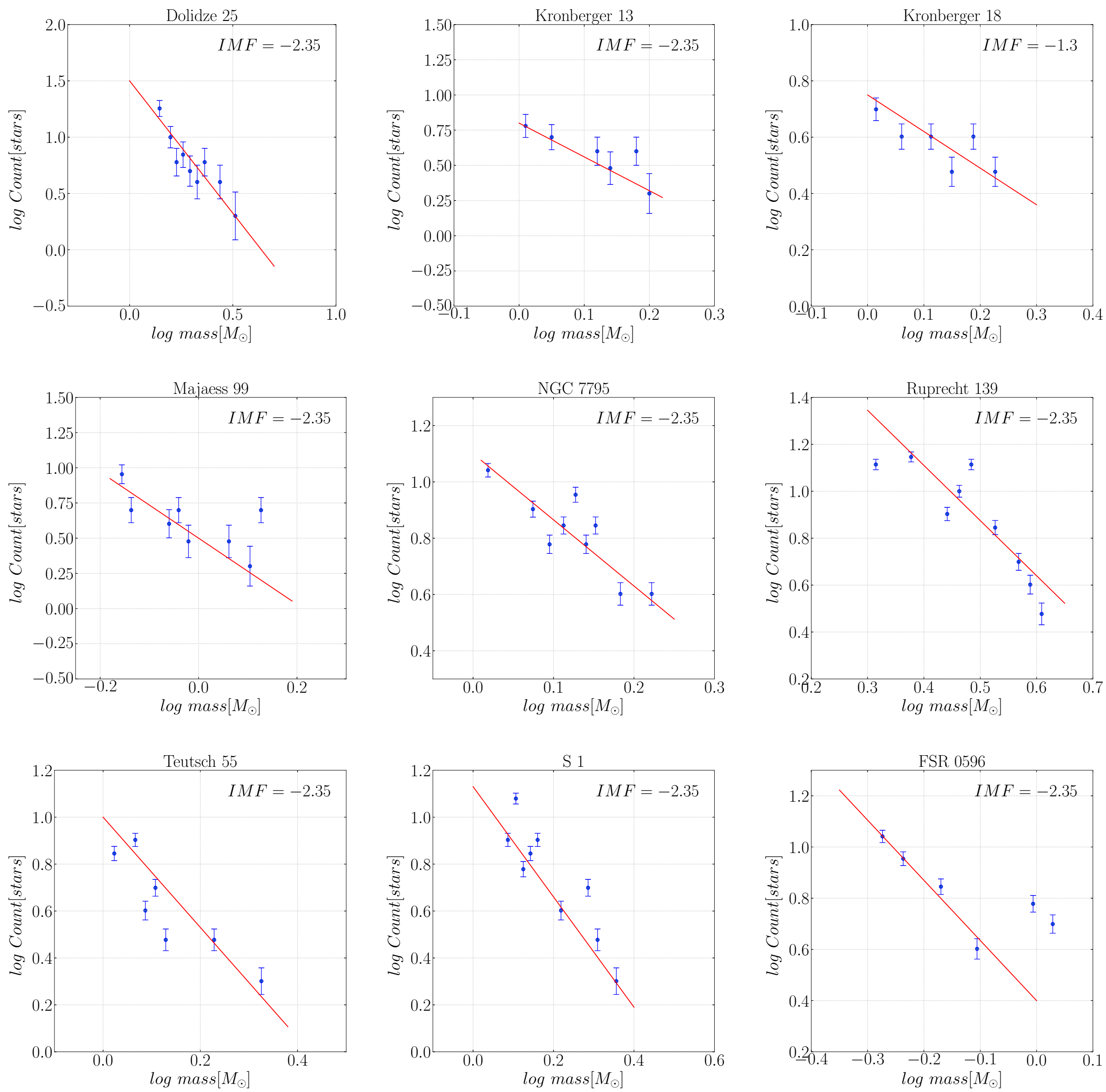

Fig. 8. The initial mass function slopes of the studied clusters. The error bars determined from the relation $1/\sqrt{N}$, where N is the number of the cluster members in each mass bin. The color figure can be viewed online.

primary link between the bright, massive members and the less massive, fainter members is provided by the IMF. It is essential for understanding the early dynamic evolution of star clusters and acts as historical evidence of the star formation process. Due to the dynamic evolution of the star system, a direct determination of IMF for the cluster is not feasible. According to Salpeter (1955) power law, which states that the number of stars in each mass range declines as the mass increases, the IMF was calculated for the bright massive stars $> 1M_\odot$. Comparing the color and magnitude of each star to the theoretical solar metallicity isochrones (Marigo et al. 2017) at the estimated age, we were able to determine the mass of each star photometrically. On the chosen isochrones, the mass of each cluster member was calculated from its closest neighbour. As a result, we calculated the current MF, which is the number of stars per mass

TABLE 3

THE PHYSICAL PARAMETERS'VALUES OF THE STUDIED CLUSTERS

Cluster	$ra(2000)$	$dec(2000)$	$l(2000)$	$b(2000)$	$E(BP-RP)$	$(m-M)$	A_G	d	Plx
...	$degree$	$degree$	$degree$	$degree$	mag	mag	mag	PC	mas
Dolidze 25	101.27	0.30	211.94	-1.27	0.90	13.80	1.67	2666	0.27
Kronberger 13	291.31	13.94	49.17	-0.98	1.60	13.5	2.98	1270	0.34
Kronberger 18	79.65	37.62	169.64	0.03	0.20	10.70	0.37	1164	0.58
Majaess 99	125.44	-42.08	259.60	-2.98	0.69	11.60	1.28	1158	0.63
NGC 7795	359.65	60.035	116.37	-2.16	0.75	13.86	1.39	3104	0.27
Ruprecht 139	270.26	-23.53	6.41	-0.23	1.30	13.50	2.42	1644	0.39
Teutsch 55	37.25	62.09	134.08	1.35	0.92	13.70	1.71	2500	0.43
S 1	27.71	61.09	130.05	-0.96	1.00	13.80	1.86	2443	0.41
FSR 0596	37.47	58.11	135.65	-2.31	0.03	10.00	0.05	977	0.41

TABLE 3. CONTINUED

Cluster	T_R	$logage$	τ	N	M_v	M_C	IMF	μ_α	μ_δ
...	Myr	yr	...	$Stars$	mag	$M_\odot$	...	mas/yr	mas/yr
Dolidze 25	12.55	7.70	3.99	81	-2.01	116.07	-2.35	-0.40	0.33
Kronberger 13	4.59	9.00	217.86	77	-6.06	79.33	-2.40	-1.76	-4.21
Kronberger 18	3.57	8.35	62.71	120	-4.08	141.24	-1.30	1.11	-3.55
Majaess 99	3.17	7.50	9.97	155	-3.71	147.34	-2.35	-4.31	5.13
NGC 7795	12.81	9.00	78.06	108	-3.83	145.76	-2.35	-10.81	-2.87
Ruprecht 139	2.86	8.00	34.96	175	-8.16	491.01	-2.35	0.02	-1.37
Teutsch 55	6.16	7.50	5.13	110	-5.71	155	-2.35	-1.22	0.18
S 1	8.58	8.50	36.83	160	-5.33	212.46	-2.35	-0.74	-0.83
FSR 0596	2.06	9.50	1534.95	116	-1.76	82.79	-2.35	-0.41	-0.98

TABLE 3. CONTINUED

Cluster	$X_\odot$	$Y_\odot$	$Z_\odot$	R_{GC}
...	pc	pc	pc	kpc
Dolidze 25	-2261.82	-1410.05	-59.09	10.56
Kronberger 13	830.21	960.81	-21.71	19.19
Kronberger 18	-1145.02	209.32	0.61	21.15
Majaess 99	-208.76	-1137.43	-60.20	8.48
NGC 7795	-1377.71	2779.03	-116.99	9.97
Ruprecht 139	1633.71	183.54	-6.60	18.37
Teutsch 55	-1738.67	1795.42	58.90	10.10
S 1	-1571.74	1869.81	-4.93	9.95
FSR 0596	-698.07	682.41	-39.38	20.71

bin, and is frequently described by the power law $\frac{dN}{dM} \propto m^{-\alpha}$, where α is the slope of MF. It can be given as

$$\log \frac{dN}{dM} = -\alpha \log M + Constant, \tag{5}$$

where $\log(dN)$ is the logarithmic number of stars per unit logarithmic mass interval (dM). Salpeter (1955) determined the slope of the mass function α as -2.35 among the solar neighborhood stars, which is typically regarded as a classical value of the MF slope, for the mass range $0.4 < M/M_\odot \leq 10$. We determined the mean mass in each magnitude bin of the G band. We provide the mass range, mean mass, and cluster members in different brightness range for the clusters. The two-stage power law in some of the MF slopes of OCs may be due to the dynamics of clusters and/or to initial conditions in star formation events (Bonatto & Bica 2005). The resulting mass function obtained for the clusters is shown in Figure 8.

8. THE DYNAMIC RELAXATION TIME

The dynamic relaxation time T_R is the time during which the velocity distribution of stars in a cluster approaches its equilibrium distribution. We estimated the dynamic relaxation time to determine if the mass segregation process in the clusters is caused by dynamical development or by the star formation process itself. According to Spitzer and Hart (1971), the relaxation time, T_R, is mathematically defined as

$$T_R = \frac{8.9 \times 10^5 \times \sqrt{N} \times R_h^{1.5}}{\sqrt{\overline{m}} \times \log(0.4 \times N)}, \tag{6}$$

where N is the total number of stars in the cluster. R_h is the star cluster's half-mass radius, and $\overline{m}$ is the average stellar mass in the cluster. To calculate R_h, we first added up the masses of each cluster member individually and calculated both the mean stellar mass and the total mass of each cluster. After determining the radius where 50% of the cluster's total mass is included, we can get R_h values, and then T_R can be obtained. We can define the dynamical evolution parameter from the following relation based on the cluster age and its relaxation time

$$\tau = \frac{age}{T_R}. \tag{7}$$

9. CONCLUSIONS

The main astrophysical parameters of the nine open stellar clusters Dolidze 25, Kronberger 13, Kronberger 18, Majaess 99, NGC 7795, Ruprecht 139, Teutsch 55, S1, and FSR 0596 were estimated in this paper for the first time using the Gaia DR3 database. Comparing the astrometric parameters obtained here for 5 OCs (Kronberger 18, Majaess 99, NGC 7795, Ruprecht 139, and Teutsch 55) with those provided by Dias et al. (2018). Kronberger 18 (radius = 3 arcmin, $\mu_\alpha = 2.01$ mas/yr, $\mu_\delta = -3.89$ mas/yr, number = 49 stars). Majaess 99 (radius = 6 arcmin, $\mu_\alpha = -6.21$ mas/yr, $\mu_\delta = 5.56$ mas/yr, number = 69 stars). NGC 7795 (radius = 11.5 arcmin, $\mu_\alpha = -1.57$ mas/yr, $\mu_\delta = -0.95$ mas/yr, number = 879 stars). Ruprecht 139 (radius = 7 arcmin, $\mu_\alpha = -0.21$ mas/yr, $\mu_\delta = -2.31$ mas/yr, number = 658 stars). Teutsch 55 (radius = 5 arcmin, $\mu_\alpha = -1.11$ mas/yr, $\mu_\delta = -0.29$ mas/yr, number = 87 stars) it is clear that they are well consistent with our results. Dolidze 25, S1, FSR 0596, and Kronberger 13 are not found in that catalog. Majaess 99 was reported only by Monteiro and Dias (2019); their results are in good agreement with ours as well. Majaess 99 (log age = 6.66 ± 0.01 yr, distance = 1.32 ± 0.08 kpc, $E(B\text{-}V) = 0.02 \pm 0.02$ mag, number = 46 stars, $\mu_\alpha = -4.37 \pm 0.002$ mas/yr, $\mu_\delta = 5.19 \pm 0.01$ mas/yr, parallax = 0.66 ± 0.03 mas). All the parameters of our studied clusters are summarized and listed in Table 3.

This work has made use of data from the European Space Agency (ESA) mission Gaia processed by the Gaia Data Processing and Analysis Consortium (DPAC), https://www.cosmos.esa.int/web/gaia/dpac/consortium. Funding for the DPAC has been provided by national institutions, in particular, the institutions participating in the Gaia Multilateral Agreement (MLA).

REFERENCES

Badawy, W. A., Tadross, A. L., Hendy, Y. H. M., et al. 2022, JAsGe, 11, 142

Bate, M. R., Bonnell, I. A., & Bromm, V. 2003, MNRAS, 339, 577, https://doi.org/10.1046/j.1365-8711.2003.06210.x

Bisht, D., Elsanhoury, W. H., Zhu, Q., et al. 2020, AJ, 160, 119, https://doi.org/10.3847/1538-3881/ab9ffd

Bisht, D., Zhu, Q., Yadav, R. K. S., Durgapal, A., & Rangwal, G. 2020, MNRAS, 494, 607, https://doi.org/10.1093/mnras/staa656

Bland-Hawthorn, J., Sharma, S., Tepper-García, T., et al. 2019, MNRAS, 486, 1167, https://doi.org/10.1093/mnras/stz217

Bonatto, C. & Bica, E. 2005, A&A, 437, 483, https://doi.org/10.1051/0004-6361:20042516

Bonatto, C., Kerber, L. O., Bica, E., & Santiago, B. X. 2006, A&A, 446, 121, https://doi.org/10.1051/0004-6361:20053573

Bossini, D., Vallenari, A., Bragaglia, A., et al. 2019, A&A, 623, 108, https://doi.org/10.1051/0004-6361/201834693

Bragaglia, A. 2017, IAUS 330, Astrometry and Astrophysica in the Gaia Sky, 119, https://doi.org/10.1017/s1743921317005294

Bressan, A., Marigo, P., Girardi, L., et al. 2012, MNRAS, 427, 127, https://doi.org/10.1111/j.1365-2966.2012.21948.x

Bukowiecki, Ł., Maciejewski, G., Konorski, P., & Strobel, A. 2011, AcA, 61, 231, https://doi.org/10.48550/arXiv.1107.5119

Cantat-Gaudin, T., Jordi, C., Vallenari, A., et al. 2018, A&A, 618, 93, https://doi.org/10.1051/0004-6361/201833476

Cantat-Gaudin, T., Anders, F., Castro-Ginard, A., et al. 2020, VizieR Online Data Catalog: Portrait Galactic disc (Cantat-Gaudin+, 2020)

Dias, W. S., Monteiro, H., Caetano, T. C., et al. 2014, A&A, 564, 79, https://doi.org/10.1051/0004-6361/201323226

Dias, W. S., Alessi, B. S., Moitinho, A., & Lepine, J. R. D. 2014, VizieR Data Catalog: Optically visible open clusters and Candidates (Dias+2002-2015)

Dias, W. S., Monteiro, H., & Assafin, M. 2018, MNRAS, 478, 5184, https://doi.org/10.1093/mnras/sty1456

Gaia Collaboration, Vallenari, A., Brown, A. G. A. et al. 2022, arXiv, https://doi.org/10.48550/arXiv.2208.00211

Harris, W. E. & Pudritz, R. E. 1994, ApJ, 429, 177, https://doi.org/10.1086/174310

Hendy, Y. & Tadross, A. 2021, AN, 342, 613, https://doi.org/10.1002/asna.202143848

Hills, S., von Hippel, T., Courteau, S., & Geller, A. M. 2015, AJ, 149, 94, https://doi.org/10.1088/0004-6256/149/3/94

Jeffries, R. D., Thurston, M. R., & Hambly, N. C. 2001, A&A, 375, 863, https://doi.org/10.1051/0004-6361:20010918

Joshi, Y. C., Joshi, S., Kumar, B., Mondal, S., & Balona, L. A. 2012, MNRAS, 419, 2379, https://doi.org/10.1111/j.1365-2966.2011.19890.x

King, I. R. 1966, AJ, 71, 64, https://doi.org/10.1086/109857

Kroupa, P. 2002, Sci, 295, 82, https://doi.org/10.1126/science.1067524

Luri, X., Brown, A. G. A., Sarro, L. M., et al. 2018, A&A, 616, 9, https://doi.org/10.1051/0004-6361/201832964

Marigo, P., Girardi, L., Bressan, A., et al. ApJ, 835, 77, https://doi.org/10.3847/1538-4357/835/1/77

Maurya, J. & Joshi, Y. C. 2020, MNRAS, 494, 4713, https://doi.org/10.1093/mnras/staa893

Monteiro, H. & Dias, W. S. 2019, MNRAS, 487, 2385, https://doi.org/10.1093/mnras/stz1455

Peterson, C. J. & King, I. R. 1975, AJ, 80, 427, https://doi.org/10.1086/111759

Riello, M., De Angeli, F., Evans, D. W., et al. 2021, A&A, 649, 3, https://doi.org/10.1051/0004-6361/202039587

Salpeter, E. E. 1955, ApJ, 121, 161, https://doi.org/10.1086/145971

Sampedro, L., Dias, W. S., Alfaro, E. J., Monteiro, H., & Molino, A. 2017, MNRAS, 470, 3937, https://doi.org/10.1093/mnras/stx1485

Spitzer, L. Jr. & Hart, M. H. 1971, ApJ, 164, 399, https://doi.org/10.1086/150855

Straižys, V., Boyle, R. P., Milašius, K., et al. 2019, A&A, 623, 22, https://doi.org/10.1051/0004-6361/201833987

Tadross, A. L. 2011, JKAS, 44, 1, https://doi.org/10.5303/JKAS.2011.44.1.1

__________. 2018, RAA, 18, 158, https://doi.org/10.1088/1674-4527/18/12/158

__________. 2021, JApA, 42, 6, https://doi.org/10.1007/s12036-020-09648-5

__________. 2022, AdSpR, 69, 467, https://doi.org/10.1016/j.asr.2021.09.014

Tadross, A. L. & Elhosseiny, E. G. 2022, RMxAA, 58, 387, https://doi.org/10.22201/ia.01851101p.2022.58.02.17

Yadav, R. K. S., Sariya, D. P., & Sagar, R. 2013, MNRAS, 430, 3350, https://doi.org/10.1093/mnras/stt136

W. A. Badawy, Y. H. M. Hendy, and A. L. Tadross: National Research Institute of Astronomy and Geophysics, Cairo, Egypt.

M. N. Ismail and A. Mouner: Faculty of Science, Al-Azhar University, Cairo, Egypt.

Revista Mexicana de Astronomía y Astrofísica, **59**, 171–175 (2023)

https://doi.org/10.22201/ia.01851101p.2023.59.02.02

ON THE CORRECT COMPUTATION OF ALL LYAPUNOV EXPONENTS IN HAMILTONIAN DYNAMICAL SYSTEMS

D. D. Carpintero[1,2] and J. C. Muzzio[1,2]

Received March 7 2023; accepted April 3 2023

ABSTRACT

The Lyapunov characteristic exponents are a useful indicator of chaos in astronomical dynamical systems. They are usually computed through a standard, very efficient and neat algorithm published in 1980. However, for Hamiltonian systems the expected result of pairs of opposite exponents is not always obtained with enough precision. We find here why in these cases the initial order of the deviation vectors matters, and how to sort them in order to obtain a correct result.

RESUMEN

Los exponentes característicos de Lyapunov constituyen un útil indicador de caos en sistemas dinámicos astronómicos. Habitualmente se los calcula mediante un algoritmo muy claro y eficiente publicado en 1980. Sin embargo, para sistemas hamiltonianos, el resultado esperable de pares de exponentes opuestos no siempre se obtiene con suficiente precisión. Aquí encontramos por qué en estos casos es importante el orden inicial de los vectores de desviación, y cómo deben distribuirse a fin de obtener un resultado correcto.

Key Words: chaos — galaxies: kinematics and dynamics — methods: numerical — planets and satellites: dynamical evolution and stability

1. INTRODUCTION

The importance of chaos in astronomical dynamical systems is generally recognized nowadays and a complete summary of this subject can be found in the textbook of Contopoulos (2002). The algorithms commonly used to determine the regularity or chaoticity of a dynamical system can be grouped into two categories: those based on the frequency analysis of the orbits (e.g. Binney & Spergel 1982; Laskar 1990; Šidlichovský & Nesvorný 1996; Carpintero & Aguilar 1998; Papaphilippou & Laskar 1998) and the so-called variational indicators, based on the behaviour of deviation vectors (e.g. Voglis & Contopoulos 1994; Contopoulos & Voglis 1996; Froeschlé et al. 1997; Voglis et al. 1999; Cincotta & Simó 2000; Sándor et al. 2000; Skokos 2001; Lega & Froeschlé 2001; Fouchard et al. 2002; Cincotta et al. 2003; Sándor et al. 2004; Skokos et al. 2007; Maffione et al. 2011; Darriba et al. 2012b,a; Maffione et al. 2013; Carpintero et al. 2014). Among the methods of the last group, the computation of the Lyapunov characteristic exponents (LCEs) (Benettin et al. 1976, 1980) stands out not only for being the oldest of them all but also for representing the very definition of chaos. They have been used to investigate chaos in elliptical galaxies, among others, by Udry & Pfenniger (1988), Merritt & Fridman (1996) and by ourselves (see Carpintero & Muzzio (2016) and its references to our previous work).

In the second part of a seminal paper, Benettin et al. (1980) gave for the first time a thorough description of an algorithm to compute all the LCEs of a system, which in turn was based on the theoretical work of the first part (Benettin et al. 1976). This algorithm quickly became a standard.

However, when dealing with a Hamiltonian system, the expected result of paired opposite LCEs is not always achieved with enough numerical precision, notwithstanding the neat procedure of the above-mentioned algorithm. We find here the origin of the problem and an easy way out.

2. SETTING THE STAGE

We assume that we are dealing with a dynamical system described by n differential equations of the first order. To compute the LCEs of one of its or-

[1]Facultad de Ciencias Astronómicas y Geofísicas, Universidad Nacional de La Plata, Argentina.

[2]Instituto de Astrofísica de La Plata, UNLP–Conicet, Argentina.

bits with the algorithm of Benettin et al. (1980), one obtains the orbit itself —which we will call the unperturbed orbit— by integrating the corresponding equations of motion, plus the time evolution of n linearly independent vectors, the deviation vectors $\delta\mathbf{w}_i$, $i = 1, \ldots, n$, representing the phase space distance between the orbit and n additional orbits —the perturbed orbits— that start near the former. The time evolution of these vectors is obtained by integrating the so-called variational equations, that is, the first variation of the equations of the motion around the original orbit (e.g. Tabor 1989, p. 148). To obtain the LCEs λ_i, $i = 1, \ldots, n$ from the deviation vectors, one computes (Benettin et al. 1980)

$$\lambda_i \simeq \frac{1}{N\tau} \sum_{k=1}^{N} \ln \alpha_i(t_k), \tag{1}$$

where $\alpha_i(t_k)$ is the modulus of $\delta\mathbf{w}_i$ after an orthogonalization of the set $\{\delta\mathbf{w}_j\}_{j=1,\ldots,n}$ at time t_k, τ is the step of integration, and N a positive integer which has to be large enough to get a good approximation. If the orthogonalization is carried out using the Gram-Schmidt method, the α_i's can be obtained on the fly. Also, since the computation does not depend on the initial moduli or initial orientation of the $\delta\mathbf{w}_i$ (Benettin et al. 1980), it is customary to set initial deviation vectors of unitary modulus, each one aligned with one of the Cartesian axes.

Let us now assume, to fix ideas, that the LCEs are ordered in descending order according to their values:

$$\lambda_1 \geq \lambda_2 \geq \cdots \geq \lambda_n. \tag{2}$$

Now we may ask: can we determine which of the $\delta\mathbf{w}_i$'s will give the α_i with which λ_1 is obtained? Clearly, by equation (1), the deviation vector that accumulates the largest modulus after the orthogonalizations will be the one that gives λ_1. This vector is identifiable thanks to three circumstances. First, the orthogonalization at times t_k includes a normalization of all the resulting vectors, in order to avoid numerical overflows due to their exponential growth. Thus, all the deviation vectors start their evolution always with the same modulus. Second, all the vectors tend to align towards the direction of maximum growth —the reason why an orthogonalization is done periodically, thus avoiding very small angles between vectors which would be numerically intractable. Therefore, all vectors tend to go into a direction with the same rate of growth; this reason, together with the previous one, allows us to claim that if the interval between t_k and t_{k+1} is not too large, all vectors will have similar moduli just before the orthonormalization step. Third, by using the Gram-Schmidt method, the first vector entering the algorithm will keep its modulus; the second one, instead, will end up with a smaller modulus because it is projected into the subspace orthogonal to the first. The third, fourth, etc. vectors will end up with even smaller moduli, each one being projected into subspaces of lesser dimension. These three reasons together allow us to answer the question posed above: although at short times any vector could be the largest, given enough time the first vector entering the Gram-Schmidt algorithm will grow more than the rest, and will be the one with which λ_1 will be computed.

By reasoning in the same way, one could claim that the second vector entering the Gram-Schmidt algorithm will always have the second-largest modulus and therefore will be the one with which λ_2 will be computed, and so on for the rest of deviation vectors and LCEs. Therefore, if we sort the subindices of $\delta\mathbf{w}_i$ in the order with which they enter the Gram-Schmidt routine (i.e., $\delta\mathbf{w}_1$ the first one, $\delta\mathbf{w}_2$ the second one, etc.), then each $\delta\mathbf{w}_i$ should give the corresponding λ_i —the latter sorted according to inequation (2). Although this is to be expected, it turns out that is not quite true in all cases.

3. THE PROBLEM: HAMILTONIAN SYSTEMS

If the dynamical system under study is Hamiltonian and autonomous, by Liouville's theorem any volume of the phase space will be conserved along its evolution. From this is not hard to see (e.g. Jackson 1989) that, for any direction of the phase space that stretches exponentially (with corresponding LCE positive), there must be another one that shrinks at the same exponential rate (with an LCE equal to the negative of the latter). Thus, Hamiltonian systems always have pairs of LCEs that are negatives of each other. Also, one of those pairs is always zero. These are strong restrictions that may be used to control whether the computation of the LCEs has been successful. But it turns out that a naïve application of equation (1) does not always achieve this. Figure 1 shows the absolute value of the computed LCEs of an orbit in the two-dimensional Binney potential (Binney 1982)

$$\Phi(x, y) = \frac{v_0^2}{2} \ln\left[R_c^2 + x^2 + \frac{y^2}{q^2} + \frac{1}{R_e}\sqrt{x^2 + y^2}(x^2 - y^2)\right], \tag{3}$$

where (x, y) are Cartesian coordinates and v_0, q, R_c and R_e are parameters. Since the system is Hamiltonian and autonomous, we expect that $\lambda_1 = -\lambda_4$ and

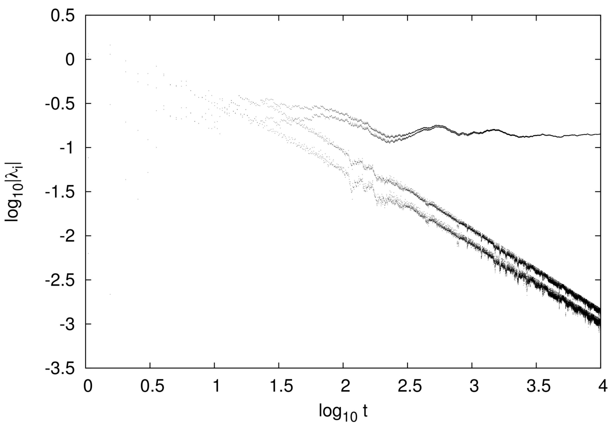

Fig. 1. LCEs of an orbit in the potential of equation (3) with parameters $v_0 = 1$, $q = 0.9$, $R_c = 0.14$ and $R_e = 3$, started at the phase space point $(x, y, \dot{x}, \dot{y}) = (0.1, 0.5, 0, 1)$. From top to bottom, the sets of dots are generated by deviation vectors originally pointing along the directions $\mathbf{e}_x$, $\mathbf{e}_y$, $\mathbf{e}_{\dot{x}}$ and $\mathbf{e}_{\dot{y}}$, respectively. All the computations were performed with double precision. Since we are plotting the absolute value of the LCEs, if two of them were the opposite of the other two —as expected for a Hamiltonian system— only two sets of dots would be seen.

$\lambda_2 = -\lambda_3$, the latter tending to zero as time goes by. However, although the computation was done with double precision, we can see that the four LCEs are not well paired in opposite pairs.

4. THE SOLUTION

An important property of Hamiltonian dynamics is that Poincaré invariants are preserved along the flow (e.g. Tabor 1989). Let $\mathbf{q}$ and $\mathbf{p}$ stand for the coordinates and momenta of a canonical set, respectively; in addition, let $\mathscr{C}_1$ be any closed curve in the n-dimensional phase space encompassing a tube of orbits, and $\mathscr{C}_2$ any other closed curve enclosing the same set of trajectories. The first Poincaré invariant can be expressed as

$$\int_{\mathscr{C}_1} \mathbf{p} \cdot \mathrm{d}\mathbf{q} = \int_{\mathscr{C}_2} \mathbf{p} \cdot \mathrm{d}\mathbf{q}. \quad (4)$$

We note that $\mathscr{C}_2$ could be the curve $\mathscr{C}_1$ evolved in time. Let us take, to fix ideas, $n = 2$ and Cartesian coordinates $(\mathbf{q}, \mathbf{p}) = (x, y, \dot{x}, \dot{y})$. If we choose for $\mathscr{C}_1$ the unit square in the plane $(q_1, p_1) = (x, \dot{x})$ at t_0, it will enclose the area spanned by $\delta\mathbf{w}_x(t_0)$ and $\delta\mathbf{w}_{\dot{x}}(t_0)$, and the Poincaré first invariant will have only the term corresponding to $\dot{x} \cdot \mathrm{d}x$. Furthermore, by virtue of Stokes's theorem, the line integral will be equal to the enclosed area. If we choose the initial deviation vectors as before (unit vectors pointing along each Cartesian axis), this area will be equal to one, and by the invariance of the integral the area of the parallelogram spanned by $\delta\mathbf{w}_x(t)$ and $\delta\mathbf{w}_{\dot{x}}(t)$ for any $t > t_0$ will remain unitary.

Now, the orthogonalization of the Gram-Schmidt algorithm allows us to compute the area of the parallelogram spanned by $\delta\mathbf{w}_x(t)$ and $\delta\mathbf{w}_{\dot{x}}(t)$ as simply $\alpha_x \cdot \alpha_{\dot{x}}$, and since this area should be always equal to 1, we should have

$$\ln \alpha_x(t) = -\ln \alpha_{\dot{x}}(t) \quad (5)$$

for all t. The same will happen with the y coordinate. Looking at equation (1), we see that the deviation vectors started on the x and $\dot{x}$ axes will give a pair of opposite LCEs, while those started on the y and $\dot{y}$ axes will give the other pair.

But here we see the problem. On the one hand, as we have just seen, if for example $\delta\mathbf{w}_1 = \delta\mathbf{w}_x$, then we must have $\delta\mathbf{w}_4 = \delta\mathbf{w}_{\dot{x}}$ in order to obtain the pair of opposite LCEs. But, on the other hand, this is not necessarily the order in which they are entered into the Gram-Schmidt routine. If these vectors are not the first and fourth, we are forcing the algorithm to find an opposite value of λ_1 with a vector that is not the expected one, thus compelling the routine to give the correct modulus to a vector that was not the one that formed a unitary parallelogram with the first. This is numerically inefficient. Therefore, since the first and last deviation vectors inserted into the Gram-Schmidt routine should give the maximum LCE and its opposite sibling, they should be those originally pointing along a Cartesian coordinate and its corresponding velocity (in any order among them). The same occurs for the second and penultimate vectors, etc.

Figure 2 shows the LCEs of the same orbit as in Figure 1, but computed with the deviation vectors ordered originally in the directions $(\mathbf{e}_x, \mathbf{e}_y, \mathbf{e}_{\dot{y}}, \mathbf{e}_{\dot{x}})$. There are four sets of points plotted in the figure, generated by the evolution of those vectors. But the sets generated by $\mathbf{e}_x$ and $\mathbf{e}_{\dot{x}}$ are superimposed, so only one set is visible (the top one in the figure). In the same way, the two sets generated by $\mathbf{e}_y$ and $\mathbf{e}_{\dot{y}}$ are superimposed (the bottom set in the figure). Thus, we can see that the very same algorithm with the same orbit used before gives now exact opposite LCEs, as expected.

Besides, using the order of the initial vectors that we propose has the additional and more practically useful advantage that it yields better defined values of the computed LCEs. As an example, we computed the LCEs of orbits in the perturbed cubic force model used by Muzzio (2017) with

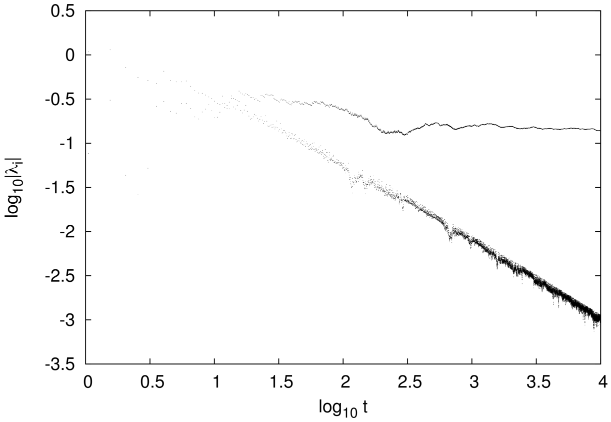

Fig. 2. LCEs of the same orbit of Figure 1, but starting with unitary deviation vectors $\delta\mathbf{w}_1 = \mathbf{e}_x$, $\delta\mathbf{w}_2 = \mathbf{e}_y$, $\delta\mathbf{w}_3 = \mathbf{e}_{\dot{y}}$ and $\delta\mathbf{w}_4 = \mathbf{e}_{\dot{x}}$. The top set of points were generated by $\mathbf{e}_x$ and $\mathbf{e}_{\dot{x}}$, though they are the same, so a unique set is seen. The same for the bottom set, which is a superposition of the sets generated by $\mathbf{e}_y$ and $\mathbf{e}_{\dot{y}}$.

$-0.166843 < e_1 < -0.166507$, $-0.324941 < e_2 < -0.323994$ and grid spacings $\Delta e_1 = 2^{-17}$ and $\Delta e_2 = 2^{-16}$ (see Muzzio, 2017, for details). The integrations were done for 5×10^6 time units in all the cases. Figure 3 presents the resulting λ_1 versus λ_2 with the usual ordering (top panel), and the same with our ordering (bottom panel). Clearly, the dispersion of the λ_2 values is smaller and their value better defined with our ordering of the initial vectors.

5. CONCLUSION

The results obtained for the LCEs of a Hamiltonian autonomous system with the Benettin et al. (1980) method depend on the order used for the initial deviation vectors. To obtain the expected opposite pairs of LCEs, the deviation vectors should be ordered by pairs, the first, second, etc. ones having to be conjugate with the last, the penultimate, etc., respectively. The results obtained with such an ordering have the additional advantage of resulting in better defined values of the computed LCEs.

The authors are very grateful to Juani Rodríguez for his technical support and they acknowledge financial support from the Universidad Nacional de La Plata, Argentina [Proyecto 11/G168] and from the Consejo Nacional de Investigaciones Científicas y Técnicas, Argentina [PIP 2169].

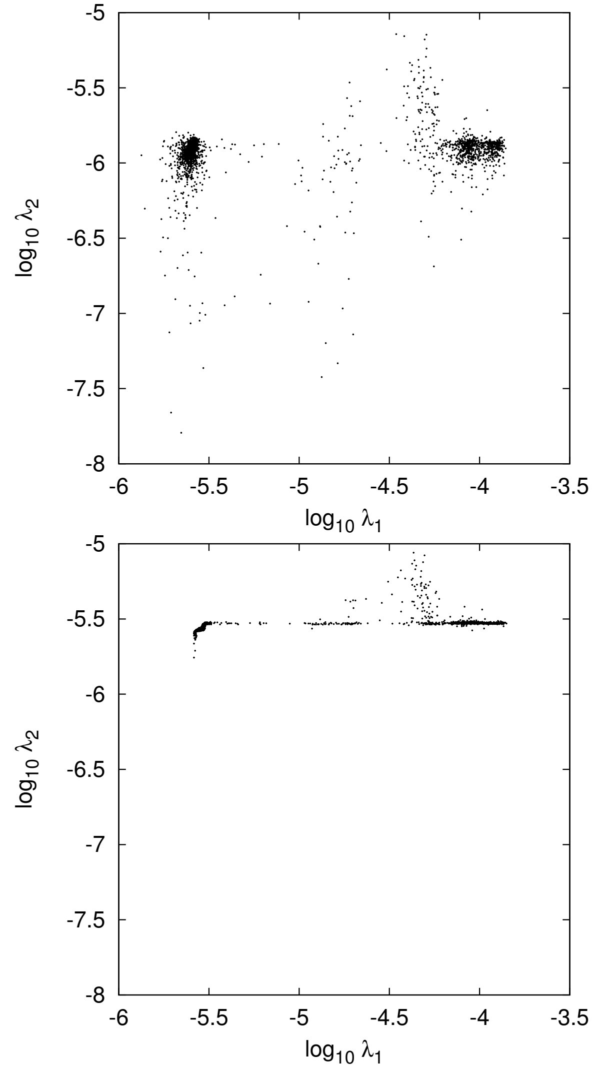

Fig. 3. Top: logarithmic plot of the largest (λ_1) versus the second largest (λ_2) LCEs for a perturbed cubic oscillator (see text for details) using the standard ordering of the deviation vectors. Bottom: the same but using the proposed ordering of the deviation vectors.

REFERENCES

Benettin, G., Galgani, L., & Strelcyn, J.-M. 1976, PhRvA, 14, 2338, https://doi.org/10.1103/PhysRevA.14.2338

Benettin, G., Galgani, L., Giorgilli, A., & Strelcyn, J.-M. 1980, Mecc, 15, 9

Binney, J. 1982, MNRAS, 201, 1, https://doi.org/10.1093/mnras/201.1.1

Binney, J. & Spergel, D. 1982, ApJ, 252, 308, https://doi.org/10.1086/159559

Carpintero, D. D. & Aguilar, L. A. 1998, MNRAS, 298, 1, https://doi.org/10.1046/j.1365-8711.1998.01320.x

Carpintero, D. D., Maffione, N., & Darriba, L. 2014, A&C, 5, 19, https://doi.org/10.1016/j.ascom.2014.04.001

Carpintero, D. D. & Muzzio, J. C. 2016, MNRAS, 459, 1082, https://doi.org/10.1093/mnras/stw720

Cincotta, P. M., Giordano, C. M., & Simó, C. 2003, PhyD, 182, 151, https://doi.org/10.1016/s0167-2789(03)00103-9

Cincotta, P. M. & Simó, C. 2000, A&AS, 147, 205, https://doi.org/10.1051/aas:2000108

Contopoulos, G. 2002, Order and chaos in dynamical astronomy (Berlin Springer)

Contopoulos, G. & Voglis, N. 1996, CeMDA, 64, 1, https://doi.org/10.1007/BF00051601

Darriba, L. A., Maffione, N. P., Cincotta, P. M., & Giordano, C. M. 2012a, in 3rd La Plata International School on Astronomy and Geophysics: Chaos, diffusion and non-integrability in Hamiltonian Systems - Application to astronomy, ed. C. E. P. M. Cincotta, C. M. Giordano (Universidad Nacional de La Plata - Asociación Argentina de Astronomía), 345

Darriba, L. A., Maffione, N. P., Cincotta, P. M., & Giordano, C. M. 2012b, IJBC, 22, 1230033, https://doi.org/10.1142/s0218127412300339

Fouchard, M., Lega, E., Froeschlé, C., & Froeschlé, C. 2002, CeMDA, 83, 205

Froeschlé, C., Gonczi, R., & Lega, E. 1997, Planet. Space Sci., 45, 881, https://doi.org/10.1016/S0032-0633(97)00058-5

Jackson, E. A. 1989, Perspectives of Nonlinear Dynamics, Volume 1 (Cambridge, MA: CUP)

Laskar, J. 1990, Icar, 88, 266, https://doi.org/10.1016/0019-1035(90)90084-M

Lega, E. & Froeschlé, C. 2001, CeMDA, 81, 129

Maffione, N. P., Darriba, L. A., Cincotta, P. M., & Giordano, C. M. 2011, CeMDA, 111, 285, https://doi.org/10.1007/s10569-011-9373-z

_________. 2013, MNRAS, 429, 2700, https://doi.org/10.1093/mnras/sts539

Merritt, D. & Fridman, T. 1996, ApJ, 460, 136, https://doi.org/10.1086/176957

Muzzio, J. C. 2017, MNRAS, 471, 4099, https://doi.org/10.1093/mnras/stx1922

Papaphilippou, Y. & Laskar, J. 1998, A&A, 329, 451

Sándor, Z., Érdi, B., & Efthymiopoulos, C. 2000, CeMDA, 78, 113, https://doi.org/10.1023/A:1011112228708

Sándor, Z., Érdi, B., Széll, A., & Funk, B. 2004, CeMDA, 90, 127, https://doi.org/10.1007/s10569-004-8129-4

Šidlichovský, M. & Nesvorný, D. 1996, CeMDA, 65, 137, https://doi.org/10.1007/BF00048443

Skokos, C. 2001, JPhA, 34, 10029, https://doi.org/10.1088/0305-4470/34/47/309

Skokos, C., Bountis, T. C., & Antonopoulos, C. 2007, PhyD, 231, 30, https://doi.org/10.1016/j.physd.2007.04.004

Tabor, M. 1989, Chaos and Integrability in Nonlinear Dynamics: An Introduction (Wiley Interscience) \href{https://books.google.com.ar/books?id=TkvvAAAAMAAJ}

Udry, S. & Pfenniger, D. 1988, A&A, 198, 135

Voglis, N., Contopoulos, G., & Efthymiopoulos, C. 1999, CeMDA, 73, 211, https://doi.org/10.1023/A:1008307332442

Voglis, N. & Contopoulos, G. J. 1994, JPhA, 27, 4899, https://doi.org/10.1088/0305-4470/27/14/017

Daniel D. Carpintero and Juan C. Muzzio: Facultad de Ciencias Astronómicas y Geofísicas, Universidad Nacional de La Plata, Paseo del Bosque s/n, 1900 La Plata, Argentina (ddc, jcmuzzio@fcaglp.unlp.edu.ar).

Daniel D. Carpintero and Juan C. Muzzio: Instituto de Astrofísica de La Plata, UNLP–Conicet, Paseo del Bosque s/n, 1900 La Plata, Argentina (ddc, jcmuzzio@fcaglp.unlp.edu.ar).

Revista Mexicana de Astronomía y Astrofísica, **59**, 177–190 (2023)

https://doi.org/10.22201/ia.01851101p.2023.59.02.03

A DEEP STUDY OF THE OPEN CLUSTER NGC 5288 USING PHOTOMETRIC AND ASTROMETRIC DATA FROM GAIA DR3 AND 2MASS

Ritika Sethi[1], D. Bisht[2], Geeta Rangwal[3], and A. Raj[2]

Received August 22 2022; accepted April 11 2023

ABSTRACT

This paper investigates a poorly studied open cluster, NGC 5288, using 2MASS JHK_S and the recently released Gaia DR3 astrometric and photometric data. The mean proper motions in right ascension and declination are estimated as (-3.840 ± 0.230) and (-1.934 ± 0.162) mas yr^{-1} respectively. We also derive the age and distance of the cluster as 510 ± 190 Myr and 2.64 ± 0.11 kpc, using color-magnitude diagrams (CMDs). We also obtain the distance as 2.77 ± 0.42 kpc using the parallax method. Interstellar reddening $E(B-V)$ in the direction of the cluster is determined as 0.45 mag using the $((J-H),(J-K))$ color-color diagram. We find the mass function slope for main-sequence stars as 1.39 ± 0.29 within the mass range $1.0-2.7$ $M_\odot$, which agrees with Salpeter's value within the uncertainty. Galactic orbits are derived using the Galactic potential model, indicating that NGC 5288 follows a circular path around the Galactic center.

RESUMEN

En este trabajo investigamos el cúmulo abierto poco estudiado NGC 5288 usando datos del 2MASS JHK_S y del Gaia DR3. Estimamos que los movimientos propios medios en ascensión recta y declinación son de (-3.840 ± 0.230) y (-1.934 ± 0.162) mas año^{-1}, respectivamente. Mediante diagramas color-magnitud derivamos edad y distancia al cúmulo de 510 ± 190 megaaños y 2.64 ± 0.11 kpc. También obtenemos una distancia de 2.77 ± 0.42 kpc con el método de la paralaje. Mediante el diagrama color-color $((J-H),(J-K))$ encontramos que el enrojecimiento interestelar $E(B-V)$ en la dirección del cúmulo es de 0.45 mag. La pendiente de la función de masa para estrellas de la secuencia principal resulta ser 1.39 ± 0.29 en el intervalo de masas $1.0-2.7$ $M_\odot$, en concordancia con el valor de Salpeter dentro de las incertidumbres. Se calculan órbitas galácticas y se encuentra que NGC 5288 describe una órbita circular alrededor del centro galáctico.

Key Words: Hertzsprung-Russell and colour-magnitude diagrams — open clusters and associations: general — proper motions — stars: luminosity function, mass function

1. INTRODUCTION

Open clusters (OCs) are loosely bound systems consisting of around a hundred to a few thousand stars. Owing to the origin of cluster members from a common molecular cloud, they have similar chemical composition, kinematic properties and distance from the Sun (Dias et al. 2002; Joshi et al. 2016). This makes them prime candidates for studying stellar formation and evolution. OCs can help us conveniently determine various astrophysical parameters and provide insights into the chemical and structural evolution of the Milky Way Galaxy (Sariya et al. 2021a; Tadross & Hendy 2021).

Global space missions like Gaia, launched in 2013, have provided the scientific community with high-precision, 3-dimensional spatial and velocity distributions of more than 3 billion stars (Gaia Collaboration et al. 2016). The mission has transformed

[1]Department of Physical Sciences, Indian Institute of Science Education and Research, India.
[2]Indian Centre for Space Physics, India.
[3]Indian Institute of Astrophysics, India.

the field of astrophysics and established a foundation for high-quality research. Although it is challenging to distinguish open cluster members from the background-field stars, the 3-D data from the Gaia mission has made the job easier (van Leeuwen et al. 2022). Much work has recently been done to estimate the membership probability of stars in the cluster region using the proper motion and parallax information (Cantat-Gaudin et al. 2018; Bisht et al. 2019; Ferreira et al. 2020; Sariya et al. 2021a). The decontaminated sample of cluster members thus obtained naturally yields cleaner color-magnitude diagrams and more accurate estimates of the astrophysical parameters.

In this study, we estimate the astrophysical properties of NGC 5288, an open cluster positioned at $\alpha_{2000} = 13^h48^m44^s$, $\delta_{2000} = -64°41'06''$ corresponding to the Galactic coordinates $l = 309°.010$ and $b = -2°.492$ according to the WEBDA open cluster database. It is located in the constellation Circinus and situated to the south of the celestial equator, mostly visible from the southern hemisphere. It is designated as Cr 278 in the Collinder catalogue of open clusters (Collinder 1931). The charge-coupled device (CCD) photometric data of the cluster observed at the Cerro Tololo Inter-American Observatory (CTIO) were analysed by Piatti et al. (2006) for determining fundamental parameters like size, age, reddening, distance and metallicity. They described NGC 5288 as a rich, strongly absorbed cluster with a small but bright nucleus and a low-density extended corona located beyond the Carina spiral feature. However, the extensive scattering caused due to atmospheric disturbances and low resolution of photometric data from ground based telescopes make it difficult to study individual stars in the cluster, differentiating them against the background field, which restricts scientists to carry out further research. The space based astrometric solutions from the Gaia mission are hence of immense importance for modern research with more accuracy. Specifically for NGC 5288, the Gaia data helped us estimate the basic parameters of the cluster more accurately. Also, completeness of Gaia photometric data is 100 percent for this cluster for a limit of 20 mag, which further helped us in finding the actual present day mass function slope of the cluster.

This paper is organized as follows. In § 2, we describe the data used, and in § 3, we elaborate on the procedure to calculate the membership probability of the stars. In § 4, we derive the cluster's structural properties and basic parameters. § 5 sheds light on fitting the derived color magnitude diagram (CMD)

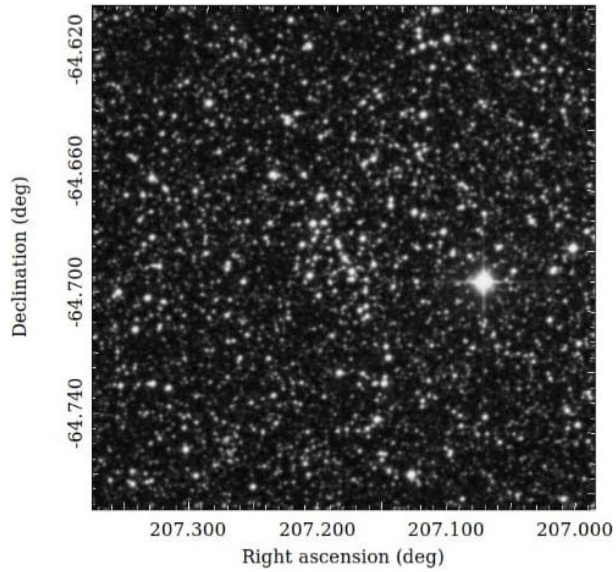

Fig. 1. Identification map of NGC 5288 taken from DSS.

of the cluster on theoretical isochrones and subsequently evaluating its age and distance. § 6 discusses the luminosity and mass functions of the cluster in detail. § 7 is devoted to the orbital dynamics of the cluster. Finally, in § 8, we conclude the study and present a summary of the results.

2. DATA USED

2.1. *2MASS*

In this paper, we have used The Two Micros All-sky Survey ($2MASS$, Skrutskie et al. 2006) data for the cluster NGC 5288. This data set uses two highly automated 1.3m telescopes, one at Mt. Hopkins, Arizona (AZ), USA and the other at CTIO, Chile, with a 3-channel camera (256×256 array of HgCdTe detectors in each channel). The $2MASS$ catalog provides J (1.25 μm), H (1.65 μm) and K_s (2.17 μm) band photometry for millions of galaxies and nearly a half-billion stars (Carpenter, 2001). The sensitivity of this catalog is 15.8 mag for J, 15.1 mag for H and 14.3 mag for K_s band at S/N=10.

2.2. *GAIA DR3*

The Gaia DR3 data gives a complete astrometric solution for more than 1.46 billion sources. It consists of their positions on the sky (α, δ), parallaxes, and proper motions within 3 to 21 mag limit in the G band (Gaia Collaboration et al. 2016; Babusiaux et al. 2022). The Gaia photometric bands: G, G_{BP}, and G_{RP} gather measurements over the wavelength ranges of $330-1050, 330-680$, and $640-1050$ nm, respectively.

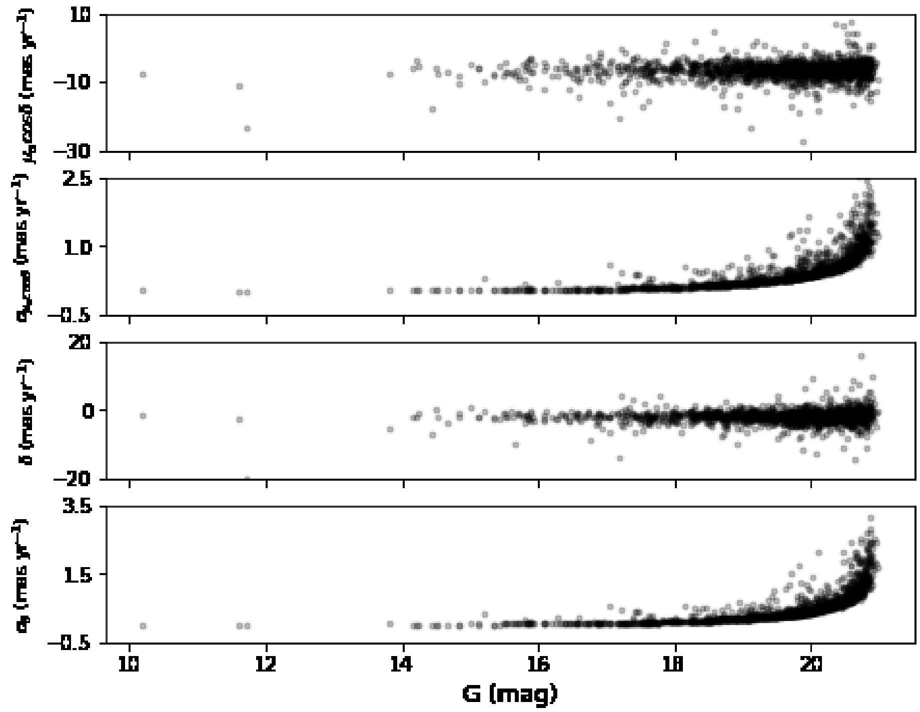

Fig. 2. Plot of proper motions and their errors against G mag

We collected the data within a radius of 10 arcmin, taking into account the estimated cluster radius of 6.3 arcmin from an earlier study (Piatti et al. 2006) of the cluster. The identification map of the cluster under study is shown in Figure 1 and is taken from the Digitized Sky Survey (DSS). The proper motions and their respective errors for all stars in the Gaia data base are plotted against G mag in Figure 2.

3. IDENTIFICATION OF CLUSTER MEMBERS

3.1. *Vector Point Diagrams*

As mentioned above, the cluster stars share similar kinematic properties and the same mean motions. Therefore, proper motions of stars are a crucial parameter for identifying cluster members and field stars (Yadav et al. 2013; Bisht et al. 2021b). A graph is plotted between the proper motion components of the stars, $\mu_\alpha \cos\delta$ (mas yr^{-1}) and μ_δ (mas yr^{-1}) to obtain a vector point diagram (VPD), as shown in the top panel of Figure 3. A CMD corresponding to each of these VPDs is plotted in the bottom panel of Figure 3. Proper motion is the change in the apparent positions of a celestial object when observed from the center of mass of the Solar System, and each point in a VPD gives the proper motion of one star. The dense region in a VPD depicts the stars that share similar motions in space compared with the background field stars. This is one of the primary conditions of being cluster members. Hence, we have used these stars for a preliminary cluster member selection. We define an eye estimated radius around dense region in the VPD as shown with red color in Figure 3. Finally we calculate the membership probability for the selected stars. The CMD in the middle of the bottom panel of Figure 3 appears much cleaner than the other two, confirming the effectiveness of this primary selection method.

3.2. *Membership Probabilities*

In this section, we aim to estimate the membership probability of stars using precise measurements of PMs and parallax from Gaia-DR3. Vasilevskis et al. (1958) described the mathematical setup for determining the membership probability of stars. For NGC 5288, we have used the method devised by Balaguer-Núñez et al. (1998) to calculate the membership probability of individual stars. This method has been used previously for both open and globular star clusters (Yadav et al. 2013, Sariya & Yadav 2015; Sariya et al. 2021a, 2021b), and a detailed description of this method can be found in Bisht et al. (2020).

To derive the two distribution functions defined in this method, ϕ_c^ν (cluster star distribution) and ϕ_f^ν (field star distribution), we considered

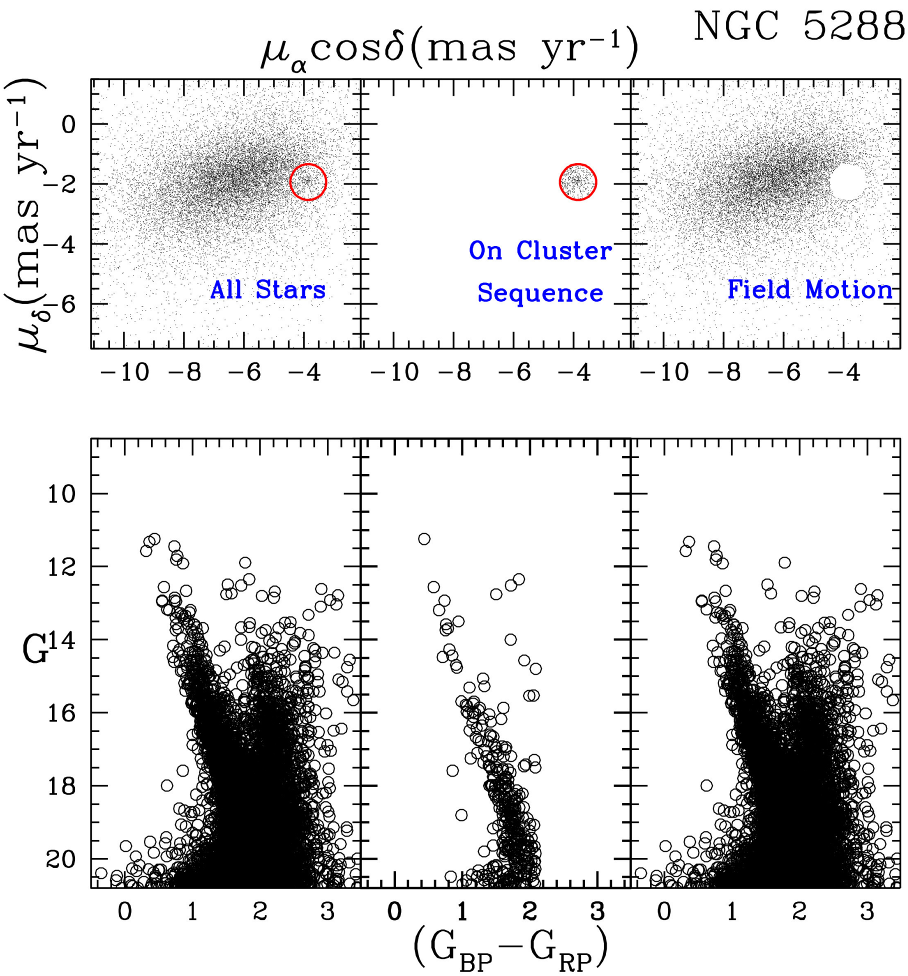

Fig. 3. (Top panel) VPDs for cluster NGC 5288. (Bottom panel) G vs $(G_{BP} - G_{RP})$ CMDs of the stars shown in the VPD above them. (Left panel) includes all stars. (Middle panel) includes only the stars within the region inside the red circle; which we classify as the probable cluster members. (Right panel) includes the probable background/foreground field stars). The color figure can be viewed online.

only those stars which have PM errors better than 1 mas yr^{-1}. A group of the cluster's preliminary members shown in the VPD is found to be centered at μ_{xc}=−3.840 mas yr^{-1}, μ_{yc}=−1.934 mas yr^{-1}. We have estimated the PM dispersion for the cluster population as $(\sigma_c) = 0.08$ mas yr^{-1}. For the field region, we have estimated $(\mu_{xf},\ \mu_{yf}) = (-6.18,\ -1.95)$ mas yr^{-1} and $(\sigma_{xf},\ \sigma_{yf}) = (0.84,\ 0.70)$ mas yr^{-1}.

The membership probabilities (P_μ) are thus determined, and they are shown as a function of Gaia's G magnitude in Figure 4. Finally, we identified 304 stars with $P_\mu > 50\%$.

To estimate the mean PM of NGC 5288, we considered the most probable cluster members and constructed the histograms for $\mu_\alpha cos\delta$ and μ_δ as shown in the right panel of Figure 6. The fitting of a Gaussian function to the histograms provides the mean PM in both directions. We obtained the mean PM of NGC 5288 as -3.840 ± 0.230 and -1.934 ± 0.162 mas yr^{-1} for $\mu_\alpha \cos\delta$ and μ_δ respectively. The estimated values of mean PM for this object is in very good agreement with the mean PM value given by Cantat-Gaudin et al. (2018) ($\mu_\alpha \cos\delta = -3.850$ mas yr^{-1}, $\mu_\delta = -1.935$ mas yr^{-1}).

3.3. *Cluster Membership Validation*

We have categorized the stars with membership probability greater than 50% as cluster members, and only these stars have been used for evaluating the properties of the cluster in the current study. To validate the accuracy of our identified cluster members, we have plotted proper motions, $\mu_\alpha \cos\delta$ (mas yr^{-1}) and μ_δ (mas yr^{-1}), and parallax as a function of G mag in Figure 5. The graph shows

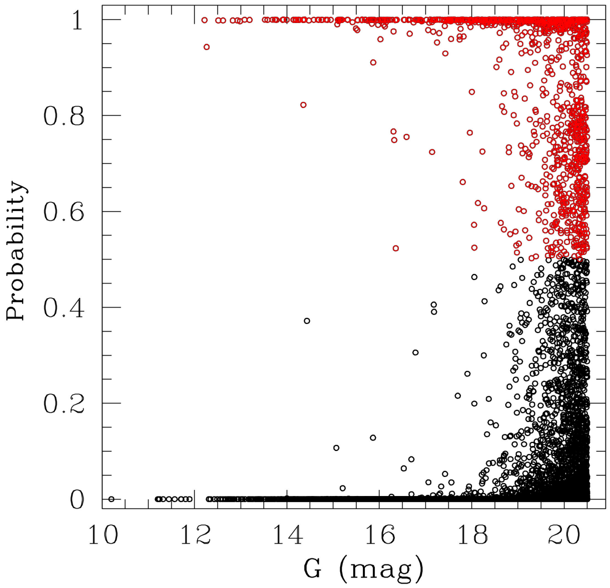

Fig. 4. Plot of cluster membership probabilities against the G mag. The red open circles represent the cluster members having membership probability greater than 50%. The color figure can be viewed online.

a narrow distance range of parallax and proper motion coordinates for the stars categorized as cluster members, but this range is significant for field stars. Hence it is fair to say that we have successfully separated the cluster members.

4. STRUCTURAL PROPERTIES

4.1. *Cluster Center*

Precise estimations of the central coordinates of a cluster play a vital role in evaluating its fundamental properties. We use a star count approach that states that the cluster center is located at the point with the highest stellar density in the cluster region to determine central coordinates (Bisht et al.2021a). For this, a histogram of the star count in RA and DEC is plotted and fitted with Gaussian profiles. The mean values of RA and DEC are estimated to be 207.188 $\pm$ 0.156 deg ($13^h48^m45^s$), and -64.679 ± 0.066 deg ($-64°40'44''$), respectively (refer to Figure 6). The center of the cluster is approximated to be at these coordinates. These values agree well with the values estimated in other studies, as shown in Table 2.

A CMD, an identification chart and the proper motion distribution of cluster members (with the cluster center highlighted) are plotted in Figure 7.

4.2. *Radial Density Profile*

The radius of a cluster gives us a direct indication of its physical dimensions. We plotted a radial

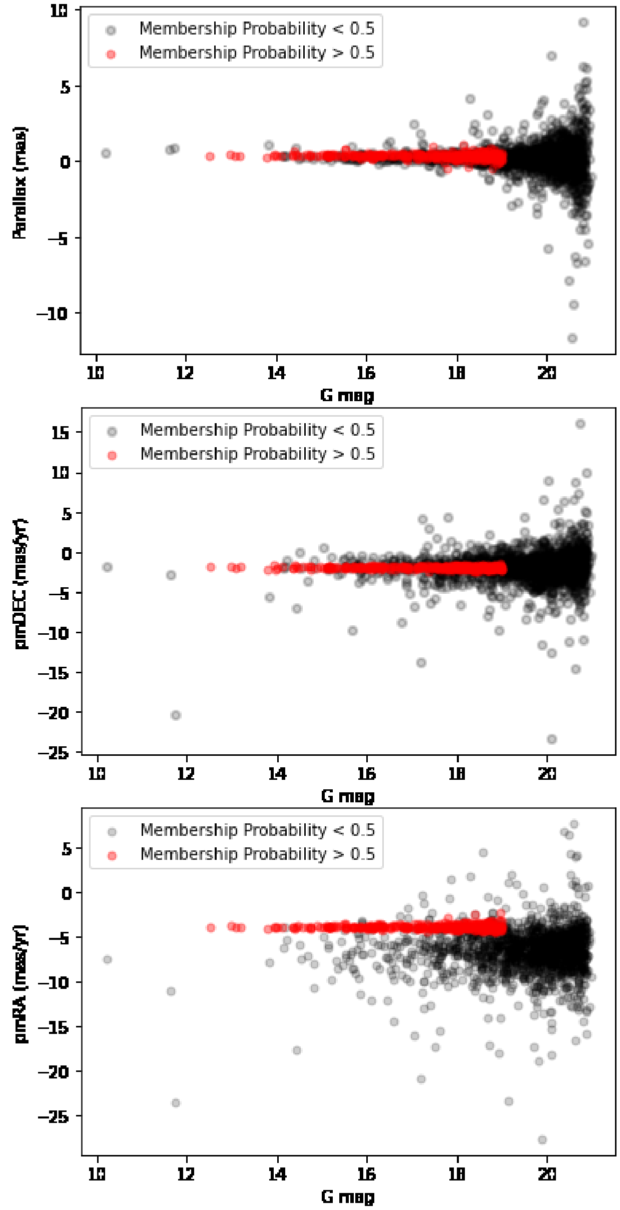

Fig. 5. Top, middle and bottom panels represent plots of parallax distribution PM in declination and PM in right ascension vs. G mag, respectively. The red dots represent the cluster members, while the black ones are the field stars. The color figure can be viewed online.

density profile (RDP) of NGC 5288 as shown in Figure 8. We divided the cluster region into several concentric circular bins and calculated the number density, $\rho_i = \frac{N_i}{A_i}$ of each bin using cluster members. ρ_i is the number of cluster members lying in the i^{th} radial bin divided by the area of the i^{th} bin, A_i. The i^{th} bin corresponds to the region between the i^{th} and $(i-1)^{th}$ concentric circles. The observed radial profile is fitted by the King (1962) model, represented as

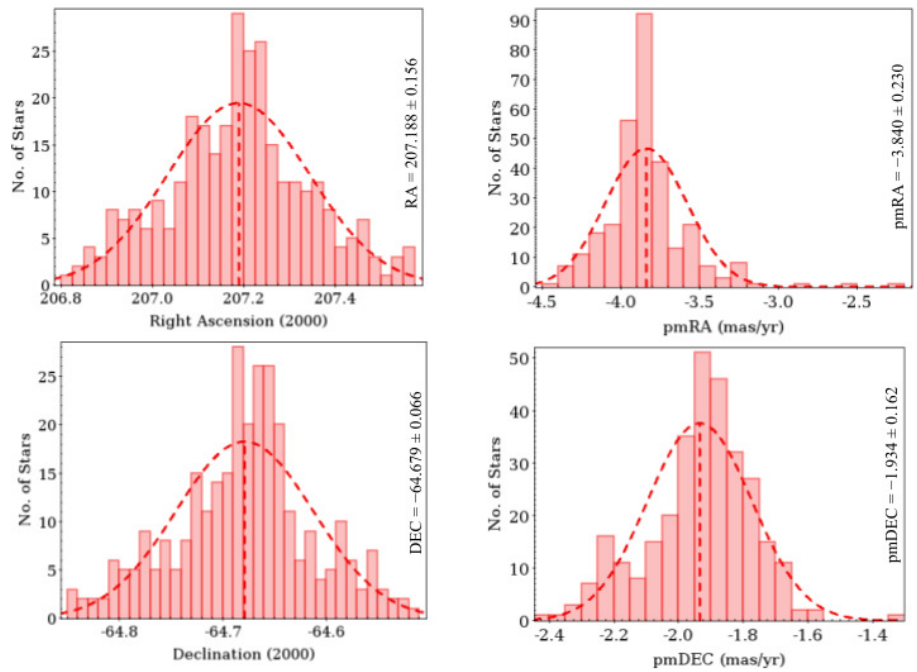

Fig. 6. Histograms of star count in RA(top left), DEC(bottom left), pmRA(top right), and pmDEC(bottom left) fitted with a Gaussian. The vertical dashed-line at the Gaussian center represents the respective mean values. The color figure can be viewed online.

TABLE 1

STRUCTURAL PARAMETERS OF NGC 5288

f_0 (stars/arcmin^2)	f_{bg} (stars/arcmin^2)	r_c (arcmin)	Cluster Radius (arcmin)	δ_c
28.60 ± 0.19	0.54 ± 0.06	1.36 ± 0.05	5.5	17 ± 2

the smooth continuous line in Figure 8. The middle one of the three horizontal lines plotted in Figure 8 corresponds to the background density, and the two lines on either side of it indicate the error in it. A mathematical expression of the model used for fitting is given as :

$$f(r) = f_{bg} + \frac{f_0}{1 + \left(\frac{r}{r_c}\right)^2} \quad , \tag{1}$$

where f_{bg}, f_0, r_c are background density, central density and core radius, respectively. Using the King (1962) fit, we estimate the structural parameters of NGC 5288, which are given in Table 1. We estimate the cluster radius as the point after which the cluster density merges with the field density. Following this criterion, we derived the cluster radius as ≈ 5.5 arcmin. The previous study by Piatti et al. (2006) estimates the radius of NGC 5288 as 6.3 arcmin using CCD photometry. We also calculate the density contrast parameter, δ_c, for the cluster using the formula, $\delta_c = 1 + \frac{f_0}{f_{bg}}$, and obtain its value as 17 ± 2. Our estimated value of δ_c lies within the limit ($7 \leq \delta_c \leq 23$) given by Bica & Bonatto (2005), suggesting that the cluster is compact.

5. DISTANCE, REDDENING AND AGE OF NGC 5288

The age and distance of open clusters give us insights into the kinematics, structure, and chemical evolution of the galaxy they are situated in (Friel & Janes 1993). We have estimated the distance using the parallax method and the isochrone fitting method as described in this section.

5.1. *Distance using the Parallax Method*

In this section, we will use one of the essential distance measurement techniques, the parallax, to approximate the cluster's distance (Luri et al. 2018). A histogram of the parallax values of cluster members

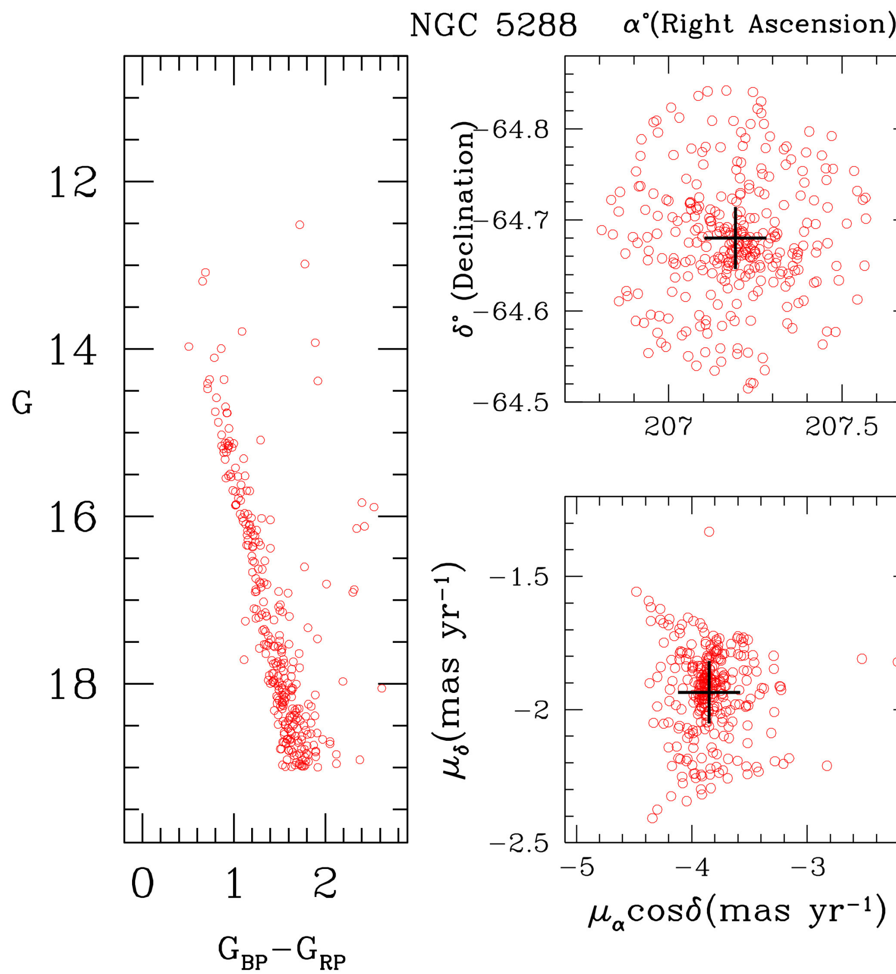

Fig. 7. Plots of CMD(($G_{BP} - G_{RP}$ vs. G), identification chart and proper motion distribution of cluster members represented as the red dots. The plus sign denotes the cluster center. The color figure can be viewed online.

is plotted in which we rejected the spurious stars having negative parallax values. It is fitted to a Gaussian profile to obtain the mean parallax, which comes out to be 0.361 ± 0.152 mas, as shown in Figure 9. This value corresponds to a distance of 2.77 ± 0.42 kpc. Since Gaia provides the most precise parallax values with a minimum error, this will provide the more accurate distance value. Also, the value of distances calculated from the parallax is more accurate than the values calculated from the photometric methods. Keeping this in mind, we fixed the value of cluster distance and then fitted the isochrones on the cluster main sequence to calculate the other fundamental parameters of the cluster.

5.2. *Interstellar Reddening from JHK Colors*

The cluster reddening in the near-IR region has been estimated using the $(J - H)$ vs $(J - K)$ color-color diagrams as shown in Figure 10. The black dots are the cluster members, the solid red line represents the cluster's zero-age main sequence (ZAMS) taken from Caldwell et al. (1993), while the red dashed line is the ZAMS displaced by the value of $E(J - H)$ and $E(J - K)$, which are estimated as 0.15 ± 0.04 and 0.28 ± 0.07 respectively. The reddening is calculated using the following equations (Fiorucci & Munari 2003) :

$$E(J - H) = 0.309 \times E(B - V)$$
$$E(J - K) = 0.48 \times E(B - V).$$

Using the above equations, we derived the interstellar reddening of the cluster, $E(B - V)$ as 0.45.

5.3. *Age and Distance from Isochrone Fitting*

We estimate important cluster parameters such as age and metallicity by fitting the theoretical isochrones of Marigo et al. (2017) to the CMDs, (G, $G_{BP} - G_{RP}$) and (J, $J - H$) as shown in Figure 11. Color-magnitude diagrams (CMDs) repre-

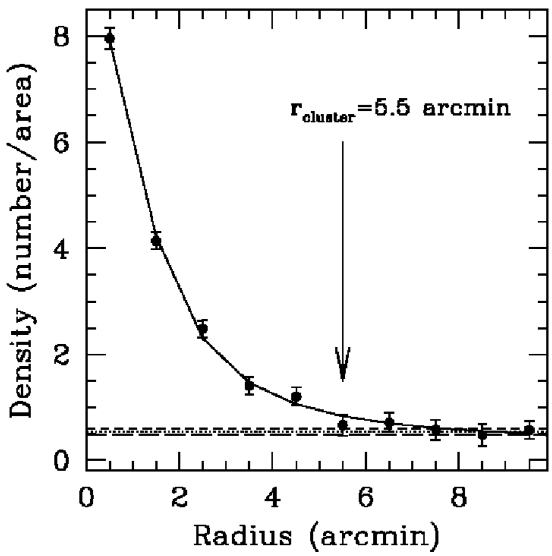

Fig. 8. Radial density profile of NGC 5288 using cluster members. The smooth continuous line represents the fitted King (1962) model. The middle dotted horizontal line depicts the background density and the long and short dashed lines represent the error in the background density.

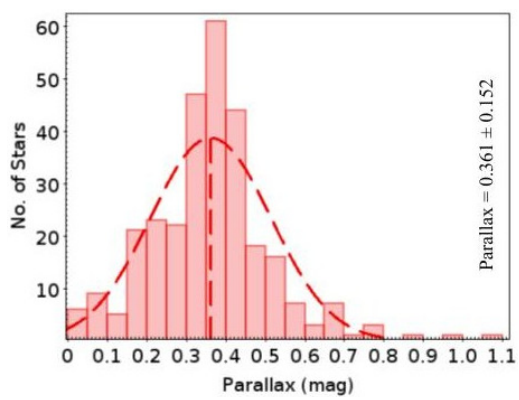

Fig. 9. Histogram of parallax values of cluster members, fitted by a Gaussian profile with a mean parallax value of 0.361 ± 0.152 mas indicated by a vertical line at the center of the Gaussian. The color figure can be viewed online.

sent the relationship between the absolute magnitudes of the stars and their surface temperatures, usually identified by their color. CMDs are extensively used to study star clusters and are beneficial for estimating their properties (Kalirai & Tosi 2004; Sariya et al. 2021b). We tried to fit many isochrones with different metallicity and ages and found the best fit at Z=0.03, which shows a good agreement with the literature value of 0.04 given by Piatti et al. (2006). In Figure 11, we have superimposed theoretical isochrones of different ages

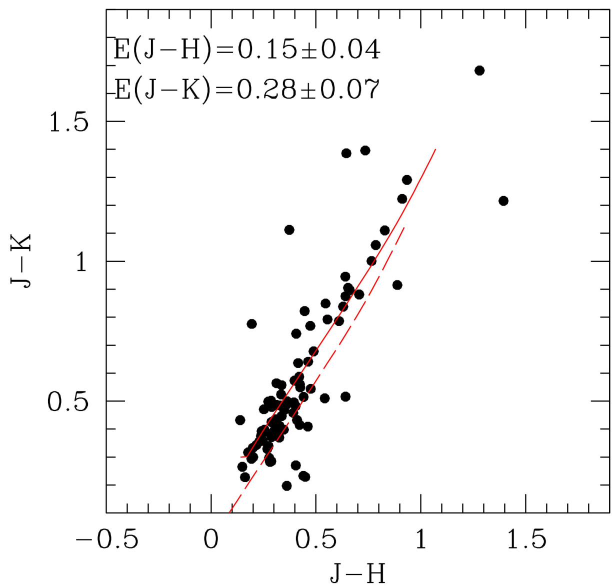

Fig. 10. $(J-H)$ vs $(J-K)$ two color diagram. The red solid and the dashed lines are the ZAMS taken from Caldwell et al. (1993). The red dashed line is the ZAMS shifted by the value given in the text. The color figure can be viewed online.

(log age = 8.5, 8.7 and 8.9) and Z=0.03 over the observed $(G,\ G_{BP}-G_{RP})$ and $(J,\ J-H)$ CMDs. We estimated the cluster's age to be 510 ± 190 Myr. Our estimated age lies between the age given by Dias et al. (2014) and Kharchenko et al. (2016). We found the color excess value, $E(G_{BP}-G_{RP})$ of the cluster as 0.60. The isochrone fitting is performed so that it will result in a cluster distance close to what we estimated from the parallax. From this fitting, we calculated the distance modulus $(m-M)$ as 13.50 ± 0.25 mag, corresponding to a heliocentric distance of 2.64 ± 0.11 kpc. This value is comparable with the distance we approximated using the parallax method in the above section. The A_G value for this cluster is 0.99 ± 0.62, which is calculated by the weighted mean method using the A_G values of cluster members from the Gaia DR3 data. The value of the total to selective extinction ratio using values determined in the present analysis is compatible with the value given by Wang & Chen (2019) within errors. A comparative analysis of the fundamental properties of cluster members derived in this study with the values in the literature is given in Table 2.

6. LUMINOSITY AND MASS FUNCTIONS

The luminosity function (LF) is the distribution of stars of a cluster in different magnitude bins. We considered cluster members with membership probability higher than 50% in the $G/(G_{BP}-G_{RP})$ CMD

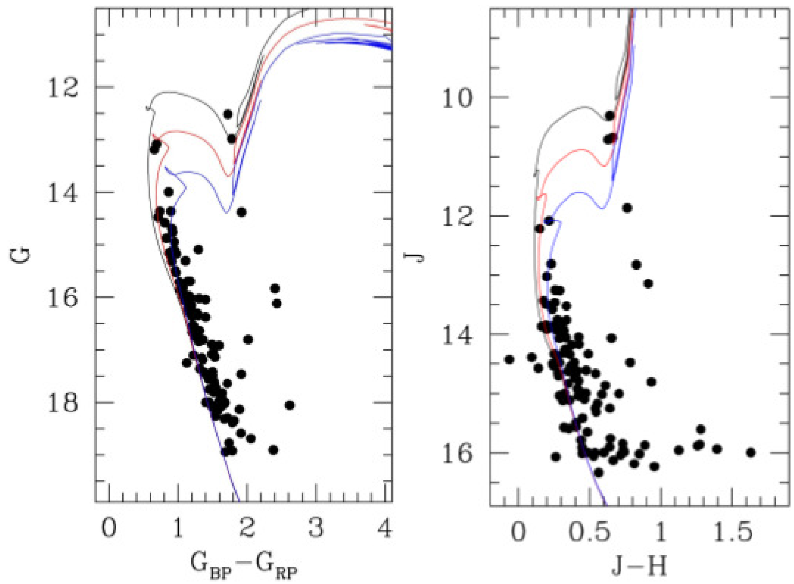

Fig. 11. The (G, $G_{BP} - G_{RP}$) and (J, $J - H$) color-magnitude diagrams of the open star cluster NGC 5288. The black dots represent cluster members and the curves represent the theoretical isochrones of three different ages (8.5, 8.7 and 8.9) with Z = 0.03. The color figure can be viewed online.

TABLE 2

COMPARISON OF OUR DERIVED FUNDAMENTAL PARAMETERS OF NGC 5288 WITH THE LITERATURE VALUES

Parameters	Numerical Values	Reference
(RA, DEC) (deg)	$(207.188 \pm 0.156, -64.679 \pm 0.066)$	Present study
	$(207.193, -64.680)$	Cantat-Gaudin et al. (2018)
	$(207.203, -64.673)$	Liu & Pang (2019)
	$(207.18333, -64.68500)$	Dias et al.(2014)
($\mu_\alpha \cos\delta$, μ_δ) (mas yr^{-1})	$(-3.840 \pm 0.230, -1.934 \pm 0.162)$	Present study
	$(-3.850 \pm 0.098, -1.935 \pm 0.087)$	Cantat-Gaudin et al. (2018)
	$(-3.841 \pm 0.169, -1.905 \pm 0.157)$	Liu & Pang (2019)
	$(-5.25 \pm 3.65, -5.79 \pm 5.58)$	Dias et al.(2014)
Cluster Radius (arcmin)	5.5	Present study
	2.50	Dias et al.(2014)
	6.3	Piatti et al.(2006)
Age (Myr)	510 ± 190	Present study
	1259	Kharchenko et al.(2016)
	178	Dias et al.(2014)
	126	Piatti et al.(2006)
Mean Parallax (mas)	0.361 ± 0.152	Present study
	0.345 ± 0.041	Cantat-Gaudin et al. (2018)
	0.345 ± 0.026	Liu & Pang (2019)
Distance (kpc)	2.77 ± 0.42	Present study
	2.6739	Cantat-Gaudin & Anders(2019)
	5.086	Kharchenko et al.(2016)
	2.158	Dias et al.(2014)
	2.1 ± 0.3	Piatti et al.(2006)

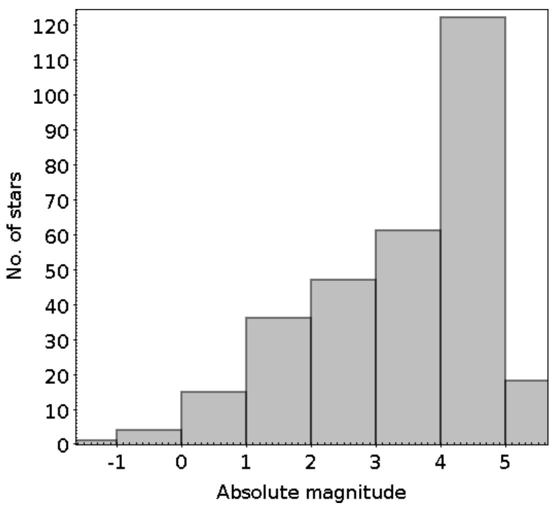

Fig. 12. Luminosity function of stars in the region of NGC 5288.

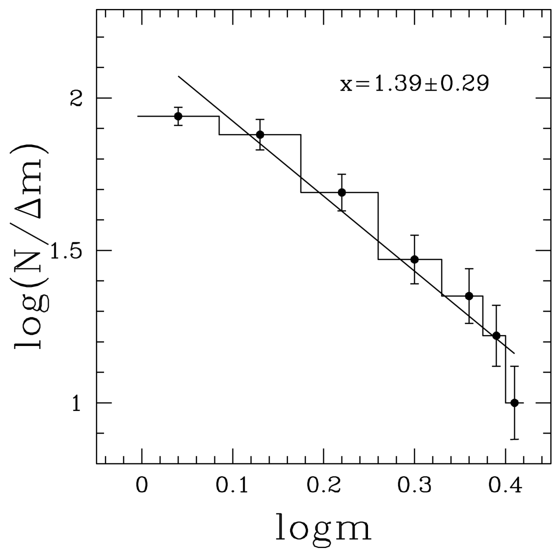

Fig. 13. Mass function histogram derived using the most probable members; the solid line indicates the power law given by Salpeter (1955). The error bars represent $\frac{1}{\sqrt{N}}$.

to construct the LF for NGC 5288. To build the LF, first we transformed the apparent G magnitudes into absolute magnitudes by using the distance modulus. Then we plotted the histogram of the LF as shown in Figure 12. The interval of 1.0 mag was chosen to have an adequate number of stars per bin for statistical usefulness. We found an increasing LF for this cluster, because it still retains its faint members.

The mass function (MF) is the distribution of masses of cluster members per unit volume. A mass-luminosity connection can transform LF into the mass function (MF). Since we could not acquire an observational transformation, we must rely on theoretical models. To convert LF into MF, we used the cluster parameters derived in this paper, and theoretical models are given by Marigo et al. (2017). The resulting MF is shown in Figure 13. The mass function slope can be derived from the linear relation

$$\log\frac{dN}{dM} = -(1+x)\times\log(M) + constant. \qquad (2)$$

In the above relation, dN symbolizes the number of stars in a mass bin dM with the central mass M, and x is the mass function slope. The Salpeter (1955) value for the mass function slope is $x = 1.35$. This form of Salpeter demonstrates that the number of stars in each mass range declines rapidly with increasing mass. Our derived MF slope value, $x = 1.39 \pm 0.29$, agrees with Salpeter's slope within the uncertainty. Utilizing this value of the mass function slope within the mass ranges 1.0 - 2.7 $M_\odot$, the total and mean mass for the cluster members were acquired as $\approx 464 M_\odot$ and $\approx 1.53 M_\odot$, respectively.

6.1. *Dynamical Relaxation Time*

In the lifetime of star clusters, encounters between their member stars gradually lead to increased energy equipartition throughout the clusters. In this process, massive stars are concentrated towards the cluster core and transfer their kinetic energy to fainter stars. The relaxation time T_R is defined as the time in which the stellar velocity distribution becomes Maxwellian and is expressed by the following formula:

$$T_R = \frac{8.9\times 10^5\sqrt{N}\times {R_h}^{3/2}}{\sqrt{\bar{m}}\times\log(0.4N)} \quad , \qquad (3)$$

where N represents the number of stars in the clusters (in our case, the ones with membership probability higher than 50%), R_h is the cluster half mass radius expressed in parsec and $\bar{m}$ is the average mass of the cluster members (Spitzer & Hart 1971) in solar units. The value of R_h is assumed as 2.56 pc, which is equal to half of the cluster's extent. Using the above formula, the value of the dynamical relaxation time T_R is determined as 24.6 Myr, significantly less than the cluster's age. Hence, we conclude that NGC 5288 is a dynamically relaxed cluster.

7. ORBIT OF THE CLUSTER

Galactic orbits are valuable tools to explore the dynamical aspects of the objects in our Galaxy. We derived orbits and orbital parameters of NGC 5288 using the Galactic potential models discussed by Irrgang et al. (2013). The galactic potentials used

TABLE 3

POSITION AND VELOCITY COMPONENTS OF NGC 5288 IN GALACTOCENTRIC COORDINATES.*

R (kpc)	Z(kpc)	ϕ	U (km/s)	V (km/s)	W (km/s)
6.919	-0.101	0.320	30.490	-243.025	5.457

*The meaning of the symbols used is described in the text.

TABLE 4

ORBITAL PROPERTIES OF NGC 5288*

e	R_a	R_p	Z_{max}	E (100 km/sec)^2	L_z (100 km/sec)^2	T_R (Myr)	T_Z (Myr)
-0.010	7.213	7.363	0.125	-12.146	-16.816	177.621	68.837

*Here e is eccentricity, R_p is the maximum distance travelled by the cluster in the x direction, R_a is the maximum distance travelled by the cluster in the y direction, E is energy, L_z is momentum, T_R is the time period for motion in plane, and T_Z is the time period for motion in the z-direction.

in the present analysis are explained by Rangwal et al. (2019). In this analysis, we adopted the refined parameters of galactic potentials from Bajkova & Bobylev (2017); they used newly available observational data to update these parameters. Information required for orbital integration such as center coordinates (α and δ), mean proper motions ($\mu_\alpha cos\delta$, μ_δ), parallax angles, age and heliocentric distance ($d_\odot$) are taken from the present analysis. The value for the radial velocity of the cluster, which is equal to -23.83 ± 1.49 km/sec is taken from Soubiran et al. (2018).

We adopted the right-handed coordinate system to convert equatorial position and velocity components into galactic position (R, ϕ, z), and galactic-space velocity components (U, V, W), where (R, U), (ϕ, V), and (z, W) are the radial, tangential, and vertical space and velocity components, respectively. Here, the x-axis is taken positive towards the galactic center, the y-axis is towards the direction of galactic rotation, and the z-axis is in the vicinity of the galactic north pole. The values of the galactic center and north-galactic pole are adopted from Reid & Brunthaler (2004) as $(17^h45^m32^s.224, -28°56'10'')$ and $(12^h51^m26^s.282, 27°7'42''.01)$ respectively. To adopt a correction for the Standard Solar Motion and the motion of the Local Standard of Rest (LSR), we utilized the Sun's position and space-velocity components as $(8.3, 0, 0.02)$ kpc and $(11.1, 12.24, 7.25)$ km/s (Schönrich et al. 2010), respectively.

The resultant orbits are shown in Figure 14. In the top left panel of the figure, we plotted the path followed by the cluster in the R and Z plane, representing the orbit's side view. The top right panel is a plot of the x and y components of the galactic distance R. The bottom panel shows a plot of the time of orbit integration and the object's height from the galactic disc. The red-filled triangle and the green-filled circle denote the cluster's birth and present-day position, respectively. The orbital parameters are summarised in Table 4.

From Figure 14 and Table 4, it is evident that the cluster is following a boxy pattern and moving in a circular orbit around the galactic center. The cluster is part of the galactic thin disc, moving inside the solar circle (the position of the Sun is at 8.3 kpc). The cluster was born very close to the galactic disc and hence highly affected by the tidal forces originating from the disc, which led to a small orbit height. This also led to a smaller time period in the vertical direction, as visible from Table 4 and the bottom panel of Figure 14. The cluster is very young, so it must contain its fainter stars, but we can notice a significant dip in the luminosity function of the cluster (Figure 12), which reflects an absence of very low mass stars in the cluster. We expect this because of the close proximity of the cluster to the galactic disc. This cluster is highly affected by the galactic tidal force and has lost its low mass stars to the field.

8. CONCLUSION

We have investigated a poorly studied open cluster, NGC 5288, using 2MASS and Gaia DR3 photometric and astrometric database. We estimated the membership probabilities of stars using their PM and parallax measurements and identified 304 cluster members with membership probability greater than 50%. We estimated the fundamental properties of the cluster, investigated its structure, conducted a dynamical study and derived its galactic orbit and orbital parameters. A summary of the major outcomes from this study follows:

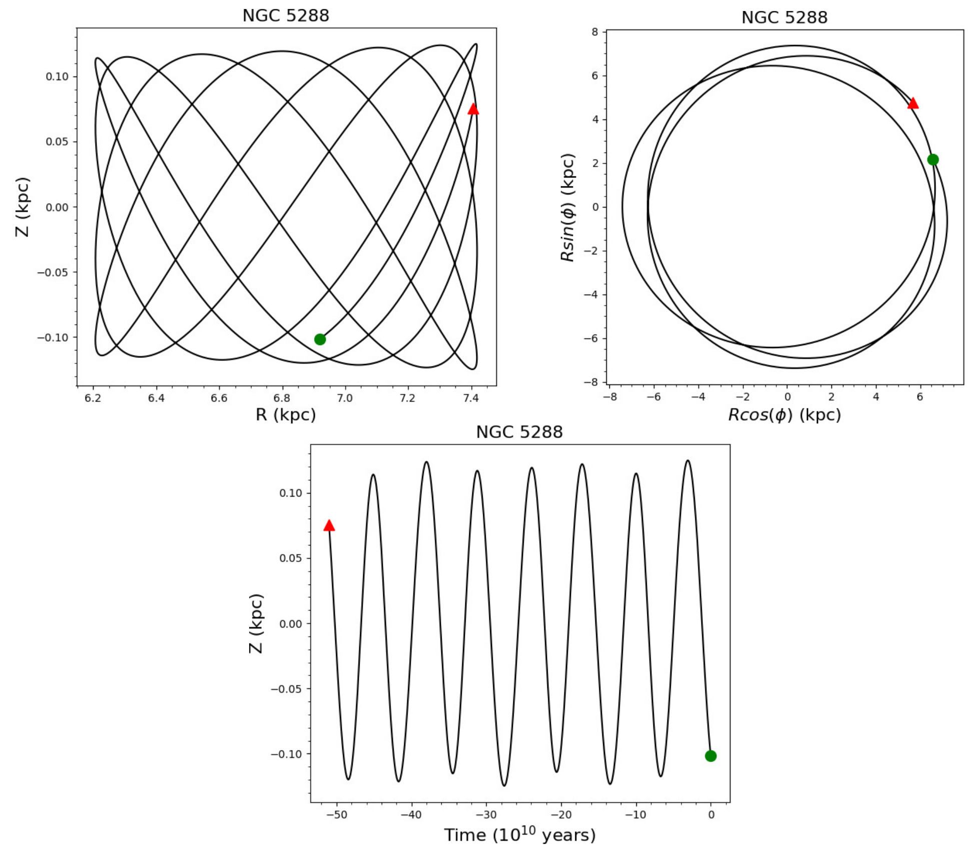

Fig. 14. The Galactic orbits of NGC 5288 were obtained with the Galactic potential model described by Rangwal et al. (2019). The time of integration is taken equal to the age of the cluster. The top left panel shows the side view, and the top right panel shows the top view of the orbits. The bottom panel shows the cluster's motion in the Galactic disk over time. The filled red triangles and the green circles denote the birth and the present-day positions of NGC 5288 in the Galaxy. The color figure can be viewed online.

1. The cluster center is estimated as $\alpha = 207.188 \pm 0.156$ deg ($13^h48^m45^s$) and $\delta = -64.679 \pm 0.066$ deg ($-64^\circ40'44''$) using the cluster members.

2. The core radius and the cluster radius are estimated as 1.36 ± 0.05 arcmin and 5.5 arcmin, respectively, using the radial density profile.

3. The mean proper motions of cluster members in right ascension and declination are calculated as (-3.840 ± 0.230) and $(-1.934 \pm 0.162)\,\mathrm{mas\,yr^{-1}}$, respectively. The interstellar reddening, $E(B-V)$ of the cluster is estimated as 0.45.

4. The heliocentric distance of the cluster is estimated using the parallax method and is equal to 2.77 ± 0.42 kpc. We determine the cluster's age as 510 ± 190 Myr by fitting the obtained CMDs of the cluster with theoretical isochrones with Z=0.03, given by Marigo et al.(2017).

5. The mass function slope of 1.39 ± 0.29 is found for NGC 5288 to be in fair agreement within the uncertainty with the value (1.35) given by Salpeter (1955). Our study also indicates that this cluster is dynamically relaxed.

6. We integrated the orbits of the cluster for a time duration equal to the cluster's age. We found that the cluster is born near the Galactic disc and moves in a circular orbit with a very small scale height. We also expect that the absence of low-mass stars of the cluster is an effect of strong tidal forces originating from the Galactic disc.

The authors are thankful to the anonymous referee for useful comments, which improved the contents of the paper significantly. This work has made use of data from the European Space Agency (ESA) mission *Gaia* (`https://www.cosmos.esa.int/gaia`), processed by the *Gaia* Data Processing and Analysis Consortium (DPAC, `https://www.cosmos.esa.int/web/gaia/dpac/consortium`). Funding for the DPAC has been provided by national institutions, in particular, the institutions participating in the *Gaia* Multilateral Agreement. This work has used TOPCAT `http://www.starlink.ac.uk/topcat`. It was developed mostly in the UK within various UK and Euro-VO projects (Starlink, AstroGrid, VOTech, AIDA, GAVO, GENIUS, DPAC) and under PPARC and STFC grants. Its underlying table processing facilities were provided by the related packages STIL and STILTS. This research has made use of the VizieR catalogue access tool, CDS, Strasbourg, France (DOI : 10.26093/cds/vizier). The original description of the VizieR service was published in 2000, A&AS 143, 23". This work has also made use of SAOImageDS9, an image visualization tool for astronomical data. This research has also made use of SIMBAD database operated at CDS, Strasbourg, France.

REFERENCES

Babusiaux, C., Fabricius, C., Khanna, S., et al. 2022, arXiv:2206.05989, https://doi.org/10.48550/arXiv.2206.05989

Balaguer-Núñez, L., Tian, K. P., & Zhao, J. L. 1998, A&AS, 133, 387, https://doi.org/10.1051/aas:1998324

Bica, E. & Bonatto, C. 2005, A&A, 431, 943, https://doi.org/10.1051/0004-6361:20042023

Bisht, D., Yadav, R. K. S., Ganesh, S., et al. 2019, MNRAS, 482, 1471, https://doi.org/10.1093/mnras/sty2781

Bisht, D., Elsanhoury, W. H., Zhu, Q., et al. 2020, AJ, 160, 119, https://doi.org/10.3847/1538-3881/ab9ffd

Bisht, D., Zhu, Q., Yadav, R. K. S., et al. 2021a, AJ, 161, 182, https://doi.org/10.3847/1538-3881/abe383

Bisht, D., Zhu, Q., Yadav, R. K. S., et al. 2021b, MNRAS, 503, 5929, https://doi.org/10.1093/mnras/stab691

Bobylev, V. V., Bajkova, A. T., & Gromov, A. O. 2017, AstL, 43, 241, https://doi.org/10.1134/S1063773717040016

Bobylev, V. V. & Bajkova, A. T. 2016, AstL, 42, 1, https://doi.org/10.1134/S1063773716010023

Caldwell, J. A. R., Cousins, A. W. J., Ahlers, C. C., van Wamelen, P., & Maritz, E. J. 1993, SAAOC, 15, 1

Cantat-Gaudin, T. & Anders, F. 2019, VizieR Online Data Catalog, J/A+A/633/A99

Cantat-Gaudin, T., Jordi, C., Vallenari, A., et al. 2018, A&A, 618, 93, https://doi.org/10.1051/0004-6361/201833476

Collinder, P. 1931, AnLun, 2, 1

Dias, W. S., Alessi, B. S., Moitinho, A., et al. 2002, VizieR Online Data Catalog, VII/229A

Dias, W. S., Monteiro, H., Caetano, T. C., et al. 2014, VizieR Online Data Catalog, J/A+A/564/A79

Ferreira, F. A., Corradi, W. J. B., Maia, F. F. S., Angelo, M. S., & Santos Jr., J. F. C. 2020, MNRAS, 496, 2021, https://doi.org/10.1093/mnras/staa1684

Fiorucci, M. & Munari, U. 2003, A&A, 401, 781, https://doi.org/10.1051/0004-6361:20030075

Friel, E. D. & Janes, K. A. 1993, A&A, 267, 75

Gaia Collaboration, Prusti, T., de Bruijne, J. H. J., et al. 2016, A&A, 595, 1, https://doi.org/10.1051/0004-6361/201629272

Hendy, Y. & Tadross, A. 2021, AN, 342, 613, https://doi.org/10.1002/asna.202143848

Irrgang, A., Wilcox, B., Tucker, E., & Schiefelbein, L. 2013, A&A, 549, 137, https://doi.org/10.1051/0004-6361/201220540

Joshi, Y. C., Dambis, A. K., Pandey, A. K., et al. 2016, VizieR Online Data Catalog, J/A+A/593/A116

Kalirai, J. S. & Tosi, M. 2004, MNRAS, 351, 649, https://doi.org/10.1111/j.1365-2966.2004.07813.x

Kharchenko, N. V., Piskunov, A. E., Schilbach, E., Röser, S., & Scholz, R.-D. 2016, A&A, 585, 101, https://doi.org/10.1051/0004-6361/201527292

King, I. 1962, AJ, 67, 471, https://doi.org/10.1086/108756

Liu, L. & Pang, X. 2019, ApJS, 245, 32, https://doi.org/10.3847/1538-4365/ab530a

Lombardi, J. C., Rasio, F. A., & Shapiro, S. L. 1996, ApJ, 468, 797, https://doi.org/10.1086/177736

Lombardi, J. C. & Rasio, F. A. 2002, ASPC 263, Stellar Collisions Mergers and their Consequences, ed. M. M. Shara (San Francisco, CA: ASP), 35

Lu, P., Deng, L. C., & Zhang, X. B. 2010, MNRAS, 409, 1013, https://doi.org/10.1111/j.1365-2966.2010.17356.x

Luri, X., Brown, A. G. A., Sarro, L. M., et al. 2018, A&A, 616, 9, https://doi.org/10.1051/0004-6361/201832964

Marigo, P., Girardi, L., Bressan, A., et al. 2017, ApJ, 835, 77, https://doi.org/10.3847/1538-4357/835/1/77

Piatti, A. E., Clariá, J. J., & Ahumada, A. V. 2006, MNRAS, 367, 599, https://doi.org/10.1111/j.1365-2966.2005.09930.x

Rangwal, G., Yadav, R. K. S., Durgapal, A., Bisht, D., & Nardiello, D. 2019, MNRAS, 490, 1383, https://doi.org/10.1093/mnras/stz2642

Reid, M. J. & Brunthaler, A. 2004, ApJ, 616, 872, https://doi.org/10.1086/424960

Salpeter, E. E. 1955, ApJ, 121, 161, https://doi.org/10.1086/145971

Sampedro, L., Dias, W. S., Alfaro, E. J., Monteiro, H. & Molino, A. 2017, MNRAS, 470, 3937, https://doi.org/10.1093/mnras/stx1485

Sariya, D. P. & Yadav, R. K. S. 2015, A&A, 584, 59, https://doi.org/10.1051/0004-6361/201526688

Sariya, D. P., Jiang, I.-G., Bisht, D., Yadav, R. K. S., & Rangwal, G. 2021a, AJ, 161, 102, https://doi.org/10.3847/1538-3881/abd31f

Sariya, D. P., Jiang, I.-G., Sizova, M. D., et al. 2021b, AJ, 161, 101, https://doi.org/10.3847/1538-3881/abd31d

Schönrich, R., Binney, J., & Dehnen, W. 2010, MNRAS, 403, 1829, https://doi.org/10.1111/j.1365-2966.2010.16253.x

Skrutskie, M. F., Cutri, R. M., Stiening, R., et al. 2006, AJ, 131, 1163, https://doi.org/10.1086/498708

Soubiran, C., Cantat-Gaudin, T., Romero-Gómez, M., et al. 2018, A&A, 619, 155, https://doi.org/10.1051/0004-6361/201834020

Spitzer, L. & Hart, M. H. 1971, ApJ, 164, 399, https://doi.org/10.1086/150855

Tadross, A. L. & Hendy, Y. H. 2021, JApA, 42, 6, https://doi.org/10.1007/s12036-020-09648-5

van Leeuwen, F., de Bruijne, J., Babusiaux, C., et al. 2022, Gaia DR3 documentation, European Space Agency; Gaia Data Processing and Analysis Consortium. Online at https://gea.esac.esa.int/archive/documentation/GDR3/index.html

Vasilevskis, S., Klemola, A., & Preston, G. 1958, AJ, 63, 387, https://doi.org/10.1086/107787

Wang, S. & Chen, X. 2019, ApJ, 877, 116, https://doi.org/10.3847/1538-4357/ab1c61

Yadav, R. K. S., Sariya, D. P., & Sagar, R. 2013, MNRAS, 430, 3350, https://doi.org/10.1093/mnras/stt136

D. Bisht and A. Raj: Indian Centre for Space Physics, 466 Barakhola, Singabari road, Netai Nagar, Kolkata 700099, India.

Geeta Rangwal: Indian Institute of Astrophysics, Koramangala II BLock, Bangalore, 560034, India.

Ritika Sethi: Department of Physical Sciences, Indian Institute of Science Education and Research, Berhampur, Odisha 760010, India.

Revista Mexicana de Astronomía y Astrofísica, **59**, 191–200 (2023)

https://doi.org/10.22201/ia.01851101p.2023.59.02.04

NEW SPECTROSCOPY OF U GEM

J. Echevarría[1], S. H. Ramírez[2], M. Fuentes[3], L. J. Sánchez[1], V. Patiño[4,5], and V. Chavushyan[4]

Received November 21 2022; accepted March 8 2023

ABSTRACT

We present new optical spectroscopic observations of U Geminorum obtained during a quiescent stage. We perform a radial velocity analysis of three Balmer emission lines yielding inconsistent results. Assuming that the radial velocity semi amplitude accurately reflects the motion of the white dwarf, we arrive at masses for the primary which are in the range of $M_{\rm wd} = 1.21 - 1.37 M_\odot$. Based on the internal radial velocity inconsistencies and results produced from the Doppler tomography – wherein we do not detect emission from the hot spot, but rather an intense asymmetric emission overlaying the disc, reminiscent of spiral arms – we discuss the possibility that the overestimation of the masses may be due to variations of gas opacities and a partial truncation of the disc.

RESUMEN

Presentamos nuevas observaciones espectroscópicas de U Geminorum obtenidas durante un estado de quietud. Realizamos un análisis de velocidades radiales para tres líneas de Balmer, cuyos resultados son inconsistentes. Asumiendo que la semi-amplitud de la velocidad radial refleja fielmente el movimiento de la componente primaria, obtuvimos valores de masa de la primaria en el intervalo $M_{\rm wd} = 1.21 - 1.37 M_\odot$. Basados en la inconsistencia de nuestros resultados y en las imágenes de tomografía Doppler – donde no detectamos emisión del punto caliente, sino que aparece una emisión sobrepuesta al disco, que asemeja brazos espirales– discutimos la posibilidad de que la sobreestimación de la masa sea debida a variaciones de las opacidades y a un disco truncado.

Key Words: novae, cataclysmic variables — stars: dwarf novae — stars: individual: U Gem — techniques: spectroscopic

1. INTRODUCTION

U Geminorum is the prototype of a subclass of dwarf novae (DN), which belong to the cataclysmic variable systems (CVs). These are semi-detached interactive binaries where the primary is a compact white dwarf (WD) accreting material from a Roche-lobe filling companion, which normally is a late type star very close to the main-sequence. According to the classical model developed by Smak (1971) and Warner & Nather (1971), the material accreted by the secondary star forms an annulus or ring in the outer regions due to its large amount of angular momentum, and eventually forms a full disc, down to the boundary of the WD, due to viscous forces within its layers. When the disc is well formed the material strikes the disc in the outer rim which results in a conspicuous bright spot. This region, also known as the hot spot, is observed as an orbital hump in the optical light-curves of U Gem during quiescence, which precedes an eclipse of the bright spot and a partial eclipse of the accretion disc.

U Gem has an orbital period of 0.1769061911 days and a mass ratio of $q = 0.35 \pm 0.05$ (Echevarría et al. 2007), with an inclination of $i = 69.7° \pm 0.7°$ (Zhang & Robinson 1987). It has an outburst recurrence of ≈ 118 days. Models from Takeo et al. (2021) predict that the inner disc is truncated in quiescence at a distance of $\approx 1.20 - 1.25$ times the WD radius, whereas in outburst it truncates at 1.012 $R_{\rm wd}$ or might even extend to the WD surface. The FUV

[1]Instituto de Astronomía, Universidad Nacional Autónoma de México, México.
[2]Department of Physics, University of Warwick, UK.
[3]Departamento de Física, Universidad de Sonora, Sonora, México.
[4]Instituto Nacional de Astrofísica, Óptica y Electrónica, Tonantzintla, Puebla, México.
[5]Max-Planck-Institut für Radioastronomie, Bonn, Germany.

lightcurve analyzed by Godon et al. (2017) shows phase-dependent modulations which are consistent with a stream overflow of the disc.

Multiple radial velocity studies have been conducted on U Gem, from which the semi-amplitudes of the components have been derived. Tracing the $H\alpha$ Balmer emission line, Echevarría et al. (2007) obtained a radial velocity for the white dwarf of $K_1 = 107 \pm 2$ kms^{-1}, in agreement with the analyses of FUV observations put forward by Long & Gilliland (1999), who reported a value of $K_1 = 107.1 \pm 2.1$ kms^{-1}.

By means of Doppler tomography – a technique that analyzes the Doppler shifts of an emission line to obtain a two-dimensional distribution of the emission in accretion discs (Marsh & Horne 1988)– this object has been observed to exhibit diverse emission structures in quiescence: from that of an extended disc dominated by the emission from the hot spot (Echevarría et al. 2007; Marsh et al. 1990), to a highly asymmetric shape similar to spiral arms overlaying the disc (e.g. Unda-Sanzana et al. 2006; Neustroev & Borisov 1998).

Despite being one of the best studied DN, and a prototype object, U Gem continues to show a behaviour far more complicated than that contemplated in the classical model. Thus, it is an object worth of continuous monitoring. With this in mind, in § 2 we present optical spectroscopic observations of U Gem obtained during quiescence. § 3 is a radial velocity study of the system implemented on three distinct emission lines: Hβ, Hγ, and Hδ, by means of which the masses of the system are derived. § 4 consists of the discussion of the derived masses. It also includes an extensive discussion on the Doppler tomography obtained for the emission lines, which we used to find clues on the spatial origin of the emission within the disc. Finally, our conclusions are presented in § 5.

2. OBSERVATIONS AND REDUCTION

Spectra were obtained with the 2.1-m telescope of the Observatorio Astrofísico Guillermo Haro at Cananea, Sonora, using the Boller and Chivens spectrograph and a E2V42-40, 2048x2048 CCD detector in the 4000 - 5000 Å range with a resolution of R $\approx$ 1700, on the nights of 2021 February 15 and 16. The exposure time for each spectrum was 600 s. Standard IRAF[6] procedures were used to reduce the data.

[6]IRAF is distributed by the National Optical Astronomy Observatories, which are operated by the Association of Universities for Research in Astronomy, Inc., under cooperative agreement with the National Science Foundation.

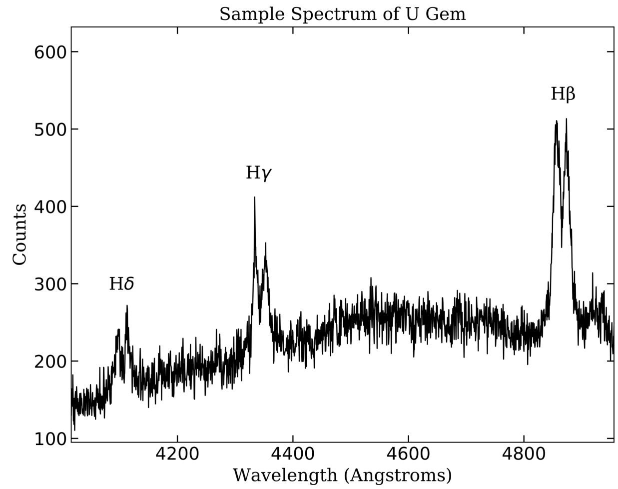

Fig. 1. Individual spectrum of U Gem showing the strong double-peaked Balmer lines.

TABLE 1

LOG OF SPECTROSCOPIC OBSERVATIONS OF U GEM

Date	Julian Date (2450000 +)	No. of spectra	Exp. Time
15 Feb 2021	9260	47	600 s
16 Feb 2021	9261	34	600 s

The log of observations is shown in Table 1. The spectra show strong double-peaked Balmer lines, as exhibited in the sample in Figure 1. The spectra are not flux calibrated, therefore the y-axis shows counts in each spectrum.

3. RADIAL VELOCITIES

The radial velocity of the emission lines of each spectrum was computed using the RVSAO package in IRAF, with the CONVRV function, developed by J. Thorstensen (2008, private communication). This routine follows the algorithm described by Schneider & Young (1980), convolving the emission line with an antisymmetric function, and assigning the centre of the line profile to the root of this convolution. As in Segura-Montero et al. (2020), we used the Double-Gaussian method (GAU2 option available in the routine), which uses a negative and a positive Gaussian to convolve the emission line. The algorithm uses as input the width and separation of the Gaussians. This method traces the emission of the wings of the line profile, presumably arising from the inner parts of the accretion disc.

Following the methodology described by Shafter et al. (1986), we made a diagnostic diagram to find

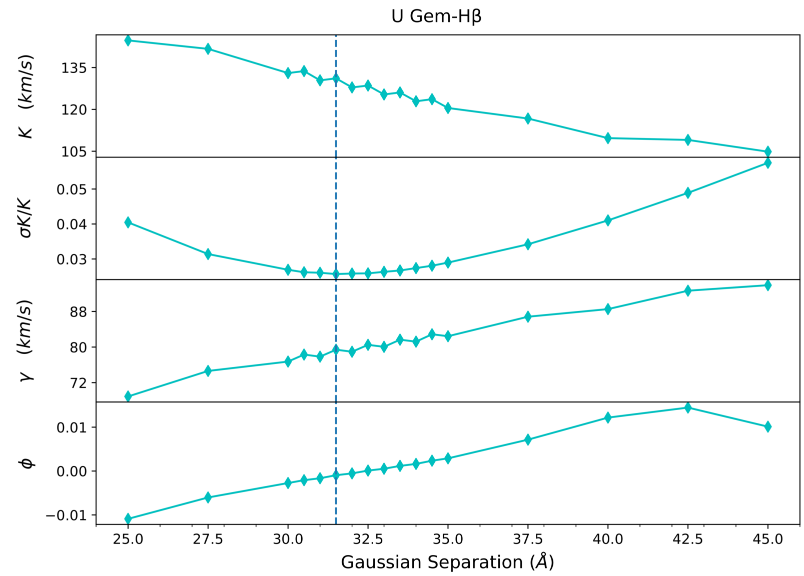

Fig. 2. Diagnostic diagram of the $H\beta$ emission line. The vertical blue dashed line indicates the best solution. See text for further discussion. The colour figure can be viewed online.

TABLE 2

ORBITAL PARAMETERS

Parameter	Hβ	Hγ	Hδ
γ (km s^{-1})	79.4 ± 2.3	81.2 ± 3.4	122.5 ± 4.9
K_1 (km s^{-1})	131.1 ± 3.3	110.0 ± 5.0	136.9 ± 7.1
$HJD_0{}^{*}$	0.0077 ± 0.0006	0.005 ± 0.001	0.008 ± 0.001
P_{orb} (min)	Fixed**	Fixed**	Fixed**

*(2459261+ days).

**0.1769061911 days.

the optimal Gaussian separation, by fitting each trial to a simple circular orbit :

$$V(t) = \gamma + K_1 \sin\left(2\pi \frac{t - t_0}{P_{orb}}\right), \qquad (1)$$

where γ is the systemic velocity, K_1 the semi-amplitude (assumed to be the WD orbital velocity), t_0 the time of inferior conjunction of the donor and P_{orb} is the orbital period. We employed χ^2 as our goodness-of-fit parameter. Note that we have fixed the orbital period in our calculations, and therefore we only fit the other three orbital parameters. This is a convenient way to improve the fit of the remaining free parameters as the orbital period has been obtained from the eclipses of the object (e.g. Echevarría et al. 2007).

Constructing a diagnostic diagram requires an interactive fitting between the CONVRV routine and a program to fit the orbital parameters. We have used ORBITAL[7] a simple least squares program to determine, in general, the three free orbital parameters. In particular, a control parameter is defined in this diagnostic, σ_K/K, whose minimum is a very good indicator of the optimal fit. In our runs we have found that the best results are obtained with a relatively small width of about 10–15 pixels. The diagnostic diagram for $H\beta$ is displayed in Figure 2, while the orbital fit for its best solution is exhibited in Figure 3. The parameters yielded for the optimal orbital fit are shown in Table 2. In a similar way, we have constructed the diagnostic diagrams for $H\gamma$ and $H\delta$. These, and the corresponding best orbital fits, are shown in Figures 4 to 7, while the orbital parametrs are also shown in Table 2.

The radial velocity fit for the $H\beta$ and $H\delta$ emission lines yield consistent K_1 values within the er-

[7] Available at `https://github.com/Alymantara/orbital_fit`

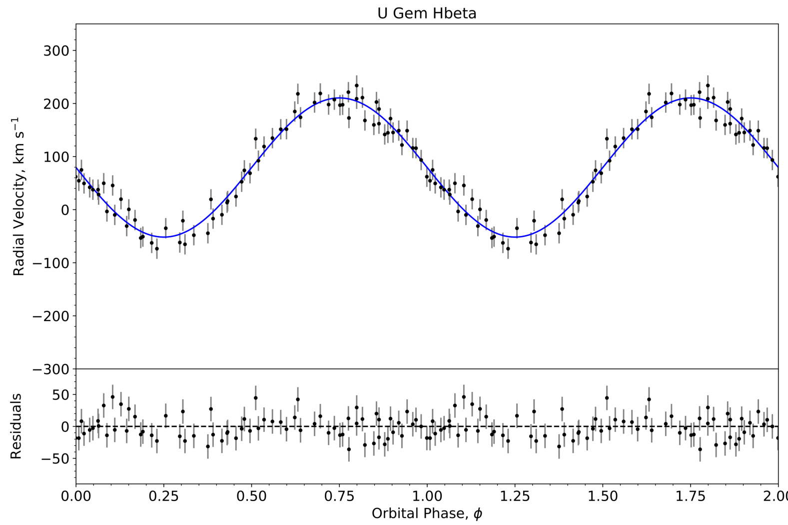

Fig. 3. Radial velocity curve for the best solution of the $H\beta$ emission line. The colour figure can be viewed online.

TABLE 3

BASIC SYSTEM PARAMETERS YIELDED BY THE K_1 AMPLITUDE VALUE OF EACH EMISSION LINE

Parameter	$H\alpha^{\dagger}$	Hβ	Hγ	Hδ
q	0.34 ± 0.01	0.42 $\pm$0.01	0.35 $\pm$0.01	0.44 $\pm$0.02
M_1 ($M_\odot$)	1.20 ± 0.05	1.34 $\pm$0.05	1.22 $\pm$0.06	1.38 $\pm$0.07
M_2 ($M_\odot$)	0.42 ± 0.04	0.57 $\pm$0.02	0.43 $\pm$0.03	0.61 $\pm$0.05
$a(R_\odot)$	1.55 ± 0.02	1.64 $\pm$0.02	1.56 $\pm$0.03	1.67 $\pm$0.03

†(Echevarría et al. 2007).

rors. They also agree with the value of $K_1 = 138 \pm 8$ kms^{-1}, obtained from an analysis of the same lines performed by Stover (1981). On the other hand $H\gamma$ agrees with the more accurate result of $K_1 = 107.1 \pm 2.1$ kms^{-1} obtained by Long & Gilliland (1999), who traced the Doppler shifts of the WD photospheric absorption lines in the FUV range; also in agreement with Echevarría et al. (2007), who followed the same methodology used in this paper, but applied to the $H\alpha$ Balmer emission line only ($K_1 = 107 \pm 2$ kms^{-1}).

4. DISCUSSION

4.1. *Basic System Parameters*

From the determination of the orbital parameters obtained in § 3 we can estimate the masses of the system components, as well as the binary separation, provided that an accurate estimation of the inclination angle is available. These mass estimates depend strongly on the assumption that the semi-amplitude derived from the emission lines accurately reflects the motion of the white dwarf, i.e. that the measurements of the wings of the lines are not distorted and present a symmetric behavior along the orbital period. The basic system parameters are obtained with the following formulae:

$$q = \frac{K_1}{K_2} = \frac{M_2}{M_1}, \tag{2}$$

$$M_1 \sin^3 i = \frac{P K_2 (K_1 + K_2)^2}{2\pi G}, \tag{3}$$

$$M_2 \sin^3 i = \frac{P K_1 (K_1 + K_2)^2}{2\pi G}, \tag{4}$$

$$a \sin i = \frac{P(K_1 + K_2)}{2\pi}, \tag{5}$$

where q is the mass ratio; M_1 is the mass of the primary; M_2 the mass of the secondary; i the inclination angle, K_1 and K_2 are the semi-amplitude of the primary and secondary, respectively; and a is the binary separation. To employ equations 2–5, we adopted the inclination derived by Zhang & Robinson (1987) of $i = 69.7° \pm 0.7°$ and the semi-amplitude of the secondary derived by Echevarría et al. (2007) of $K_2 = 310 \pm 5$ kms^{-1}.

Table 3 shows a summary for the system parameters yielded when using each of the K_1 values from

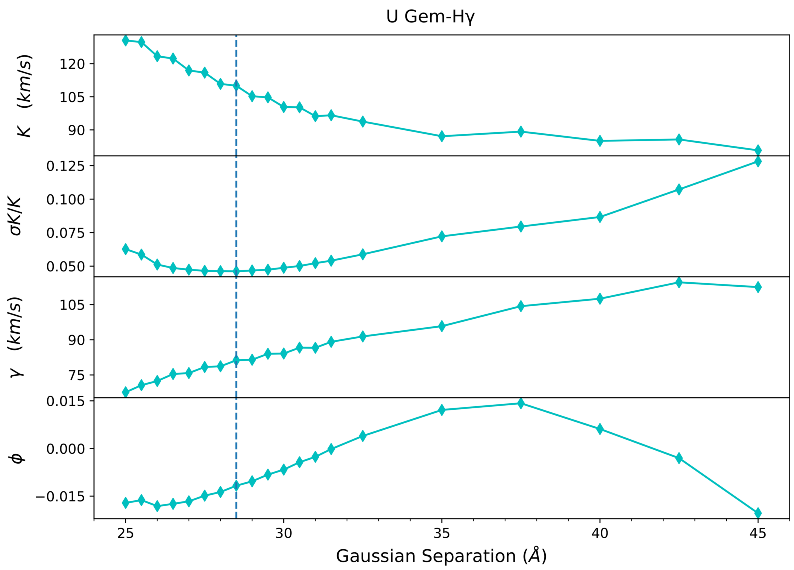

Fig. 4. Diagnostic diagram of the $H\gamma$ emission line. The vertical blue dashed line indicates the best solution. See text for further discussion. The colour figure can be viewed online.

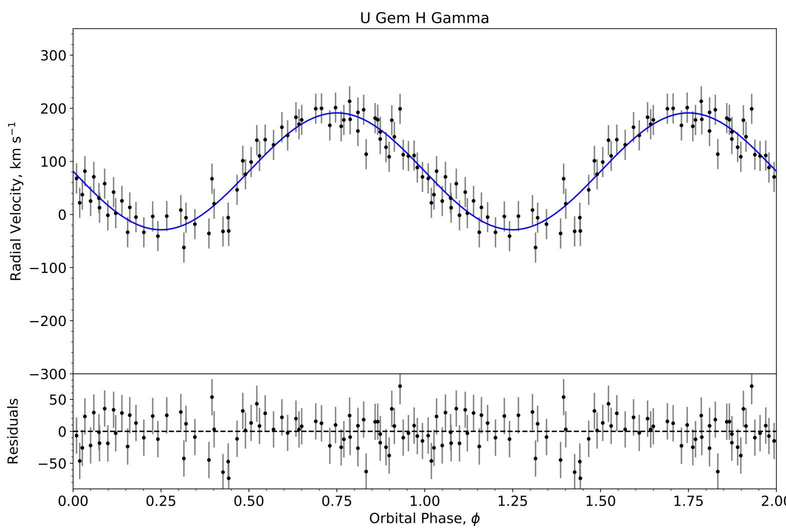

Fig. 5. Radial velocity curve for the best solution of the $H\gamma$ emission line. The colour figure can be viewed online.

the three lines, obtained in § 3. For comparison, we also include the parameters reported for $H\alpha$ by Echevarría et al. (2007).

As expected from the high K_1 values for Hβ and Hδ, and because we are using the same i and K_2 constraints as Echevarría et al. (2007), the system parameters for these lines resulted in an overestimation with respect to those obtained from the $H\alpha$ analysis of the aforementioned authors (See Table 3). On the other hand, the parameters yielded for $H\gamma$ are consistent with those reported by Echevarría et al. (2007), because of the agreement of the K_1 value.

A possible explanation for our radial velocity parameter overestimation and thus for our mass parameter calculations could be made based on the X-ray analysis of Takeo et al. (2021), whose models predict that the accretion disc is truncated at 1.25 Rwd during quiescence, as expected by the theory (Narayan & Popham 1993). Given that the Double-Gaussian method, employed in § 3, traces the inner region of the disc, this truncation could result in higher values for the radial velocity of the WD.

It is possible that the inner part of the disc does contain mass, but at such low density and low surface brightness that it is optically thin (e.g. Pringle

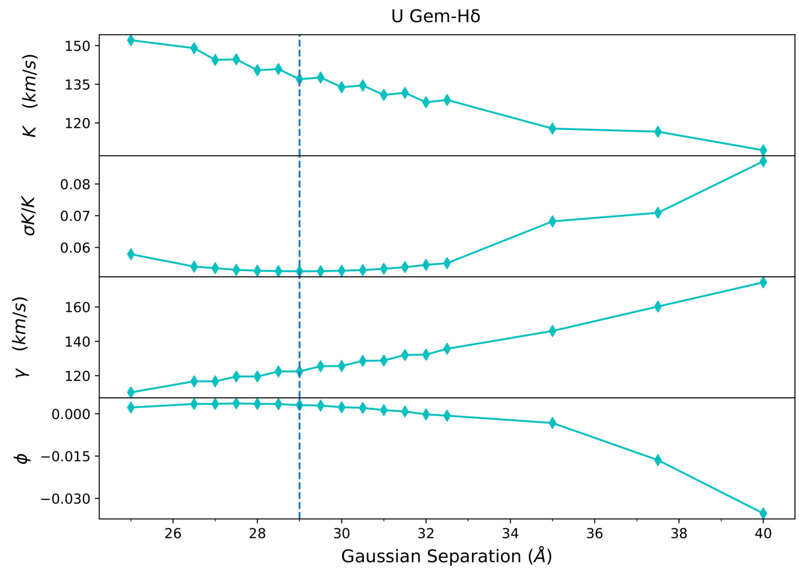

Fig. 6. Diagnostic diagram of the $H\delta$ emission line. The vertical blue dashed line indicates the best solution. See text for further discussion. The colour figure can be viewed online.

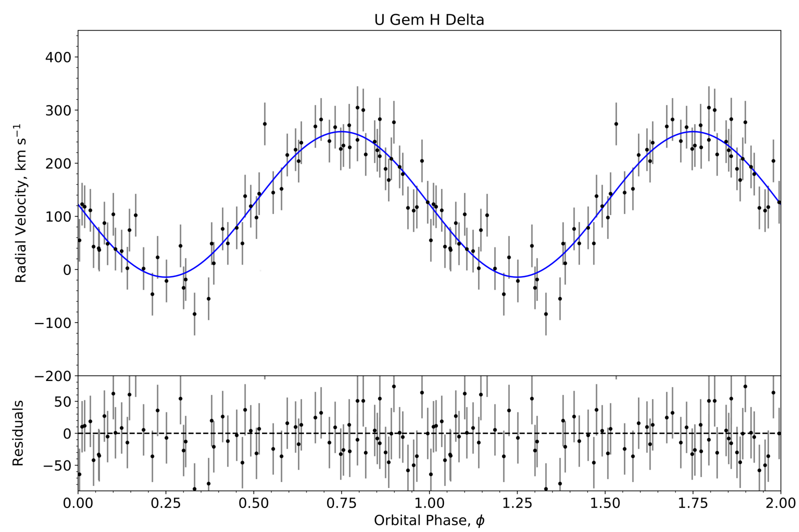

Fig. 7. Radial velocity curve for the best solution of the $H\delta$ emission line. The colour figure can be viewed online.

1981). Furthermore, as explained in § 4.2, we detect an asymmetry overlaying the disc in our Doppler tomograms. These circumstances could imply abrupt variations of opacities within the disc, which would explain our internal inconsistencies in the radial velocity analysis (e.g. Mason et al. 2000).

4.2. *Doppler Tomography*

Doppler tomography is an indirect imaging technique developed by Marsh & Horne (1988). It produces two-dimensional mappings of the emission intensity in velocity space of the accretion disc, using the phase-resolved profiles of the spectral emission lines. We produced the Doppler tomography of the $H\beta$, $H\gamma$ and $H\delta$ Balmer emission lines, using a Python wrapper [8] (Hernandez Santisteban 2021) of the FORTRAN routines published by Spruit (1998) within an IDL environment. Figures 8-10, show the resulting images from the analysis, with the following layout: in the top left panel we show the observed trailed spectra; the tomography is displayed in the bottom panel; and the reconstructed trailed spectra, which are created by collapsing the tomography

[8] Available at `https://github.com/Alymantara/pydoppler`

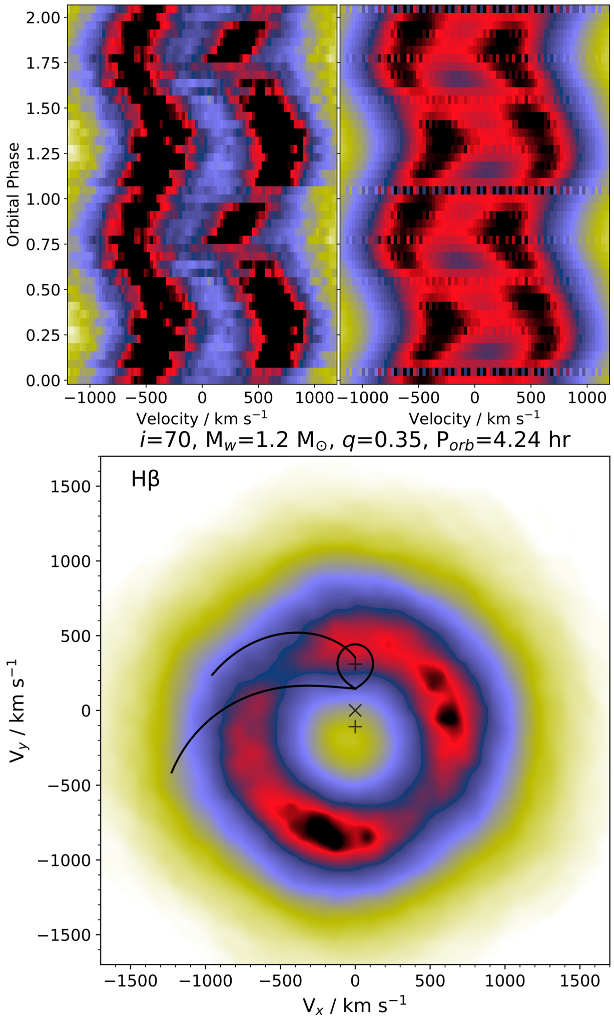

Fig. 8. Trail spectra and Doppler tomography of the $H\beta$ emission line. The relative emission intensity is shown in a scale of colours, where the strongest intensity is represented by black, followed by red, then blue, and finally yellow. The cross markings represent (from top to bottom) the position of the secondary, the centre of mass and the primary component. The Roche lobe of the secondary is depicted around its cross. The Keplerian and ballistic trajectories of the gas stream are marked as the upper and lower : curves, respectively. The colour figure can be viewed online.

image along the direction defined by the respective orbital phase (Marsh 2005), appear in the top right panel.

The trailed spectra of all three Balmer lines show a conspicuous double-peaked structure, characteristic of the line profiles of discs in systems of high inclination (Horne & Marsh 1986; Marsh & Horne 1988). The spectrograms exhibit an evident lack of a hot-spot signature, which would appear as an s-wave oscillating from peak to peak.

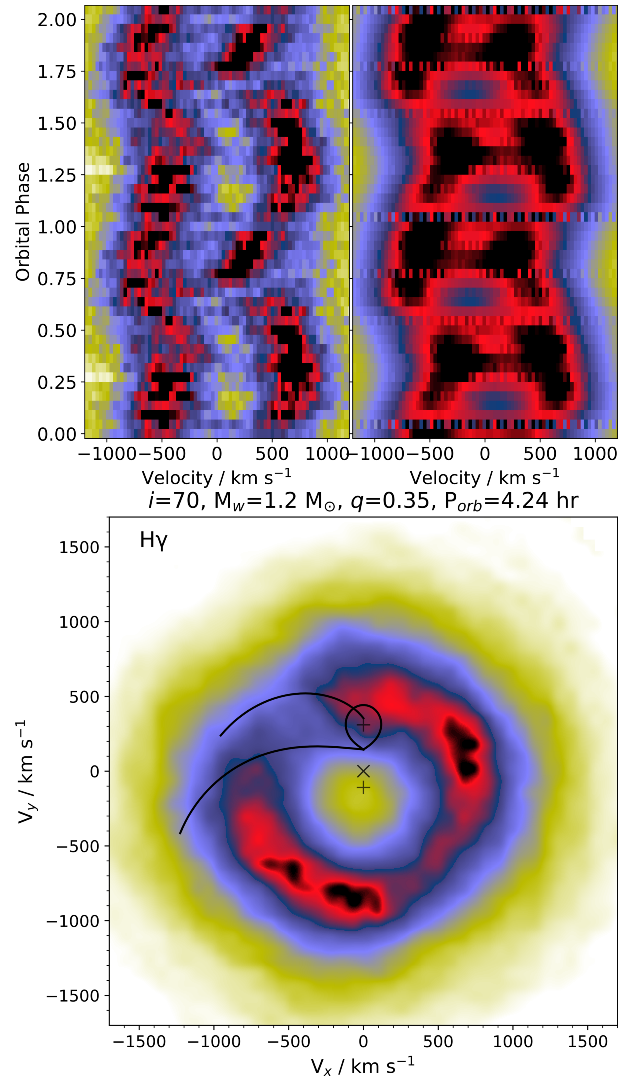

Fig. 9. Trail spectra and Doppler tomography of the $H\gamma$ emission line. The relative emission intensity is shown in a scale of colours, where the strongest intensity is represented by black, followed by red, then blue, and finally yellow. The cross markings represent (from top to bottom) the position of the secondary, the centre of mass and the primary component. The Roche lobe of the secondary is depicted around its cross. The Keplerian and ballistic trajectories of the gas stream are marked as the upper and lower curves, respectively. The colour figure can be viewed online.

The overall structure in our three tomography images is in contrast to most previous Doppler tomography studies of U Gem in quiescence, which were dominated by an intense emission corresponding to a hot spot component (e.g. Marsh et al. 1990; Echevarría et al. 2007). Instead, we find an asymmetric region of enhanced emission overlaying the disc, consistent with the structure exhibited by spiral

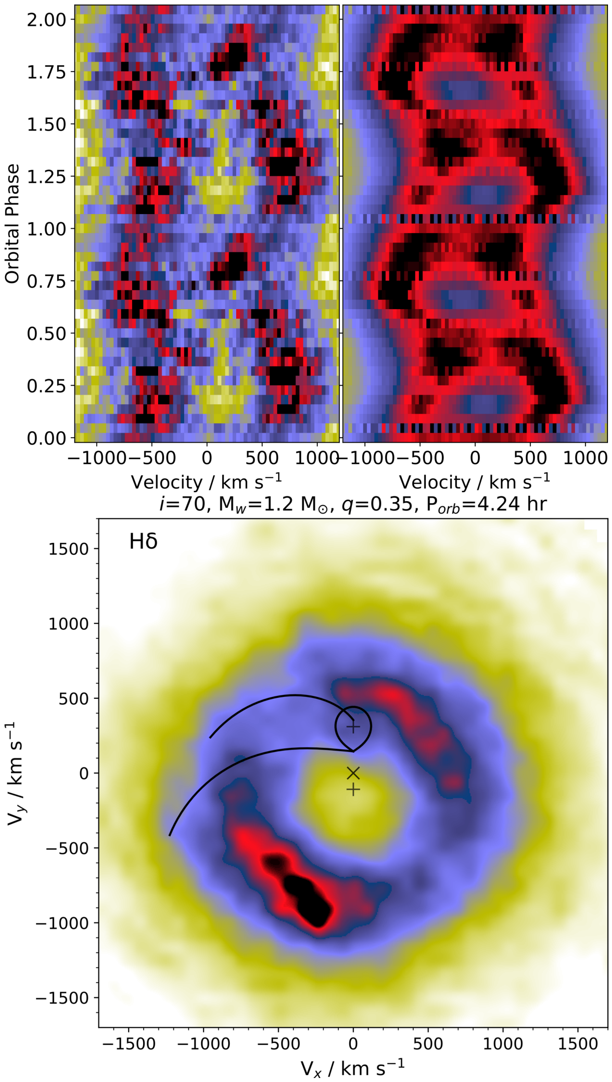

Fig. 10. Trail spectra and Doppler tomography of the $H\delta$ emission line. The relative emission intensity is shown in a scale of colours, where the strongest intensity is represented by black, followed by red, then blue, and finally yellow. The cross markings represent (from top to bottom) the position of the secondary, the centre of mass and the primary component. The Roche lobe of the secondary is depicted around its cross. The Keplerian and ballistic trajectories of the gas stream are marked as the upper and lower curves, respectively. The colour figure can be viewed online.

density waves (eg. Steeghs et al. 1997). While U Gem has been observed to show this structure in Doppler tomograms before (Neustroev & Borisov 1998; Unda-Sanzana et al. 2006), the presence of fully formed spiral shocks in U Gem must be regarded with caution: the study of the evolution of spiral shocks in U Gem performed by Groot (2001) shows that they fade during the decline of the outburst. And even if spiral arms were present in U Gem in quiescence, they would be expected to be tightly wrapped during this stage (Steeghs & Stehle 1999); hence very difficult to detect with Doppler tomography (Ruiz-Carmona et al. 2020). As discussed by Unda-Sanzana et al. (2006), the spiral feature in the tomography could instead be explained by irradiation from the WD of regions of the disc that become thickened from tidal distortion.

Nonetheless, our understanding of spiral shocks from 2D models has shown limitations before, as in the simulations by Godon et al. (1998) which predicted an unrealistically hot disc in order to reproduce the two-armed spiral pattern exhibited in the tomography of IP Peg by Steeghs et al. (1997). Moreover, a previous detection in quiescence makes the limitations evident: the Doppler maps reported by Pala et al. (2019) exhibit a clear signature of spiral shocks in a quiescent state of the WZ Sge object SDSS J123813.73-033933.0; confirmed by the double hump modulation of the white dwarf in their *HST* data, caused by the interface between the white dwarf and the inner edge of the spiral shocks. And since the mass ratio of U Gem, $q = 0.35 \pm 0.03$ (Echevarría et al. 2007), sets it right on the limit that allows the disc to achieve the 3:1 resonance ($q \lesssim 0.3$) (Hellier 2001), spiral arms cannot be completely discarded.

Another possible explanation is provided by Smak (2001), who argues that the high radial velocity of $K_1 = 138 \pm 8$ kms^{-1} obtained by Stover (1981) (in accordance with our own values yielded for $H\beta$ and $H\delta$) could be caused by stream overflow of the disc. This would explain the absence of a hot spot in our tomography images, since the stream overshoot would avoid (or ameliorate) the initial impact with the rim of the disc. Stream material overshooting the disc edge and re-impacting at radii with lower velocity can create a second hot spot (Lubow 1989) which usually shows up in regions within the lower quadrants of the Doppler tomograms, as is the case in SW Sextantis systems (Schmidtobreick 2017). This scenario is further supported by the phase-dependent modulation of the FUV light curve and absorption lines velocity reported by Froning et al. (2001), which can be explained by the stream overflowing the edge of the disc (Godon et al. 2017; Godon 2019).

In any case, it is puzzling that our tomography shows similar emission distributions for all three emission lines, implying that they arise from the same regions in the disc. This raises the question: why is it that for $H\beta$ and $H\delta$ we obtain values that are consistent with Stover (1981), which are likely corrupted by some additional effect on the disc; while on the other hand $H\gamma$ appears unaffected and agrees better with the more reliable WD radial velocity measured from *HST* FUV observations by Long & Gilliland (1999)? As mentioned in § 4.1, we expect this internal inconsistency to be caused by different gas opacities in the accretion disc (Mason et al. 2000), occurring as a consequence of some combination of the phenomena discussed above: WD irradiation of tidally thickened regions, stream overflow, a partially truncated disc, and perhaps even fully formed spiral arms.

However, this inconsistency is a clear example of the issues arising from measuring the radial velocity of the WD from optical data, even when presumably tracing the inner regions of the disc as is done in the Double-Gaussian method (see § 3).

5. CONCLUSIONS

We presented a spectroscopic analysis of the dwarf nova U Geminorum. We obtained the radial velocity of the system for three distinct Balmer emission lines: Hβ, Hγ, and Hδ, by tracing the outer regions of the profile (which arise from the inner sections of the accretion disc), with the purpose of obtaining the WD radial velocity K_1. The resulting semi-amplitude for Hγ is consistent with previous canonic results of $K_1 = 107.1 \pm 2.1$ kms^{-1} (Echevarría et al. 2007; Long & Gilliland 1999). However, the other two lines show a considerable discrepancy, agreeing instead with the value obtained by Stover (1981) of $K_1 = 138 \pm 8$ kms^{-1}. We expected to find the source of this inconsistency in the Doppler tomography study, but the tomograms show that all three lines arise from the same region. However, it must be noted that the tomography does not show a typical disc: in particular there is no evidence whatsoever of a hot spot; instead it exhibits a spiral arm structure unexpected for a system in quiescence. This unusual shape (which can be a product of stream overflow, WD irradiation or actual spiral arms), along with a partial truncation of the inner regions of the disc, could together amount to considerable differences of gas opacities within the accretion disc, which could explain the different values of K_1 obtained for our three emission lines (e.g. Mason et al. 2000).

U Gem stands as one of the best studied DN. However, as it is made evident in this paper, more ingredients than those prescribed by the classical model must come into play to better explain its behaviour. Therefore, we propose further observations of this source to help shed light on the mechanisms giving rise to its rich and interesting nature.

The authors are indebted to DGAPA (Universidad Nacional Autónoma de México) support, PAPIIT Projects IN114917 and IN103120. This project has received funding from the European Research Council (ERC) under the European Union's Horizon 2020 research and innovation programme (Grant Agreement No. 101020057). This work was supported by CONACyT (Consejo Nacional de Ciencia y Tecnología) Research Grants 280789 and 320987. This work was supported by the MPlfR-Mexico Max Planck Partner group led by V.M.P.-A. We thank the staff at the Observatorio Astrofísico Guillermo Haro for facilitating and helping us to obtain our observations. This research made extensive use of ASTROPY, a community-developed core Python package for Astronomy (Astropy Collaboration et al. 2013), Python's SciPy signal processing library (Virtanen et al. 2020), and MATPLOTLIB (Hunter 2007).

REFERENCES

Astropy Collaboration, Robitaille, T. P., Tollerud, E. J., et al. 2013, A&A, 558, 33, https://doi.org/10.1051/0004-6361/201322068

Echevarría, J., de la Fuente, E., & Costero, R. 2007, AJ, 134, 262, https://doi.org/10.1086/518562

Froning, C. S., Long, K. S., Drew, J. E., Knigge, Ch., & Proga, D. 2001, ApJ, 562, 963, https://doi.org/10.1086/323860

Godon, P., Livio, M., & Lubow, S. 1998, MNRAS, 295, 11, https://doi.org/10.1046/j.1365-8711.1998.29510584.x

Godon, P., Shara, M. M., Sion, E. M., & Zurek, D. 2017, ApJ, 850, 146, https://doi.org/10.3847/1538-4357/aa9616

Godon, P. 2019, ApJ, 870, 112, https://doi.org/10.3847/1538-4357/aaf3a2

Groot, P. J. 2001, ApJ, 551, 89, https://doi.org/10.1086/319826

Hameury, J. M. & Lasota, J. P. 2017, A&A, 602, 102, https://doi.org/10.1051/0004-6361/201730760

Hellier, C. 2001, Cataclysmic Variable Stars (Springer)

Hernandez Santisteban, J. V. 2021, PyDoppler: Wrapper for Doppler Tomography Software, ascl.soft 06003H

Horne, K. & Marsh, T. R. 1986, MNRAS, 218, 761, https://doi.org/10.1093/mnras/218.4.761

Hunter, J. D. 2007, CSE, 9, 90, https://doi.org/10.1109/MCSE.2007.55

Long, K. S. & Gilliland, R. L. 1999, ApJ, 511, 916, https://doi.org/10.1086/306721

Lubow, S. H. 1989, ApJ, 340, 1064, https://doi.org/10.1086/167458

Marsh, T. R. & Horne K. 1988, MNRAS, 235, 269, https://doi.org/10.1093/mnras/235.1.269

Marsh, T. R., Horne, K., Schlegel, E. M., Honeycutt, R. K., & Kaitchuck, R. M. 1990, ApJ, 364, 637, https://doi.org/10.1086/169446

Marsh, T. R. 2005, Ap&SS, 296, 403, https://doi.org/10.1007/s10509-005-4859-3
Mason, E., Skidmore, W., Howell, S. B., et al. 2000, MNRAS, 318, 440, https://doi.org/10.1046/j.1365-8711.2000.03780.x
Narayan, R. & Popham, R. 1993, Natur, 362, 820, https://doi.org/10.1038/362820a0
Neustroev, V. V. & Borisov, N. V. 1998, A&A, 336, 73, https://doi.org/10.48550/arXiv.astro-ph/9807076
Neustroev, V.V., Zharikov, S.V. & Borisov, N.V. 2016, A&A, 585, 10, https://doi.org/10.1051/0004-6361/201526363
Pala, A. F., Gänsicke, B. T., Marsh, T. R., et al. 2019, MNRAS, 483, 1080, https://doi.org/10.1093/mnras/sty3174
Patterson, J., Thorstensen, J. R., Vanmunster, T., et al. 2004, PASP, 116, 516, https://doi.org/10.1086/421034
Pringle, J. E. 1981, ARA&A, 19, 137, https://doi.org/10.1146/annurev.aa.19.090181.001033
Rodríguez-Gil, P., Gänsicke, B. T., Araujo-Betancor, S., et al. 2004, MNRAS, 349, 367, https://doi.org/10.1111/j.1365-2966.2004.07512.x
Ruiz-Carmona, R., Groot, P. J., & Steeghs, D. 2020, MNRAS, 491, 2217, https://doi.org/10.1093/mnras/stz2992
Schneider, D. P. & Young, P. 1980, ApJ, 238, 946, https://doi.org/10.1086/158059
Segura-Montero, O., Ramírez, S & Echevarría, J. 2020, MNRAS, 494, 4110, https://doi.org/10.1093/mnras/staa856
Schmidtobreick, L. 2017, arXiv:1705.09332, https://doi.org/10.48550/arXiv.1705.09332
Shafter, A. W., Szkody, P., & Thorstensen, J. R. 1986, ApJ, 308, 765, https://doi.org/10.1086/164549
Smak, J. 1971, AcA, 21, 15
Smak, J. 2001, AcA, 51, 279
Smak, J. & Waagen, E. O. 2004, AcA, 54, 433
Spruit, H. C. 1998, arXiv: astro-ph/9806141, https://doi.org/10.48550/arXiv.astro-ph/9806141
Steeghs, D., Harlaftis, E. T., & Horne, K. 1997, MNRAS, 290, 28, https://doi.org/10.1093/mnras/290.2.L28
Steeghs, D. & Stehle, R. 1999, MNRAS, 307, 99, https://doi.org/10.1046/j.1365-8711.1999.02634.x
Stepanyan, D. A. 1982, PZ, 21, 691
Stover, R. J. 1981, ApJ, 248, 684, https://doi.org/10.1086/159193
Takeo, M., Hayashi, T., Ishida, M., et al. 2021, PASJ, 73, 143, https://doi.org/10.1093/pasj/psaa111
Unda-Sanzana, E., Marsh, T. R., & Morales-Rueda, L. 2006, MNRAS, 369, 805, https://doi.org/10.1111/j.1365-2966.2006.10336.x
Virtanen, P., Gommers, R., Oliphant, T. E., et al. 2020, NatMe, 17, 261, https://doi.org/10.1038/s41592-019-0686-2
Warner, B. 1995, Cataclysmic Variable Stars, (Cambridge University Press)
Warner, B. & Nather, R. E. 1971, MNRAS, 152, 219, https://doi.org/10.1093/mnras/152.2.219
Zhang, E. H. & Robinson, E. L. 1987, ApJ, 321, 813, https://doi.org/10.1086/165674

V. Chavushyan and V. Patiño: Instituto Nacional de Astrofísica, Óptica y Electrónica, Luis Enrique Erro #1, Tonantzintla, Puebla 72840, México.
J. Echevarría and L. J. Sánchez[1]: Instituto de Astronomía, Universidad Nacional Autónoma de México, Apartado Postal 70-264, Ciudad Universitaria, México D.F., C.P. 04510, México.
M. Fuentes: Departamento de Física, Universidad de Sonora, Unidad Regional Centro, Hermosillo, Blvd. Luis Encinas J, Calle Av. Rosales S/N, Centro, 83000, Sonora, México.
V. Patiño: Max-Planck-Institut für Radioastronomie, Auf dem Hügel 69, D-53121 Bonn, Germany.
S. H. Ramírez: Department of Physics, University of Warwick, Coventry CV4 7AL, UK.

Revista Mexicana de Astronomía y Astrofísica, **59**, 201–211 (2023)

https://doi.org/10.22201/ia.01851101p.2023.59.02.05

SPECTROSCOPIC & PHOTOMETRIC STUDY OF THE ALGOL-TYPE BINARY V1241 TAURI

R. H. Nelson[1,2,3], K. B. Alton[2], and M. Kendurkar[3]

Received November 21 2022; accepted March 8 2023

ABSTRACT

New radial velocity (RV) data obtained at the Dominion Astrophysical Observatory (DAO) in Victoria, British Columbia along with light curve (LC) data for the Algol-type binary V1241 Tau have been simultaneously analysed with the 2003 version of the Wilson-Devinney code (WD2003). There were two distinct LC datasets: one was from the Transiting Exoplanet Survey Satellite (TESS) and the others (BVI_c) from the (land-based) Desert Blooms Observatory (DBO). The TESS data were considered to have the least photometric uncertainty; consequently, we derived estimates for M_1 (1.91(8) $M_\odot$), M_2 (1.04(4) $M_\odot$), R_1 (1.86(1) $R_\odot$), R_2 (1.73(1) $R_\odot$), q_{WD} (0.54(3)), L_1 (10.7(8) $L_\odot$), and L_2 (1.7(2) $L_\odot$) following simultaneous analysis (RV+LC) with the WD2003 code. Evolutionary modeling revealed that the primary star is somewhat evolved past the zero age main sequence (ZAMS) while the secondary is much evolved past the terminal age main sequence (TAMS).

RESUMEN

Se analizan simultáneamente datos sobre la velocidad radial de la binaria tipo Algol V1241 Tau obtenidos en el Dominion Astrophysical Observatory en Victoria, Columbia Británica junto con datos sobre su curva de luz. Se usa la versión 2003 del código Wilson-Devinney (WD2003). Los datos sobre la curva de luz provienen de TESS y del Desert Blooms Observatory. Consideramos que los datos de TESS tienen la mejor incertidumbre fotométrica y derivamos estimaciones para M_1 (1.91(8) $M_\odot$), M_2 (1.04(4) $M_\odot$), R_1 (1.86(1) $R_\odot$), R_2 (1.73(1) $R_\odot$), q_{WD} (0.54(3)), L_1 (10.7(8) $L_\odot$), y L_2 (1.7(2) $L_\odot$) después del análisis simultáneo (curva de luz y velocidad radial) con el código WD2003. El análisis evolutivo reveló que la estrella primaria ya se ha alejado un poco de la secuencia principal de edad cero, mientras que la secundaria ya se alejó mucho de la secuencia principal terminal.

Key Words: binaries: eclipsing — binaries: spectroscopic — stars: evolution — stars: fundamental parameters — stars: imaging

1. INTRODUCTION

Following the examination of photographic plates, V1241 Tau (AN 201-1907, BD-01 484, HD 21102, and TYC 4709-1181-1) was discovered to be a variable star in the constellation Taurus by Henrietta Leavitt (Pickering 1908). It was similarly observed by Hoffmeister (1934) who identified the system as Algol-type but the period was not disclosed. Jensch (1934) provided a period of 0.823272 d, along with a light curve and nine times of minima (ToM). Interestingly, this same variable located very near the Eridanus/Taurus border was reported by Gaposchkin (1953) but was instead identified as WX Eri. Not until Kazarovets et al. (2006) did the nomenclature for this eclipsing binary finally change to V1241 Tau. Roman (1956) classified the system (also listed as WX Eri) as A7+F6V. Sarma & Abhyankar (1979) analysed new B and V light curves using the rectification method and tentatively classified WX Eri as detached with the F3 primary pulsating like a δ-Scuti variable with two periods of about 0.16 and 0.14 d. Giuricin & Mardirossian (1981) concluded from their own data that this system was unlikely to be a simple main sequence (MS) detached system. Russo & Milano

[1]Mountain Ash Observatory, BC, Canada.
[2]Desert Blooms Observatory, AZ, USA.
[3]Guest investigator, Dominion Astrophysical Observatory, Victoria, BC, Canada.

(1983) were the first to analyze light curves using a Roche-based (physical) model, namely that of Wilson & Devinney (1971). Srivastava & Kandpal (1986) performed their own photometry in the B and V passbands and detected no δ-Scuti type light variations. After plotting eclipse timings from 1930 to 1980, they concluded that the orbital period was constant. Arentoft et al. (2004) analyzed their own light curve data with the Wilson and Devinney code and also found no evidence for oscillations in the data. Furthermore as reported by Yang et al. (2012), this Algol-type system should be removed as an "oscillating EA" star as defined by Mkrtichian et al. (2003). Finally, sparsely sampled monochromatic light curve data from V1241 Tau were also acquired during the All Sky Automated Survey (Pojmanski 2003) between 2001 and 2009.

Although primarily designed to capture very small host star brightness changes during an exoplanet transit, the TESS Mission (Ricker et al. 2015; Caldwell 2020) also provides a wealth of LC data for many variable stars. A pre-selected number of dwarf main-sequence stars for photometric study were initially targeted using effectively two minutes of total exposure time (2 sec $\times$ 60). The TESS CCD detector bandpass ranges between 600-1000 nm and is centered near the Cousins I band (I_c). One such imaging campaign which captured LC data from V1241 Tau started on October 19, 2018 and ran continuously every 2 min through November 13, 2018. Another 120 s cadence imaging campaign followed between October 22, 2020 and November 16, 2020. Raw flux readings were processed by the TESS Science Processing Operations Center (TESS-SPOC) to remove long term trends using so-called co-trending basis vectors (CBVs). These results identified as pre-search data conditioning simple aperture (PDCSAP) flux are usually cleaner data than the SAP flux. A large number (n=102) of minimum light timings were produced (MAVKA: Andrych & Andronov (2019); Andrych et al. (2020)) from both imaging campaigns. These along with 18 more ToM literature values were used to determine whether any secular changes in the orbital period could be detected from the eclipse timing residuals (Table 2) evaluated between 2012 and 2020. TESS results expressed in BJD$-$TDB were converted to JD in UTC according to Eastman et al. (2010).

Yang et al. (2012) presented new photometry in B and V which they analyzed with the WD2003 code. However, a spatial model newly rendered with Binary Maker 3 (Bradstreet 1993) using their parameters (i=79.9° and q=0.545) reveals that the eclipses

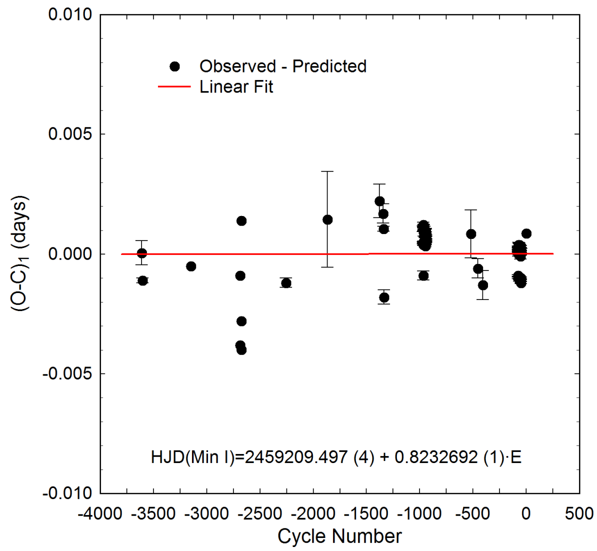

Fig. 1. V1241 Tau: Eclipse Timing Diagram showing straight line fit of O$-$C residuals suggesting no obvious change in the orbital period from 2012 to 2020. The colour figure can be viewed online.

are only partial. This is problematic since it has been shown (Terrell & Wilson 2005; Terrell 2022) that for overcontact and semi-detached binaries undergoing partial eclipses, the mass ratio is indeterminate. Therefore, a radial velocity study (RV) was required to reliably determine the mass ratio and total mass. Accordingly, the necessary spectra were obtained at the Dominion Astrophysical Observatory (DAO).

2. PERIOD VARIATION

The first comprehensive period study, using timing data from 1928 to 2011, was by Yang et al. (2012). In it they concluded a linear ephemeris with a light time (LiTE) component due to the orbital movement in conjunction with a supposed third star. Our analysis ignored these data and focused on determining a new linear ephemeris which only included ToM results between 2012 and 2020. This covers the time periods for radial velocity experiments (2014-2015) and the multicolor photometric acquisition of light curve data (2017-2019). These (Table 1) include 18 literature values and 102 ToM estimates extracted from light curve observations made by the TESS Satellite Mission (Ricker et al. 2015; Caldwell 2020) in 2018 and 2020. An eclipse timing difference (O$-$C) plot, is presented in Figure 1. Initially we used the eclipse elements (equation 1) taken from the General Catalogue of Variable Stars (Samus et al. 2017) to seed the linear regression

TABLE 1

V1241 TAU TIMES OF MINIMUM (ToM), MEASUREMENT UNCERTAINTY, EPOCH AND ECLIPSE TIMING DIFFERENCES (ETD) USED TO CALCULATE A LINEAR EPHEMERIS

ToM (HJD-2400000)	Err	Cycle No.	ETD	Ref.
56235.4376	0.00050	-3612.5	0.0000	1
56242.4342	0.00010	-3604	-0.0011	1
56617.0223	nr	-3149	-0.0005	2
56996.9578	nr	-2687.5	-0.0038	3
56996.9607	nr	-2687.5	-0.0009	3
57006.0135	nr	-2676.5	-0.0040	3
57006.0147	nr	-2676.5	-0.0028	3
57006.0189	nr	-2676.5	0.0014	3
57351.7894	0.0002	-2256.5	-0.0012	4
57672.8670	0.0020	-1866.5	0.0014	5
58073.7999	0.0007	-1379.5	0.0022	6
58101.7905	0.0004	-1345.5	0.0017	6
58106.3178	0.0001	-1340	0.0010	7
58109.6081	0.0003	-1336	-0.0018	6
58411.3391	0.0001	-969.5	0.0011	8
58411.7501	0.0001	-969	0.0005	8
58412.1623	0.0001	-968.5	0.0010	8
58412.5733	0.0001	-968	0.0004	8
58412.9856	0.0001	-967.5	0.0010	8
58413.3967	0.0001	-967	0.0005	8
58413.8069	0.0001	-966.5	-0.0009	8
58414.2200	0.0001	-966	0.0005	8
58414.6323	0.0001	-965.5	0.0012	8
58415.0432	0.0001	-965	0.0005	8
58415.4555	0.0001	-964.5	0.0011	8
58415.8664	0.0001	-964	0.0004	8
58416.2787	0.0001	-963.5	0.0011	8
58416.6897	0.0001	-963	0.0004	8
58417.1018	0.0001	-962.5	0.0009	8
58417.5130	0.0001	-962	0.0005	8
58417.9253	0.0001	-961.5	0.0011	8
58418.3362	0.0001	-961	0.0004	8
58421.6293	0.0001	-957	0.0004	8
58422.0416	0.0001	-956.5	0.0010	8
58422.4526	0.0001	-956	0.0004	8
58424.9224	0.0001	-953	0.0004	8
58425.3344	0.0001	-952.5	0.0008	8
58425.7456	0.0001	-952	0.0004	8
58426.1576	0.0001	-951.5	0.0008	8
58426.5690	0.0001	-951	0.0005	8
58426.9809	0.0001	-950.5	0.0008	8
58427.3923	0.0001	-950	0.0005	8
58427.8042	0.0001	-949.5	0.0008	8
58428.2155	0.0001	-949	0.0004	8
58428.6273	0.0001	-948.5	0.0007	8
58429.0387	0.0001	-948	0.0003	8
58429.4507	0.0001	-947.5	0.0008	8
58429.8620	0.0001	-947	0.0004	8
58430.2739	0.0001	-946.5	0.0007	8
58430.6854	0.0001	-946	0.0005	8
58431.0973	0.0001	-945.5	0.0008	8
58431.5086	0.0001	-945	0.0005	8
58431.9207	0.0001	-944.5	0.0009	8
58432.3318	0.0001	-944	0.0004	8
58432.7439	0.0001	-943.5	0.0008	8
58433.1551	0.0001	-943	0.0004	8
58435.6250	0.0001	-940	0.0005	8
58436.0367	0.0001	-939.5	0.0006	8
58436.4483	0.0001	-939	0.0006	8
58781.8100	0.0010	-519.5	0.0008	9
58835.7327	0.0004	-454	-0.0006	9
58872.7791	0.0006	-409	-0.0013	10
59144.8711	0.0001	-78.5	0.0003	8
59145.2815	0.0001	-78	-0.0010	8
59145.6943	0.0001	-77.5	0.0002	8
59146.1048	0.0001	-77	-0.0010	8
59146.5175	0.0001	-76.5	0.0001	8
59146.9281	0.0001	-76	-0.0009	8
59147.3409	0.0001	-75.5	0.0002	8
59147.7513	0.0001	-75	-0.0010	8
59148.1643	0.0001	-74.5	0.0004	8
59148.5745	0.0001	-74	-0.0010	8
59148.9873	0.0001	-73.5	0.0001	8
59149.3979	0.0001	-73	-0.0010	8
59149.8105	0.0001	-72.5	0.0000	8
59150.2211	0.0001	-72	-0.0010	8
59150.6339	0.0001	-71.5	0.0002	8
59151.0444	0.0001	-71	-0.0010	8
59151.4571	0.0001	-70.5	0.0001	8
59151.8676	0.0001	-70	-0.0010	8
59152.2807	0.0001	-69.5	0.0004	8
59152.6910	0.0001	-69	-0.0010	8
59153.1037	0.0001	-68.5	0.0001	8
59153.5142	0.0001	-68	-0.0010	8
59153.9272	0.0001	-67.5	0.0004	8
59154.3374	0.0001	-67	-0.0011	8
59154.7502	0.0001	-66.5	0.0001	8
59155.1607	0.0001	-66	-0.0011	8
59155.5736	0.0001	-65.5	0.0002	8
59159.2770	0.0001	-61	-0.0011	8
59159.6900	0.0001	-60.5	0.0003	8
59160.1003	0.0001	-60	-0.0011	8
59160.5133	0.0001	-59.5	0.0003	8
59160.9235	0.0001	-59	-0.0011	8
59161.3364	0.0001	-58.5	0.0001	8
59161.7468	0.0001	-58	-0.0011	8
59162.1598	0.0001	-57.5	0.0003	8
59162.5701	0.0001	-57	-0.0011	8
59162.9829	0.0001	-56.5	0.0001	8
59163.3934	0.0001	-56	-0.0011	8
59163.8062	0.0001	-55.5	0.0002	8
59164.2166	0.0001	-55	-0.0011	8
59164.6292	0.0001	-54.5	-0.0001	8
59165.0398	0.0001	-54	-0.0011	8
59165.4527	0.0001	-53.5	0.0000	8
59165.8632	0.0001	-53	-0.0010	8
59166.2761	0.0001	-52.5	0.0002	8
59166.6865	0.0001	-52	-0.0010	8
59167.0992	0.0001	-51.5	0.0000	8
59167.5096	0.0001	-51	-0.0011	8
59167.9226	0.0001	-50.5	0.0002	8
59168.3328	0.0001	-50	-0.0012	8

a: nr=not reported.

1. Karampotsiou et al. (2016); 2. Nagai (2014); 3. Nagai (2015); 4. Nelson (2016); 5. Nelson (2017); 6. Nelson (2018); 7. Lehký et al. (2021); 8. This study derived from TESS: Ricker et al. (2015); 9. Nelson (2020a); 10. Samolyk (2020); 11. Nagai (2021).

TABLE 1. CONTINUED

ToM (HJD-2400000)	Err	Cycle No.	ETD	Ref.	ToM (HJD-2400000)	Err	Cycle No.	ETD	Ref.
58433.5673	0.0001	-942.5	0.0010	8	59168.7459	0.0001	-49.5	0.0002	8
58433.9785	0.0001	-942	0.0006	8	59169.1563	0.0001	-49	-0.0011	8
58434.3902	0.0001	-941.5	0.0006	8	59169.5691	0.0001	-48.5	0.0001	8
58434.8017	0.0001	-941	0.0005	8	59209.9100	nr	0.5	0.0009	11
58435.2135	0.0001	-940.5	0.0007	8					

a: nr=not reported.
1. Karampotsiou et al. (2016); 2. Nagai (2014); 3. Nagai (2015); 4. Nelson (2016); 5. Nelson (2017); 6. Nelson (2018); 7. Lehký et al. (2021); 8. This study derived from TESS: Ricker et al. (2015); 9. Nelson (2020a); 10. Samolyk (2020); 11. Nagai (2021).

model fit:

$$Min(HJD) = 2\,427\,531.687 + 0.82327038 \cdot E\,, \quad (1)$$

which ultimately led to the following (unweighted) least squares best-fit linear ephemeris used for all phasing:

$$MinI(HJD) = 2\,459\,209.497(6) + 0.8232692(1) \cdot E. \quad (2)$$

3. SPECTROSCOPIC OBSERVATIONS

In September of 2014, and again in September-October of 2015, we obtained a total of 12 medium-resolution ($R{\approx}10{,}000$) spectra at the Dominion Astrophysical Observatory (DAO) in Victoria, British Columbia, Canada using the 1.83-m Plaskett telescope. The spectrograph was fitted with a 21181Yb grating (1800 lines/mm and blazed at 5000 Angstroms), producing a reciprocal dispersion of approximately 10 Å/mm. The wavelength range was from 5000 to 5250 Å, and chosen to include the strong iron absorption lines at 5167.487 and 5171.595 Å. Spectra from an iron-argon lamp taken immediately before and after each stellar spectrum were used for wavelength calibration. RV standard stars were selected from the 1986 *Astronomical Almanac* (Section H42-3), many of which were also listed as suitable IAU radial velocity standard stars (Stefanik et al. 1999). These have proven to be extremely reliable and consistent with the results achieved in over 20 publications using the same 1.83-m telescope. In general, stars were selected near in spectral type (and luminosity class) to the target stars (typically A-F, luminosity class V) and as bright as possible. Typical exposures of standards (running from magnitude 2 to 8) on a 1.5-2 metre class telescope run from a few seconds to perhaps 10 or 20 min. Windows software *RaVeRe*, written by the first author and available on his website (Nelson 2013), was used for reduction. The radial velocities were determined by the broadening functions (BF) routine (Ruciński 1969, 1992, 2004) as implemented in the Windows-based software *Broad* (Nelson 2013); details regarding this procedure are provided in Nelson (2010). The elements used for all phasing are given in equation 2. A log of observations and the derived heliocentric radial velocities ($RV_{1,2}$) is presented in Table 2. The calibrated one-dimensional spectra, sorted by phase, are presented in Figure 2. To disentangle the components, Gaussian profile curve fitting was used; see Nelson (2022) for details of the procedure. Figure 3 shows the broadening peaks at phase 0.248 (top) and phase 0.758 (bottom) for the standard and target spectra as indicated in the figure captions.

Derived (heliocentric) RV values are listed in Table 2 along with the uncertainty estimate for each, the latter being the standard deviation of values from the different comparison stars. A double sinusoidal fit to the RV curves yielded the following values: $K_1 = 101.6 \pm 1.8$ km·s^{-1}, $K_2 = 205.5 \pm 4.0$ km·s^{-1}, $V_\gamma = 17.4 \pm 1.8$ km·s^{-1} (systemic velocity), and q_{sp} $(M_2/M_1) = 0.495 \pm 0.012$.

4. PHOTOMETRIC OBSERVATIONS

Photometric observations were carried out at Desert Blooms Observatory (DBO) in 2017 (November, December), 2018 (October) and in 2019 (October, December) during which a total of 1080, 997, and 1081 observations in B, V, and I_c were respectively obtained. The telescope is a 40 cm Schmidt-Cassegrain optical assembly operating at $f/6.8$; data acquisition in 2017 and 2018 was with a SBIG STT-1603; however, in 2019 a QSI 683 CCD camera was used instead (see Nelson 2020b for more details).

In Table 3, J2000 coordinates for the stars of interest are from Gaia EDR3 (Gaia Collaboration 2021) while magnitudes are taken from the AAVSO Photometric All-Sky Survey (APASS DR9; Henden et al. (2009). The colour index ($B{-}V$) of the comparison was higher than one would like; unfortunately, most candidates in the same field-of-view had similar values. The star chosen for the comparison had the advantage of close proximity on the image

TABLE 2

LOG OF DAO OBSERVATIONS AND RESULTS

DAO Image #	Mid-time HJD-2400000	Exposure (s)	Phase at Mid-exp	RV_1 ($km \cdot s^{-1}$)	RV_2 ($km \cdot s^{-1}$)
15-13226	57297.9750	2400	0.133	-50.5 (3.1)	179.7 (5.6)
15-13235	57298.0082	1804	0.174	-71.5 (3)	201.2 (9.4)
15-13082	57293.9532	1200	0.248	-81.8 (3.4)	217.7 (8.2)
14-24522	56911.9805	1200	0.278	-87.6 (7.0)	214.1 (17.8)
14-24524	56911.9952	1200	0.296	-80.9 (6.9)	214.5 (15.6)
14-24526	56912.0105	1200	0.314	-78.3 (7.0)	203.2 (16.9)
15-13254	57298.9642	2400	0.335	-67.0 (3.4)	193.3 (9.1)
15-13296	57299.9917	2400	0.583	69.8 (4.0)	...
14-24429	56909.0123	836	0.672	98.3 (8.1)	-154.7 (11.1)
14-24432	56909.0364	1200	0.702	114.7 (3.1)	-181.0 (13.2)
15-13018	57291.9030	1200	0.758	126.1 (3.1)	-192.3 (8.7)
15-13182	57296.9164	1800	0.847	104.9 (3.1)	-160.4 (4.8)

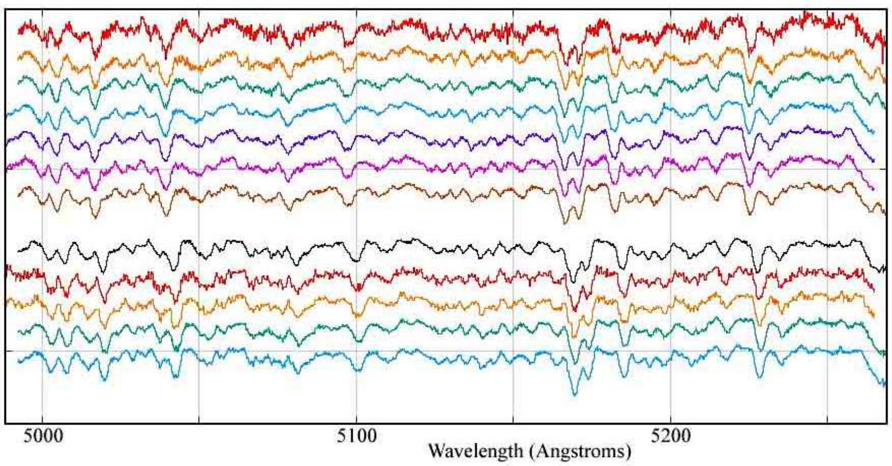

Fig. 2. V1241 Tau spectra, offset for clarity. The vertical scale is arbitrary. The phases (from top to bottom) correspond to those in Table 2, top to bottom. The colour figure can be viewed online.

and being close in brightness to the program star. For all runs, the Comp-Check difference was constant to within ≈0.01 magnitude, with no systematic variation. As described in Nelson (2020b), automatic focusing was required to accommodate the large swings in desert temperature throughout each night. The usual bias, dark subtraction, and flat fielding, as well as aperture photometry was accomplished with MIRA (`https://www.mirametrics.com/`).

5. LIGHT CURVE ANALYSIS

All light curves were normalized relative to maximum flux. RV and light curve data from this paper were simultaneously fit with the WD2003 code which implemented Kurucz atmospheres (Wilson & Devinney 1971; Wilson 1990; Kurucz 1993; Kallrath et al. 1998). This was conveniently packaged as a Windows compatible front-end program with a GUI interface ($WDwint56c$ (Nelson 2013)).

As mentioned earlier, the spectral classification assigned by Roman (1956) was A7 + F6V. Tables from Pecaut & Mamajek (2013) estimate an effective temperature for the primary star, where $T_{\rm eff1}$= 7760 (125) K and log g = 4.282 (1) (cgs); the errors correspond to differences over one-half spectral subclass. An interpolation program (Nelson 2013) provided the van Hamme (1993) limb darkening values using the logarithmic (LD=2) law and are listed in Table 4. Values for the gravity darkening exponent g = 1.00 and albedo A = 1.0, appropriate for radiative stars (Lucy 1967; Ruciński 1969), respec-

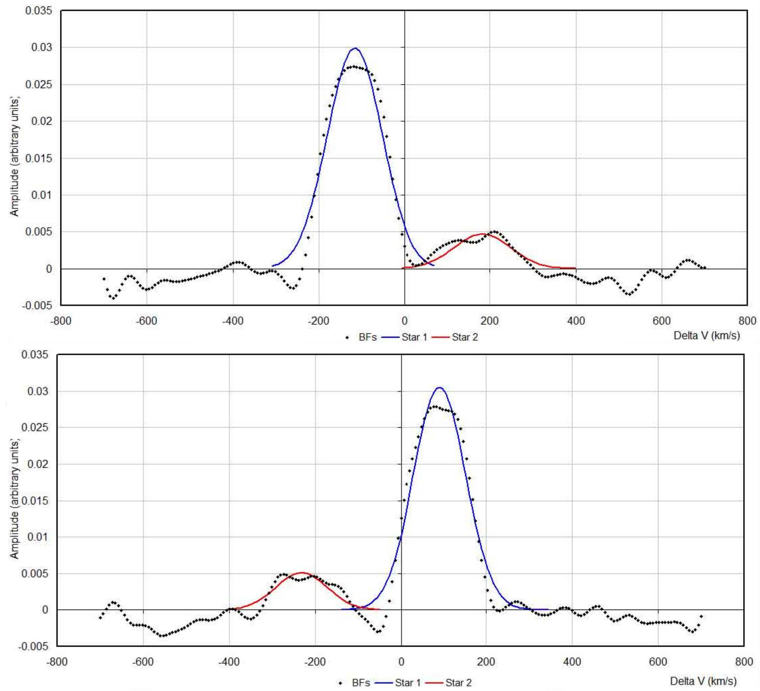

Fig. 3. Top: Broadening function for V1241 Tau at phase 0.248 and the fitted Gaussian profiles. The standard spectrum is 15-12961 (HD 187691) and the program spectrum, 15-13082. Bottom: Broadening function for V1241 Tau at phase 0.758 and the fitted Gaussian profiles. The standard spectrum is 15-12961 (HD 187691) and the program spectrum, 15-13018. The colour figure can be viewed online.

TABLE 3

V1241 TAU, COMPARISON AND CHECK STARS FOR APERTURE PHOTOMETRY

Object	GSC	RA (J2000)	Dec (J2000)	V-mag	$(B-V)$
V1241 Tau	4709-1181	03:24:23.25	-00:42:14.93	9.43	0.61 (35)
Comp.	4709-1022	03:24:28.57	-00:37:13.92	10.16 (4)	1.14 (4)
Check	4709-1298	03:24:42.57	-00:45:58.62	11.47 (1)	1.23 (2)

TABLE 4

LIMB DARKENING VALUES FROM VAN HAMME (1993)*

Band	x_1	x_2	y_1	y_2
B	0.829	0.843	0.851	0.035
V	0.719	0.795	0.791	0.152
I_c	0.506	0.656	0.639	0.205
Bol	0.673	0.635	0.647	0.174

*Based on spectral type A7, K0 for stars 1 and 2 respectively.

tively, were chosen. Model fit optimization was accomplished by differential corrections.

Final models using the TESS (2018) and land-based (2017-2019) light curves produced very similar effective temperatures for the secondary, where T_{eff2}=5087 K and 5073 K, respectively. These values are much cooler than what would be expected from its putative F6V classification (6340 K) and correspond more closely to spectral class K0. In this case, the secondary limb darkening coefficients x_2, y_2 provided in Table 4 were determined using the mean value (5080 K).

Based on the shape of the BVI$_\mathrm{c}$ light curves (Figure 4), mode 5 (classical Algol) was selected but with the understanding that other modes such as mode 2-detached, mode 4-reverse Algol, etc. would need to be checked. Initially, convergence by the method of multiple subsets was reached. The subsets were: (a, i, Ω_1, $L1$), (i, q), (T_2, Ω_1), and (a, V_γ, ϕ). However, despite multiple iterations using different starting points, the resulting fits were rather poor.

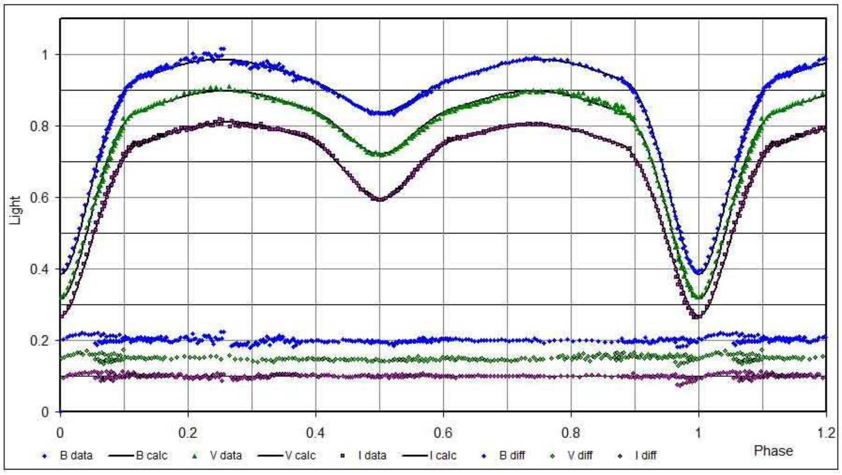

Fig. 4. Peak normalized V1241 Tau light curves from DBO with the WD results, separated by fixed offsets (0.1 light curve units). Plotted are, top to bottom: B, V, I_{c}. At the bottom of the figure, the model fit residuals are provided in the same order as the light curves. The colour figure can be viewed online.

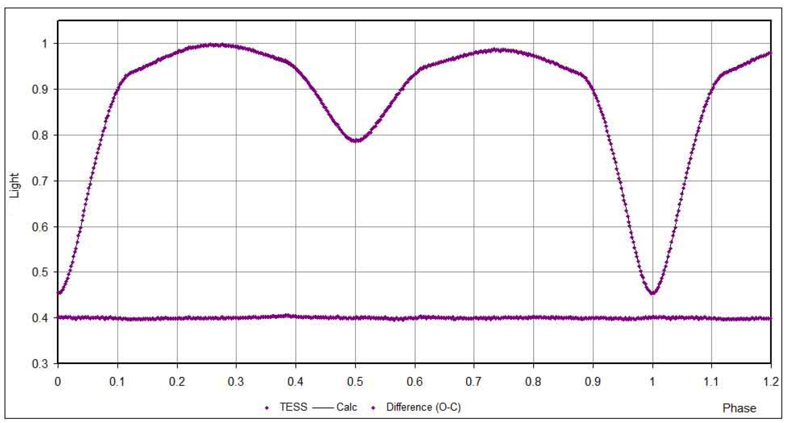

Fig. 5. Peak normalized V1241 Tau light curve and the WD results from the TESS Mission (2018). At the bottom of the figure, the residual differences between the observed and simulated light curve fits are plotted with a fixed offset (0.4). The colour figure can be viewed online.

As a consequence we turned to the light curve data taken by the TESS satellite in 2018. Parameter estimates for the best-fit TESS model are listed in Table 5 while the light curve (data and computed) are presented in Figure 5. Next, we returned to the DBO data and used the best-fit TESS parameters to get started. A reasonable fit quickly ensued with only minor adjustments required to reach an acceptable solution (Figure 4). The DBO parameters, listed in Table 5, differ only slightly from those obtained from the TESS data. The spot parameters (cool spot on the secondary star), which might be expected to change in the time interval between the two data sets, do so, but only by a small amount. Although secular analysis of minimum times (Yang et al. 2012) suggested the presence of a third gravitationally bound stellar object ($P{\approx}47.4$ y), it was not necessary to invoke a third light correction (l_3) to produce a satisfactory Roche-lobe model fit. Furthermore, no evidence for oscillation of either star in this binary system was found, thereby confirming that V1241 Tau should not be classified as an oEA system (Mkrtichian et al. 2003).

The radial velocity observations with the best double-sine curve model fit are plotted in Figure 6. This analysis yielded values for K_1 (101.6 ± 1.8 km$\cdot$s^{-1}), K_2 (205.5 ± 4.0 km$\cdot$s^{-1}) and V_γ (17.4 ± 1.8 km$\cdot$s^{-1}). When modeled without any light curve data, the spectroscopic mass ratio ($q_{\mathrm{sp}}{=}M_2/M_1$) was determined to be 0.495 ± 0.012.

TABLE 5

WILSON-DEVINNEY PARAMETERS FOR THE BEST-FIT SOLUTION FROM V1241 TAU LIGHT CURVES

WD Quantity[a]	TESS	DBO
T_{eff1} (K)[b]	7760	7760
T_{eff2} (K)	5087 (3)	5073 (8)
q ($\mathrm{m_2/m_1}$)	0.543 (2)	0.544 (1)
Ω_1	3.465 (5)	3.470 (8)
i°	80.18 (4)	79.69 (3)
a ($\mathrm{R_{\odot}}$)	5.30 (3)	5.39 (5)
V_{γ} (km·s^{-1})	18.7 (7)	18.7 (2)
$A_{\mathrm{P}} = T_{\mathrm{S}}/T_{\star}$[c]	0.832 (1)	0.855 (5)
Θ_{P}(spot co-latitude)[c]	86 (1)	92 (4)
ϕ_{P} (spot longitude)[c]	288 (1)	310 (2)
$\mathrm{r_P}$ (angular radius)[c]	19.0 (1)	14.5 (5)
$L_1/(L_1+L_2)_{\mathrm{B}}$[d]	···	0.937 (1)
$L_1/(L_1+L_2)_{\mathrm{V}}$	···	0.888 (1)
$L_1/(L_1+L_2)_{\mathrm{TESS,\ I_c}}$	0.817 (1)	0.811 (1)
r_1 (pole)	0.3389 (6)	0.3390 (9)
r_1 (point)	0.3708 (10)	0.3700 (13)
r_1 (side)	0.3499 (7)	0.3500 (10)
r_1 (back)	0.3611 (8)	0.3610 (12)
r_2 (pole)	0.3064 (3)	0.3060 (20)
r_2 (side)	0.3199 (3)	0.3200 (20)
r_2 (back)	0.3523 (3)	0.3520 (20)

[a]All uncertainty estimates for $T\mathrm{eff}_2$, q, $\Omega_{1,2}$, i, $r_{1,2}$, and L_1 from *WDwint56a* (Nelson 2013).
[b]Fixed with no error during DC.
[c]Spot parameters in degrees (Θ_{P}, ϕ_{P} and r_{P}); $\mathrm{A_P}$ equals the spot temperature (T_{S}) divided by star temperature, T_*.
[d]L_1 and L_2 refer to scaled luminosities of the primary and secondary stars, respectively.

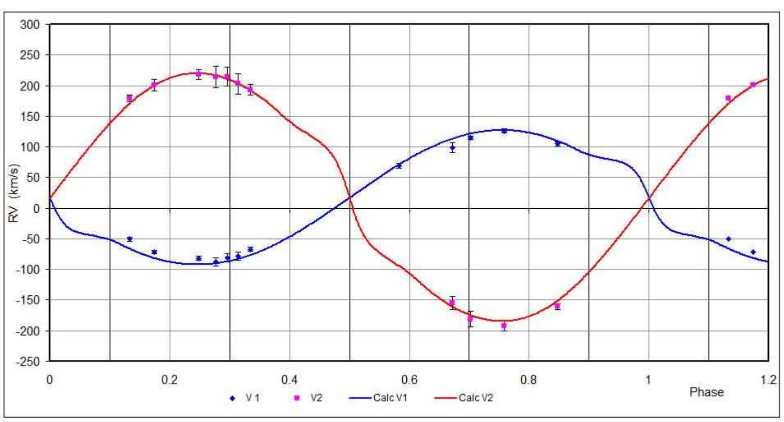

Fig. 6. V1241 Tau radial velocities and WD solution. As the computed curves from the DBO and TESS data sets were visually identical, only one RV plot is presented. The colour figure can be viewed online.

Simultaneous WD2003 analysis using the TESS data (regarded to have the least uncertainty) yielded M_1=1.91(8) $\mathrm{M_{\odot}}$, M_2=1.04(4) $\mathrm{M_{\odot}}$, R_1=1.86(1) $\mathrm{R_{\odot}}$, R_2=1.73(1) $\mathrm{R_{\odot}}$, q_{WD}=0.54(3), L_1=10.7(8) $\mathrm{L_{\odot}}$, and L_2=1.7(2) $\mathrm{L_{\odot}}$. Note that the mass ratio in Table 5 derived from combined (RV+LC) fitting differs

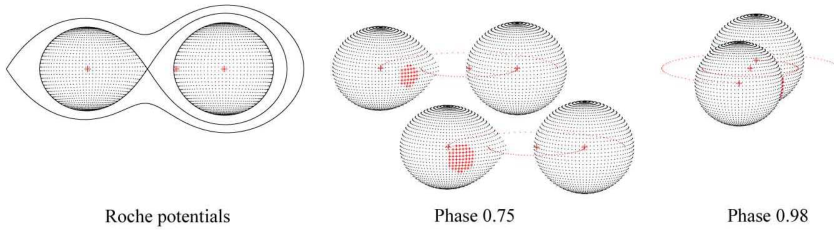

Fig. 7. Roche surface potentials and spatial representations of V1241 Tau from Binary Maker 3 showing a cool spot on the secondary star. At phase 0.75, the upper middle figure is from the DBO data (2017–2019), while the lower is from the TESS Mission (2018). The spatial orientation at phase 0.98 clearly shows the V1241 Tau is partially eclipsing. The colour figure can be viewed online.

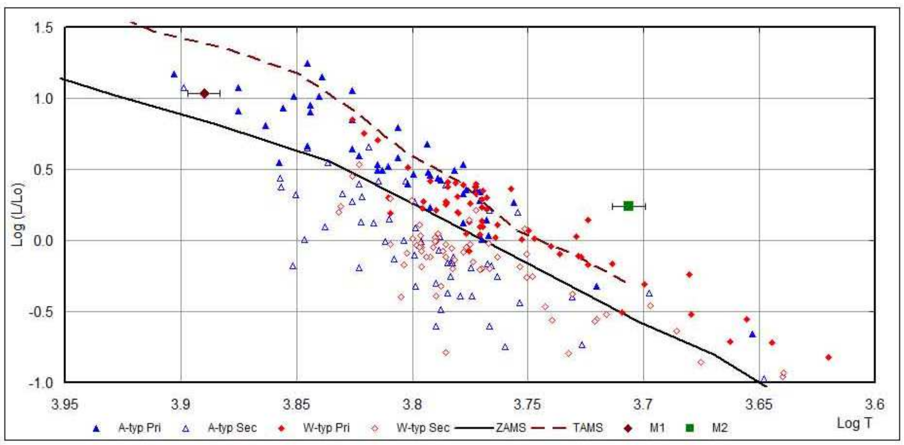

Fig. 8. log $L/\mathrm{L}_{\odot}$ vs log T plot for close binaries from Yakut and Eggleton (2005). The ZAMS (solid line) and the TAMS (dashed line) are from the evolutionary tracks of the Geneva Group (Schaller et al. 1992) when Z = 0.02 (solar-like). Results from the TESS satellite have been added: the large diamond (brown in the online version) is for the primary star while the large (green) square is for the secondary. The (half) width of each error bar is the standard deviation of the values for $T_{\mathrm{eff}1,2}$ and log $L_{1,2}$ from each solution. The colour figure can be viewed online.

somewhat from the spectroscopic mass ratio directly calculated from the K_1/K_2 ratio. This is not unexpected; however, the latter value (0.543 ± 0.002) is considered more reliable since it is derived from all the data (Wilson 1990). In any case, WD parameter uncertainty from both light curve sources are quite comparable.

A word about error estimation is appropriate here (all error values in this paper are one sigma). For the errors in K_1 and K_2, the reader should consult Alton et al. (2020). For the individual RV data points in the present data set, each RV is the mean of values obtained from eight different standards; the error estimate is simply the standard deviation of the group. Actual errors from systematic effects are obviously larger but not directly calculable. That is why the sample standard deviation (i.e., sigma divided by root n) is not used as it would imply a greater precision than what is experienced. WD2003 parameter values with associated uncertainty following Roche-lobe modeling are listed in Table 5. These are statistical values known to be smaller than the total uncertainty because the latter contains systematic experimental errors not readily determined. Spatial representations of V1241 Tau rendered with Binary Maker 3 (Bradstreet 1993) are illustrated in Figure 7.

6. EVOLUTIONARY STATUS OF V1245 TAU

We can attempt to describe the evolutionary status of this variable using our estimates for luminosity and effective temperature. These values are plotted in the theoretical Hertzsprung-Russell diagram (HRD) from Yakut & Eggleton (2005) who evaluated 72 close binary systems for which reliable data existed. Types included were low-temperature overcontact binaries, near-contact binaries and detached close binaries. A reproduction of this log $L/\mathrm{L}_{\odot}$ vs. log T plot (Figure 8) includes zero-age main sequence

(ZAMS) values for selected stars from Cox (2000), and the terminal-age main sequence (TAMS) values from the evolutionary tracks of the Geneva Group (Schaller et al. 1992) when Z = 0.02 (solar). This analysis suggests that both stars have evolved, while the secondary might be past the TAMS. Nonetheless, one should regard plots of this type with much caution, as we do not know the metallicity plus there is a fairly large degree of uncertainty with the temperatures and luminosities for this system. The error bars hint at that uncertainty.

7. CONCLUSIONS

New radial velocity and light curve data for V1241 Tau, an Algol-type binary, have been simultaneously analysed with the Wilson-Devinney (WD2003) code. There were two distinct LC datasets: One was from the TESS space satellite and the other from a land-based (Desert Blooms) observatory. The RV data alone yielded results for K_1 (101.6 ± 1.8 km·s^{-1}), K_2 (205.5 ± 4.0 km·s^{-1}), RV_γ (17.4 ± 1.8 km·s^{-1}), and q_{sp} (0.495 ± 0.012). Simultaneous analyses (RV+LC) using the TESS data resulted in the best estimates for M_1 (1.91 ± 0.08 $\mathrm{M}_\odot$), M_2 (1.04 ± 0.04 $\mathrm{M}_\odot$), R_1 (1.86 ± 0.01 $\mathrm{R}_\odot$), R_2 (1.73 ± 0.01 $\mathrm{R}_\odot$), q_{WD} (0.54 ± 0.03), L_1 (10.7 ± 0.8 $\mathrm{L}_\odot$), and L_2 (1.7 ± 0.02 $\mathrm{L}_\odot$). Simultaneous analysis with the DBO data yielded similar parameter values but often with greater uncertainties. Evolutionary analysis using an HRD model from Yakut and Eggleton (2005) suggested that the primary star in V1241 Tau is somewhat evolved past the zero age main sequence (ZAMS) while the secondary has evolved past the terminal age main sequence (TAMS). This is typical behaviour for many Algol-type binaries.

This research has made use of the SIMBAD database operated at Centre de Données astronomiques de Strasbourg, France. This work also presents results from the European Space Agency (ESA) space mission Gaia. Gaia data are being processed by the Gaia Data Processing and Analysis Consortium (DPAC). Funding for the DPAC is provided by national institutions, in particular those participating in the Gaia MultiLateral Agreement (MLA). The Gaia mission website is https://www.cosmos.esa.int/gaia, while the Gaia archive website is https://archives.esac.esa.int/gaia. This paper also makes use of TESS data obtained from the Mikulski Archive for Space Telescopes (MAST) at the Space Telescope Science Institute. STScI is operated by the Association of Universities for Research in Astronomy, Inc., under NASA contract NAS5-26555. Support to MAST for these data is provided by the NASA Office of Space Science via grant NAG5-7584 and by other grants and contracts. It is a pleasure to thank the staff members at the DAO (David Bohlender, Dmitry Monin) for their usual splendid help and assistance. Thanks are also due to Environment Canada for the website satellite images (https://weather.gc.ca/canada_e.html) that were essential in predicting clear times for observing runs in this cloudy locale, and to Attilla Danko and Allan Rahill of the CMC for their Clear Sky Chart (http://cleardarksky.com/). The diligence and dedication shown by all associated with these organizations is very much appreciated.

REFERENCES

Alton, K. B., Nelson, R. H., & Stępień, K. 2020, JApA, 41, 26, https://doi.org/10.1007/s12036-020-09641-y

Andrych, K. D. & Andronov, I. L. 2019, OEJV, 197, 65, https://doi.org/10.48550/arXiv.1812.06949

Andrych, K. D., Andronov, I. L., & Chinarova, L. L. 2020, JPhSt, 24, 1902, https://doi.org/10.30970/jps.24.1902

Arentoft, T., Lampens, P., van Cauteren, P., et al. 2004, A&A, 418, 249, https://doi.org/10.1051/0004-6361:20034543

Bradstreet, D. H. 1993, IAUS 151, Light Curve Modelling of Eclipsing Binary Stars, 151

Caldwell, D. A. 2020, RNAAS, 4, 201, https://doi.org/10.3847/2515-5172/abc9b3

Cox, A. N. 2000, Allen's Astrophysical Quantities, (New York, NY: Springer-Verlag)

Eastman, J., Siverd, R., & Guadi, B. S. 2010, PASP, 122, 935, https://doi.org/10.1086/655938

Gaia Collaboration et al. 2021, A&A, 649, 1, https://doi.org/10.1051/0004-6361/202039657

Gaposchkin, S. 1953, AnHar, 113, 67

Giuricin, G. & Mardirossian, F. 1981, A&AS, 45, 85

Henden, A. A., Welch, D. L., Terrell, D., & Levine, S. E. 2009, AAS, 41, 669

Hoffmeister, C. 1934, AN, 251, 19, https://doi.org/10.1002/asna.19342510203

Jensch, A. 1934, AN, 251, 327, https://doi.org/10.1002/asna.19342512104

Kallrath, J., Milone, E. F., Terrell, D., & Young, A. T. 1998, ApJ, 508, 308, https://doi.org/10.1086/306375

Karampotsiou, E., Gazeas, K., Petropouou, M., & Tzouganatos, L. 2016, IBVS, 6158, 1

Kazarovets, E. V., Samus, N. N., Durlevich, O. V., Kireeva. N. N., & Pastukhova, E. N. 2006, IBVS, 5721, 1

Kholopov, P. 1982, New catalogue of stars suspected of variability containing data on 14810 variable stars which have not received definite nomenclature until 1980 (Moskva: Nauka)

Kurucz, R. L. 1993, IAUCB 21, Light Curve Modeling of Eclipsing Binary Stars, 93, (New York, NY: Springer)
Lehký, M., Hoňková, K., Šmelcer, L., et al. 2021, OEJV, 211, 11, https://doi.org/10.5817/OEJV2021-0211
Lucy, L. B. 1967, ZA, 65, 89
Mkrtichian, D. E., Nazarenko, V., Gamarova, A. Y., et al. 2003, ASPC 292, Interplay of Periodic, Cyclic and Stochastic Variability in Selected Areas of the H-R Diagram, ed. C. Sterken (San Francisco, CA: ASP), 113
Nagai, K. 2014, VSOLJ Variable Star Bulletin, 56, 1
__________. 2015, VSOLJ Variable Star Bulletin, 59, 6
__________. 2021, VSOLJ Variable Star Bulletin, 69, 12
Nelson, R. H. 2010, Spectroscopy for Eclipsing Binary in The Alt-Az Initiative, Telescope Mirror & Instrument Developments, ed. R. M. Genet, J. M. Johnson, & V. Wallen (Santa Margarita, CA: Collins Foundation Press)
__________. 2013, Software, http://binaries.boulder.swri.edu/binaries/
__________. 2016, IBVS, 6164, 1
__________. 2017, IBVS, 6195, 1
__________. 2018, IBVS, 6234, 1
__________. 2020a, JAVSO, 48, 169
__________. 2020b, NewA, 77, 101362, https://doi.org/10.1016/j.newast.2020.101362
__________. 2022, RMxAA, 58, 223, https://doi.org/10.22201/ia.01851101p.2022.58.02.05
Pecaut, M. J. & Mamajek, E. E. 2013, ApJ, 208, 9, https://doi.org/10.1088/0067-0049/208/1/9
Pickering, E. C. 1908, AN, 178, 157, https://doi.org/10.1002/asna.19081781003
Pojmanski, G. 2003, AcA, 53, 341
Ricker, G. R., Winn, J. N., Vanderspek, R., et al. 2015, JATIS, 1, 014003
Roman, N. G. 1956, ApJ, 123, 246, https://doi.org/10.1086/146155
Russo, G. & Milano, L. 1983, A&AS, 52, 31
Ruciński, S. M. 1969, AcA, 19, 245
__________. 1992, AJ, 104, 1968, https://doi.org/10.1086/116372
__________. 2004, IAUS 215, Stellar Rotation, ed. A. Maeder & P. Eenens (San Francisco, CA: IAUS, 17)
Samolyk, G. 2020, JAVSO, 48, 87
Samus N. N., Kazarovets E. V., Durlevich O. V., Kireeva, N. N., & Pastukhova, E. N. 2017, ARep, 61, 80, https://doi.org/10.1134/S1063772917010085
Sarma, M. B. K. & Abhyankar, H. D. 1979, Ap&SS, 65, 443, https://doi.org/10.1007/BF00648509
Schaller, G., Schaerer, D., Meynet, G., & Maeder, A. 1992, A&AS, 96, 269
Stefanik, R. P., Latham, D. W., & Torres, G. 1999, ASPC 185, Precise Stellar Radial Velocities, ed. J. B. Hearnshaw & C. D. Scarfe, 354
Srivastava, J. B. & Kandpal, C. D. 1986, Ap&SS, 121, 301, https://doi.org/10.1007/BF00653701
Terrell, D. 2022, Galaxies, 10, 8, https://doi.org/10.3390/galaxies10010008
Terrell, D. & Wilson, R. W. 2005, Ap&SS, 296, 221, https://doi.org/10.1007/s10509-005-4449-4
van Hamme, W. 1993, AJ, 106, 2096, https://doi.org/10.1086/116788
Wilson, R. E. & Devinney, E. J. 1971, ApJ., 166, 605, https://doi.org/10.1086/150986
Wilson, R. E. 1990, ApJ, 356, 613, https://doi.org/10.1086/168867
Yakut, K. & Eggleton, P. P. 2005, ApJ, 629, 1055
Yang, Y.-G., Zhang, X.-B., Li, H.-L., & Dai, H. F. 2012, AJ., 144, 136, https://doi.org/10.1088/0004-6256/144/5/136

Kevin B. Alton: Desert Blooms Observatory, 70 Summit Ave., Cedar Knolls, AZ, USA (mail@underoakobservatory.com).
M. Kendurkar: Dominion Astrophysical Observatory, 5071 W Saanich Rd, Victoria, BC V9E 2E7, Canada.
R. H. Nelson: Mountain Ash Observatory, 1393 Garvin Street, Prince George, BC, Canada, V2M 3Z1.

Revista Mexicana de Astronomía y Astrofísica, **59**, 213–258 (2023)

https://doi.org/10.22201/ia.01851101p.2023.59.02.06

SDSS-IV MANGA: THE RADIAL DISTRIBUTION OF PHYSICAL PROPERTIES WITHIN GALAXIES IN THE NEARBY UNIVERSE

J. K. Barrera-Ballesteros[1], S. F. Sánchez[1], C. Espinosa-Ponce[1], C. López-Cobá[2], L. Carigi[1], A. Z. Lugo-Aranda[1], E. Lacerda[1], G. Bruzual[3], H. Hernandez-Toledo[1], N. Boardman[4], N. Drory[5], Richard R. Lane[6], and J. R. Brownstein[7]

Received May 26 2022; accepted May 25 2023

ABSTRACT

Using the largest sample of galaxies observed with an optical integral field unit (IFU, the SDSS-IV MaNGA survey, ≈10000 targets), we derive the radial distribution of the physical properties obtained from the stellar continuum and the ionized-gas emission lines. Given the large sample, we are able to explore the impact of the total stellar mass and morphology by averaging those radial distributions for different bins of both global properties. In general, we find that most of the properties exhibit a negative gradient, with a secondary impact by global properties. Our results confirm the intimate interplay between the properties of the stellar component and those of the ionized gas at local (kpc) scales to set the observed radial gradients. The resemblance of the gradients for similar global properties indicates statistical similar histories of star formation and chemical enrichment, with an initial radial gas distribution following the potential of the galaxy.

RESUMEN

Usando la muestra más grande de galaxias con observaciones espacialmente resueltas (el cartografiado SDSS-IV MaNGA, ≈10000 objetos) estimamos las distribuciones radiales de las propiedades obtenidas a través del continuo y de las líneas de emisión del espectro óptico. La muestra permite explorar el impacto que parámetros como la masa estelar total y la morfología tienen en los gradientes. De manera general, encontramos que la mayoría de las propiedades muestran un gradiente cuya pendiente es negativa con un impacto secundario de la masa estelar y la morfología. Nuestros resultados confirman la relación entre las propiedades de las estrellas con el gas ionizado a escalas locales (kpc), las cuales fijan los perfiles radiales observados. Las similitud entre gradientes para galaxias con propiedades similares indican historias de formación estelar y enriquecimiento químico parecidas con una distribución inicial de gas que sigue el potencial de la galaxia.

Key Words: galaxies: fundamental parameters — galaxies: stellar content — surveys — techniques: spectroscopic

1. INTRODUCTION

Projected on the sky, galaxies are spatially resolved objects. To truly assess the physical processes that drive the galaxy formation and evolution it is necessary to measure their observables in a spatially-resolved fashion. One of the most well-known techniques to estimate structural properties of a galaxy is through the measurement and fitting of its surface brightness radial profile (e.g., de Vaucouleurs 1958; Sersic 1968; Freeman 1970; Kormendy 1977; Kent 1985). In general, the surface brightness (from broad-band photometry) decreases with radius, in-

[1]Universidad Nacional Autónoma de México, Instituto de Astronomía, CDMX, México.
[2]Institute of Astronomy and Astrophysics, Academia Sinica, Taipei, Taiwan.
[3]IRyA, Universidad Nacional Autónoma de México, Campus Morelia, Michoacán, México.
[4]School of Physics and Astronomy, University of St Andrews, UK.
[5]University of Texas at Austin, McDonald Observatory, Austin, TX, USA.
[6]Centro de Investigación en Astronomía, Universidad Bernardo O'Higgins, Santiago, Chile.
[7]Department of Physics and Astronomy, University of Utah, UT, USA.

dicating that the amount of stars is larger in the central regions of galaxies.

Similarly, there are studies exploring the radial profiles of the Hα emission line using narrow-band filters (e.g., Martin & Kennicutt 2001; Bigiel et al. 2008). Although the Hα emission usually is small in the outskirts in comparison to central regions, these studies showed that not for all galactocentric distances the Hα emission monotonically decreases with radius. Long-slit spectroscopy has also been a powerful tool to measure the radial distributions of physical properties from both the stellar continuum and the ionized gas emission lines (e.g., Pagel & Edmunds 1983; Peletier 1989). Through the analysis of different features of the stellar absorption lines and emission lines, such studies have provided a new way to estimate physical properties from each component at different galactocentric distances (e.g., stellar ages, and metallicities; star-formation rates, oxygen abundances, among many others).

Despite these significant efforts, these studies have been performed in samples of galaxies targeted to explore a specific scientific goal. Furthermore, the above techniques do not fully capture the angular distribution of the observables from both components. These issues have been successfully overcome thanks to large samples of galaxies observed using the Integral Field Spectroscopy (IFS) technique. This observational technique allows to obtain spectra for different positions of a galaxy across its optical extension. Thus, for each of the physical parameters derived from spectroscopy, it is possible to estimate a two-dimensional distribution. Different collaborations have acquired IFS datacubes for large samples of galaxies (e.g., Sánchez et al. 2012; Croom et al. 2012, CALIFA, and SAMI). Of particular interest is the MaNGA survey included in the SDSS-IV collaboration (Bundy et al. 2015). This collaboration has recently achieved its goal to observe a sample of 10000 galaxies using an integral field unit (IFU). Given the large sample probed by these surveys, they have unveiled the radial distribution of physical properties for a wide demographic range of galaxies in the local universe for both the stellar and ionized gas components. In particular, these surveys allow us to quantify the impact that global and structural parameters, such as the total stellar mass or the morphology, have in modulating the slopes and absolute values of those radial profiles (see Sánchez 2020, and references therein).

In this study we explore the radial distribution of physical parameters from the stellar and ionized gas component using the entire MaNGA dataset. Our goal is to quantify the impact that global parameter have in shaping the radial profiles of those properties. Furthermore, to give a more accurate description than a single gradient for those profiles will provide, we make use of a piece-wise analysis which allows us to measure different slopes and breaks for a given radial distribution of a physical property. In § 2 we provide a brief description of the MaNGA sample, the IFU datacubes, and the analysis pipeline used to estimate the map for a given observable. In this section we describe the criteria to select a set of the closest galaxies with the best spatial coverage and physical spatial resolution from which we will derive their radial profiles (known as *Golden Sample*). We also describe the piece-wise analysis to measure the slopes of those profiles. In § 3 and § 4 we present the piece-wise analysis of the radial distribution of the properties derived from the stellar and ionized gas components, respectively. In § 5 we present the radial distribution of the line-of-sight velocity and velocity dispersion from both components, as well as comparisons between them. In § 6 we compare the results from § 3 and § 4 with those using the entire sample of MaNGA galaxies (excluding only highly-inclined targets, ≈ 7000 galaxies). Finally, in § 8 we summarize our main results and conclusions.

2. SAMPLE, DATACUBES, AND ANALYSIS

2.1. *The MaNGA Survey*

The MaNGA survey (Bundy et al. 2015) was part of the forth generation of surveys included in the Sloan Digital Sky Survey (SDSS-IV, Blanton et al. 2017). The goal of this spectroscopic survey was to obtain datacubes in the optical for more than 10000 galaxies via IFU observations. The final sample includes galaxies observed from March of 2014 to September of 2020 (10245 unique datacubes). This sample is publicly available in the final data release of the SDSS-IV surveys (Abdurro'uf et al. 2021). For this study we use the latest MaNGA data release (v3.1.1). In this section we provide a brief description of the most relevant features of this survey.

Observations for the MaNGA survey took place at the Apache Point Observatory using its 2.5-m telescope (Gunn et al. 2006). This survey used two spectrographs from the BOSS survey (Baryon Oscillation Spectroscopic Survey, Smee et al. 2013). These spectrographs achieve a nominal spectral resolution of $R \equiv \lambda/\Delta\lambda \approx 1900$ covering a large portion of the optical spectra (from 3000 to 10000 Å). These spectrographs were fed by joined fibers in bundles distributed in a hexagon-like array. The number of fibers in a given bundle varies from 19 to 127. Given

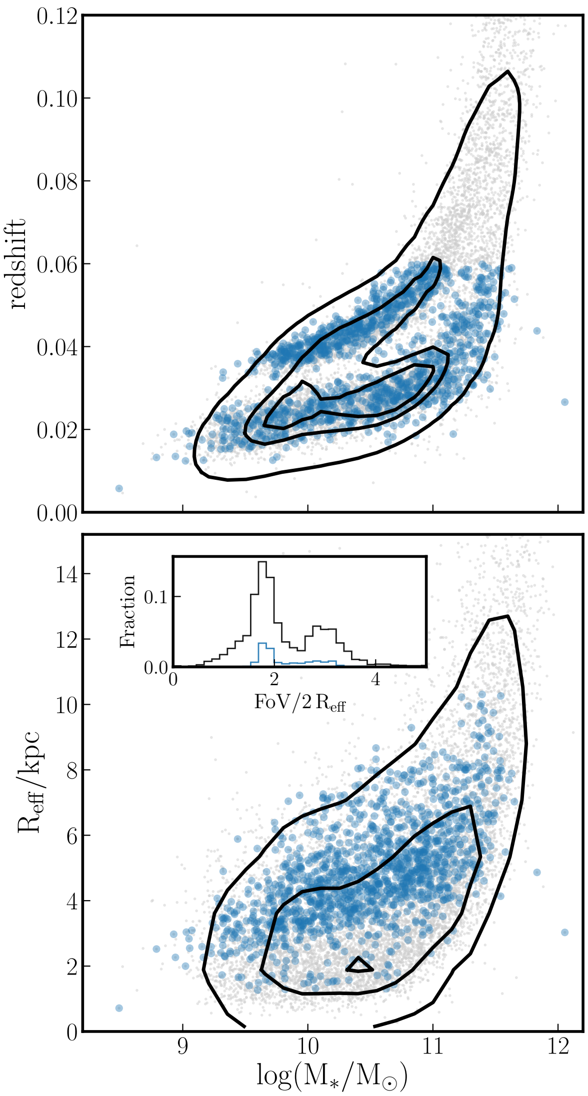

Fig. 1. Comparing the Golden Sample (GS) with its parent, the MaNGA sample according to their distance (redshift), size ($R_{\rm eff}$) and stellar mass, M_* (top and bottom panels, respectively). The gray points represent the entire MaNGA survey, while the contours enclose 90%, 80%, and 50% of this sample. The blue circles represent the GS. The inset in the bottom panel shows the distribution of the radial coverage of both samples. The spatial-resolution criteria required to drawn the GS reduces its size to ≈10% the entire MaNGA survey (see details in § 2.2). The color figure can be viewed online.

that the diameter of each fiber is $\approx 2.5''$, thus the field-of-view (FoV) varies from $12''$to $32''$. A detailed description of the instrumentation of the survey can be found in Drory et al. (2015). The reader is refereed to Law et al. (2016) for a detailed explanation of the data strategy (acquisition, reduction, etc). The MaNGA reduction pipeline includes wavelength calibration, corrections from fiber-to-fiber transmission, subtraction of the sky spectrum and flux calibration (Yan et al. 2016). The final product is a datacube with x and y coordinates corresponding to the sky coordinates and the z-axis corresponds to the wavelength. As result for each datacube, the spaxel size is $0.5''$ with a spatial resolution of $2.5''$ corresponding to a mean physical scale of $\approx$ 2 kpc.

In Figure 1 the contours show the distribution of the entire MaNGA sample in three fundamental parameters, their redshift (z), size ($R_{\rm eff}$), and total stellar mass (M_*)[8]. From the top panel of Figure 1 it is evident that this sample covers both a wide range in redshift and M_* ($0.01 < z < 0.14$ and $9.0 < \log(M_*/{\rm M}_\odot) < 11.5$, respectively). A wide coverage of redshift implies a large dynamical range in the physical spatial resolution of the survey. The strong correlation between these two parameters is also clear: massive galaxies are located further away from us than low-mass galaxies. Furthermore, the MaNGA sample shows a bimodality in this plane. This is a result of the intrinsic selection criteria of the survey where $\approx 2/3$ of the sample is selected in a way that for each galaxy the fiber bundle covers at least 1.5 $R_{\rm eff}$, for the remaining fraction of the sample, the bundle covers $\approx$ 2.5 $R_{\rm eff}$ for each galaxy. Thus, to satisfy this criterion, for a given range of M_* the sample has a fraction of galaxies closer and another further away from us. The bottom panel of Figure 1 shows an expected behavior of $R_{\rm eff}$ with M_*: massive galaxies are bigger in comparison to low-mass ones. The distribution of the FoV weighted by $R_{\rm eff}$ shows the bimodality presented in the z-M_* plane (see inset in bottom panel of Figure 1). The reader is addressed to Wake et al. (2017) for a detailed description of the selection criteria for the MaNGA survey.

The statistical strength of this survey allows us to explore not only the spatially resolved properties of individual galaxies but also their integrated properties. In Figure 2 we show the integrated star formation rate (SFR) against the M_* for the entire MaNGA sample (black contours and gray points). The distribution of this sample in the SFR-M_* plane shows the bimodality observed in larger samples of galaxies using integrated properties. We note that a significant fraction of galaxies are located in the so-called 'Star-Formation Main Sequence' (SFMS, e.g., Brinchmann et al. 2004; Renzini & Peng 2015), that

[8]A full description of the integrated properties derived from the IFU datacubes for the entire MaNGA survey is presented in Sanchez et al. (submitted).

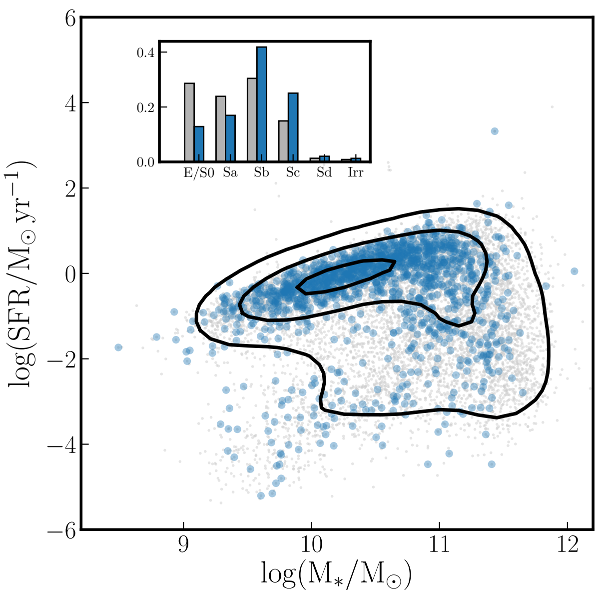

Fig. 2. Comparison of the Golden Sample and the entire MaNGA sample in the SFR-M_* plane. As in the previous figure, the blue points represent the golden sample whereas the gray points and the contours represent the MaNGA sample. The blue bars in the histogram in the inset shows the number of galaxies for a given morphology for the golden sample while the gray bars show the morphological distribution for the entire sample. Given our selection criteria from the golden sample, it includes a significant fraction of star-forming Sb galaxies in comparison to the MaNGA sample. The color figure can be viewed online.

is, galaxies that actively form new stars. The remaining fraction of the sample occupy the so-called 'Retired-Galaxies Sequence' (RGS), galaxies with little or no formation of new stars, and the so-called Green Valley, that is, galaxies located in the middle of the SFMS and the RGS in the SFR-M_* plane. Finally, when we study the morphological distribution of the MaNGA survey we find that this sample covers a wide range of morphological types from early to late types (see inset in Figure 2). In a dedicated article on the integrated properties of the MaNGA survey, Sanchez et al. (submitted) present a detailed description and analysis of the above properties.

2.2. *Sample Selection: The Golden Sample*

The main goal of this work is to explore the radial distribution of the properties of galaxies using the MaNGA survey. Therefore, we require to have a sample in which the fiber bundle of the MaNGA instrumentation provides a good spatial coverage for each of the galaxies in the sample (Ibarra-Medel et al. 2019). From the MaNGA sample we select a sub-sample of galaxies according to the following criteria: (*i*) galaxies observed with the largest fiber bundles (i.e., 91 and 127 fibers); (*ii*) the effective diameter of the galaxy (i.e., 2 $R_{\rm eff}$) has to be larger than 2 times the spatial resolution (≈5″); (*iii*) the FoV has to cover at least 3.5 times the effective diameter (this is motivated from the distribution of the sample in the coverage of the MaNGA FoV, see inset in Figure 1); (*iv*) the major/minor axis ratio has to be smaller than 0.45; and (*v*) the redshift of the galaxy has to be in the range $0.005 < z < 0.06$. The above selection criteria ensure that we select galaxies with a reliable coverage of the galaxy as well as a significant independent data within each galaxy. In particular, the selection criteria (*v*) ensures that within this sample we are considering a consistent physical spatial resolution and that the evolution of the galaxies is similar. These criteria yield a final sample of 1347 galaxies, representing ≈ 13% of the total MaNGA sample. We are referring to this sample in this article as the *Golden Sample (GS)*. Although we could impose more restrictive selection criteria to obtain the GS, this would lead to a sub-sample that it is not representative of the entire MaNGA population.

We overplot the GS in Figures 1 and 2 (blue circles). We note that in general the GS follows similar trends as those observed by the entire MaNGA sample. In Figure 1, the GS shows a bimodality in the redshift-M_* plane and an increment of $R_{\rm eff}$ as M_* increases. It is also clear the cut on redshift from the GS is due to our selection criteria. In the inset of the bottom panel of Figure 1 we compare the spatial coverage of the GS with respect to its parent sample. The GS follows the distribution of the MaNGA sample. However, given our constrains to have both a reliable spatial coverage and good spatial sampling, its size is heavily reduced in comparison to the total sample of the MaNGA survey. In § 6 we explore the impact of deriving the azimuthal-averaged radial distributions using the entire low-inclined MaNGA sample.

2.3. PYPIPE3D: *The Data-Analysis Pipeline*

To analyze the large amount of datacubes provided from the MaNGA survey we use the PYPIPE3D analysis pipeline (Lacerda et al. 2022). This is an update in python language of the FIT3D and PIPE3D software and analysis pipeline (Sánchez et al. 2015, 2016) with significant improvements. Here we highlight the main features of this pipeline, while in Sanchez et al. (submitted) we provide a detailed description of the use of this pipeline for the entire MaNGA dataset.

In a nutshell, the PYPIPE3D analysis pipeline disentangles the contributions of the stars and the ionized gas emission in the observed spectrum for each spaxel for each datacube. To obtain the contribution from the stellar component, the pipeline provides the best fit of the continuum using a linear combination of single-stellar populations (SSPs) spectra. To account for the line-of-sight velocity distribution function (LOSVD) first and second moments (i.e., the systemic stellar velocity, $V_{\rm los}$, and the stellar velocity dispersion, σ) the set of SSPs is shifted and convolved with a Gaussian function, as well as dust attenuated, adopting a Cardelli extinction curve (Cardelli et al. 1989). Details on how PYPIPE3D estimates $V_{\rm los}$ and σ are described in Sánchez et al. (2015, 2016). The decomposition of the stellar continuum in different SSPs of a spectrum provides fundamental parameters of the stellar component. Thus, for each datacube PYPIPE3D provides two-dimensional distributions (or maps) of the derived properties as well as their uncertainties. Among the many properties derived from the stellar continuum (see § 5 in Sanchez et al., submitted), we use in this study the maps of the following properties: the mass-to-light ratio (M/L), stellar mass density (Σ_*), the luminosity-weighted stellar age and metallicity (Age, [Z/H]), the dust attenuation ($\mathrm{Av_{SSP}}$), and the systemic stellar velocity ($V_{\rm los}$) and velocity dispersion (σ). Once the stellar continuum has been modeled by the SSPs for each datacube, it is removed from the observed datacube. This continuum-free datacube is thus used to estimate the properties from the emission lines. PYPIPE3D pipeline provides a moment analysis to derive the physical properties for a large set of emission lines. For each emission line, the pipeline provides the map of its integrated flux, its systemic velocity, its velocity dispersion, and its equivalent width. We use these properties to build the radial profiles presented in this study for both the stellar and the ionized gas components.

2.4. *Radial Profiles and Gradients*

From the two-dimensional map of each galaxy's parameter derived by PYPIPE3D we build its azimuthal-average radial profile. This procedure is performed for the entire MaNGA survey. For each map in each galaxy we make radial bins of 0.15 $R_{\rm eff}$ width up to $\approx$3 $R_{\rm eff}$. Projected in the sky each of these bins is an elliptical annulus centered on the optical (V-band) brightest region, with an ellipticity and position angle drawn from the NSA survey (Blanton et al. 2011). In Figure 3 we plot as example the radial distribution of the stellar mass surface density, Σ_*, for the MaNGA GS. Instead of plotting the radial gradients for individual galaxies, we plot for each morphological type (each panel in Figure 3) the median radial distribution for different bins of total stellar mass (each shaded area colored in Figure 3). The borders of those shaded areas show the 1-σ distribution for each galactocentric distance. To ensure a reliable estimation of the radial gradient we select those radial bins with good signal-to-noise ratio in the continuum (SNR > 3) for stellar-derived properties, whereas for the emission-line-derived measurements, besides using a SNR cut in the continuum, we also impose a SNR cut in the Hα line (SNR > 2). Furthermore, when calculating the median value for each morphology - stellar mass bin we exclude those radial bins where there are less than ten measurements.

As in other studies exploring the radial profiles of galaxy's properties (e.g., Sánchez-Menguiano et al. 2018), we note that a single-slope gradient for a large fraction of radial distributions is not accurate to describe them. In other words, to provide a proper description on how the physical properties of galaxies change at different galactocentric distances, it is required to use a procedure that fits more than one gradient. To account for these different variations in slopes we fit those radial distributions with a two-piece function. We fit the following functional form for a given radial profile $P(r)$:

$$P(r)=\begin{cases} P_0+k_0(r/R_{\rm eff}), & r/R_{\rm eff}\le r_0; \\ P_{\rm ini}+k_1(r-r_0/R_{\rm eff}), & r_0\le r/R_{eff}\le r_1; \\ P_{\rm med}+k_2(r-r_1/R_{\rm eff}), & r_1\le r/R_{\rm eff}; \end{cases} \quad (1)$$

where $P_{\rm ini}=P_0+k_0(r_0/R_{\rm eff})$ and $P_{\rm med}=P_{\rm ini}+k_1(r_1-r_0/R_{\rm eff})$. The solid lines in Figure 3 represent the best fit of equation 1 for each radial distribution of Σ_*. Although we intended to constrain this fit to the typical size of the IFU ($\approx r/R_{\rm eff}<2.5$), the piece-wise analysis provided an $r_0/R_{\rm eff}$ larger than 2.5. In turn, this suggests that the entire radial profile is well described by a single slope. It is evident that this functional form provides an accurate representation of the radial distribution for each morphology and stellar mass bin. In Appendix A we show the radial distribution, as well as the best-fit gradients, using equation 1 for the set of parameters explored using the MaNGA GS.

In the next sections (§ 3 and § 4), we present the best-fit parameters using equation 1 (i.e., the slopes of each line: k_0, k_1, k_2, and the break radius: r_0,

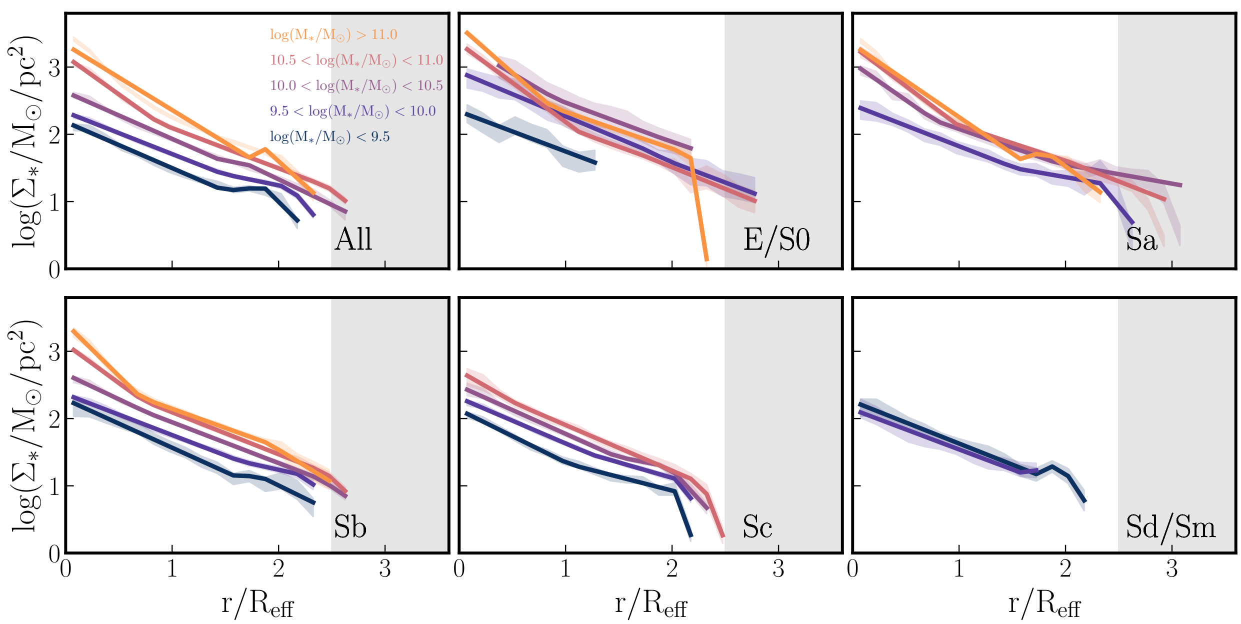

Fig. 3. The average radial distribution of the stellar mass density, Σ_*, as an example of the radial distribution of the physical properties derived for the GS of the MaNGA sample. The gradients are averaged by morphology (panels from left to right and top to bottom) and total stellar mass bins (shaded colored areas; each color represents a stellar mass bin see the legend in the top-left panel). The gray shaded area in each panel represent the typical maximum radius covered by the FoV ($R_{eff} \approx 2.5$). The solid lines in each panel represent the best fit derived from fitting a piecewise function to the radial distribution (see details in § 2.4). The color figure can be viewed online.

r_1), the differences between these slopes (Δ slope), and the value of each parameter at $R_{\rm eff}$. For the slopes as well as for the values derived at $R_{\rm eff}$ we show the uncertainty derived from the best fit. In general we find that the trends presented below for k_0, and k_1 with respect to the stellar mass are reliable in the sense that the uncertainties of these parameters are small in comparison to those trends. On the other hand, we find significantly large uncertainties for the outermost slope k_2, suggesting that the trends with respect to the stellar mass are not reliable. To avoid spurious results, in the following analysis we exclude those slopes derived where the range in galactocentric distance is smaller than $r/R_{\rm eff} < 0.3$ (i.e., $r_0 < 0.3$, and $r_1 - r_0 < 0.3$). This criteria exclude those slopes where the radial range is comparable to the size of the MaNGA PSF. We show for each of these parameters the variation with morphology for the different stellar mass bins (see as example Figure 4). When required, we also consider the uncertainties of these parameters in describing the observed trends. In other words, we describe these trends taking into account the associated error for each bin of stellar mass and morphology.

3. STELLAR PROPERTIES

3.1. *The M/L Ratio, and Stellar Mass Surface Density,* Σ_*

As we mention above, galaxies show in general a decreasing radial distribution of their surface brightness in the optical(e.g., de Vaucouleurs 1958; Sersic 1968; Freeman 1970; Kormendy 1977). These surface brightness profiles are correlated mainly with the amount of stars that produce the observed flux via the mass-to-light ratio, M/L (e.g., Portinari & Salucci 2010). In Figure 33 we plot the median values of the M/L ratio for different morphologies and stellar masses, whereas in Figure 4 we summarize the best-fit parameters derived from the piece-wise analysis. From this analysis we find that the central slope, k_0, has mostly negative values and decreases with the total stellar mass – with little variation with respect to the morphology. Except for the Sb type, our analysis is not able to detect a significant value of k_1. For Sb galaxies the best-fit values of k_1 are negative and increase with M_* (except for most massive galaxies). For the outermost parts of the galaxies, the gradient of the M/L ratio, k_2, varies depend-

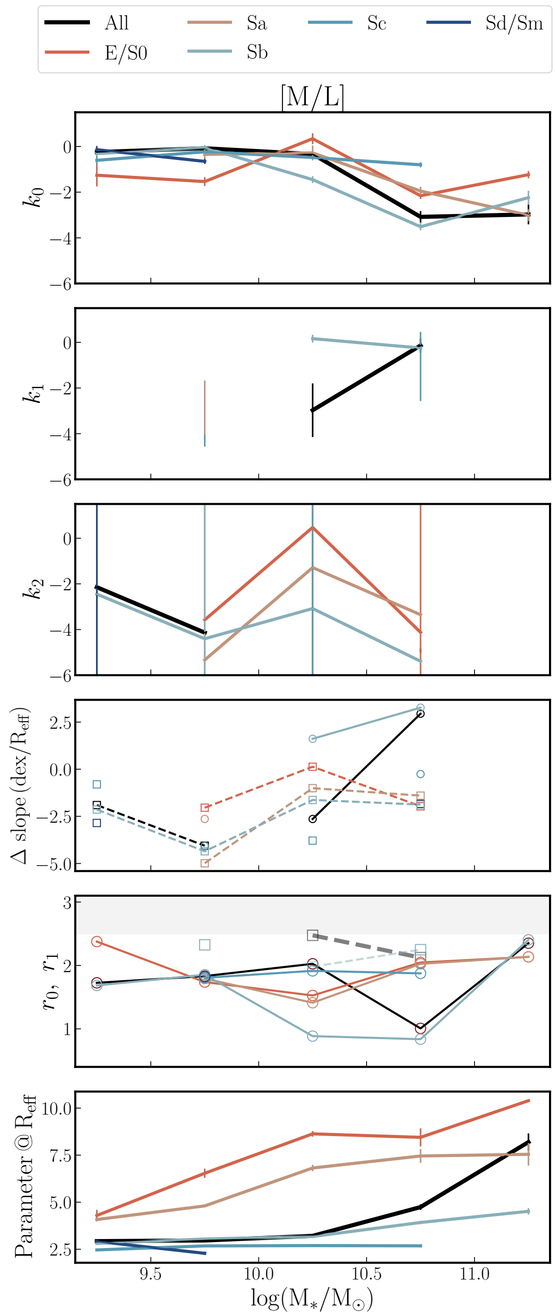

Fig. 4. Parameters derived from the radial distribution of the M/L ratio for different bins of total stellar mass. The color code of each symbol and line represents a morphological type (see legend). From top to bottom each panel shows: k_0, k_1, and k_2 from equation 1; the differences between those slopes (solid and dashed lines represent the $k_1 - k_0$, and $k_2 - k_0$ differences, respectively); r_0, and r_1 from equation 1 (solid and dashed lines, respectively); and the value of M/L at $R_{\rm eff}$. The color figure can be viewed online.

ing on both the stellar mass and morphology. For early-type galaxies with intermediate stellar mass, k_2 is positive or flat in comparison to the rest of mass-bins, where the slope is negative. For late-type galaxies k_2 is also negative with a more negative trend with M_* than k_0. These differences are highlighted in the fourth panel of Figure 4, suggesting a sharper drop of the M/L ratio in the outskirts of galaxies. We note a sharply negative slope for the most massive E/S0 galaxies bin (see top-middle panel in Figure 33). As this is a gradient derived with few data it is not reported in Figure 4. The fifth panel of Figure 4 indicates that those breaks of the gradients occur between ≈ 1.7 and $2.0\ R_{\rm eff}$. Finally, we note that for a given stellar mass bin, the M/L ratio at $R_{\rm eff}$ changes significantly for different morphologies. On average, late type galaxies present mild variations with M_* whereas early-type galaxies show significant variations of this ratio. This highlights the combined role of M_* and the morphology in shaping the radial distribution of the M/L ratio. These results reflect the different amount of old stars vs young stars for the different morphological types. Although less bright, old low-mass stars are the main contributor to the stellar mass in galaxies, at least for the mass and morphological ranges explored in this study.

One of the more significant parameters that represents a galaxy is its total stellar mass. Similarly, at spatially resolved scales, its local analog, the stellar mass surface density, Σ_*, has been observed to be a fundamental parameter to understand the angular distributions of different observables (e.g., Cano-Díaz et al. 2016; González Delgado et al. 2015; Sánchez 2020). In Figure 3 we show the average radial distributions of Σ_* for different masses and morphologies, as well as the gradients from the piece-wise analysis. In Figure 5 we show the best-fit parameters from that analysis. We find similar distributions as those reported previously in the literature (e.g., González Delgado et al. 2015; Sánchez 2020). In general, regardless of the morphological type and the total stellar mass, Σ_* decreases with the galactocentric distance, with relatively similar slopes. The piece-wise analysis reveals that the slope for Σ_* at small galactocentric distances decreases from $k_0 \approx -0.5$ to $k_0 \approx -1.5$ dex/$R_{\rm eff}$, as M_* increases. We do not find a significant impact of morphology in setting the k_0 slope. The k_1 slope is rather stable for different masses and morphologies (except for low-mass galaxies where we find a flat gradient), although we note that it is not derived for low-mass or massive early-type galaxies, suggesting

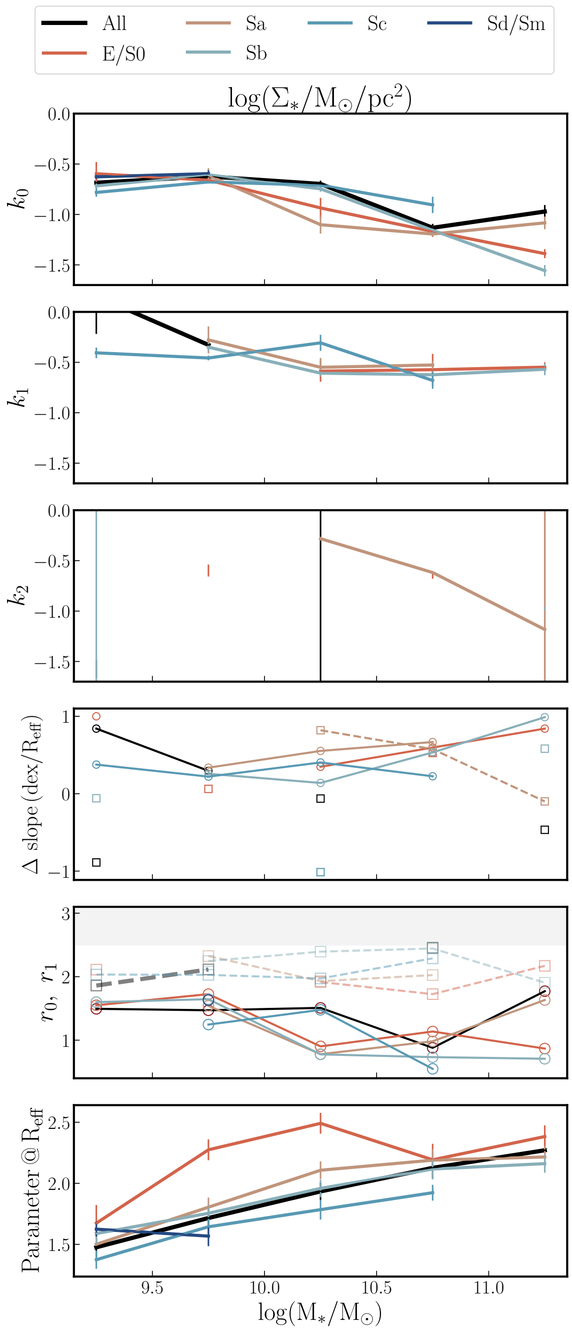

Fig. 5. Similar to Figure 4. Parameters derived from the piece-wise analysis for the stellar mass surface density gradients. The color figure can be viewed online.

that a single slope is required to estimate the gradient of these galaxies. Except for early-type galaxies, the analysis does not derive k_2 slopes, suggesting that for most bins of the M_*-morphology parameter space only a single or double slope is required to describe the Σ_* radial distribution. The difference between slopes suggest that in general the external gradient has a slightly more positive gradient than the inner one (i.e., $k_1 > k_0$). The break where the change of slope occurs is $r_0 \approx 0.5$ to $2.0\ R_{\rm eff}$, depending on the stellar mass and morphology. For those radial distributions with estimations of k_2, r_1 varies between 2.0 to 2.5 $R_{\rm eff}$. The characteristic value of Σ_* at $R_{\rm eff}$ increases with M_* with little effect from the morphology (except for early-type E/S0 galaxies where the characteristic value of Σ_* is larger in comparison to other morphologies).

3.2. *Luminosity Weighted Age, Metallicity, and Extinction*

Other than Σ_*, the SSP analysis also provides estimations of the average stellar age and metallicity, [Z/H]. In Figure 6 we show the parameters derived from the piece-wise analysis of the radial distribution of the luminosity-weighted stellar age (see Figure 34). The slope of the central gradient is in general negative ($k_0 \approx -0.3$ dex/$R_{\rm eff}$, although there are some stellar mass bins that exhibit an almost flat gradient, e.g., E/S0 low mass galaxies). When considering the morphology, this slope appears to decrease for late-type galaxies, while early-type galaxies tend to have either flat or mildly positive gradients. On average, the k_1 slope is slightly flatter than k_0, while the outer gradient (k_2) has a significantly larger negative value than the central gradient. For this analysis we exclude the sharp drops observed for k_2 in Figure 34, as those slopes are spurious. The radii where the change of slope occurs are relatively well confined ($r_0 \approx 1.0$ - $1.5\ R_{\rm eff}$, and $r_1 \approx 2\ R_{\rm eff}$). By exploring the average stellar age at $R_{\rm eff}$, we find that early-type galaxies show the oldest ages in comparison to other morphological types. Furthermore, the stellar age measured at $R_{\rm eff}$ increases with M_* (black solid line in bottom panel of Figure 34). However, morphology may play a more significant role: late-type galaxies are in general younger than early-type ones. These results are in agreement with different studies presented in the literature (e.g., Sánchez-Blázquez et al. 2014a,b; González Delgado et al. 2015; Morelli et al. 2015; Zheng et al. 2017; Parikh et al. 2021). In order to describe these mild negative gradients, these studies suggest a 'inside-out' growth of the galaxies. We note that contrary to these studies, Goddard et al. (2017) found positive mass-weighted stellar age gradients for early-type galaxies (using the same dataset as this study), suggesting that an 'outside-in' growth for these galaxies. In this study, we find that in general, the age gradients are – mildly – negative, regardless the morphological type suggesting

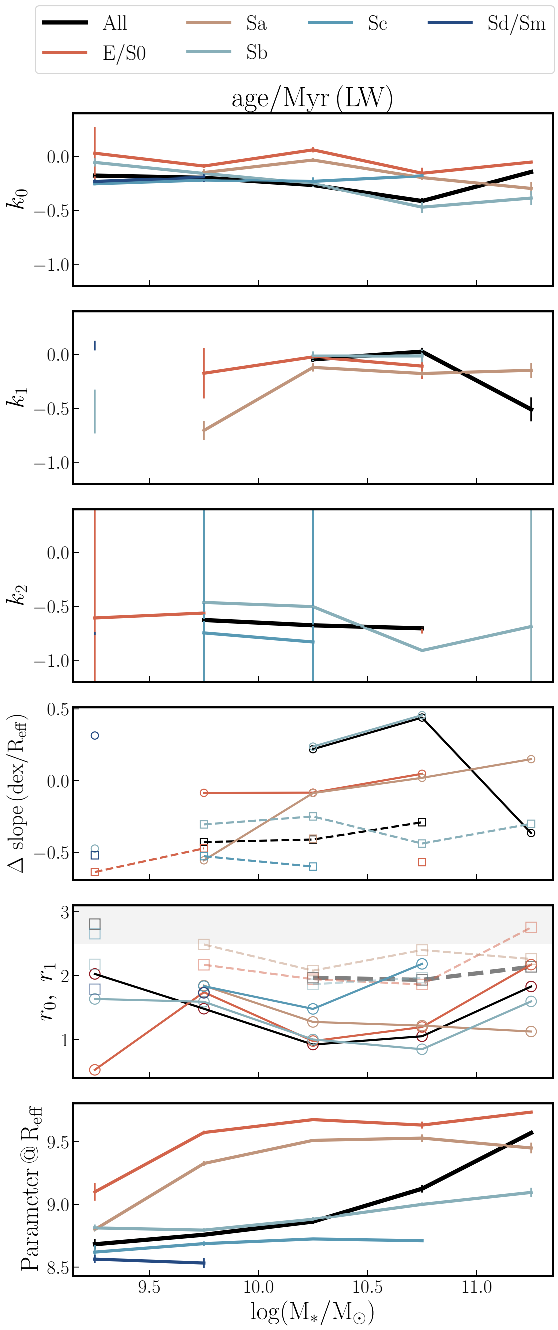

Fig. 6. Similar to Figure 4. Parameters derived from the piece-wise analysis for the luminosity-weighted age of the stellar population. The color figure can be viewed online.

an 'inside-out' growth for all the different morphological types or stellar masses.

In Figure 7 we show the result of the piece-wise analysis for the stellar metallicity radial profiles for our MaNGA GS (see Figure 35). We find that regardless of the morphology (except for intermediate-mass early-type galaxies), the gradient of the central radial profile (k_0) slightly decreases with M_*. For low-mass galaxies, this gradient is nearly flat, whereas most massive galaxies have a mild negative gradient ($k_0 \approx -0.1$ dex/$R_{\rm eff}$). Similar results have been found in the literature assuming a single gradient for the entire radial distribution of metals (e.g., S20). The slopes of the central gradients have been usually interpreted as an inside-out growth, more evident in massive galaxies. However, those galaxies where we are able to measure an external metallicity gradient (k_1, and k_2), usually have a flatter behavior than k_0. Even more, in some cases (e.g., Sb-Sc galaxies), we detect positive gradients, suggesting a radical change: an increment of metallicity at the outskirts of these galaxies. Since the gradients of the stellar metallicity have been usually described with a single negative slope (e.g., González Delgado et al. 2015; Zheng et al. 2017; Sánchez 2020), this could be an artifact due to either the lack of statistics at large galactocentric distances (although as we will explore in § 6, these trends are also observed when using a much larger sample) and/or the low signal-to-noise from the spectra at the outskirts of galaxies. Finally, we note that contrary to the stellar age at $R_{\rm eff}$, [Z/H] at $R_{\rm eff}$ depends significantly on M_* rather than on the morphology. The metallicity of the stellar component at this radius increases with M_*. Similar results have been found using the same dataset (Zheng et al. 2017).

From the stellar continuum fitting, the SSP analysis also allows us to have an estimation of the optical extinction afecting the stellar continuum, $Av_{\rm SSP}$. In Figure 8 we show the results of the piece-wise analysis to the radial distribution of $Av_{\rm SSP}$ (see Figure 36). From the piece-wise analysis we note that in the central portion of the galaxies the radial distribution of $Av_{\rm SSP}$ is almost flat with mild negative gradients for most morphological types ($k_0 \approx -0.1$ dex/$R_{\rm eff}$), except for early-type galaxies where these gradients are slightly positive. On the other hand, k_1 values change their sign, exhibiting a slight increment of $Av_{\rm SSP}$ as the galactocentric distance increases. For those sub-samples where we are able to measure k_2, we find stark drops in the values of $Av_{\rm SSP}$ as the galactocentric distance increases. Similar radial trends have been described in the literature using different IFU dataset (e.g., González Delgado et al. 2015). From the measurement of $Av_{\rm SSP}$ at $R_{\rm eff}$ we note that the absolute values are rather small ($Av_{\rm SSP} < 0.3$ mag). Contrary to other stellar properties derived from the SSP analysis, for the radial

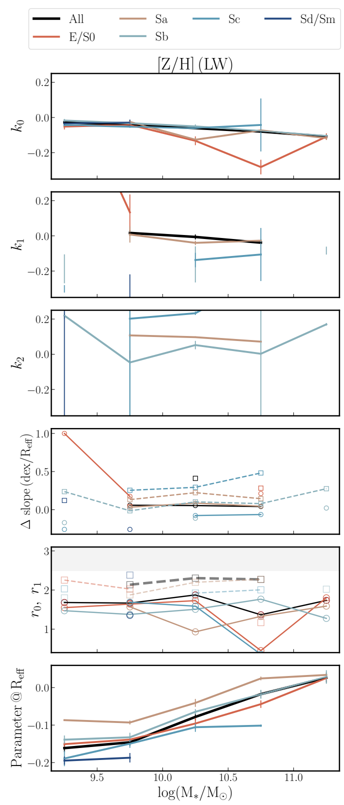

Fig. 7. Similar to Figure 4. Parameters derived from the piece-wise analysis for the luminosity-weighted stellar metallicity. The color figure can be viewed online.

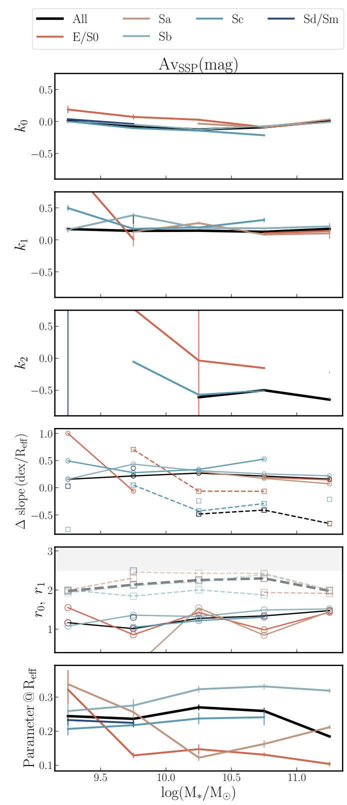

Fig. 8. Similar to Figure 4. Parameters derived from the piece-wise analysis for the optical extinction derived from the SSP analysis. The color figure can be viewed online.

distribution of the optical extinction it is not clear to disentangle the impact of either the morphology or M_*. Our analysis suggests that both structural parameters play a similar role in shaping the radial distribution of $\mathrm{Av}_{\mathrm{SSP}}$. In § 4.2.1 we show the ratio between $\mathrm{Av}_{\mathrm{SSP}}$ and the optical extinction derived from the Balmer decrement.

4. EMISSION LINES PROPERTIES

As we mention in § 2.3, the pyPipe3D analysis pipeline provides the angular distribution of the properties of different emission lines observed in the optical (i.e., the integrated flux, equivalent width, velocity, and velocity dispersion) for each of the galaxies included in the MaNGA survey. These properties, including their ratios, has been widely used to explore physical properties of the ionized gas component of the ISM. In this section we explore the radial distribution of the properties derived directly by the pipeline (§ 4.1), and those derived from the flux ratios of these emission lines (§ 4.2, § 4.3, § 4.4, and § 4.5).

4.1. *Fluxes, and Equivalent Widths*

In Figure 9 we show the results of the piece-wise analysis for the four brightest emission lines in the optical regime: Hα, Hβ, [NII], and [OIII][9] (see their radial profiles in Figures 37, 38, 39, and 40). We first note that due to our SNR selection criteria, in particular the one from the Hα emission line, there are some bins of morphology/M_* where it is not possible to derive the gradients from these emission lines. This is the case for low-mass early-type (Sa) galaxies.

For those stellar masses and morphologies where we measure a gradient, the slope in the central region ($r < 1.5\ R_{\mathrm{eff}}$) is negative regardless of the emission line ($-1 < k_0 < 0$). For the Balmer emission lines, Hα and Hβ, we find little dependence of k_0 with respect to M_*. For late-type galaxies, $k_0 \approx -0.5$ dex/R_{eff}. On the other hand, for early-type galaxies k_0 tends to be stepper in comparison

[9]Apart from these emission lines, the pyPipe3D analysis pipeline also allows us to derive the flux from low-brightness emission lines.

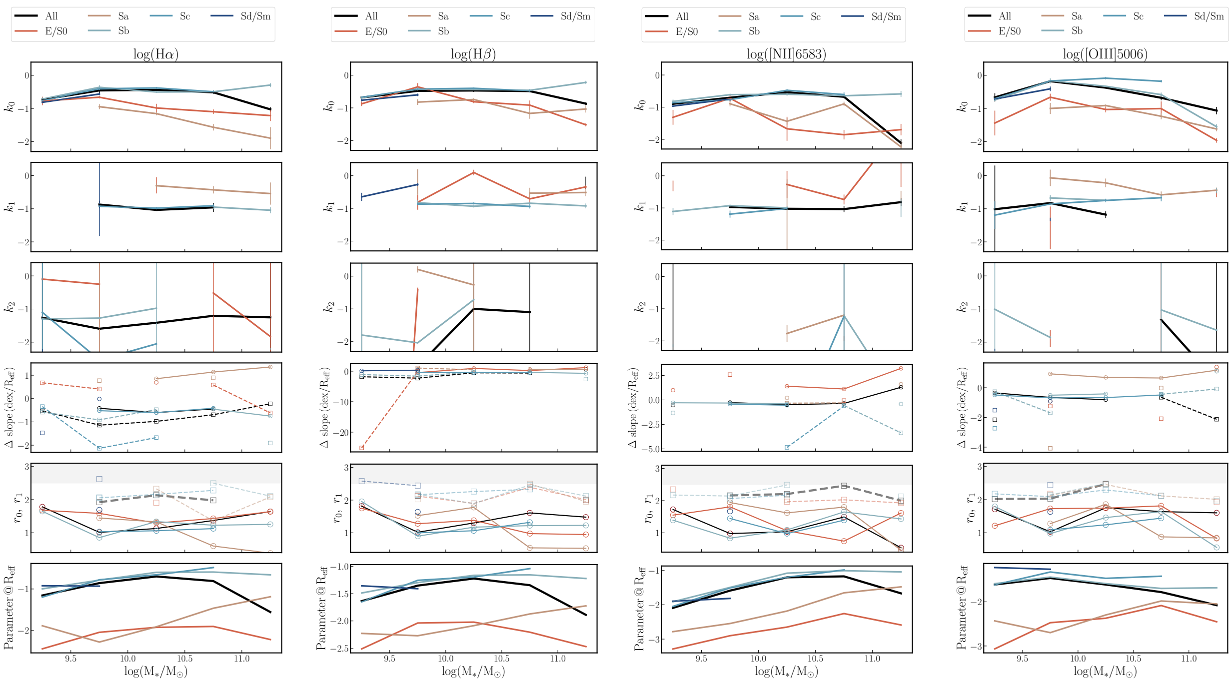

Fig. 9. Parameters derived from the piece-wise analysis for the four brightest emission lines in the optical. From left to right: Hα, Hβ, [NII], and [OIII]. The color figure can be viewed online.

to that derived for late type ones at the same stellar mass bin. For those galaxies where we are able to estimate an external gradient (k_1), we find, in general, steeper negative gradients in comparison to k_0 for late-type galaxies, whereas for early galaxies $k_1 > k_0$. For the [NII] emission line k_0 slightly increases with M_*, reaching a constant value of $k_0 \approx -0.5$ dex/$R_{\rm eff}$ (except for the most massive bin where k_0 is significantly steeper, $k_0 \approx -2$ dex/$R_{\rm eff}$). Similar to the Balmer lines, the slope of the central gradient for the [NII] lines for early-type galaxies is steeper in comparison to late-type galaxies for the same stellar mass bin. For this emission line the outer gradients are steeper than those derived in central regions. On the other hand, for the [OIII] emission line we find that the central gradient, k_0, decreases with the stellar mass: low-mass galaxies have a flatter gradient in comparison to massive ones. Similar to the other emission lines, we estimate negative steeper gradients for the outskirts of galaxies (k_1). The sharp drop of the gradients at the outskirts for the different emission lines could be expected given the low signal-to-noise from these lines at those large galactocentric radii. For the Hα, Hβ, and [NII] emission lines their fluxes at $R_{\rm eff}$ slightly increase with the stellar mass. For early-type galaxies the flux of these emission lines at $R_{\rm eff}$ is significantly fainter than that derived for late-type galaxies. On the other hand, the flux of the [OIII] slightly decreases with the stellar mass.

The equivalent width of the Hα emission line, EW(Hα), has been extensively used to explore the star-formation activity of galaxies at both integrated and spatially resolved scales (e.g., Sánchez et al. 2012; Lacerda et al. 2018). Therefore, it is quite relevant to understand how this parameter changes with radius. In Figure 10 we present the piece-wise analysis of the radial distribution for the EW(Hα). The radial distributions of EW(Hα) for different bins of stellar mass and morphology are presented in Figure 41. We find that the slope of the central gradient of EW(Hα) is nearly constant for different bins of M_*, regardless of morphology. However, we note that although late-type galaxies show a positive gradient, early-type galaxies show a nearly flat gradient. Interestingly, we find a change in the slope of the radial distribution of EW(Hα) for the outskirts of late-type galaxies (i.e., k_1, and k_2 are negative). This change in the slope occurs at ≈1.0 - 1.5 $R_{\rm eff}$. This may reflect the impact of morphological features on setting the radial distribution of the EW(Hα) in these galaxies. Finally, when we explore the value of EW(Hα) at $R_{\rm eff}$, we find that low-mass late-type galaxies (Sd/Sm) have the largest values of EW(Hα). For the other late-type morphological bins we note that as M_* increases the value of EW(Hα) at $R_{\rm eff}$

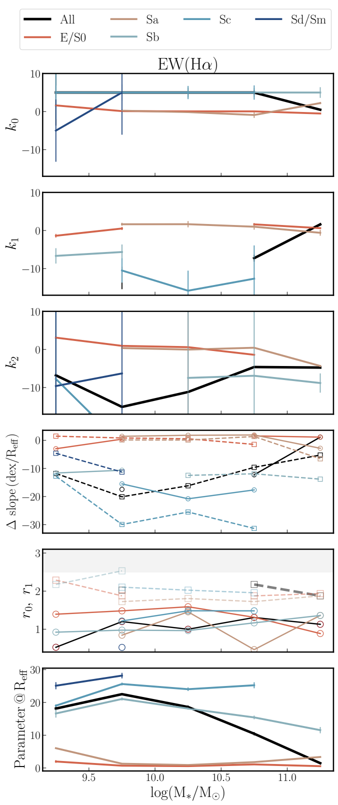

Fig. 10. Parameters derived from the piece-wise analysis for the Hα emission line equivalent width. The layout of the figure is similar to Figure 4. The color figure can be viewed online.

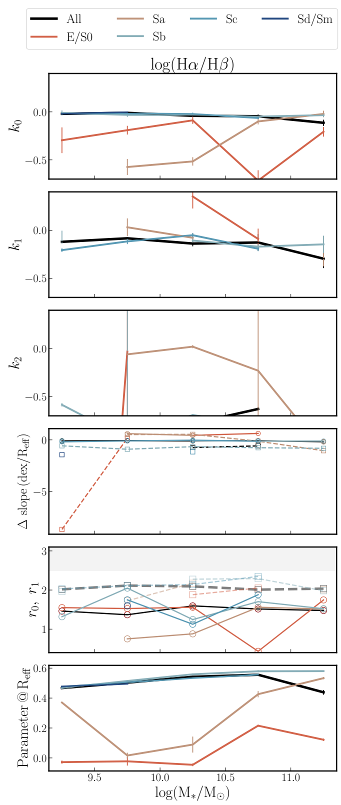

Fig. 11. Parameters derived from the piece-wise analysis for the Balmer decrement. The layout of the figure is similar to Figure 4. The dashed lines represent the expected value of this ratio from a Case B of recombination (Hα/Hβ= 2.86). The color figure can be viewed online.

tends to decrease. On the other hand, for early-type galaxies, the EW(Hα) measured at $R_{\rm eff}$ is constant regardless M_* (EW(Hα) < 6 Å). This value has been used to differentiate star-forming regions from other ionization mechanisms (e.g., Cid Fernandes et al. 2011; Lacerda et al. 2018, see dashed line in Figure 41). As derived in other studies, we find that the star-formation activity is largely affected by the morphology rather than by the stellar mass (e.g., Sánchez 2020, and references therein).

4.2. *Line Ratios*

The ratios between fluxes of different emission lines have been essential to explore physical properties of the ISM. In this section we describe the radial gradients and the best-fit gradients of three emission-line ratios from the brightest lines presented in the previous section (Hα, Hβ, [NII], and [OIII]).

4.2.1. *Balmer Decrement,* Av$_{\rm gas}$ *, and* $\Sigma_{\rm mol,Av}$

The Hα/Hβ flux lines ratio (also known as the Balmer decrement, BD) has been extensively used to estimate the effect of the dust on the optical extinction (Av$_{\rm gas}$; e.g., Kennicutt 1992; Brinchmann et al. 2004; Moustakas et al. 2006; Domínguez et al. 2013). Recently, in Barrera-Ballesteros et al. (2020) we provided a proxy between Av$_{\rm gas}$ and the molecular gas surface mass density, $\Sigma_{\rm mol}$, at kpc scales using the spatially resolved data from the optical and the molecular gas of the EDGE-CALIFA survey.

In Figure 11 we present the piece-wise analysis of the Hα/Hβ radial profiles for our MaNGA Golden Sample, whereas in Figure 42 we show the radial distribution of the BD as well as the best-fit gradients derived from this analysis. In Figure 42 we also indicate the theoretical value of this ratio $\approx$ 2.86 (see dashed lines; this is the expected value for the Hα/Hβ ratio for a temperature of 10^4 K and Case B of recombination, Osterbrock & Ferland 2006; Raga et al. 2015). From the piece-wise analysis we find that the central gradient (k_0) for late-type galaxies is rather constant and flat for different stellar mass bins (i.e., $k_0 \approx 0$ dex/$R_{\rm eff}$). For the early-type galaxies the central gradients vary significantly between negative and flat for the different bins of probed stellar mass. For those galaxies where we are able to estimate external gradients (i.e., k_1 and k_2) we find that these are mostly negative. The values of the Balmer decrement measured at $R_{\rm eff}$ show that this parameter increases with M_* for late-type galaxies. Furthermore, we find that for all late-type galaxies – at least within 1 $R_{\rm eff}$ – the BD is larger than the expected value from theory (see dashed line in Figure 11). On the other hand, only the most massive Sa galaxies have a BD larger than 2.86. For the rest of the early-type galaxies the BD measured at $R_{\rm eff}$ is smaller than this value. Furthermore we note that for E/S0 galaxies BD ≈ 1, suggesting that the flux from these two lines is close to the values expected from fluctuations within the noise. The fact that for most of the late-type galaxies, regardless of the stellar mass, the BD distribution is larger than 2.86 suggests that it is possible to have a radial measurement of the optical extinction from this ratio. On the other hand, for early-type galaxies it is not possible to estimate the optical extinction from the Hα/Hβ ratio since their values are smaller than the one expected from the case B of recombination.

We follow Barrera-Ballesteros et al. (2020) and Catalán-Torrecilla et al. (2015) to estimate the optical extinction for the Hα emission line, A(Hα). Assuming a Cardelli extintion curve with $R_V = 3.1$ (Cardelli et al. 1989), the optical extinction is given by:

$$\mathrm{Av_{gas}} = A(\mathrm{H}\alpha)/0.817. \tag{2}$$

Thus to estimate $\mathrm{Av_{gas}}$ we do not consider those radial bins in galaxies where BD < 2.86. In Figure 12 we present the result of the piece-wise analysis of the radial distribution of $\mathrm{Av_{gas}}$ (see Figure 43). As in the previous analysis, for early-type galaxies it is not possible to derive $\mathrm{Av_{gas}}$ from the Balmer decrement because most of the radial bins have a value of the BD smaller than 2.86. Therefore, most of the results presented in Figure 12 are for late-type galaxies, in particular Sb, and Sc ones. For a wide range of stellar masses (i.e., $9.2 < \log(M_*/M_\odot < 10.7)$, the gradient of $\mathrm{Av_{gas}}$, k_0, decreases with M_* (from $k_0 \approx -0.2$ mag/$R_{\rm eff}$ to $k_0 \approx -0.4$ mag/$R_{\rm eff}$). For the most massive bin, the gradients are flatter. The radial extension of $\mathrm{Av_{gas}}$ goes up to $\approx 1.5\ R_{\rm eff}$. When measuring $\mathrm{Av_{gas}}$ at $R_{\rm eff}$, we find that this extinction increases with M_*. For low-mass galaxies $\mathrm{Av_{gas}} \approx 0.2$ mag, whereas massive ones show values of $\mathrm{Av_{gas}} \approx 1.0$ mag. Our results show the impact that M_* has in setting the radial distribution

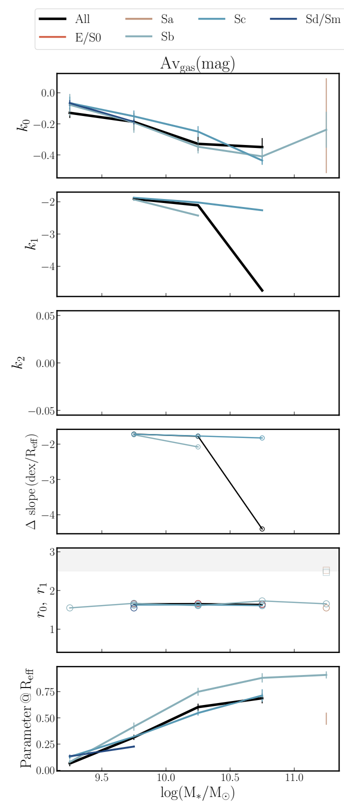

Fig. 12. Parameters derived from the piece-wise analysis for the optical extinction derived from the Balmer decrement, $\mathrm{Av_{gas}}$. The layout of the figure is similar to Figure 4. The color figure can be viewed online.

of $\mathrm{Av_{gas}}$ in late-type galaxies: the more massive is the galaxy the steeper is the gradient of $\mathrm{Av_{gas}}$.

Since we have the estimation of the optical extinction from both the stellar continuum ($\mathrm{Av_{SSP}}$) and the emission lines ($\mathrm{Av_{gas}}$) we are able to compare the radial variations of the ratio of these values. Different studies have explored this ratio for integrated and angular resolved scales. On the one hand, some studies suggested that this ratio is constant for late-type galaxies in both integrated and spatially-resolved measurements (e.g., Calzetti 1997; Calzetti et al. 2000; Kreckel et al. 2013). On the other hand, other studies have suggested variations of this ratio for different local and global properties (e.g., Wild et al. 2011; Koyama et al. 2015, 2019; Qin et al. 2019; Lin & Kong 2020; Li et al. 2021).

In Figure 13 we present the results of the piece-wise analysis of the radial distribution of the $\mathrm{Av_{gas}}/\mathrm{Av_{SSP}}$ ratio (see Figure 44). We first note that the ratio of these two estimations of the optical extinction is not constant with radius. Furthermore the gradient of this ratio varies depending on the

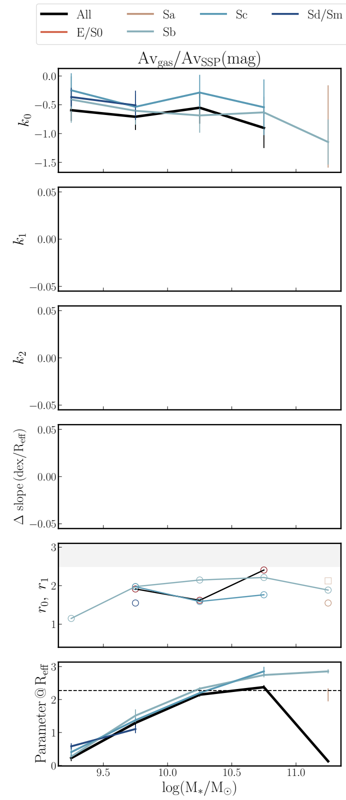

Fig. 13. Parameters derived from the piece-wise analysis for the Av_{gas} /Av_{SSP} ratio. The layout of the figure is similar to Figure 4. The dashed line in the bottom panel shows the value derived from Calzetti (1997): Av_{gas} /$Av_{SSP} \approx 2.27$. The color figure can be viewed online.

stellar mass. As for Av_{gas} , the radial extension of this ratio is limited by the Hα SNR selection criteria. Therefore, for most radial distributions, a single gradient (k_0) describes well the entire radial distribution. Also similar to Av_{gas} , this ratio is derived mostly for late-type galaxies. We find a similar trend in k_0 as the one described by Av_{gas} with respect to the stellar mass. The gradient of this ratio decreases with M_* ; massive galaxies have steeper negative gradients in comparison to low-mass ones. The value of this ratio at $R_{\rm eff}$, increases with M_* ; going from values below 1 to 3 from low-mass to massive galaxies, respectively. The bottom panel of Figure 13 shows that only intermediate mass Sb galaxies have a similar ratio as the one expected in the literature (Calzetti 1997). Our results suggest that the estimation of the optical extinction varies depending on the adopted proxy (i.e., ionized gas or stellar). Furthermore, this ratio shows a significant variation radially, as well as with the stellar mass. In contrast to studies that proposed a constant stellar-gas extinction ratio (Calzetti 1997; Calzetti et al. 2000; Kreckel et al. 2013), we find significant variations of this ratio across the optical extension of the probed galaxies. Different studies have suggested that a possible scenario to explain these differences is due mainly to geometrical effects (e.g., Price et al. 2014; Reddy et al. 2015; Koyama et al. 2019). Nevertheless, using a sample of galaxies also included in the MaNGA survey, Lin & Kong (2020) and Li et al. (2021) found that the difference in this ratio is due to different properties from both the stellar and the ionized gas components. On the one hand, Lin & Kong (2020) found that this ratio strongly depends on the oxygen abundance as well as on the ionization stage at kpc scales. On the other hand, Li et al. (2021) found that this ratio also depends on the luminosity-weigthed age, thus the Av_{gas} /Av_{SSP} ratio. Therefore, our results favor the scenario presented by these works where the extinction (i.e., the dust properties) is affected (mainly) by local physical conditions, such as the chemical enrichment of the ISM and/or the ionization parameter.

As we mention above, using a sample of galaxies with spatially resolved observations of the molecular gas and the optical properties we estimate a calibrator between the optical extinction derived from the Balmer decrement (Av_{gas}), and the molecular gas surface density, $\Sigma_{\rm mol}$ (Barrera-Ballesteros et al. 2020). Using this calibration, we present in Figure 14 the piece-wise analysis of the radial distribution of the molecular gas density, $\Sigma_{\rm mol,Av}$, derived from the optical extinction, Av_{gas} (see radial profiles in Figure 45). As expected, we find similar trends of the gradients and values of $\Sigma_{\rm mol,Av}$ at $R_{\rm eff}$ with respect to the stellar mass and morphology in comparison to those derived for Av_{gas} . The gradient of $\Sigma_{\rm mol,Av}$ decreases with respect to M_* and is available in general only for late-type galaxies. However, we note that the gradients from $\Sigma_{\rm mol,Av}$ are flatter in comparison to those derived from Av_{gas} . The value of $\Sigma_{\rm mol,Av}$ at $R_{\rm eff}$ increases with the stellar mass. Following this calibrator as a reliable estimation of $\Sigma_{\rm mol}$ at kpc scales, our results suggest that, except for low-mass galaxies, the radial distribution of $\Sigma_{\rm mol}$ slightly decreases with radius.

Finally, given the estimation of $\Sigma_{\rm mol,Av}$, we can also provide a measurement of the ratio between the molecular and stellar gas surface mass density – $f_{\rm mol}= \Sigma_{\rm mol,Av}$ / Σ_*. In Figure 15 we show the piece-wise analysis of the radial distribution of log($f_{\rm mol}$) (see Figure 46). We find that, in general, regardless of the stellar masses and morphologies probed, $f_{\rm mol}$

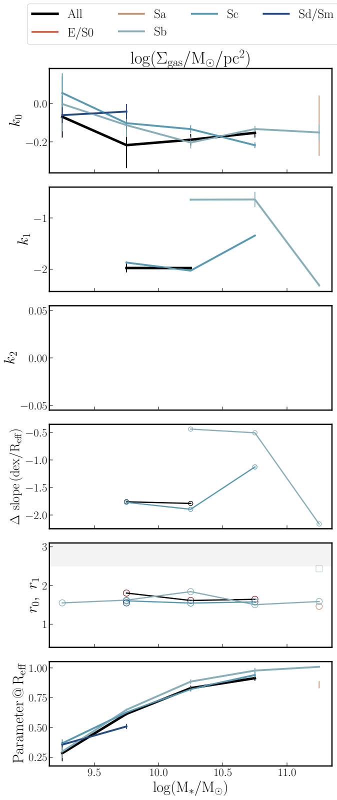

Fig. 14. Parameters derived from the piece-wise analysis for the molecular gas mass derived from $\mathrm{Av_{gas}}$, $\Sigma_{\mathrm{mol,Av}}$. The layout of the figure is similar to Figure 4. The color figure can be viewed online.

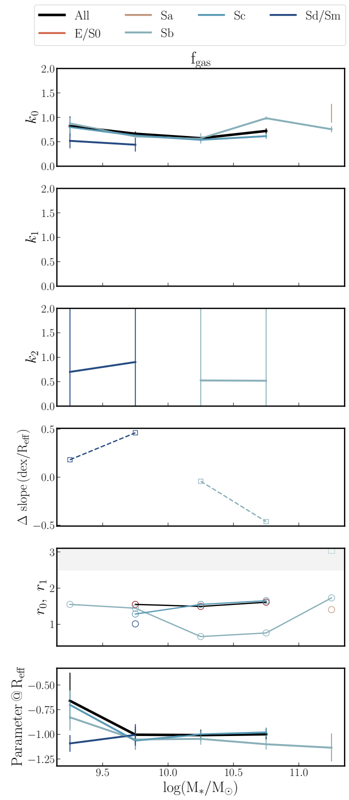

Fig. 15. Parameters derived from the piece-wise analysis for the gas fraction, $\mathrm{f_{mol}}$. The layout of the figure is similar to Figure 4. The color figure can be viewed online.

has a positive constant gradient ($k_0 \approx 0.7$ dex/R_{eff}). We also find that, except for the low mass galaxies, the gas fraction measured at the effective radius is relatively constant for the range of probed stellar masses with $\log(\mathrm{f_{mol}}) \approx -1.1$. Our results suggest that the gas density, with respect to the stellar mass density, increases at large radii. In other words, in comparison to the radial gradient of Σ_*, the radial distribution of $\Sigma_{\mathrm{mol,Av}}$ is rather flat. The small variations in both slope and $\mathrm{f_{mol}}$ at R_{eff} for different stellar masses suggest that this radial trend is an ubiquitous property for late-type galaxies.

4.2.2. *Other Line Ratios*

Apart from the Hα/Hβ ratio, there are other emission line ratios that provide insights on the physical condition of the ISM – and even on the very young stellar population – in galaxies. This is the case of the [NII]/Hα ratio. In star-forming galaxies, this ratio has been linked to the fraction of young stellar population (e.g., Sánchez et al. 2015). In Figure 16 we present the parameters derived from the piece-wise analysis from the radial distribution of this emission line ratio (see Figure 47). Except for E/S0 low-mass galaxies, we find that regardless of M_*, the central gradient (k_0) has negative values with a mild decrease with stellar mass. On the other hand, for early-type galaxies we find a change from positive to negative gradients as stellar mass increases. For the external part of the galaxies, we note that the piece-wise analysis yields positive gradients (in some cases sharp ones, e.g., Sb galaxies). We consider that those strong radial variations of the [NII]/Hα ratio at the outskirts of these galaxies could be spurious, induced by low SNR values of both emission lines. At low SNRs, emission lines fluxes tend to be similar to each other, in other words, the ratio is close to $\approx$ 1. The [NII]/Hα ratio measured at R_{eff} increases with M_* from $\log([\mathrm{NII}]/\mathrm{H}\alpha) \approx -0.8$ dex to $\log([\mathrm{NII}]/\mathrm{H}\alpha) \approx -0.2$ dex, for late-type galaxies. For early-type galaxies, this ratio measured at R_{eff} does not significantly changes with M_* , with a constant value of $\log([\mathrm{NII}]/\mathrm{H}\alpha) \approx -0.2$ dex.

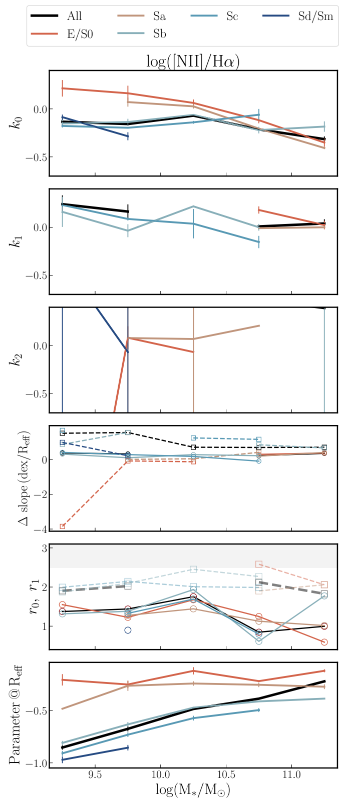

Fig. 16. Parameters derived from the piece-wise analysis for the [NII]/Hα emission lines ratio. The layout of the figure is similar to Figure 4. The color figure can be viewed online.

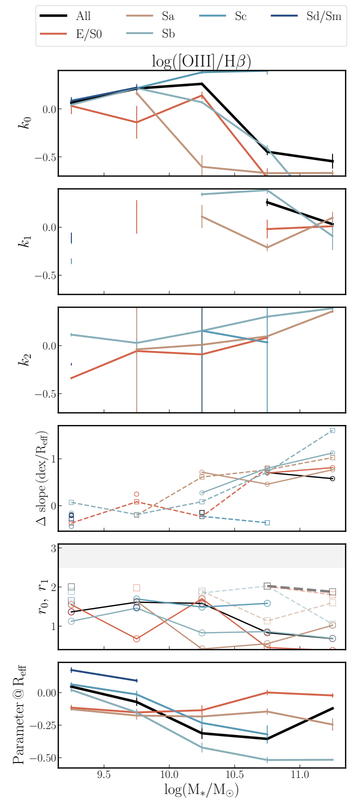

Fig. 17. Parameters derived from the piece-wise analysis for the [OIII]/Hβ emission lines ratio. The layout of the figure is similar to Figure 4. The color figure can be viewed online.

In Figure 17 we show the results of the piece-wise analysis for the radial distribution of the [OIII]/Hβ ratio (see Figure 48). The central gradient (k_0) of this ratio has significant variations for both different morphologies and stellar masses. On the one hand, for late-type galaxies k_0 is positive and increases from low to intermediate stellar masses. However, for massive galaxies k_0 is negative becoming larger (negative and stepper) as M_* increases. On the other hand, for early-type galaxies k_0 varies from positive to negative for different bins of stellar mass. In contrast to k_0, k_1 and k_2 have larger positive gradient indicating the strong radial variation of the [OIII]/Hβ ratio. Given the fact that these variations occur at smaller radius than the [NII]/Hα ratio (≈ 1 $R_{\rm eff}$, and ≈ 2 $R_{\rm eff}$, respectively), we suggest that these variations may have a physical origin. For instance, large central [OIII]/Hβ ratios could be indicating the presence of a hard ionizing source (e.g., an active nucleus), whereas large ratios at the outskirts could be due to ionization from a large star formation activity. Nevertheless, we cannot rule out that, as for the [NII]/Hα ratio, these variations in gradients are due to low SNR measurements. Contrary to the [NII]/Hα ratio, we find that both M_* and the morphology play a significant role in setting the observed [OIII]/Hβ ratio at $R_{\rm eff}$. For late-type galaxies, [OIII]/Hβ measured at $R_{\rm eff}$ decreases with M_* . However, for a given stellar mass bin, this ratio decreases from Sd/Sm to Sb galaxies. On the other hand, for early-type galaxies this ratio is rather constant for different bins of M_* . Furthermore, the value of this ratio is similar to the one derived from the [NII]/Hα ratio for this morphological type. In the next section, using these two line ratios, we explore the possible ionization mechanism that could explain their radial distribution.

4.2.3. *The BPT Diagram*

Diagnostic diagrams using emission-line ratios are very useful tools to probe the ionization stage of entire galaxies and kpc regions within them. Depending on the position of the galaxy/region in this diagram it can be associated with a different ioniza-

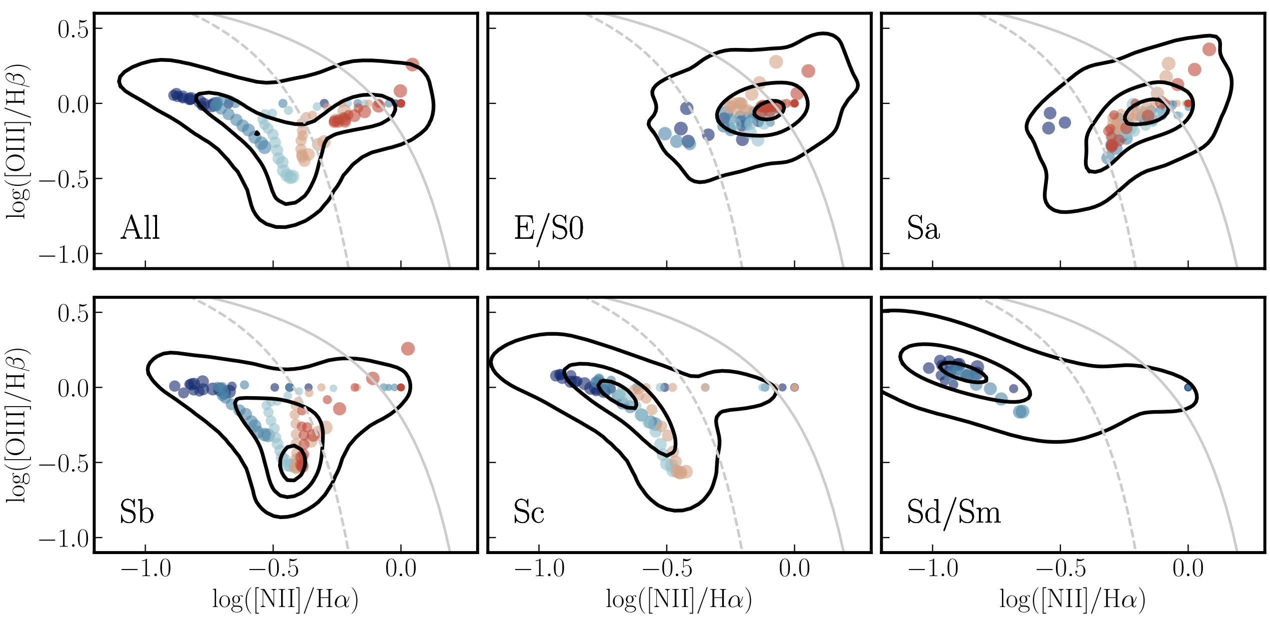

Fig. 18. The BPT diagnostic diagram using the radial averages for the Golden Sample. The contours enclose 90%, 50%, and 10% of the line ratios for the radial bins. In each panel we segregate the samples according to their morphology (see the label in each panel). The circles represent the averaged values for different bins of stellar mass. The color of each circle represents the stellar mass, following the same color code as in Figure 3. The sizes of the circles decrease with galactocentric distance. The solid and dashed gray lines represent the demarcation lines in this diagram by Kewley et al. (2001) and Kauffmann et al. (2003), respectively. The color figure can be viewed online.

tion process. The ionizing stage is segregated by the so-called demarcation lines. Prior to the large IFU surveys mapping, a large number of targets, galaxies with line ratios below the Kauffmann demarcation line (Kauffmann et al. 2003), were considered as star-forming, whereas galaxies above the Kewley demarcation line (Kewley et al. 2001) were considered as AGNs or LINERs. Galaxies in between were considered as ‘composite’, that is, a mixture between both types of ionization. This picture has significantly changed thanks to angular-resolved observations (for a review see Sánchez 2020; Sánchez et al. 2021). In Figure 18 we show the best known of those diagrams, the BPT diagram (Baldwin et al. 1981) for the ratios derived for the radial bins of the MaNGA GS. We find that the distribution of flux ratios varies depending on the morphology, the stellar mass, and the galactocentric distance. For the entire GS (top left panel in Figure 18), we find a significant difference between low-mass and massive galaxies. On the one hand, central regions of massive galaxies are above the Kewley et al. (2001) demarcation lines, suggesting that the ionizing source for those regions is dominated by processes other than star formation. Furthermore, as distance increases the flux ratios from massive galaxies move below the demarcation lines indicating that the ionization could be due to star formation. The massive galaxies follow what has been identified as the composite/AGN branch using single-fiber spectroscopy(e.g., Kauffmann et al. 2003, using SDSS dataset). On the other hand, as stellar mass decreases, most of the radial bins are below the Kauffmann demarcation line. This suggests that the ionization source for those galaxies, regardless of the galactocentric distance, is due to star formation. Furthermore, the lowest mass bin exhibits the lowest values of the [NII]/Hα ratio. The radial bins follow the star-formation branch observed using the SDSS dataset (e.g., Kauffmann et al. 2003).

For the E/S0 morphological bin (top-middle panel of Figure 18), the radial values of these emission line ratios (black contours) are mostly above the Kauffmann et al. (2003) demarcation line (gray-dashed line). Similar to the contours, these values are slightly below the Kewley et al. (2001) demarcation line. Although this could indicate that the ionization source could be due to an AGN (e.g., Husemann et al. 2010, 2014), this is only plausible in the central regions of these galaxies. It could also be that the ionization is due to hot-evolved stars (also known as HOLMES, e.g., Binette et al. 1994; Flores-Fajardo et al. 2011). To further constrain the

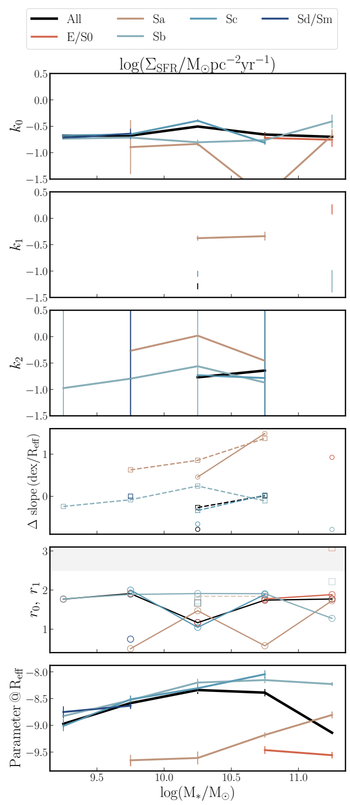

Fig. 19. Parameters derived from the piece-wise analysis for the radial distribution of the $\Sigma_{\rm SFR}$. The layout of the figure is similar to Figure 4. The color figure can be viewed online.

source that ionizes the ISM it has been also required to measure the EW(Hα) (e.g., Cid Fernandes et al. 2010, 2011; Barrera-Ballesteros et al. 2016; Lacerda et al. 2020). Similarly, Sánchez (2020) explored the distribution of the EW(Hα) for a large sample of IFS datasets at kpc scales within the BPT diagram for different stellar masses and morphologies. His results showed that indeed for massive E/S0 galaxies the distribution of the emission line ratios in the BPT diagram is between the Kauffman and Kewley demarcation lines, with EW(Hα) values smaller than 6Å (below this threshold it is expected that the ionization source is mainly due to HOLMES; e.g., Cid Fernandes et al. 2011). We should also note that most of the averaged values for different stellar mass bins at the outskirts of E/S0 galaxies (small circles of different colors) are located close to the region where both ratios are close to one. As we mention above, we cannot rule out that these positions of the flux ratios in the BPT diagram are simply due to measured fluxes with low SNR. For Sa galaxies the distribution of the flux ratios measured in their radial bins spreads wider across the BPT diagram than for E/S0 galaxies. Nevertheless, as we mention for E/S0 galaxies, the outer radial bins, regardless of M_* are mostly concentrated where the ratios are close to one. For the central radial bins of the most massive galaxies the ratios are well above the Kewley demarcation line, whereas the ratios from central regions in low-mass galaxies are well below the Kauffmann demarcation line. The Sb galaxies show a similar distribution as the entire sample, with low-mass galaxies lying below the Kauffmann demarcation line and massive galaxies spreading along the 'non star-forming' branch. The flux ratios from most of the radial bins of Sc galaxies lie below the Kauffmann demarcation line; furthermore, they lie in the so-called 'star-forming' branch. This suggests that for galaxies of this morphological type the ionization is due mostly to star formation across their optical extension, regardless of the stellar mass. For the irregular galaxies (Sd/Sm), we find that the [OIII]/Hβ ratio is rather constant for the probed galaxies ([OIII]/H$\beta \approx 1$). The [NII]/Hα ratio, on the other hand, covers a wider dynamical range than any other morphological type ($0.1 <$ [NII]/Hα < 3). For the irregular galaxies, we find flux ratios only for low-mass galaxies. In the BPT diagram, these ratios are located well below the Kauffmann demarcation line, suggesting that these ratios are the result of ionization due to star formation. Finally, we note that for those radial bins at the outskirts of galaxies both flux ratios tend to be close to one. We observe a similar behavior for the radial distribution of each line ratio (see § 4.2.2). Rather than indicating an ionization source other than star formation, this suggests that the low SNR from these emission lines at external radii do not allow us to derive their true ionization source.

4.3. *Star-Formation Parameters*

The Balmer emission lines are also a powerful tools to gauge the star formation rate (SFR) for galaxies/regions (Kennicutt & Evans 2012, and references therein). From the optical, following Kennicutt (1998), we can use the extinction-corrected luminosity of the Hα emission line as proxy of the star formation rate. This calibration has been widely used in IFS studies (e.g., Sánchez et al. 2012; Cano-Díaz et al. 2016, 2019). Apart from the SNR threshold for the Hα emission line, we did not use other selection criteria to derive the radial distribution of the SFR; thus, for some morphological types (e.g., E/S0) the radial profiles should be considered as upper limits of star formation. In this section we

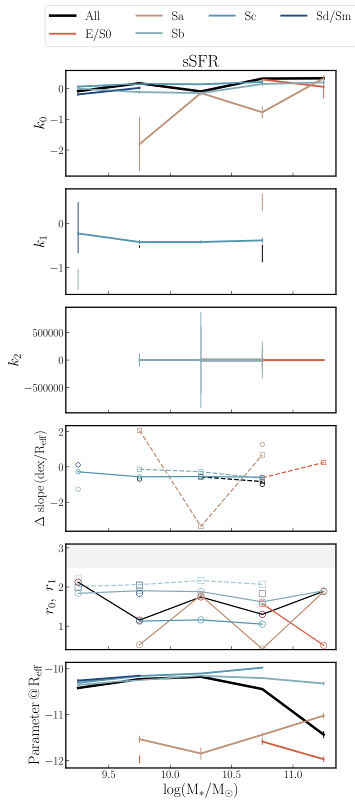

Fig. 20. Parameters derived from the piece-wise analysis for the radial distribution of the sSFR. The layout of the figure is similar to Figure 4. The color figure can be viewed online.

explore the radial distribution of the SFR density, $\Sigma_{\rm SFR}$, as well as its ratio, with the different components of the baryonic mass: the specific SFR, sSFR $= \Sigma_{\rm SFR}/\Sigma_*$; and the star formation efficiency, SFE $= \Sigma_{\rm SFR}/\Sigma_{\rm mol,Av}$. The radial distribution of these parameters is fundamental to understand what drives or halts the star-formation activity in galaxies (e.g., Colombo et al. 2020; Ellison et al. 2020).

4.3.1. *SFR Surface Density,* $\Sigma_{\rm SFR}$

In Figure 19 we plot the piece-wise analysis of the radial distribution of $\Sigma_{\rm SFR}$ (see Figure 49). We find that the central gradient of $\Sigma_{\rm SFR}$, k_0, is negative regardless of the stellar mass or morphology. Furthermore, k_0 is quite similar for the late-type galaxies regardless of M_* ($k_0 \approx -0.7$ dex/$R_{\rm eff}$). For the Sa galaxies, the central slopes are slightly steeper than for late-type galaxies (except for intermediate stellar mass galaxies, where($k_0 \approx -2.0$ dex/$R_{\rm eff}$). On the other hand, for E/S0 galaxies we estimate the central gradient only for the two most massive bins of M_*. These central gradients are similar to those derived for late-type galaxies with similar M_*. For those bins of M_* and morphology where the analysis detects an external gradient (i.e., k_1 and/or k_2), we find a mix of flatter and steeper gradients; in any case, they are still negative. Regarding the characteristic value of $\Sigma_{\rm SFR}$(i.e., measured at $R_{\rm eff}$), we find that for late-type galaxies it increases as M_* increases. For Sa-type galaxies, this $\Sigma_{\rm SFR}$ is approximately one order of magnitude smaller for a given bin of M_*. The difference is larger for E/S0 galaxies, where the characteristic $\Sigma_{\rm SFR}$ is $\approx 10^{-9.5}$ M$_\odot$ pc^{-2} yr^{-1}. These results are in good agreement with previous measurements of the gradients and characteristic values of $\Sigma_{\rm SFR}$ (Sánchez 2020).

4.3.2. *Specific SFR, sSFR*

In Figure 20 we show the results of the piece-wise analysis of the radial distribution of the sSFR (see Figure 50). We find that the values of k_0 are relatively consistent for different bins of M_* within the late-type galaxies. There is a mild increment of the slope (from negative to positive gradients) as M_* increases. As for the gradients of $\Sigma_{\rm SFR}$, the Sa galaxies lie in the only morphological bin that shows significant variations in k_0. For those bins of M_* or morphology where we measure an external gradient (k_1 or k_2) the values are usually negative. Regarding the characteristic value of the radial distribution of sSFR (i.e., at $R_{\rm eff}$), we find that it varies significantly depending on the morphology. The characteristic sSFR from early-type galaxies is at least one order of magnitude smaller in comparison to late-type galaxies. For each morphological type we do not see significant variations of the characteristic sSFR for different stellar mass bins. Qualitatively, these gradients are in agreement with previous results using a larger heterogeneous sample of galaxies (Sánchez 2020).

4.3.3. *Star-Forming Efficiency, SFE*

In Figure 21 we show the piece-wise analysis of the average of the radial distribution of the SFE segregated by morphology for different stellar mass bins (see Figure 51). Contrary to the gradients of sSFR, for the SFE the slopes for all the bins of M_* and morphology are negative (i.e., $k_0 < 0$). The value of this slope for late-type galaxies varies depending on both stellar mass and morphology ($-1.0 < k_0 < -0.4$ dex/$R_{\rm eff}$). Although for most of the radial profiles a single gradient suffices to describe the radial trend of the SFE, for some morphological bins the piece-wise analysis detected another gradient at their outskirts (k_2, e.g., Sb galaxies). We exclude from this analysis those external gradients

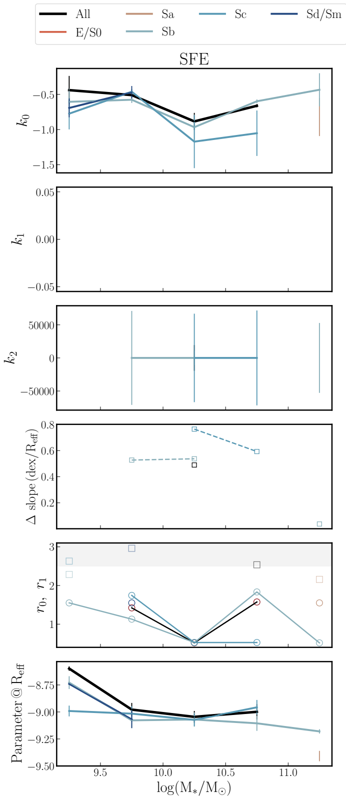

Fig. 21. Parameters derived from the piece-wise analysis for the radial distribution of the SFE. The layout of the figure is similar to Figure 4. The color figure can be viewed online.

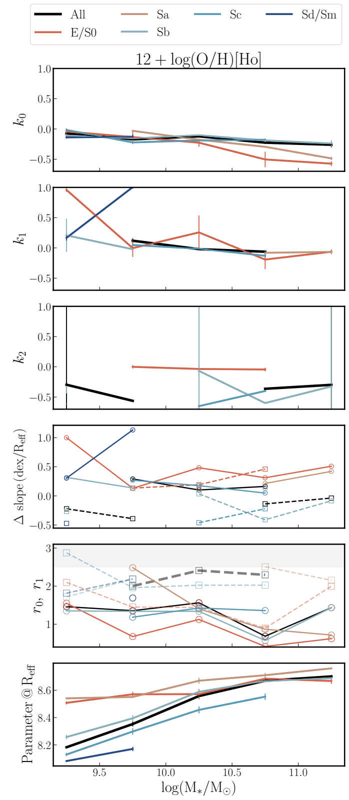

Fig. 22. The radial distribution of the oxygen abundance using the Ho calibrator. The layout of the figure is similar to Figure 4. The color figure can be viewed online.

with large values of k_2, as they are spurious. The value of this gradient depends on M_* with low and high masses having steeper gradients than the derived central values for the same mass bin. However, we note that these values may not be representative of the radial trend at these galactocentric distances, as they measure the very outer part of the galaxies. Similar to the characteristic values of sSFR, we find that for the SFE these values are similar for late-type galaxies regardless of the probed M_* (SFE $\approx 10^{-9.1}$ yr^{-1}). The trends presented here are in agreement with previous studies exploring the radial distribution of the SFE using spatially resolved observations of the molecular gas (e.g., Leroy et al. 2008; Villanueva et al. 2021).

4.4. *Chemical Abundances*

Thanks to the emission of different chemical species in the optical it has been possible to have an estimation of the amount of elements heavier than hydrogen or helium in the ISM. There is a plethora of chemical abundance calibrators in the literature, in particular of the oxygen abundance (Maiolino & Mannucci 2019, and references therein). In this analysis we present the radial distribution of the oxygen abundances using a fiducial calibrator for this abundance. However, in Appendix B we present the impact on the radial profiles of using different calibrators.

4.4.1. *Oxygen Abundance*

The oxygen abundance has been widely used to gauge the chemical stage of galaxies as well as its evolution (e.g., Maiolino & Mannucci 2019, and references therein). As we mention above, there is a large amount of abundance calibrators in the literature using different methodologies (e.g., direct estimations, photoionization models, or hybrid ones). In this section we present the analysis of the radial distribution of the oxygen abundance with an empirical calibrator derived using a neuronal network analysis from Ho (2019). Nevertheless, we present the same analysis of the radial distribution of the oxygen abundance using different calibrators in Appendix B [10]. When necessary, we briefly discuss the differences in the results using different calibrators. Although we try to minimize the impact of other sources of ionization, we note that the radial distribution of the oxygen abundance could be affected by ionization sources other than star-formation. For this reason we consider these gradients as upper limits of the abundances.

In Figure 22 we show the result of the piece-wise analysis of the radial distribution of the oxygen abundance for the MaNGA Golden Sample (see Figure 52). We find that the central gradient, k_0, is negative regardless of the morphology or M_*. For late-type galaxies (from Sb to Sd/Sm) we find little changes of k_0 with respect to M_* with an average value of $k_0 \approx -0.13$ dex/$R_{\rm eff}$. If any, we find a slightly flatter gradient for the lowest mass bin in comparison to massive ones. Interestingly, we find similar central gradients for early-type low-mass galaxies ($\log M_*/{\rm M}_\odot < 10.5$). For larger masses, early-type galaxies tend to have steeper gradients in comparison to late-type ones. For those radial profiles where we are able to measure an external gradient (k_1 and k_2) we find that these gradients range from positive to negative values (with most of the k_1 slopes being positive and k_2 being negative). For the characteristic oxygen abundance (measure at $R_{\rm eff}$), we find that for late-type galaxies it increases with M_*. On the other hand, it is relatively constant for early-type galaxies 12+log(O/H) ≈ -8.6. Furthermore, massive early-type galaxies tend to have characteristic abundances similar to their late-type counterparts.

These results are in partial agreement with previous results using the MaNGA dataset and other IFS data. On the one hand, we find more subtle variations of the slope (k_0) with M_* than those reported by Belfiore et al. (2017). Differences between that study and the work presented here are expected due to the differences in the samples (selection, sizes, etc) as well as the different oxygen calibrator adopted for each work. It could also be the case that the methodology for deriving the slopes of the gradients has an impact on these different works. In this work we employ a piece-wise analysis to take into account that the radial distribution could have different gradients at different galactocentric distances, whereas Belfiore et al. (2017) employed a linear fit with a single slope to describe the radial gradient of the oxygen abundance. On the other hand, regarding the morphology we find differences in the slope of the oxygen abundance only for early-type massive galaxies. Similar results have been reported recently using a larger sample of MaNGA galaxies (Boardman et al. 2021). Our results suggest that, at least for this sample of galaxies and for the adopted calibrator, the central gradient for late-type galaxies is rather constant for a wide range of M_*.

[10] Oxygen and nitrogen abundances presented in this study are derived using the script `pyOxy` (`https://github.com/cespinosa/pyOxy`).

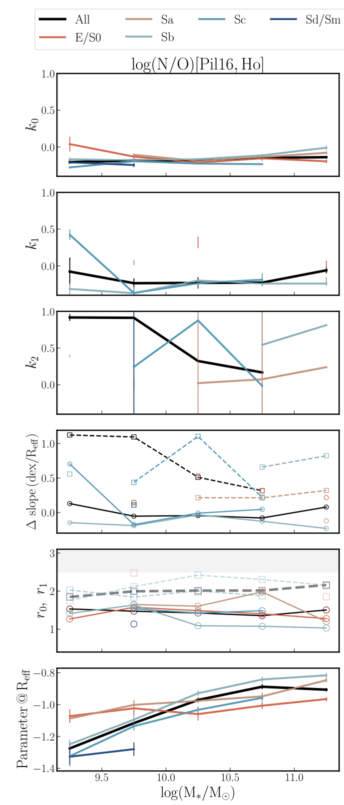

Fig. 23. The radial distribution of the N/O ratio. The layout of the figure is similar to Figure 4. The color figure can be viewed online.

The above results could vary significantly depending on the adopted calibrator. In Appendix B we present a similar analysis as the one derived above using two other calibrators (the empirical calibrator O3N2 from Marino et al. 2013 and the theoretical one from Kobulnicky & Kewley 2004). In this appendix we describe the differences in the gradients depending on the used abundance calibrator. In general, we find that the adopted calibrator could have a significant impact on the derived gradients for different morphologies and stellar masses.

4.4.2. *Nitrogen/Oxygen Abundances Ratio*

Having a measurement of chemical abundances with different nucleosynthesis origins, or their ratios, allows us in principle to quantify the scales of star formation across the evolution of galaxies. On the one hand, the oxygen abundance measures the chemical enrichment from short-lived massive stars. On the other hand, the nitrogen abundance partially measures the enrichment of the ISM from stars with a smaller mass and longer lifetimes. In this section we explore the radial distribution of their ratio in our sample of MaNGA golden galaxies. For the oxygen abundance we use the same calibrator described in the previous section, whereas for the nitrogen abundance we use the calibrator derived by Pilyugin & Grebel (2016).

In Figure 23 we present the piece-wise analysis of the radial distribution of the N/O ratio for our sample of galaxies. Contrary to the oxygen abundance analysis of the previous section, we find a significant impact of both the stellar mass and morphology in setting the gradient of the N/O ratio in the central portion of our sample, k_0. For late-type Sb galaxies, k_0 increases with M_*. In other words, for this morphological type the central slope changes from negative to almost flat gradients as M_* increases. The flatness in the central region for the most massive Sb galaxies could be a consequence of the line ratios tracing diffuse ionized gas in regions dominated by a bulge, instead of tracing star formation. Thus, the measurements of the N/O ratio for the central region may not be reliable – a similar scenario is likely occurring for E/S0 low-mass galaxies. However, we note that Espinosa-Ponce et al. (2022) found similar results using a large sample of HII regions with spectroscopic information. For Sc galaxies, k_0 is negative and similar regardless of the stellar mass, except for the lowest mass bin where the slope is steeper. For Sd/Sm galaxies the slope is similar to those derived from the Sc-type. For most of the bins of morphology and M_* where the piece-wise fit is able to measure k_1, we find that it is negative, slightly steeper than k_0. However, for those bins with three gradients we find that the outer one (i.e., k_2) is positive and significantly steeper. We consider that this may be an spurious artifact due to the lax cut in SNR. This affects the radial values of the N/O ratio at the outskirts of galaxies. According to our analysis, the change in slopes for the radial distributions occurs at $\approx 1.5\ R_{\rm eff}$, regardless of the stellar mass or morphology. The characteristic values of the N/O ratio at $R_{\rm eff}$ increases monotonically with M_*, regardless of the morphology. However, for a given stellar mass bin, the average value for the Sb galaxies is the largest in comparison to other morphological types among late-type galaxies. For early-type galaxies this characteristic value is relatively similar regardless of M_* $(\log(\mathrm{N/O}) \approx -1.0)$.

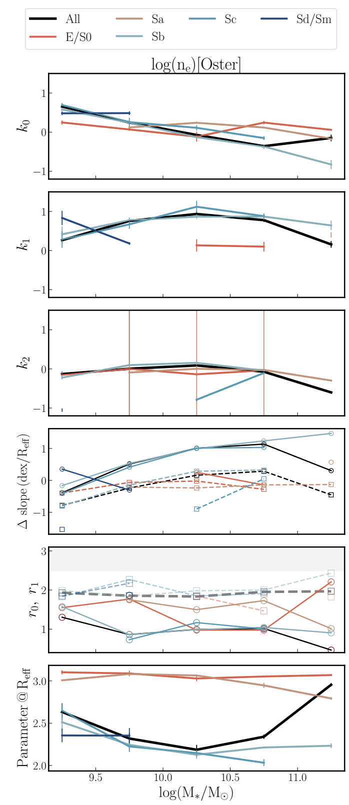

Fig. 24. The radial distribution of the electronic density derived from the Oster et al. calibrator. The layout of the figure is similar to Figure 4. The color figure can be viewed online.

Considering only our late-type sample, our central gradients from the N/O ratio differ from those derived by Belfiore et al. (2017) using a smaller sample of the MaNGA survey. Contrary to our results, they found that the gradient of the radial distribution decreases with M_*. As for the radial distribution of the oxygen abundance, these differences could be caused by the difference in the sample or by the adopted calibrators. Our results thus suggest that for late-type massive galaxies there is a flattening in the central gradient of N/O. On the other hand, using a large sample of HII regions with spectroscopic information drawn from the CALIFA survey and the same abundance calibrators, Espinosa-Ponce et al. (2022) found similar results as those derive in this study. In particular they also found flat gradients in the central part of massive Sb galaxies. This may suggest that even when using spectral information from HII the dominant ionization mechanism detected could be due to diffuse ionized gas.

4.5. *ISM Properties*

The ratio of the flux of different emission lines allows us to provide estimations of the physical properties of the ISM. In this section we explore the radial distribution of two parameters that are fundamental to understand the energetics of the ISM, the electron density, n_e, and the ionization parameter, U.

4.5.1. *Electron Density, n_e*

Usually the electron density is estimated using the emission line ratio from a single ion. To gauge n_e, we follow Espinosa-Ponce et al. (2022). They derived this density using the [S II] doublet solving the equation:

$$\frac{[\mathrm{SII}]\lambda6717}{[\mathrm{SII}]\lambda6731} = 1.49\frac{1+3.77x}{1+12.8x}\,, \tag{3}$$

where $x = 10^{-4} n_e t^{-1/2}$ and t is the electron temperature in units of 10^4 K (McCall et al. 1985). They assume a fiducial electron temperature expected for the usual conditions of an H II region ($t = 10^4$ K). Although this doublet is sensitive only to a narrow range of densities (≈50 to ≈7000 cm^{-3}, Osterbrock & Ferland 2006), it is still useful to gauge the radial distribution of n_e in our sample of MaNGA galaxies.

In Figure 24 we plot the results of the piece-wise analysis of the radial distribution of n_e for our Golden Sample (see Figure 54). We find that the central gradient of the radial distribution of n_e, k_0, changes significantly with M_*, going from positive to negative as the stellar mass increases. We find rather flat gradients for early-type galaxies. For those galaxies where we are able to estimate an external gradient, k_1, we find steeper positive values in almost all the bins of morphology and stellar mass. We find that the characteristic electron density measure at R_{eff} for late-type galaxies at different stellar mass bins is relatively constant ($n_e \approx 10^{2.1} - 10^{2.5}$ cm^{-3}). On the other hand, we find larger densities for massive early-type galaxies ($n_e \approx 10^{3.0}$ cm^{-3}). Radial trends similar to those derived in this study have been reported using large spectroscopic data sets of H II regions (Espinosa-Ponce et al. 2022). These trends have been attributed to the fact that denser material is located in regions of high pressure. Usually regions of high pressure are located at the central part of galaxies with little dependence on stellar mass or morphology (Barrera-Ballesteros et al. 2021).

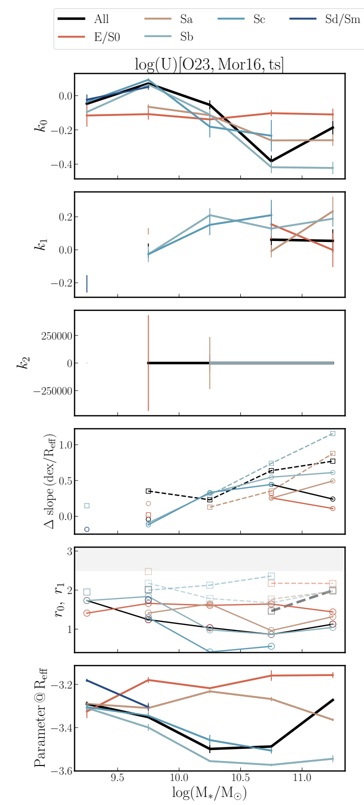

Fig. 25. The radial distribution of the ionization parameter derived from the calibrator presented by Morisset et al. (2016). The layout of the figure is similar to Figure 4. The color figure can be viewed online.

4.5.2. *Ionization Parameter*

The ionization parameter (U) measures the ratio between the number of ionizing photons and the number of atoms of hydrogen. Despite its importance, it is rather difficult to estimate U observationally. Although it is usually gauged using emission line ratios from a given element (e.g., [O III]/ [O II]), this parameter depends on the geometry of the explored regions, and the hardness of the ionizing spectra, among other properties. For this study, we estimate the ionization parameter and the above line ratio. We follow the relation derived from recent photoionization models from Morisset et al. (2016).

In Figure 25 we show the results from the piece-wise analysis of the radial distribution of the ionization parameter in our sample (Figure 55). In contrast to the early-type galaxies where the central gradient has small variations ($k_0 \approx -0.1$ dex/R_{eff}), late-type galaxies have significant variations of their central gradients for different bins of stellar mass. Late-type galaxies in the lowest mass bin tend to have a similar negative gradient as those derived

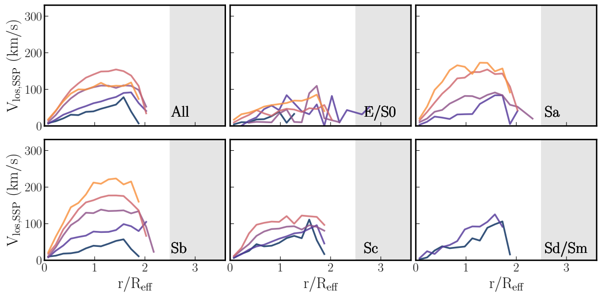

Fig. 26. The average radial distribution of the line-of-sight stellar velocity, $V_{\rm los,SSP}$. Similar to the distribution of Figure 3, the gradients are averaged by stellar mass and morphology. In each panel, each solid line represents the average profile per total stellar mass bin. The color figure can be viewed online.

for early-type galaxies, whereas for the next mass bin ($\log(M_* / \mathrm{M}_\odot) < 9.7$) we find that galaxies have a positive gradient. For the next two mass bins, late-type galaxies have negative gradients with k_0 decreasing as M_* increases. For the most massive bin (where it is only possible to measure the central gradient from Sb galaxies) k_0 remains with a similar negative slope as in the previous mass bin. Regardless of the stellar mass or the morphology, we find positive steep gradients in the outskirts of the galaxies in our sample. We find that the characteristic value of U measured at $R_{\rm eff}$ decreases with M_* for late-type galaxies, whereas for early-type objects this value of U is relatively constant for different bins of M_* ($U \approx 10^{-3.2}$). Qualitatively, our results are in partial agreement to those derived using a sample of H II regions from the CALIFA survey (Espinosa-Ponce et al. 2022), namely that in the central region of the galaxies the slopes of the gradients of U are usually negative or mildy possitive.

5. KINEMATIC PROPERTIES

To provide a reliable estimation of the properties of the stellar component from the continuum, the SSP fitting technique must be able to also provide an estimation of at least the first two moments of the line-of-sight velocity distribution (LOSVD) of the stellar component. In a similar fashion, the emission-line analysis should also provide an estimation of at least the two moments of the LOSVD of the ionized gas. Given the fact that the kinematic radial profiles follow different trends and that their shape is usually fitted by a non-linear function (e.g., López-Cobá et al. 2017; Barrera-Ballesteros et al. 2018), in this section we will provide a qualitative description of these kinematic features.

In Figure 26 we plot the radial distribution of the first moment of the LOSVD, $V_{\rm los,ssp}$, averaged for different stellar masses and morphologies. To create these radial profiles of $V_{\rm los,ssp}$ for each galaxy and each radial bin, we averaged the absolute values of velocity from the receding and the approaching sides of the stellar velocity field. The shape of the $V_{\rm los,ssp}$ profiles segregated only by stellar mass depends strongly on it (top left panel of Figure 26): massive galaxies exhibit a rising profile with a flattening at $\approx 1.5\ R_{\rm eff}$, whereas low-mass galaxies shows a monotonically increasing of $V_{\rm los,ssp}$. Furthermore, the absolute values of each radial profile increase with the stellar mass (e.g., measuring $V_{\rm los,ssp}$ at $R_{\rm eff}$), except for the most massive bin where the radial profile $V_{\rm los,ssp}$ is below the profile from the second most massive bin. We also find that, regardless of M_*, at large galactocentric distance $V_{\rm los,ssp}$ has a significant drop. These drops could be indicating the maximum radii at which it is possible to have a reliable measurement of the rotational curve for the galaxies; beyond those radii the measurements of the SNR of the continuum may not allow a proper estimation of $V_{\rm los,ssp}$. For consistency with the radial analysis of the other stellar properties we do not attempt any further selection of the radial profiles of $V_{\rm los,ssp}$. Segregated by morphology and stellar mass, the radial profiles of $V_{\rm los,ssp}$ reveal interesting features. For E/S0 galaxies (top middle panel of Figure 26) we find strong radial variations of $V_{\rm los,ssp}$ for different bins of M_*, except for the most massive bin, where we observe a monotonic increment of $V_{\rm los,ssp}$ with radius. These strong variations could suggest that early-type galaxies are supported by random motions instead of ordered ones. However, when we plot the radial distribution of the $\lambda_{\rm ssp}$ parameter, we find that these galaxies appear to be supported by these two components. We will come to this point below. For Sa galaxies we find a trend for the radial distributions of $V_{\rm los,ssp}$ similar to those observed using the entire GS for different bins of M_*; the gradient of $V_{\rm los,ssp}$ becomes steeper as M_* increases. Only the lowest probed mass bin shows a monotonically increment of $V_{\rm los,ssp}$, while the other profiles show a plateau at large galactocentric distances. For late-type galaxies (Sb, bottom left panel of Figure 26) we find that the shape of the radial profile of $V_{\rm los,ssp}$ varies for different stellar masses. Massive galaxies show a steeper gradient, and a flattening at large radii in comparison to low-mass galaxies that exhibit a monotonically increase of $V_{\rm los,ssp}$. For Sc galaxies (bottom middle panel of Figure 26) we observe a monotonically increment of $V_{\rm los,ssp}$ with radius, with

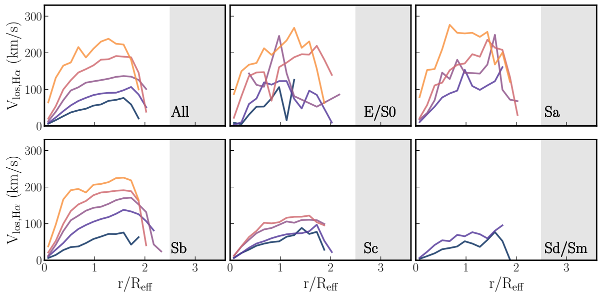

Fig. 27. The radial distribution of the line-of sight ionized gas velocity, $V_{\rm los,H\alpha}$. The layout of the figure is similar to Figure 26. The color figure can be viewed online.

little dependence on the stellar mass. As for the other stellar properties, for Sd/Sm galaxies we are able to measure the radial gradients of $V_{\rm los,ssp}$ only for low-mass galaxies. Thus the radial profiles of $V_{\rm los,ssp}$ show a monotonical increase with no signature of a plateau.

In comparison to $V_{\rm los,ssp}$, we find similar trends in the radial distribution of the velocity derived for the ionized gas, $V_{\rm los,H\alpha}$ (Figure 27). Averaging the gradients only over stellar mass, the increments for massive galaxies are stepper in comparison to low-mass galaxies. Similar trends are also observed when we average $V_{\rm los,H\alpha}$ over morphology and M_* bins in comparison to those derived for $V_{\rm los,ssp}$. Although the radial averages are similar, we note that $V_{\rm los,H\alpha}$ shows larger velocities in comparison to $V_{\rm los,ssp}$.

To further quantify these differences, we plot in Figure 28 the radial distribution of the $V_{\rm los,H\alpha}/V_{\rm los,ssp}$ ratio using the radial profiles of $V_{\rm los,H\alpha}$ and $V_{\rm los,ssp}$ presented in Figures 27 and 26, respectively. We find interesting features for the radial profiles of this ratio. When segregating the entire GS only by M_* we find that the most massive M_* bin shows a significant increment of $V_{\rm los,H\alpha}$ in comparison to $V_{\rm los,ssp}$ across the optical extension of the galaxies; furthermore, the radial profile of the $V_{\rm los,H\alpha}/V_{\rm los,ssp}$ ratio spikes at the central region of the galaxies with $V_{\rm los,H\alpha}/V_{\rm los,ssp} \approx 4$. For the rest of the stellar mass bins, the shape and values of this ratio are relatively similar. For the very center of galaxies the ratio is slightly below, or close to, 1. As the galactocentric distance increases this ratio remains relatively constant with $V_{\rm los,H\alpha}/V_{\rm los,ssp} \approx 1.2$; for radii larger than $r/R_{\rm eff} \approx 1.5$, this ratio drops to values close to zero. For early-type galaxies, this ratio strongly varies across the radial extension of the galaxies; therefore, it is not possible to provide a reliable description of it. For massive Sa galaxies ($\log(M_*/{\rm M}_\odot) \gtrsim 10.5$) we find that the radial profiles of the $V_{\rm los,H\alpha}/V_{\rm los,ssp}$ ratio have similar shapes and values as those derived for the entire sample. Sa galaxies with smaller stellar mass exhibit strong variations in the radial profiles of their velocity ratio. Except for the lowest-mass bin of Sb galaxies, these galaxies show a rather constant $V_{\rm los,H\alpha}/V_{\rm los,ssp}$ ratio across their optical extension, $V_{\rm los,H\alpha}/V_{\rm los,ssp} \approx 1.4$. Low-mass galaxies exhibit a rising profile reaching a peak of $V_{\rm los,H\alpha}/V_{\rm los,ssp} \approx 2$ at $r/R_{\rm eff} \approx 1.2$. After this radius the ratio decreases to values close to zero. For Sc galaxies the radial distribution of this ratio is relatively constant for the different mass bins ($V_{\rm los,H\alpha}/V_{\rm los,ssp} \approx 1$). Finally, for the Sd/Sm galaxies the $V_{\rm los,H\alpha}/V_{\rm los,ssp}$ ratio decreases as the radius increases. We note that we are only able to estimate this ratio for low-mass galaxies. Although the ratio at the center of these galaxies is larger than 1, it decreases reaching values close to zero at their outskirts. This analysis highlights the well-known interplay between the morphology and kinematic structure of galaxies (e.g., Cappellari 2016). For Sa galaxies, where the $V_{\rm los,H\alpha}/V_{\rm los,ssp}$ ratio is the largest, $V_{\rm los,H\alpha}$ traces ionized gas probably located in the mid-plane of the galaxy, whereas $V_{\rm los,ssp}$ is coupled with non-ordered motion in the line-of sight. On the other hand, for late-type galaxies both stars and ionized gas trace similar velocities, as both trace the ordered motions from the disk.

The SSP as well as the emission line analysis provides an estimation of the second momentum of the LOSVD, also known as the stellar and ionized gas velocity dispersions, ($\sigma_{\rm ssp}$, $\sigma_{\rm H\alpha}$, respectively). In Figure 29 we plot the radial distribution of $\sigma_{\rm ssp}$ for different stellar masses and morphologies. The top left panel of this figure shows the large impact that stellar mass has in the radial profiles of $\sigma_{\rm ssp}$. Massive galaxies ($\log M_*/{\rm M}_\odot > 11.0$, dark red profile) have the largest values of $\sigma_{\rm ssp}$. The central velocity dispersion for these massive galaxies reach the largest value (≈ 200 km s^{-1}) and their average radial profile decreases with galactocentric distance. For the lowest stellar mass bin ($10.5 < \log M_*/{\rm M}_\odot < 11.0$, yellow profile), the shape of the $\sigma_{\rm ssp}$ radial profile is similar, although its central value is significantly smaller than the one derived for the most massive galaxies; for large radius it reaches a flat gradient close to 10 km s^{-1}. For the remaining stellar mass bins the radial profiles are basically flat with a constant velocity dispersion of ≈ 10 km s^{-1}. For massive E/S0 galaxies $\sigma_{\rm ssp}$ decreases with radius; the central dispersion for the most massive galaxies is the largest of the entire sample (≈ 250 km s^{-1}). For

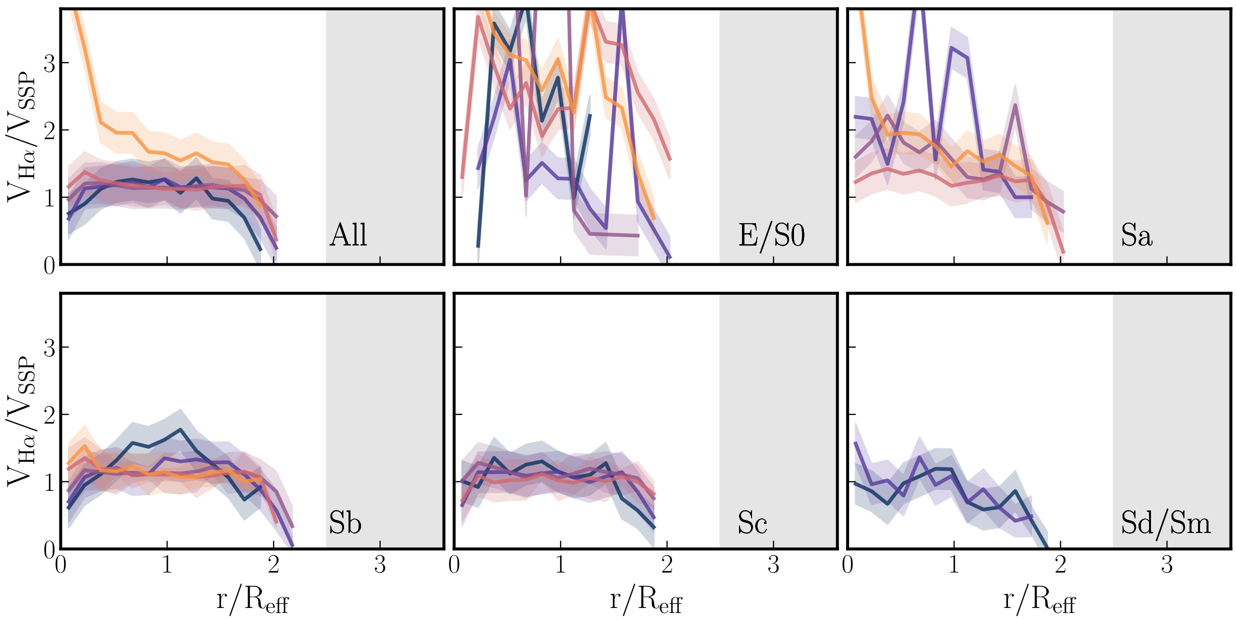

Fig. 28. The ratio of the radial profiles presented in Figures 27 and 26. The shaded area represents the standard deviation of the radial distribution in each radial beam. The layout of the figure is similar to Figure 26. The color figure can be viewed online.

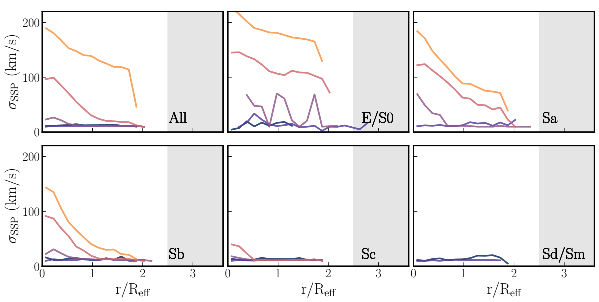

Fig. 29. The radial distribution of the stellar velocity dispersion, σ_{SSP}. The layout of the figure is similar to Figure 26. The color figure can be viewed online.

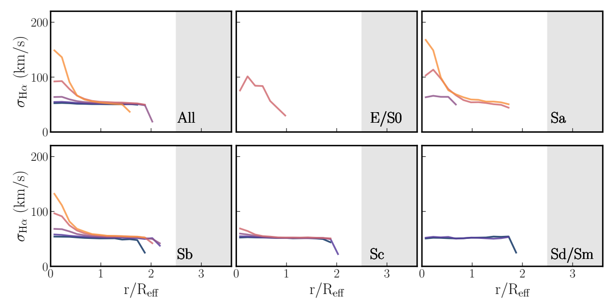

Fig. 30. The radial distribution of the stellar velocity dispersion, $\sigma_{\mathrm{H}\alpha}$. The layout of the figure is similar to Figure 26. The color figure can be viewed online.

low-mass E/S0 the radial profiles are flat, with values close to 0 km s^{-1}. Sa galaxies show a similar trend as those described for E/S0 galaxies, although the drop of σ_{ssp} with radius is sharper for massive Sa galaxies than for their E/S0 counterparts. For Sb galaxies the trends are similar to Sa galaxies. However, the drop for massive galaxies is even sharper than for Sa galaxies. For Sc and Sd/Sm galaxies we report flat gradients of σ_{ssp} with dispersions close to 0 km s^{-1}.

Similar to σ_{ssp}, in Figure 30 we plot the radial distribution of $\sigma_{\mathrm{H}\alpha}$. We find similar trends for different stellar masses and morphologies in comparison to those reported above for σ_{ssp}. However, we note two significant differences. On the one hand, the flattening of the $\sigma_{\mathrm{H}\alpha}$ radial profiles occurs at a higher velocity dispersion than for σ_{ssp}. This is expected, since the estimation of $\sigma_{\mathrm{H}\alpha}$ is significantly limited by the spectral resolution of the instrument ($\approx$ 45 km s^{-1}, Law et al. 2021). On the other hand, we find smaller values of $\sigma_{\mathrm{H}\alpha}$ in comparison of σ_{ssp}, as well as sharper drops of the velocity dispersion for massive galaxies. To account for these differences we follow a similar analysis as for the line-of-sight velocities, namely, we derive the ratio $\sigma^{corr}_{\mathrm{H}\alpha}/\sigma_{\mathrm{ssp}}$, where $\sigma^{corr}_{\mathrm{H}\alpha}$considers a correction in quadrature to $\sigma_{\mathrm{H}\alpha}$ in order to account for the instrumental resolution ($\sigma^{corr\,2}_{\mathrm{H}\alpha} = \sigma_{\mathrm{H}\alpha}{}^2 - \sigma^2_{ins}$), with σ_{ins} = 45 km s^{-1} (Sanchez et al., submitted).

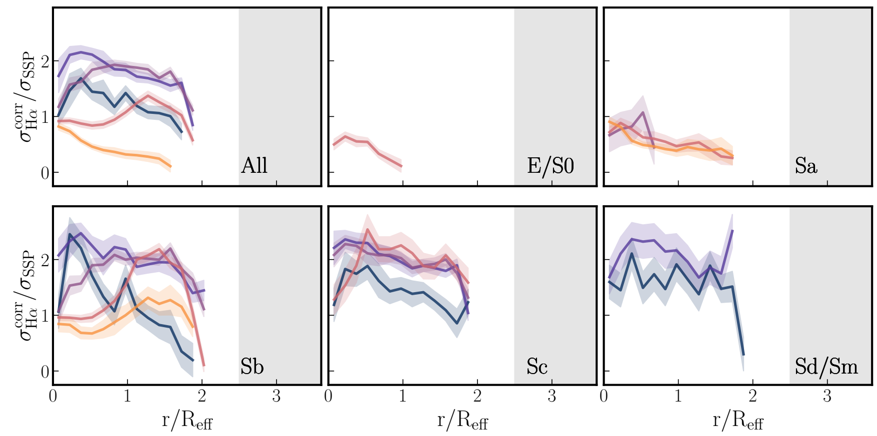

Fig. 31. The radial distribution of the $\sigma^{corr}_{\rm H\alpha}/\sigma_{\rm ssp}$ ratio. The layout of the figure is similar to Figure 26. The color figure can be viewed online.

In Figure 31 we show the radial distribution of the above ratio. When the sample is segregated only by stellar mass (top left panel), we observe different trends for the different stellar mass bins. For low and intermediate-mass galaxies we find that for the radial profiles $\sigma^{corr}_{\rm H\alpha}/\sigma_{\rm ssp} > 1$, suggesting that $\sigma_{\rm H\alpha}$ across these galaxies is larger than $\sigma_{\rm ssp}$. Furthermore the radial profiles of this ratio increase and peak up to certain galactocentric distance ($r/R_{\rm eff} \approx 0.5$); beyond this radius this ratio decreases with distance. On the other hand, for the most massive galaxies $\sigma^{corr}_{\rm H\alpha}/\sigma_{\rm ssp} < 1$ for all the radial bins. Although the central value is close to one, this ratio decreases with radius reaching values close to zero. For the intermediate stellar mass bin ($10.5 < \log M_*/{\rm M}_\odot < 11.0$, yellow profile) the central portion of the ratio is rather flat with $\sigma^{corr}_{\rm H\alpha}/\sigma_{\rm ssp} \approx 1$. However, at $r \approx R_{\rm eff}$ this ratio increases to ≈ 1.5, suggesting that for galaxies of that M_*, the dispersions are similar in their central portion, with an increase of $\sigma_{\rm H\alpha}$ at larger radii in comparison to $\sigma_{\rm ssp}$.

For early-type galaxies (top middle panel of Figure 31), we are able to make this comparison only for one stellar mass bin ($10.5 < \log M_*/{\rm M}_\odot < 11.0$, yellow profile). This profile shows $\sigma^{corr}_{\rm H\alpha}/\sigma_{\rm ssp} < 1$ with values decreasing with radius. As expected, $\sigma_{\rm ssp}$ is larger for E/S0 galaxies in comparison to $\sigma^{corr}_{\rm H\alpha}$. For Sa galaxies the radial distributions of $\sigma^{corr}_{\rm H\alpha}/\sigma_{\rm ssp}$ decreases with radius. However, all the values are below 1, except for the lowest mass bin sampled, although the values are highly variable. For these galaxies, as for the E/S0 sample, $\sigma_{\rm ssp}$ dominates over $\sigma^{corr}_{\rm H\alpha}$. For late-type Sb galaxies we find different trends for different mass bins (bottom left panel of Figure 31). The most massive Sb galaxies show central values of $\sigma^{corr}_{\rm H\alpha}/\sigma_{\rm ssp}$ slightly smaller than 1. However, as the galactocentric distance increases $\sigma^{corr}_{\rm H\alpha}/\sigma_{\rm ssp}$ has values above one for radii beyond 1.5 $R_{\rm eff}$. This change in tendency suggests that although for the central portion of massive Sb galaxies $\sigma_{\rm ssp}$ is larger than $\sigma^{corr}_{\rm H\alpha}$, at larger radii the situation is the other way around: turbulent motions of the ionized gas component dominate the ones from the stellar component. The lower mass bin of Sb galaxies (yellow profile) has a similar, yet more evident, radial trend of the $\sigma^{corr}_{\rm H\alpha}/\sigma_{\rm ssp}$ ratio in comparison to the red profile. For distances smaller than the $R_{\rm eff}$ this ratio is 1. However, it increases reaching values close to 2 around 1.5 $R_{\rm eff}$. Regardless of the galactocentric distance, we find for intermediate mass bins that the $\sigma^{corr}_{\rm H\alpha}/\sigma_{\rm ssp}$ ratio is larger than 1. For Sb galaxies with $10.0 < \log M_*/{\rm M}_\odot < 10.5$ (cyan profile), we find that this ratio increases with radius up to $R_{\rm eff}$; beyond that point the ratio is relatively flat reaching a constant value of $\sigma^{corr}_{\rm H\alpha}/\sigma_{\rm ssp} \approx 2$. For Sb galaxies with $9.5 < \log M_*/{\rm M}_\odot < 10.0$, the dispersion ratio decreases with distance from $\approx$2 to 1. For Sb galaxies, the radial profile with the sharpest variation of this ratio is the one corresponding to the lowest mass bin ($9.5 < \log M_*/{\rm M}_\odot$, dark-blue profile). For Sb galaxies, these objects have the largest $\sigma^{corr}_{\rm H\alpha}/\sigma_{\rm ssp}$ ratio at their center. However, as the galactocentric distance increases this ratio decreases, reaching values close to zero at their outskirts. For Sc galaxies, the $\sigma^{corr}_{\rm H\alpha}/\sigma_{\rm ssp}$ ratio is larger than 1 regardless of the probed stellar mass and radii. In general, for the probed bins of M_* we find that this ratio decreases with distance, with values close to 2 in the center to values close to 1 in

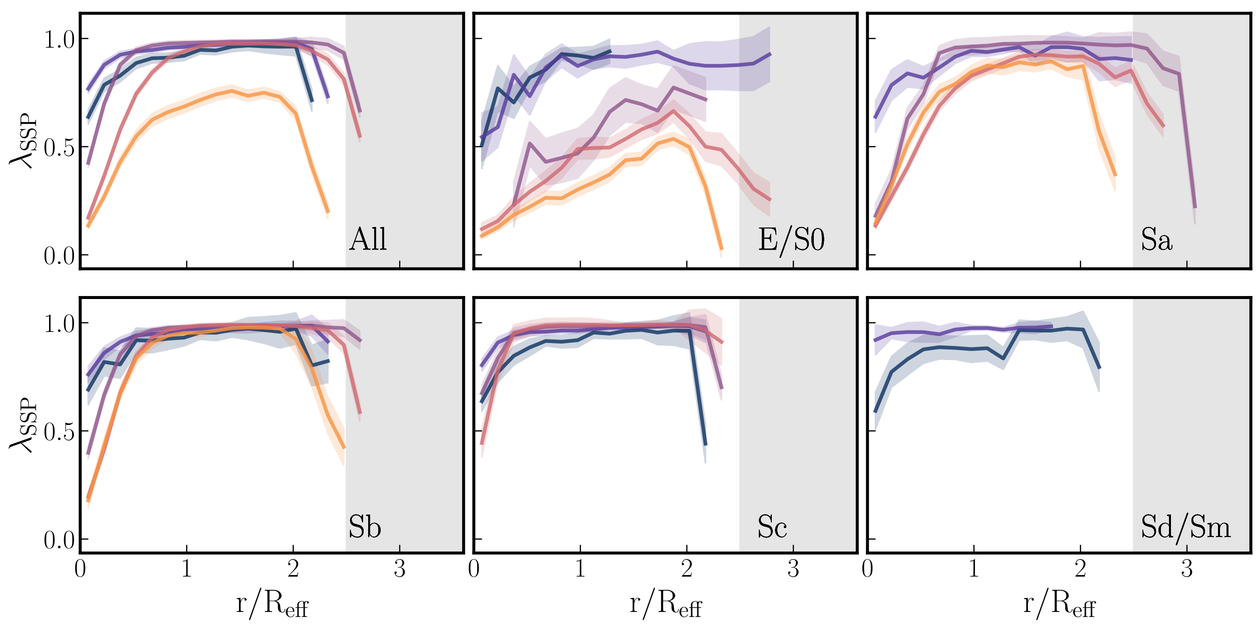

Fig. 32. The radial distribution of the λ parameter for the stellar component. The layout of the figure is similar to Figure 5. The color figure can be viewed online.

their outskirts. Finally, for the Sd/Sm galaxies we also find that this ratio is larger than 1 for the probed bins of M_* (low-mass galaxies) and radii. The values of this ratio are relatively constant for different radii, with $\sigma_{\mathrm{H}\alpha}^{corr}/\sigma_{\mathrm{ssp}} \approx 1.5$ - 2.

Thanks to the spatially resolved information of the MaNGA survey, we are able to probe the kinematic stage of the demographics in the nearby universe by comparing the kinematic properties of the stellar and the ionized gas. Furthermore, these radial profiles are also useful to explore dynamical differences in these components. For instance, by measuring the differences between $V_{\mathrm{los,ssp}}$ and $V_{\mathrm{los,H}\alpha}$ as well as σ_{ssp} and $\sigma_{\mathrm{H}\alpha}^{corr}$ we are able to explore how each of these components traces the potential well of the galaxies.

In Figure 32 we plot the radial distribution of the so-called apparent spin parameter for the stellar component λ_{ssp} (Emsellem et al. 2007) for different stellar masses and morphologies. This parameter is defined as:

$$\lambda_{\mathrm{ssp}} = \frac{\sum_{r'<r} f_\star \; r \; |v_\star|}{\sum_{r'<} f_\star \; r' \; \sqrt{v_\star^2 + \sigma_\star^2}}, \tag{4}$$

where $f_\star$, $v_\star$ and $\sigma_\star$ correspond to the stellar flux-intensity in the V-band at any position (x, y) within the FoV, the stellar velocity and the stellar velocity dispersion in each spaxel within the considered apertures, and r is the deprojected galactocentric distance. λ_{ssp}, which varies between 0 and 1, and gauges what sets the kinematic structure of a galaxy (Cappellari 2016). Values of λ_{ssp} close to 1 suggest that the region/galaxy is rotationally supported, whereas values close to zero suggest that the region/galaxy is supported by non-ordered motions. In general λ_{ssp} increases with distance, although the central shape of this increment varies depending on the stellar mass and morphology. Segregated only by stellar mass, the central value of λ_{ssp} decreases with M_*. This parameter increases steeply with distance, reaching the value of 1 at small galactocentric distances for most of the stellar mass bins, except for the most massive bin, where the radial profiles of λ_{ssp} reach a plateau at $\lambda_{\mathrm{ssp}} \approx 0.7$. For E/S0 galaxies the radial distributions of λ_{ssp} vary significantly depending on M_*. For low-mass galaxies the radial distribution rises very steeply becoming almost flat with values close to 1. For intermediate-mass and massive galaxies the radial profiles of λ_{ssp} monotonically increases. We note that the two more massive bins show a strong drop of λ_{ssp} at their outskirts. As we mention above, kinematic properties such as $V_{\mathrm{los,ssp}}$ may not be reliable at large radii due to our conservative cuts in SNR. These results suggest that for galaxies with this morphology the stellar mass plays a major role in setting the kinematic stage of the stellar component; low-mass E/S0 galaxies appear to be kinematically supported by rotation, while massive

E/S0 galaxies are supported by random motions or rotation, depending on the location. For the rest of the morphological bins the trends are similar for different bins of M_*. Most of the profiles exhibit an almost flat radial distribution close to 1 – except for the most massive galaxies. Other than the E/S0 morphological bin, we are able to measure the radial profile of $\lambda_{\rm ssp}$ for the most massive stellar bin only for Sa and Sb galaxies. In these morphological bins the radial profile of the most massive bin shows a sharp drop in their central region, suggesting that for these galaxies their centers are supported by random motions while the rest of the galaxy is supported by ordered motions. These results highlight the fact that, in comparison to morphology, M_* appears to play a major role in setting the radial distribution of $\lambda_{\rm ssp}$.

6. RADIAL PROFILES FROM THE ENTIRE MANGA SAMPLE

As we mention in § 2.2, in order to provide a reliable estimation of the radial distribution of the physical properties, we select from the entire MaNGA sample ($\approx$ 10000 targets) those galaxies that satisfy several criteria, including good radial coverage from the fiber bundle as well as reliable spatial sampling and resolution. These selection criteria yield what we refer in this study as the *Golden Sample, GS* ($\approx$ 13 % of the entire MaNGA sample). In this section we derive the radial distribution of the physical properties studied above for a much larger sample of MaNGA galaxies. The only selection criteria for this analysis is low-inclined galaxies (i.e., the major/minor axis ratio has to be smaller than 0.45). This criterion yields a sample of $\approx$ 7500 galaxies. Evidently, the entire sample provides a much better coverage on M_* and morphology. Since the GS includes those galaxies with the best spatial coverage and resolution, here we only provide a qualitatively comparison between the radial profiles from the GS and those derived from the entire sample. We refer the reader to the following web page, where we include the same analysis for the entire sample: `http://ifs.astroscu.unam.mx/MaNGA/Pipe3D_v3_1_1/radial/figures/`

M/L **ratio, and** Σ_***:** In general, the radial profiles of the M/L ratio for the entire sample show negative trends similar to those derived for the GS (see Figures 4 and 33). As for the GS, the central gradient of the radial profiles of M/L ratio depends mainly on M_*. Furthermore, the characteristic value of this ratio strongly depends on the morphology. Similarly, for the entire sample the radial profiles of Σ_* decrease with radius as for the GS. However, we note sharp drops at large radii for low-mass galaxies regardless of the morphology. On the other hand, contrary to the GS, the characteristic value of Σ_* for the entire sample appears to depend strongly on both M_* and morphology.

Stellar age, metallicity, and extinction: The central gradients of the stellar age are slightly flatter for the entire sample in comparison to the GS. As for Σ_*, we note that for some bins of morphology and M_* the age shows a sharp drop at the outskirts of galaxies. As for the gradients of stellar metallicity, although we find similar negative central slopes in both the complete and the Golden Sample, for the entire sample we find step positive external gradients in different bins of morphologies and stellar mass. As for other measurements, such as those derived from the emission lines, we are finding that for galaxies with positive gradients at the outskirts the continuum flux is dominated by the noise; therefore those values of metallicity are not reliable. Finally, for the optical extinction we find that the gradients of the entire sample are similar to the GS; however, they are slightly smoother, that is, the gradients at the outskirts tend to be similar to those derived for the central part of galaxies.

Emission lines fluxes, EW(Hα), and line ratios: Although the general behavior of the slopes of the radial gradients of different emission lines (Hα,Hβ, [NII], and [OIII]) for the entire sample is similar to the one measured from the GS (i.e., negative gradients), we find that regardless of the emission line, the central gradients for early-type galaxies are similar to those derived for late-type galaxies. We recall that in § 4.1 we found that the early-type galaxies showed sharper negative gradients in comparison to late-type for the probed bins of M_*. In contrast to the GS, in the eintire sample it is more difficult to observe the difference between the characteristic flux measured at $R_{\rm eff}$ for early-type galaxies and for late-type ones. For the radial distribution of the EW(Hα) using the entire sample, we find similar trends as those measured in the GS, both in slopes and characteristic radii. As we discuss in the next section, we consider that those variations in the gradients are caused mainly by the impact of the bulge. Regarding the radial distribution of the emission line ratios (Hα/Hβ, [NII]/Hα, and [OIII]/Hβ), we find trends similar to the GS, as well as similar characteristic values. Other properties derived from the emission line ratios for the entire sample, such as $\rm Av_{gas}$, the $\rm Av_{gas}/Av_{SSP}$ ratio, $\Sigma_{\rm mol,Av}$, and $\rm f_{mol}$, show radial distributions similar to those derived from the GS.

$\Sigma_{\rm SFR}$, sSFR, and SFE: The radial distribution of the $\Sigma_{\rm SFR}$ for the entire sample is similar to the one derived for the GS. We find a negative gradient across the entire extension of the galaxies. Although we note some deviations from this gradient depending on the stellar mass and morphology (e.g., an almost flat gradient for the lowest-mass bin of early-type galaxies). The characteristic values of $\Sigma_{\rm SFR}$ measured at $R_{\rm eff}$ vary depending on both M_* and the morphology: they usually increase from early to late type galaxies for a given bin of M_*. Similar to the GS, the entire sample shows an almost flat gradient for the sSFR (although at large radii some profiles show drops), regardless of the stellar mass and morphology. As for the GS, there is a clear segregation between the sSFR measure at $R_{\rm eff}$ for early and late-type galaxies: early galaxies have significantly smaller sSFR in comparison to late-types for the same stellar mass bin. For the radial distribution of the SFE we find a characteristic negative gradient regardless of the stellar mass and morphology. However, we find significant variations of the SFE measured at $R_{\rm eff}$ for both stellar bins of M_* and morphology.

Oxygen abundance, N/O ratio, electron density, and ionization parameter: The radial distribution of the oxygen abundance using the entire sample, and the Ho calibrator (Ho 2019), is very similar to the one derived from the GS adopting the same calibrator. However, the piece-wise analysis provides a better description of the radial profiles when using the entire sample in comparison to the GS. For the entire sample, the slope of the central gradient decreases, k_0 with M_*. It is important to note, that the extension of the central gradient also varies depending on M_*. The extension where the piece-wise analysis detects k_0 is significantly smaller for massive galaxies in comparison to galaxies with lower mass. When comparing the large extension of the galaxies, the slope of the radial distribution is similar for different bins of M_*,except for the lowest-mass bin, where the slope is flatter in comparison to other mass bins. The characteristic oxygen abundances are the same, regardless of the sample. These results are in agreement with those presented previously in the literature using the same sample of galaxies (e.g., Barrera-Ballesteros et al. 2016; Boardman et al. 2021). We also find similar distributions for the N/O ratio, the electron density, and the ionization parameter for both samples. These results suggest that the GS is a representative sample of the entire MaNGA sample regarding the estimation of radial properties of the ionized gas.

Stellar and ionized gas kinematics: For the entire sample we find that the radial distribution of $V_{\rm los,ssp}$ is similar to the one derived for the GS for most of the bins of morphology and M_*. We only find significant differences for E/S0 low-mass galaxies: instead of strong radial variations in $V_{\rm los,ssp}$, we find that their radial profile is flat and close to zero km s $^{-1}$. Similar to $V_{\rm los,ssp}$, we find common trends between the entire sample and the GS for the radial distribution of $V_{\rm los,H\alpha}$. As above, the entire sample provides a smoother radial profiles of $V_{\rm los,H\alpha}$ for E/S0 galaxies in comparison to those derived for the GS. From the comparisons above it is clear that the radial distribution of the $V_{\rm los,H\alpha}/V_{\rm los,ssp}$ ratio is similar when using the entire sample or the GS. Nevertheless, we note that for the entire sample the most massive E/S0 galaxies are those responsible for the large ratio observed for the entire population of massive galaxies (e.g., top left panel of Figure 28). Although the radial distribution of both $\sigma_{\rm ssp}$, and $\sigma_{\rm H\alpha}$ are similar for both the entire and the GS, we find significant differences when we compare the radial distribution of the $\sigma_{\rm H\alpha}^{corr}/\sigma_{\rm ssp}$ ratio between the two samples. Contrary to the GS, the radial distribution of this ratio when using the entire sample segregated only by M_* is relatively flat and close to one. Similar trends are observed for the Sb galaxies. Finally, we find similar radial trends for $\lambda_{\rm ssp}$ between the entire sample and the GS. The above results show that the most significant difference, kinematically speaking, when using a sample that provides the best conditions to derive radial profiles and the entire MaNGA sample is observed in their velocity dispersion of both components. This could indicate that, rather than affecting the systemic velocity of the galaxies, using a large sample of galaxies averages a non-linear property such as the velocity dispersion.

7. DISCUSSION

Along this study we explore the radial distribution of the different physical properties that can be derived from the optical spectra (i.e., the stellar and ionized gas properties). We use a piece-wise analysis to account for possible variations on the slopes of the gradients from those radial distributions. In general, we find that for those parameters that relate to an absolute property, a gradient with a single slope usually suffices to describe them (e.g., Σ_*, $\mathrm{Av}_{\rm SSP}$, emission-line fluxes). On the other hand, we find that for some relative properties a gradient with different slopes is needed to provide a good representation of the radial distribution of those parameters (e.g., M/L, EW(Hα), emission-line ratios). We also find that the election of a gradient with a single or several slopes for the radial distribution of a given property also depends on both the morphology and the stellar mass: for a significant fraction of parameters the slopes for early-type galaxies differ from those measured for late-type ones. This is also valid for the absolute values of the radial distributions (measured by their characteristic value at $R_{\rm eff}$).

One of the physical properties that best exemplifies the need of using gradients with different slopes to describe its radial distribution is the EW(Hα): see the piece-wise analysis and the radial distribution in Figures 10 and 41, respectively (see also the line ratios [NII]/Hα and [OIII]/Hβ). As we describe in § 4.1, the signs of the slopes vary from positive to negative for the central and external parts of the radial distribution of the EW(Hα), respectively. This transition of gradients is evident for Sb galaxies, regardless of the total stellar mass. On the other hand, early-type galaxies (E/S0, Sa) show a flat gradient regardless of M_*. As we mention in § 4.1 the EW(Hα) measures the star-formation activity. Thus, regions with an EW(Hα) $\lesssim$ 6Å correspond to an ionization source different than star formation (e.g., diffuse ionized gas, DIGs, from HOLMES), whereas larger values of EW(Hα) are associated with star-formation: the larger the value of EW(Hα) the more star-formation activity is occurring.

The change in the slopes for Sb galaxies reflects what we consider is the impact of the galaxy's structure, in particular, the presence of a bulge in the center of galaxies. For instance, the central value of EW(Hα) from the most massive Sa galaxies is similar to those derived from E/S0 and Sa galaxies (i.e., below 6Å) suggesting that even though the galaxy has a late-type morphology in its center it has properties similar to an early-type galaxy. As the galactocentric distance increases the EW(Hα) increases reaching a peak around $\approx 1.2R_{\rm eff}$. This could indicate a composite stage where DIGs and star-forming regions cohabit, and as the galactocentric distance increases the star-formation increases overcoming the contribution from DIGs, reaching a maximum contribution at $\approx 1.2R_{\rm eff}$. For galactocentric distances larger than $\approx 1.2R_{\rm eff}$, EW(Hα) decreases with radius reaching again values below 6Å. The slope of this decrease is similar to the negative slope derived from other late-type galaxies (Sc and Sd/Sm). This indicates that for farther distances the properties of an Sb galaxy resemble those expected for late-type galaxies. Our results thus suggest that particular types of galaxies, such as the Sb galaxies, can be considered as a composition between an early-type galaxy in their center and a disk one in their outskirts.

Using IFS data, different works have suggested a similar scenario for galaxies with bulges. Using a photo-spectral decomposition of galaxies Méndez-Abreu et al. (2019) obtain the spectra for individual structural components of S0 galaxies, in particular, their bulges and disks (see also, Johnston et al. 2017; Méndez-Abreu et al. 2021). They find that indeed the physical properties of these galaxies are different between their center and their outskirts. For instance, the properties of the ionized gas in the central region resemble those of early-type galaxies, whereas the properties of the outskirts are consistent with those derived from late-type galaxies. In other words, our results suggest that for those galaxies where we find significant differences in the slopes of their gradients, this is due to the fact that the physical properties are different across their optical extension. Furthermore, for bulge galaxies our results also agree with the scenario in which bulges (or central parts of the galaxies) were formed at early ages of the universe, either by monolithic collapse or by major mergers, whereas the outskirts of galaxies were likely formed after the formation of the bulge via different evolutionary channels (e.g., gas accretion or wet minor-mergers). Moreover, for the entire sample of galaxies our results also support the scenario in which galaxies form in an inside-out fashion.

8. SUMMARY AND CONCLUSIONS

Using the MaNGA sample (the largest IFU sample up to date, with $\approx$ 10000 galaxies), we present one of the most comprehensive explorations of the radial distribution of physical properties derived from both the stellar continuum and the ionized gas emission lines in the optical (including their main kinematic properties). From the entire sample we select a so-called *Golden Sample*, in other words, we select the closest targets with the best spatial coverage ($\approx$1400 galaxies). Given the size of the sample we are able to disentangle the impact of two fundamental global properties: the total stellar mass, M_*, and the morphology. To quantify the gradients of those radial distributions, we make use of a piece-wise analysis allowing us to measure changes in the slope of those radial profiles as well as its characteristic value (i.e., measured at $R_{\rm eff}$). This allows us to quantify how the absolute values of a given property change depending on either the stellar mass or the morphology. We also explore how these radial distributions vary when considering larger samples of galaxies at different distances (or physical spatial resolution) and with different spatial coverage ($\approx$ 7000 galaxies).

In general, we find that most of the physical properties from both components decrease with distance (e.g., Σ_*, and Hα flux) with M_* and the morphology, modulating their gradient as well as their characteristic values for some observables. Here we summarize the main results from this study for the different properties derived from the stellar continuum and ionized gas emission lines using the *Golden Sample*:

- The stellar mass surface density, Σ_*, as well as the stellar mass-to-light ratio, M/L, decrease with radius. Their slopes and characteristic values at $R_{\rm eff}$ become steeper and larger as M_* increases. Although morphology does not seem to significantly affect these slopes, the characteristic values for early-type galaxies are larger in comparison to late-type ones for a given bin of M_*. These results are in agreement with those derived for a heterogeneous sample of galaxies (Sánchez et al. 2021).

- Both the luminosity-weighted stellar age and metallicity show in general negative central slopes regardless of M_* and morphology. Although these gradients are close to flat, we find a mild trend with M_*, with the slopes becoming stepper as M_* increases. The characteristic values of both properties increase with M_*. Early-type galaxies are older and more metal rich in comparison to late-type galaxies of similar M_*. The central slope of the radial distribution of the stellar optical extinction, Av$_{\rm SSP}$, is close to zero for late-type galaxies and positive for early-type ones; external slopes are positive. The characteristic stellar extinction is significantly affected by morphology; late-type galaxies have larger values of Av$_{\rm SSP}$ in comparison to early-type object of similar M_*.

- The radial distributions of the flux from the brightest emission lines have a negative slope, with similar values for the probed lines. We do not find significant differences in their slope for different stellar mass or morphology. However, depending on the emission line, their fluxes at $R_{\rm eff}$ depend on M_* and morphology.

- From these emission lines we derive the radial distribution of their ratios. Depending on the ratio, the slope of the gradients can depend on both M_* and morphology. The Hα/Hβ line ratio allows us to estimate the optical extinction, Av$_{\rm gas}$ which in turn allows us to estimate the radial distribution of the molecular gas mass density, $\Sigma_{\rm mol,Av}$. We also present the radial distribution of properties derived from Av$_{\rm gas}$: Av$_{\rm gas}$/Av$_{\rm SSP}$, and $f_{\rm mol}$. As explored by previous spatially resolved studies (Li et al. 2021), we find that the radial distribution of the Av$_{\rm gas}$/Av$_{\rm SSP}$ ratio is not constant, but decreases with radius. Furthermore, the slope becomes steeper as M_* increases. On the other hand, $f_{\rm mol}$ has positive gradients regardless of M_* or the morphology.

- The slopes of the $\Sigma_{\rm SFR}$ gradients are negative with a similar value regardless of M_* or the morphology. On the other hand, the central slopes of the sSFR radial distribution have a mild variation from negative to positive, whereas the outer gradients have negative slopes. The slope of the gradient of SFE has negative values. For these three parameters, late-type galaxies have large characteristic values in comparison to early-type galaxies at similar M_*.

- We find that in general the radial gradients from the central portion of the oxygen abundance derived from emission-line calibrators have negative slopes. The exact values of those gradients depend on the calibrator. Contrary to previous studies, we do not find a strong impact of M_* on those gradients for late-type galaxies. The values of the oxygen abundance at $R_{\rm eff}$ strongly depend on both M_* and the adopted calibrator.

- The MaNGA dataset allows us to measure the radial distribution of the line-of-sight velocity from the stellar and ionized gas components. We find that, for both components, massive galaxies have a steeper increase in $V_{\rm los}$; these galaxies reach the expected plateau at smaller galactocentric distances in $V_{\rm los}$ than low-mass galaxies. Morphology also has a significant role in shaping those radial profiles: late-type galaxies have steeper gradients than those derived from early-type galaxies. On the other hand, the velocity dispersion of both components decreases with radius for the most massive galaxies, whereas for the low-mass galaxies the profiles are flat and close to 0 km/s.

- Using the kinematic information from each component we explore the radial distribution of the $V_{\rm los,H\alpha}/V_{\rm los,ssp}$ and $\sigma^{corr}_{\rm H\alpha}/\sigma_{\rm ssp}$ ratios. Although the $V_{\rm los,H\alpha}/V_{\rm los,ssp}$ is relatively constant (close to unity) for different bins of M_* and morphology, we find that in the center of massive galaxies this ratio reaches values larger than 3. This is due to the large central value of $V_{\rm los,H\alpha}$ in comparison to $V_{\rm los,ssp}$ in early-type galaxies. On the other hand, the radial distribution of the $\sigma^{corr}_{\rm H\alpha}/\sigma_{\rm ssp}$ ratio varies significantly depending on both M_* and the morphology.

- In general, we find that the radial properties derived from the *Golden Sample* for the stellar and ionized gas components are similar to those derived from a larger low-inclined sample (≈7500 galaxies).

The radial distributions observed for the different parameters presented in this study are a significant evidence that the main processes responsible to shape the formation and evolution of galaxies appear to occur at kpc scales. These radial profiles are the result of the scaling relations derived at kpc scales; thus, at the same galactocentric distance the physics that regulates the properties of both the stellar component, the ionized gas, and the interplay between them is similar. Furthermore, these radial distributions suggest an inside-out formation scenario. Global properties, such as the stellar mass or morphology, play a secondary role in setting the local properties of galaxies in the local universe.

J.B-B acknowledges support from the grant IA-101522 (DGAPA-PAPIIT, UNAM) and funding from the CONACYT grant CF19-39578. L.C. thanks the support from the grant IN103820 (DGAPA-PAPIIT, UNAM). This research made use of Astropy,[11] a community-developed core Python package for Astronomy (Astropy Collaboration et al. 2013, 2018).

Funding for the Sloan Digital Sky Survey IV has been provided by the Alfred P. Sloan Foundation, the U.S. Department of Energy Office of Science, and the Participating Institutions.

SDSS-IV acknowledges support and resources from the Center for High Performance Computing at the University of Utah. The SDSS website is www.sdss.org.

SDSS-IV is managed by the Astrophysical Research Consortium for the Participating Institutions of the SDSS Collaboration including the Brazilian Participation Group, the Carnegie Institution for Science, Carnegie Mellon University, Center for Astrophysics — Harvard & Smithsonian, the Chilean Participation Group, the French Participation Group, Instituto de Astrofísica de Canarias, The Johns Hopkins University, Kavli Institute for Physics and Mathematics of the Universe (IPMU) / University of Tokyo, the Korean Participation Group, Lawrence Berkeley National Laboratory, Leibniz Institut für Astrophysik Potsdam (AIP), Max-Planck-Institut für Astronomie (MPIA Heidelberg), Max-Planck-Institut für Astrophysik (MPA Garching), Max-Planck-Institut für Extraterrestrische Physik (MPE), National Astronomical Observatories of China, New Mexico State University, New York University, University of Notre Dame, Observatário Nacional / MCTI, The Ohio State University, Pennsylvania State University, Shanghai Astronomical Observatory, United Kingdom Participation Group, Universidad Nacional Autónoma de México, University of Arizona, University of Colorado Boulder, University of Oxford, University of Portsmouth, University of Utah, University of Virginia, University of Washington, University of Wisconsin, Vanderbilt University, and Yale University.

[11]http://www.astropy.org

APPENDICES

A. RADIAL PROFILES AND GRADIENTS

In this Appendix we include the averaged radial profiles for the properties explored in this study. As we mention in § 2.4, we present these radial profiles for different bins of morphology and stellar mass.

B. OXYGEN ABUNDANCES USING DIFFERENT CALIBRATORS

As we mention in § 4.4.1, thanks to the `pyOxy` script, we are able to estimate the oxygen abundance using a large suite of strong-line calibrators. Although the script allows an estimation of the oxygen abundance for more than 20 calibrators, in this appendix we present the radial distribution and the piece-wise analysis using two of them, which we consider to be representative of this large set of calibrators: the empirical calibrator using the O3N2 ratio from Marino et al. (2013), and the theoretical calibrator using different line ratios proposed by Kobulnicky & Kewley (2004).

In Figure 56 we present the radial distribution of the oxygen abundance using the O3N2 abundance calibrator derived in Marino et al. (2013), whereas in Figure 58, we show the result from the piece-wise analysis of these radial profiles. In comparison to the results derived using the calibrator derived by Ho (2019, see Figure 22), we find that the central gradients (k_0) using this O3N2 calibrator are flatter (and in some cases of opposite sign). The trend from k_0 for different bins of M_* for the Sb galaxies using the O3N2 calibrator is similar to those described by Belfiore et al. (2017): k_0 increases as M_* increases (except for the lowest-mass bin). However, for Sc galaxies we find that k_0 decreases with M_*. A similar trend is observed for Sd/Sm galaxies. For early-type galaxies we find flat gradients regardless of M_*. For the outskirts of galaxies the piece-wise analysis shows that the gradients ($k1$) change from positive to negative as M_* increases. This piece-wise analysis provides a more complete description of the radial gradients in comparison to assuming a single gradient to the entire radial distribution of the oxygen abundance (e.g., Sánchez-Menguiano et al. 2018). Finally, we find trends of the characteristic abundance using the O3N2 calibrator similar to those derive using the calibrator derived by Ho (2019). For late-type galaxies this abundance increases with M_* despite some variation among galaxies of this type: For a given stellar mass bin the oxygen abundance increases from Sd/Sm galaxies to Sb ones. For early-type galaxies the characteristic value of the oxygen abundance remains constant regardless of the morphological type (E/S0 or Sa) and M_* ($12 + \log(\mathrm{O/H}) \approx -8.5$).

In Figure 57 we present the radial distribution of the oxygen abundance using the O3N2 abundance calibrator derived in Kobulnicky & Kewley (2004), whereas in Figure 59, we show the result from the piece-wise analysis of these radial profiles. In general, we find results similar to those derived using the O3N2 calibrator.

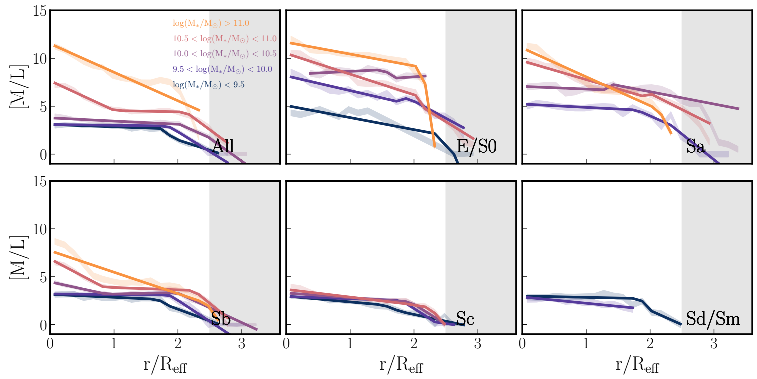

Fig. 33. Similar to Figure 3 for the M/L ratio. The gradients are averaged by morphology (panels from left to right and top to bottom) and total stellar mass bins (shaded colored areas; each color represents a stellar mass bin; see the legend at the top-left panel). The gray shaded area in each panel represents the typical maximum radius covered by the FoV ($R_{\rm eff} \approx 2.5$). The solid lines in each panel represent the best fit derived from fitting a piecewise function to the radial distribution. The color figure can be viewed online.

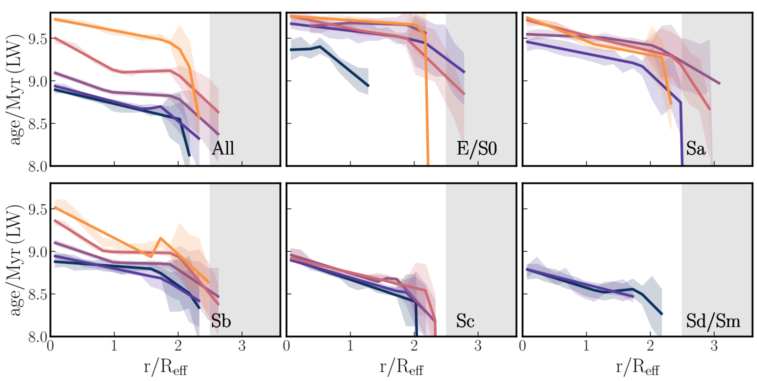

Fig. 34. Similar to Figure 3 for the luminosity-weighted age of the stellar population. The color figure can be viewed online.

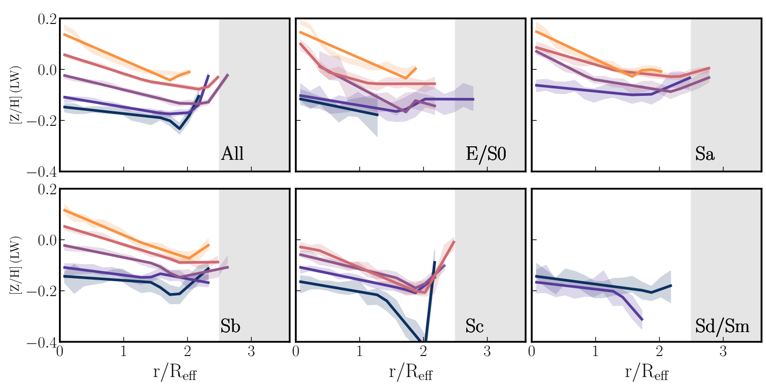

Fig. 35. Similar to Figure 3 for the luminosity-weighted stellar age. The color figure can be viewed online.

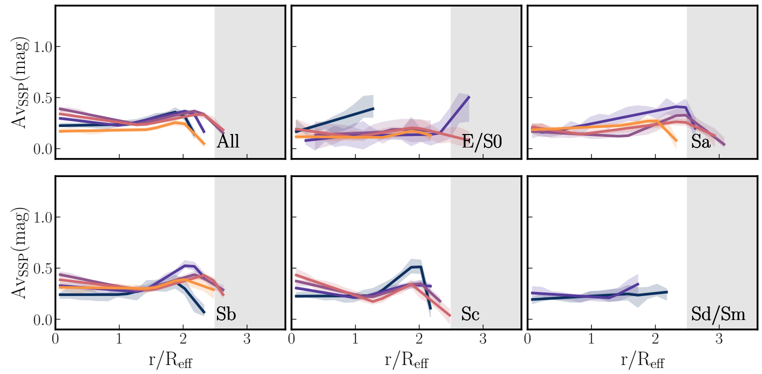

Fig. 36. Similar to Figure 3 for the luminosity-weighted stellar age. The color figure can be viewed online.

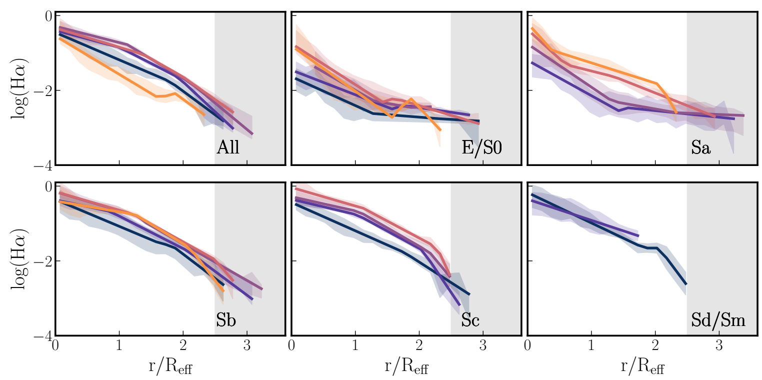

Fig. 37. Similar to Figure 3 for the Hα emission line. The color figure can be viewed online.

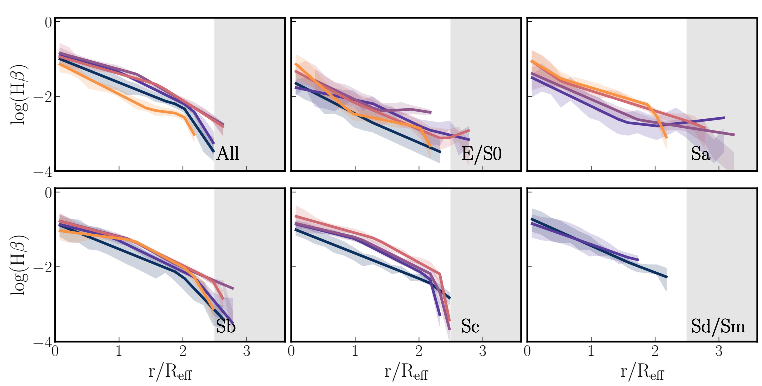

Fig. 38. Similar to Figure 3 for the Hβ emission line. The color figure can be viewed online.

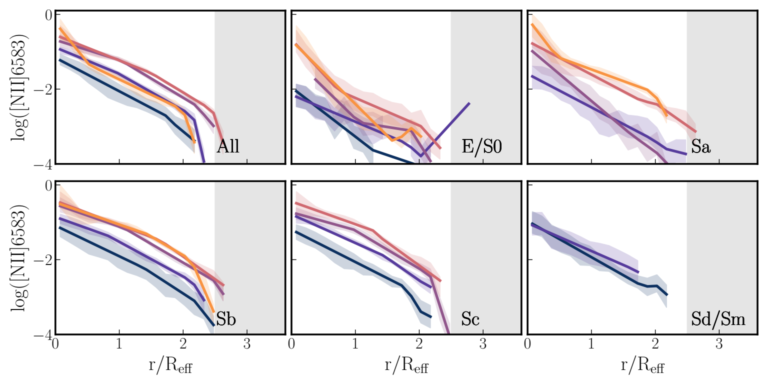

Fig. 39. Similar to Figure 3 for the [NII] emission line. The color figure can be viewed online.

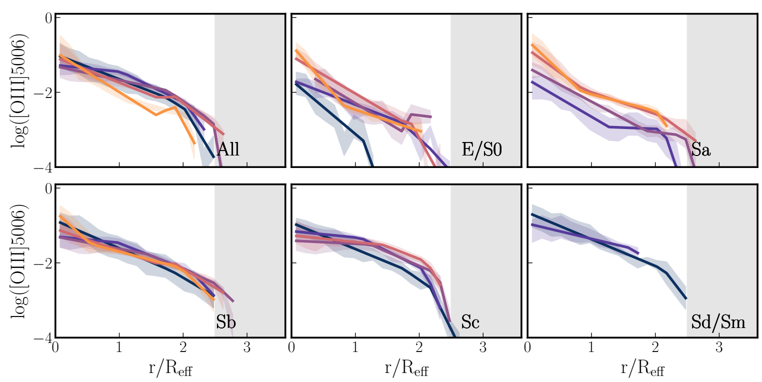

Fig. 40. Similar to Figure 3 for the [OIII] emission line. The color figure can be viewed online.

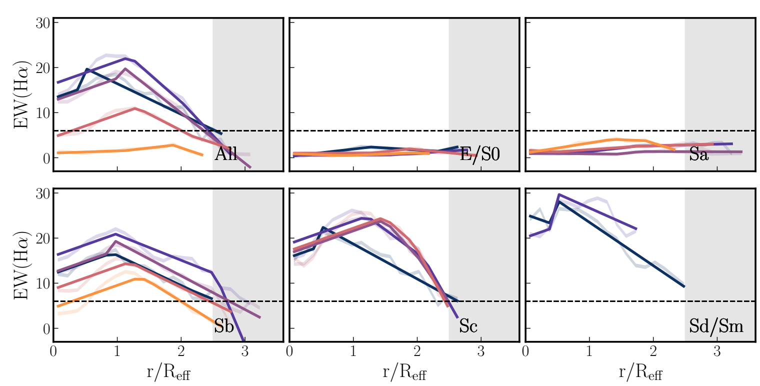

Fig. 41. Similar to Figure 3 for EW(Hα). The dashed horizontal lines in all the panels represent an EW(Hα) of 6Å. The color figure can be viewed online.

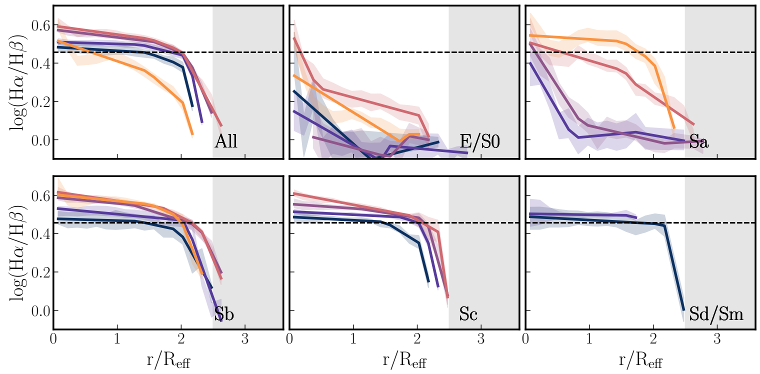

Fig. 42. Similar to Figure 3 for the Hα/Hβ line ratio. The dashed horizontal lines in all the panels represent the canonical value of this ratio. The color figure can be viewed online.

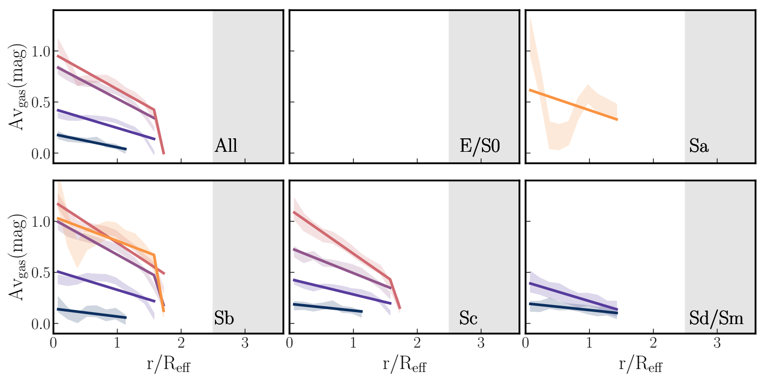

Fig. 43. Similar to Figure 3 for the optical extinction derived from the Balmer decrement. The color figure can be viewed online.

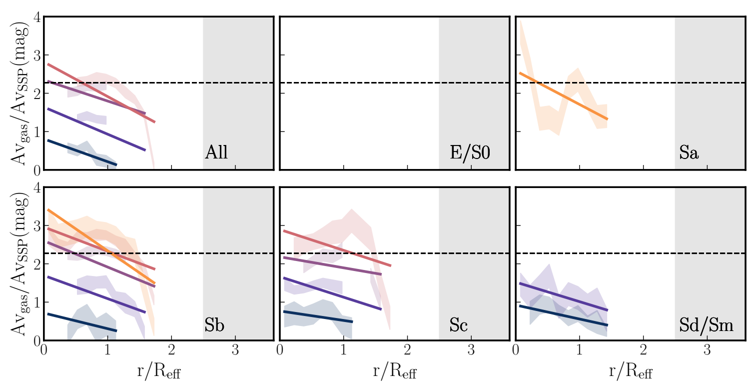

Fig. 44. Similar to Figure 3 for the $\mathrm{Av_{gas}}$ /$\mathrm{Av_{SSP}}$ ratio. The dashed line in all the panels represents the value derived from Calzetti (1997):$\mathrm{Av_{gas}}$ /$\mathrm{Av_{SSP}} \approx 2.27$. The color figure can be viewed online.

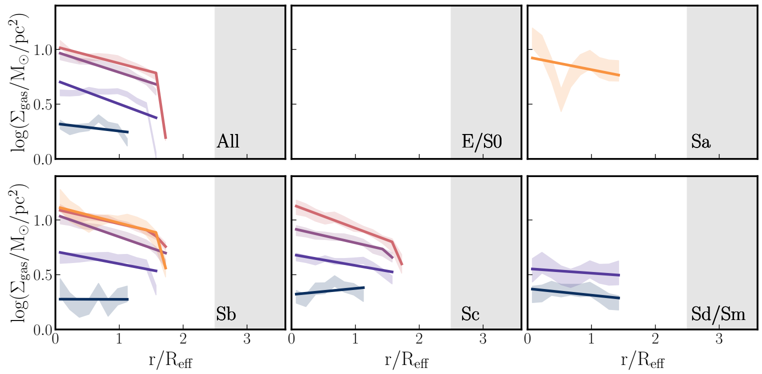

Fig. 45. Similar to Figure 3 for $\Sigma_{\rm mol,Av}$. The color figure can be viewed online.

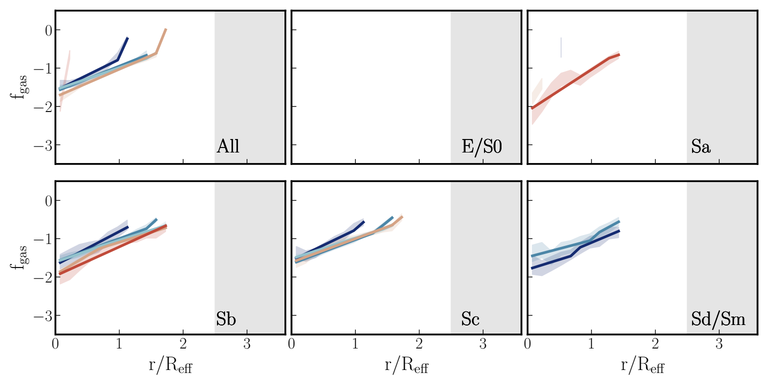

Fig. 46. Similar to Figure 3 for gas fraction, $f_{\rm mol}$. The color figure can be viewed online.

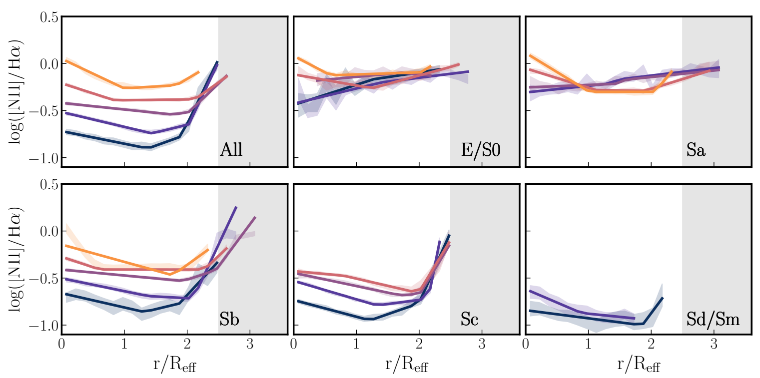

Fig. 47. Similar to Figure 3 for emission lines ratio [NII]/Hα. The color figure can be viewed online.

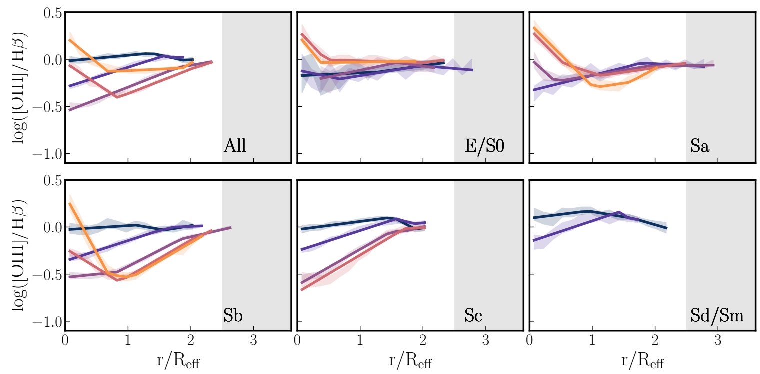

Fig. 48. Similar to Figure 3 for emission lines ratio [OIII]/Hβ. The color figure can be viewed online.

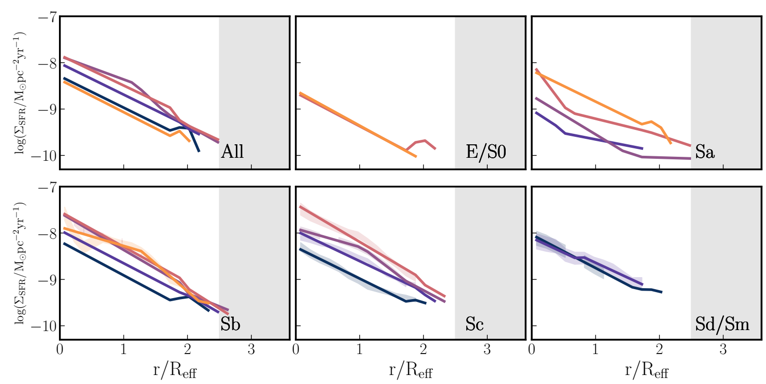

Fig. 49. Similar to Figure 3 for Σ_{SFR}. The color figure can be viewed online.

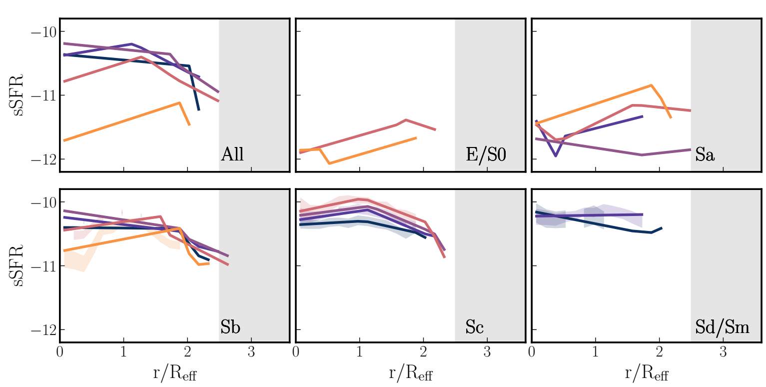

Fig. 50. Similar to Figure 3 for sSFR. The color figure can be viewed online.

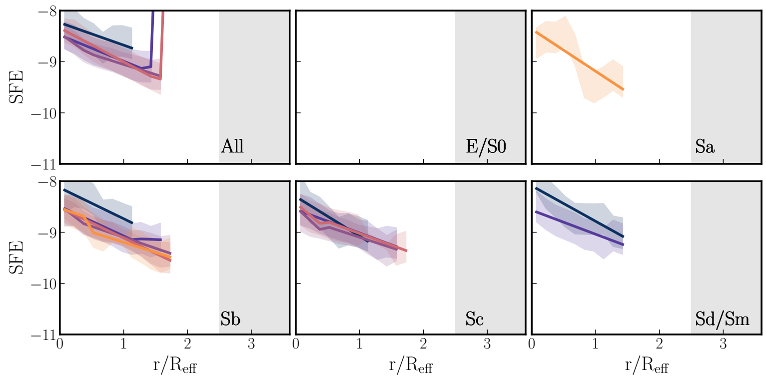

Fig. 51. Similar to Figure 3 for SFE. The color figure can be viewed online.

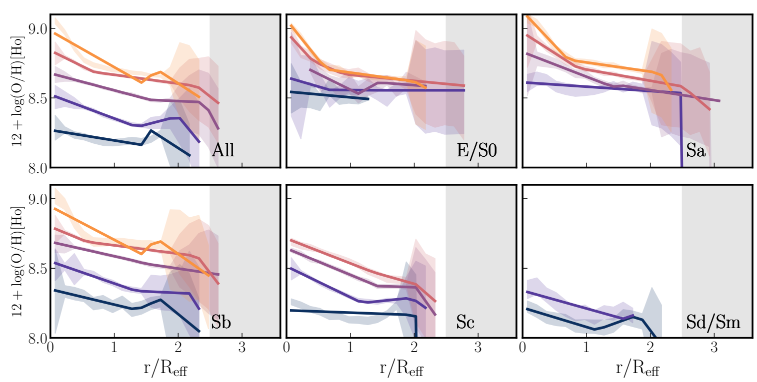

Fig. 52. Similar to Figure 3 for the oxygen abundance derived using the calibrator presented in Ho (2019). The color figure can be viewed online.

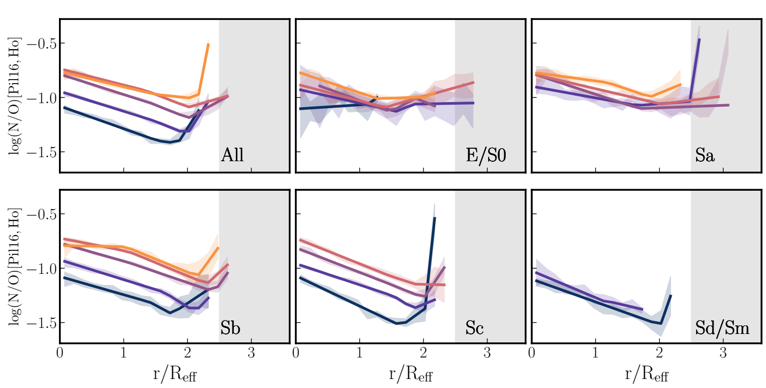

Fig. 53. Similar to Figure 3 for the N/O ratio. The color figure can be viewed online.

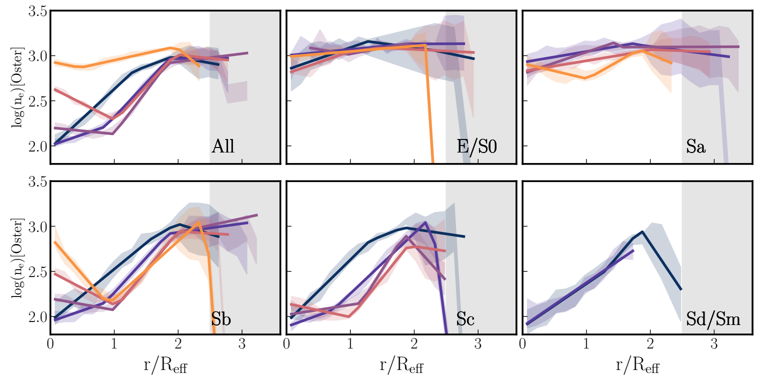

Fig. 54. Similar to Figure 3 for the electron density. The color figure can be viewed online.

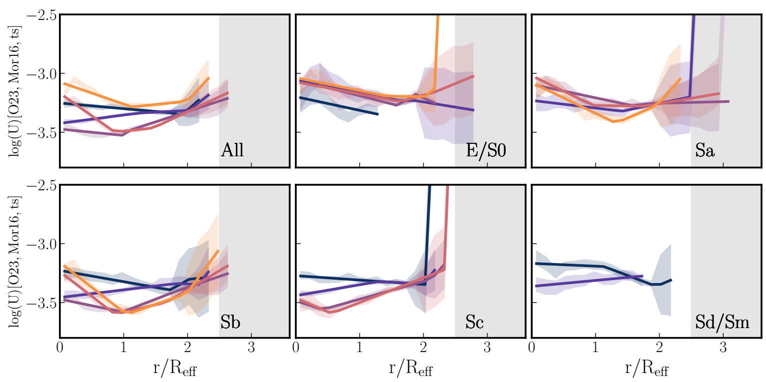

Fig. 55. Similar to Figure 3 for the ionization parameter. The color figure can be viewed online.

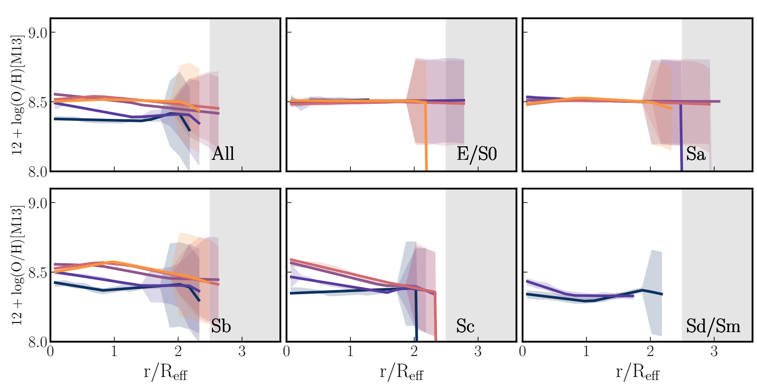

Fig. 56. Similar to Figure 3 for the oxygen abundance derived using the calibrator presented in Marino et al. (2013). The color figure can be viewed online.

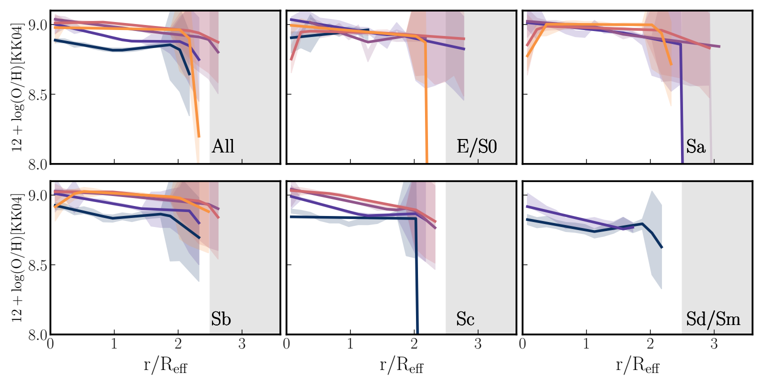

Fig. 57. Similar to Figure 3 for the oxygen abundance derived using the calibrator presented in Kobulnicky & Kewley (2004). The color figure can be viewed online.

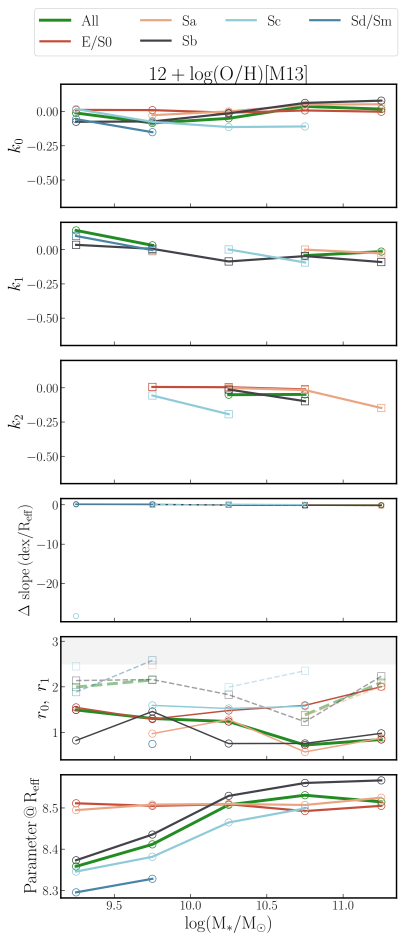

Fig. 58. Similar to Figure 3 for the oxygen abundance derived using the calibrator presented in Ho (2019). The color figure can be viewed online.

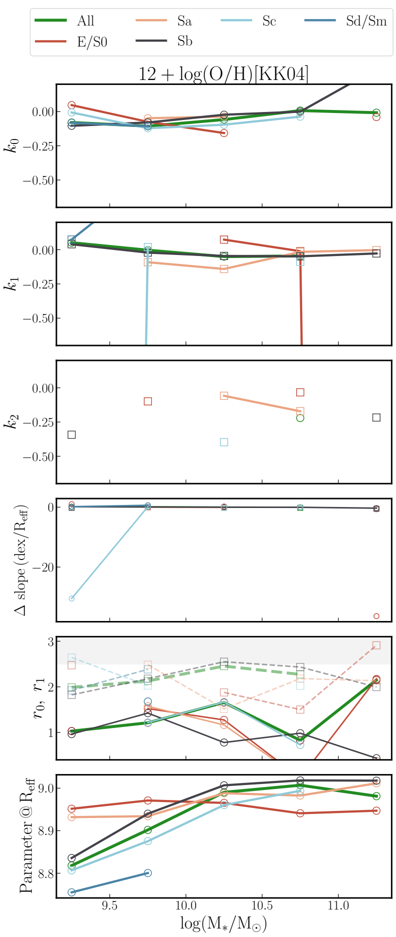

Fig. 59. Similar to Figure 3 for the oxygen abundance derived using the calibrator presented in Ho (2019). The color figure can be viewed online.

REFERENCES

Abdurro'uf, Accetta, K., Aerts, C., et al. 2022, ApJS, 259, 35, https://doi.org/10.3847/1538-4365/ac4414

Astropy Collaboration, Price-Whelan, A. M., SipHocz, B. M., et al. 2018, AJ, 126, 153, https://doi.org/10.3847/1538-3881/aabc4f

Astropy Collaboration, Robitaille, T. P., Tollerud, E. J., et al. 2013, A&A, 558, 33, https://doi.org/10.1051/0004-6361/201322068

Baldwin, J. A., Phillips, M. M., & Terlevich, R. 1981, PASP, 93, 5, https://doi.org/10.1086/130766

Barrera-Ballesteros, J. K., Heckman, T., Sánchez, S. F., et al. 2018, ApJ, 852, 74, https://doi.org/10.3847/1538-4357/aa9b31

Barrera-Ballesteros, J. K., Heckman, T. M., Zhu, G. B., et al. 2016, MNRAS, 463, 2513, https://doi.org/10.1093/mnras/stw1984

Barrera-Ballesteros, J. K., Sánchez, S. F., Heckman, T., et al. 2021, MNRAS, 503, 3643, https://doi.org/10.1093/mnras/stab755

Barrera-Ballesteros, J. K., Utomo, D., Bolatto, A. D., et al. 2020, MNRAS, 492, 2651, https://doi.org/10.1093/mnras/stz3553

Belfiore, F., Maiolino, R., Tremonti, C., et al. 2017, MNRAS, 469, 151, https://doi.org/10.1093/mnras/stx789

Bigiel, F., Leroy, A., Walter, F., et al. 2008, AJ, 136, 2846, https://doi.org/10.1088/0004-6256/136/6/2846

Binette, L., Magris, C. G., Stasińska, G., & Bruzual, A. G. 1994, A&A, 292, 13

Blanton, M. R., Bershady, M. A., Abolfathi, B., et al. 2017, AJ, 154, 28, https://doi.org/10.3847/1538-3881/aa7567

Blanton, M. R., Kazin, E., Muna, D., Weaver, B. A., & Price-Whelan, A. 2011, AJ, 142, 31, https://doi.org/10.1088/0004-6256/142/1/31

Boardman, N. F., Zasowski, G., Newman, J. A., et al. 2021, MNRAS, 501, 948, https://doi.org/10.1093/mnras/staa3785

Brinchmann, J., Charlot, S., White, S. D. M., et al. 2004, MNRAS, 351, 1151, https://doi.org/10.1111/j.1365-2966.2004.07881.x

Bundy, K., Bershady, M. A., Law, D. R., et al. 2015, ApJ, 798, 7, https://doi.org/10.1088/0004-637X/798/1/7

Calzetti, D. 1997, AIPC 408, The ultraviolet universe at low and high redshift, 403, https://doi.org/10.1063/1.53764

Calzetti, D., Armus, L., Bohlin, R. C., et al. 2000, ApJ, 533, 682, https://doi.org/10.1086/308692

Cano-Díaz, M., Ávila-Reese, V., Sánchez, S. F., et al. 2019, MNRAS, 488, 3929, https://doi.org/10.1093/mnras/stz1894

Cano-Díaz, M., Sánchez, S. F., Zibetti, S., et al. 2016, ApJ, 821, 26, https://doi.org/10.3847/2041-8205/821/2/L26

Cappellari, M. 2016, ARA&A, 54, 597, https://doi.org/10.1146/annurev-astro-082214-122432

Cardelli, J. A., Clayton, G. C., & Mathis, J. S. 1989, ApJ, 345, 245, https://doi.org/10.1086/167900

Catalán-Torrecilla, C., Gil de Paz, A., Castillo-Morales, A., et al. 2015, A&A, 584, 87, https://doi.org/10.1051/0004-6361/201526023

Cid Fernandes, R., Stasińska, G., Mateus, A., & Vale Asari, N. 2011, MNRAS, 413, 1687, https://doi.org/10.1111/J.1365-2966.2011.18244.x

Cid Fernandes, R., Stasińska, G., Schlickmann, M. S., et al. 2010, MNRAS, 403, 1036, https://doi.org/10.1111/j.1365-2966.2009.16185.x

Colombo, D., Sanchez, S. F., Bolatto, A. D., et al. 2020, A&A, 644, 97, https://doi.org/10.1051/0004-6361/202039005

Croom, S. M., Lawrence, J. S., Bland-Hawthorn, J., et al. 2012, MNRAS, 421, 872, https://doi.org/10.1111/j.1365-2966.2011.20365.x

de Vaucouleurs, G. 1958, ApJ, 128, 465, https://doi.org/10.1086/146564

Domínguez, A., Siana, B., Henry, A. L., et al. 2013, ApJ, 763, 145, https://doi.org/10.1088/0004-637X/763/2/145

Drory, N., MacDonald, N., Bershady, M. A., et al. 2015, AJ, 149, 77, https://doi.org/10.1088/0004-6256/149/2/77

Ellison, S. L., Thorp, M. D., Lin, L., et al. 2020, MNRAS, 493, 39, https://doi.org/10.1093/mnrasl/slz179

Emsellem, E., Cappellari, M., Krajnović, D., et al. 2007, MNRAS, 379, 401, https://doi.org/10.1111/j.1365-2966.2007.11752.x

Espinosa-Ponce, C., Sánchez, S. F., Morisset, C., et al. 2022, MNRAS, 512, 3436, https://doi.org/10.1093/mnras/stac456

Flores-Fajardo, N., Morisset, C., Stasińska, G., & Binette, L. 2011, MNRAS, 415, 2182, https://doi.org/10.1111/j.1365-2966.2011.18848.x

Freeman, K. C. 1970, ApJ, 160, 811, https://doi.org/10.1086/150474

Goddard, D., Thomas, D., Maraston, C., et al. 2017, MNRAS, 466, 4731, https://doi.org/10.1093/mnras/stw3371

González Delgado, R. M., García-Benito, R., Pérez, E., et al. 2015, A&A, 581, 103, https://doi.org/10.1051/0004-6361/201525938

Gunn, J. E., Siegmund, W. A., Mannery, E. J., et al. 2006, AJ, 131, 2332, https://doi.org/10.1086/500975

Ho, I.-T. 2019, MNRAS, 485, 3569, https://doi.org/10.1093/mnras/stz649

Husemann, B., Jahnke, K., Sánchez, S. F., et al. 2014, MNRAS, 443, 755, https://doi.org/10.1093/mnras/stu1167

Husemann, B., Sánchez, S. F., Wisotzki, L., et al. 2010, A&A, 519, 115, https://doi.org/10.1051/0004-6361/201014559

Ibarra-Medel, H. J., Avila-Reese, V., Sánchez, S. F., González-Samaniego, A., & Rodríguez-Puebla, A. 2019, MNRAS, 483, 4525, https://doi.org/10.1093/mnras/sty3256
Johnston, E. J., Häußler, B., Aragón-Salamanca, A., et al. 2017, MNRAS, 465, 2317, https://doi.org/10.1093/mnras/stw2823
Kauffmann, G., Heckman, T. M., White, S. D. M., et al. 2003, MNRAS, 341, 54, https://doi.org/10.1046/j.1365-8711.2003.06292.x
Kennicutt, R. C., Jr. 1992, ApJ, 388, 310, https://doi.org/10.1086/171154
_________. 1998, ARA&A, 36, 189, https://doi.org/10.1146/annurev.astro.36.1.189
Kennicutt, R. C., Jr. & Evans, N. J. II. 2012, ARA&A, 50, 531, https://doi.org/10.1146/annurev-astro-081811-125610
Kent, S. M. 1985, ApJS, 59, 115, https://doi.org/10.1086/191066
Kewley, L. J., Dopita, M. A., Sutherland, R. S., Heisler, C. A., & Trevena, J. 2001, ApJ, 556, 121, https://doi.org/10.1086/321545
Kobulnicky, H. A. & Kewley, L. J. 2004, ApJ, 617, 240, https://doi.org/10.1086/425299
Kormendy, J. 1977, ApJ, 217, 406, https://doi.org/10.1086/155589
Koyama, Y., Kodama, T., Hayashi, M., et al. 2015, MNRAS, 453, 879, https://doi.org/10.1093/mnras/stv1599
Koyama, Y., Shimakawa, R., Yamamura, I., Kodama, T., & Hayashi, M. 2019, PASJ, 71, 8, https://doi.org/10.1093/pasj/psy113
Kreckel, K., Groves, B., Schinnerer, E., et al. 2013, ApJ, 771, 62, https://doi.org/10.1088/0004-637x/771/1/62
Lacerda, E. A. D., Cid Fernandes, R., Couto, G. S., et al. 2018, MNRAS, 474, 3727, https://doi.org/10.1093/mnras/stx3022
Lacerda, E. A. D., Sánchez, S. F., Cid Fernandes, R., et al. 2020, MNRAS, 492, 3073, https://doi.org/10.1093/mnras/staa008
Lacerda, E. A. D., Sánchez, S. F., Mejía-Narváez, A., et al. 2022, https://doi.org/10.48550/arXiv.2202.08027
Law, D. R., Cherinka, B., Yan, R., et al. 2016, AJ, 152, 83, https://doi.org/10.3847/0004-6256/152/4/83
Law, D. R., Westfall, K. B., Bershady, M. A., et al. 2021, AJ, 161, 52, https://doi.org/10.3847/1538-3881/abcaa2
Leroy, A. K., Walter, F., Brinks, E., et al. 2008, AJ, 136, 2782, https://doi.org/10.1088/0004-6256/136/6/2782
Li, N., Li, C., Mo, H., et al. 2021, ApJ, 917, 72, https://doi.org/10.3847/1538-4357/ac0973
Lin, Z. & Kong, X. 2020, ApJ, 888, 88, https://doi.org/10.3847/1538-4357/ab5f0e
López-Cobá, C., Sánchez, S. F., Moiseev, A. V., et al. 2017, MNRAS, 467, 4951, https://doi.org/10.1093/mnras/stw3355
Maiolino, R. & Mannucci, F. 2019, A&A Rev., 27, 3, https://doi.org/10.1007/s00159-018-0112-2
Marino, R. A., Rosales-Ortega, F. F., Sánchez, S. F., et al. 2013, A&A, 559, 114, https://doi.org/10.1051/0004-6361/201321956
Martin, C. L. & Kennicutt, R. C., Jr. 2001, ApJ, 555, 301, https://doi.org/10.1086/321452
McCall, M. L., Rybski, P. M., & Shields, G. A. 1985, ApJS, 57, 1, https://doi.org/10.1086/190994
Méndez-Abreu, J., de Lorenzo-Cáceres, A., & Sánchez, S. F. 2021, MNRAS, 504, 3058, https://doi.org/10.1093/mnras/stab1064
Méndez-Abreu, J., Sánchez, S. F., & de Lorenzo-Cáceres, A. 2019, MNRAS, 484, 4298, https://doi.org/10.1093/mnras/stz276
Morelli, L., Corsini, E. M., Pizzella, A., et al. 2015, MNRAS, 452, 1128, https://doi.org/10.1093/mnras/stv1357
Morisset, C., Delgado-Inglada, G., Sánchez, S. F., et al. 2016, A&A, 594, 37, https://doi.org/10.1051/0004-6361/201628559
Moustakas, J., Kennicutt, R. C., Jr., & Tremonti, C. A. 2006, ApJ, 642, 775, https://doi.org/10.1086/500964
Osterbrock, D. E. & Ferland, G. J. 2006, Astrophysics of gaseous nebulae and active galactic nuclei (2nd ed.; Sausalito, CA: University Science Books)
Pagel, B. E. J. & Edmunds, M. G. 1983, Natur, 304, 488, https://doi.org/10.1038/304488a0
Parikh, T., Thomas, D., Maraston, C., et al. 2021, MNRAS, 502, 5508, https://doi.org/10.1093/mnras/stab449
Peletier, R. F. 1989, Eliptical galaxies: structure and stellar content, PhD. Thesis, University of Groningen
Pilyugin, L. S. & Grebel, E. K. 2016, MNRAS, 457, 3678, https://doi.org/10.1093/mnras/stw238
Portinari, L. & Salucci, P. 2010, A&A, 521, 82, https://doi.org/10.1051/0004-6361/200811444
Price, S. H., Kriek, M., Brammer, G. B., et al. 2014, ApJ, 788, 86, https://doi.org/10.1088/0004-637x/788/1/86
Qin, J., Zheng, X. Z., Wuyts, S., Pan, Z., & Ren, J. 2019, ApJ, 886, 28, https://doi.org/10.3847/1538-4357/ab4a04
Raga, A. C., Castellanos-Ramírez, A., Esquivel, A., Rodríguez-González, A., & Velázquez, P. F. 2015, RMxAA, 51, 231
Reddy, N. A., Kriek, M., Shapley, A. E., et al. 2015, ApJ, 806, 259, https://doi.org/10.1088/0004-637X/806/2/259
Renzini, A. & Peng, Y.-j. 2015, ApJ, 801, 29, https://doi.org/10.1088/2041-8205/801/2/L29
Sánchez, S. F. 2020, ARA&A, 58, 99, https://doi.org/10.1146/annurev-astro-012120-013326
Sánchez, S. F., Kennicutt, R. C., Gil de Paz, A., et al. 2012, A&A, 538, 8, https://doi.org/10.1051/0004-6361/201117353

Sánchez, S. F., Pérez, E., Sánchez-Blázquez, P., et al. 2016, RMxAA, 52, 21, https://doi.org/10.48550/arXiv.1509.08552

Sánchez, S. F., Pérez, E., Sánchez-Blázquez, P., et al. 2016, RMxAA, 52, 171, https://doi.org/10.48550/arXiv.1602.01830

Sánchez, S. F., Walcher, C. J., Lopez-Cobá, C., et al. 2021, RMxAA, 57, 3, https://doi.org/10.22201/ia.01851101p.2021.57.01.01

Sánchez-Blázquez, P., Rosales-Ortega, F., Diaz, A., & Sánchez, S. F. 2014a, MNRAS, 437, 1534, https://doi.org/10.1093/mnras/stt1984

Sánchez-Blázquez, P., Rosales-Ortega, F. F., Méndez-Abreu, J., et al. 2014b, A&A, 570, 6, https://doi.org/10.1051/0004-6361/201423635

Sánchez-Menguiano, L., Sánchez, S. F., Pérez, I., et al. 2018, A&A, 609, 119, https://doi.org/10.1051/0004-6361/201731486

Sersic, J. L. 1968, Atlas de Galaxias Australes (Cordoba, Argentina: Observatorio Astronómico)

Smee, S. A., Gunn, J. E., Uomoto, A., et al. 2013, AJ, 146, 32, https://doi.org/10.1088/0004-6256/146/2/32

Villanueva, V., Bolatto, A., Vogel, S., et al. 2021, ApJ, 923, 60, https://doi.org/10.3847/1538-4357/ac2b29

Wake, D. A., Bundy, K., Diamond-Stanic, A. M., et al. 2017, AJ, 154, 86, https://doi.org/10.3847/1538-3881/aa7ecc

Wild, V., Charlot, S., Brinchmann, J., et al. 2011, MNRAS, 417, 1760, https://doi.org/10.1111/j.1365-2966.2011.19367.x

Yan, R., Tremonti, C., Bershady, M. A., et al. 2016, AJ, 151, 8, https://doi.org/10.3847/0004-6256/151/1/8

Zheng, Z., Wang, H., Ge, J., et al. 2017, MNRAS, 465, 4572, https://doi.org/10.1093/mnras/stw3030

J. K. Barrera-Ballesteros, L. Carigi, C. Espinosa-Ponce, H. Hernandez-Toledo, E. Lacerda, A. Z. Lugo-Aranda, and S. F. Sánchez: Universidad Nacional Autónoma de México, Instituto de Astronomía, AP 70-264, CDMX 04510, México.

N. Boardman: School of Physics and Astronomy, University of St Andrews, North Haugh, St Andrews KY16 9SS, UK.

J. R. Brownstein: Department of Physics and Astronomy, University of Utah, 115 S. 1400 E., Salt Lake City, UT 84112, USA.

G. Bruzual: IRyA, Universidad Nacional Autónoma de México, Campus Morelia, Michoacan, México C.P. 58089, México.

N. Drory: University of Texas at Austin, McDonald Observatory, 1 University Station, Austin, TX 78712, USA.

Richard R. Lane: Centro de Investigación en Astronomía, Universidad Bernardo O'Higgins, Avenida Viel 1497, Santiago, Chile.

C. López-Cobá: Institute of Astronomy and Astrophysics, Academia Sinica, No. 1, Section 4, Roosevelt Road, Taipei 10617, Taiwan.

Revista Mexicana de Astronomía y Astrofísica, **59**, 259–277 (2023)

https://doi.org/10.22201/ia.01851101p.2023.59.02.07

MASS PROFILES OF LATE GALAXIES USING A GENETIC ALGORITHM. I - TESTING THE ALGORITHM

Rodolfo de J. Zermeño and Ana M. Hidalgo-Gámez

Escuela Superior de Física y Matemáticas, Instituto Politécnico Nacional, Unidad Profesional Adolfo López Mateos, CDMX, México.

Received March 27 2023; accepted June 8 2023

ABSTRACT

The rotation curve of a galaxy contains a wealth of information about its dynamical properties, being the mass distribution one of the most important. The rotation curve fitting procedures used to estimate the mass profiles of disc galaxies have become more sophisticated over the years, providing ever more reliable results. However, the time-cost and data requirements (e.g. high-resolution NIR photometry) necessary to put to use some of them have restricted these kind of studies to small samples of galaxies. We propose a simple procedure that could be used as a good first approximation for the study of large galaxy samples. It is based on a parameter-fitting method along with a recent optimization algorithm, called the Asexual Genetic Algorithm (AGA). With this procedure, we were able to replicate previously published results, within uncertainties, suggesting that it will provide a reliable first estimation, suitable for its application to large galaxy samples.

RESUMEN

La curva de rotación de una galaxia proporciona vasta información acerca de sus propiedades dinámicas, siendo la distribución de masa una de las más importantes. Los procedimientos de ajuste de curvas de rotación usados para estimar los perfiles de masa en galaxias de disco han mejorado con el tiempo, y han proporcionado resultados cada vez más confiables. Sin embargo, los requisitos en tiempo y calidad de datos (e.g. fotometría NIR de alta resolución) necesarios para poner en uso a algunos de ellos han restringido este tipo de estudios a pequeñas muestras de galaxias. Proponemos un procedimiento simple que podría ser utilizado para obtener una buena primera aproximación en el estudio de grandes muestras. Se basa en un método de ajuste de parámetros en conjunto con un algoritmo genético. Con este procedimiento, fue posible replicar los resultados en la literatura, dentro incertidumbres, lo que sugiere que éste provee una estimación confiable, adecuada para grandes muestras de galaxias.

Key Words: dark matter — galaxies: statistics — galaxies: structure — methods: data analysis

1. INTRODUCTION

The idea of the existence of a halo composed by non-baryonic matter in which the galaxy is completely embedded (Freeman 1970; Rubin et al. 1978; Bosma 1978) was considered after the discovery of an unexpected fast rotation in the outer edges of galaxies, even beyond the optical radius (Bosma 1981; Van Albada & Sancisi 1986). Although over the years alternative models have appeared to explain the rapid rotation of the outer parts of galaxies (Milgrom 1983), the Λ-Cold Dark Matter (hereafter, ΛCDM) paradigm still remains as the most popular, mainly for its simplicity in modelling a great host of phenomena on a vast range of scales (Peebles 2020).

Over the years, several models of dark matter (hereafter, DM) density profiles have been proposed to explain the behavior of the measured rotation curves (hereafter, RCs). Most of the earlier results provided by cosmological DM simulations (Navarro et al. 1997) based on the ΛCDM model predicted a DM density profile with an abrupt rise in density towards the center (i.e., a cusp). However, many studies analyzing RCs from late-type galaxies (mostly Scd - Irr) have systematically found an overestimation of the rotation velocity in the inner regions when a cusp-type DM density profile is considered (McGaugh et al. 2001; Marchesini et al. 2002; Simon et al. 2005; Kuzio de Naray et al. 2008; Walker & Penarrubia 2011), obtaining better fits with core-type profiles, which show a near constant density at small radius. The disparity between the results of the simulations and the analysis of observed RCs of late galaxies is called the *core-cusp discrepancy* (De Blok 2010).

Such discrepancy, along with the so called disc-halo degeneracy (Carignan & Freeman 1985; van Albada et al. 1985), which describes the situation observed when a certain RC may produce multiple, same-quality, fits (i.e., with comparable χ^2_R) with different stellar disc contributions have encouraged the development of more sophisticated fitting procedures over the years (Blais-Ouellette et al. 2001; Sofue 2012; Katz et al. 2017; Aniyan et al. 2018; Li et al. 2020). However, while all these methods have provided ever more reliable results, the time-cost and data requirements (i.e., high-resolution NIR photometry) needed to implement some of them have restricted these kinds of studies to small samples of galaxies.

With this in mind, we propose a simple procedure based on a parameter fitting method (Sofue 2012, 2013) along with the use of a recent optimization algorithm, called the Asexual Genetic Algorithm (AGA, Cantó et al. 2009). This algorithm has been implemented with success in other studies where a high-accuracy, low-time optimization algorithm was needed, such as orbital parameter fitting from radial velocity data in the search for exoplanets around υ Andromedae (Curiel et al. 2011) and the multi-component analysis of Hα spectra from the jet of the Herbig-Haro object HH34 (Rodríguez-González et al. 2012).

In addition, although some works have explored the influence of using different observational techniques and criteria in the mass profile estimation of disc galaxies (Katz et al. 2017; Korsaga et al. 2019; Li et al. 2020), the influence of some specific aspects of the fitting procedure, such as the chosen optimization algorithm and stellar disc model have not yet been studied in detail. We think that the analysis of RCs extracted from a homogenized data catalog using different fitting procedures [e.g. SPARC database (Lelli et al. 2016b; Li et al. 2020)] is important to find the influence that those considerations might have over the resulting fits, such as possible systematic effects visible through a direct comparison between them. For this reason, we think that this simple approach might prove to be really useful, serving also as a complement to previous studies.

The main goal of this manuscript is twofold: First, to check the reliability of our procedure. In order to achieve this we analyze a set of RC data extracted from the SPARC database (Lelli et al. 2016b), and then compare our results to those available in the literature (Li et al. 2020), previously obtained through a different procedure on the same dataset (i.e. SPARC). And second, to search for any systematic effects that could be attributed to a difference between procedures. Therefore, proving our procedure to be reliable, i.e. finding that our results do not deviate significantly from the ones already published, would imply that:

- The optimization algorithm (AGA) does a competent job providing a simple, low time-cost method to fit kinematical data for the mass profile estimation of late galaxies. Moreover, it does not require high spatial resolution photometry (which is not always available) to provide reliable results. These latter characteristics would make it suitable for analyzing samples with a great number of galaxies, using photometry data from widely available standardized digital surveys [e.g. SDSS (Abdurro'uf et al. 2022)].

- Would reinforce the argument that the use of an homogenized RC database serves as one of the most important factors in reducing the scatter between results (Li et al. 2020), limiting the influence of the assumed stellar disc models and optimization algorithms.

On the contrary, if the results obtained here show a systematic difference from those already published, independently of the assumed DM density profiles, it might be concluded that our assumed optimization algorithm and set of constraints show a bias, or that the simple stellar disc model assumed in this work is not a good approximation for practical purposes.

The present work comprises seven sections: in § 2, we make a brief description of the optimization algorithm, the Asexual Genetic Algorithm (AGA), and some of its characteristics. § 3 describes the test sample along with its selection criteria. In § 4 we detail the adopted mass models for each component, information about the photometry and M/L used as constraints in the fitting procedure, along with a description on how the fitting procedure was implemented. Finally, § 5 and 6 contain our results and conclusions, respectively.

2. ASEXUAL GENETIC ALGORITHM (AGA)

AGA is an optimization algorithm based on the selection of the fittest *individuals* (points in a N-dimensional space of parameters) through successive generations until convergence is achieved. These individuals are evaluated with the theoretical model and then compared with the observational data using a previously established *survival criterion*, a function (e.g. the reduced χ^2 function,

χ^2_R) whose value determines if the evaluated point is conserved for the next generation. A detailed description of this function is given in § 4.4.

According to the AGA main paper (Cantó et al. 2009), the most important difference between AGA and other 'standard' genetic algorithms (Holland et al. 1992) lies in the way the new generations are constructed. Standard genetic algorithms involve *sexual reproduction*, which involves the union of 'male' and 'female' reproductive individuals. Instead, AGA uses *asexual reproduction with mutation*, where a single individual can produce offspring by generating a random point within a narrow neighborhood around it. The size of this neighborhood can be specified by the user to reduce convergence time (Rodríguez-González et al. 2012). It is important to note that every new generation a clone of the parent individual is always conserved in case their offspring is less suited. When the first guess is far from the solution, AGA is capable of *migrating* the search to the optimal true solution. The optimal solution is normally obtained after a few hundred iterations. The combination of these characteristics makes AGA a reliable and fast-converging optimization algorithm, suitable for problems with many local minima/maxima close to the true solution.

3. TEST SAMPLE

Our test sample consists of 100 late-type galaxies selected from the *Spitzer Photometry and Accurate Rotation Curves* (SPARC) database (Lelli et al. 2016b). This catalog contains kinematical data (hybrid Hα+HI RCs) for 175 late-type galaxies along with their near-infrared (NIR) Spitzer 3.6μm photometry. Additionally, it contains a set of disk mass models calculated using the Casertano formula (Casertano 1983), a solution of the Poisson equation considering a finite thickness disc with an arbitrary radial density distribution. Since all the RCs in the SPARC catalog have been treated in a homogeneous manner, it provides the community with a *standardized* data sample, which works as an ideal reference to study the influence of the adopted fitting procedure in the mass estimation problem. The complete list of galaxies considered in the present work is condensed in Table 1 along with their most important characteristics. To simplify our analysis, as a first implementation of our procedure we selected galaxies that are classified in the SPARC database as lacking a bulge component, considering only the stellar disk, HI disk and dark matter halo. Since we are considering the same components as the ones assumed for the extraction of the published fits, this will allow us to make a reliable comparison between results.

4. FITTING PROCEDURE

In this section we detail the chosen disc and dark matter halo mass models as well as the main characteristics of our fitting procedure. We also include a subsection which describes briefly how the optimization algorithm was implemented, along with the method used to estimate the uncertainty of our results.

4.1. *Disc and Halo Models*

In this work, we use the method described by Sofue (2012), where the total rotation velocity at radius R is defined as:

$$V_t^2 = V_b^2 + V_d^2 + V_h^2 + V_{HI}^2, \tag{1}$$

where V_t is the total rotation velocity and V_b,V_d,V_h,V_{HI} are the rotation velocity components for the bulge, disc, DM halo and HI disc, respectively. For the present study, since our sample is composed of late spiral and irregular galaxies, we will consider the velocity contribution of a bulge component as negligible.

The stellar disc velocity component, V_d, was determined with the analytical expression obtained from the Poisson equation for a thin disc following an exponential surface density profile and a constant M/L along the radius (Freeman 1970; Binney & Tremaine 1987).

$$V_d\left(R\right) = \sqrt{\frac{GM_d}{a_d}} D\left(X\right), \tag{2}$$

where M_d is the total stellar disc mass, a_d the exponential scale radius and $D\left(X\right)$ is defined as:

$$D\left(X\right) = \left(\frac{X}{\sqrt{2}}\right)\left[I_0\left(\frac{X}{2}\right)K_0\left(\frac{X}{2}\right) - I_1\left(\frac{X}{2}\right)K_1\left(\frac{X}{2}\right)\right]^{1/2}, \tag{3}$$

being I_i y K_i the modified Bessel functions and $X = \frac{R}{a_d}$. The two free parameters are the total stellar disc mass, M_d, and the exponential scale radius, a_d. In the present investigation, the DM halo was modelled assuming three different density profiles: Navarro-Frenk-White (hereafter, NFW) (Navarro et al. 1997), pseudo-isothermal (ISO) (Kent 1986), and Burkert-type (BURK) (Burkert 1995). They are described as:

$$\rho_h^{NFW}\left(R\right) = \frac{\rho_0}{\frac{R}{h}\left(1+\frac{R}{h}\right)^2}; \tag{4}$$

$$\rho_h^{ISO}\left(R\right) = \frac{\rho_0}{\left(1+\left(\frac{R}{h}\right)^2\right)}; \tag{5}$$

$$\rho_h^{BURK}\left(R\right) = \frac{\rho_0}{\left(1+\frac{R}{h}\right)\left(1+\left(\frac{R}{h}\right)^2\right)}, \tag{6}$$

where ρ_0 is the *core density* and h is the *scale length* of the DM halo. Considering spherical symmetry, the total halo mass is obtained by integrating along the radius, giving

TABLE 1

MAIN PROPERTIES OF SPARC TEST SAMPLE[a]

Name	Hubble Type	D (Mpc)	i (°)	L (3.6 μm) ($10^{10} L_\odot$)	a_d (pc)	μ_0 ($L_\odot$/pc^2)	HI total mass ($10^{10} M_\odot$)
D512-2	Im	15.2 ± 4.56	56 ± 10	0.0325 ± 0.0022	1240	93.94	0.0081
D564-8	Im	8.79 ± 0.28	63 ± 7	0.0033 ± 0.0004	610	21.13	0.0029
D631-7	Im	7.72 ± 0.18	59 ± 3	0.0196 ± 0.0009	700	115.04	0.029
DDO064	Im	6.8 ± 2.04	60 ± 5	0.0157 ± 0.0007	690	151.65	0.0211
DDO154	Im	4.04 ± 0.2	64 ± 3	0.0053 ± 0.0002	370	71.26	0.0275
DDO161	Im	7.5 ± 2.25	70 ± 10	0.0548 ± 0.0015	1220	169.37	0.1378
DDO168	Im	4.25 ± 0.21	63 ± 6	0.0191 ± 0.0005	1020	92.22	0.0413
DDO170	Im	15.4 ± 4.62	66 ± 7	0.0543 ± 0.003	1950	73.93	0.0735
ESO079-G014	Sbc	28.7 ± 7.17	79 ± 5	5.17 ± 0.05	5080	2295.25	0.314
ESO116-G012	Sd	13 ± 3.9	74 ± 3	0.4292 ± 0.007	1510	1320.78	0.1083
ESO444-G084	Im	4.83 ± 0.48	32 ± 6	0.007 ± 0.0003	460	66.81	0.0135
ESO563-G021	Sbc	60.8 ± 9.1	83 ± 3	31.12 ± 0.26	5450	6558.89	2.4298
F563-1	Sm	48.9 ± 9.8	25 ± 5	0.19 ± 0.02	3520	41.77	0.32
F563-V1	Im	54 ± 10.8	60 ± 10	0.15 ± 0.017	3790	40.63	0.061
F563-V2	Im	59.7 ± 11.9	29 ± 10	0.2986 ± 0.0267	2430	146.16	0.2169
F565-V2	Im	51.8 ± 10.4	60 ± 10	0.06 ± 0.01	2170	40.26	0.0699
F567-2	Sm	79 ± 11.8	20 ± 10	0.2134 ± 0.0305	3080	46.65	0.2449
F568-1	Sc	90.7 ± 9.7	26 ± 5	0.6252 ± 0.0564	5180	57.13	0.4498
F568-3	Sd	82.4 ± 8.24	40 ± 10	0.8346 ± 0.0592	4990	132.08	0.3195
F568-V1	Sd	80.6 ± 8.06	40 ± 10	0.3825 ± 0.0384	2850	90.54	0.2491
F571-8	Sc	53.3 ± 10.7	85 ± 5	1.0164 ± 0.0412	3560	87.26	0.1782
F571-V1	Sd	80.1 ± 8	30 ± 10	0.1849 ± 0.0267	2470	64.39	0.1217
F574-1	Sd	96.8 ± 9.68	65 ± 10	0.6537 ± 0.0596	4460	128.48	0.3524
F574-2	Sm	89.1 ± 8.91	30 ± 10	0.2877 ± 0.0384	3760	41.38	0.1701
F579-V1	Sc	89.5 ± 8.95	26 ± 10	1.1848 ± 0.0742	3370	201.76	0.2245
F583-1	Sm	35.4 ± 8.85	63 ± 5	0.0986 ± 0.0093	2360	60.93	0.2126
F583-4	Sc	53.3 ± 10.7	55 ± 10	0.1715 ± 0.0185	1930	83.34	0.0641
IC2574	Sm	3.91 ± 0.2	75 ± 7	0.1016 ± 0.0012	2780	80.32	0.1036
KK98-251	Im	6.8 ± 2.04	59 ± 5	0.0085 ± 0.0007	1340	52.1	0.0115
NGC0024	Sc	7.3 ± 0.36	64 ± 3	0.3889 ± 0.0036	1340	1182.58	0.0676
NGC0055	Sm	2.11 ± 0.11	77 ± 3	0.4628 ± 0.0013	6110	391.59	0.1565
NGC0247	Sd	3.7 ± 0.19	74 ± 3	0.7332 ± 0.0027	3740	506.79	0.1746
NGC1003	Scd	11.4 ± 3.42	67 ± 5	0.682 ± 0.0075	1610	1345.33	0.588
NGC2403	Scd	3.16 ± 0.16	63 ± 3	1.0041 ± 0.0028	1390	1408.74	0.3199
NGC3109	Sm	1.33 ± 0.07	70 ± 5	0.0194 ± 0.0002	1560	140.87	0.0477
NGC3198	Sc	13.8 ± 1.4	73 ± 3	3.8279 ± 0.0212	3140	1602.62	1.0869
NGC3741	Im	3.21 ± 0.17	70 ± 4	0.0028 ± 0.0001	200	143.49	0.0182
NGC3769	Sb	18 ± 2.5	70 ± 2	1.8679 ± 0.0189	3380	160.26	0.5529
NGC3893	Sc	18 ± 2.5	49 ± 2	5.8525 ± 0.0377	2380	2055.09	0.5799
NGC3917	Scd	18 ± 2.5	79 ± 2	2.1966 ± 0.0202	2630	1226.96	0.1888
NGC3992	Sbc	23.7 ± 2.3	56 ± 2	22.6932 ± 0.0836	4960	3257.09	1.6599
NGC4010	Sd	18 ± 2.5	89 ± 1	1.7193 ± 0.019	2810	2611.14	0.2832
NGC4100	Sbc	18 ± 2.5	73 ± 2	5.9394 ± 0.0328	2150	8970.78	0.3102
NGC4183	Scd	18 ± 2.5	82 ± 2	1.084 ± 0.015	2790	1098.58	0.3506
NGC4559	Scd	9 ± 2.7	67 ± 1	1.9377 ± 0.0107	2100	1602.62	0.5811
NGC5585	Sd	7.06 ± 2.12	51 ± 2	0.2943 ± 0.0033	1530	297.05	0.1683
NGC6015	Scd	17 ± 5.1	60 ± 2	3.2129 ± 0.0237	2300	1926.77	0.5834
NGC7793	Sd	3.61 ± 0.18	47 ± 9	0.705 ± 0.0026	1210	1068.64	0.0861
UGC00128	Sdm	64.5 ± 9.7	57 ± 10	1.2 ± 0.06	5950	88.89	0.7431
UGC00191	Sm	17.1 ± 5.1	45 ± 5	0.2004 ± 0.0063	1580	207.41	0.1343

TABLE 1. CONTINUED

Name	Hubble Type	D (Mpc)	i (°)	L (3.6 μm) ($10^{10} L_\odot$)	a_d (pc)	μ_0 ($L_\odot/pc^2$)	HI total mass ($10^{10} M_\odot$)
UGC00634	Sm	30.9 ± 7.7	37 ± 8	0.2989 ± 0.0146	2450	126.13	0.3663
UGC00731	Im	12.5 ± 3.75	57 ± 3	0.0323 ± 0.0019	2300	82.57	0.1807
UGC00891	Sm	10.2 ± 3.1	60 ± 5	0.0374 ± 0.0017	1430	113.98	0.0428
UGC01230	Sm	53.7 ± 10.7	22 ± 10	0.762 ± 0.0379	4340	69.32	0.643
UGC02259	Sdm	10.5 ± 3.1	41 ± 3	0.1725 ± 0.0038	1620	172.52	0.0494
UGC04325	Sm	9.6 ± 2.88	41 ± 3	0.2026 ± 0.0035	1860	213.22	0.0678
UGC04483	Im	3.34 ± 0.31	58 ± 3	0.0013 ± 0.0001	180	82.57	0.0032
UGC04499	Sdm	12.5 ± 3.75	50 ± 3	0.1552 ± 0.0043	1730	127.3	0.11
UGC05005	Im	53.7 ± 10.7	41 ± 10	0.41 ± 0.0283	3200	65.59	0.3093
UGC05414	Im	9.4 ± 2.82	55 ± 3	0.1123 ± 0.0028	1470	127.3	0.0574
UGC05716	Sm	21.3 ± 5.3	54 ± 10	0.0588 ± 0.0042	1140	90.54	0.1094
UGC05721	Sd	6.18 ± 1.85	61 ± 5	0.0531 ± 0.0011	380	913.76	0.0562
UGC05750	Sdm	58.7 ± 11.7	64 ± 10	0.3336 ± 0.0264	3460	124.98	0.1099
UGC05764	Im	7.47 ± 2.24	60 ± 10	0.0085 ± 0.0006	1170	33.79	0.0163
UGC05829	Im	8.64 ± 2.59	34 ± 10	0.0564 ± 0.0019	1990	63.22	0.1023
UGC05918	Im	7.66 ± 2.3	46 ± 5	0.0233 ± 0.0011	1660	24.94	0.0297
UGC05986	Sm	8.63 ± 2.59	90 ± 3	0.4695 ± 0.0048	1670	1725.16	0.2667
UGC05999	Im	47.7 ± 9.5	22 ± 10	0.3384 ± 0.0231	3220	51.62	0.2022
UGC06399	Sm	18 ± 2.5	75 ± 2	0.2296 ± 0.0072	2050	311.05	0.0674
UGC06446	Sd	12 ± 3.6	51 ± 3	0.0988 ± 0.0032	1490	86.46	0.1379
UGC06667	Scd	18 ± 2.5	89 ± 1	0.1397 ± 0.0066	5150	614.94	0.0809
UGC06917	Sm	18 ± 2.5	56 ± 2	0.6832 ± 0.012	2760	261.11	0.2023
UGC06923	Im	18 ± 2.5	65 ± 2	0.289 ± 0.0077	1440	347.4	0.0809
UGC06930	Sd	18 ± 2.5	32 ± 5	0.8932 ± 0.014	3940	189.16	0.3237
UGC06983	Scd	18 ± 2.5	49 ± 1	0.5298 ± 0.0102	3210	121.57	0.2967
UGC07089	Sdm	18 ± 2.5	80 ± 3	0.3585 ± 0.0089	2260	520.99	0.1214
UGC07125	Sm	19.8 ± 5.9	90 ± 3	0.2712 ± 0.008	3380	103	0.4629
UGC07151	Scd	6.87 ± 0.34	90 ± 3	0.2284 ± 0.0025	1250	965.67	0.0616
UGC07261	Sdm	13.1 ± 3.93	30 ± 10	0.1753 ± 0.0048	1200	566.02	0.1388
UGC07399	Sdm	8.43 ± 2.53	55 ± 3	0.1156 ± 0.0024	1640	135.78	0.0745
UGC07524	Sm	4.74 ± 0.24	46 ± 3	0.2436 ± 0.0025	3460	106.86	0.1779
UGC07559	Im	4.97 ± 0.25	61 ± 3	0.0109 ± 0.0004	580	55.06	0.0169
UGC07603	Sd	4.7 ± 1.41	78 ± 3	0.0376 ± 0.0008	530	520.99	0.0258
UGC07608	Im	8.21 ± 2.46	25 ± 10	0.0264 ± 0.0012	1500	46.65	0.0535
UGC07690	Im	8.11 ± 2.43	41 ± 5	0.0858 ± 0.0018	570	395.21	0.039
UGC07866	Im	4.57 ± 0.23	44 ± 5	0.0124 ± 0.0004	610	97.46	0.0118
UGC08286	Scd	6.5 ± 0.21	90 ± 3	0.1255 ± 0.0018	1050	1488.78	0.0642
UGC08490	Sm	4.65 ± 0.53	50 ± 3	0.1017 ± 0.0012	670	576.54	0.072
UGC08550	Sd	6.7 ± 2	90 ± 3	0.0289 ± 0.0009	450	1284.78	0.0288
UGC09037	Scd	83.6 ± 8.4	65 ± 5	6.8614 ± 0.1769	4280	841.07	1.9078
UGC10310	Sm	15.2 ± 4.6	34 ± 6	0.1741 ± 0.0053	1800	158.79	0.1196
UGC11455	Scd	78.6 ± 11.8	90 ± 1	37.4322 ± 0.3792	5930	9568.2	1.3335
UGC11557	Sdm	24.2 ± 6.05	30 ± 10	1.2101 ± 0.0212	2750	337.93	0.2605
UGC11820	Sm	18.1 ± 5.43	45 ± 10	0.097 ± 0.0047	2080	34.11	0.1977
UGC12506	Scd	100.6 ± 10.1	86 ± 4	13.9571 ± 0.3214	7380	5608.28	3.5556
UGC12632	Sm	9.77 ± 2.93	46 ± 3	0.1301 ± 0.003	2420	66.81	0.1744
UGC12732	Sm	13.2 ± 4	39 ± 6	0.1667 ± 0.0048	1980	120.46	0.366
UGCA281	BCD	5.68 ± 0.28	67 ± 3	0.0194 ± 0.0007	1720	12.05	0.0062
UGCA442	Sm	4.35 ± 0.22	64 ± 7	0.014 ± 0.0005	1180	116.1	0.0263
UGCA444	Im	0.98 ± 0.05	78 ± 4	0.0012 ± 0	830	22.74	0.0067

[a]Properties of selected SPARC test sample. The galaxy name is given in the first Column while the morphological type, according to SPARC, is shown in the second Column. The distance and inclination are shown in Columns 3 and 4, while the 3.6 μm luminosity is tabulated in Column 5. Finally, the exponential scale radius (a_d), the central surface brightness (μ_0) and the estimated HI total mass are listed in Columns 6, 7 and 8, respectively.Data extracted from the SPARC database website (Lelli et al. 2016b).

the following expressions for the NFW, ISO and BURK profiles, respectively:

$$M_h^{NFW}(R) = 4\pi\rho_0 h^3 \left\{ \ln\left(1+\frac{R}{h}\right) - \frac{\frac{R}{h}}{1+\frac{R}{h}} \right\}; \quad (7)$$

$$M_h^{ISO}(R) = 4\pi\rho_0 h^2 \left\{ R - h\arctan\left(\frac{R}{h}\right) \right\}; \quad (8)$$

$$M_h^B(R) = 4\pi\rho_0 h^3 \left\{ \ln\frac{\sqrt{h+R}(R^2+h^2)^{1/4}}{h} - \frac{1}{2}\arctan\left(\frac{R}{h}\right) \right\}. \quad (9)$$

The rotation velocity component for the dark matter halo at radius R is:

$$V_h(R) = \sqrt{\frac{GM_h}{R}}. \quad (10)$$

DM density profiles are often expressed in terms of the rotation velocity at the virial radius, V_{200}, and the concentration parameter, c, defined as:

$$V_{200} = \sqrt{\frac{GM_{200}}{R_{200}}}; \quad (11)$$

$$c = \frac{R_{200}}{h}, \quad (12)$$

where R_{200} is the radius of a spherical halo with a mass equal to M_{200} and the virial mass M_{200} is defined as the total mass contained within a sphere whose *mean* density equals 200 times the critical density of the Universe (ρ_c) at $z = 0$

$$M_{200} = \frac{4}{3}\pi R_{200}^3(200\rho_c). \quad (13)$$

We have considered a Hubble constant value of $H_0 = 73\,km\,s^{-1}Mpc^{-1}$ (Riess et al. 2022) throughout this investigation. This value is the same as the one assumed in the published fits used as comparison (Li et al. 2020).

4.2. *HI Disc Velocity Component*

Since all the elements in our sample are classified as late-type galaxies (mostly Sm and Irr), it should be necessary to take into account the dynamical effects of a separate HI disc component because such galaxies tend to have an important fraction of their total baryonic mass in the form of HI (Roberts 1962; Huchtmeier & Richter 1989; Korsaga et al. 2019). In this work, the HI disc velocity component is obtained from the SPARC database HI mass model for each galaxy. This component is calculated with the Casertano (1983) formula. In this investigation, in order to isolate the contributions of the stellar disc and DM halo, the HI disc velocity component for each point in the RC is subtracted from the observed rotation velocity using the following expression:

$$V_{corr}(R) = \sqrt{V_{obs}^2 - V_{HI}^2}, \quad (14)$$

where V_{obs} is the observed rotation velocity , V_{HI} the HI disc velocity component and V_{corr} the *corrected velocity*. This latter component is then inserted in the fitting algorithm and analysed.

4.3. *Photometry and $(M/L)_\star$ Ratio*

In all the problems that involve the fitting of observational data using a certain theoretical model it is important to select a suitable set of constraints to ensure that our algorithm does not give unrealistic results. One important constraint in RC analysis is the surface brightness photometry (Katz et al. 2017; Korsaga et al. 2019; Li et al. 2020). The surface brightness profile of the galaxy provides information about how the stars are distributed throughout the disc. In recent years, many studies have shown that near-infrared (NIR) surface photometry can be used as an excellent stellar disc mass tracer, since these bands are less susceptible to systematic uncertainties caused by dust emission that afflict the optical bands (Kennicutt et al. 2003; Leroy et al. 2008; Meidt et al. 2014). Another reason is that most of the stellar disc total mass is composed of low-mass stars, whose main emission is at NIR bands (Kroupa & Jerabkova 2021). This is seen as a low dispersion on the (M/L)-color correlation at NIR bands compared to the optical bands (Bell & de Jong 2001). In this work, we used the exponential disc scale length (a_d) and the 3.6 μm total luminosity ($L_T^{3.6\mu m}$), extracted from the SPARC database (Table 1). It is important to note that, although the thin disk model (Freeman 1970; Binney & Tremaine 1987) represents a simplification with respect to models used in other studies, it has the advantage of only depending on two photometric parameters (L_T, a_d) to estimate the stellar disk contribution, instead of requiring a complete luminosity profile obtained with high spatial resolution observations (Casertano 1983). In the case of low-mass galaxies, the exponential profile is usually a good approximation for a large interval of radii (Lelli et al. 2016b). However, it is common to find small deviations on the disc caused by secondary structures, such as bars or spiral arms.

Another important constraint in our model is the $(M/L)_\star$ ratio for the stellar disc. As mentioned in the Introduction, the uncertainty in this parameter is mainly responsible for the disc-halo degeneracy. A way to counter this degeneracy is by considering the *maximal disc hypothesis*, where the contribution of the disc mass to the RC is considered to be as large as the RC itself allows it. Qualitatively, it is defined as a disc whose contribution to the total potential exceeds the contribution of the dark matter halo in the inner regions. However, in recent years evidence was found suggesting that the application of the maximum disc hypothesis usually resulted in $(M/L)_\star$ values that were too high compared to those predicted by the stellar population synthesis (SPS) models (McGaugh & Schombert 2014; Schombert & McGaugh 2014). This effect is more noticeable in late type galaxies (Sc, Sd, Irr), where the contribution of a bulge is small or nonexistent. Thus, when a plausible range for $(M/L)_\star$ is considered, the resulting fits show DM halos whose contributions to the total rotation velocity are dominant at all radii. The discs that show this property are classified as *submaximal* (Sackett 1997).

For this first implementation and testing of our procedure, we decided to fix the $(M/L)_\star$ ratio instead of considering it as a free parameter. This was done in order to avoid adding another free parameter to the algorithm, hampering the interpretation of our results. We fixed this ratio at $(M/L)_\star = 0.5$, constant along the disc, which many studies have converged to take as the fiducial value at 3.6 μm (McGaugh & Schombert 2014; Schombert & McGaugh 2014; Lelli et al. 2016a), consistent with the results of stellar population synthesis (SPS) models (Bruzual & Charlot 2003; Meidt et al. 2014).

4.4. *AGA Selection Criterion, the χ^2_R Function*

As we briefly mentioned in the Introduction, in the present work we use the χ^2_R function as the selection criterion for AGA, which is defined as:

$$\chi^2_R = \frac{1}{N-P} \sum_{i=1}^{N} \frac{\left(V_i^{obs} - V_i^t\right)^2}{\sigma_i^2}; \tag{15}$$

where N is the number of RC data points, P the number of free parameters, V_i^{obs} the observed rotation velocity, V_i^t the calculated total rotation velocity and σ_i the observational uncertainties. After establishing the photometry constraints, the remaining free parameters are the ones corresponding to the DM halo (ρ_0 and h), thus $P = 2$.

4.5. *Uncertainty Estimation*

In order to estimate the uncertainty range of our results, we use the methodology described in the AGA main paper (Cantó et al. 2009), based in the generation of *synthetic data sets*. The process is quite simple: for each data point of the measured curve, a random data point is generated inside the observational velocity uncertainty interval 2σ. The procedure is repeated until a set of synthetic RCs is obtained. These synthetic curves serve as *statistical equivalents* on the uncertainty estimation. Each one is treated and analysed in the same way as the measured RCs. The formula used for the generation of synthetic RCs is:

$$V'(R) = V_{obs}(R) + \sigma(2\xi - 1), \tag{16}$$

where $V'(R)$ is the synthetic rotation velocity value, $V_{obs}(R)$ the measured rotation velocity, σ the observational error and ξ is a random variable in the interval $[0, 1]$. In the present work, the uncertainties were estimated using sets with an average of 6 synthetic RCs per galaxy. This number was chosen after some tests designed to find the best compromise between time and accuracy. The uncertainties are defined as the standard deviation of the parameter distribution for the synthetic data set.

4.6. *Python Subroutine*

Adapting AGA to our procedure required to implement some modifications in the code. As mentioned in section 4, the stellar disc contribution is calculated from equation (2), which contains the first and second order modified Bessel functions. The language in which AGA is compiled (FORTRAN90) does not support these functions implicitly, so it was necessary to add them as an external module. These functions were adapted from the FORTRAN special function package, SPECFUN (Cody 1993). Individual tests were performed for each function to ensure they worked correctly.

The fitting procedure was compiled as a Python subroutine, whose main purpose was to provide AGA with all the information needed from a set of machine-readable tables containing the SPARC data for each galaxy in the sample. These data consisted of the measured RC, the disc exponential scale length (a_d), the galaxy total luminosity at 3.6 μm ($L_\odot^{3.6\mu m}$) and the HI velocity component. Once a fit was obtained for the specified RC, the subroutine then estimated the corresponding c, V_{200}, M_{200} and R_{200} values by using the numerical solver included in the SYMPY package (Meurer et al. 2017). In order to guarantee a good coverage of the parameter space, we established a set of loose constraints for our fitting variables. In the case of the DM profile core density, ρ_0, we set a range between $0 \leq \rho_0 \leq 1$ $M_\odot$ pc^{-3}, while the scale parameter h could vary between $0 \leq h \leq 100$ kpc. The typical values of ρ_0 and h tend to be of the order of $\rho_0 \approx 10^{-2} M_\odot$ pc^{-3} and $h \approx 10^3 - 10^4$ pc (Sofue 2012, 2013).

Each AGA run consisted of 150 generations, containing 1000 individual points in the parameter space (200 *parent* + 800 *offspring*), with a *box size* factor of 0.5 between generations. The box size factor reduces the parameter-space volume from which new points can be generated around each individual between one generation and the next. Every AGA run starts with a box size spanning the full specified parameter range. The result is then stored and used as a starting point for the next run. This procedure may seem redundant at first, but it is important to note that for each run, the sizes of the sampling boxes

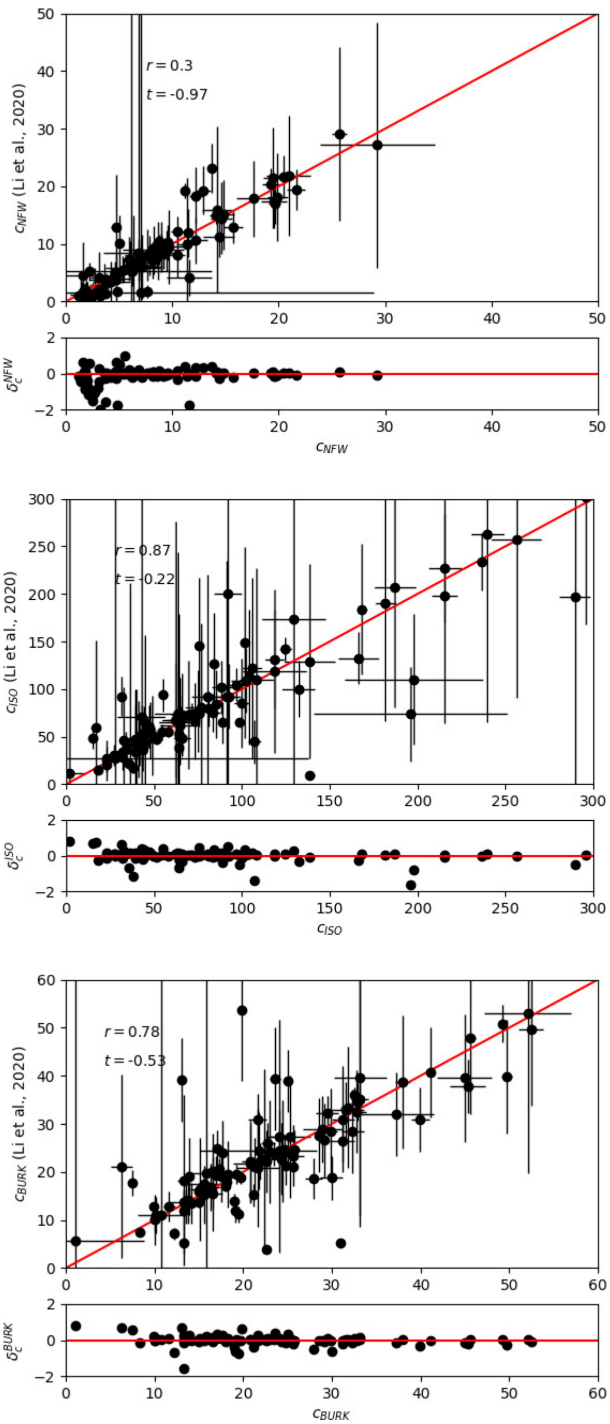

Fig. 1. Comparison diagrams of the best-fit c values obtained with our procedure against their corresponding published fits in the SPARC database (Li et al. 2020). The $y = x$ line is indicated in red. The corresponding residual graphs, described in terms of the deviation parameter δ_c (Equation 17) are located below each comparison diagram. On all DM profiles, most galaxies in our sample ($\gtrsim$ 90%) lie within $\delta_c \leq 1$. The color figure can be viewed online.

are reset to their initial values, so each run starts searching for the solution using boxes of the same size as the ones used in the first run, but centered on improved initial values (Cantó et al. 2009). This enhances the accuracy of the algorithm and reduces the probability of converging on a local minimum. Finally, after 6 consecutive runs, the results are stored as the best-fit parameters.

5. RESULTS

Tables A1, A2 and A3 (Appendix A) list the obtained best-fit c, M_{200}, R_{200}, V_{200} and χ_R^2 values for all the galaxies in this sample, assuming a NFW, ISO and BURK DM halo profiles, respectively. In the present work, for the comparison between obtained and published fits we will focus on two independent parameters: the concentration parameter, c, and the virial rotation velocity, V_{200}. As explained in § 4.1, the DM profile can be completely characterized by these two parameters.

In the analyzed sample, the typical values found for the concentration parameter c depend on the assumed DM profile. For example, for a NFW profile, the typical values are around $c_{NFW} \approx 10 - 20$, while for ISO and BURK, the typical values are around $c_{ISO} \approx 80$ and $c_{BURK} \approx 20 - 30$. In the case of the parameter V_{200}, for all DM profiles, the typical values are around $V_{200} \approx 100\,\mathrm{km\,s^{-1}}$. It can be seen from Tables A1, A2 and A3 that only a handful of galaxies show values far-off from the average ones for c or V_{200}, being the BURK profile the one with the least number of outlying galaxies (only two of them) while the ISO profile shows the largest number of outliers.

5.1. *Comparison with Previous Results*

Figures 1 and 2 compare our obtained best-fit parameter values against their corresponding values found in the literature (Li et al. 2020) assuming each DM density profile for the parameters c and V_{200}, respectively. A qualitative analysis shows that most galaxies in these diagrams lie near the red $y = x$ line, within uncertainties, implying a great degree of consistency between studies. However, some deviations were found (e.g. Figure 2, top), which will be addressed below.

In order to verify in a quantitative manner if our results are consistent with those found in the literature, we compared our obtained best-fit c and V_{200} samples against their corresponding published values through a set of paired t-tests. According to these tests, for a sample size of 100 galaxies with a 95% confidence level, the critical t value, T (from which we can reject the same-mean hypothesis) is equal to 1.98. If the absolute values of t_c or $t_{V_{200}}$ are higher than T, we can consider that the difference between the means of our compared samples is statistically significant. The t-test results, along with their corresponding Pearson correlation values for the parameters c (r_c) and V_{200} ($r_{V_{200}}$) are condensed in Table 2.

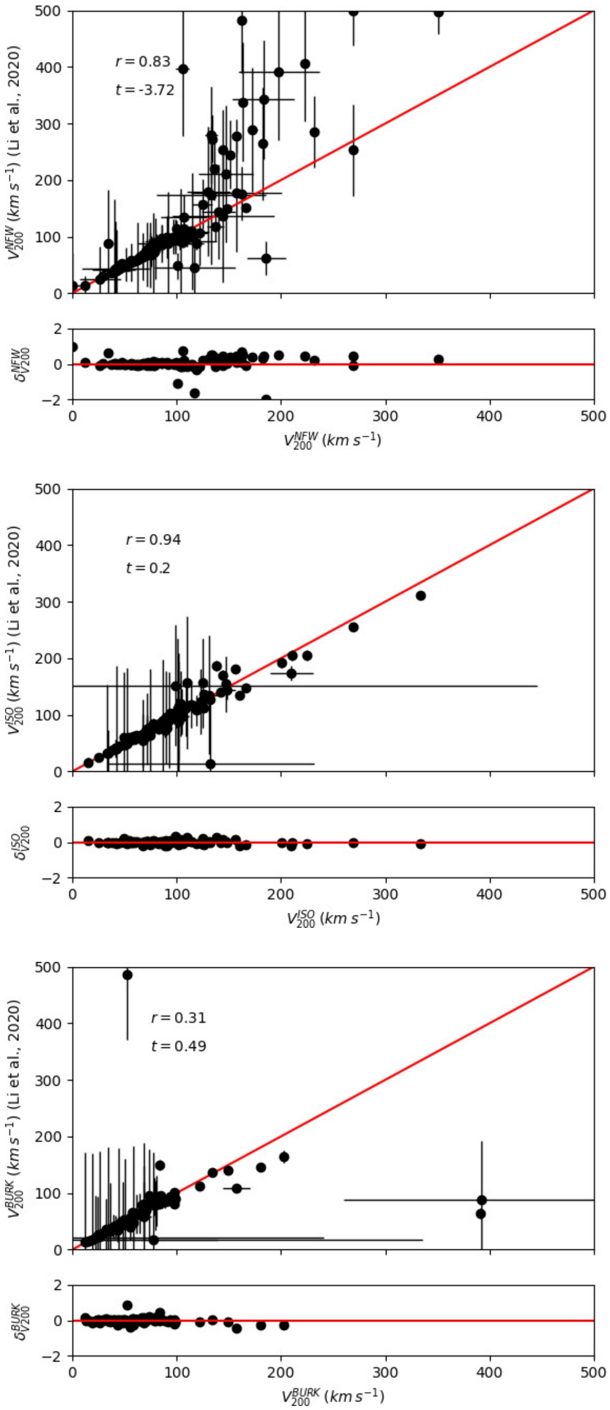

Fig. 2. Comparison diagrams of the best-fit V_{200} values obtained with our procedure against their corresponding published fits in the SPARC database (Li et al. 2020). The $y = x$ line is indicated in red. The corresponding residual graphs, described in terms of the deviation parameter δ_{V200} (equation 18) are located below each comparison diagram. On all DM profiles, most galaxies in our sample ($\gtrsim$ 90%) lie within $\delta_{V200} \leq 1$. The color figure can be viewed online.

The t-test analysis shows that our fits pass the equal-mean hypothesis in 5 out of the 6 possible tests (2 fit parameters, 3 DM profiles). The only t-test that did not pass corresponds to the comparison between our obtained vs the published V_{200}^{NFW} samples. This is seen in the V_{200}^{NFW} comparison diagram (Figure 2, top) as a divergence from the $y = x$ line at $V_{200}^{NFW} \gtrsim 200$ km s^{-1} . It is interesting to note that most of the galaxies that deviate from the $y = x$ line show h values that lie near the upper limit imposed for our procedure ($h \approx 100$ kpc), indicating that the global minimum probably did not fall inside our specified h range. In order to explore this, several runs were performed assuming different upper range values for h. We found that, although the χ^2_R global minimum was reached, the resulting parameter values would not be physical (i.e. $V_{200} > 500$ km s^{-1}) (Li et al. 2020). This behaviour was found exclusively when a NFW profile was considered.

Along with the t-tests, to quantify the deviation between the obtained and the published parameter values for each individual galaxy, we define a *deviation parameter* (δ_c and $\delta_{V_{200}}$ for c and V_{200}, respectively) by using the following expressions:

$$\delta_c = 1 - \frac{c}{c^{bib}}, \tag{17}$$

$$\delta_{V_{200}} = 1 - \frac{V_{200}}{V_{200}^{bib}}, \tag{18}$$

where c^{bib} and V_{200}^{bib} are the published c and V_{200} values from SPARC, respectively. The number of galaxies in our sample with δ_c and $\delta_{V_{200}}$ below different thresholds is described in Table 3.

Table 3 shows that in the case of the ISO and BURK profiles the fraction of galaxies in our sample with $|\delta_c|, |\delta_{V_{200}}| \leq 1$ is 95% and 94%, respectively, while the NFW profile only reached 85%. These results indicate that the core-type profiles, such as ISO and BURK, are closer to the respective published values than those obtained assuming a NFW profile.

Regarding the Pearson correlation (r_c, r_{V200}) between datasets (Table 2), high values ($r_c, r_{V200} \approx 0.8 - 0.94$) are observed in 4 out of the 6 comparison diagrams (Figures 1 and 2), implying a good compliance of our results with the literature. In contrast, two of these cases show low correlation values ($r_c, r_{V200} \approx 0.3$), specifically in the c_{NFW} comparison diagram (Figure 1, top) and the V_{200}^{BURK} diagram (Figure 2, bottom). These low values are consequence of a handful of outlying galaxies with exceptionally high δ_c or $\delta_{V_{200}}$: one in the c_{NFW} diagram (F571-8) and three in the V_{200}^{BURK} diagram (NGC0247, UGC11557 and D631-7). The main cause for the observed inconsistencies in these galaxies may be attributed to multiple factors, e.g. a divergence from a pure exponential profile in the stellar disk produced by secondary

TABLE 2

COMPARISON WITH LITERATURE VALUES[d]

Profile	$\overline{c}$	$\overline{c_{bib}}$	r_c	t_c	$\overline{V_{200}}$	$\overline{V_{200}^{bib}}$	r_{V200}	t_{V200}
NFW	8.02	9.75	0.3	-0.97	104.16	130.67	0.83	-3.72
ISO	84.39	85.26	0.87	-0.22	99.00	99.22	0.94	0.20
BURK	23.19	23.56	0.78	-0.53	67.45	64.32	0.31	0.49

[d]Results of the t-test analysis between obtained and published (Li et al. 2020) best-fit parameter samples. The first column describes the halo profile, while the second and third columns correspond to the obtained ($\overline{c}$) and the published ($\overline{c_{bib}}$) c parameter sample-average values. Columns 4 and 5 indicate the corresponding Pearson correlation coefficient (r_c) and t-value (t_c) between the c parameter samples. Finally, Columns 6 to 9 describe the obtained ($\overline{V_{200}}$) and published ($\overline{V_{200}^{bib}}$) sample-average values for the parameter V_{200}, along with the corresponding Pearson correlation coefficient (r_{V200}) and t-value (t_{V200}) between the V_{200} parameter samples.

TABLE 3

DEVIATION PARAMETER DISTRIBUTION[e]

	c			V_{200}			c and V_{200}		
$\lvert\delta_i\rvert$	**NFW**	**ISO**	**BURK**	**NFW**	**ISO**	**BURK**	**NFW**	**ISO**	**BURK**
$\leq$ **0.25**	66	73	77	76	96	93	63	73	75
$\leq$ **0.5**	77	87	87	90	99	96	65	87	86
$\leq$ **0.75**	81	94	96	96	99	96	79	94	94
$\leq$ **1**	88	96	97	97	99	97	85	95	94

[e]Number of galaxies in our sample with deviation parameter values ($|\delta_c|$ and $|\delta_{V200}|$) below different thresholds.

features (i.e. a bar or bulge), or artifacts produced by the use of different numerical solver routines between studies. Without taking into account the outlying galaxies, the correlation values between the samples are $r_c = 0.93$ and $r_{V200} = 0.92$ for the c_{NFW} and V_{200}^{BURK} comparison diagrams, respectively. It is important to emphasize that these galaxies represent a small fraction of the total sample. Most of the galaxies analysed with our procedure ($\gtrsim 85\%$), show consistency with the literature. The influence of other factors, such as the assumed stellar disc (M/L)* value and the consideration of a separate HI disc component in the resulting mass profile fits, will be explored in a future work.

5.2. *Comparison Between Our Results*

A comparison of our best-fit parameter samples assuming different DM models serves as an internal consistency check for our procedure. Figures 3 and 4 show all the comparison diagrams (ISO vs NFW, BURK vs NFW and BURK vs ISO) between our best-fit parameter samples c and V_{200}, respectively. A qualitative analysis shows that all comparison diagrams display a positive trend, with varying degrees of dispersion. In the case of the c parameter (Figure 3), we found high correlation values ($r \approx 0.9$) in all comparisons, displaying a nearly linear trend. For the case of V_{200}, the diagrams show lower correlation values ($0.43 \leq r \leq 0.71$) and in general, a greater dispersion. This could imply a difference in the sensibility between fitting parameters. From this comparison, we conclude that in general our results show consistency between different models.

6. CONCLUSIONS

The main conclusions of this investigation can be summarized as follows:

1. By using an independent fitting procedure, with its own stellar disc model, optimization algorithm and set of constraints, we were able to marginally replicate the results published in the literature (Li et al. 2020). Our results suggest that the use of a homogenized kinematical data catalogue along with a set of simple physically-based constraints is enough to achieve consistent results, at least with the simplifying assumptions made in the present work.

2. The t-test analysis shows that most of the results obtained here are consistent with those published in the literature, within uncertainties. However, some deviations were observed in a small set of particular galaxies. These inconsistencies could be attributed to multiple causes, like deviations of the stellar disc from an exponential profile (i.e. a bar or bulge), or inconsistencies produced by the use of different numerical solver routines.

3. Our analysis indicates that the use of a different stellar disc model from the one assumed in the literature (Casertano 1983) apparently does not generate large

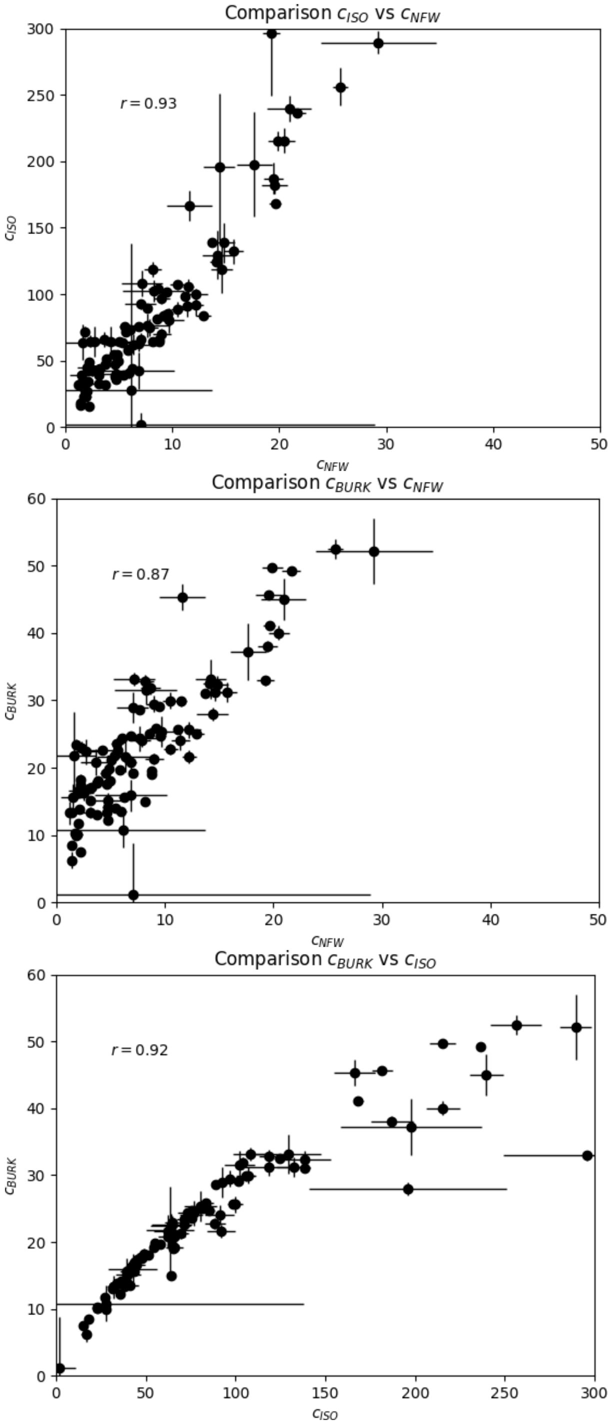

Fig. 3. *Comparison diagrams between our obtained best-fit c samples assuming different DM profiles.*

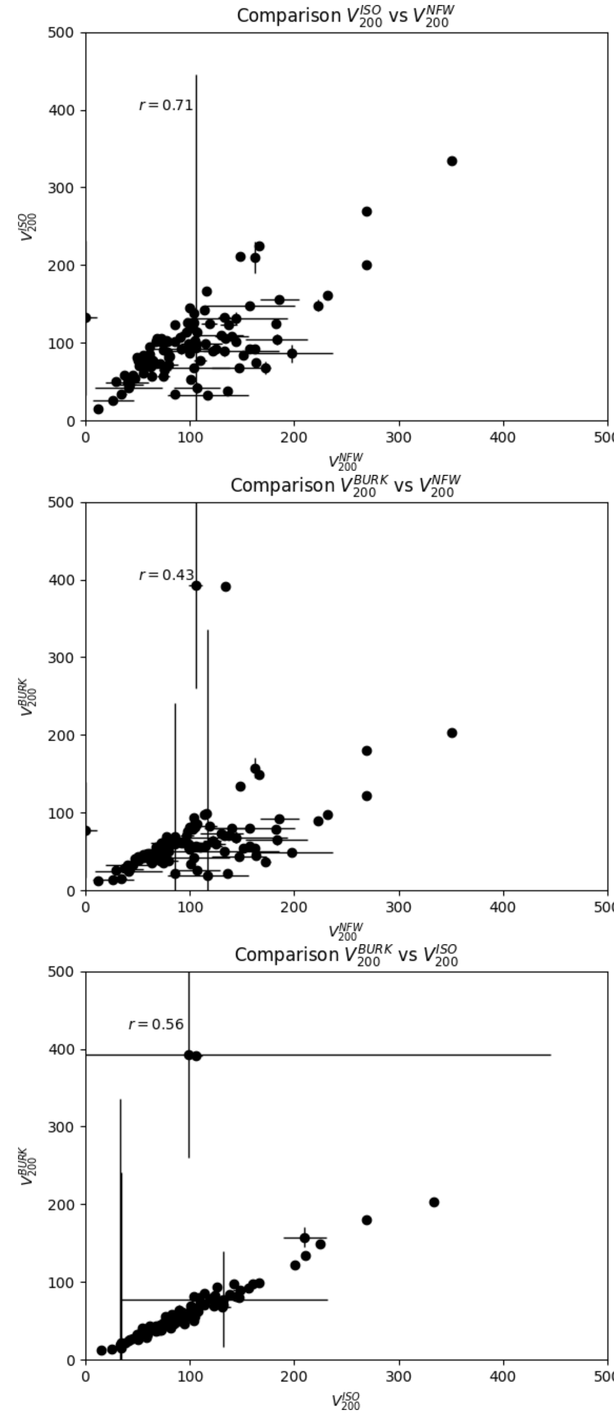

Fig. 4. *Comparison diagrams between our obtained best-fit V_{200} samples assuming different DM profiles.*

deviations in the resulting fits, at least in those cases where a *core* type DM profile (ISO and BURK) is considered. In addition, our assumption of a fixed (M/L)* ratio did not seem to produce any major deviations when compared to the published fits, even when the latter considered a variable (M/L)* ratio, imposing priors around the fiducial (M/L)*=0.5 for the stellar disc (Li et al. 2020).

4. The V_{200}^{NFW} comparison diagram (Figure 2, top), clearly shows a dispersion that is consistently higher

(i.e. not produced by a handful of outlying galaxies) in comparison to the same diagrams for the ISO and BURK profiles. This effect could be explained by two different scenarios: the presence of a bias inherent to the fitting procedure produced by one of its features (e.g. the assumed stellar disk model, optimization algorithm and/or set of constraints), or the fact that a cusp type DM density profile like NFW is simply not adequate to model the RCs of the late-type galaxies analyzed in our test sample, thus producing the observed scatter between studies. This latter scenario is supported by a great amount of evidence obtained over the years, showing a preference for core-type profiles over cusp profiles in late galaxies (McGaugh et al. 2001; Marchesini et al. 2002; Simon et al. 2005; Kuzio de Naray et al. 2008; Walker & Penarrubia 2011). Another reason to support the latter scenario relies on the fact that if our fitting procedure had any inherent bias produced by some its features, we would notice systematic deviations in the results for all the assumed DM profiles, not just for one.

5. As an internal consistency check for our results, a comparison was made between our best fit parameter samples obtained by assuming different DM density models. The qualitative analysis shows that all comparison diagrams (Figures 3 and 4) display a positive trend, with varying degrees of dispersion. The *c* comparison diagrams display high correlation values between DM models ($r \approx 0.9$), while the corresponding V_{200} diagrams show quite lower values ($0.43 \leq r \leq 0.71$). The difference in the dispersion between the *c* and V_{200} diagrams is probably caused by a variation in the sensibility between fitting parameters. However, based in the results of this analysis, we conclude that in general our parameter samples are consistent with each other.

6. The analysis of the χ^2_R values in our sample suggests that the best fits are obtained when an ISO DM profile is assumed (i.e. with the lowest sample-averaged χ^2_R), followed by the BURK and finally the NFW profile. From these last results, we conclude that our sample shows a clear tendency to obtain better fits when a core-type profile is assumed. This agrees with a previously published analysis of the sample (Li et al. 2020), providing observational evidence for the *core-cusp* discrepancy.

7. In recent years, homogenized RC+photometry data catalogues such as SPARC (Lelli et al. 2016b), have provided the means to estimate the influence of different optimization algorithms and observational techniques in the search of a consistent RC-fitting procedure that can provide accurate results. This work serves as a first step for a more general approach with our procedure (e.g. adding a bulge component) that would provide a simple, low time-cost method to fit kinematical data for the mass profile estimation of disc galaxies. These latter characteristics would make it suitable for analyzing samples with a great number of galaxies, using photometry data from widely available standardized digital surveys [e.g. SDSS (Abdurro'uf et al. 2022)].

This research was supported by the Instituto Politécnico Nacional (Mexico) under the research projects SIP-20210556, and SIP-20220744. This work is part of MSc. Rodolfo de J. Zermeño's Ph.D. thesis, sponsored by CONACyT. The authors would like to thank Dr. Isaura Fuentes-Carrera, Dr. Janos Zsargó and Dr. Ary Rodríguez for all their valuable discussions and feedback in the preparation of this work. And of course, we sincerely thank the referee for the valuable comments and suggestions in the preparation of this work.

This work is dedicated to the memory of Dr. Héctor Castañeda-Fernández: a beloved researcher, teacher and friend.

APPENDIX

BEST FIT PARAMETER TABLES

Table A1 contains the obtained best-fit values (in tabulated form) of the DM halo parameters for each galaxy in our sample. The complete set of RC plots detailing the velocity contributions for each component (stellar disc, HI disc and DM halo) and tables containing their corresponding best-fit parameter values in machine-readable format, along files with the Asexual Genetic Algorithm (AGA) code in FORTRAN90 language is available to download at the Harvard Dataverse website:
https://dataverse.harvard.edu/privateurl.xhtml?token=66a59351-4b9b-4a1b-a2b5-d25fc4cd5f27
The published data used for comparison in the present work are available to download in machine readable table format at the SPARC catalog website:
http://astroweb.cwru.edu/SPARC/

TABLE A1

BEST-FIT PARAMETER VALUES, ASSUMING A NFW PROFILE.[b]

Name	c	M_{200} $(10^{10} M_{\odot})$	R_{200} (kpc)	V_{200} (km/s)	$\log \rho_0$ $\left(\frac{M_{\odot}}{pc^3}\right)$	$\log h$ (pc)	χ^2_R
D512-2	6.32 ± 2.54	2.2 ± 22.5	56.3 ± 44.3	41 ± 32	-2.66	3.95	0.41
D564-8	1.17 ± 0.03	19.8 ± 1.5	116.9 ± 2.8	85 ± 2	-4.17	5.00	1.18
D631-7	1.84 ± 0.01	77.5 ± 1.9	184.3 ± 1.5	135 ± 1	-3.81	5.00	8
DDO064	2.36 ± 0.06	163 ± 12	236.4 ± 6.1	173 ± 4	-3.59	5.00	0.73
DDO154	4.93 ± 0.16	8 ± 0.7	86.5 ± 2.4	63 ± 2	-2.91	4.24	12.52
DDO161	1.83 ± 0.14	42.5 ± 6.8	150.8 ± 8.1	110 ± 6	-3.81	4.91	1.42
DDO168	2.23 ± 0.02	136 ± 3.2	222.3 ± 1.8	162 ± 1	-3.65	5.00	11.53
DDO170	5.49 ± 0.28	5.35 ± 0.3	75.6 ± 1.7	55 ± 1	-2.80	4.14	2.02
ESO079-G014	3.69 ± 0.02	623 ± 7.9	369.1 ± 1.6	269 ± 1	-3.18	5.00	4.31
ESO116-G012	6.06 ± 0.48	81.7 ± 12.8	187.6 ± 10.9	137 ± 8	-2.70	4.49	2.99
ESO444-G084	8.18 ± 0.83	16.1 ± 6.3	109.1 ± 12.7	80 ± 9	-2.39	4.13	0.79
ESO563-G021	4.81 ± 0.02	1375 ± 18	480.6 ± 2.1	351 ± 2	-2.93	5.00	23.21
F563-1	7.84 ± 0.86	29 ± 6	132.8 ± 9.1	97 ± 7	-2.43	4.23	1.04
F563-V1	6.11 ± 7.64	0.06 ± 0.1	17.1 ± 5.7	12 ± 4	-2.69	3.45	0.36
F563-V2	7.17 ± 1.89	95.7 ± 177	198 ± 67	144 ± 49	-2.53	4.44	1.3
F565-V2	2.5 ± 0.88	196 ± 64	251 ± 40	183 ± 29	-3.54	5.00	0.4
F567-2	6.8 ± 3.3	2 ± 11.4	55 ± 29	40 ± 21	-2.58	3.90	0.47
F568-1	7.01 ± 1.46	124 ± 188	215.4 ± 59.4	157 ± 43	-2.55	4.49	0.82
F568-3	2.5 ± 0.03	194 ± 6.8	250.3 ± 3	183 ± 2	-3.54	5.00	3.35
F568-V1	14.62 ± 0.99	20.1 ± 2.5	117.6 ± 4.8	86 ± 3	-1.77	3.91	0.21
F571-8	5.56 ± 0.57	204 ± 69	254.4 ± 25.4	186 ± 19	-2.78	4.66	1.07
F571-V1	4.69 ± 1.56	24.6 ± 39.8	125.7 ± 40	92 ± 29	-2.95	4.43	0.34
F574-1	8.61 ± 0.34	20 ± 1.6	117.5 ± 3.2	86 ± 2	-2.34	4.14	1.46
F574-2	7.05 ± 21.87	0 ± 0.5	0 ± 15.8	0 ± 12	-2.54	-0.33	0.17
F579-V1	20.93 ± 2.09	9.7 ± 0.9	92.2 ± 3	67 ± 2	-1.37	3.64	0.21
F583-1	4.61 ± 0.28	30.4 ± 5.7	134.9 ± 8.2	98 ± 6	-2.97	4.47	1.63
F583-4	3.63 ± 1.39	36 ± 50	142.8 ± 47.1	104 ± 34	-3.20	4.59	0.17
IC2574	1.44 ± 0	37.2 ± 0.3	144.2 ± 0.4	105 ± 0	-4.01	5.00	43.75
KK98-251	1.39 ± 0.03	33.1 ± 2.2	138.8 ± 3.1	101 ± 2	-4.04	5.00	2.08
NGC0024	21.63 ± 0.87	10.1 ± 0.7	93.4 ± 2.1	68 ± 2	-1.34	3.64	0.95
NGC0055	3.12 ± 0.27	61.6 ± 13.7	170.7 ± 12.6	125 ± 9	-3.34	4.74	1.4
NGC0247	5.64 ± 0.24	31.9 ± 3.8	137.1 ± 5.3	100 ± 4	-2.77	4.39	1.75
NGC1003	4.72 ± 0.1	38.8 ± 1.2	146.3 ± 1.5	107 ± 1	-2.95	4.49	2.78
NGC2403	11.24 ± 0.07	29.7 ± 0.3	133.9 ± 0.4	98 ± 0	-2.05	4.08	11.41
NGC3109	2.15 ± 0.01	123.7 ± 2.2	215.3 ± 1.3	157 ± 1	-3.67	5.00	10.17
NGC3198	8.77 ± 0.07	47.2 ± 0.5	156.2 ± 0.6	114 ± 0	-2.32	4.25	2.57
NGC3741	3.83 ± 0.41	13.3 ± 3.4	102.4 ± 8.8	75 ± 6	-3.15	4.43	0.37
NGC3769	14.38 ± 1.48	14.9 ± 1.7	106.3 ± 4.1	78 ± 3	-1.79	3.87	0.69
NGC3893	17.69 ± 1.62	32.1 ± 4.6	137.3 ± 6.5	100 ± 5	-1.56	3.89	0.55
NGC3917	3.18 ± 0.02	397.9 ± 6.3	317.9 ± 1.7	232 ± 1	-3.32	5.00	7.5
NGC3992	12.23 ± 0.68	145.8 ± 6.2	227.5 ± 3.3	166 ± 2	-1.96	4.27	1.27
NGC4010	3.05 ± 0.03	350.4 ± 11.6	304.7 ± 3.3	222 ± 2	-3.36	5.00	2.49
NGC4100	12.92 ± 0.7	50.2 ± 4	159.4 ± 4.1	116 ± 3	-1.90	4.09	3.58
NGC4183	10.52 ± 0.64	15.5 ± 1.2	107.7 ± 2.7	79 ± 2	-2.12	4.01	0.18
NGC4559	4.71 ± 0.44	53.1 ± 11.2	162.5 ± 10.6	119 ± 8	-2.95	4.54	0.81
NGC5585	5.06 ± 0.12	37.7 ± 2.2	144.9 ± 3	106 ± 2	-2.88	4.46	8.93
NGC6015	13.74 ± 0.2	35.3 ± 0.8	141.7 ± 1.1	103 ± 1	-1.84	4.01	6.55
NGC7793	10.48 ± 0.72	13.4 ± 2.1	102.6 ± 5.1	75 ± 4	-2.13	3.99	1.19
UGC00128	8.21 ± 0.08	35.3 ± 0.3	141.8 ± 0.4	104 ± 0	-2.39	4.24	2.97
UGC00191	9.52 ± 0.24	8.4 ± 0.3	87.9 ± 0.9	64 ± 1	-2.23	3.97	3.12
UGC00634	6.25 ± 0.53	34.8 ± 5.8	141.1 ± 7.4	103 ± 5	-2.67	4.35	3.3
UGC00731	9.57 ± 0.51	5.9 ± 0.6	78 ± 2.4	57 ± 2	-2.23	3.91	0.33
UGC00891	2.08 ± 0.01	110.6 ± 1.3	207.4 ± 0.8	151 ± 1	-3.71	5.00	3.49
UGC01230	11.44 ± 0.85	14.9 ± 1.9	106.4 ± 4.2	78 ± 3	-2.04	3.97	1.01
UGC02259	19.48 ± 0.89	5.5 ± 0.3	76.2 ± 1.2	56 ± 1	-1.45	3.59	0.69
UGC04325	19.56 ± 1.2	7.4 ± 0.8	84.4 ± 3.1	62 ± 2	-1.45	3.63	3.11
UGC04483	8.25 ± 2.88	0.6 ± 4.7	36.3 ± 26.7	26 ± 19	-2.38	3.64	0.71
UGC04499	6.81 ± 0.59	10 ± 2.2	93.1 ± 6.3	68 ± 5	-2.58	4.14	0.62
UGC05005	1.91 ± 0.52	86.9 ± 23.3	191.4 ± 22	140 ± 16	-3.78	5.00	0.24
UGC05414	2.24 ± 0.03	138.7 ± 6.4	223.7 ± 3.4	163 ± 2	-3.64	5.00	1.26
UGC05716	8.74 ± 0.11	6.7 ± 0.1	81.5 ± 0.6	59 ± 0	-2.32	3.97	2.01
UGC05721	25.7 ± 0.72	3.7 ± 0.1	67 ± 0.9	49 ± 1	-1.14	3.42	1.08

TABLE A1. CONTINUED

Name	c	M_{200} ($10^{10} M_{\odot}$)	R_{200} (kpc)	V_{200} (km/s)	$\log \rho_0$ $\left(\frac{M_{\odot}}{pc^3}\right)$	$\log h$ (pc)	χ^2_R
UGC05750	1.67 ± 0.18	57.4 ± 10.7	166.7 ± 11.6	122 ± 8	-3.89	5.00	1.16
UGC05764	19.62 ± 0.52	1.7 ± 0.1	51.4 ± 0.8	38 ± 1	-1.45	3.42	6.61
UGC05829	2.01 ± 0.89	101 ± 34	201.3 ± 35.8	147 ± 26	-3.73	5.00	0.1
UGC05918	7.67 ± 2.09	2.4 ± 4.9	57.5 ± 18.9	42 ± 14	-2.46	3.88	0.15
UGC05986	7.67 ± 0.38	75.6 ± 10.9	182.7 ± 8.4	133 ± 6	-2.46	4.38	7.69
UGC05999	3.13 ± 0.82	70 ± 33	178 ± 28	130 ± 21	-3.34	4.76	2.23
UGC06399	5.4 ± 0.7	48 ± 28	157 ± 23	115 ± 17	-2.82	4.47	0.74
UGC06446	14.8 ± 1	6 ± 0.6	78.4 ± 2.6	57 ± 2	-1.75	3.72	0.22
UGC06667	6.86 ± 0.66	31 ± 7	135.9 ± 10.3	99 ± 8	-2.57	4.30	1.29
UGC06917	9.16 ± 0.62	23.7 ± 4	124.1 ± 6.6	91 ± 5	-2.27	4.13	0.38
UGC06923	4.28 ± 1.73	75.3 ± 113	182.5 ± 71.8	133 ± 52	-3.04	4.63	0.61
UGC06930	12.25 ± 1.11	12.8 ± 1.5	101.2 ± 4.1	74 ± 3	-1.96	3.92	0.17
UGC06983	15.72 ± 0.92	12.4 ± 0.7	99.9 ± 2	73 ± 1	-1.69	3.80	0.53
UGC07089	1.97 ± 0.04	95.1 ± 6.5	197.3 ± 4.4	144 ± 3	-3.75	5.00	0.74
UGC07125	5.96 ± 0.49	3.4 ± 0.3	64.9 ± 1.8	47 ± 1	-2.72	4.04	0.55
UGC07151	9.02 ± 0.76	7.9 ± 1.8	85.9 ± 6.3	63 ± 5	-2.29	3.98	2.83
UGC07261	14.25 ± 1.41	4.3 ± 0.9	70.2 ± 4.6	51 ± 3	-1.80	3.69	0.04
UGC07399	19.9 ± 0.95	11 ± 1	96.1 ± 3	70 ± 2	-1.43	3.68	0.74
UGC07524	5.87 ± 0.43	15.8 ± 2.3	108.5 ± 5.4	79 ± 4	-2.73	4.27	0.56
UGC07559	1.47 ± 1.02	38.7 ± 13.3	146.2 ± 30.8	107 ± 22	-4.00	5.00	0.64
UGC07603	8.7 ± 0.9	11.6 ± 5.8	97.9 ± 12.3	71 ± 9	-2.33	4.05	1.9
UGC07608	2.71 ± 1.1	247 ± 82	271 ± 53	198 ± 39	-3.47	5.00	0.45
UGC07690	29.3 ± 5.4	0.8 ± 0.2	40 ± 2.7	29 ± 2	-0.99	3.14	0.18
UGC07866	1.63 ± 2.05	51 ± 25	160.3 ± 53.1	117 ± 39	-3.91	4.99	0.05
UGC08286	14 ± 0.53	7.4 ± 0.4	84.2 ± 1.6	61 ± 1	-1.81	3.78	2.68
UGC08490	20.48 ± 0.97	4.2 ± 0.2	69.7 ± 1.2	51 ± 1	-1.40	3.53	0.11
UGC08550	11.5 ± 0.48	3.06 ± 0.3	62.8 ± 2	46 ± 1	-2.03	3.74	1.74
UGC09037	2.23 ± 0.03	136.7 ± 4.8	222.7 ± 2.5	163 ± 2	-3.65	5.00	3.32
UGC10310	9.72 ± 1.4	5.8 ± 1.5	77.6 ± 6.6	57 ± 5	-2.21	3.90	0.68
UGC11455	3.69 ± 0.03	623 ± 15	369.2 ± 2.9	269 ± 2	-3.18	5.00	5.86
UGC11557	1.45 ± 0.09	37.4 ± 7.6	144.6 ± 9.3	106 ± 7	-4.01	5.00	1.44
UGC11820	4.68 ± 0.32	16.6 ± 1.9	110.3 ± 4.2	81 ± 3	-2.96	4.37	2.02
UGC12506	19.25 ± 0.84	102.8 ± 4.1	202.4 ± 2.7	148 ± 2	-1.47	4.02	0.15
UGC12632	9.01 ± 0.87	5.9 ± 1	77.9 ± 4.1	57 ± 3	-2.29	3.94	0.31
UGC12732	7.03 ± 0.34	15.6 ± 1.4	107.9 ± 3.2	79 ± 2	-2.55	4.19	0.19
UGCA281	11.6 ± 2.11	1.3 ± 0.5	47.2 ± 6.4	34 ± 5	-2.02	3.61	1.03
UGCA442	4.53 ± 0.46	14 ± 3	104 ± 7.7	76 ± 6	-2.99	4.36	2.18
UGCA444	1.86 ± 0.02	79.5 ± 3	185.8 ± 2.3	136 ± 2	-3.80	5.00	0.06

[b]Best-fit parameter values, assuming a NFW profile. Column 1 the galaxy name as listed in Table 1, while c, M_{200}, R_{200} and V_{200} are listed in Columns 2, 3, 4 and 5, respectively. In Columns 6 and 7 are shown the core density (ρ_0) and the scale length (h) of the DM halo, respectively. Finally, the χ^2_R values are given in Column 8.

TABLE A2

BEST-FIT PARAMETER VALUES, ASSUMING AN ISO PROFILE.[c]

Name	c	M_{200} ($10^{10} M_\odot$)	R_{200} (kpc)	V_{200} (km/s)	$\log \rho_0$ $\left(\frac{M_\odot}{pc^3}\right)$	$\log h$ (pc)	χ^2_R
D512-2	62.24 ± 7.7	2.33 ± 0.3	57.3 ± 2.8	42 ± 2	-1.41	2.96	0.16
D564-8	32.07 ± 3.76	1.26 ± 0.4	46.7 ± 4.8	34 ± 3	-1.97	3.16	0.11
D631-7	27.59 ± 0.62	37.68 ± 5.7	144.9 ± 7.7	106 ± 6	-2.10	3.72	1.8
DDO064	64.5 ± 4.3	9.74 ± 3.9	92.3 ± 11.1	67 ± 8	-1.38	3.16	0.31
DDO154	49.53 ± 0.3	6.08 ± 0.1	78.9 ± 0.4	58 ± 0	-1.60	3.20	2.65
DDO161	23.09 ± 0.32	14.4 ± 0.3	105.1 ± 0.6	77 ± 0	-2.25	3.66	0.29
DDO168	45.16 ± 0.82	25.36 ± 2.3	127 ± 3.7	93 ± 3	-1.68	3.45	4.36
DDO170	39.27 ± 1.34	7.51 ± 0.3	84.6 ± 1	62 ± 1	-1.80	3.33	1.2
ESO079-G014	46.89 ± 1.13	257.64 ± 11.5	275 ± 4.1	201 ± 3	-1.65	3.77	1.47
ESO116-G012	73.17 ± 2.68	60.39 ± 2.1	169.6 ± 2	124 ± 1	-1.27	3.36	1.1
ESO444-G084	118.62 ± 5.41	11.57 ± 0.7	97.7 ± 2	71 ± 1	-0.85	2.92	0.93
ESO563-G021	54.79 ± 0.86	1184.47 ± 29	457.3 ± 3.7	334 ± 3	-1.52	3.92	13.38
F563-1	75.18 ± 6.47	47.05 ± 4.3	156 ± 4.9	114 ± 4	-1.24	3.32	0.54
F563-V1	27.55 ± 110.35	0.11 ± 0.1	20.7 ± 3.7	15 ± 3	-2.10	2.88	0.36
F563-V2	108.31 ± 9.61	71.89 ± 12.5	179.7 ± 10.6	131 ± 8	-0.93	3.22	0.33
F565-V2	42.02 ± 4.03	36.24 ± 7.3	143 ± 9.6	104 ± 7	-1.74	3.53	0.06
F567-2	42.66 ± 13.74	3.75 ± 0.8	67.2 ± 4.9	49 ± 4	-1.73	3.20	0.36
F568-1	92.36 ± 3.75	101.29 ± 7	201.5 ± 4.4	147 ± 3	-1.07	3.34	0.12
F568-3	42.89 ± 0.97	62.28 ± 4.6	171.3 ± 4.3	125 ± 3	-1.73	3.60	1.03
F568-V1	118.58 ± 17.92	59.01 ± 7.4	168.3 ± 7	123 ± 5	-0.85	3.15	0.13
F571-8	75.35 ± 1.28	120.54 ± 4.3	213.5 ± 2.5	156 ± 2	-1.24	3.45	1.34
F571-V1	40.18 ± 6.85	25.32 ± 5.8	126.9 ± 8.9	93 ± 6	-1.78	3.50	0.08
F574-1	81.15 ± 2.16	33.09 ± 1.1	138.7 ± 1.5	101 ± 1	-1.18	3.23	0.19
F574-2	1.82 ± 0.2	73.96 ± 50	181.4 ± 17	132 ± 13	-4.10	5.00	0.13
F579-V1	239.65 ± 9.5	33.51 ± 2.2	139.3 ± 3	102 ± 2	-0.24	2.76	0.06
F583-1	47.61 ± 0.88	27.06 ± 1.4	129.7 ± 2.4	95 ± 2	-1.64	3.44	0.36
F583-4	65.82 ± 5.95	9.93 ± 0.8	92.9 ± 2.5	68 ± 2	-1.36	3.15	0.31
IC2574	18.3 ± 0.23	35.56 ± 3.8	142.1 ± 4.9	104 ± 4	-2.44	3.89	1.98
KK98-251	32.32 ± 1.21	4.62 ± 1.1	72 ± 5.5	53 ± 4	-1.97	3.35	0.3
NGC0024	236.4 ± 2.17	37.02 ± 0.8	144 ± 1	105 ± 1	-0.26	2.78	0.35
NGC0055	39.15 ± 0.74	25.24 ± 1.3	126.8 ± 2.2	93 ± 2	-1.80	3.51	0.23
NGC0247	71.24 ± 1.38	21.22 ± 0.7	119.6 ± 1.2	87 ± 1	-1.29	3.23	2.61
NGC1003	35.97 ± 0.92	47.4 ± 0.8	156.4 ± 0.8	114 ± 1	-1.88	3.64	3.21
NGC2403	98.73 ± 0.53	64.25 ± 0.2	173.1 ± 0.2	126 ± 0	-1.01	3.24	16.89
NGC3109	42.31 ± 0.88	25.02 ± 1.7	126.4 ± 2.9	92 ± 2	-1.74	3.48	0.16
NGC3198	65.53 ± 0.92	91.01 ± 0.5	194.4 ± 0.4	142 ± 0	-1.36	3.47	1.67
NGC3741	51.29 ± 1.51	5.77 ± 0.4	77.5 ± 1.7	57 ± 1	-1.57	3.18	0.91
NGC3769	195.74 ± 55.12	35.03 ± 2.2	141.4 ± 2.8	103 ± 2	-0.42	2.86	0.28
NGC3893	197.8 ± 39.28	95.98 ± 5.1	197.9 ± 3.5	144 ± 3	-0.41	3.00	0.54
NGC3917	43.99 ± 1.08	131.99 ± 3.2	220 ± 1.8	161 ± 1	-1.70	3.70	3.36
NGC3992	91.91 ± 8.04	360.5 ± 7	307.6 ± 1.9	225 ± 1	-1.07	3.52	1.57
NGC4010	43.28 ± 2.32	104 ± 16.3	203.3 ± 10.4	148 ± 8	-1.72	3.67	1.31
NGC4100	83.77 ± 2.68	147.33 ± 3	228.3 ± 1.6	167 ± 1	-1.15	3.44	3.22
NGC4183	88.46 ± 5.6	33.16 ± 0.8	138.8 ± 1.1	101 ± 1	-1.11	3.20	0.21
NGC4559	36.42 ± 1.58	61.21 ± 3.9	170.3 ± 3.7	124 ± 3	-1.86	3.67	0.41
NGC5585	64.06 ± 1.55	26.27 ± 0.6	128.5 ± 1	94 ± 1	-1.38	3.30	20.67
NGC6015	138.63 ± 2.82	83.73 ± 1.3	189.1 ± 0.9	138 ± 1	-0.72	3.13	5.76
NGC7793	107 ± 3.54	23.87 ± 2.1	124.4 ± 3.6	91 ± 3	-0.94	3.07	1.52
UGC00128	64.19 ± 0.59	63.92 ± 0.2	172.8 ± 0.1	126 ± 0	-1.38	3.43	3.33
UGC00191	101.7 ± 2.25	14.8 ± 0.2	106.1 ± 0.5	77 ± 0	-0.98	3.02	1.16
UGC00634	43.69 ± 2.41	53.78 ± 2.5	163.1 ± 2.5	119 ± 2	-1.71	3.57	1.55
UGC00731	85.58 ± 2.57	11.22 ± 0.6	96.7 ± 1.6	71 ± 1	-1.13	3.05	0.17
UGC00891	33.9 ± 0.93	19.09 ± 1.1	115.5 ± 2.4	84 ± 2	-1.93	3.53	0.2
UGC01230	91.05 ± 8.14	33.03 ± 2.7	138.7 ± 3.5	101 ± 3	-1.08	3.18	0.74
UGC02259	187 ± 11.9	19.33 ± 0.5	116 ± 1	85 ± 1	-0.46	2.79	0.48
UGC04325	181.7 ± 5.9	27.35 ± 1	130.2 ± 1.5	95 ± 1	-0.48	2.86	1.53
UGC04483	102.4 ± 8	0.53 ± 0.1	35 ± 1.2	26 ± 1	-0.98	2.53	0.31
UGC04499	62.6 ± 5.6	12.81 ± 1.4	101.1 ± 3.5	74 ± 3	-1.40	3.21	0.12
UGC05005	23.2 ± 1.9	40.66 ± 6.1	148.6 ± 7.3	108 ± 5	-2.25	3.81	0.03
UGC05414	48.9 ± 2.8	13.37 ± 1.6	102.6 ± 4.4	75 ± 3	-1.61	3.32	0.08
UGC05716	64.48 ± 1.25	13.03 ± 0.2	101.7 ± 0.6	74 ± 0	-1.38	3.20	2.57
UGC05721	256.2 ± 14	17 ± 0.8	111 ± 1.8	81 ± 1	-0.19	2.64	0.88

TABLE A2. CONTINUED

Name	c	M_{200} ($10^{10} M_{\odot}$)	R_{200} (kpc)	V_{200} (km/s)	$\log \rho_0$ $\left(\frac{M_{\odot}}{pc^3}\right)$	$\log h$ (pc)	χ_R^2
UGC05750	23.12 ± 1.41	22.72 ± 3.4	122.4 ± 6.5	89 ± 5	-2.25	3.72	0.3
UGC05764	168.37 ± 2.91	6.38 ± 0.1	80.1 ± 0.3	59 ± 0	-0.55	2.68	4.37
UGC05829	45 ± 4.41	9.82 ± 3	92.6 ± 7.8	68 ± 6	-1.68	3.31	0.14
UGC05918	76.69 ± 8.84	3.06 ± 0.4	62.8 ± 2.9	46 ± 2	-1.23	2.91	0.01
UGC05986	89.13 ± 2.07	74.01 ± 1.9	181.4 ± 1.5	132 ± 1	-1.10	3.31	2.54
UGC05999	32.56 ± 1.68	42.51 ± 4.4	150.8 ± 5.5	110 ± 4	-1.96	3.67	0.96
UGC06399	63.32 ± 2.84	31.27 ± 5.7	136.2 ± 7.7	99 ± 6	-1.39	3.33	0.11
UGC06446	138.58 ± 14.65	16.34 ± 1.1	109.7 ± 2.5	80 ± 2	-0.72	2.90	0.2
UGC06667	75.4 ± 3.18	30.35 ± 1.4	134.8 ± 2.1	98 ± 2	-1.24	3.25	0.21
UGC06917	83.7 ± 3.89	39.8 ± 2.8	147.6 ± 3.4	108 ± 2	-1.15	3.25	0.17
UGC06923	64.64 ± 11.26	22.7 ± 4.5	122.4 ± 8.2	89 ± 6	-1.37	3.28	0.41
UGC06930	99.63 ± 4.11	31.6 ± 0.8	136.6 ± 1.1	100 ± 1	-1.00	3.14	0.1
UGC06983	132.3 ± 9.23	37.39 ± 1.5	144.5 ± 1.9	105 ± 1	-0.76	3.04	0.48
UGC07089	27.23 ± 0.7	33.18 ± 2.5	138.9 ± 3.6	101 ± 3	-2.11	3.71	0.08
UGC07125	41.14 ± 4.85	5.25 ± 0.3	75.1 ± 1.5	55 ± 1	-1.76	3.26	0.35
UGC07151	96.94 ± 4.58	10.63 ± 0.5	95 ± 1.6	69 ± 1	-1.03	2.99	1.27
UGC07261	129.54 ± 18.26	11.48 ± 1.3	97.5 ± 3.6	71 ± 3	-0.78	2.88	0.02
UGC07399	215.14 ± 7.26	36.14 ± 0.7	142.9 ± 0.9	104 ± 1	-0.34	2.82	0.24
UGC07524	58.18 ± 1.97	16.86 ± 0.6	110.8 ± 1.3	81 ± 1	-1.46	3.28	0.43
UGC07559	39.21 ± 3.41	2.4 ± 1.3	57.8 ± 8.9	42 ± 6	-1.80	3.17	0.16
UGC07603	103.94 ± 2.73	12.31 ± 0.5	99.8 ± 1.4	73 ± 1	-0.97	2.98	0.5
UGC07608	64.07 ± 11.2	20.45 ± 9.8	118.2 ± 15.3	86 ± 11	-1.38	3.27	0.06
UGC07690	289.45 ± 8.66	3.97 ± 0.3	68.5 ± 1.7	50 ± 1	-0.08	2.37	0.25
UGC07866	63.6 ± 13.43	1.13 ± 0.4	45 ± 4.8	33 ± 3	-1.39	2.85	0.04
UGC08286	124.71 ± 3.38	19.91 ± 0.1	117.1 ± 0.2	86 ± 0	-0.81	2.97	0.81
UGC08490	215.43 ± 9.38	14.68 ± 0.2	105.8 ± 0.5	77 ± 0	-0.34	2.69	0.2
UGC08550	105.71 ± 5.43	6.57 ± 0.2	80.9 ± 0.9	59 ± 1	-0.95	2.88	0.67
UGC09037	15.41 ± 0.38	295.1 ± 106	287.7 ± 28	210 ± 21	-2.59	4.27	1
UGC10310	80.27 ± 9.14	11.71 ± 1.4	98.1 ± 4	72 ± 3	-1.19	3.09	0.31
UGC11455	31.59 ± 0.65	618.55 ± 15.5	368.2 ± 3.1	269 ± 2	-1.99	4.07	2.54
UGC11557	16.72 ± 2.76	30 ± 11	135 ± 18	99 ± 13	-2.52	3.91	0.94
UGC11820	38.23 ± 0.85	18.19 ± 0.3	113.7 ± 0.6	83 ± 0	-1.82	3.47	8.64
UGC12506	296.1 ± 47	299 ± 10.6	289 ± 3.4	211 ± 2	-0.06	2.99	0.27
UGC12632	69.73 ± 3.96	11.5 ± 0.4	97.6 ± 1.2	71 ± 1	-1.31	3.15	0.12
UGC12732	65.88 ± 4.79	22.03 ± 1.2	121.2 ± 2.2	88 ± 2	-1.36	3.26	0.48
UGCA281	166.34 ± 11.23	1.3 ± 0.2	47.1 ± 2	34 ± 1	-0.56	2.45	0.23
UGCA442	54.17 ± 1.6	8.87 ± 0.3	89.5 ± 1	65 ± 1	-1.53	3.22	0.72
UGCA444	71.29 ± 4.01	1.72 ± 0.2	51.8 ± 1.9	38 ± 1	-1.29	2.86	0.21

[c]Best-fit parameter values, assuming an ISO profile. Columns as in Table A1.

TABLE A3

BEST-FIT PARAMETER VALUES, ASSUMING A BURK PROFILE.[d]

Name	c	M_{200} ($10^{10} M_\odot$)	R_{200} (kpc)	V_{200} (km/s)	$\log \rho_0$ $\left(\frac{M_\odot}{pc^3}\right)$	$\log h$ (pc)	χ^2_R
D512-2	21.67 ± 2.38	0.46 ± 0.2	33.4 ± 4.5	24 ± 3	-1.37	3.19	0.08
D564-8	13.27 ± 0.6	0.35 ± 0.08	30.4 ± 2	22 ± 1.6	-1.91	3.36	0.12
D631-7	9.9 ± 0.1	1910 ± 39	536 ± 4	391 ± 3	-2.23	4.73	3.72
DDO064	23 ± 1	1.6 ± 0.3	50 ± 3	36 ± 2	-1.30	3.34	0.31
DDO154	18.1 ± 0.07	1.38 ± 0	48.1 ± 0.2	35 ± 0	-1.57	3.42	1.37
DDO161	10.08 ± 0.14	5.35 ± 0.2	75.6 ± 0.8	55 ± 1	-2.21	3.88	0.22
DDO168	17.35 ± 0.34	5.29 ± 1.6	75.3 ± 6.6	55 ± 5	-1.62	3.64	4.54
DDO170	13.96 ± 0.33	2.57 ± 0.1	59.2 ± 0.9	43 ± 1	-1.86	3.63	1.6
ESO079-G014	17.69 ± 0.51	57.91 ± 3.5	167.2 ± 3.4	122 ± 2	-1.59	3.98	1.25
ESO116-G012	24.32 ± 0.51	11 ± 0.6	96.1 ± 1.7	70 ± 1	-1.24	3.60	0.82
ESO444-G084	32.84 ± 1.02	1.74 ± 0.1	52 ± 1.3	38 ± 1	-0.89	3.20	1.33
ESO563-G021	19.9 ± 0.2	266.3 ± 0.9	278 ± 0.3	203 ± 0	-1.46	4.15	13.14
F563-1	24.03 ± 0.99	11.2 ± 1	96.7 ± 2.8	71 ± 2	-1.25	3.60	0.54
F563-V1	10.81 ± 2.68	0.06 ± 0	16.5 ± 2.2	12 ± 2	-2.13	3.18	0.3
F563-V2	33.12 ± 0.97	10.28 ± 1.5	94 ± 4.7	69 ± 3	-0.88	3.45	0.21
F565-V2	16.28 ± 1.15	8.63 ± 2.9	88.6 ± 8.4	65 ± 6	-1.69	3.74	0.06
F567-2	15.88 ± 2.33	1.08 ± 0.3	44.3 ± 4.5	32 ± 3	-1.71	3.45	0.26
F568-1	28.97 ± 2.24	16.34 ± 2.9	109.7 ± 6.5	80 ± 5	-1.04	3.58	0.08
F568-3	16.56 ± 0.39	15.22 ± 2.3	107.1 ± 5.2	78 ± 4	-1.67	3.81	1.03
F568-V1	31.26 ± 1.3	10.37 ± 1.2	94.3 ± 3.5	69 ± 3	-0.95	3.48	0.05
F571-8	23.64 ± 0.61	24.93 ± 2.1	126.3 ± 3.4	92 ± 3	-1.27	3.73	1.64
F571-V1	15.14 ± 1.09	7.31 ± 1.1	83.9 ± 3.8	61 ± 3	-1.77	3.74	0.04
F574-1	25.03 ± 0.47	6.88 ± 0.4	82.2 ± 1.7	60 ± 1	-1.20	3.52	0.05
F574-2	1.1 ± 7.68	14.8 ± 37	106 ± 84	77 ± 62	-4.07	4.98	0.13
F579-V1	44.96 ± 3.06	5.47 ± 0.3	76.2 ± 1.5	56 ± 1	-0.53	3.23	0.36
F583-1	17.56 ± 0.17	6.83 ± 0.2	82 ± 0.9	60 ± 1	-1.60	3.67	0.21
F583-4	20.81 ± 1.98	2.33 ± 1.2	57.3 ± 7	42 ± 5	-1.41	3.44	0.45
IC2574	8.4 ± 0.09	16.81 ± 2	110.7 ± 4.7	81 ± 3	-2.40	4.12	1.76
KK98-251	13.33 ± 0.2	1.26 ± 0.3	46.6 ± 3.5	34 ± 3	-1.91	3.54	0.32
NGC0024	49.19 ± 0.46	5.65 ± 0.1	77 ± 0.6	56 ± 0	-0.43	3.19	0.73
NGC0055	15.05 ± 0.12	6.99 ± 0.3	82.7 ± 1.1	60 ± 1	-1.77	3.74	0.19
NGC0247	22.68 ± 0.31	4.65 ± 0.2	72.1 ± 1	53 ± 1	-1.32	3.50	4.88
NGC1003	12.19 ± 0.17	19.66 ± 0.4	116.6 ± 0.8	85 ± 1	-2.00	3.98	5.12
NGC2403	25.64 ± 0.02	14.01 ± 0	104.2 ± 0.1	76 ± 0	-1.18	3.61	24.35
NGC3109	16.28 ± 0.25	5.94 ± 0.4	78.3 ± 1.8	57 ± 1	-1.69	3.68	0.16
NGC3198	19.05 ± 0.07	30.09 ± 0.2	134.4 ± 0.3	98 ± 0	-1.51	3.85	1.26
NGC3741	18.03 ± 0.28	1.47 ± 0.1	49.2 ± 0.8	36 ± 1	-1.57	3.44	1.05
NGC3769	27.9 ± 0.96	9.44 ± 0.2	91.3 ± 0.8	67 ± 1	-1.08	3.51	1.66
NGC3893	37.24 ± 4.22	17.22 ± 2.1	111.6 ± 4.6	81 ± 3	-0.75	3.48	1.43
NGC3917	17 ± 0.28	29.71 ± 2.4	133.9 ± 3.6	98 ± 3	-1.64	3.90	3.32
NGC3992	21.62 ± 1.01	104.81 ± 5.4	203.8 ± 3.5	149 ± 3	-1.37	3.97	0.64
NGC4010	16.95 ± 0.35	22.43 ± 1.9	121.9 ± 3.7	89 ± 3	-1.64	3.86	1.25
NGC4100	25.04 ± 0.35	31.06 ± 0.7	135.9 ± 1	99 ± 1	-1.20	3.73	2.08
NGC4183	22.79 ± 0.76	8.98 ± 0.3	89.8 ± 1.2	66 ± 1	-1.31	3.60	0.41
NGC4559	14.1 ± 0.48	18.4 ± 1.3	114.1 ± 2.7	83 ± 2	-1.84	3.91	0.26
NGC5585	21.21 ± 0.15	6.13 ± 0.1	79.1 ± 0.4	58 ± 0	-1.39	3.57	20.46
NGC6015	31.03 ± 0.15	18.82 ± 0.1	115 ± 0.2	84 ± 0	-0.96	3.57	12.43
NGC7793	29.95 ± 1.23	4.36 ± 0.3	70.6 ± 1.6	52 ± 1	-1.00	3.37	1.44
UGC00128	14.99 ± 0.13	25.87 ± 0.3	127.8 ± 0.5	93 ± 0	-1.78	3.93	7.83
UGC00191	29.15 ± 0.39	2.98 ± 0.1	62.2 ± 0.4	45 ± 0	-1.03	3.33	4.1
UGC00634	15.56 ± 0.52	15.75 ± 1	108.3 ± 2.3	79 ± 2	-1.74	3.84	0.39
UGC00731	24.76 ± 0.4	2.56 ± 0.1	59.1 ± 0.9	43 ± 1	-1.22	3.38	0.6
UGC00891	13.79 ± 0.37	5.15 ± 0.6	74.6 ± 2.6	54 ± 2	-1.87	3.73	0.17
UGC01230	24.06 ± 1.39	10.46 ± 0.6	94.5 ± 1.7	69 ± 1	-1.25	3.59	0.23
UGC02259	38 ± 0.82	3.14 ± 0.1	63.3 ± 0.4	46 ± 0	-0.73	3.22	2.19
UGC04325	45.64 ± 0.52	3.2 ± 0.1	63.7 ± 0.6	46 ± 0	-0.51	3.14	0.39
UGC04483	31.52 ± 2.09	0.07 ± 0	18.1 ± 0.8	13 ± 1	-0.94	2.76	0.29
UGC04499	20.82 ± 0.99	2.92 ± 0.2	61.8 ± 1.2	45 ± 1	-1.41	3.47	0.15
UGC05005	10.08 ± 0.26	16.36 ± 2.4	109.7 ± 5.4	80 ± 4	-2.21	4.04	0.01
UGC05414	18.28 ± 0.68	2.83 ± 0.8	61.1 ± 5.1	45 ± 4	-1.56	3.52	0.08
UGC05716	19.51 ± 0.18	3.53 ± 0.1	65.8 ± 0.4	48 ± 0	-1.49	3.53	3.75
UGC05721	52.44 ± 1.45	2.1 ± 0.1	55.4 ± 0.8	40 ± 1	-0.35	3.02	0.41

TABLE A3. CONTINUED

Name	c	M_{200} ($10^{10}M_\odot$)	R_{200} (kpc)	V_{200} (km/s)	$\log\rho_0$ $\left(\frac{M_\odot}{pc^3}\right)$	$\log h$ (pc)	χ^2_R
UGC05750	10.22 ± 0.65	8.44 ± 2.7	88 ± 9.2	64 ± 7	-2.19	3.94	0.25
UGC05764	41.17 ± 0.29	0.79 ± 0	40 ± 0.2	29 ± 0	-0.63	2.99	2.44
UGC05829	16.54 ± 1.06	2.55 ± 0.4	59.1 ± 3.4	43 ± 3	-1.67	3.55	0.18
UGC05918	24.38 ± 1.86	0.61 ± 0.1	36.6 ± 1.9	27 ± 1	-1.23	3.18	0.04
UGC05986	28.52 ± 0.17	11.36 ± 0.2	97.2 ± 0.6	71 ± 0	-1.06	3.53	1.71
UGC05999	13.35 ± 0.83	12.69 ± 2	100.8 ± 5.2	74 ± 4	-1.90	3.88	0.76
UGC06399	21.84 ± 1.02	6.13 ± 0.8	79.1 ± 3.3	58 ± 2	-1.36	3.56	0.06
UGC06446	32.33 ± 1.28	3.05 ± 0.2	62.7 ± 1.4	46 ± 1	-0.91	3.29	0.54
UGC06667	24.69 ± 0.48	5.57 ± 0.4	76.6 ± 1.6	56 ± 1	-1.22	3.49	0.09
UGC06917	25.82 ± 0.49	7.54 ± 0.4	84.7 ± 1.5	62 ± 1	-1.17	3.52	0.25
UGC06923	22.64 ± 0.52	4.01 ± 0.4	68.6 ± 2.3	50 ± 2	-1.32	3.48	0.38
UGC06930	25.61 ± 1.24	7.47 ± 0.5	84.5 ± 1.8	62 ± 1	-1.18	3.52	0.18
UGC06983	31.18 ± 1.41	7.33 ± 0.4	83.9 ± 1.6	61 ± 1	-0.95	3.43	0.54
UGC07089	11.66 ± 0.69	10.21 ± 3.6	93.8 ± 10.1	68 ± 7	-2.05	3.91	0.08
UGC07125	13.51 ± 0.57	2.07 ± 0.1	55.1 ± 1	40 ± 1	-1.89	3.61	0.26
UGC07151	29.49 ± 1.27	1.7 ± 0.1	51.6 ± 0.9	38 ± 1	-1.02	3.24	1.3
UGC07261	33.17 ± 2.97	1.98 ± 0.4	54.2 ± 3.2	40 ± 2	-0.88	3.21	0.13
UGC07399	49.68 ± 0.6	3.92 ± 0.1	68.1 ± 0.5	50 ± 0	-0.41	3.14	1.3
UGC07524	19.68 ± 0.21	4.13 ± 0.1	69.3 ± 0.8	51 ± 1	-1.48	3.55	0.43
UGC07559	15.64 ± 1.84	0.54 ± 0.3	35.3 ± 7	26 ± 5	-1.73	3.35	0.17
UGC07603	31.8 ± 0.87	1.73 ± 0.1	51.9 ± 0.7	38 ± 1	-0.93	3.21	0.36
UGC07608	22.39 ± 1.89	3.67 ± 0.9	66.6 ± 5.9	49 ± 4	-1.33	3.47	0.07
UGC07690	52.12 ± 4.92	0.53 ± 0.1	34.9 ± 1.7	25 ± 1	-0.36	2.83	0.05
UGC07866	21.72 ± 3.3	0.23 ± 0.1	26.3 ± 3.7	19 ± 3	-1.36	3.08	0.05
UGC08286	32.49 ± 0.36	3.42 ± 0.1	65.1 ± 0.3	48 ± 0	-0.91	3.30	0.94
UGC08490	39.98 ± 1.06	2.62 ± 0.1	59.6 ± 0.8	44 ± 1	-0.67	3.17	0.56
UGC08550	29.87 ± 0.71	1.15 ± 0.1	45.3 ± 0.7	33 ± 1	-1.00	3.18	0.74
UGC09037	7.46 ± 0.2	124.84 ± 33	216 ± 17.9	158 ± 13	-2.52	4.46	1.03
UGC10310	25.34 ± 2.28	2.32 ± 0.3	57.2 ± 2.6	42 ± 2	-1.19	3.35	0.13
UGC11455	13 ± 0.4	187 ± 14	247 ± 6	180 ± 4	-1.93	4.28	2.55
UGC11557	6.27 ± 1.21	1927 ± 858	537 ± 181	393 ± 132	-2.70	4.93	1
UGC11820	13.3 ± 0.26	6.48 ± 0.3	80.6 ± 1.1	59 ± 1	-1.91	3.78	10.49
UGC12506	32.9 ± 0.7	76.6 ± 1.3	184 ± 1	134 ± 1	-0.89	3.75	0.7
UGC12632	21.31 ± 0.76	2.89 ± 0.1	61.6 ± 0.8	45 ± 1	-1.39	3.46	0.08
UGC12732	19.1 ± 0.5	6.4 ± 0.3	80.2 ± 1.4	59 ± 1	-1.51	3.62	1.29
UGCA281	45.4 ± 2	0.12 ± 0	21.5 ± 1	16 ± 1	-0.52	2.68	0.13
UGCA442	19.2 ± 0.22	2.08 ± 0	55.2 ± 0.3	40 ± 0	-1.50	3.46	0.52
UGCA444	23.41 ± 0.88	0.33 ± 0	30 ± 1.1	22 ± 1	-1.28	3.11	0.23

[d]Best-fit parameter values, assuming a BURK profile. Columns as in Table A1.

REFERENCES

Abdurro'uf, Accetta, K., Aerts, C., et al. 2022, ApJS, 259, 35, https://doi.org/10.3847/1538-4365/ac4414

Aniyan, S., Freeman, K., Arnaboldi, M., et al. 2018, MNARAS, 476, 1909, https://doi.org/10.1093/mnras/sty310

Bell, E. F. & de Jong, R. S. 2001, ApJ, 550, 212, https://doi.org/10.1086/319728

Binney, J. & Tremaine, S. 1987, Galactic Dynamics, (Pincenton, NJ: PUP)

Blais-Ouellette, S., Amram, P., & Carignan, C. 2001, AJ, 121, 1952, https://doi.org/10.1086/319944

Bosma, A. 1978, The distribution and kinematics of neutral hydrogen in spiral galaxies of various morphological types, PhD. Thesis, Groningen Univ.

__________. 1981, AJ, 86, 1825, https://doi.org/10.1086/113063

Bruzual, G. & Charlot, S. 2003, MNRAS, 344, 1000, https://doi.org/10.1046/j.1365-8711.2003.06897.x

Burkert, A. 1995, AJ, 447, 25, https://doi.org/10.1086/309560

Cantó, J., Curiel, S., & Martínez-Gómez, E. 2009, A &A, 501, 1259, https://doi.org/10.1051/0004-6361/200911740

Carignan, C. & Freeman, K. C. 1985, ApJ, 294, 494, https://doi.org/10.1086/163316

Casertano, S. 1983, MNRAS, 203, 735, https://doi.org/10.1093/MNRAS/203.3.735

Cody, W. J. 1993, ACM Transactions on Mathematical Software, 19, 22, https://doi.org/10.1145/151271.151273

Curiel, S., Cantó, J., Georgiev, L., Chávez, C., & Poveda, A. 2011, A&A, 525, 78, https://doi.org/10.1051/0004-6361/201015693

de Blok, W. J. G. 2010, AdAsT, 2010, https://doi.org/10.1155/2010/789293

Freeman, K. C. 1970, ApJ, 160, 811, https://doi.org/10.1086/150474

Holland, J. H. et al. 1992, Adaptation in Natural and Artificial Systems. An Introductory Analysis with Applications to Biology, Control, and Artificial Intelligence, (Cambridge, MA: MIT Press)

Huchtmeier, W. & Richter, O.-G. 1989, A&A, 210, 1

Katz, H., Lelli, F., McGaugh, S. S.,et al. 2017, MNRAS, 466, 1648, https://doi.org/10.1093/mnras/stw3101

Kennicutt, R. C. Jr., Armus, L., Bendo, G., et al. 2003, PASP, 115, 928, https://doi.org/10.1086/376941

Kent, S. M. 1986, AJ, 91, 1301, https://doi.org/10.1086/114106

Korsaga, M., Epinat, B., Amram, P., et al. 2019, MNRAS, 490, 2977, https://doi.org/10.1093/mnras/stz2678

Kroupa, P. & Jerabkova, T. 2021, arXiv:2112.10788, https://doi.org/10.48550/arXiv.2112.10788

Kuzio de Naray, R., McGaugh, S. S., & de Blok, W. J. G. 2008, ApJ, 676, 920, https://doi.org/10.1086/527543

Lelli, F., McGaugh, S. S., & Schombert, J. M. 2016a, ApJ, 816, 14, https://doi.org/10.3847/2041-8205/816/1/L14

__________. 2016b, AJ, 152, 157, https://doi.org/10.3847/0004-6256/152/6/157

Leroy, A. K., Walter, F., Brinks, E., et al. 2008, AJ, 136, 2782, https://doi.org/10.1088/0004-6256/136/6/2782

Li, P., Lelli, F., McGaugh, S., & Schombert, J. 2020, ApJs, 247, 31, https://doi.org/10.3847/1538-4365/ab700e

Marchesini, D., D'Onghia, E., Chincarini, G., et al. 2002, ApJ. 575, 801, https://doi.org/10.1086/341475

McGaugh, S. S., Rubin, V. C., & De Blok, W.J.G. 2001, AJ, 122, 2381, https://doi.org/10.1086/323448

McGaugh, S. S. & Schombert, J. M. 2014, AJ, 148, 77, https://doi.org/10.1088/0004-6256/148/5/77

Meidt, S. E., Schinnerer, E., Van de Ven, G., et al. 2014, AJ, 788, 144, https://doi.org/10.1088/0004-637X/788/2/144

Meurer, A., Smith, C. P., Paprocki, M., et al. 2017, Peer J. Computer Science, 3, 103, https://doi.org/10.7717/peerj-cs.103

Milgrom, M. 1983, ApJ, 270, 365, https://doi.org/10.1086/161130

Navarro, J. F., Frenk, C. S., & White, S. D. M. 1997, ApJ, 490, 493, https://doi.org/10.1086/304888

Peebles, P. J. E. 2020, Cosmology's Century: An Inside History of our Modern Understanding of the Universe (Princeton, NJ: PUP)

Riess, A. G., Yuan, W., Macri, L. M., et al. 2022, ApJL, 934, 7, https://doi.org/10.3847/2041-8213/ac5c5b

Roberts, M. S. 1962, AJ, 67, 437, https://doi.org/10.1086/108752

Rodríguez-González, A., Esquivel, A., Raga, A., et al. 2012, AJ, 143, 60, https://doi.org/10.1088/0004-6256/143/3/60

Rubin, V. C., Ford, W. K. Jr., Strom, K. M., Strom, S. E., & Romanishin, W. 1978, ApJ, 224, 782, https://doi.org/10.1086/156426

Sackett, P. D. 1997, ApJ, 483, 103, https://doi.org/10.1086/304223

Schombert, J. & McGaugh, S. 2014, PASA, 31, 36, https://doi.org/10.1017/pasa.2014.32

Simon, J. D., Bolatto, A. D., Leroy, A., Blitz, L., & Gates, E. L. 2005, ApJ, 621, 757, https://doi.org/10.1086/427684

Sofue, Y. 2012, PASJ, 64, 75, https://doi.org/10.1093/pasj/64.4.75

__________. 2013, Planets, Stars and Stellar Systems Vol. 5, 985, https://doi.org/10.1007/978-94-007-5612-0_19

van Albada, T. & Sancisi, R. 1986, RSPTA, 320, 447, https://doi.org/10.1098/rsta.1986.0128

van Albada, T. S., Bahcall, J. N., Begeman, K., & Sancisi, R. 1985, ApJ, 295, 305, https://doi.org/10.1086/163375

Walker, M. G. & Penarrubia, J. 2011, ApJ, 742, 20, https://doi.org/10.1088/0004-637X/742/1/20

Ana M. Hidalgo-Gámez and Rodolfo de J. Zermeño: Escuela Superior de Física y Matemáticas, Instituto Politécnico Nacional, Unidad Profesional Adolfo López Mateos, Gustavo A. Madero, 07738, México, (amhidalgog@ipn.mx, rzermenop1800@alumno.ipn.mx).

Revista Mexicana de Astronomía y Astrofísica, **59**, 279–298 (2023)

https://doi.org/10.22201/ia.01851101p.2023.59.02.08

SEARCH AND STUDY OF ULTRACOMPACT H II REGIONS

D. Quiroga-González[1,2], M. A. Trinidad[1,3], E. de la Fuente[4], J. M. Masqué[1], and T. Rodríguez–Esnard[5]

Received March 1 2023; accepted June 12 2023

ABSTRACT

We present results from a sample of 106 high-luminosity IRAS sources observed with the Very Large Array in the B and C configurations. 96 sources were observed in the X-band and 52 in the K-band, with 42 of them observed at both wavelengths. We also used previously published observations in the C-band for 14 of them. The detection rate of sources with 3.6 cm continuum emission was ≈ 25%, while only 10% have emission at 1.3 cm. In order to investigate the nature of these sources, their physical parameters were calculated mainly using the 3.6 cm continuum emission, and for sources detected at two wavelengths, we used the best fit of three H II region models with different geometries. As a final result, we present a catalog of the detected sources, which includes their basic physical parameters for further analysis. The catalog contains 17 ultracompact H II regions and 3 compact H II regions.

RESUMEN

Presentamos resultados de una muestra de 106 fuentes IRAS de alta luminosidad observadas con el interferómetro Very Large Array en las configuraciones B y C. 96 fuentes se observaron en la banda X y 52 en la banda K, con 42 de ellas observadas en ambas longitudes de onda. También usamos observaciones previamente publicadas en la banda C para 14 de ellas. La tasa de detección de fuentes con emisión de continuo a 3.6 cm fue del ≈ 25%, mientras que sólo un 10% tienen emisión a 1.3 cm. Para investigar la naturaleza de estas fuentes se calcularon sus parámetros físicos usando principalmente la emisión de continuo a 3.6 cm y para fuentes detectadas en dos longitudes de onda usamos el mejor ajuste de tres modelos de regiones H II con diferentes geometrías. Como resultado final, presentamos un catálogo de las fuentes detectadas y proporcionamos sus parámetros físicos básicos para su posterior análisis. El catálogo contiene 17 regiones H II ultracompactas y 3 regiones H II compactas.

Key Words: HII regions — ISM: general — radio continuum: ISM — stars: early type — stars: formation

1. INTRODUCTION

The study of high-mass star formation is crucial for understanding the physical and chemical evolution of galaxies. Because forming massive stars takes ≈ 10^6 yr, the process of high mass star formation is less understood than the formation of low-mass stars (time-scales of ≈ 10^9 yr). Currently, it is not completely clear how massive stars form, being monolithic collapse, protostar collision and/or coalescence, and competitive accretion the most widely accepted models (see Motte, Bontemps & Louvet 2018, and references therein). Studying the evolution of the earliest phases of high-mass star formation is key to understanding how this process occurs. In this sense, two of the earliest phases of massive star formation are the young stellar object and the H II region(e.g Garay & Lizano 1999). While both stages have been extensively studied, new questions continue to arise about their formation and evolution process. Further study of these evolutionary phases will undoubtedly contribute to a better understand-

[1]Departamento de Astronomía, Universidad de Guanajuato, Guanajuato, México.
[2]Universidad Autónoma Metropolitana, México.
[3]Corresponding author.
[4]Departamento de Física, CUCEI, Universidad de Guadalajara, Jalisco, México.
[5]Instituto de Geofísica y Astronomía de la República de Cuba.

TABLE 1

PHYSICAL PARAMETERS OF H II REGIONS[a]

Type of H II region	Size (pc)	EM (cm^{-6} pc)	n_e (cm^{-3})	$M_{H\ II}$ ($M_\odot$)	Reference[b]
Hypercompact	≈ 0.003	$\gtrsim 10^{10}$	$\gtrsim 10^6$	$\approx 10^{-3}$	1
Ultracompact	$\lesssim 0.1$	$\gtrsim 10^7$	$\gtrsim 10^4$	$\approx 10^{-3}$	2,3
Compact	$\lesssim 0.5$	$\gtrsim 10^7$	$\gtrsim 5\times10^3$	≈ 1	4
Ultracompact with Extended Emission	1–20	10^4–10^5	$\gtrsim 10^2$-10^3	5–10^3	5

[a]Adapted from Kurtz & Franco (2002); de la Fuente et al. (2020b).

[b]1.- Sewiło et al. (2008, 2004), 2.- Wood & Churchwell (1989), 3.- Kurtz et al. (1994), 4.- Lumsden et al. (2013), 5.- (de la Fuente et al. 2020a,b, and references therein).

ing of massive star formation and provide evidence for or against the proposed models.

One way to contribute to solving the puzzle of high-mass star formation is to study the H II regions related to this process: the hypercompact (HC), ultra-compact (UC), and compact H II regions. These objects are thought to be related to the evolutionary sequence as the massive star approaches the zero-age main sequence or ZAMS (e.g Beuther et al. 2007, and references therein). The physical parameters that define HC H II , UC H II , and compact HII regions following this evolutionary sequence are shown in Table 1.

On the other hand, density gradients are highly noticeable in H II regions (e.g. de Pree, Rodriguez, & Goss 1995; Jaffe & Martin-Pintado 1999; Franco et al. 2000a,b, 2001; Phillips 2007, 2008). These gradients are important and useful to describe the dynamics of an H II region. For example, density gradients with a power law of $n_e \propto r^\beta$, where r is the distance from the ionization front, accurately describe expanding H II regions when $\beta \gtrsim 1.5$ (e.g Franco, Tenorio-Tagle, and Bodenheimer 1990; Franco et al. 2000a,b, 2001, and references therein). Thus, the presence of these gradients should be taken into consideration in models and studies of HC H II , UC H II , and compact H II regions.

In order to advance in the understanding of the earliest stages of the high-mass star formation process and to find evidence in favor of one of the models mentioned above, we perform a physical characterization of the ionized gas in a sample of 106 IRAS sources to identify H II regions in their different evolutionary stages. We calculate physical parameters at 3.6 cm in the standard way, and we apply density gradient models for sources with multiple wavelength observations. We aim to confirm if they are H II regions and, if applicable, to determine their nature and classify them as HC H II , UC H II , or compact H II region, taking into consideration the presence of protostellar thermal jets.

The sample, radio continuum observations, and data reduction are described in § 2. Results and discussion are presented in § 3 and § 4, respectively. Finally, we give the conclusions in § 5 and individual sources comments are provided in Appendix A.

2. OBSERVATIONS

We retrieve 3.6 and 1.3 cm data for a sample of 104 IRAS sources from the Very Large Array (VLA[6]) archive using the B and C configurations, respectively (unpublished data from the AC295 project; P.I. Ed Churchwell). Out of the 104 sources, 94 were observed in the X band and 52 in the K band, with 42 observed at both wavelengths. We also included two sources (IRAS 18094-1823 and G45.47+0.05) observed in the X band with the VLA D configuration (AK559 project; P.I. Stan Kurtz; see de la Fuente et al. 2018, 2020a), bringing the final sample to 106 sources. The observations of the AC295 project, at both wavelengths, were carried out in snapshot mode using a bandwidth of 50 MHz, with an integration time of 5 and 10 minutes for 3.6 and 1.3 cm, respectively, over a time span of about 4.5 months (1992 January and May) for both bands. Table 2 lists the 106 sources in the sample observed at 3.6 and 1.3 cm. Additionally, we also used 6 cm data, observed with the VLA-B and reported by Urquhart et al. (2009), for some sources detected at 3.6 and/or 1.3 cm. All sources in the sample are located in star-forming regions associated with high luminosity IRAS sources ($L_{FIR} \gtrsim 500\ L_\odot$), and are situated more than 1 kpc away. They cover a range from $\approx 21^h$ to 08.5^h in right ascension (J2000), and from $\approx -41°$ to $66°$ in

[6]The National Radio Astronomy Observatory is a facility of the National Science Foundation operated under cooperative agreement by Associated Universities, Inc.

TABLE 2

THE SAMPLE OF 106 IRAS SOURCES: 96 OBSERVED AT 3.6 CM, 10 AT 1.3 CM, AND 42 OBSERVED AT BOTH WAVELENGTHS

IRAS Source	RA (J2000) (h:m:s)	DEC (J2000) (°: ′: ″)	IRAS Source	RA (J2000) (h:m:s)	DEC (J2000) (°: ′: ″)	IRAS Source	RA (J2000) (h:m:s)	DEC (J2000) (°: ′: ″)
00117+6412*	00:14:27.72	64:28:46.3	05554+2013	05:58:24.56	20:13:57.5	07528-3441	07:54:49.97	-34:49:45.9
00338+6312**	00:36:47.51	63:29:02.1	06055+2039*	06:08:32.82	20:39:16.2	07530-3436**	07:54:56.18	-34:49:38.3
00412+6638*	00:44:15.23	66:54:40.6	06073+1249*	06:10:12.43	12:48:45.5	08007-2829	08:02:46.36	-28:25:47.4
00468+6508	00:49:55.82	65:43:38.7	06084+1727	06:11:24.52	17:26:26.5	08008-3423	08:02:42.30	-34:31:46.8
00468+6527**	00:49:55.82	65:43:38.7	06089+1727**	06:11:44.41	17:26:05.1	08088-3554*	08:10:43.49	-36:03:29.8
00556+6048	00:58:40.13	61:04:44.0	06103+1523	06:13:18.21	15:23:16.1	08140-3556	08:15:58.98	-36:08:20.0
00578+6233	01:00:55.81	62:49:28.5	06104+1524A**	06:13:21.32	15:23:56.9	08159-3543	08:17:52.89	-35:52:49.9
01045+6505*	01:07:50.70	65:21:21.4	06105+1756*	06:13:28.33	17:55:29.5	08189-3602*	08:20:47.86	-36:12:34.4
01133+6434*	01:16:37.39	64:50:38.8	06114+1745*	06:14:23.69	17:44:36.5	08212-4146	08:23:02.96	-41:55:48.5
02044+6031*	02:08:05.05	60:45:56.7	06155+2319A	06:18:35.15	23:18:11.4	08245-4038*	08:26:17.70	-40:48:35.1
02395+6244	02:43:28.72	62:57:05.3	06208+0957*	06:23:34.41	09:56:22.1	08274-4111	08:29:13.94	-41:10:44.4
02437+6145*	02:47:40.43	61:58:26.3	06306+0437*	06:33:16.36	04:34:56.8	18094–1823[a]	18:12:23.63	-18:22:53.7
02455+6034	02:49:23.23	60:47:01.2	06331+1102	06:35:56.01	11:00:17.5	19120+1103[b]	19:14:25.67	11:09:26.0
02461+6147	02:50:08.11	61:59:47.1	06337+1051	06:36:29.48	10:49:05.1	21074+4949	21:09:08.09	50:01:59.8
03233+5809**	03:27:22.33	58:19:45.8	06381+1039	06:40:58.00	10:36:48.8	21080+4950	21:09:42.83	50:08:29.5
03235+5808*	03:27:31.15	58:19:21.3	06412-0105*	06:43:44.97	-01:08:06.7	21202+5157*	21:21:53.18	52:10:43.6
04034+5107	04:07:11.93	51:24:44.7	06426+0025	06:45:15.50	00:22:25.9	21290+5535	21:30:38.70	55:48:59.6
04324+5102	04:36:16.08	51:08:12.8	06446+0029	06:47:12.87	00:26:06.5	21306+4927**	21:05:15.62	49:40:01.2
04324+5106*	04:36:19.70	51:12:44.6	06501+0143	06:52:45.57	01:40:14.9	21306+5540*	21:32:11.56	55:53:23.7
04366+5022*	04:40:26.12	50:28:24.7	06547-0109A	06:57:16.69	-01:13:39.5	21334+5039*	21:35:09.18	50:53:09.2
04547+4753*	04:58:29.66	47:58:27.6	06567-0355*	06:59:15.76	-03:59:39.0	21334+5329	21:35:05.86	53:43:01.2
04579+4703	05:01:39.74	47:07:23.1	06570-0401	06:59:30.95	-04:05:35.1	21407+5441*	21:42:23.68	54:55:06.7
05100+3723	05:13:25.43	37:27:04.5	07024-1102	07:04:45.65	-11:07:14.5	21413+5442*	21:43:01.36	54:56:16.3
05271+3059	05:30:21.22	31:01:27.2	07069-1045	07:04:45.65	-11:07:14.5	22134+5834*	22:15:09.08	58:49:09.3
05274+3345*	05:30:45.62	33:47:51.6	07061-0414*	07:08:38.75	-04:19:07.5	22308+5812*	22 32 46.01	58 28 21.8
05281+3412	05:31:26.60	34:14:57.7	07207-1435	07:23:01.28	-14:41:32.5	22475+5939*	22:49:29.47	59:54:56.6
05305+3029*	05:33:44.81	30:31:04.5	07295-1915**	07:33:10.45	-19:28:42.9	22502+5944**	22:51:59.86	59:59:16.9
05334+3149	05:36:41.08	31:51:13.8	07298-1919	07:32:02.46	-19:26:02.3	22506+5944*	22:52:38.63	60:00:55.8
05358+3543*	05:39:10.39	35:45:19.2	07299-1651*	07:32:10.00	-16:58:14.7	22539+5758	22:56:00.01	58:14:45.9
05361+3539	05:39:27.66	35:40:43.0	07333-1838	07:35:34.31	-18:45:32.5	22551+6139	22:57:11.23	61:56:03.4
05375+3536	05:40:52.52	35:38:23.8	07334-1842	07:35:40.95	-18:48:59.0	22570+5912*	22:59:06.50	59:28:27.7
05375+3540*	05:40:53.64	35:42:15.7	07422-2001	07:44:27.85	-20:08:31.9	23030+5958*	23:05:10.62	60:14:40.4
05490+2658	05:52:12.93	26:59:32.9	07427-2400*	07:44:51.90	-24:07:40.6	23033+5951	23:05:25.16	60:08:11.6
05480+2545*	05:51:10.75	25:46:14.3	07311-2204*	07:33:20.24	-22:10:57.7	23139+5939	23:16:09.32	59:55:22.8
05553+1631*	05:58:13.87	16:32:00.1	07434-2044	07:45:35.47	-20:51:38.6	23151+5912	23:17:21.09	59:28:48.8
						23545+6508**	23:57:05.23	65:25:10.8

*Sources observed at 3.6 and 1.3 cm at high resolution.

**Sources observed at 1.3 cm at high resolution.

[a]Source refereed as 18094–G12.20. Low resolution at 3.6 cm observation only. See text for details.

[b]Source refereed as 19120–G45.47. Arguable designation: the IRAS source is more related with G45.45+0.06. Low resolution at 3.6 cm only. See text for details.

declination (J2000). These characteristics make the sources in the sample excellent candidates for identifying and studying HII regions, as well as for expanding the dataset of these objects to better understand their properties. Additional information about each source can be found in Appendix A.

We performed the data editing, calibration, and further mapping of all sample sources at 3.6 and 1.3 cm wavelengths following the standard techniques using the Common Astronomy Software Applications (CASA) of the NRAO version 5.3.0-143 (McMullin et al. 2007). The flux calibrator for observations at 3.6 and 1.3 cm was 3C48, and several phase calibrators were used (see Table 3). 6 cm data were calibrated using the same procedure as was used for the 3.6 and 1.3 cm data. In order to obtain a similar angular resolution for continuum sources detected at two and three wavelengths, we convolved the data with the same beam. All observational parameters of the detected sources (position, flux density, and deconvolved angular size) were obtained with the task IMFIT of CASA.

From the subsample of 96 IRAS sources observed at 3.6 cm, we detect only 25 of them, while from the subsample of 52 sources observed at 1.3 cm, we detect only five. These five sources were also detected

TABLE 3

PHASE CALIBRATOR'S OBSERVATIONAL PARAMETERS

Calibrator	RA (J2000) (h:m:s)	DEC (J2000) (∘: ′: ″)	3.6 Bootstrapped Flux Density (Jy)
2023+544	20h 23m 55.844s	54°27′35.83″	1.12±0.01
2230+697	22h 30m 36.470s	69°46′28.08″	0.44±0.01
0228+673	02h 28m 50.051s	67°21′03.03″	0.78±0.02
0359+509	03h 59m 29.747s	50°57′50.16″	1.47±0.03
0555+398	05h 55m 30.806s	39°48′49.17″	4.86±0.08
0530+135	05h 30m 56.417s	13°31′55.15″	1.40±0.02
0700+171	07h 00m 01.525s	17°09′21.70″	1.11±0.01
0725–009	07h 25m 50.640s	00°54′56.54″	0.95±0.01
0730–116	07h 30m 19.112s	–11°41′12.60″	4.63±0.05
0828–375	08h 28m 04.780s	–37°31′06.28″	1.07±0.01

TABLE 4

SOURCES DETECTED AT 3.6 CM

IRAS[a] Source	VLA 3.6 cm Source	RA (J2000) (h:m:s)	Dec (J2000) (∘: ′: ″)	Distance[b] (kpc)	$L_{\rm FIR}$[b] ($10^4 L_\odot$)
01045+6505	01045–VLA	01:07:51.34	65:21:22.4	10.7[1]	8.00[17]
01133+6434	01133–VLA	01:16:36.67	64:50:42.4	4.1[2]	0.84[2]
03235+5808	03235–VLA	03:27:31.34	58:19:21.7	4.2[2]	1.30[2]
04324+5106	04324–VLA	04:36:21.03	51:12:54.7	5.8[3]	6.00[3]
04366+5022	04366–VLA	04:40:27.20	50:28:29.2	5.9[3]	3.00[3]
05305+3029	05305–VLA	05:33:45.83	30:31:18.0	10.4[4]	0.60[4]
05358+3543	05358–VLA1	05:39:15.62	35:46:42.1	1.8[5]	0.66[5]
————	05358–VLA2	05:39:15.13	35:46:41.6	1.8[5]	0.66[5]
05553+1631	05553–VLA	05:58:13.53	16:31:58.4	1.2[3]	0.20[3]
06055+2039	06055–VLA	06:08:35.44	20:39:03.5	2.9[3]	3.00[3]
06412–0105	06412–VLA	06:43:48.42	-01:08:20.5	7.1[3]	9.00[3]
06567–0355	06567–VLA	06:59:15.74	-03:59:36.8	2.3[6]	1.80[18]
07299–1651	07299–VLA	07:32:09.79	-16:58:12.2	1.4[3]	0.70[3]
07311–2204	07311–VLA	07:33:19.92	-22:10:57.5	8.0[7]	20.00[7]
07427–2400	07427–VLA	07:44:52.03	-24:07:42.1	6.9[3]	50.10[19]
07528–3441	07528–VLA	07:54:56.12	-34:49:37.8	1.2[8]	20.00[8]
08189–3602	08189–VLA	08:20:54.92	-36:13:02.5	7.6[3]	30.00[20]
18094–1823[c]	18094–G12.20	18:12:23.63	-18:22:53.7	14.0[13]	86.80[14]
19120+1103[d]	19120–G45.47	19:14:25.67	11:09:26.0	8.4[15]	49.2[16]
21306+5540	21306–VLA	21:32:11.76	55:53:40.9	3.7[9]	1.10[3]
21334+5039	21334–VLA	21:35:11.13	50:52:13.1	5.0[10]	2.10[10]
21413+5442	21413–VLA	21:43:01.47	54:56:18.0	7.9[11]	1.45[11]
22134+5834	22134–VLA	22:15:09.25	58:49:08.9	2.3[3]	1.34[3]
22308+5812	22308–VLA	22:32:45.62	58:28:18.2	5.7[3]	9.00[3]
23030+5958	23030–VLA	23:05:10.20	60:14:47.2	4.4[12]	10.00[3]

[a]The observed source does not necessary coincide with the IRAS source.

[b]The distance and the FIR luminosity are from the IRAS region, and do not necessary correspond to the observed sources at 3.6 cm. Values taken from: 1.- Rudolph De Geus & Wouterloot (1996), 2.- Maud et al. (2015), 3.- Wouterloot & Brand (1989), 4.- Lumsden et al. (2013), 5.- Lu et al. (2014), 6.- Tapia et al. (1997), 7.- May, Alvarez, & Bronfman (1997), 8.- Preite–Martínez (1988), 9.- Kim, Kim, & Kim (2015), 10.- McCutcheon et al. (1991), 11.- Navarrete et al. (2015), 12.- Lee, Murray, & Rahman (2012), 13.- Hill et al. (2005), 14.- We assume the IRAS FIR luminosity of G12.21–0.10 (de la Fuente et al. 2018, 2020a), 15.- Wu et al. (2019), 16.- We assume the IRAS FIR luminosity of G45.45+0.06 (de la Fuente et al. 2020a), 17.- Snell, Carpenter & Heyer (2002), 18.- Klein et al. (2005), 19.- MacLeod et al. (1998), 20.- Planck Collaboration et al. (2015).

[c]This source was not included in the original sample of 94 sources (see Table 3).

[d]This source was not included in the original sample of 94 sources (see Table 3). The nearest IRAS source is 19120+1103, but this coincides in position with the UC H II region with extended emission G45.455+0.058 or G45.45+0.06 (de la Fuente et al. 2020a). See text for discussion. The distance is adopted from Wu et al. (2019).

TABLE 5

OBSERVATIONAL PARAMETERS OF THE SOURCES DETECTED AT 1.3, 3.6, AND 6.0 CM

VLA 3.6 cm Source	λ (cm)	S_ν (mJy)	Beam Size (″×″)	PA (deg)	RMS Noise (mJy beam^{-1})	Size (″×″)
01045–VLA	6.0	140.4±4.2	1.57×1.05	134	0.25	3.13×2.91
———	3.6	289.8±6.7	1.57×1.05	120	0.41	3.10×2.92
———	1.3	100.5±5.4	1.57×1.05	27	0.67	3.12×3.00
01133–VLA	6.0	1.5±0.3	1.61×1.07	168	0.06	3.11×1.73
———	3.6	2.1±0.1	1.61×1.07	129	0.06	1.75×1.15
03235–VLA	6.0	1.7±0.1	1.41×1.10	146	0.03	1.50×1.13
———	3.6	6.6±0.2	1.41×1.10	144	0.07	1.48×1.16
04324–VLA	6.0	50.0±2.1	1.34×1.08	47	0.06	8.82×7.27
———	3.6	97.7±3.3	1.34×1.08	46	0.12	8.85×8.31
04366–VLA	6.0	1.8±0.1	1.30×1.08	141	0.03	2.41×1.73
———	3.6	5.0±0.4	1.30×1.08	158	0.03	2.72×2.27
05305–VLA	6.0	0.4±0.1	1.26×1.15	146	0.02	1.32×1.15
———	3.6	0.21±0.01	1.26×1.15	120	0.02	1.30×1.21
05358–VLA1	3.6	1.8±0.2	0.88×0.74	139	0.02	3.04×1.05
05358–VLA2	3.6	0.8±0.1	0.88×0.74	30	0.02	2.35×1.49
05553–VLA	3.6	0.8±0.1	1.00×0.62	135	0.03	1.11×0.82
06055–VLA	3.6	0.8±0.1	1.11×0.74	124	0.09	1.30×0.82
06412–VLA	6.0	850.0±47.0	1.51×1.25	57	0.67	13.85×12.17
———	3.6	685.0±48.0	1.51×1.25	62	0.90	12.97×10.74
———	1.3	660.0±44.0	1.51×1.25	146	1.90	12.59×12.36
06567–VLA	6.0	49.3±3.2	1.69×1.24	161	0.21	4.58×3.65
———	3.6	37.0±1.1	1.69×1.24	166	0.07	3.68×3.53
07299–VLA	3.6	0.26±0.01	1.40×0.76	148	0.01	1.44×0.86
07311–VLA	3.6	4.0±0.3	1.50×0.76	165	0.01	6.26×5.28
07427–VLA	3.6	2.3±0.2	1.65×0.77	160	0.02	1.81×0.95
07528–VLA	6.0	16.0±1.1	4.52×1.14	153	0.08	5.57×3.30
———	3.6	17.4±1.3	4.52×1.14	163	0.12	6.08×2.85
08189–VLA	3.6	16.5±1.6	4.24×1.17	176	2.72	26.66×16.20
———	1.3	18.2±1.8	4.24×1.17	179	2.45	19.43×10.77
18094–G12.20	3.6	7.2±0.1	12.54×7.26	167	0.15	12.84×7.31
19120–G45.47	3.6	112.4±1.7	8.23×7.64	159	1.34	8.34×7.63
21306–VLA	6.0	74.0±3.3	1.81×1.14	116	0.46	3.87×3.37
———	3.6	39.9±2.6	1.81×1.14	128	0.40	3.35×2.76
21334–VLA	6.0	7.7±0.1	1.80×1.15	93	0.12	1.82×1.21
———	3.6	5.7±0.1	1.80×1.15	93	0.06	1.84×1.17
21413–VLA	6.0	115.7±3.7	1.87×1.13	93	0.29	2.18×1.40
———	3.6	177.1±4.4	1.87×1.13	91	0.73	2.13×1.32
———	1.3	441.8±9.8	1.87×1.13	90	1.89	2.04×1.24
22134–VLA	3.6	4.7±0.3	0.82×0.72	116	0.20	0.98×0.84
22308–VLA	6.0	203.0±13.0	1.90×1.07	86	0.47	7.66×5.02
———	3.6	433.0±25.0	1.90×1.07	79	1.14	7.67×5.07
23030–VLA	6.0	945.0±44.0	1.62×1.19	95	1.40	14.79×7.50
———	3.6	1226.0±72.0	1.62×1.19	90	2.52	12.79×5.52
———	1.3	1670.0±110.0	1.62×1.19	96	5.86	12.19×5.65

at 3.6 cm (see Table 4). The low detection rate may be due to the low sensitivity of the observations carried out in snapshot mode, but other reasons cannot be ruled out (see § 4.1).

Observational parameters of all detected IRAS sources at 1.3, 3.6, and 6 cm are listed in Table 5, and their respective radio contour maps are shown in Figures 1, 2, 3, and 4. Detailed results for each of the sources are provided in Appendix A.

3. RESULTS

3.1. *3.6 cm Continuum Emission: Physical Parameters*

In order to investigate the nature of the radio continuum sources detected toward the IRAS regions, we used the 3.6 cm flux density to determine their physical parameters as if they were optically thin H II regions at this wavelength. We also assumed an homogeneous and isothermal gas, with a spherically symmetric distribution, composed of

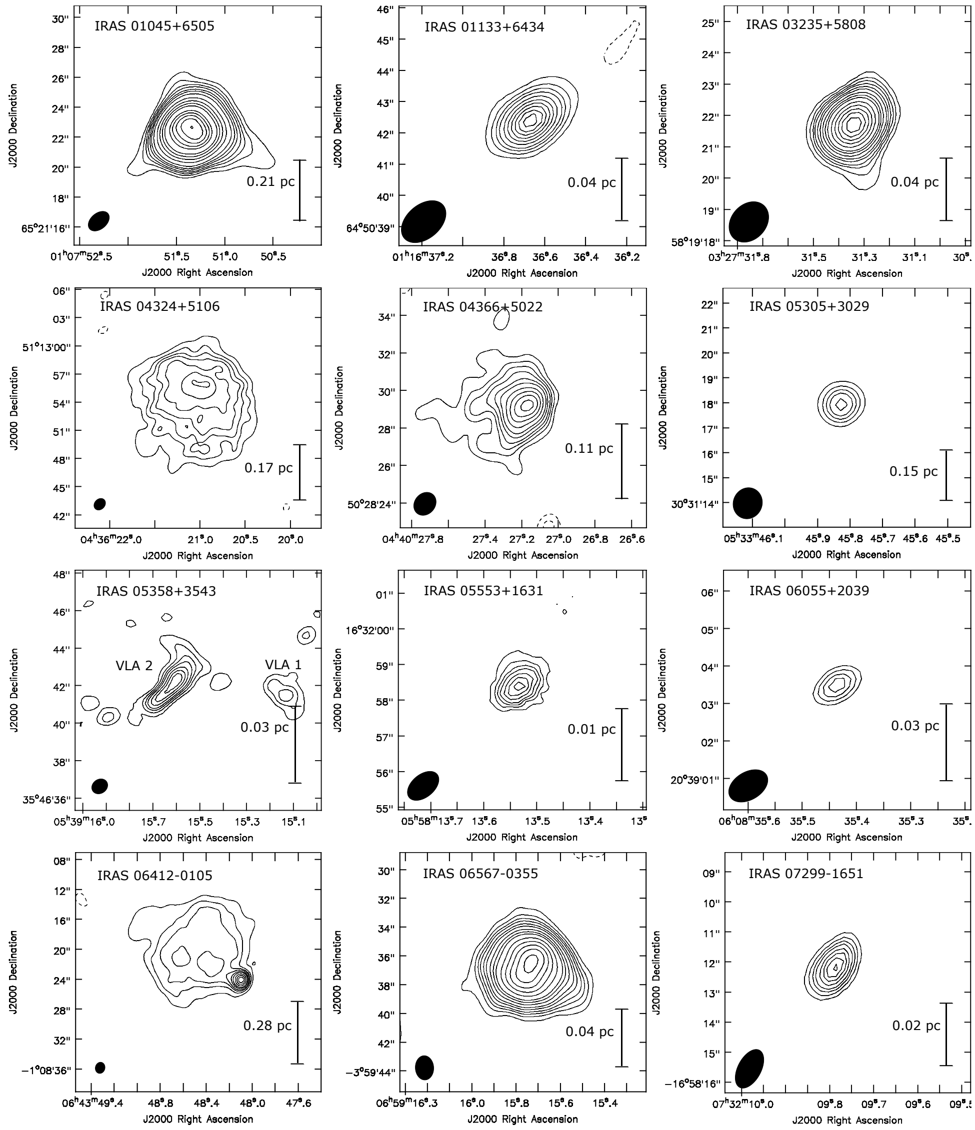

Fig. 1. Continuum contour maps of the sources detected at 3.6 cm. The contours for each source are: IRAS 01045+6505: -5, 5, 10, 15, 30, 60, 90, 120, 150, 180; IRAS 01133+6434: -5, -3, 3, 5, 7, 9, 12, 15, 18, 21, 24, 27; IRAS 03235+5808: -5, -3, 3, 5, 7, 9, 12, 15, 20, 25, 30, 40, 50, 60, 70, 80; IRAS 04324+5106: -5, -3, 3, 5, 7, 9, 12, 15, 18; IRAS 04366+5022: -5, -3, 3, 5, 7, 9, 12, 15, 20, 25, 30, 35; IRAS 05305+3029: -5, -3, 3, 5, 7, 9, 12, 15, 18; IRAS 05358+3543: -5, -3, 3, 5, 7, 9, 12, 15, 18; IRAS 05553+1631: -5, -3, 3, 5, 7, 9, 12, 15, 18; IRAS 06055+2039: -5, -3, 3, 4, 5, 6, 7; IRAS 06412-0105: -5, -3, 3, 5, 7, 9, 12, 15, 20, 25, 30; IRAS 06567-0355: -5, -3, 3, 5, 7, 9, 12, 15, 20, 25, 30, 40, 50, 60, 70, 80, and IRAS 07299-1651: -5, -3, 9, 12, 15, 18, 21 times the respective rms listed in Table 5. The beam size is shown at bottom left and given in Table 5.

pure hydrogen and a canonical value for the electronic temperature of 10^4 K. The electronic density ($n_{\rm e}$), emission measure (EM), the mass of the ionized gas ($M_{\rm HII}$), and the total rate of Lyman continuum photons of the ionizing star ($N'_{\rm c}$) were calculated in the standard way using equations 1 to 4 (Schraml & Mezger 1969; Kurtz et al. 1994):

$$\left(\frac{n_{\rm e}}{\rm cm^{-3}}\right) = 7.8\times10^{3}\left(\frac{\nu}{4.9\,{\rm GHz}}\right)^{0.05}\left(\frac{S_\nu}{\rm mJy}\right)^{0.5}\left(\frac{T_{\rm e}}{10^4\,{\rm K}}\right)^{0.175} \times\left(\frac{\Theta_{\rm s}}{\rm arcsec}\right)^{-1.5}\left(\frac{D}{\rm kpc}\right)^{-0.5}, \tag{1}$$

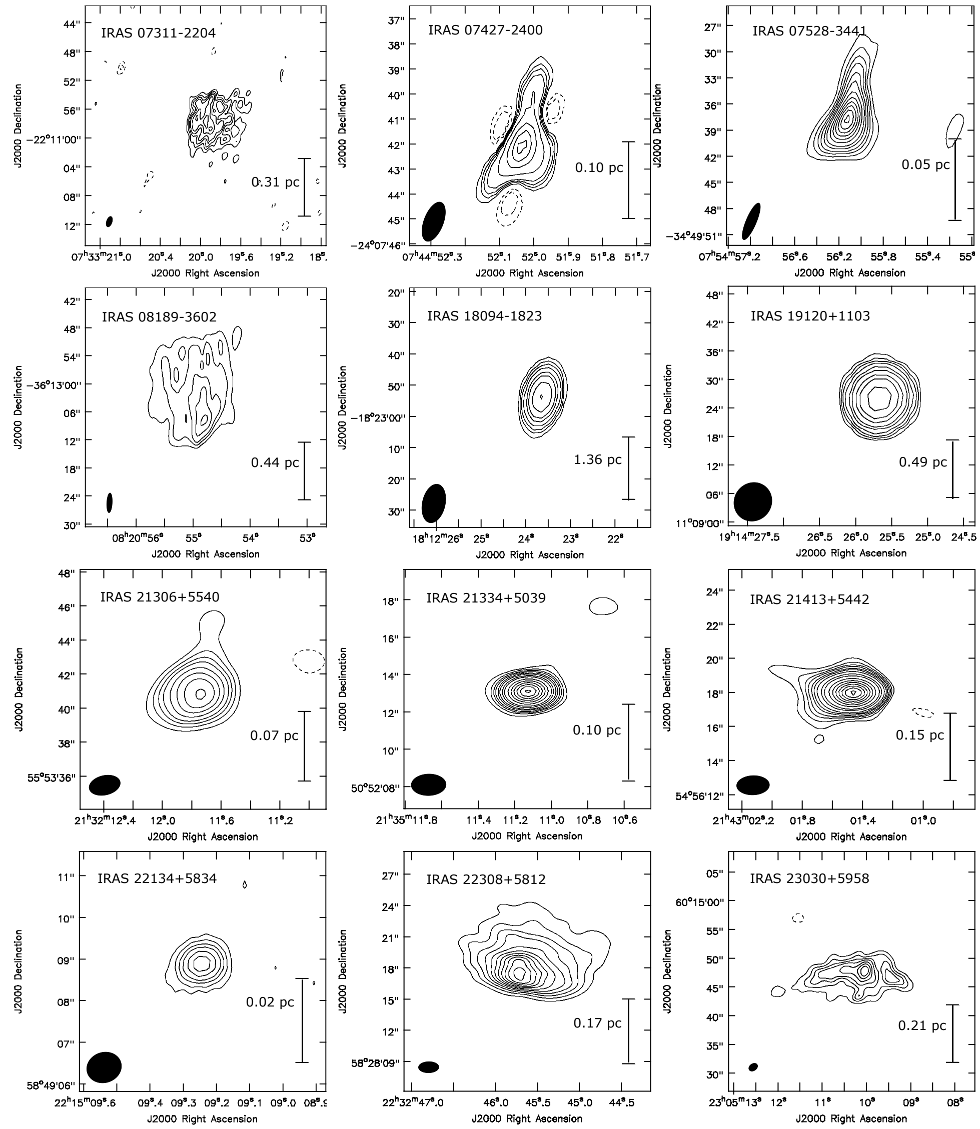

Fig. 2. Continuum contour maps of the sources detected at 3.6 cm. The contours for each source are: IRAS 07311-2204: -5, -3, 3, 5, 7, 9, 12, 15, 18; IRAS 07427-2400: -5, 5, 10, 20, 40, 60, 80; IRAS 07528-3441: -5, -3, 3, 5, 7, 9, 12, 15, 20, 25, 30, 35, 40, 45; IRAS 08189-3602: -4, -3, 3, 4, 5, 7, 9, 11, 13; IRAS 18094-1823: -5, -3, 3, 5, 7, 10, 15, 20, 30, 45; IRAS 19120+1103: -5, -3, 3, 5, 7, 10, 15, 20, 30, 40, 60, 80, 100, 150, 200, 250; IRAS 21306+5540: -5, -3, 3, 5, 7, 9, 12, 15, 18, 21; IRAS 21334+5039: -5, -3, 3, 5, 7, 9, 12, 15, 20, 25, 35, 45, 55, 65, 75, 85; IRAS 21413+5442: -5, -3, 3, 5, 7, 9, 12, 15, 20, 30, 40, 60, 80, 100, 120, 140, 160, 180; IRAS 22134+5834: -5, -3, 3, 5, 7, 9, 12, 15, 18; IRAS 22308+5812: -5, -3, 3, 5, 7, 9, 11, 13, 15, 17, 19, 21, 23, and IRAS 23030+5958: -5, -3, 3, 5, 7, 9, 12, 15, 18 times the respective rms listed in Table 5. The beam size is shown at bottom left and given in Table 5.

$$\left(\frac{EM}{\text{pc cm}^{-6}}\right) = 4.4\times 10^{5}\left(\frac{\nu}{4.9\,\text{GHz}}\right)^{0.1}\left(\frac{S_\nu}{\text{mJy}}\right)\left(\frac{T_\text{e}}{10^4\,\text{K}}\right)^{0.35} \times\left(\frac{\Theta_\text{s}}{\text{arcsec}}\right)^{-2}, \quad (2)$$

$$\left(\frac{M_\text{HII}}{M_\odot}\right) = 3.7\times 10^{-5}\left(\frac{\nu}{4.9\,\text{GHz}}\right)^{0.05}\left(\frac{S_\nu}{\text{mJy}}\right)^{0.5}\left(\frac{T_\text{e}}{10^4\,\text{K}}\right)^{0.175} \times\left(\frac{\Theta_\text{s}}{\text{arcsec}}\right)^{1.5}\left(\frac{D}{\text{kpc}}\right)^{2.5}, \quad (3)$$

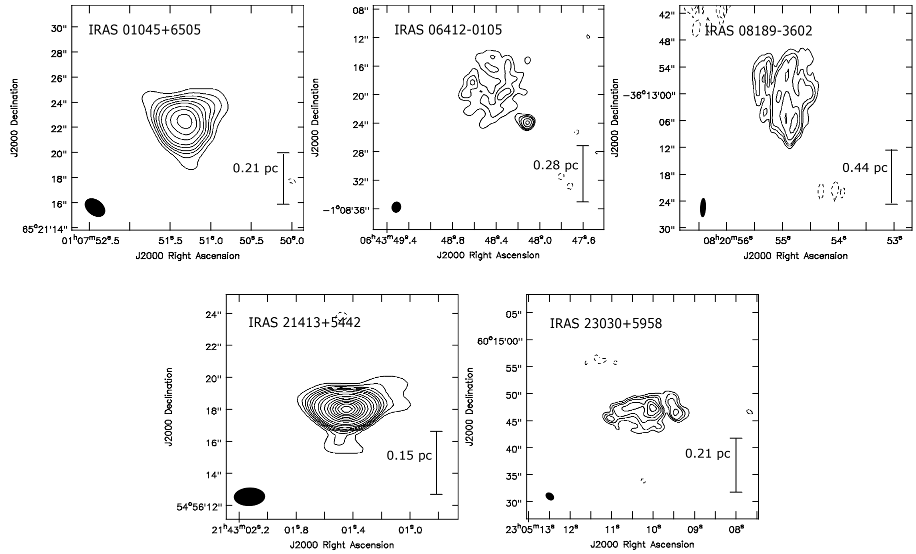

Fig. 3. Contour maps of the continuum emission from sources detected at 1.3 cm The respective contour levels for each source are: IRAS 01045+6505: -5, -3, 3, 5, 10, 15, 20, 25, 30; IRAS 06412-0105: -4, -3, 3, 4, 5, 7, 9; IRAS 08189-3602: -4, -3, 3, 4, 5, 7, 9, 11; IRAS 21413+5442: -5, -3, 3, 5, 7, 9, 12, 15, 20, 30, 40, 60, 80, 100, 120, 140, 160, 180, and IRAS 23030+5958: -4, -3, 3, 4, 5, 7, 9, 11 times the respective rms reported in Table 5. The beam size is shown at bottom left and given in Table 5.

TABLE 6

PHYSICAL PARAMETERS OF THE SOURCES USING THEIR 3.6 CM CONTINUUM EMISSION

VLA 3.6 cm Source	Size (pc)	EM (10^6cm^{-6} pc)	n_e (10^3cm^{-3})	$M_{\rm H\ II}$ (M$_\odot$)	N_i (s^{-1})	Spectral Type	H II region[a] Type
01045–VLA	0.16	21.30	11.68	0.5792	48.39	O8	C
01133–VLA	0.03	0.67	4.80	0.0015	45.41	B1	UC
03235–VLA	0.03	2.54	9.72	0.0025	45.93	B0.5	UC
04324–VLA	0.24	0.88	1.91	0.3501	47.38	B0	C
04366–VLA	0.07	0.53	2.71	0.0129	46.10	B0.5	UC
05305–VLA	0.06	0.09	1.18	0.0039	45.22	B1	UC
05358–VLA1[b]	0.02	0.29	4.03	0.0003	44.64	B2	UC
05358–VLA2	0.02	0.14	2.92	0.0002	44.27	B2	UC
05553–VLA	0.01	0.57	10.08	0.00002	43.93	B3	UC
06055–VLA	0.01	0.47	5.61	0.0002	44.69	B2	UC
06412–VLA	0.41	3.24	2.82	2.4979	48.40	O8	C
06567–VLA	0.04	1.89	6.85	0.0058	46.16	B0.5	UC
07299–VLA	0.01	0.13	4.10	0.00003	43.57	B3	UC
07311–VLA	0.22	0.08	0.60	0.0873	46.27	B0.5	C
07427–VLA	0.05	0.82	4.21	0.0054	45.91	B0.5	UC
07528–VLA	0.03	0.58	4.72	0.0011	45.26	B1	UC
08189–VLA	0.79	0.02	0.17	1.1159	46.84	B0	UC
18094–G12.20	0.68	0.05	0.26	1.0963	47.02	B0	UC
19120–G45.47	0.33	1.17	1.90	0.8519	47.76	O9.5	C
21306–VLA	0.05	2.84	7.19	0.0155	46.60	B0.5	UC
21334–VLA	0.04	1.66	6.74	0.0043	46.02	B0.5	UC
21413–VLA	0.07	39.41	24.39	0.0924	47.91	O9.5	UC
22134–VLA	0.01	3.78	19.30	0.0003	45.26	B1	UC
22308–VLA	0.18	7.10	6.35	0.4514	48.01	O9	C
23030–VLA	0.20	9.73	7.06	0.6858	48.24	O8.5	C

[a]UC = UC H II region and C = Compact H II region.
[b]This source has an elongated, jet-like morphology. See Appendix A.

$$\left(\frac{N'_c}{\rm s^{-1}}\right) \geq 8.04\times10^{46}\left(\frac{T_e}{\rm K}\right)^{-0.85}\left(\frac{r}{\rm pc}\right)^{3}\left(\frac{n_e}{\rm cm^{-3}}\right)^{2}. \quad (4)$$

where ν is the frequency, S_ν the flux density, T_e the electronic temperature, D the distance, r is the radius of the sphere, and Θ_s is its size. The distance

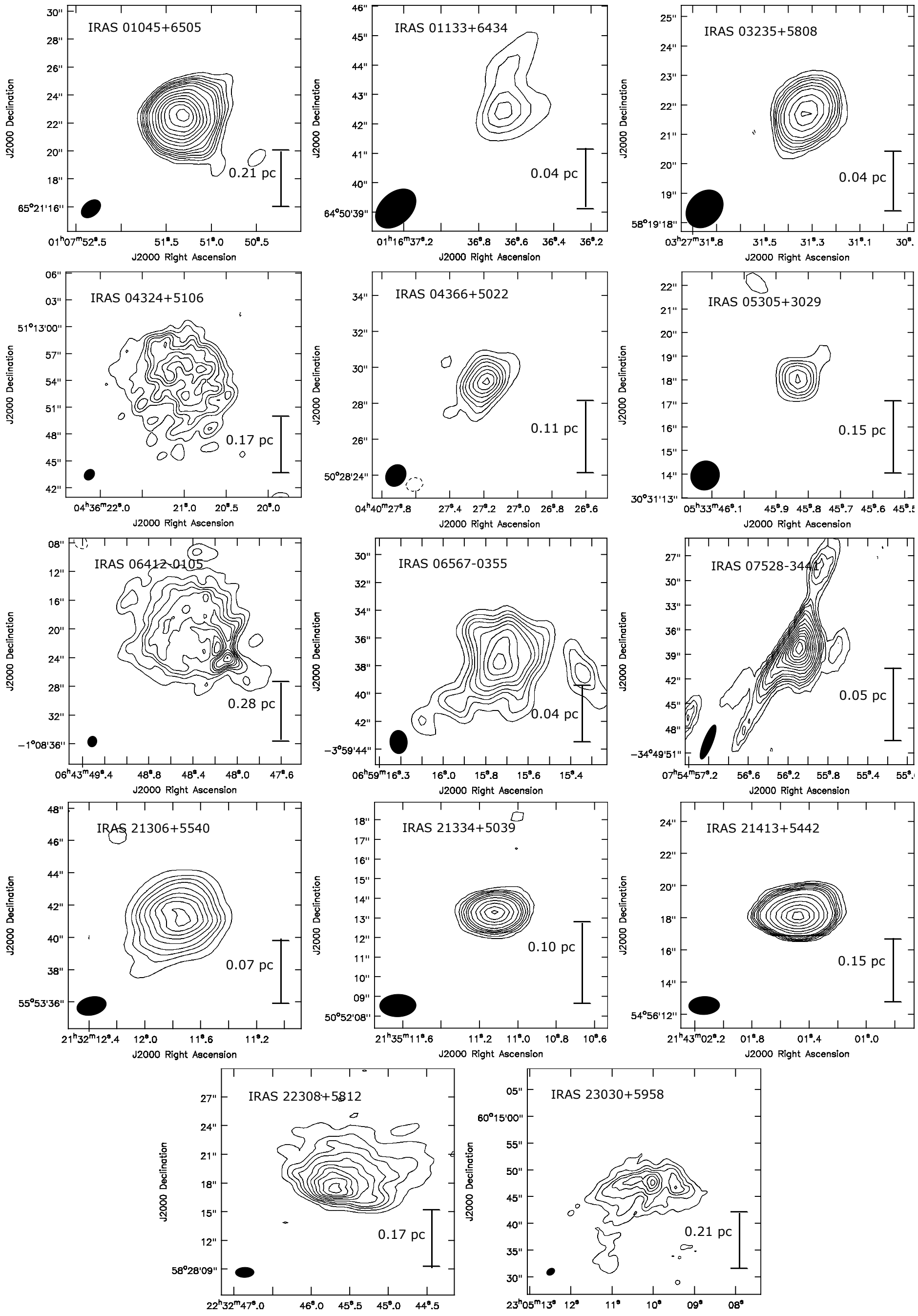

Fig. 4. Continuum contour maps of the sources with 6 cm emission (these observations have been reported previously by Urquhart et al. (2009); see § 2). The contours for each source are: Continuum contour maps of the sources detected at 6.0 cm. The contours for each source are: IRAS 01045+6505: 5, 10, 15, 20, 40, 60, 100, 140, 200; IRAS 01133+6434: -5, -3, 3, 5, 7, 9, 12, 15, 18; IRAS 03235+5808: -5, -3, 3, 5, 7, 9, 12, 15, 20, 30, 40, 50; IRAS 04324+5106: -5, -3, 3, 5, 7, 9, 12, 15, 18; IRAS 04366+5022: -5, -3, 3, 5, 7, 9, 12, 15, 18, 21; IRAS 05305+3029: -3, 3, 5, 7, 9, 12, 15, 18; IRAS 06412-0105: -5, -3, 3, 5, 7, 9, 12, 15, 20, 25, 30; IRAS 06567-0355: -5, -3, 3, 5, 7, 9, 12, 15, 20, 25, 30; IRAS 07528-3441: -5, -3, 3, 5, 7, 9, 12, 15, 20, 25, 30, 35, 40, 45, 50, 55; IRAS 21306+5540: -5, -3, 3, 5, 7, 9, 12, 15, 18, 21, 24; IRAS 21334+5039: -5, -3, 3, 5, 7, 9, 12, 15, 20, 30, 40, 50, 60; IRAS 21413+5442: -5, -3, 3, 5, 7, 9, 12, 15, 20, 40, 60, 100, 150, 200, 250; IRAS 22308+5812: -5, -3, 3, 5, 7, 9, 12, 15, 18, 21, 24, 27, and IRAS 23030+5958: -5, -3, 3, 5, 7, 9, 12, 15, 18 times the respective rms listed in Table 5. The beam size is shown at bottom left and given in Table 5.

and flux density values at 3.6 cm for all continuum sources were taken from Tables 4 and 5, respectively, and the size of the sources was calculated using the mean of their two axes. In addition, the ionizing spectral type was determined following Panagia (1973), considering zero-age main-sequence (ZAMS) objects.

The physical parameters calculated from the 3.6 cm flux density are listed in Table 6. Most of the calculated parameters for the continuum sources meet the definition of the UC H II region according to Wood & Churchwell (1989); Kurtz et al. (1994). Although the determination of the physical parameters using the flux density at 3.6 cm is an acceptable approximation, a better characterization requires observations in at least two wavelengths to estimate their spectral index. For this reason, caution must be taken when interpreting these results.

3.2. *Spectral Indices*

The spectral index provides more reliable information about the nature of the sources. However, to calculate it requires that the sources are detected in at least two wavelengths. The spectral index, α is calculated using a power-law function $S_\nu \propto \nu^\alpha$ (being S the flux density at the frequency ν), and its value indicates whether the continuum emission is thermal or non-thermal in nature. For example, at centimeter wavelengths, optically thin H II regions are associated with a spectral index around -0.1, while optically thick H II regions have an index ≈ 2 (e.g Trinidad et al. 2003). Thermal jets, on the other hand, have a spectral index of approximately 0.6 (e.g Anglada, Rodríguez, & Carrasco-González 2018, and references therein). In contrast, the active magnetosphere of some young low-mass stars has a spectral index ranging from -2 to 2 (e.g Rodríguez et al. 2012), while starburst galaxies have a spectral index ranging from -1.2 to -0.4 (e.g Deeg et al. 1993). Furthermore, the spectral index allows to infer the degree of optical depth of the emission. In the case of thermal emission, its value, together with the morphology, could indicate whether the source is consistent with an H II region or a thermal jet.

As mentioned, only five sources in the sample were detected at both 3.6 and 1.3 cm. To increase the number of characterized sources, we also used observations at 6 cm from 14 sources reported by Urquhart et al. (2009). Out of the 25 sources listed in Table 5, 14 were found to have emission at 3.6 and 6 cm, while only one source showed emission at both 1.3 and 3.6 cm and four sources were detected at 1.3, 3.6, and 6 cm.

TABLE 7

SPECTRAL INDEX OF THE SOURCES DETECTED*

VLA 3.6 cm Source	Wavelength (cm)	Spectral Index
01045–VLA	3.6 & 6	1.3±0.2
01133–VLA	3.6 & 6	0.6±0.8
03235–VLA	3.6 & 6	2.4±0.2
04324–VLA	3.6 & 6	1.2±0.2
04366–VLA	3.6 & 6	1.9±0.5
05305–VLA	3.6 & 6	–1.2±0.5
06412–VLA	1.3, 3.6 & 6	–0.2±0.4
06567–VLA	3.6 & 6	–0.5±0.3
07528–VLA	3.6 & 6	0.2±0.4
08189–VLA	1.3 & 3.6	0.1±0.3
21306–VLA	3.6 & 6	–1.1±0.3
21334–VLA	3.6 & 6	–0.6±0.1
21413–VLA	1.3, 3.6 & 6	0.9±0.2
22308–VLA	3.6 & 6	1.4±0.4
23030–VLA	1.3, 3.6 & 6	0.4±0.3

*At two and/or three wavelengths.

Because of the 1.3 and 3.6 cm observations have a similar (u,v) coverage and were carried out using the same calibrators with a time difference of about 4.5 months, assuming that their flux density had no significant variations over time, we can estimate a reliable spectral index for the continuum sources detected at these two wavelengths. Although 6 cm observations were carried out over a decade later and with slightly lower angular resolution than those at 1.3 and 3.6 cm, they can still be used to estimate a rough spectral index. As mentioned in § 2, all data were convolved to have a similar angular resolution (see Table 5). The calculated spectral indices are reported in Table 7.

Based on spectral indices and morphology (size, shape, and internal structure, mainly at 3.6 cm), we confirm that the majority of continuum sources could be consistent with H II regions, five of them associated with optically thick emission, three with optically thin emission, and three with partially optically thin emission. Additionally, we identified four continuum sources with a negative spectral index, which indicates non-thermal emission.

3.3. *H II Region Models*

In general, the physical parameters of H II regions are calculated assuming a homogeneous electron density. However, models that account for specific density distributions, such as the outwardly decreasing density model, are expected to provide a more reliable understanding of the ionized gas physics than the ideal Stromgren sphere model, which does not consider these gradients. One of such model was developed by Olnon (1975).

Olson's models assume ionized hydrogen gas, circular symmetry for the radius perpendicular along the line of sight, and uniform electron temperature (T_e). In the Rayleigh-Jeans regime, the total flux density is given by

$$S_\nu = \frac{4\,\pi k\,T_e\,\nu^2}{c^2\,D^2}\int_0^\infty \rho\left[1-e^{-\tau_\nu(\rho)}\right]d\rho,$$

where ρ is the radius perpendicular to the line of sight and D is the distance to the object.

The optical depth is defined as:

$$\tau_\nu(\rho) = f(\nu, T_e)E(\rho) = 8.235\times10^{-2}\,T_e^{-1.35}\,\nu^{-2.1}E(\rho).$$

The emission measure can be expressed as

$$E(\rho) = 2\int_0^\infty n_e^2(r)dz,$$

where $r^2 = \rho^2 + z^2$ and the distance along the line of sight is z. With this background and following Olnon (1975), we explored models with cylindrical, spherical, and Gaussian distributions.

For the *cylindrical distribution*, we considered a cylinder with radius=R and length=$2R$, where the electron density n_e is constant inside, and zero outside. Therefore:

$$S_\nu = \frac{2\,\pi k\,T_e R^2\,\nu^2}{c^2\,D^2}\left(1-e^{-\tau'}\right). \quad (5)$$

In a similar way, the *spherical distribution* is given by

$$S_\nu = \frac{2\,\pi k\,T_e R^2\,\nu^2}{c^2\,D^2}\left[1-\frac{2}{\tau'^2}[1-(\tau'-1)e^{-\tau'}]\right], \quad (6)$$

while the *Gaussian distribution* is defined by

$$S_\nu = \frac{2\,\pi k\,T_e R^2\,\nu^2}{c^2\,D^2}\left[\gamma + ln\,\tau'' + E_1(\tau'')\right], \quad (7)$$

where the H II region has spherical symmetry, but the electron density distribution is not constant; there is a density gradient with a Gaussian distribution.

In these equations, R is the source radius, D is the distance, $\tau' = 2n_0^2Rf$, $\tau'' = n_0^2Rf\sqrt{\pi}$, γ is Euler's constant, and $E_1(\tau)$ is the exponential integral, defined as $E_1(x) \equiv \int_x^\infty (\exp^{-t}/t)dt$. We used the least-squares fit method in all these models to find the best values for the radius and density using the minimizing function in Python software. We have

$$\chi^2 = \sum_i^N \frac{\left[S_{\nu i}^{obs} - S_{\nu i}^{mod}(a)\right]^2}{\epsilon_i^2}, \quad (8)$$

where $S_{\nu i}^{obs}$ is the set of observed data, $S_{\nu i}^{mod}$ is the model, a is the set of parameters in the model to be optimized in the fit, ϵ_i is the estimated uncertainty in the flux density equal to $(SN/2)(0.15S_{\nu i}^{obs})$, where SN is the signal to noise ratio.

4. DISCUSSION

We employed the Olson models with cylindrical, spherical, and Gaussian distribution to confirm the nature of the H II regions suggested by the morphology (see Figures 1 and 2), 3.6 cm continuum emission (Table 5), and spectral indices (Table 7) for sources detected at two and three wavelengths. The first two models assume a homogeneous electron density, while the third model uses a density gradient with a Gaussian distribution. For sources detected at two or three bands, we obtained physical parameters using H II region models with cylindrical (equation 5), spherical (equation 6), and Gaussian (equation 7) geometries.

Assuming an isothermal ionized gas with a temperature of 10^4 K, we minimized equation 8 to obtain the best spectral fit for each source. H II region models were applied to 11 sources from Table 7 with a spectral index greater than ≈ -0.1. Of these, eight were detected at two wavelengths, and three were detected at three wavelengths. The resulting best fits for each source are shown in Figure 5, and their respective physical parameters, as determined by the best fit, are listed in Table 8. However, from our two or three wavelength dataset, we were unable to accurately discriminate between specific models for the symmetry and structure of H II regions, highlighting the need for additional multi-band observations. In this way, elements such as morphology and inferred substructure from observations can help us to characterize H II regions more accurately. For more details on each source, please refer to Appendix A.

We present the results in the form of a final catalog, (see Table 9), that summarizes the calculated physical parameters for 20 sources. These were calculated from 3.6 cm emission for sources detected at a single wavelength and from H II models for sources with two or three observations. Of these sources, 17 show physical parameters consistent with those typical of ultracompact H II regions (one with cometary morphology) and 3 are compatible with being compact H II regions. Of the remaining five sources listed

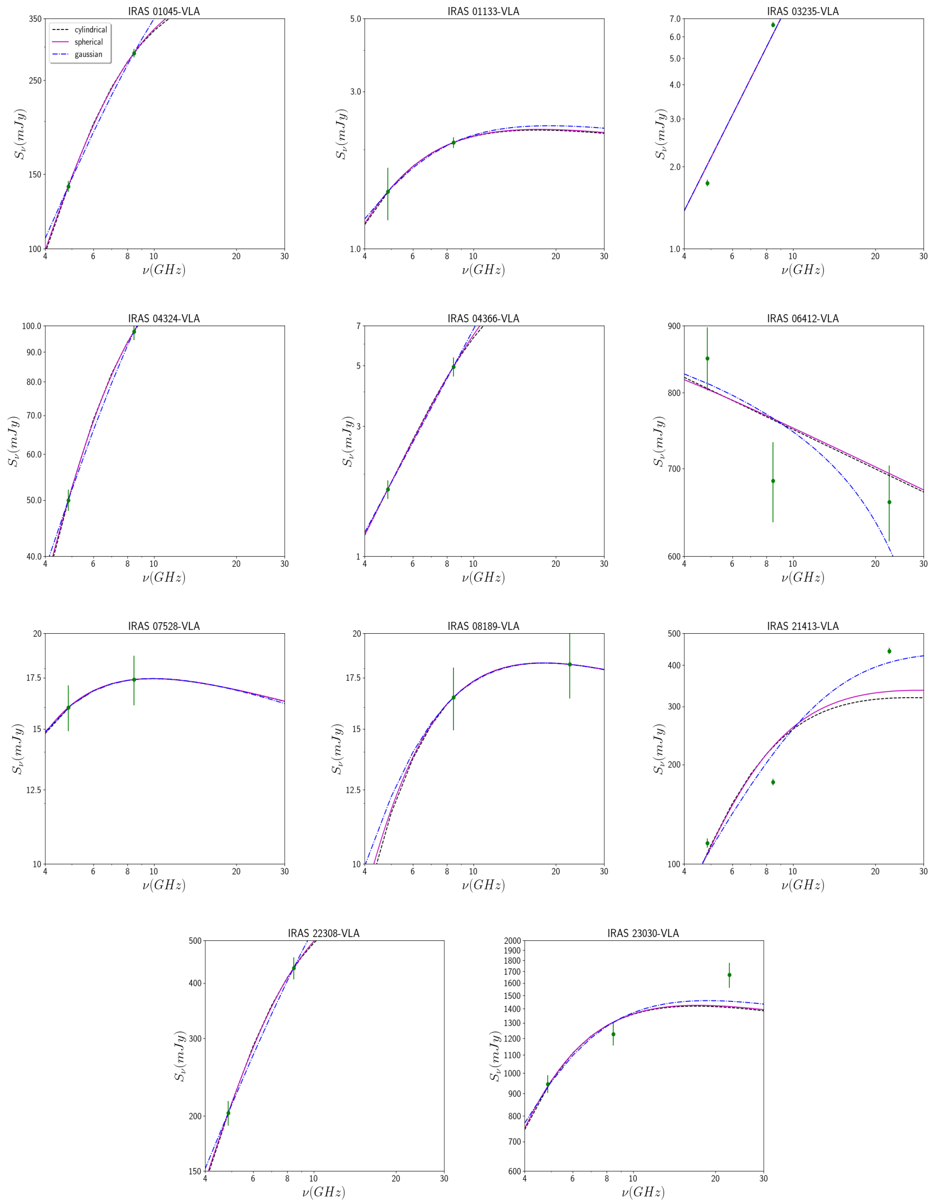

Fig. 5. Fits of the three models of the IRAS sources detected at two or three wavelengths. Dots are the observational data. Dash, continuous, and dash-dot lines are for cylindrical, spherical and Gaussian models, respectively. See the text for details.

in Table 6, 05358-VLA1 has an elongated jet-like morphology, while 05305-VLA, 06567-VLA, 21306-VLA, and 21334-VLA have a negative spectral index (< -0.5).

4.1. *Detection Rate of H II Regions in the Sample*

As mentioned, the sample consists of 106 IRAS sources, 96 of which were observed at 3.6 cm and 52 at 1.3 cm, with 42 of them observed at both wavelengths. The detection rate at 3.6 cm was $\approx$ 25% (25 sources), while at 1.3 cm it was only around 10% (five sources). There are several reasons that could account for this low detection rate, which will be explored below.

One possible reason for the low detection rate could be the poor sensitivity of the observations, which were made in snapshot mode, with integration times of 5 and 10 minutes at 3.6 and 1.3 cm, respectively. However, even with these integration

TABLE 8

PHYSICAL PARAMETERS: H II REGION MODELS

VLA 3.6 cm Source	Size[a] (pc)	EM cm^{-6} pc	n_e cm^{-3}	N_i (s^{-1})	Spectral Type	Morphology	H II [b] Type
01045-VLA	0.16	4.39×10^8	8.92×10^4	6.25×10^{48}	O6.5	Spherical	UC
01133-VLA	0.03	1.60×10^8	2.51×10^5	4.80×10^{45}	B1	Spherical	UC
03235-VLA	0.03	6.68×10^9	1.63×10^6	1.97×10^{47}	B0	Spherical	UC
04324-VLA	0.24	4.67×10^8	3.87×10^5	6.11×10^{47}	O9.5	Gaussian	C
04366-VLA	0.07	1.37×10^9	6.41×10^5	7.06×10^{46}	B0	Spherical	UC
06412-VLA	0.41	1.19×10^6	2.88×10^3	3.26×10^{48}	O7.5	Gaussian	UC[c]
07528-VLA	0.03	3.59×10^7	1.02×10^5	1.96×10^{45}	B1	Cylindrical	UC
08189-VLA	0.79	1.71×10^8	1.16×10^5	1.30×10^{47}	B0	Spherical	UC
21413-VLA	0.07	5.75×10^8	3.10×10^5	2.76×10^{48}	O8	Gaussian	UC
22308-VLA	0.18	9.14×10^8	4.04×10^5	3.85×10^{48}	O7.5	Gaussian	UC
23030-VLA	0.20	1.07×10^8	8.85×10^4	2.67×10^{48}	O8	Gaussian	UC

[a]Taken from the 3.6 cm RC emission.
[b] UC = UC H II region and C = Compact H II region.
[c] UC with cometary morphology.

TABLE 9

FINAL CATALOG OF H II REGIONS[a]

IRAS Source	VLA 3.6 cm Source	Size (arcsec)	Size (pc)	EM ($10^6 cm^{-6}$ pc)	n_e ($10^3 cm^{-3}$)	$M_{H\ II}$ ($M_\odot$)	H II [a] Type
01045+6505	01045–VLA	3.02	0.16	21.30	11.68	0.5792	UC
01133+6434	01133–VLA	0.83	0.03	0.67	4.80	0.0015	UC
03235+5808	03235–VLA	0.87	0.03	2.54	9.72	0.0025	UC
04324+5106	04324–VLA	8.56	0.24	0.88	1.91	0.3501	C
04366+5022	04366–VLA	2.30	0.07	0.53	2.71	0.0129	UC
05358+3543	05358–VLA2	1.84	0.02	0.14	2.92	0.0003	UC
05553+1631	05553–VLA	0.95	0.01	0.57	10.08	0.00002	UC
06055+2039	06055–VLA	0.95	0.01	0.47	5.61	0.0002	UC
06412–0105	06412–VLA	0.41	3.24	1.19	2.82	2.4979	UC[b]
07299–1651	07299–VLA	1.11	0.01	0.13	4.10	0.00003	UC
07311–2204	07311–VLA	5.75	0.22	0.08	0.60	0.0873	C
07427–2400	07427–VLA	1.31	0.05	0.82	4.21	0.0054	UC
07528–3441	07528–VLA	3.78	0.03	0.58	4.72	0.0011	UC
08189–3602	08189–VLA	3.48	0.79	0.02	0.17	1.1159	UC
18094–1823	18094–G12.20	2.10	0.68	0.05	0.26	1.0963	UC
19120–1103	19120–G45.47	2.20	0.33	1.17	1.90	0.8519	C
21413+5442	21413–VLA	1.70	0.07	39.41	24.39	0.0924	UC
22134+5834	22134–VLA	0.91	0.01	3.78	19.30	0.0003	UC
22308+5812	22308–VLA	6.24	0.18	7.10	6.35	0.4514	UC
23030+5958	23030–VLA	4.30	0.20	9.73	7.06	0.6858	UC

[a] UC = UC H II region and C = Compact H II region.
[b] UC with cometary morphology.

times, sources with a flux density of $\approx$ 2 mJy at 3.6 cm and $\approx$ 4 mJy at 1.3 cm could still be detected at 3σ. Thus, this factor can only account for a few cases of non-detection. On the other hand, it is also known that the lifetime of the H II regions is relatively short, which could also contribute to the low detection rate.

We cannot rule out the possibility that the emission measure of potential H II regions is very large ($> 10^9$ pc cm^{-6}), making it optically thick at centimeter/millimeter wavelengths and resulting in a turnover frequency for optically thin emission of around 30 GHz or higher (Kurtz et al. 1994). This would mean that they cannot be detected at 3.6 cm or even at 1.3 cm. On the other hand, Sewiło et al. (2011) observed a small sample of UC and HC H II region candidates at several bands and achieved a successful detection rate with flux density ranging from 60 to 350 mJy at 1.3 and 3.6 cm, respectively. Their sources span a range of distances up to 14.0 kpc, which is close to the upper end of the range of distances in our sample. However, the large sample of sources we have explored may include some objects, especially the most compact ones, that could be affected by opacity and become undetectable, particularly in the 6 cm band. Nonetheless, as shown by Sewiło et al. (2011), this effect is not dominant, at least for the majority of H II regions observed at wavelengths above a few cm.

4.2. *Non-thermal Emission*

In general, the nature of emission from astronomical sources can be classified as thermal (e.g Olnon 1975; Reynolds 1986) and non-thermal (e.g Deeg et al. 1993), if the spectral indices are larger than -0.1 or less than -0.5, respectively. We explore some scenarios that could explain the nature of the continuum sources with a negative spectral index.

Negative spectral indices were found in four continuum sources (05305-VLA, 06567-VLA, 21306-VLA, and 21334-VLA), with values ranging from -1.3 to -0.5, which indicate non-thermal emission. Young sources with spectral indices between -0.5 and -0.1 have been associated to gyro-synchrotron radiation, produced in strong collisions in radio jets (e.g Trinidad, Rodríguez, & Rodríguez 2009) or in the corona of young low-mass stars (e.g Launhardt et al. 2022). Since the sample sources are related to massive star formation regions, the first scenario could be the most likely; however, strong collisions are not expected in H II regions. Spectral indices as low as $-1.2 < \alpha < -0.4$ are typically only found in starburst galaxies (e.g Deeg et al. 1993).

The variability of continuum sources could also explain these negative values of the spectral index, since the observations at 3.6 and 6 cm were carried out about a decade apart. Another possibility is that the spectral index of these sources could be a result of the emission produced by two or more continuous sources. For example, for the sources IRAS 06567-VLA and IRAS 21306-VLA, there is marginal evidence that the continuous emission is not associated with a single source. In either case, to investigate the nature of these sources, new observations with higher sensitivity and angular resolution at multiple wavelengths are needed.

5. CONCLUSIONS

The UC H II regions are good tracers for places where early-type massive stars form; thus their study and characterization can provide important insights to understand the formation process of high-mass stars. However, due to their short lifetime, the number of known UC H II regions is relatively small. In this context, this paper is intended to increase the number of known H II regions (mainly ultra-compact) and to provide the basic data that can be used for further detailed investigations.

We conducted a study on the 1.3 and 3.6 cm continuum emission from a sample of 106 high-luminosity IRAS sources observed with the VLA in its C and B configuration, respectively. 52 sources of the sample were observed at 1.3 cm and 96 at 3.6 cm, with 42 of them observed at both wavelengths. Additionally, we used 6 cm observations reported in the literature for the detected sources. From the 3.6 cm observations, we detected 25 sources, while only 5 sources were detected from the 1.3 cm observations. In general, a single radio continuum source was detected toward each IRAS region, although there is marginal evidence of double systems in some regions. We only detected two independent sources in one region.

Using the 3.6 cm emission, we performed an initial characterization of the ionized gas in all detected sources by calculating their traditional physical parameters. For sources that were also detected at 1.3 cm and for those with reported 6 cm emission, we determined the spectral index and calculated models of H II regions with cylindrical, spherical, and Gaussian morphologies. Based on these results, we present a catalog of candidate H II regions detected in the sample.

APPENDIX

A. COMMENTS ON INDIVIDUAL SOURCES

General information is given below for the 25 sources detected at 3.6 cm, as well as the most relevant results of the study carried out in this paper. Table 4 lists the luminosity and distance for all sources, while Table 6 gives the physical parameters calculated from the 3.6 emission. In addition, Figures 1 and 2 display the 3.6 cm contour maps, and Figure 3 shows the 1.3 cm contour maps of the detected sources in the sample. Contour maps of sources with 6 cm emission are shown in Figure 4. The physical parameters obtained from the models of the H II regions with cylindrical, spherical and Gaussian symmetry, as well as the best fits to the observational data are given in Table 8 and Figure 5, respectively.

IRAS 01045+6505 is located in the HCS 6236 molecular cloud (Snell, Carpenter & Heyer 2002). An UC H II region, spatially coincident with a CS molecular clump, and two submillimeter sources have been detected toward it (Mookerjea, Sandell & Wouterloot 2007). We detect 1.3 and 3.6 cm continuum emission toward IRAS 01045+6505. In the field, we observe only one compact source, which is also detected at 6 cm and coincides with the millimeter source 01045-SMM1 and the UC H II region reported by Mookerjea, Sandell & Wouterloot (2007). A spectral index, $\alpha \approx 0.3$ is estimated using the flux density of the three wavelengths. However, the flux density at 1.3 cm appears to be very low compared to those obtained at 3.6 and 6 cm, which makes the estimated spectral index unreliable. It is possible that the flux density of the source is variable with the time.

Using only the 3.6 and 6 cm flux densities, we estimated a value of $\alpha \approx 1.3$. We interpret this spectral index as an optically partially thick UC H II region, which is consistent with the interpretation given by Mookerjea, Sandell & Wouterloot (2007). No significant variations are observed in Figure 5 between the cylindrical, spherical and Gaussian geometries of the UC H II region; however, based on its morphology at 1.3 and 3.6 cm, the spherical model could be the most suitable.

IRAS 01133+6434. It was previously observed in radio continuum by Urquhart et al. (2009), finding only one radio source. In our study, we detected a single compact and spherical source in the field at 3.6 cm. However, at 6 cm, this continuum source exhibits two emission peaks, with the strongest one coinciding with the 3.6 cm emission. Using its 3.6 and 6 cm flux density, we estimated a spectral index of ≈ 0.6, which is consistent with an optically partially thin H II region. The physical parameters obtained from the H II region models are given in Table 8, suggesting that it is an UC H II region sustained by a ZAMS B1 star. We did not find significant differences between the three models applied.

IRAS 03235+5808. This source has been little studied. Urquhart et al. (2009) detected a continuum source and NH_3 emission in the region. A continuum source was detected at 3.6 and 6 cm, which has a compact and spherical morphology at both wavelengths and coincides spatially with the IRAS center position. Its spectral index ($\alpha \approx 2.4$) and physical parameters suggest that it could be an optically thick UC H II region, which is confirmed by analyzing the H II region with three symmetries. The central source of the UC H II region is a ZAMS B0 star.

IRAS 04324+5106. A radio continuum source and four millimeter sources were detected in the region by Urquhart et al. (2009) and Klein et al. (2005), respectively. We observed a continuum source at 3.6 cm, that is very extended and shows a cometary morphology. This source is also detected at 6 cm with a similar morphology. Based on its spectral index between 3.6 and 6 cm (1.2) and applying the H II region models, we find that the continuum source is consistent with a compact H II region with Gaussian symmetry (see Figure 5 and Table 8), which is associated with a ZAMS O9.5 star.

IRAS 04366+5022. Urquhart et al. (2009) detected a single continuum source at 6 cm, which has NH_3 emission (Urquhart et al. 2011). We detected a continuum source toward IRAS 04366+5022 at wavelengths of 3.6 and 6 cm. This source, at 3.6 cm, shows an irregular morphology with several protuberances, suggesting the presence of more than one embedded continuum source (Figure 1). However, high angular resolution observations will be necessary to confirm this speculation.

Assuming that the continuum emission is produced by a single source, we estimated a spectral index of ≈ 1.9. This value could be consistent with an optically thick H II region. Based on the H II region models, we found that its physical parameters are consistent with this assumption (see Figure 5 and Table 8).

IRAS 05305+3029. This source has been poorly studied and no ammonia or other molecular tracer has been detected in the region. A compact continuum source was detected in the field at 3.6 cm, located about $14.3''$ northeast of the IRAS position. Although it was not detected at 1.3 cm, the continuum source was detected at 6 cm. It shows a compact morphology at 3.6 cm with a protuberance observed at 6 cm, suggesting that the continuum source could be a binary system. More sensitive observations will be necessary to verify this hypothesis.

We calculated a spectral index of ≈ -1.2, which is too negative to be credible. This value could be explained by invoking variability of the continuum source and/or the possibility that it could be a double system. The physical parameters of this continuum source, using its 3.6 cm emission, are consistent with an UC H II region harboring a ZAMS B1 star. However, simultaneous multi-wavelength observations with high angular resolutions are necessary to confirm its nature.

IRAS 05358+3543 is located toward the star cluster S233 (Yao et al. 2000) and has been studied at several wavelengths. Although it is strong at millimeter wavelengths (Beuther et al. 2002a), centimeter continuum emission has not been detected (e.g Sridharan et al. 2002). In addition, a massive bipolar outflow with a high degree of collimation has been detected (Beuther et al. 2002b).

The 3.6 cm continuum map reveals two sources in the field. The strongest source, IRAS 05358-VLA1, shows an elongated morphology in the northwest-southeast direction, while the second source, IRAS 05358-VLA2, is weaker and more compact. Although IRAS 05358-VLA1 has a jet-like morphology, it was not detected at 1.3 cm nor at 6 cm; hence, its spectral index was not calculated. Moreover, this continuum source is not associated with the millimeter source detected by Beuther et al. (2002a) or the bipolar SiO outflow detected by Beuther et al. (2002b), whose center is about 75″ to the southeast. Nonetheless, the elongation of the IRAS 05358-VLA1 is similar to that of the SiO bipolar outflow (northwest-southeast direction). Although IRAS 05358-VLA1 does not seem to be the driver source of the SiO outflow, there may be some relationship. Furthermore, using its 3.6 cm emission, we estimated a mass-loss rate of $\dot{M} = 2.71\times10^{-10}$ M$_\odot$ yr^{-1}, and a momentum rate of $\dot{P} = 1.35\times10^{-7}$ M$_\odot$ yr^{-1} km s^{-1}, suggesting this source is a thermal jet (e.g. Anglada, Rodríguez, & Carrasco-González 2018).

On the other hand, the derived physical parameters of the weak continuum source, IRAS 05358-VLA2, seem to be consistent with an UC H II region hosting a ZAMS B2 star.

IRAS 05553+1631 is one of the nearest regions in the sample ($\approx$ 1.2 kpc; (Wouterloot & Brand 1989)). A millimeter source was detected by Williams, Fuller, & Sridharan (2004) in the region. We detected one compact and spherical continuum source at 3.6 cm, which is offset by approximately $\approx$ 2.5″ from the millimeter source. Based on its physical parameters, we suggest that it could be an UC H II region, harboring a ZAMS B3 star.

IRAS 06055+2039 is located toward S235. Six-millimeter sources and ammonia emission were observed in the region by Klein et al. (2005). We detected a weak continuum source toward the IRAS region at 3.6 cm. However, it is shifted about $\approx$ 49″ from the IRAS position. Besides, this continuum source is not spatially coincident with any of the other millimeter sources detected by Klein et al. (2005), the closest one being 1″ away. Our calculated physical parameters suggest that this compact source is an H II region with a ZAMS B2 star.

IRAS 06412–0105 is located toward the WB870 region. A millimeter source was detected in the region by Klein et al. (2005), which was interpreted as a low-mass dust core embedded in the extended emission. Contour maps at 3.6 and 1.3 cm show a source with cometary morphology that has a size of about 13″ × 11″ at 3.6 cm and is spatially coincident with the IRAS source. A similar morphology is also observed at 6 cm, but the compact source seems to split into a double system.

Taking into account the compact and extended emission of the continuum source, we estimated a spectral index of ≈ -0.2, which is interpreted as an optically thin H II region. In addition, H II region models indicate that this source is an UC H II region with Gaussian morphology, associated with a ZAMS O7.5 star.

IRAS 06567–0355. Both millimeter and IR sources were detected in this region by Klein et al. (2005) and Zhang & Wu (1996), respectively. NH_3 (1,1) and (2,2) emission, as well as a bipolar outflow were also reported by Klein et al. (2005) and Wu, Huang & He (1996), respectively.

We detected a nearly spherical 3.6 cm continuum source that is shifted about $\approx$ 290″ from the IRAS source and is not spatially coincident with the millimeter source. In addition, this continuum source was detected at 6 cm, but with a slightly elongated morphology and showing several protuberances. Using the centimeter emission, we calculated a spectral index of ≈ -0.5 between 3.6 and 6 cm, which is consistent with non-thermal emission. This spectral index value could be explained by the presence of variability in the flux density, or the continuum source could be a multiple system. Simultaneous and high angular resolution observations will be necessary to confirm its nature.

IRAS 07299–1651. A millimeter and infrared sources, separated by $\approx$ 2.4″, were detected by Klein et al. (2005) and Rosero et al. (2019), respectively. A single continuum source is detected at 3.6 cm in the field, but not at 1.3 cm. It is spatially coincident with the millimeter source, and based on its continuum emission, this source is consistent with an UC H II region maintained by a ZAMS B3 star.

IRAS 07311–2204 is located toward BRAN 45 region, which has a diameter of $\approx$ 25′ and CO emission (May, Alvarez, & Bronfman 1997). We detected an extended continuum source at 3.6 cm with angular size $\approx$ 6″. This continuum source is spatially coincident with the IRAS source and lies within the BRAN 45 region. Assuming it to be an H II region and based on its 3.6 cm continuum emission, we found that the ionizing star is a ZAMS B0.5 star.

IRAS 07427–2400 is a high-mass star-forming region (MacLeod et al. 1998). Trinidad (2011) found a cluster of at least three radio continuum sources, two of which are UC H II regions, while the strongest source is a jet. These sources have also been detected at millimeter wavelengths by Qiu et al. (2009). We detect a continuum source at 3.6 cm; however, we note a peculiar morphology that resembles neither an H II region nor thermal jets. This fact could be explained as due to the low angular resolution of the observations at 3.6 cm, which do not spatially separate the embedded sources detected by Trinidad (2011).

IRAS 07528–3441. Using CS(2–1) and ^{12}CO observations, Bronfman, Nyman & May (1996) found an UC H II region and a molecular outflow toward IRAS 07528–3441. In addition, NH_3 (1–1) has been also detected by Urquhart et al. (2011).

The 3.6 cm continuum emission shown in Figure 2 seems to be elongated in the north-south direction, as is also observed at 6 cm. A continuum peak is clearly detected and there is evidence of a weaker second peak. However, the second peak detected at 6 cm is not coincident with the one detected at 3.6 cm. In addition, the continuum emission does not spatially coincide with the UC H II region detected by Bronfman, Nyman & May (1996), which is offset by $\approx 2'$. Based on the spectral index (≈ 0.15) and the H II region models, we find that this continuum source is consistent with an UC H II region harboring a B1 ZAMS star.

IRAS 08189–3602 was observed as a radio continuum source by Wouterloot & Brand (1989), while Planck Collaboration et al. (2015) found a compact H II region through mm and sub–mm observations. We detect a continuum source at 3.6 and 1.3 cm with a large angular size of $\approx 20''$ at 3.6 cm. A strong peak at 3.6 cm is observed, but other less defined peaks are also observed. These peaks are probably not associated with other continuum sources, but rather are irregularities of extended emission. To investigate the possibility of the secondary emission peaks being associated with compact embedded sources, we made contour maps removing the shorter baselines, both at 1.3 and 3.6 cm. However, no additional compact sources were detected.

Considering the 1.3 and 3.6 cm emission of the source, Figure 5 shows that the three H II region models fit the data very well. Based on its morphology and physical parameters, we adopt the cylindrical model. However, spherical or Gaussian models could also be consistent. This UC H II region is separated by $\approx 15''$ from the compact H II region detected at mm wavelengths by Planck Collaboration et al. (2015).

IRAS 18094–1823 (G12.20–0.03) is a high–mass star-forming region (Hill et al. 2005) and is not part of the original of the AC295 project. It is located about $\approx 4'$ to the west of the UC H II region G12.21–0.10 (e.g. de la Fuente et al. 2020a, and references therein). It stands out because the presence of low-resolution VLA emission at 3.6 cm (size $\approx 20'$) that coincides with IRAS 18094–1823 in the radio–continuum study for G12.21–0.10 presented by de la Fuente et al. (2018). In addition, using 6 cm observations from the CORNISH survey, Kalcheva et al. (2018) suggested that this object is an UC H II region. The 3.6 cm contour map shows a spherical compact source, whose emission is produced by an UC H II region. We found the ionizing star to be a ZAMS B0 star.

IRAS 19120+1103 (G45.47+0.05) is also not included in the original sample of 104 sources, but VLA low-resolution emission at 3.6 cm was detected in a study by de la Fuente et al. (2020a). Its continuum emission is rather associated with the UC H II region with extended emission G45.45+0.06 (see de la Fuente et al. 2020a, and references therein). This source was confirmed as a star-forming region by the detection of H_2O and OH maser emission by Kim, Kim, & Kim (2019). It was classified as an irregular UC H II region based on its 6 cm emission (Wood & Churchwell 1989). The physical parameters and morphology of the 3.6 cm emission are consistent with a compact H II region, with the central source being a ZAMS O9.5 star.

IRAS 21306+5540 is located towards S128, which has been studied at radio wavelengths by Ho, Haschick, & Israel (1981) and Fich (1986). Three compact H II regions were found by Ho, Haschick, & Israel (1981), labeled as S128A, S128B, and S128N with exciting stars O6, O6, and O9.5, respectively. In addition, an IR and submillimeter source has been detected by Umana et al. (2008), and the presence of a bipolar outflow in the east-west direction has been reported by Kim, Kim, & Kim (2015).

We detected a nearly compact continuum source at 3.6 cm, with a protuberance toward the north. This compact source was also detected at 6 cm and coincides with the source S128N detected by Ho, Haschick, & Israel (1981). We estimate a spectral index of about -1.1, which is interpreted as non-thermal emission. Such negative spectral indices are generally associated with extra-galactic sources. However, this continuum source is embedded in a star-forming region and has been catalogued as a compact H II region. We could explain this spectral index due to the variability of the source or to the fact that the continuum emission is not associated with a single source (e.g., a protuberance can be observed at 3.6 cm). Its physical parameters are reported in Table 6, assuming it is an H II region.

IRAS 21334+5039. A compact H II region, with a ZAMS B0 star, was discovered in this region through radio continuum observations by Mc-

Cutcheon et al. (1991), which coincides with NH_3 emission detected by Urquhart et al. (2011). In addition, Obonyo et al. (2019) searched for non-thermal radio emission toward this region, but the results were negative.

We detected one continuum source in the field at 3.6 cm, with a compact spherical morphology. A similar morphology was also observed at 6 cm. However, this source has an offset of $\approx 60''$ from the compact H II region detected by McCutcheon et al. (1991). We determined a spectral index of about -0.55, which could indicate a non-thermal nature or variability of the source (observations were carried out with a separation of about ten years). Further simultaneous observations will be necessary to determine its nature.

IRAS 21413+5442. Two radio continuum sources have been detected by Miralles, Rodríguez & Scalise (1994) and classified as a compact H II and a UC H II region, respectively. In addition, IR observations by Anandarao et al. (2008) showed the presence of a stellar cluster.

We detected a source in the field at 6, 3.6 and 1.3 cm. The morphology of the source is compact, showing slight protrusions in all three wavelengths. It coincides with the IRAS source and one of the IR sources detected by Anandarao et al. (2008), which was interpreted as a massive young stellar object. However, this continuum source is offset by about $20'$ from the H II regions reported by Miralles, Rodríguez & Scalise (1994). Using the 1.3, 3.6 and 6 cm flux densities, we obtained a spectral index of 0.85, suggesting that this source is an optically partially thick H II region. By modeling this continuum source as an H II region, we find that its physical parameters are consistent with an UC H II region with Gaussian morphology, harboring a ZAMS O8 star.

IRAS 22134+5834. NH_3 and water maser emission were detected toward the IRAS region by Sunada et al. (2007). We detected a continuum source at 3.6 cm, located about $3.5''$ from the IRAS source. This source shows a compact spherical morphology, and based on its derived physical parameters from the 3.6 cm emission, it could be classified as an UC H II region with a ZAMS B1 star.

IRAS 22308+5812 is located towards Sh2–138 (Wouterloot & Brand 1989). A compact H II region was studied by Martín-Hernández et al. (2002) and NH_3 (1,1) emission was reported by Urquhart et al. (2011).

We detected a continuum source at 3.6 cm with a cometary-like H II region morphology, with its emission peak about $2''$ from the IRAS source. A similar morphology was also observed at 6 cm. Based on its spectral index (≈ 1.4), physical parameters and morphology observed (Figure 2), we suggest this source is an UC H II region with a ZAMS O7.5 star and a Gaussian distribution (see Figure 5).

IRAS 23030+5958 is located towards S156 (Lee, Murray, & Rahman 2012) and it is one of the most luminous regions of the sample. Using low angular resolution observations at 6 cm, Israel (1977) found a group of H II regions (S156) with at least two O stars and three B stars.

We detected continuum emission at 3.6 and 1.3 cm, but the morphology does not have a well–defined structure; rather, it shows a complicated morphology with at least three continuum peaks detected at both wavelengths (VLA1, VLA2, and VLA3), aligned in the east-west direction. This morphology is also observed at 6 cm. All continuum peaks are contained in the S156A source and interpreted as an H II region. In general, the morphology of S156A and the other sources detected by Israel (1977) was explained by the quasi-stationary blister type model. Considering that all the emission detected in the field is part of a single H II region and based on its spectral index information and derived physical parameters, we find that its continuum emission is consistent with an optically partially thin UC H II region excited by ZAMS O8 stars.

REFERENCES

Anandarao, B. G., Venkata Raman, V., Ghosh, S. K., Ojha, D. K., & Kumar, M. S. N., 2008, MNRAS, 390, 1185, https://doi.org/10.1111/j.1365-2966.2008.13820.x

Anglada, G., Rodríguez, L. F., & Carrasco-González, C., 2018, A&ARv. 26, 3, https://doi.org/10.1007/s00159-018-0107-z

Beuther, H., Schilke, P., Menten, K. M., et al. 2002a, ApJ, 566, 945, https://doi.org/10.1086/338334

Beuther, H., Schilke, P., Gueth, F., et al. 2002b, A&A387, 931, https://doi.org/10.1051/0004-6361:20020319

Beuther, H., Churchwell, E. B., McKee, C. F., & Tan, J. C. 2007, Protostars and Planets V, (Tuczon, AZ: UAP), 165, https://doi.org/10.48550/arXiv.astro-ph/0602012

Bronfman, L., Nyman, L.-A., & May, J. 1996, A&AS, 115, 81

Deeg, H.-J., Brinks, E., Duric, N., Klein, U., & Skillman, E. D. 1993, ApJ, 410, 626, https://doi.org/10.1086/172780

de la Fuente, E., Porras, A., Trinidad, M. A., et al. 2020a, MNRAS, 492, 895, https://doi.org/10.1093/mnras/stz3482

de la Fuente, E., Tafoya, D., Trinidad, M. A., et al. 2020b, MNRAS, 497, 4436, https://doi.org/10.1093/mnras/staa2149
de la Fuente, E., Trinidad, M. A., Porras, A., et al. 2018, RMxAA, 54, 129
de Pree, C. G., Rodríguez, L. F., & Goss, W. M. 1995, RMxAA, 31, 39
Fich, M., 1986, AJ, 92, 787, https://doi.org/10.1086/114212
Franco, J., Kurtz, S. E., García-Barreto, J. A., et al. 2001, ApSSS, 277, 71, https://doi.org/10.1023/A:1012779627430
Franco, J., García-Barreto, J. A., & de la Fuente, E. 2000a, ApJ, 544, 277, https://doi.org/10.1086/317189
Franco, J., Kurtz, S., Hofner, P., et al. 2000b, ApJ, 542, 143, https://doi.org/10.1086/312938
Franco, J., Tenorio-Tagle, G., & Bodenheimer, P. 1990, ApJ, 349, 126, https://doi.org/10.1086/168300
Garay, G. & Lizano, S. 1999, PASP, 111, 1049, https://doi.org/10.1086/316416
Hill T., Burton, M. G., Minier, V., et al. 2005, MNRAS, 366, 405, https://doi.org/10.1111/j.1365-2966.2005.09347.x
Ho, P. T. P., Haschick, A. D., & Israel, F. P. 1981, ApJ, 243, 526, https://doi.org/10.1086/158617
Israel, F. P. 1977, A&A, 59, 27
Jaffe, D. T. & Martín-Pintado, J., 1999, ApJ, 520, 162, https://doi.org/10.1086/307440
Kalcheva, I. E., Hoare, M. G., Urquhart, J. S., et al. 2018, A&A, 615, 103, https://doi.org/10.1051/0004-6361/201832734
Kim, K.-T., Kim, W.-J., & Kim, C.-H. 2015, JKAS, 48, 365, https://doi.org/10.5303/JKAS.2015.48.6.365
Kim, W.-J., Kim, K.-T., & Kim, K.-T. 2019, ApJS, 244, 2, https://doi.org/10.3847/1538-4365/ab2fc9
Klein, R., Posselt, B., Schreyer, K., Forbrich, J., & Henning, Th. 2005, ApJS, 161, 361, https://doi.org/10.1086/496962
Kurtz, S. & Franco, J. 2002, RMxAC, 12, 16
Kurtz, S., Churchwell, E., & Wood, D. O. S. 1994, ApJS, 91, 659, https://doi.org/10.1086/191952
Launhardt, R., Loinard, L., Dzib, S. A., et al. 2022, ApJ, 931, 43, https://doi.org/10.3847/1538-4357/ac5b09
Lee, E. J., Murray, N., & Rahman, M. 2012, ApJ, 752, 146, https://doi.org/10.1088/0004-637X/752/2/146
Lu, X., Zhang, Q., Liu, H. B., Wang, J., & Gu, Q. 2014, ApJ, 790, 84, https://doi.org/10.1088/0004-637X/790/2/84
Lumsden, S. L., Hoare, M. G., Urquhart, J. S., et al. 2013, ApJS, 208, 11, https://doi.org/10.1088/0067-0049/208/1/11
MacLeod, G, C., Scalise, E. Jr., Saedt, S., Galt, J. A., & Gaylard, M. J. 1998, AJ, 116, 1897, https://doi.org/10.1086/300538
Martín-Hernández, N. L., Peeters, E., Morisset, C., et al. 2002, A&A, 381, 606, https://doi.org/10.1051/0004-6361:20011504
Maud, L. T., Moore, T. J. T., Lumsden, S. L., et al. 2015, MNRAS, 453, 645, https://doi.org/10.1093/mnras/stv1635
May, J., Alvarez, H., & Bronfman, L. 1997, A&A, 327, 325
McCutcheon, W. H., Dewdney, P. E., Purton, C. R., & Sato, T. 1991, AJ, 101, 1435, https://doi.org/10.1086/115776
McMullin, J. P., Waters, B., Schiebel, D., Young, W., & Golap, K., 2007, ASPC 376, Astronomical Data Analysis Software and Systems, ed. R. A. Shaw, F. Hill, & D. J. Bell, 127
Miralles, M. P., Rodríguez, L. F., & Scalise, E. 1994, ApJS, 92, 173, https://doi.org/10.1086/191965
Mookerjea, B., Sandell, G., Stutzki, J., & Wouterloot, J. G. A., 2007, A&A, 473, 485, https://doi.org/10.1051/0004-6361:20077878
Motte, F., Bontemps, S., & Louvet, F. 2018, ARA&A, 56, 41, https://doi.org/10.1146/annurev-astro-091916-055235
Navarrete, F., Damineli, A., Barbosa, C. L., & Blum, R. D. 2015, MNRAS, 450, 4364, https://doi.org/10.1093/mnras/stv914
Obonyo, W. O., Lumsden, S. L., Hoare, M. G., et al. 2019, MNRAS, 486, 3664, https://doi.org/10.1093/mnras/stz1091
Olnon, F. M., 1975, A&A, 39, 217
Panagia, N. 1973, AJ, 78, 929, https://doi.org/10.1086/111498
Phillips, J. P. 2007, MNRAS, 380, 369, https://doi.org/10.1111/j.1365-2966.2007.12078.x
Phillips, J. P. 2008, NewA, 13, 60, https://doi.org/10.1016/j.newast.2007.06.013
Planck Collaboration, Arnaud, M., Atrio-Barandela, et al. 2015, A&A, 573, 6, https://doi.org/10.1051/0004-6361/201423836
Preite-Martínez, A. 1988, A&AS, 76, 317
Qiu, K., Zhang, Q., Wu, J., & Chen, H.-R. 2009, ApJ, 696, 66, https://doi.org/10.1088/0004-637x/696/1/66
Reynolds, S. P. 1986, ApJ, 304, 713, https://doi.org/10.1086/164209
Rodríguez, L. F., González, R. F., Montes, G., et al. 2012, ApJ, 755, 152, https://doi.org/10.1088/0004-637X/755/2/152
Rosero, V., Tanaka, K. E. I., Tan, J. C., et al. 2019, ApJ, 873, 20, https://doi.org/10.3847/1538-4357/ab0209
Rudolph, A. L., Brand, J., De Geus, E. J., & Wouterloot, J. G. A. 1996, ApJ, 458, 653, https://doi.org/10.1086/176847
Schraml, J. & Mezger, P. G. 1969, ApJ, 156, 269, https://doi.org/10.1086/149964
Sewiło, M., Churchwell, E., Kurtz, S., Goss, W. M., & Hofner, P. 2011, ApJS, 194, 44, https://doi.org/

10.1088/0067-0049/194/2/44
———. 2008, ApJ, 681, 350, https://doi.org/10.1086/588422
———. 2004, ApJ, 605, 285, https://doi.org/10.1086/382268
Snell, R. L., Carpenter, J. M., & Heyer, M. H. 2002, ApJ, 578, 229, https://doi.org/10.1086/342424
Sridharan, T. K., Beuther, H., Schilke, P., Menten, K. M., & Wyrowski, F. 2002, ApJ, 566, 931, https://doi.org/10.1086/338332
Sunada, K., Nakazato, T., Ikeda, N., et al. 2007, PASJ, 59, 1185, https://doi.org/10.1093/pasj/59.6.1185
Tapia, M., Persi, P., Bohigas, J., & Ferrari-Toniolo, M. 1997, AJ, 113, 1769, https://doi.org/10.10.1086/118390
Trinidad, M. A., Curiel, S., Cantó, J., et al. 2003, ApJ, 589, 386, https://doi.org/10.1086/374618
Trinidad, M. A., Rodríguez, T., & Rodríguez, L. F. 2009, ApJ, 706, 244, https://doi.org/10.1088/0004-637x/706/1/244
Trinidad, M. A. 2011, AJ, 142, 147, https://doi.org/10.1088/0004-6256/142/5/147
Umana, G., Leto, P., Trigilio, C., et al. 2008, A&A, 482, 529, https://doi.org/10.1051/0004-6361:20078796
Urquhart, J. S., Hoare, M. G., Purcell, C. R., et al. 2009, A&A, 501, 539, https://doi.org/10.1051/0004-6361/200912108
Urquhart, J. S., Morgan, L. K., Figura, C. C., et al. 2011, MNRAS, 418, 1689, https://doi.org/10.1111/j.1365-2966.2011.09594
Williams, S. J., Fuller, G. A., & Sridharan, T. K. 2004, A&A, 417, 115, https://doi.org/10.1051/0004-6361:20031733
Wood, D.O.S. & Churchwell, E. 1989, ApJS, 69, 831, https://doi.org/10.1086/191329
Wouterloot, J. G. A. & Brand, J. 1989, A&AS, 80, 149
Wu, Y. W., Reid, M. J., Sakai, N., et al. 2019, ApJ, 874, 94, https://doi.org/10.3847/1538-4357/ab001a
Wu, Y., Huang, M., & He, J. 1996, A&AS, 115, 283
Yao, Y., Ishii, M., Nagata, T., Nakaya, H., & Sato, S. 2000, ApJ, 542, 392, https://doi.org/10.1086/309515
Zhang, W.-H. & Wu, Y.-F. 1996, ChA&A, 20, 326, https://doi.org/10.1016/0275-1062(96)00046-X

Eduardo de la Fuente: Departamento de Física, CUCEI, Blvd. Gral. Marcelino García Barragán 1421, Olímpica, 44430, Guadalajara, Jalisco, México (eduardo.delafuente@academicos.udg.mx).
Josep M. Masqué: Departamento de Astronomía, Universidad de Guanajuato, Apartado Postal 144, 36000, Guanajuato, Guanajuato, México (jmasque@ugto.mx).
Daniel Quiroga-González: Universidad Autónoma Metropolitana-Iztapalapa, México (dquirogag@gmail.com).
Tatiana Rodríguez–Esnard: Instituto de Geofísica y Astronomía de la Republica de Cuba, calle 212 # 2906 e/ 29 y 31 la Coronela, la Lisa 11600, C. Habana, Cuba (tatiana@iga.cu) (esnard73@gmail.com).
Miguel Angel Trinidad: Departamento de Astronomía, Universidad de Guanajuato, Apdo. Postal 144, 36000 Guanajuato, México (trinidad@ugto.mx).

Revista Mexicana de Astronomía y Astrofísica, **59**, 299–312 (2023)

https://doi.org/10.22201/ia.01851101p.2023.59.02.09

SOLAR-TYPE ECLIPSING BINARY KIC 4832197: PHYSICAL PROPERTIES AND INTRINSIC VARIABILITY OF THE COMPONENTS

O. Özdarcan, H. A. Dal, and E. Yoldaş

Department of Astronomy and Space Sciences, Faculty of Science, Ege University, İzmir, Turkey.

Received March 30 2023; accepted June 13 2023

ABSTRACT

Comprehensive analysis of optical spectroscopy and space photometry of the solar type eclipsing binary system KIC 4832197 is presented. The system is composed of F7V + F9V components with masses of $M_1 = 1.16 \pm 0.12$ M$_\odot$, $M_2 = 1.07 \pm 0.10$ M$_\odot$ and radii of $R_1 = 1.26 \pm 0.04$ R$_\odot$, $R_2 = 1.03 \pm 0.03$ R$_\odot$. The position of the components on the Log T_{eff} − Log $L/L_\odot$ plane suggests an age of 2.8 ± 0.8 Gyr for the system. Inspection of out-of-eclipse brightness in time reveals a wave-like variability pattern, whose amplitude and shape quickly change on order of days. Frequency analysis of this variability results in two significant peaks in the amplitude spectrum, which are interpreted as rotational modulation of spots on the components. Assuming both spots are on the same component, a lower limit for the differential rotation coefficient is computed as $k = 0.12$, which is weaker compared to the solar value of $k_\odot = 0.189$.

RESUMEN

Presentamos un análisis de la espectroscopía óptica y fotometría de la binaria eclipsante tipo solar KIC 4832197. El sistema se compone de dos estrellas F7V + F9V, con masas de $M_1 = 1.16 \pm 0.12$ M$_\odot$, $M_2 = 1.07 \pm 0.10$ M$_\odot$ y radios de $R_1 = 1.26 \pm 0.04$ R$_\odot$, $R_2 = 1.03 \pm 0.03$ R$_\odot$. La posición de las componentes en el plano Log T_{eff} − Log $L/L_\odot$ sugiere una edad de 2.8 ± 0.8 Gyr. La inspección del brillo fuera de eclipse revela una variabilidad ondulatoria, cuya amplitud y forma cambian rápidamente, en días. El análisis de la frecuencia de esta variabilidad arroja dos picos significativos en el espectro de amplitud, que se interpretan como una modulación rotacional de manchas en las componentes. Si suponemos que ambas manchas están en una de las componentes, calculamos un límite inferior para el coeficiente de rotación diferencial de $k = 0.12$, más pequeño que el valor solar, que es $k_\odot = 0.189$.

Key Words: binaries: eclipsing — stars: activity — stars: fundamental parameters — stars: individual: KIC 4832197

1. INTRODUCTION

Observed rotational modulation of brightness in a light curve of a solar-type star is interpreted as a strong photometric evidence of cool star spots on the stellar surface, which co-rotate with the surface. These spots might emerge in various locations on the surface of the star as a manifestation of the magnetic activity, which is commonly observed among solar-type stars. Such a light curve allows one to trace the temporal and spatial evolution of spots, as well as to determine the photometric period of the star. Finding the photometric period of a single star is crucial because that period can be considered as the rotation period the star. In the case of binary stars, it is possible to determine the photometric and orbital period separately. If the components of the binary system are solar-type stars, then a comparison between the photometric period and the orbital period provides hints on the surface differential rotation, which is one of the key parameter that drives the dynamo mechanism in stellar interiors.

Until the era of very high precision space photometry, photometric studies of the magnetic activity of solar-type stars had relied on long-term time-series photometry obtained from dedicated ground-based telescopes (Henry & Eaton 1995; Strassmeier et al. 1997; Rodonò et al. 2001) or on all sky surveys (Pojmanski 1997; Kochanek et al. 2017). These sources provided photometric data with an uncertainty of a few percent of a magnitude (rarely at milimag level; e.g. Henry & Eaton 1995) and enabled to trace the short and long-term magnetic activity behaviour of solar-type stars in terms of mean brightness, light curve amplitude and photometric period.

After entering the era of groundbreaking space photometry, astronomers had extremely high precision photometric data obtained in a wide wavelength range. Especially, the *Kepler* space telescope (Borucki et al. 2010; Howell et al. 2014) reached a photometric precision down to a few tens of part-per-million. Such a precision not only enabled to detect a planetary transit in a light curve, which was the primary mission of the *Kepler* space telescope, but also sub-millimag amplitude variability of stars. In the case of magnetic activity of solar-type stars, such precision allowed detection of very small amplitude rotational modulation of brightness, which could not be distinguished in ground-based photometry due to the typical observational scatter of a few per-cent of a magnitude. In addition to its very high precision, *Kepler* photometry spans over four years without any considerable time gap, which enables one to trace low amplitude photometric signs of magnetic activity of solar-type stars. All these properties encouraged research for more detailed and comprehensive photometric studies of stellar flares and differential rotation of large sample of stars (Balona 2015; Reinhold & Gizon 2015) or of individual targets, (particularly eclipsing binaries; Yoldaş & Dal 2021; Özdarcan et al. 2018). In some cases, *Kepler* photometry revealed effects of two separate variability mechanisms, (e.g. pulsation and cool spot activity), in eclipsing binary system (see, e.g., Özdarcan & Dal 2017).

In this study, we present a comprehensive analysis of a solar-type eclipsing binary system KIC 4832197. Our analysis is based on ground-based medium resolution optical spectroscopy and *Kepler* photometry. KIC 4832197 draws attention with its very shallow eclipse depths in its light curve and its remarkable out-of-eclipse variability with an amplitude that is comparable to the eclipse depths. Neither eclipses nor out-of-eclipse variability of the system were discovered until the advent of very high precision *Kepler* photometry. The system was included in the planet candidate catalogue due to its shallow eclipse depths (Coughlin et al. 2016). However, no confirmed exoplanet in this system has been reported so far. KIC 4832197 appeared as a late A spectral type star according to Tycho-2 measurements ($B-V = 0\overset{\mathrm{m}}{.}202 \pm 0\overset{\mathrm{m}}{.}111$, Høg et al. 2000). On the other hand, more recent and precise broadband UBV colours and magnitudes of the system are $V = 11\overset{\mathrm{m}}{.}673 \pm 0\overset{\mathrm{m}}{.}018$, $B-V = 0\overset{\mathrm{m}}{.}496 \pm 0\overset{\mathrm{m}}{.}030$ and $U-B = -0\overset{\mathrm{m}}{.}002 \pm 0\overset{\mathrm{m}}{.}032$ (Everett et al. 2012), which indicate an F7 spectral type for the system (Gray 2005).

Remarkable out-of-eclipse variability may indicate cool spot activity or pulsations on one or both components. Furthermore, shallow eclipses may indicate a possible third light, which may reduce eclipse amplitudes in the light curve depending on its contribution to the total light of the system. All these properties of KIC 4832197 are promising not only for testing stellar evolution models, but also for further studies on the variability mechanism currently occurring in one or both components. Analysis of very high precision *Kepler* photometry is excellent for such studies.

In this context, we combine ground-based optical spectroscopy and space photometry to determine the physical properties of the system and its evolutionary status. We further analyse brightness variability at out-of-eclipse phases, which can shed light into the current variability mechanism on the components of KIC 4832197. We organize the remaining parts of our study as follows. We describe the observational data and reduction in the next section. Section 3 includes light time variation analysis, spectroscopic and photometric modelling of the system, including atmospheric parameter estimation of each component, spectroscopic orbit of the system and light curve analysis. In the last section, we summarize our findings and discuss our results.

2. DATA

2.1. *Spectroscopy*

Medium resolution optical spectra of KIC 4832197 were obtained at TÜBİTAK National Observatory (TNO) with the 1.5 m Russian-Turkish telescope and the Turkish Faint Object Spectrograph Camera (TFOSC[1]). An Andor DW436-BV 2048 × 2048 pixels CCD camera with a pixel size of 13.5 × 13.5 μm^2 was used, which allows recording optical spectra between 3900 − 9100 Å in 11 échelle orders. This instrumental set-up provided an average resolution of $R = \lambda/\Delta\lambda = 2700 \pm 500$ around the $\lambda = 5500$ Å wavelength region. Observations

[1] https://tug.tubitak.gov.tr/en/teleskoplar/rtt150-telescope-0

were carried out on eight nights between July 2014 and April 2017. Ten spectra were recorded in total.

Conventional procedures for reducing échelle spectrum images were followed. These steps are applied under IRAF environment[2] and start with the removal of bias level and continue by division of bias-removed object and calibration lamp images by a normalized flat-field image. Then, scattered light correction and cosmic rays removal steps are applied to the bias and flat-field corrected images. Finally, object and calibration lamp spectra are extracted from the échelle orders. Wavelength calibration of the extracted object spectra is done by using a Fe-Ar calibration lamp spectrum recorded on the same observing night. After completing standard reduction steps, all object spectra were normalized to unity by applying 4th or 5th order cubic spline functions.

2.2. *Kepler Photometry*

Very high precision space photometry of KIC 4832197 was obtained by *Kepler* spacecraft. The spacecraft recorded images in 6.02 second exposure times with 0.52 second read-out times in a broad wavelength range between 4100 Å and 9100 Å (Gilliland et al. 2010). The broad wavelength range allows to record more photons in a single exposure, which increases precision, at the expense of losing colour information. From the recorded images, two data sets were created depending on two separate integration times; 58.9 second (short cadence data) and 29.4 minute (long cadence data). These integrations were grouped as separate data sets, where each set covered approximately three months, called quarters, except the first quarter, which covered ten days of commissioning phase and is called quarter zero (Q0). During operation of the spacecraft over 4 years (between 2009 and 2013) photometric data were collected for eighteen quarters in total (from Q0 to Q17). Continuous long cadence photometry obtained in each quarter is available for the majority of *Kepler* targets, including KIC 4832197. Long cadence photometry of KIC 4832197 for each quarter is obtained from Mikulski Archive for Space Telescopes (MAST). Prior to analyses, it is necessary to remove instrumental effects from the long cadence data. For each quarter, simple aperture photometry (SAP) fluxes are considered. These fluxes are de-trended as described in Slawson et al. (2011) and Prša et al. (2011). De-trended fluxes are then normalized to unity. The analysis and modelling process is based on these normalized fluxes. We show the long cadence light curve of KIC 4832197 in Figure 1.

[2]The Image Reduction and Analysis Facility is hosted by the National Optical Astronomy Observatories in Tucson, Arizona at URL iraf.noao.edu

3. ANALYSIS

3.1. *Light Time Variations*

The first step of the analysis is to determine mid-eclipse times of KIC 4832197 for primary eclipses. In principle, mid-eclipse times can be determined straightforwardly by applying the Kwee - van Woerden method (Kwee & van Woerden 1956) to observations close by to mid-eclipse time. An alternative way is to fit a function to the observational data around the estimated mid-eclipse time and determine the extremum point of this function, which corresponds to the mid-eclipse time. These methods may work flawlessly for a light curve of an ordinary eclipsing binary, which shows symmetric eclipse light curves with respect to the mid-eclipse time and exhibits flat or slightly distorted maxima at out-of-eclipse phases. Such light curves indicate the absence of intrinsic variability for any of the component. Looking at Figure 1, one may easily notice the variable nature of the light curve. Because of the relatively short orbital period and integration time of long cadence data, a few data points can be found around the expected mid-eclipse time for a given orbital cycle. Combination of these two effects gives a complex shape to the light curve and makes the methods mentioned above unsuited for the precise determination of mid-eclipse times. In such cases, one of the most reliable ways is to find a best-fitting light curve model and then only adjust the mid-eclipse time of the primary minimum in the model for each cycle. We follow exactly this way for a precise determination of mid-eclipse times from long cadence data.

Actually, this is an iterated process, which starts by preparing a phase-folded light curve with initial light elements, i.e. an ephemeris reference time (T_0) and an orbital period (P), then continues by finding the best-fitting light curve model. In the case of KIC 4832197, initial T_0 and P values are adopted from the Kepler Eclipsing Binary Catalogue[3] (Prša et al. 2011; Slawson et al. 2011) given in equation 1:

$$T_0(\mathrm{BJD}) = 2,454,954.965798 + 1^{\mathrm{d}}.8954655 \times E. \quad (1)$$

After finding the best-fitting light curve model, T_0 is adjusted for each orbital cycle separately, by keeping all other model parameters fixed. In this step, time-based long cadence data are considered,

[3]http://keplerebs.villanova.edu/

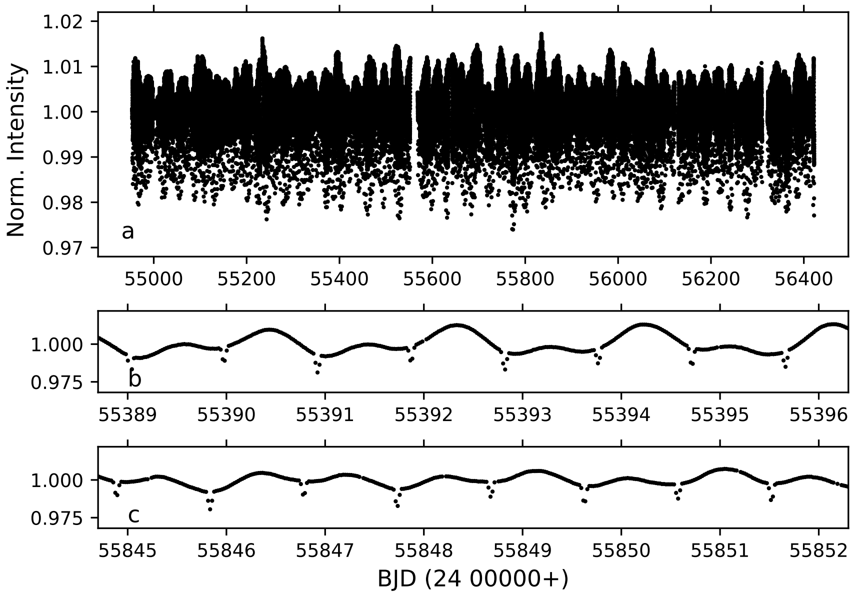

Fig. 1. In panel a the long cadence light curve of KIC 4832197 is shown. In panels b and c, different portions of the long cadence light curve are shown, where the shape of the ligh

instead of phase-folded light curve. Thus, the mid-eclipse time of each orbital cycle can be determined precisely together with formal errors. Practical application of this method is done with the Wilson-Devinney code (see later sections for details). After determination of mid-eclipse times, a simple eclipse time variation (etv) diagram is constructed and linear corrections are determined and applied to both T_0 and P. Then the whole process is repeated by using the corrected T_0 and P. In most cases, two iterations are enough to obtain self consistent T_0, P, and light curve model parameters. The converged solution leads to the corrected light elements given in equation 2:

$$T_0(\mathrm{BJD}) = 2,454,954.9661(2) + 1^{\mathrm{d}}.8954650(4) \times E. \quad (2)$$

The numbers in parentheses are statistical uncertainties for the last digit of the corresponding parameter. These uncertainties are computed from a linear least squares fit. T_0 and P values given in equation 2 are adopted for further analyses and kept fixed. The resulting eclipse time variation diagram is shown in Figure 2. In the figure, an irregular undulating variation is noticeable among the scatter, with an approximate amplitude of $0^{\mathrm{d}}.003$. Since that pattern does not repeat itself strictly over four years, it is not likely to be due to a possible third body. A more likely explanation of this pattern might be the out-of-eclipse variability of the system, which can be noticed in the b and c panels of Figure 1.

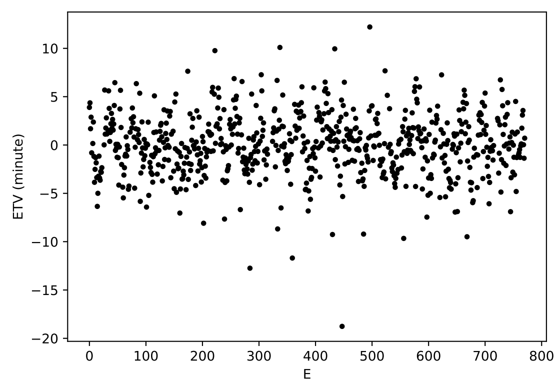

Fig. 2. ETV diagram for KIC 4832197.

3.2. *Radial Velocities and Spectroscopic Orbit*

The next step of our analysis is to determine radial velocities of each component from each observed spectrum and to model the spectroscopic orbit of the system. In order to determine radial velocities of the components, we use the optical spectrum of HD 184499 (T_{eff} = 5743, log g = 4.07; Prugniel et al. 2011) as a template spectrum, which was recorded with the same instrumental set-up on 20th August, 2014. Then, each observed spectrum of KIC 4832197 was cross-correlated with the spectrum of HD 184499 by following the method proposed by Tonry & Davis (1979). The practical application of this method used the *fxcor* task (Fitzpatrick 1993) under IRAF environment. All clear absorption lines (except strongly blended or very broad spectral lines) were considered in the 5th and 6th

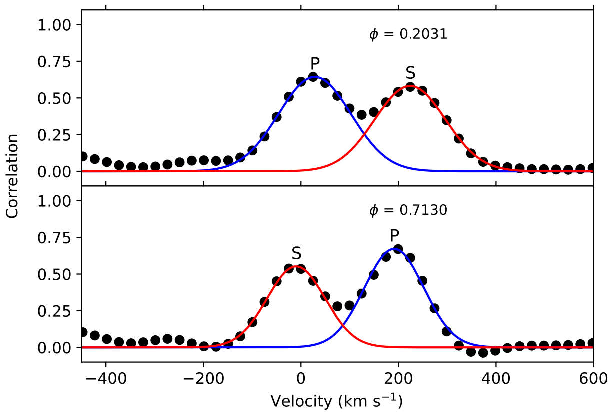

Fig. 3. Cross-correlation functions of two observed spectra recorded around orbital quadratures. P and S denote the primary and the secondary component, ϕ the orbital phase. The colour figure can be viewed online.

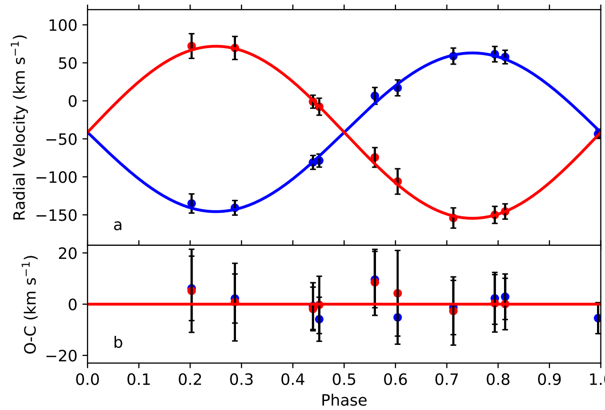

Fig. 4. Phase-folded radial velocities of the primary (blue) and the secondary (red) components are shown as filled circles. The best-fitting spectroscopic orbit model is over-plotted for each component as a continuous line. The colour figure can be viewed online.

échelle orders, which cover a wavelength range between 4900 Å and 5700 Å. In this wavelength range, it was possible to detect strong signals of both components. We show cross-correlation functions of two spectra of KIC 4832197, recorded at two separate orbital quadratures, in Figure 3. The heliocentric radial velocities are tabulated in Table 1.

Preliminary inspection of the phase-folded light curve shows that the mid-primary and the mid-secondary eclipses precisely occur at 0.0 and 0.5 orbital phases, respectively. This finding strongly suggests a circular orbit. Therefore, the spectroscopic orbit of the system is determined assuming zero eccentricity (i.e. $e = 0$). In this case, the longitude of the periastron (ω) is undefined; thus the T_0 value found in the light time variation analysis step is adopted instead of the periastron passage time. T_0 and P values are kept fixed during the modelling, while radial velocity semi-amplitudes of the components (K_1 and K_2), center-of-mass velocity of the system (V_γ) are adjusted. Application of a linear least squares fitting method to the observed radial velocities results in the best-fitting spectroscopic orbit parameters tabulated in Table 2. The agreement between the observed radial velocities and their best-fitting model is shown in Figure 4.

3.3. *Spectral Type*

Medium resolution TFOSC spectra allow us to determine spectral types and global atmospheric parameters for each component of KIC 4832197. A spectrum recorded around any of the orbital quadrature is suitable for the atmospheric parameter determination of individual components, since the spectral lines of both components are often sufficiently separated from each other and can be distinguished at those orbital phases. This is observed in the TFOSC spectrum recorded on 30th July 2016, corresponding to 0.7130 orbital phase (see lower panel of Figure 3). Spectral types and atmospheric parameters are determined from this spectrum.

Determination of spectral types and atmospheric parameters is an iterated process, as in the case of determination of mid-eclipse times described in § 3.1. During the analysis, we fix the micro-turbulence velocity of each component at 2 km s^{-1}. Actually, analysing high resolution optical spectra it is possible to determine the micro-turbulence velocity and the [Fe/H] abundance simultaneously, via the Blackwell diagram (Blackwell & Shallis 1979). However, due to the insufficient resolution of TFOSC spectra, we were unable to do so. Instead, we implicitly assume a 2 km/s micro-turbulence velocity and fix this value during the analysis. Although there is no strict relation in the literature to estimate micro-turbulence velocities reliably, limited observational studies indicate that 2 km s^{-1}is appropriate for solar type stars (Landstreet et al. 2009).

It is possible to apply a constraint on the logarithm of gravity (log g) of the components. To do this, spectroscopic orbit model parameters are combined with preliminary light curve solution parameters. This step allows computation of the masses and radii of the components. Then, log g values are computed via the computed masses and radii of the components. Computed log g values are fixed in the spectral type analysis and effective temperatures of the components (T_{eff1} and T_{eff2}) are estimated together with overall metallicity ([Fe/H]). Then, the

TABLE 1

SUMMARY OF SPECTROSCOPIC OBSERVATIONS*

HJD (24 00000+)	Orbital Phase	Exposure time (s)	SNR	Primary V_r	Primary σ	Secondary V_r	Secondary σ
56842.4581	0.7936	3200	120	61	10	-150	11
56842.4963	0.8138	3200	95	58	9	-146	10
56843.3937	0.2872	3200	90	-141	10	70	15
56887.3009	0.4516	3200	140	-79	9	-8	11
56887.5063	0.5599	3200	95	7	11	-74	13
56888.3307	0.9949	3200	120	-43	6	—	—
57592.3910	0.4395	3600	90	-81	9	-1	9
57600.4912	0.7130	3600	110	59	11	-154	13
57617.3447	0.6045	3600	90	17	10	-106	17
57853.5170	0.2031	2700	100	-135	13	72	16

*Along with the measured radial velocities and their corresponding standard errors (σ) in $\mathrm{km\,s^{-1}}$. SNR denotes the signa-to-noise ratio around 5500Å wavelength.

TABLE 2

BEST-FITTING SPECTROSCOPIC ORBIT PARAMETERS OF KIC 4832197.*

Parameter	Value
$P_{\rm orb}$ (day)	1.8954655 (fixed)
T_0 (HJD24 00000+)	54954.965798 (fixed)
V_γ ($\mathrm{km\,s^{-1}}$)	-41 ± 2
K_1 ($\mathrm{km\,s^{-1}}$)	104 ± 4
K_2 ($\mathrm{km\,s^{-1}}$)	113 ± 5
e	0 (fixed)
$a\sin i$ ($\mathrm{R_\odot}$)	8.15 ± 0.26
$M\sin^3 i$ ($\mathrm{M_\odot}$)	2.03 ± 0.14
Mass ratio ($q = M_2/M_1$)	0.92 ± 0.06
rms1 ($\mathrm{km\,s^{-1}}$)	5
rms2 ($\mathrm{km\,s^{-1}}$)	4

*M_1 and M_2 denote the masses of the primary and the secondary component, respectively, while M shows the total mass of the system and $a\sin i$ is the projected semi-major axis, depending on the orbital inclination i.

estimated temperature of the primary component and the overall metallicity are adopted as fixed parameters, and combined light curve and radial velocity modelling is repeated. Two or three iterations are usually enough to reach a self-consistent solution.

Effective temperatures and overall metallicity are estimated by the spectrum synthesis method. ATLAS9 (Castelli & Kurucz 2004) model atmospheres, which adopt a plane-parallel atmosphere, are used for synthetic spectrum computation. A grid of synthetic spectra is computed for a temperature range of 6000 K to 7000 K with a step of 100 K. This computation is repeated for metallicities between solar ([Fe/H]=0) and sub-solar ([Fe/H]=-1.0), with a step of 0.25. The computation of synthetic spectra is done by a PYTHON framework, *iSpec* software (Blanco-Cuaresma et al. 2014). Among various radiative transfer codes provided in *iSpec*, the SPECTRUM code (Gray & Corbally 1994) is adopted. *iSpec* also includes a comprehensive line list compiled from the third version of the Vienna atomic line database (VALD3, Ryabchikova et al. 2015). Each computed synthetic spectrum is convolved with a Gaussian line spread function to reduce the spectral resolution to the resolution of the TFOSC spectra. After that, a trial synthetic spectrum is chosen for each component among the computed spectra, and a composite spectrum of the system is computed. In order to compute the composite spectrum of the system, each individual spectrum is shifted in wavelength with respect to the radial velocity of the corresponding component and scaled with respect to the square of the ratio of the radii of the components.

Self-consistent effective temperatures and overall metallicities are determined in the third iteration, which gives T_{eff1} = 6300 K, T_{eff2} = 6100 K and [Fe/H] = -0.25. The estimated uncertainties are around 200 K for temperature and 0.25 for metallicity. The adopted ratio of radii is $R_1/R_2 = 1.27$ and log g values are log $g_1 = 4.30$ and log $g_2 = 4.47$ (see next section for details). These results indicate F7V and F9V spectral types for the primary and the secondary components (Gray 2005), respectively. The observed TFOSC spectrum and the best-fitting composite spectrum are shown in Figure 5.

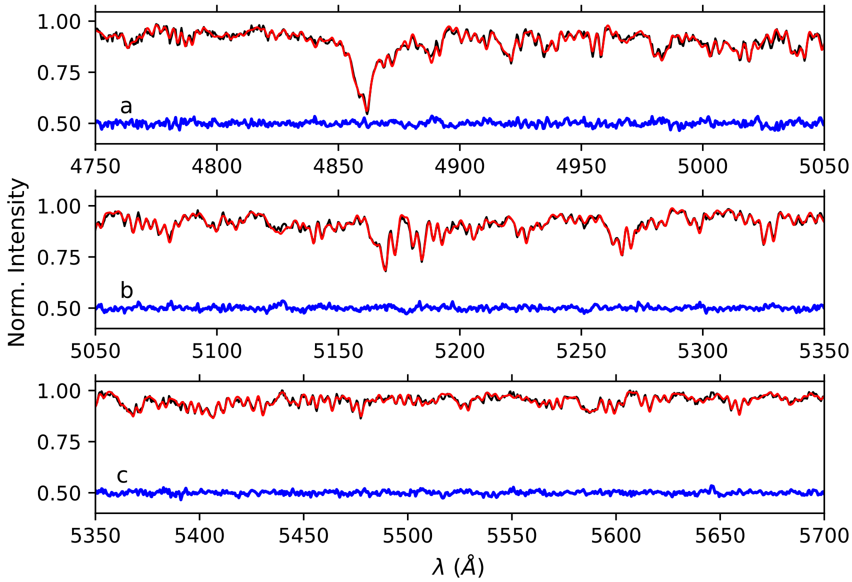

Fig. 5. Observed (blue) and computed composite spectrum (red) for KIC 4832197 in three different portions of the optical wavelengths. Residuals from the best-fitting model are plotted as shifted upwards by 0.5 (blue) for a better viewing purpose. The colour figure can be viewed online.

3.4. *Light Curve Analysis and Evolutionary Status*

Long cadence photometric data of KIC 4832197 include 65190 individual data points in total, which means that a large amount of CPU time is required to find a best-fitting light curve model. Therefore, an average phase-folded light curve is prepared by computing an average in every 0.01 phase at out-of eclipse phases. Around mid-eclipse phases a phase step of 0.0005 is adopted in order to detect the ingress and egress phases of eclipses precisely. The average phase-folded light curve includes 556 data points in total, which enormously reduces the required CPU time for light curve modelling. Weighting of each normal data point in the phase-folded average light curve is done by considering the total number of data points, which produces the normal data point.

Light curve modelling is done with the 2015 version of the well-known Wilson–Devinney (WD) eclipsing binary light curve modelling code (Wilson & Devinney 1971; Wilson & Van Hamme 2014). Its practical application is done by the user friendly PYTHON GUI $PyWD2015$ (Güzel & Özdarcan 2020). $PyWD2015$ allows the use of almost all features of the 2015 version of the WD code. In addition to the capabilities of the WD code, $PyWD2015$ includes many useful features and tools to speed up the modelling process and to trace successive iterations visually.

Two most critical parameters for an accurate light curve modelling are T_{eff1} and q. These have already been determined in previous sections, and are kept fixed during modelling. Effective temperatures of the components clearly indicate that both components possess a convective outer envelope; thus, gravity darkening (g) and albedo (A) values of each component are set to 0.32 (Lucy 1967) and 0.5 (Ruciński 1969), respectively. The low resolution of TFOSC spectra does not allow to determine reliable rotational velocities of the components; so, considering the non-eccentric orbit of the system, synchronous rotation is implicitly assumed for both components by fixing the rotation parameter (F) of each component to unity. A logarithmic limb darkening law (Klinglesmith & Sobieski 1970) is adopted for both components and limb darkening coefficients are taken from van Hamme (1993) for the Kepler passband. Adjustable parameters are: inclination of the orbit (i), effective temperature of the secondary component (T_{eff2}), dimensionless potentials of the components (Ω_1, Ω_2) and luminosity of the primary component (L_1). Coarse and fine grid numbers for the stellar surface are set to 60. Modelling attempts with a possible third light contribution do not yield a reasonable model, which indicates extremely small or negative third light contribution. Therefore, the modelling process is carried out with no third light contribution. Convergence is not very quick due to the shallow eclipse depths. However, successive it-

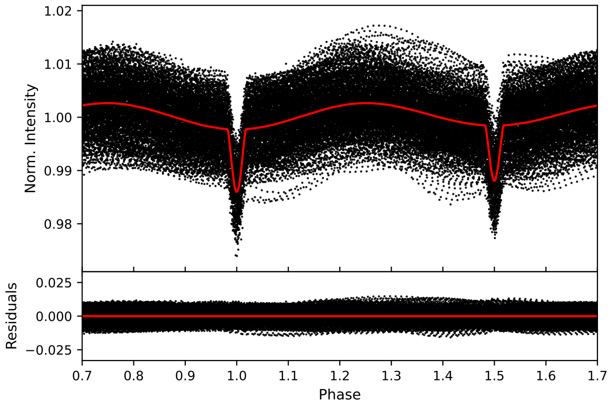

Fig. 6. Phase-folded long cadence Kepler observations and the best-fitting light curve model of KIC 4832197 are shown along with residuals from the model. The colour figure can be viewed online.

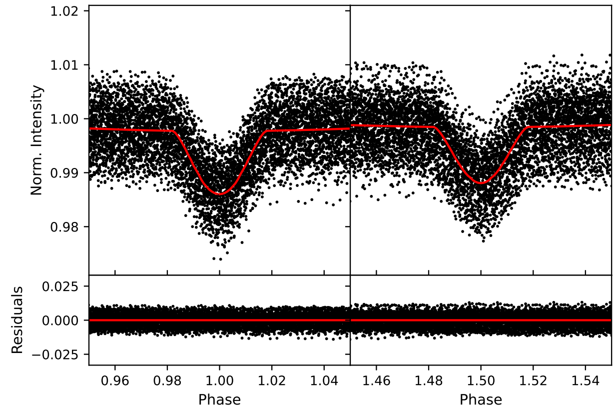

Fig. 7. Close-up view of observations and the best-fitting light curve model around eclipse phases. The colour figure can be viewed online.

TABLE 3

BEST-FITTING LIGHT CURVE MODEL PARAMETERS FOR KIC 4832197.*

Parameter	Value
q	0.92 (fixed)
$T_1(K)$	6500 (fixed)
$g_1 = g_2$	0.32
$A_1 = A_2$	0.5
$F_1 = F_2$	1.0
i (°)	75.67(5)
$T_2(K)$	6060(200)
Ω_1	7.605(22)
Ω_2	8.520(44)
$L_1/(L_1{+}L_2)$	0.639(3)
x_1, x_2	0.685, 0.700
y_1, y_2	0.270, 0.259
$\langle r_1\rangle, \langle r_2\rangle$	0.1498(5), 0.1219(8)
Model rms	2.8×10^{-4}

*$\langle r_1\rangle$ and $\langle r_2\rangle$ show mean fractional radii of the primary and the secondary components, respectively. Uncertainties of the adjusted parameters are internal to the Wilson-Devinney code and are given in parentheses for the last digits, except T_2. The uncertainty of T_2 is assumed to be the same as that of T_1.

TABLE 4

ABSOLUTE DIMENSION OF KIC 4832197.*

Parameter	Primary	Secondary
Spectral Type	F7V	F9V
Mass ($M_\odot$)	1.16(12)	1.07(10)
Radius ($R_\odot$)	1.26(4)	1.03(3)
log $L/L_\odot$	0.35(6)	0.11(6)
log g (cgs)	4.30(2)	4.44(2)
M_{bol} (mag)	3.87(15)	4.48(16)
[Fe/H]	−0.25(0.25)	
Separation ($R_\odot$)	8.41(26)	
Distance (pc)	459(40)	

*The statistical error of each parameter is given in parentheses for the last digits.

erations converge slowly but firmly to a global minimum. Model parameters for the best-fitting light curve are tabulated in Table 3. In Figure 6, the phase-folded light curve and and the best-fitting light curve model are shown. A separate close-up view of each eclipse is shown in Figure 7.

Combination of the best-fitting spectroscopic orbit and light curve model parameters allows us to compute the absolute dimension of the system as well as its distance. Both the UBV colours (Everett et al. 2012) and the optical spectrum of the system indicate an F7 spectral type, which means that reddening and interstellar extinction should be negligible. Trial plotting of the system on the UBV colour-colour diagram gives $E(B-V) = 0\overset{\mathrm{m}}{.}009$, which is well below the observational error of $B-V$. Hence might be ignored for the distance computation. Considering P, K_1, K_2, i, $\langle r_1\rangle$ and $\langle r_2\rangle$ along with the published UBV magnitudes, the absolute dimension of the system is computed with the JKTABSDIM code[4] (Southworth et al. 2005) and tabulated in Table 4. Calibrations given in Kervella et al. (2004) are adopted for the bolometric correction and distance computation.

Comparing the locations of the components with stellar evolutionary tracks on the Log T_{eff} − Log $L/L_\odot$ plane, it is possible to es-

[4]https://www.astro.keele.ac.uk/jkt/codes/jktabsdim.html

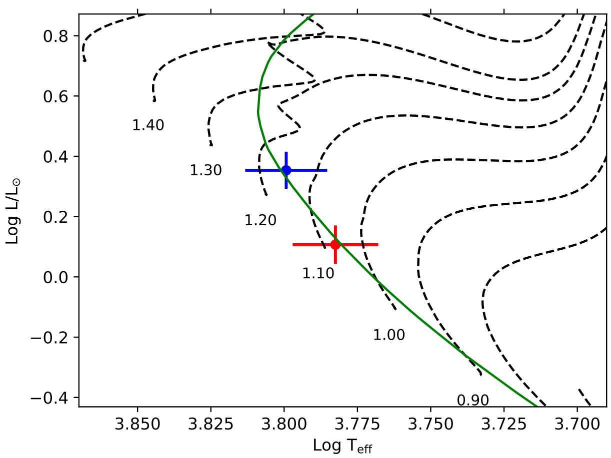

Fig. 8. Positions of the primary and the secondary components on log T_{eff}−log $L/L_{\odot}$ plane. Dashed lines show evolutionary tracks for different masses. Each track is labelled with its corresponding mass. The continuous curve shows the isochrone for log(age)=9.45. The tracks are for a slightly sub-solar metallicity with $Y = 0.273$ and $Z = 0.014$. The colour figure can be viewed online.

timate the age of the system. In Figure 8, the components of KIC 4832197 are plotted along with stellar evolutionary tracks computed with the PAdova and TRieste Stellar Evolution Code (PARSEC, Bressan et al. 2012). The best-matching isochrone to the positions of the components has log(age)=9.45, which indicates an age of 2.8 Gyr for the system. The estimated uncertainty for this age is approximately 0.8 Gyr. The primary source of this uncertainty is the uncertainty of the estimated effective temperatures and its propagation to the computed luminosities. Both components are still on the main sequence. However, the primary component is almost half-way through its main sequence life.

3.5. *Out-of-Eclipse Variability*

A scatter of ±0.01 is clearly noticeable in the phase-folded light curve (see Figure 7). This scatter is a natural result of dominant brightness variability at out-of-eclipse phases (see Figure 1, lower panels). For further investigation of this variability, the best-fitting light curve model is subtracted from observations, and residuals from the model are obtained. In principle, these residuals do not include variability due to eclipses nor proximity effects of the components, and give hints on intrinsic variability of one or both components. Residuals from the best-fitting light curve model are obtained with PyWD2015 by inputting all long cadence data into the WD code and making a single differential corrections iteration. The obtained residuals are plotted in Figure 9. Quick changes in the residual light curve shape and amplitude are remarkable.

TABLE 5

FIRST TWO DOMINANT FREQUENCIES (F_1, F_2)*

Frequency number	Frequency (c/d)	Amplitude (Flux $\times 10^3$)	Phase (radian)
f_1	0.4995769(76)	3.70(2)	0.4947(8)
f_2	0.5339561(88)	2.79(2)	0.807(1)
f_{orb}	0.5275750(1)	—	—

*Resulting from the frequency analysis of the residual light curve of KIC 4832197 along with the orbital frequency (f_{orb}) of the system. Uncertainties are given in parentheses for the last digits.

In order to see the reflection of this variability in the frequency-amplitude plane, a Lomb-Scargle periodogram (Lomb 1976; Scargle 1982) is applied to the whole long cadence residuals via a Python script PYSCA (Herzberg & Glogowski 2014). PYSCA allows quick and practical computation of the amplitude spectrum and can extract significant frequencies above a defined noise level. Adopting a 24.498 cycle/day (c/d) as Nyquist frequency, a single PYSCA run results in the amplitude spectrum given in Figure 10. The adopted Nyquist frequency corresponds to twice (≈ 59 min) the integration time of a single long cadence exposure. In the resulting amplitude spectrum, two dominant peaks are clearly seen around the orbital frequency, but no signal appears at the precise location of the orbital frequency. Frequency values of the two dominant peaks are tabulated in Table 5, together with the orbital frequency.

It is also possible to trace the behaviour of the detected frequency peaks for each Kepler quarter separately. A close view of the f_1 and f_2 peaks is shown in Figure 11 for each Kepler quarter, separately. It is apparent that f_1 strongly appears in most of quarters while f_2 weakens or disappears in some quarters.

The corresponding frequencies of the first two dominant peaks in the amplitude spectrum give the phase folded residual light curves shown in Figure 12. Phase folding is done with respect to the reference ephemeris given in equation 2 and the corresponding period values of the frequencies listed in Table 5. A wave-like light curve pattern can be noticed easily in both panels of the figure. This picture appears to be the reflection of a double-humped structure of the light curve (see Figure 1, Panels *b* and *c*), which is the frequently observed through four years of long

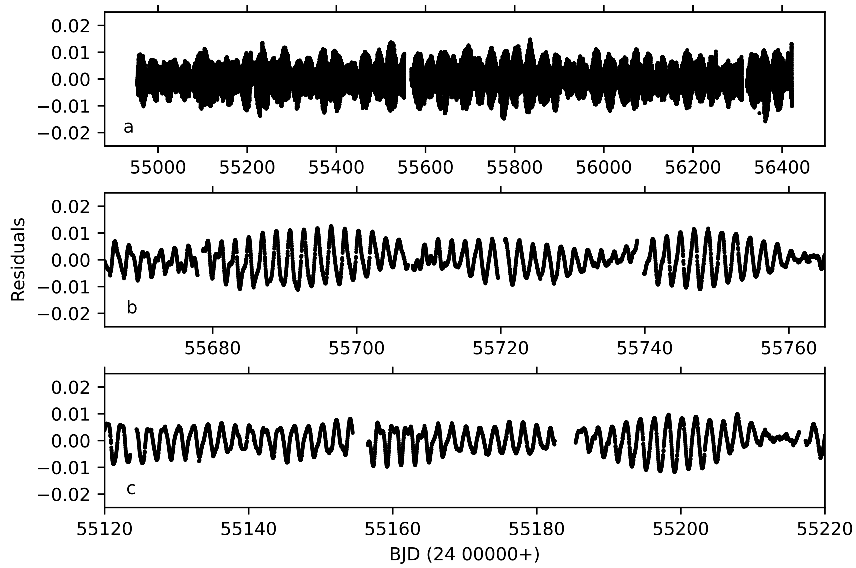

Fig. 9. Residuals from the best-fitting light curve model are plotted against time (BJD). Panel a shows the whole long cadence residuals,

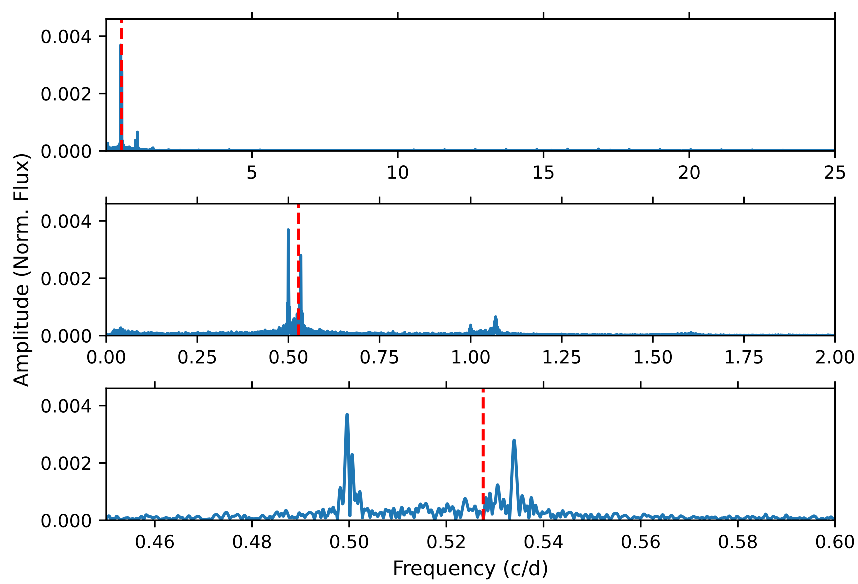

Fig. 10. Amplitude spectrum of light curve residuals. The uppermost panel shows the whole amplitude spectrum between 0 and 24.498 c/d. The middle panel focuses on 0 and 2 c/d, where dominant peaks appear. The lowermost panel shows a detailed view of the two most dominant peaks and the orbital frequency. In each panel, the orbital frequency is marked with a vertical dashed (red) line. The colour figure can be viewed online.

cadence data. Estimated spectral types of the components in § 3.3 suggest that these f_1 and f_2 frequencies are likely the result of cool spot activity on one or both components.

4. SUMMARY AND DISCUSSION

Analyses of medium resolution ground-based optical spectroscopy and very high precision Kepler photometry show that KIC 4832197 is composed of F7V and F9V stars possessing slightly sub-solar metallicity ([Fe/H]=-0.25 ± 0.25). The components move around the center-of-mass of the system in a circular orbit with a period of $1\overset{d}{.}8954650$. The Kepler long cadence light curve of the system is dominated by a wave-like brightness variability whose amplitude is comparable to the eclipse depths. In some

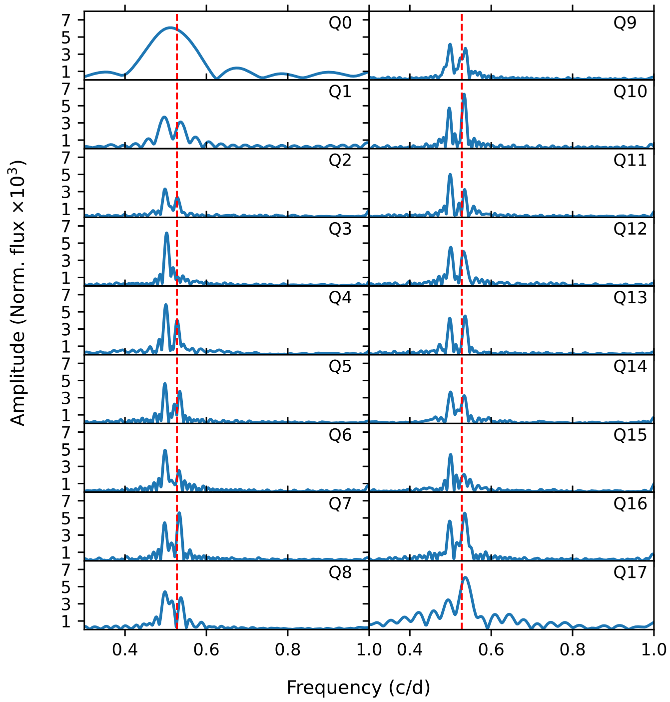

Fig. 11. Close view of the amplitude the spectrum of light curve residuals for each quarter of Kepler data. Panels are focused on the frequency region around f_{orb}, which is shown by a vertical (red) dashed line. Each panel is labelled with its corresponding qua

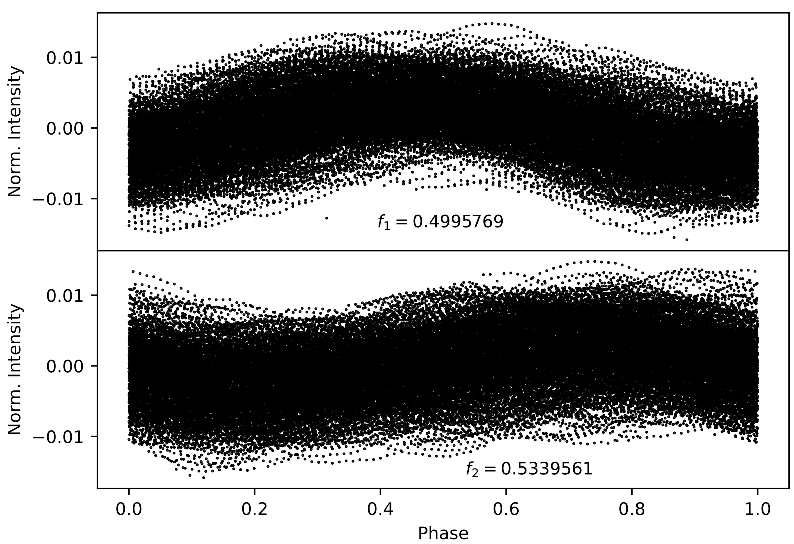

Fig. 12. Phase folded light curve residuals with respect to f_1 and f_2 frequencies. Each frequency is shown in the corresponding panel.

epochs, the amplitude of this variability exceeds the amplitude of eclipses, which are very shallow and hardly exceed 0.01 in normalized flux units.

Shallow eclipse depths could be result of a possible third light contribution. However, the best-fitting light curve model indicates no third light contribution. The ETV diagram does not show any sign for a possible third body, but only a scatter of ± 5 minutes with some vaguely undulating patterns among this scatter. A remaining possible explanation is that the undulating pattern could be the reflection of the variability observed at out-of-eclipse phases. Considering the spectral types of the components, such irregular patterns in ETV diagrams could be attributed to an intrinsic photometric variability originating from magnetic activity of one or both components. (Balaji et al. 2015). Comparing the ETV diagrams of KIC 4832197 and a very active eclipsing binary KIC 12418816 (Dal & Özdarcan 2018, see Figure 1 in their study), it is clearly seen that our target system does not exhibit clear patterns, which indicates a much lower level of magnetic activity.

Combining the best-fitting spectroscopic orbit and light curve models, absolute physical properties of the components of the system are computed. Using these parameters, the components are plotted on the log T_{eff}−log $L/L_{\odot}$ plane. The positions of the components on this plane suggest an age of 2.8±0.8 Gyr for the system. The primary component of KIC 4832197 appears to have burnt almost half of its main sequence fuel.

UBV colours (Everett et al. 2012) of the system enable us to estimate interstellar reddening. Trial plots of the $U-B$ and $B-V$ colours of the system on the UBV colour-colour diagram yields $E(B-V) = 0\overset{\mathrm{m}}{.}009$. This indicates a distance of 452±40 pc. Considering the reported observational errors of the UBV colours and the small amount of $E(B-V)$, interstellar reddening can be neglected. In this case, the distance becomes 459±40 pc. Both distance values agree within the computed statistical error. The computed error of the distance is mainly dominated by the estimated 200 K uncertainty of the effective temperatures of the components. The distance of the system based on precise parallax measurement of GAIA (Gaia Collaboration et al. 2016, 2022; Babusiaux et al. 2022) is given as 449±2 pc, which is in good agreement with the computed distance in this study.

Removing the best-fitting light curve model from the long cadence Kepler light curve, a residual light curve is obtained, which shows clear brightness variability at out-of-eclipse phases. The residual light curve exhibits remarkable changes, with a time scale of a few orbital cycles. These changes occur both in amplitude and shape of the light curves. For instance, an asymmetric single-humped light curve can become a double-humped one with a noticeable amplitude change in a few days, and then can return to another asymmetric light curve with a different amplitude. Considering the spectral types of the components the most likely explanation for the source of the out-of-eclipse brightness variability is cool spot activity on one or both components. Such a spot activity is the result of magnetic activity in cool stars and causes emission features to appear in particular activity-sensitive spectral lines throughout the optical spectrum (e.g. Hα, Ca II H& K lines). However, no emission features are observed, neither in the Hα nor in the Ca II H& K lines in the TFOSC spectra of KIC 4832197. Nevertheless, several very weak stellar flares, which can be considered photometric evidence of cool spot activity, are detected in the long cadence Kepler light curve of the system. Such a situation was observed before for the eclipsing binary KIC 9451096 (Özdarcan et al. 2018), where no emission was detected in activity-sensitive lines but a significant number of flares were detected in the Kepler light curve. On the other hand, although the amplitude of the rotational modulation signal reaches up to 0.01 in normalized flux units, this is still a low amplitude brightness variability. Thus, observing no emission in activity-sensitive spectral lines may not be unexpected. Actually, a low level of magnetic activity is in agreement with the physical properties of the system. Masses of the components are slightly higher than the solar mass, which means that both of them possess more shallow outer convective envelopes compared to the Sun. Therefore, one may expect a decrease in the level of magnetic activity. Comparing KIC 4832197 with KIC 12418816 (Dal & Özdarcan 2018), which is a lower mass eclipsing binary with shorter orbital period and high level of magnetic activity, confirms this situation. The components of KIC 12418816 possess a deeper convective envelope compared to the components of our target. As a result of the combination of faster rotation and deeper convective envelopes, a high level of magnetic activity in KIC 12418816 is not surprising. In the case of KIC 4832197, the situation is opposite. Hence, a low level of magnetic activity is not unexpected for KIC 4832198.

Frequency analysis of the residual light curve shows two dominant frequency peaks around the orbital frequency (see the amplitude spectrum plotted in Figure 10). However, the lowermost panel of the figure clearly shows that almost no signal appears at the exact location of the orbital frequency. This means that the best-fitting light curve model precisely represents binarity effects. As a result, removing the best-fitting light curve model from the observations perfectly removes the binarity effects from the long cadence light curve. Comparing the frequencies (f_1, f_2 and f_{orb}) and their statistical error (listed in Table 5), one can notice that the separation of frequencies exceeds the statistical errors. No major splitting is observed for the peaks of f_1

and f_2, except for a remarkable side component of f_1 located at a slightly higher frequency compared to f_1. We interpret these frequencies as the result of two separate spots or spot groups located at different latitudes on the surface of one or both components. Looking at the lowermost panel of the Figure 10, it is quickly seen that the f_1 and f_2 frequencies are smaller and larger than f_{orb}, respectively. Assuming that both components possess solar type differential rotation on their surfaces, a spot (or spot group) causing variability with an f_1 frequency is assumed to be located at lower latitudes, which are expected to rotate faster than at the latitude rotating with f_{orb}. (The latitude that rotates with f_{orb} is often called co-rotation latitude). In this case, the other spot (or spot group), which rotates with an f_2 frequency must be located at higher latitudes compared to the co-rotation latitude. These latitudes are expected to rotate slower than the co-rotation latitude as well. Further inspection of these frequencies reveals that f_1 persistently appears in each separate Kepler quarter while f_2 weakens or disappears occasionally. In this case, the spot (or spot group) related to f_1 is more persistent and exhibits stronger activity compared to the spot or spot group related to f_2. Four years of persistence of the f_1 frequency is not surprising in the context of solar and stellar activity since similar persistent active longitudes were reported previously for our Sun (Berdyugina & Usoskin 2003).

With the current data, it is difficult to distinguish which component possesses a spot(s) on its surface. However, we may make an implicit assumption by considering two mechanisms, depth of the outer convective envelope and rotation, which trigger the magnetic activity on cool stars. Although the system is composed of two similar stars, the secondary component is 500 K cooler than the primary. This means that the secondary star possesses a deeper convective envelope. Considering that the axial rotation periods of the components are synchronized with the orbital period, this finding indicates that the secondary component may exhibit stronger magnetic activity, because of its deeper convective outer envelope. Then, we may assume that the spots occur in the cool secondary component.

Assuming that both f_1 and f_2 come from spot or spot groups on the cool secondary component, a lower limit for the differential rotation can be set. Following the procedure described in Hall & Busby (1990), we compute the corresponding period for f_1 and f_2, and adopt them as minimum (P_{min}) and maximum (P_{max}) periods. Assuming a solar type differential rotation, P_{min} can be adopted as the equatorial rotation period. Then, the relative surface shear can be computed via $P_{max} - P_{min}/P_{min} = kf$, where k is the differential rotation coefficient and f is a constant depending on the range of spot forming latitudes. Assuming that f varies between 0.5 and 0.7, which corresponds to 45 degrees of latitude range for spot forming, k varies between 0.14 and 0.10, which indicates an average $\bar{k} = 0.12$. This is half of the solar differential rotation coefficient ($k_\odot = 0.189$, see Hall & Busby (1990) and references therein) but twice the differential rotation coefficient of the eclipsing binary KIC 9451096 ($k = 0.069$, Özdarcan et al. 2018). This finding appears to contradict the theory of stellar magnetic activity since KIC 9451096 possesses a higher level of magnetic activity but a weaker differential rotation compared to our target system.

Increasing the number of precisely analysed solar type eclipsing binaries will provide a global look of the photometric properties of magnetic activity eclipsing binaries, and on the influence on light curves of differential rotation, which is one of the two key mechanisms responsible for magnetic activity in cool stars. Continuous photometric data provided by space telescopes is key to achieve this purpose.

We acknowledge an anonymous referee for his/her valuable comments that improved the quality of the paper. We thank TÜBİTAK for partial support to use the RTT150 (Russian-Turkish 1.5-m telescope in Antalya) with project number 14BRTT150-667. This paper includes data collected by the Kepler mission. Funding for the Kepler mission is provided by the NASA Science Mission Directorate.

REFERENCES

Babusiaux, C., Fabricius, C., Khanna, S., et al. 2022, arXiv e-prints, arXiv:2206.05989, https://doi.org/10.48550/arXiv.2206.05989

Balaji, B., Croll, B., Levine, A. M., & Rappaport, S. 2015, MNRAS, 448, 429, https://doi.org/10.1093/mnras/stv031

Balona, L. A. 2015, MNRAS, 447, 2714, https://doi.org/10.1093/mnras/stu2651

Berdyugina, S. V. & Usoskin, I. G. 2003, A&A, 405, 1121, https://doi.org/10.1051/0004-6361:20030748

Blackwell, D. E. & Shallis, M. J. 1979, MNRAS, 186, 673, https://doi.org/10.1093/mnras/186.4.673

Blanco-Cuaresma, S., Soubiran, C., Heiter, U., & Jofré, P. 2014, A&A, 569, 111, https://doi.org/10.1051/0004-6361/201423945

Borucki, W. J., Koch, D., Basri, G., et al. 2010, Sci, 327, 977, https://doi.org/10.1126/science.1185402

Bressan, A., Marigo, P., Girardi, L., et al. 2012, MNRAS, 427, 127, https://doi.org/10.1111/j.1365-2966.2012.21948.x

Castelli, F. & Kurucz, R. L. 2004, A&A, 419, 725, https://doi.org/10.1051/0004-6361:20040079

Coughlin, J. L., Mullally, F., Thompson, S. E., et al. 2016, ApJS, 224, 12, https://doi.org/10.3847/0067-0049/224/1/12

Dal, H. A. & Özdarcan, O. 2018, MNRAS, 474, 326, https://doi.org/10.1093/mnras/stx2875

Everett, M. E., Howell, S. B., & Kinemuchi, K. 2012, PASP, 124, 316, https://doi.org/10.1086/665529

Fitzpatrick, M. J. ASPC 52, Astronomical Data Analysis Software and Systems II, ed. R. J. Hanisch, R. J. V. Brissenden, & J. Barnes, 472

Gaia Collaboration, Prusti, T., de Bruijne, J. H. J., et al. 2016, A&A, 595, 1, https://doi.org/10.1051/0004-6361/201629272

Gaia Collaboration, Vallenari, A., Brown, A. G. A., et al. 2022, arXiv:2208.00211, https://doi.org/10.48550/arXiv.2208.00211

Gilliland, R. L., Jenkins, J. M., Borucki, W. J., et al. 2010, ApJ, 713, 160, https://doi.org/10.1088/2041-8205/713/2/L160

Gray, D. F. 2005, The Observation and Analysis of Stellar Photospheres, 3rd ed. (Cambridge, UK: CUP)

Gray, R. O. & Corbally, C. J. 1994, AJ, 107, 742, https://doi.org/10.1086/116893

Güzel, O. & Özdarcan, O. 2020, CoSka, 50, 535, https://doi.org/10.31577/caosp.2020.50.2.535

Hall, D. S. & Busby, M. R. 1990, ASIC 319, Proceedings of the NATO Advanced Study Institute on Active Close Binaries, ed. C. Ibanoglu, 377

Henry, G. W. & Eaton, J. A. 1995, ASPC 79, Robotic telescopes: current capabilities, present developments, and future prospects for automated astronomy: proceedings of a symposium held as part of the 106th annual meeting of the Astronomical Society of the Pacific, Arizona, 28-30 June 1994

Herzberg, W. & Glogowski, K. 2014, IAUS, Precision Asteroseismology, 421, https://doi.org/10.1017/S1743921313014853

Høg, E., Fabricius, C., Makarov, V. V., et al. 2000, A&A, 355, 27

Howell, S. B., Sobeck, C., Haas, M., et al. 2014, PASP, 126, 398, https://doi.org/10.1086/676406

Kervella, P., Thévenin, F., Di Folco, E., & Ségransan, D. 2004, A&A, 426, 297, https://doi.org/10.1051/0004-6361:20035930

Klinglesmith, D. A. & Sobieski, S. 1970, AJ, 75, 175, https://doi.org/10.1086/110960

Kochanek, C. S., Shappee, B. J., Stanek, K. Z., et al. 2017, PASP, 129, 104502, https://doi.org/10.1088/1538-3873/aa80d9

Kwee, K. K. & van Woerden, H. 1956, BAN, 12, 327

Landstreet, J. D., Kupka, F., Ford, H. A., et al. 2009, A&A, 503, 973, https://doi.org/10.1051/0004-6361/200912083

Lomb, N. R. 1976, Ap&SS, 39, 447, https://doi.org/10.1007/BF00648343

Lucy, L. B. 1967, ZA, 65, 89

Özdarcan, O. & Dal, H. A. 2017, PASA, 34, 17, https://doi.org/10.1017/pasa.2017.11

Özdarcan, O., Yoldaş, E., & Dal, H. A. 2018, RMxAA, 54, 37, https://doi.org/10.48550/arXiv.1709.01129

Pojmanski, G. 1997, AcA, 47, 467, https://doi.org/10.48550/arXiv.astro-ph/9712146

Prugniel, P., Vauglin, I., & Koleva, M. 2011, A&A, 531, 165, https://doi.org/10.1051/0004-6361/201116769

Prša, A., Batalha, N., Slawson, R. W., et al. 2011, AJ, 141, 83, https://doi.org/10.1088/0004-6256/141/3/83

Reinhold, T. & Gizon, L. 2015, A&A, 583, 65, https://doi.org/10.1051/0004-6361/201526216

Rodonò, M., Cutispoto, G., Lanza, A. F., & Messina, S. 2001, AN, 322, 333, https://doi.org/10.1002/1521-3994(200112)322:5/6<333::AID-ASNA333>3.0.CO;2-6

Ruciński, S. M. 1969, AcA, 19, 245

Ryabchikova, T., Piskunov, N., Kurucz, R. L., et al. 2015, PhyS, 90, 054005, https://doi.org/10.1088/0031-8949/90/5/054005

Scargle, J. D. 1982, ApJ, 263, 835, https://doi.org/10.1086/160554

Slawson, R. W., Prša, A., Welsh, W. F., et al. 2011, AJ, 142, 160, https://doi.org/10.1088/0004-6256/142/5/160

Southworth, J., Maxted, P. F. L., & Smalley, B. 2005, A&A, 429, 645, https://doi.org/10.1051/0004-6361:20041867

Strassmeier, K. G., Boyd, L. J., Epand, D. H., & Granzer, T. 1997, PASP, 109, 697, https://doi.org/10.1086/133934

Tonry, J. & Davis, M. 1979, AJ, 84, 1511, https://doi.org/10.1086/112569

van Hamme, W. 1993, AJ, 106, 2096, https://doi.org/10.1086/116788

Wilson, R. E. & Devinney, E. J. 1971, ApJ, 166, 605, https://doi.org/10.1086/150986

Wilson, R. E. & Van Hamme, W. 2014, ApJ, 780, 151, https://doi.org/10.1088/0004-637x/780/2/151

Yoldaş, E. & Dal, H. A. 2021, RMxAA, 57, 335, https://doi.org/10.22201/ia.01851101p.2021.57.02.07

H. A. Dal, O. Özdarcan, and E. Yoldaş: Ege University, Faculty of Sciences, Department of Astronomy and Space Sciences, 35100 Bornova, İzmir, Turkey (orkun.ozdarcan@ege.edu.tr).

Revista Mexicana de Astronomía y Astrofísica, **59**, 313–322 (2023)

https://doi.org/10.22201/ia.01851101p.2023.59.02.10

A NEW PROPOSAL OF THE TERM METEOROID

G. Cordero-Tercero[1], D. Maravilla[1], and M. Covarrubias-Saavedra[2]

Received November 29 2022; accepted June 15 2023

ABSTRACT

In this document we briefly review the evolution of the term meteoroid and we make several proposals for a definition, emphasizing the importance of the criteria used for it. Finally, we propose a definition based on observations rather than on the instrument of observation.

RESUMEN

En este documento realizamos una breve reseña de la evolución del término meteoroide y hacemos varias propuestas para una definición enfatizando la importancia de los criterios empleados para ello. Finalmente proponemos una definición basada en observaciones más que en el instrumento de observación

Key Words: meteorites, meteors, meteoroids — minor planets, asteroids: general

1. SHORT HISTORICAL EVOLUTION OF THE TERM METEOROID

Since ancient times, humanity has observed the sky discovering countless bodies that inhabit the vicinity of the Earth and beyond. From the Egyptians to the Greeks and the civilizations of the East, the passage of "shooting stars" or "meteors" through the sky was captured in their writings and/or records [e.g. Yang et al. (2005)]. Many of these discoveries are currently linked to the smaller bodies that are part of the Solar System and/or to those bodies that cross the interplanetary medium by approaching or interacting with the Earth. Such bodies are what we recognize and study now as asteroids and comets (Marvin 1996; Williams 2002, 2011). The former range from the structure known as the asteroid belt and the conglomerates in the vicinity of our planet known as the Aton, Apollo, Amor and Atira families, to the groups that exist in the Jovian or Trans-Neptunian regions, while the latter, from the Kuiper Belt or the Oort Cloud, cross the interplanetary medium leaving behind a trail of rocks and dust. Asteroids and comets are linked to bodies that reach Earth or that intercept its orbit; in some cases, they can not only cross the Earth's atmosphere but also impact the surface of our planet or settle at the bottom of the sea. The observation of bodies that come from space has been documented in many research works, and since the 19th century the observations carried out of the phenomena called "shooting stars" were collected in works such as those of Herschel (1802) and Newton (1865). Before the nineties of the 20th century a difference had already been established between asteroids and bodies that travel in space, which were given the name of meteoroids.

This last term was coined by Millman (1961) to differentiate these bodies from each other on the basis that asteroids were bodies larger than 100 meters. According with Millman (1961) a meteoroid could be defined as a solid body travelling in the interplanetary medium of a size much smaller than an asteroid but much larger than an atom or molecule. For many years this definition worked well, but it was not until the end of the last century that the scientific community started to analyze the meteoroid concept not only as to the body size but also as to the phenomena produced by these bodies when they cross the terrestrial atmosphere.

Along with the definition for asteroid and meteoroid, in 1961 the definitions for meteor, fireball and micrometeorite were also established. These definitions, approved by the IAU were: (a) Meteorite: body that has reached the surface of the Earth without being completely evaporated. (b) Meteoroid: solid body that moves in the interplanetary medium with a size considerably smaller than that of an asteroid but considerably larger than that of an atom or molecule. (c) Meteor: luminous phenomenon that occurs when a particle from space enters the Earth's atmosphere. (d) Fireball: bright meteor with a luminosity equal to or greater than the brightness of the

[1]Instituto de Geofísica, UNAM, México.
[2]Secretaría de Educación Pública, México.

planets. (e) Micrometeorite: very small meteorite or particular meteorite with a diameter of less than one millimeter.

By 1990, the discovery of the asteroid 1990UN, which has a diameter of 100 meters and an absolute magnitude greater than 23 ($H > 23$, Borovička 2016), as well as the arrival of a few meter objects to our planet, led to a revaluation of the concept *meteoroid* that was beginning to be obsolete by then; thus, in the last three decades it has become necessary to classify with greater precision the bodies that come from space, attending mainly to their size, although in this century, other parameters have also begun to be considered within the proposed definitions, such as speed, albedo and chemical composition, among others. Thus, since the nineties of the last century, the new definitions that have been proposed have been based on observations made with various techniques and state-of-the-art instruments, and these have been discussed in scientific sessions of the International Astronomical Union (IAU).

In 1995, Beech and Steel proposed a definition based on the size of the object. According to their work, "any solid natural object in space of a cometary or planetary nature, with a size greater than 10 meters could be considered an asteroid or minor planet, while an object much smaller than 10 meters, which could even be cometary in nature, but larger than 100 microns could be defined as a meteoroid". With this definition, a new question arose related to those bodies smaller than 100 microns, based on the phenomenon produced by meteoroids when they enter the Earth's atmosphere which is known as a "meteor". These authors mention that, for a meteor to be produced, the object has to be larger than 100 microns (Bronshten 1981); that is, if the body is larger than 100 microns then we are talking about a meteoroid, but if its size is less than this value then it is a dust particle. The 100 microns barrier represents the frontier between meteoroids and smaller bodies.

With these arguments, the definition that was finally proposed was the following: "a meteoroid is a solid body that moves in space, with a size smaller than 10 meters but larger than 100 microns". The authors also proposed that the definitions of dust and micrometeorite could be modified, which by then had already been discussed in the IAU work sessions being those: (a) Dust: finely divided rocky matter with particle sizes much smaller than the size of a micrometeorite. (b) Micrometeorite: very small meteorite or meteorite particle with a diameter of less than one millimeter.

Even so, Beech & Steel (1995) proposed the following modifications for these last definitions: (a) Dust: Particles that originate or exist in space with sizes much smaller than 100 microns. (b) Micrometeorite: Small meteorite whose size exceeds 100 microns.

While these changes were taken into account, the IAU also considered that the definition of meteorite did not need to be modified under the definition of meteoroid proposed by Beech and Stell (1995), since by then the definition for a meteorite had gone through a long process of modifications (Craig 1849; Rubin & Grossman 2010; Cohen 1894; Farrington 1915; Nininger 1933; Millman 1961; Mason 1962; Gomes & Keil 1980; McSween 1987; Krot et al. 2003). Therefore, by 2003 the definition of a meteorite was established as: a solid body of extraterrestrial material that penetrates the atmosphere and reaches the Earth's surface (Krot et al. 2003). Seven years later, Rubin & Grossman (2010) gave a new version of the concept of meteorite and meteoroid based on the fact that meteorites have also fallen on the Moon and Mars, and small interplanetary objects can impact a spacecraft. These researchers proposed that:

(a) A meteorite is a natural solid body larger than 10 microns and that comes from a celestial body. (b) A meteoroid is a natural solid body that moves in the interplanetary medium and has a size between 10 microns and one meter.

Additionally, these authors provide a definition for micrometeoroid and for micrometeorite, these being the following:

(a) Micrometeoroid: meteoroid with a size between 10 microns and 2 mm. (b) Micrometeorite: meteorite with a size between 10 microns and 2 mm.

Six years after the work of Rubin & Grossman (2010), Borovička (2016) published a work with new and more precise definitions based on physical and astronomical arguments. These new definitions arose as a need to identify the rocky matter that travels in the interplanetary medium and that can impact the Earth's surface. The definitions were born from the discussions carried out by several researchers who were part of Commission 22 of the IAU and are listed below:

(a) Comet: active solid body with a diameter greater than 1 m and smaller than a dwarf planet that moves across, or comes from, the interplanetary medium. (b) Asteroid: non-active solid body with a diameter greater than 1 m and smaller than a dwarf planet that moves across, or comes from, the interplanetary space. (c) Meteorite: solid body that survives the meteor phase as it passes through a gaseous atmosphere without being completely evaporated. (d) Meteoroid: solid body with a diameter between 30 microns and one meter that moves across, or comes from, the interplanetary medium. This body becomes a meteorite when the ablation process stops and the object enters the phase of dark flight towards the Earth's surface. In particular, a meteorite smaller than a millimeter is called a micrometeorite. (e) Meteor: it is referred to light and the associated phenomenon that results from the entry of a solid object from space into a gaseous atmosphere. The phenomenon can be caused by a meteoroid, a comet, an asteroid or any particle with a certain mass, speed and mean free path crossing a planetary atmosphere. This phenomenon can occur in any planet or satellite that has an atmosphere dense enough for the meteoroid to evaporate, totally or partially, as it passes through the atmosphere. Meteors with an absolute magnitude smaller than -4 are called fireballs, while those with an absolute magnitude smaller than -17 are called superbolides. (f) Dust: finely divided rocky matter smaller than the size of meteoroids that moves through the interplanetary medium and can be observed in the zodiacal cloud (Lasue et al. 2020), zodiacal dust lines, and cometary tails. Dust from cometary tails can have sizes that place it in the meteoroid classification. Due to their size, very small dust particles do not produce meteors when they enter a planetary atmosphere, only heat below the melting point, and can reach Earth without being altered. When they are collected in the atmosphere, they are called interplanetary dust particles (IDPs) or Brownlee particles (Brownlee 1985). (g) Meteorite smoke: solid matter that has condensed in the gaseous atmosphere from material that evaporated during the meteor phase. The size of meteorite smoke particles is in the subnanometer range.

In recent years and considering other phenomena such as the YORP effect and the Yarkovsky effect, the above definitions could be modified. In this paper we propose a new definition for the term meteoroid based on both physical effects.

2. THE IMPORTANCE OF THE CRITERIA

In the class "Introduction to Space Physics" at the Sciences Faculty at UNAM, I (Cordero-Tercero) show to my students a slide with several little animals: ladybug, mantis, butterfly, centipede, stick insect, snail, and spider; and I ask them how many insects do they see. I get several answers, but when I tell them that an insect is a small invertebrate animal that has six legs and generally one or two pairs of wings, they answer correctly. After that we discuss the importance of a definition and the criteria to adopt it. To exemplify, we discuss the definition of a planet expressed in Resolution 5 of the General Assembly of the IAU in 2006. From our point of view, this definition does not consider small planetary bodies as important, only as points moving around the Sun's gravitational force. The definition may not please many, but it is adequate according to a dynamic criterion. However, from the point of view of geology, geophysics or astrobiology, they are indeed important. In the next sections, we propose several definitions of the term *meteoroid* based on an equal number of criteria. Several of them have been discussed by the scientific community, and we only collect them here. We are conscious that the definition proposed by Commission 22 of the IAU is valuable and that it was result of hard work. However we consider that we can show another valid point of view.

3. PROPOSED DEFINITIONS

In this section, we propose several criteria to define the term *meteoroid* and analyse their advantages and disadvantages.

3.1. *About the Lower Limit to Define a Meteoroid*

Another example of the difficulty in agreeing on the way in which an object is defined is the dust. According to Mann et al. (2014) the terminology used to refer to dust comes from the different ways that it is studied; thus, the dust size has a wide range and includes meteors, meteoroids, meteoric smoke, meteorites, IDPs, zodiacal dust particles and β-meteoroids. This is strange because in the same category are placed meteors that are light phenomena, objects like meteorites that can be several meters in size, and particles as small as zodiacal dust. On the other hand, Krüger & Grün (2014) say that dust in the Solar System, also called micrometeoroids, are fine particles whose size ranges from a few molecules to tenths of millimeters. These particles are subject to various forces: gravity, radiation pressure, Lorentz force, Poynting-Robertson drag and ion drag. In consonance with these, particles of different sizes (between 0.01 μm and 100 μm), and in all rigor physical properties like their mineralogy, are affected mainly by one or several of these forces.

In our Solar System, particularly in the interplanetary medium, dust particles modify their orbital parameters when they interact with the solar radiation field, absorbing, scattering and re-emitting part of the energy intercepted by the cross section that the small body presents to the radiation flux.

The radiation force that results from such an interaction has two components, the first is a radial force called radiation pressure that points away from the star when the particles are considered to be spherically symmetric; and the second is an azimuthal force known as the Poynting-Robertson effect (P-R drag) which causes dust particles in bounded orbits to spiral towards the Sun as their orbits become circular.

The relationship between the radiation pressure force and the solar gravity force is known as the β parameter and depends only on the properties of the particle (Mignard 1984; Mann 2009)

Paying attention to the wavelength of the energy intercepted by dust, $\beta \approx 1/r$ for $s \gg \lambda$ (where r is the heliocentric distance of the particle from the star, s is the dust particle radius, and λ the wavelength of the incident radiation); $\beta \approx$ constant for particles with $s \ll \lambda$ (Rayleigh limit) i.e. β depends on the size, geometry and chemical composition of the particle as well as on the wavelength of the incident light. When the radiation pressure force is greater than the solar gravity force, the particles with $\beta > 1$ are not bounded and can leave the Solar System describing hyperbolic trajectories. These types of particles are known as β meteoroids (Berg & Grün 1973; Zook & Berg 1975; Burns et al. 1979; Mann 2009), and their dynamics depend on their kinetic energy, orbital angular momentum, and potential energy that the dust particle had at the time it was formed. The maximum value of β corresponds to $s \approx \lambda$.

On the other hand, when $\beta > 1$, dust particles have zero angular momentum, which corresponds to a fictitious case, since as it has been shown by several researchers, β can have very small values that allow a circumsolar orbit to be open (Dohnanyi 1973) and dust particles can be ejected. For dust particles produced by comets, if they are small enough to be disturbed by solar radiation, they will reach any region or point of their orbital plane in relatively short times, moving away from the original orbit of the parent body (comet) due to the direct radiation pressure, or will spiral towards the Sun by the P-R effect (Kresák 1976). In particular, when all the incident radiation does not transfer momentum effectively, β acquires very small values and the orbit described by cometary dust particles will be elliptical or hyperbolic with a new semi-major axis given by:

$$a' = a_0\ (1-\beta)\ (1-e_0)\ (1-e_0-2\beta)^{-1}, \qquad (1)$$

where a_0 and e_0 are the comet original semi-major axis and eccentricity values, respectively (Kresák 1976). Then, the escape limits of a cometary particle ejected at perihelion β_P and aphelion β_A are, respectively:

$$\beta_P = \frac{1}{2}(1-e_0) \quad and \quad \beta_A = \frac{1}{2}(1+e_0). \qquad (2)$$

These equations represent two critical values of β and their magnitude depends on the orbital eccentricity. The values for the cometary particles that come from the Encke comet are: $\beta_P = 0.076$ at perihelion and $\beta_A = 0.924$ at aphelion (Kresák 1976). In the Solar System, most of the Beta meteoroids have values in the interval: $0.5 < \beta < 1$, although the ejected bodies do not reach high speeds and their size is a fraction of microns (Mann 2009).

In recent decades, small bodies and dust have been discovered forming debris disks around stars of spectral types B, A, F, G, K and M (Mann 2009) as well as planets around stars of type G, K and M.

In particular, protoplanetary disks have been detected around the stars β Pictoris, Vega, UA Microscopii (UA Mic) and Fomalhaut. These protoplanetary disks contain large amounts of dust where the ejection process could be occurring. In the case of β Pictoris and its debris disk, the studies indicate that Beta meteoroids can escape with speeds between ≈ 50 and 90 km/s, the lowest speed being associated with ice dust, while the highest speed is related to dust particles made up of carbon. Escaping dust particles from β Pictoris have sizes of several microns (Mann 2009). On the other hand, in protoplanetary disks, dust particles that could be influenced by the P-R drag are those for which $\beta \approx 0.5$ which implies that the P-R drag does not affect the evolution of any dust particle in the disk (Wyatt 2009), as is the case of particles that have bounded orbits and whose collision time is shorter than the lifetime related to the P-R drag.

Wyatt (2009) states that there are two types of disks: the dense ones that are dominated by collisions and have few grains under the influence of P-R drag; and the thin disks that are dominated by P-R drag and dust particles in the disk are affected by this drag. The ejection processes, as well as the collisions and the influence of the P-R effect on dust particles, are associated with the star life stage, since in the case of young stars, radiation fluxes and winds are highly variable compared to those of mature stars.

Visible meteors are associated to centimeter-sized objects (Krüger & Grün 2014), but strictly speaking this depends on their velocity, entry angle and composition. This can be a criterion to mark the lower limit of a meteoroid, but according to the previous paragraphs, there could be many criteria to define this lower limit; they will depend on what physical properties of the objects are important and why.

In 2016, Borovička (2016) mentioned that the maximum influx of particles that enter Earth's atmosphere have a size of 100 μm, but considers that a better dust-meteoroid boundary could be 10 μm or even 30 μm. This last value was the chosen as the lower limit to define the term meteoroid according to Commission 22 of the IAU.

3.2. *Yarkovsky and YORP Effects*

The interaction of solar radiation with the surface of bodies smaller than few tens of kilometers (< 30-40 km) (Bottke et al. 2006; Fenucci & Novaković 2021) generates a force able to produce small changes in the asteroids' orbital parameters, moving them away or closer to the Sun depending on their prograde o retrograde rotation (Yarkovsky effect), and torques capable of modifying the spin rates and axis orientations of asteroids (YORP effect, by Yarkovsky-O'Keefe-Radzievskii-Paddack).

The Yarkovsky effect has two components: seasonal and diurnal (the latter commonly larger than the former) that significantly affect asteroids of tens of meters to $\approx$ 10 km (Burbine 2017). Chesley et al. (2003) carried out the first measure of this effect on a planetary object: the asteroid 6489 Golevka, of 530 m diameter. Before, the Yarkovsky effect had been detected only in the motion of artificial satellites (Chesley et al. 2003). Using OSIRIS-REx spacecraft tracking data and a thermophysical model of Bennu, Farnocchia et al. (2021) estimate that Bennu's semi-major axis drifts -284.6 ± 0.2 m/yr. In addition, Greenberg et al. (2020), using optical and radar data of 600 NEAs, made a list of 247 asteroids for which it is possible to quantify the Yarkovsky effect.

The YORP effect has been detected in around nine asteroids (Zegmott et al. 2021). This is important for asteroids of size less than $\approx$ 10 km, and is considered to be the main cause of the spin change of small asteroids (Golubov & Scheeres 2019).

Bottke et al. (2006) and Grieve & Shoemaker (1994) among others, think that the number of near Earth objects has been constant during the last 3 billion years; this means that there must be a mechanism to supply new asteroids into the inner Solar System (to renew those that have impacted with other planetary bodies). Morbidelli & Vokrouhlický (2003) think that impacts between main belt asteroids are not enough to explain the constant number and that the Yarkovsky and YORP effects can help to restock the inner Solar System with asteroids.

Models about the Yarkovsky and YORP effects take into consideration several characteristics of the asteroid, such as diameter, density, thermal conductivity, semi-major axis, heat capacity of the surface, obliquity, rotation period, emissivity and absorption coefficient (e.g. Fenucci & Novaković 2021).

Given the above, we can say that the Yarkovsky and YORP effects are important for the dynamics of asteroids, and that they implicitly provide information about the physical properties of these objects. In this context, we could say that a meteoroid *is an object that is affected by the Yarkovsky and YORP effect.* According to Bottke et al. (2006), the Yarkovsky effect works on objects of sizes between 0.1 m and 40 km, and the YORP effect is important in the variation of the spin rates of main belt asteroids with diameters less than 40 km.

According to the previous paragraphs, we propose that a *meteoroid is a solid body with a diameter greater than 0.1 m and less than $\approx$ 40 km, considering the lower and the upper limits of the objects influenced by the Yarkovsky and YORP effects.*

Advantages of this definition: it gives lower and upper limits that are independent of the observation.

Disadvantages: determining the asteroid size depends on the albedo and whatever it is measured in the visible or IR bands. In addition, many observations are necessary to determine it. Asteroids with a size near the upper limit could be difficult to classify.

3.3. *Completeness*

From the Small-Body Database Query (`https://ssd.jpl.nasa.gov/tools/sbdb_query.html#!#results`), we obtained a list of 31889 objects with a determined H from orbit classes Atira, Apollo, Aten, and Amor (data updated to February 3, 2023); and we made a completeness test. According to Figure 1 (lineal behavior), the sample is complete between $11 \leqslant H < 19$.

Based on this, another way of defining the term meteoroid would be: a *meteoroid is a solid object with magnitude H less than 11 and whose size is* ≥ 30 *microns.* In this sense, it would mean that meteoroids are objects whose sample is not complete and that are greater than micrometeorites.

Advantages of this definition: It gives well defined lower and an upper limits. In addition, we do not know many things about asteroids, but we do have the H of all of them (at least in the list that we used to make the completeness test).

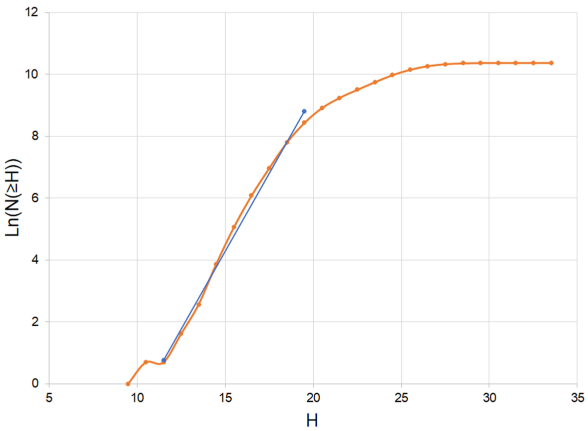

Fig. 1. Test of completeness. The intervals are such that $n \leq H < n+1$, n=9,10,11,...,32. The blue segment shows the range inside which the sample is complete. The color figure can be viewed online.

Disadvantages: The upper limit is going to move to $H > 19$ due to the efforts to complete the sample of all Near Earth Asteroids with $H < 22$ (e.g. Asteroid Day 100X Declaration).

3.4. *Society Risk*

3.4.1. *The Torino Scale*

The Torino scale was created by Binzel in 1995 and adopted in 1999 during a Conference of the International Astronomical Union in Torino, Italy. In 2004, Morrison et al. presented a new version of this scale and a very nice and clear exposition about several risk scales and the importance to communicate the public, in a simple and realistic way, the degree of hazard that an asteroid could present (Morrison et al. 2004). The Torino scale is a numerical scale, graduated in integer values between 0 and 10. Each value considers the impactor kinetic energy and the probability of impact. In the scientific community, it has been considered as an oversimplification of a multi-dimensional problem, but it is a proposal whose aim is to tell people if they must be concerned or not.

Number **0**, in the Torino scale means “No hazard”, **1**, “Normal”, numbers **2**,**3**, and **4**, “Meriting attention”, numbers **5**, **6**, and **7**, “Threatening”, and numbers **8**, **9**, and **10** mean “Certain collisions”. In particular, number **2**, is defined as: “A somewhat close but not highly unusual pass near the Earth meriting attention by astronomers. An actual collision is very unlikely, with no cause for public attention or public concern. New telescopic observations very likely will lead to re-assignment to level 0”. This number in the Torino scale is the greatest number that does not merit public attention (Morrison et al. 2004).

In this context, the proposal is to define meteoroid *as a solid object of size greater than 30 microns, whose Torino scale is* ≤ 2*; namely an object that is not a motive for public concern.*

Advantages of this definition: The physical meaning is simple: an object whose Torino scale is ≤ 2 means that we do not have to be worried about it, “it is only” a meteoroid.

Disadvantages: This does not provides much information about the physical parameters of the object, but the essence of Torino scale is to be a simple way to communicate to the public the importance of a collision with an object; so we must admit that this definition of meteoroid would not be useful to the scientific community.

3.4.2. *The Palermo Scale*

Another scale that assesses the risk of a collision is the Palermo scale. This one not only considers impact energy and probability of impact but also the time until an event occurs. Unlike the Torino scale, this one is not intended for communication with the public, but among astronomers (Chesley et al. 2002). Chesley and co-authors propose a value $\mathcal{P}$ that gives an idea about the impact risk compared to the background hazard that is the “threat from the entire asteroid and comet population averaged over very long time spans”.

$\mathcal{P} > 0$ means that an asteroid at a given time is more threatening that the background hazard. $\mathcal{P} > -2$ implies an event greater than 0 on the Torino scale.

So, in this case, a meteoroid could be defined as *a solid object of size greater than 30 microns with* $\mathcal{P} < -2$.

Advantages of this definition: the lower and upper limits are well defined, and they indicate when an object is, or is not, a public concern.

Disadvantages: The upper limit will have uncertainties due to approximations to their diameters and masses. It is possible that e. g. asteroids can change their value of $\mathcal{P}$ due to better observations.

3.5. *Kinetic Energy and Size*

In the page of the Center for Near Earth Objects Studies there are data for 953 fireballs sensed by US Government sensors from April 15, 1988 to April 15 2023. These data include date/time (UT) of the peak brightness, latitude (deg), longitude (deg), altitude (km), velocity (km/s) and its components, total

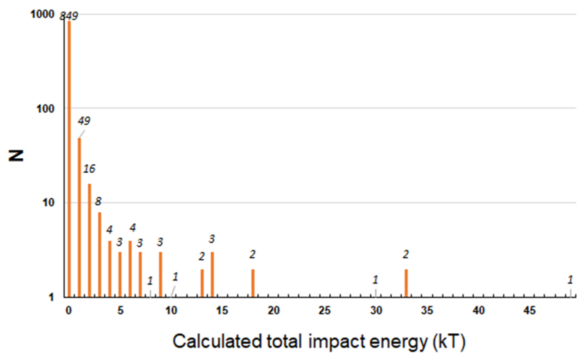

Fig. 2. Energy distribution function. Data from 952 fireballs sensed by the US Government. Figures placed above bars indicate the number of events with an energy, E, such that $n \leq E < n + 1$, n=0,1,2...49. The color figure can be viewed online.

radiated energy (J), and calculated total impact energy (kt) (https://cneos.jpl.nasa.gov/fireballs/). Velocity, when given, refers to the speed of the object before it impacts Earth's atmosphere. The total radiated energy is the integrated energy of the meteor brightness, which is an indicator of the pre-impact kinetic energy of the impactor (Brown et al. 2002). In the introduction of the consulted fireball database, it can be read that the calculated total impact energy is the kinetic energy of the impactor according to a relationship proposed by Brown et al. (2002):

$$\tau = (0.1212 \pm 0.0043)E_0^{0.115\pm0.075}, \qquad (3)$$

where τ is the radiation efficiency, and E_0 is the observed radiation energy. Thus, the initial kinetic energy of the impactor, E, is

$$E = E_0/\tau = 8.2508 E_0^{0.885}. \qquad (4)$$

Although Brown et al. (2002) discuss that equation (3) has several assumptions, like that bolids radiate as black bodies at 6,000 K which can be a poor approximation, Edwards et al. (2006) mention that this approximation is quite consistent with other estimations.

Figure 2 shows the energy distribution of these 952 fireballs (we excluded one with an energy of 440 kt that correspond to the Chelyabinsk event).

According to Korotev (2021), 95.1 % of the falls worldwide are stony meteorites, of which 93.1 % are chondrites, and 93.9 % of these are ordinary chondrites; so, in a first approximation, we can consider that the density of the typical material that falls into the Earth's atmosphere is similar to the mean

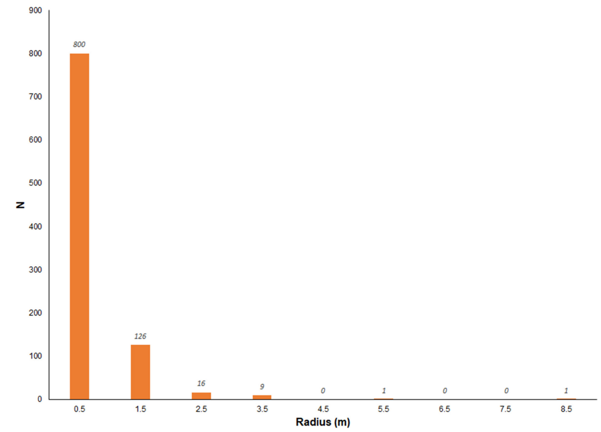

Fig. 3. Radius distribution function. Data from 953 fireballs sensed by the US Government. Figures placed above bars indicate the number of objects with a radius, r, such that $n \leq r < n + 1$, n=0,1,2...,8. The last data with a radius of ≈ 9 m correspond to Chelyabinsk. The color figure can be viewed online.

density of the ordinary chondrites (H, L, LL), i.e. 3.54 g/cm^3 (Britt & Consolmagno 2004).

From previous data, and considering impactors as spheres, we converted the energy distribution function into a size distribution function using the kinetic energy equation and isolating the radius, r:

$$r = \sqrt[3]{\frac{3E}{2\pi\rho v^2}}, \qquad (5)$$

where E is the calculated total impact energy, ρ is the mean density of the ordinary chondrites, and v is the velocity. We used the velocity given in the fireball database, whenever it datum exists (290 out of 953); otherwise, we used a mean velocity of 20.3 km/s (Brown et al. 2002). Thus, we obtained the distribution function given in Figure 3. 99.6 % of the elements of this sample (i.e. almost all of them) have a radius $\leqslant 3.5$ m, so we can define a meteoroid as an object whose diameter is less than 7 m.

Advantages of this definition: (a) It gives lower and upper limits that are independent of the observation instrument; and (b) under this definition, a meteoroid will be a typical object that entries the Earth's atmosphere and that does not represent a risk to people.

In a certain sense, the upper limit that we propose to define a meteoroid is similar to the lower limit proposed by Borovička (2016), because just as he considered the size of the particle as related to the maximum rate of influx of particles into our atmosphere, we are considering the largest size of common objects as the upper limit.

Disadvantages: The upper limit is obtained from two suppositions: a mean density and a mean velocity (in the most of the cases), so it is not very precise; however, we consider that it is a good approximation in round numbers.

4. COMMENTS AND DISCUSSION ABOUT SOME EVENTS

In this section we address some events and discuss them in the light of our definitions.

The Tunguska event occurred on the morning of June 30, 1908, when an object of an asteroidal or cometary nature (Robertson & Mathias 2019), with a radius of between 30 and 50 m (Hills & Goda 1993) or a diameter between 43 and 64 m (Jenniskens et al. 2019) exploded between 6 and 10.5 km above the Podkamennaya Tunguska river and damaged around 2,150 km^2 of Siberian taiga (Farinella et al. 2001). According to several studies, the energy released by the airburst could be between 3 and 50 Mt (Robertson & Mathias 2019; Jenniskens et al. 2019), although some authors mention that the most probable value could be between 10 and 15 Mt (Farinella et al. 2001; Jenniskens et al. 2019). This is the most intense event recorded historically, although there is geological evidence that an airburst and a series of ground impacts occurred near Abt Hureyra, Syria, approximately 12,800 years ago, and that this event may actually have been one of a series of impacts that could have affected an entire terrestrial hemisphere (Moore et al. 2020).

Geological and archaeological evidence indicate that another Tunguska-like event, perhaps even slightly more intense, destroyed the city of Tall el-Hammam, located northeast of the Dead Sea, approximately 3600 years ago (Bunch et al. 2021).

These three events could be classified as 8 or 9 on the Torino scale, but they would definitely not be considered meteoroids, according to the definition proposed in § 3.5.

The Chelyabinsk event, Russia, occurred on February 15, 2013. On this occasion, it is estimated that a rocky body 19.8 ± 4.6 m in diameter entered the Earth's atmosphere with a kinetic energy of 590 ± 50 kT. On this occasion, in the city of Chelyabinsk, some 1,210 people were injured, mainly due to the broken glass from the windows that were ejected (Popova et al. 2013). In this case, due to the energy of the object and its size, it is definitely an asteroid according to any of the proposed definitions, but once its approximate size or energy is known, it is evident that it is an asteroid also according to the definition proposed in § 3.5.

On February 12, 2023, the object 2023 CX1 was discovered, only several hours before it entered the Earth's atmosphere. According to the International Meteor Organization (IMO), this object, of around 1 m, is the 7th one to be discovered before colliding with our planet (https://www.imo.net/imminent-asteroid-entry-over-the-channel/). According to our definition in § 3.5, this object was a meteoroid, i.e. a common cosmic object that additionally was not a cause of concern for the public.

At around 3:50 p.m. on February 10, 2010, near the border between the Mexican states of Puebla and Hidalgo, a cosmic object entered causing great commotion among the population. Many people heard a loud crash, but we only found 12 people who saw it. Thanks to these witnesses we were able to determine that the direction of movement of the object was between west-east and 30° to the northeast (Cordero et al. 2011). Comparing the effects of this event (vibration of windows and the floor, the observation of a fireball and the noise) with the event of Curuça that was more intense (Cordero & Poveda 2011), it is very likely that the object had a size of a few meters at most. On February 22, 2011, a similar event occurred, this time between the states of Zacatecas and Aguascalientes. According to the definition in § 3.5, both events would correspond to a meteoroid. Here it is necessary to remark that some important events have occurred in February. These cases could be at the limit of the size or energy of our last definition, but they could be considered to be meteoroids because they did not represent a real risk for the people, and their energies were much less than Chelyabinsk's.

5. CONCLUSIONS

The objective of this work was to propose a definition for the term meteoroid. To do this, we analysed several criteria, some of them discussed by other authors: Yarkovsky and YORP effects, completeness of NEAs sample, society risk, kinetic energy and size.

As we mentioned before, with these criteria we only analysed the upper limit of the size of a meteoroid which coincided with the lower limit established by the IAU.

In each subsection we proposed a definition and gave advantages and disadvantages of each one.

Beech & Steel (1995), established the upper limit of a meteoroid at 10 m, because objects with sizes smaller than that were difficult to detect, i.e. a meteoroid was an object that telescopes could hardly observe. With this in mind, better telescopes would decrease the upper limit of a meteoroid. Rubin & Grossman (2010) do not clarify explicitly why they adopt 1 m as the upper limit of a meteoroid, but it looks like they considered that our telescopes are able to detect objects as small as this size. Whatever the reason, we consider that if we based the definition on our capacity to detect objects, the definition of a meteoroid would be nonsense in the future. Even now, we consider that the meteoroid definition is rather arbitrary and does not give information about the object.

As it was commented in previous sections, the definitions proposed here have advantages and disadvantages. But we consider that among them there is one that can be useful: *a meteoroid is a solid body that comes from the interplanetary medium and whose diameter is between 30 microns and 7 m.* In other words, meteoroids are objects greater than 30 microns whose entry into the Earth's atmosphere is very common and does not represent a risk to people. This definition is supported by 34 years of observations.

Previous definition do not make clear the nature of the body. It could be an asteroid, comet, planet or even a rocket, a satellite, or a part of them. In this sense, we propose that *a meteoroid is a natural solid body, that comes from interplanetary medium and whose diameter is between 30 microns and 7 m.* Rockets, artificial satellites or their remains could be named *artificial objects*, in general, no matter their sizes or materials. We are aware that to distinguish between natural and artificial bodies is not always possible, but the latter do not have the same size distribution function as the former, so they do not necessarily can be described in the same manner. Thus, they do not enter in the proposed definition.

All the authors would like to thank an anonymous reviewer because his/her comments improved this manuscript.

REFERENCES

Beech, M. & Steel, D. 1995, QJRAS, 36, 281

Berg, O. E. & Grün, E. 1973, Space Research, 2, 1047

Borovička, J. 2016, JIMO, 44, 31

Bottke, W. F., Vokrouhlický, Jr. D., Rubincam, D. P., & Nesvorný, D. 2006, AREPS, 34, 157, https://doi.org/10.1146/annurev.earth.34.031405/125154

Britt, D. T. & Consolmagno, G. J. 2004, LPI, 35, 2108

Bronshten, V. A. 1981, Physics of Meteoric Phenomena (Dordrecht Reidl)

Brown, P., Spalding, R. E., ReVelle, D. O., Tagliaferri, E., & Worden, S. P. 2002, Natur, 420, 294, https://doi.org/10.1038/nature01238

Brownlee, D. E. 1985, AREPS, 13, 147, https://doi.org/10.1146/annurev.ea.13.050105.001051

Bunch, T. E., LeCompte, M. A., Adedeji, A. V., Wittke, J. H. et al. 2021, NatSR, 11, 18632

Burbine. T. H. 2017, Asteroids: Astronomical and Geological Bodies (Cambridge, UK: CUP), https://doi.org/10.1017/9781316156582

Burns, J. A., Lamy, P., & Soter, S. 1979, Icar, 40, 1, https://doi.org/10.1016/0019-1035(79)90050-2

Chesley S. R., Chodas, P. W., Milani, A., Valsecchi, G. B. & Yeomans, D. K. 2002, Icar, 159, 423, https://doi.org/10.1006/icar.2002.6910

Chesley, S. R., Ostro, S. J., Vokrouhlický, C. D., et al. 2003, Sci, 302, 1739, https://doi.org/10.1126/science.1091452

Cohen E. 1894, Meteoritenkunde (Stuttgart: Koch)

Cordero, G., Cervantes de la Cruz, K. & Gómez, E. 2011, Geof Int, 50, 77

Cordero, G. & Poveda, A. 2011, P&SS, 59, 10, https://doi.org/10.1016/j.pss.2010.10.012

Craig, J. 1849, A new universal etymological, technological and pronouncing dictionary of the English language embracing all terms used in art, science, and literature (London: H. G. Collins)

Dohnanyi, J. S. 1973, IAU 13, Evolutionary and Physical Properties of Meteroids, ed. C. L. Hemenway, P. M. Millman, & A. F. Cook, 363

Edwards, W. N., Brown, P. G., & Revelle, D. O. 2006, JASTP, 68, 1136, https://doi.org/10.1016/j.jastp.2006.02.010

Farinella, P., Foschini, L., Froeschlé, Ch., et al. 2001, A&A, 377, 1081, https://doi.org/10.1051/0004-6361:20011054

Farnocchia, D., Chesley, S. R., Takahashi, Y., et al. 2021, Icar, 369, 114594, https://doi.org/10.1016/j.icarus.2021.114594

Farrington O. C. 1915, Meteorites. Their structure, composition, and terrestrial relations (Chicago: Published by the Author)

Fenucci, M. & Novaković, B. 2021, AJ, 162, 227, https://doi.org/10.3847/1538-3881/ac2902

Golubov, O. & Scheeres, D. J. 2019, AJ, 157, 105, https://doi.org/10.3847/1538-3881/aafd2c

Gomes, C. B. & Keil, K. 1980, Brazilian stone meteorites: with a brief, general introduction on the significance, classification, mineralogy, bulk composition, and recognition of stone meteorites (Albuquerque, NM: University of New Mexico Press)

Greenberg, A. H., Margot, J. -L., Verma, A. K., Taylor, P. A., & Hodge, S. E. 2020, AJ, 159, 92, https://doi.org/10.3847/1538-3881/ab62a3

Grieve, R. A. F. & Shoemaker, E. M. 1994, in Hazards due to comets and asteroids ed. T. Gehrels, M. S. Matthews, & A. Schumann, (Tucson: UAP)

Herschel, W. 1802, RSPT, 92, 213

Hills, J. G. & Goda, P. 1993, AJ, 105, 1114, https://doi.org/10.1086/116499

Jenniskens, P., Popova, O. P., Glazachev, D. O., Podobnaya, E. D., & Kartashova, A. P. 2019, Icar, 327, 4, https://doi.org/10.1016/j.icarus.2019.01.001

Korotev, R. L. 2021, Meteorite statistics, https://sites.wustl.edu/meteoritesite/items/some-meteorite-statistics/

Kresák, L. 1976, BAICz, 27, 35

Krot, A. N., Keil K., Goodrich C. A., Scott E. R. D., & Weisberg M. K. 2003, in Treatise on Geochemistry, ed. A. M. Davis, H. D. Holland, Elsevier, 83, https://doi.org/10.1016/B0-08-043751-6/01062-8

Krüger, H. & Grün, E. 2014, in Encyclopedia of the Solar System, ed. T. Spohn, D. Breuer & T. V. Johnson, (Elsevier)

Lasue, J., Levasseur-Regourd, A.- Ch., & Renard, J. B. 2020, P&SS, 190, 104973, https://doi.org/10.1016/j.pss.2020.104973

Levasseur-Regourd, A.- Ch., Renard, J. B., & Dumont, R. 1991, AdSpR, 11, 175, https://doi.org/10.1016/0273-1177(91)90560-7

Mann, I. 2009, in Small Bodies in Planetary Systems, ed. I. Mann, A. M. Nakamura, & T. Mukai (Springer-Verlag)

Mann, I., Meyer-Vernet, N., & Czechowski, A. 2014, PhR, 536, 1, https://doi.org/10.1016/j.physrep.2013.11.001

Mason, B. 1962, Meteorites (New York, NY: Wiley)

Marvin, U. B. 1996, M&PS, 31, 545, https://doi.org/10.1111/j.1945-5100.1996.tb02031.x

McSween, H. Y. 1987, Meteorites and their parent planets, (Cambridge, MA: CUP)

Mignard, F. 1984, in Planetary Rings, ed. R. Greenberg & A. Brahic (Tuczon, AZ: UAP)

Millman, P. M. 1961, JRASC, 55, 137

Moore, A. M. T., Kennett, J. P., Napier, W. M., et al. 2020, NatSR, 10, 4185, https://doi.org/10.1038/s41598-020-60867-w

Morbidelli, A. & Vokrouhlický, D. 2003, Icar, 163, 120, https://doi.org/10.1016/S0019-1035(03)00047-2

Morrison, D. et al. 2004, in Mitigation of hazardous comets and asteroids, ed. M. Belton, T. H. Morgan, N. Samarasinha, & D. K. Yeomans (UK: CUP)

Newton, H. A. 1865, AmJS, 39, 193, https://doi.org/10.2475/ajs.s2-39.116.193

Nininger, H. H. 1933, Our stone-pelted planet (Boston, MA: Houghton Mifflin)

Popova, O. P. Jenniskens, P., Emel'yanenko, V. et al. 2013, Sci, 342, 1069, https://doi.org/10.1126/science1242642

Robertson, D. K. & Mathias, D. L. 2019, Icar, 327, 36, https://doi.org/10.1016/j.icarus.2018.10.017

Rubin, A. E. & Grossman, J. N. 2010, M&PS, 45, 114, https://doi.org/10.1111/j.1945-5100.2009.01009.x

Vokrouhlický, D., Bottke, W. F., Chesley, S. R., Scheeres, D. J., & Statier, J. S. 2015, in Asteroids IV, ed. P. Michel, F. E. DeMeo, & W. F. Bottke (Tuczon, AR: UAP)

Warner, B. D. & Harris, A. W. 2011, Icar, 216, 610, https://doi.org/10.1016/j.icarus.2011.10.007

Wehry, A. & Mann, I. 1999, A&A, 341, 296

Williams, I. P. 2002, in Meteors in the Earth's Atmosphere, ed. I. Mann, A. M. Nakamura, & T. Mukai (Springer-Verlag)

Williams, I. P. 2011, A&G, 52, 20, https://doi.org/10.1111/j.1468-4004.2011.52220.x

Wyatt, M. C. 2009, In *Small bodies in planetary systems* Eds. I. Mann, A. M. Nakamura & T. Mukai (Springer-Verlag)

Yang, H.-J., Park, Ch., & Park, M.-G. 2005, Icar, 175, 215, https://doi.org/10.1016/j.icarus.2004.10.007

Zegmott, T. J., Lowry, S. C., Rozek, A., et al. 2021, MNRAS, 507, 4914, https://doi.org/10.1093/mnras/stab2476

Zook, H. A. & Berg, O. E. 1975, P&SS, 23, 183, https://doi.org/10.1016/0032-0633(75)90078-1

Guadalupe Cordero-Tercero and D. Maravilla: Instituto de Geofísica, Universidad Nacional Autónoma de México, Circuito exterior Ciudad Universitaria. Coyoacán (gcordero@igeofisica.unam.mx).

M. Covarrubias-Saavedra: Secretaría de Educación Pública, México.

Revista Mexicana de Astronomía y Astrofísica, **59**, 323–326 (2023)

https://doi.org/10.22201/ia.01851101p.2023.59.02.11

A PECULIAR GALAXY NEAR M104

E. Quiroga[1]

Received April 24 2023; accepted July 3 2023

ABSTRACT

Messier 104, NGC 4594, also known as the Sombrero Galaxy, has been extensively studied, especially its structure and stellar halo. Its abundance of globular clusters has given rise to many theories and much speculation. However, other objects in the vicinity of such a spectacular galaxy are sometimes ignored. While studying HST images available on the HST Legacy website of the halo of M104 (HST proposal 9714, PI: Keith Noll), the author observed at 12:40:07.829 -11:36:47.38 (in j2000) an object about 4 arc seconds in diameter. A study with VO tools suggests that the object is a SBc galaxy with an AGN (Seyfert).

RESUMEN

Messier 104, NGC 4594, conocida como la Galaxia del Sombrero, ha sido extensamente estudiada, especialmente su estructura y halo estelar. La abundancia de cúmulos globulares que presenta ha dado lugar a muchas teorías y especulaciones. Sin embargo, otros objetos en las cercanías de una galaxia tan espectacular a veces son pasados por alto. Mientras estudiaba las imágenes del HST disponibles en el sitio web HST Legacy del halo de M104 (propuesta HST 9714, investigador principal: Keith Noll), el autor observó en las coordenadas 12:40:07.829 -11:36:47.38 (en j2000) un objeto de aproximadamente 4 segundos de arco de diámetro. Un estudio con herramientas de VO sugiere que el objeto es una galaxia SBc con un AGN (Seyfert).

Key Words: catalogues — galaxies: peculiar — galaxies: spiral — virtual observatory tools

METHODS AND DISCUSSION

The author, studying Hubble Space Telescope (HST) images of M104 available on the HST Legacy website (HST proposals 9714, PI: K. Noll, and 13364, PI: D. Calzetti), observed at coordinates 12:40:07.829 -11:36:47.38 an object located in the halo of the galaxy, about 4 arc seconds in diameter. It is catalogued by Simbad as a Globular Cluster Candidate. The Nasa/IPAC Extragalactic Database (NED)[2] shows its classification as an IrS (Infrared Source), not as a galaxy, with an available spectral energy distribution (SED) plot. A search of the Pan-STARRS1 data archive returns objName PSO J190.0326-11.6132, which in VizieR shows a more complete SED plot [3] with data from 5 catalogues: PAN-STARRS PS1, SDSSz, 2MASSJ, Spitzer:IRAC3.6 and VISTA:Z. After a new search in NED, the object in region #710, SSTSL2 J124007.83-113647.1, seems to be the one.

The author has compared the object's SED plot with those of spiral galaxy models in Optical-NIR-MIR (Nicole 2012), and the object's NED plot points fit quite well.

HST Legacy has some images taken with the 435 and 555 filters, which are equivalent to B, V and R filters. So the bandwidth is from B to NIR. The results of an RGB of the images in Aladin Sky Atlas, (Figure 1b) show (limited by the resolution) a galactic centre and a central bar with reddish hues (555 filter, R of the Wide Field and Planetary Camera 2 [WFPC2]) and a blue ring around it (435 filter, $B+V$ of the Advanced Camera for Surveys [ACS]).

[1]Universidad del Atlántico Medio, Facultad de Comunicación, Canary Islands, Spain.

[2]https://ned.ipac.caltech.edu/byname?objname=SSTSL2+J124007.83-113647.1&hconst=67.8&omegam=0.308&omegav=0.692&wmap=4&corr_z=1

[3]http://vizier.cds.unistra.fr/vizier/sed/?-c=12+40+07.83277+-11+36+47.0442&c.rs=5.0

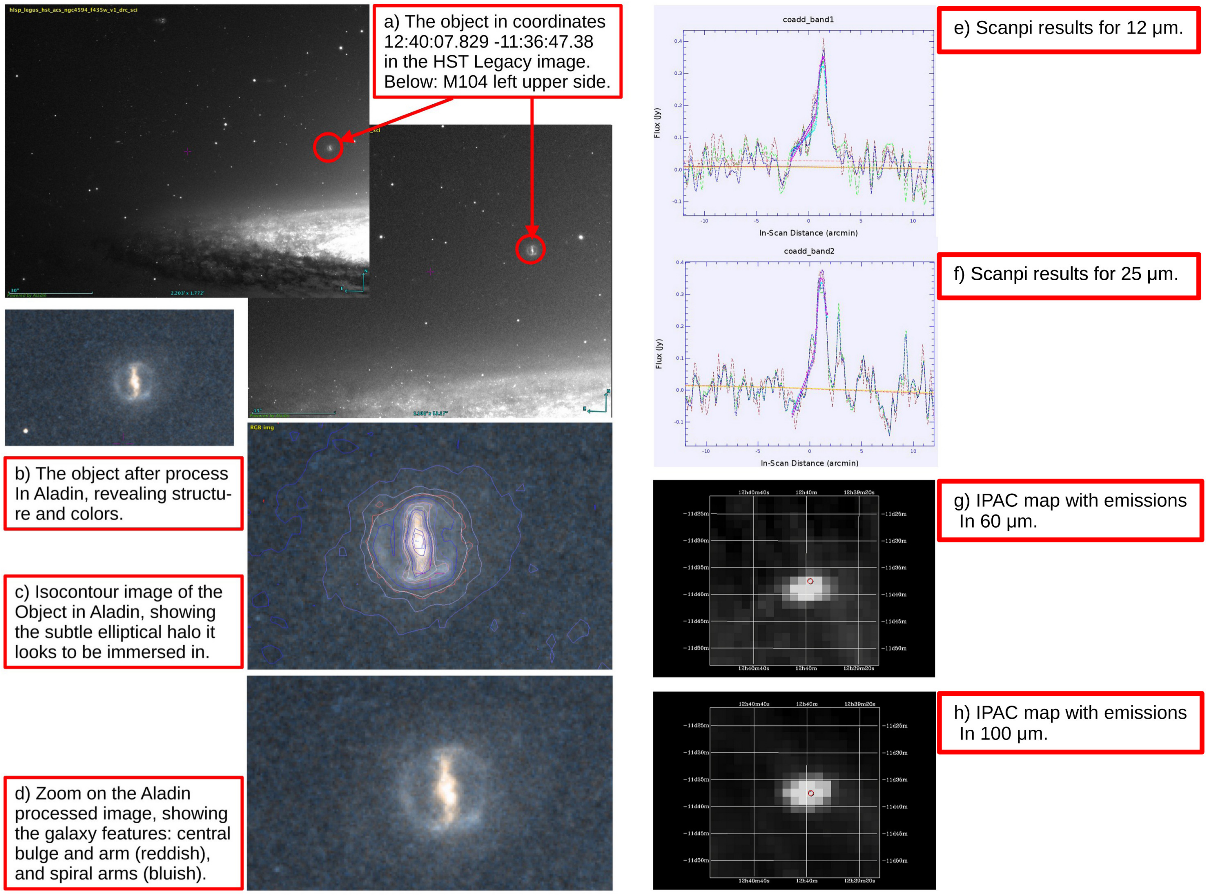

Fig. 1. The adjusted and zoomed RGB of the object in Simbad (a, b, c), the Scanpi results for 12 micrometers (d) and for 25 micrometers (e), and the IPAC map with emissions at 60 (f) and 100 micrometers (h) in the halo area shown in b.

This may suggest a central region of cool, old stars and two possible spiral arms with star-forming regions.

In addition, the approximately circular object (which appears to be face-on) has a subtle elliptical halo twice its size (Figure 1c), possibly a feature of the PSF due to the low signal-to-noise ratio in the area. The author obtained an IPAC map (with data from the Spitzer Space Telescope, Wide-field Infrared Survey Explorer WISE) showing emissions at 60 and 100 micrometers, within an approximate radius of 7 arc seconds around the coordinates of the object (Figures 1g and 1h), which is 4 arc seconds wide; it shows that the halo has an infrared emission, which is not a feature of the PSF. In Figure 1e, Scanpi results for the object show a flux gap at 12 micrometers (silicate absorption feature), which may be indicative of an AGN Seyfert galaxy (Köhler & Li 2010, Hao et al. 2007). Also shown in Figure 1f are the Scanpi results at 25 micrometers, which show a peak. The 25 micrometers emission is a good measure of AGN luminosity (Severgnini et al. 2012). The WISE satellite offers a spatial resolution of approximately 6 arcsec [4] while Spitzer provides about 2 arcsec [5], so it is probable that the origin of the infrared emission is the galaxy, not the halo.

The silicate absorption feature may indicate that this galaxy once hosted massive stars (type O or B) capable of burning silicon in their final stages (Vollmer et al 2008). Supernova explosions may also have created a silicon-rich interstellar medium around the galaxy's core (Woosley, 2005).

In terms of redshift and angular size, Simbad[6] gives us a radial velocity for the object of 1359 km/s and a $z = 0.004545 \pm 0.000027$. M104 has a

[4] `https://wise2.ipac.caltech.edu/docs/release/allsky/`

[5] https://lweb.cfa.harvard.edu/~mmarengo/me/irac.html

[6] http://simbad.cds.unistra.fr/simbad/sim-id?Ident=%4012370942&Name=PSO%20J190.0301-11.6124&submit=submit

$z = 0.003416$, so these data should be taken with the necessary caution. The measured redshift of a galaxy results from a combination of the cosmological redshift due to the expansion of the Universe and a Doppler shift due to the peculiar motions of the galaxy, and it is widely accepted that for galaxy collections, if the difference in redshift corresponds to a velocity difference below 500 km/s, or 1000 km/s for clusters, one cannot affirm with certainty that the objects are gravitationally unbound (Capelato et al. 1991). In this case the velocity difference is about 300 km/s. The author cannot confirm that the object is not gravitationally bound to M104, so it could be a satellite of the Sombrero galaxy with an angular size around 0.3 kpc.

As an alternative scenario, assuming the object is not associated with M104, it could be located at 20 Mpc ($H0 = 67.04$, $\Omega m = 0.3183$ and $\Omega\Lambda = 0.6817$) with an angular size ≈ 22 Kpc, i.e. two thirds the size of the Milky Way. The object has a Fe/H metallicity of -0.309 dex (Alves-Brito et al. 2011), a relatively low value (metal-poor). Finally, there is an entry in HEASARC [7] from the CXOGSGSRC table of the CHANDRA observatory database for the object at coordinates 12 40 06.24−11 36 47.7 with an X-ray flux emission of 2.410×10^{-15} erg/cm^2/s, i.e. an X-ray luminosity of $L_X \approx 1.80 \times 10^{43}$ erg/s; assuming the alternative scenario with a distance of 20 Mpc; such a luminosity may indicate an active galactic nucleus (AGN), which is in the range observed for Seyfert galaxies (Panessa et al. 2006). Further studies would be needed to determine whether this is a Type 1 or Type 2 AGN.

CONCLUSIONS

The author has recognized an object (erroneously catalogued by Simbad as a Globular Cluster Candidate) as an SBc AGN Seyfert galaxy, $z = 0.004545 \pm 0.000027$, using VO tools. The Aladin Sky Atlas RGB suggests an SBc galaxy with a dominant central arm, a nucleus, and possibly two spiral arms with hot young stars and dust. VizieR and NED SED plots are consistent with a spiral galaxy. The object has a subtle elliptical halo twice the size of the central object, almost unnoticeable in the visible, with far-infrared emission in a radius of 7 arc seconds. Scanpi results at 12 micrometers show a silicate absorption feature and a peak at 25 micrometers suggests a possible AGN. The object has an X-ray emission luminosity of $L_X \approx 1.80 \times 10^{43}$ erg/s assuming a distance of 20 Mpc, suggesting a possible Seyfert galaxy in the AGN Unification Model (Singh et al. 2011).

The author recommends adding the object to the "Galaxy" category, especially in public catalogues such as NED or Simbad, where it is still classified as an "Infrared Source" or "Globular Cluster Candidate". The author proposes that it be named The Iris Galaxy.

[7] bit.ly/46x1yrJ

Thanks to Adrian B. Lucy in the Space Telescope Science Institute for his kind help. Thanks to Alex Fraser for the English revision. Thanks to Agustin Trujillo (ULPGC) for the LaTeX translation help.

This research has made use of the Aladin Sky Atlas developed at CDS, Strasbourg Observatory, France, the NASA/IPAC Extragalactic Database (NED), the VizieR catalogue access tool, the Pan-STARRS1 Surveys (PS1), the Two Micron All Sky Survey (2MASS), the SDSS catalogue, the SIMBAD astronomical database, the European Space Agency (ESA) Gaia mission, and the Chandra X-Ray Center (CXC), operated for NASA by the Smithsonian Astrophysical Observatory. This research is based on observations made with the NASA/ESA Hubble Space Telescope obtained from the Space Telescope Science Institute.

This research has made use of the NASA/IPAC Infrared Science Archive, which is funded by the National Aeronautics and Space Administration and operated by the California Institute of Technology.

DATA AVAILABILITY STATEMENT

VO tables for the VizieR and NED SEDs plus data in Simbad and Heasarc are in the footnote links.

The short link for HEASARC stays for the url: `https://heasarc.gsfc.nasa.gov/db-perl/W3Browse/w3hdprods.pl?files=P&Target=heasarc%5Fxray%20%7C%7C%7C%5F%5Frow%3D1386796%7C%7C&Coordinates=Equatorial&Equinox=2000.`

REFERENCES

Alves-Brito, A., Hau, G. K. T., Forbes, D. A., 2011, MNRAS, 417, 1823, https://doi.org/10.1111/j.1365-2966.2011.19368.x

Capelato, H. V., Mazure, A., Proust, D., et al. 1991, A&AS, 90, 355

Ford, H. C., Hui, X. Ciardullo, R., Jacoby, G. H., & Freeman, K. C. 1996, ApJ, 458, 455, https://doi.org/10.1086/176828

Köhler, M. & Li, A. 2010, MNRAS, 406, 6, https://doi.org/10.1111/j.1745-3933.2010.00870.x

Noll, K. 2002. HST Proposal, 9714

Panessa, F., Bassani, L., Cappi, M., et al. 2006, A&A, 455, 173, https://doi.org/10.1051/0004-6361:20064894

Severgnini, P., Caccianiga, A., & Della Ceca, R. 2012, A&A, 542, 46, https://doi.org/10.1051/0004-6361/201118417

Singh, V., Shastri, P., & Risaliti, G. 2011, A&A, 532, 84, https://doi.org/10.1051/0004-6361/201016387

Spoon, H. W. W., Marshall, J. A., Houck, J. R., et al. 2006, ApJ, 654, 49, https://doi.org/10.1086/511268

Vollmer, C., Hoppe, P., & Brenker, F. E. 2008, ApJ, 684, 611, https://doi.org/10.1086/589913

Woosley, S. & Janka, T. 2005, NatPh, 1, 147, https://doi.org/10.1038/nphys172

Elio Quiroga Rodríguez: Lecturer, Universidad del Atlántico Medio, Facultad de Comunicación, Ctra. de Quilmes, 37, 35017 Tafira Baja, Gran Canaria, Islas Canarias, España (elio.quiroga@pdi.atlanticomedio.es).

Revista Mexicana de Astronomía y Astrofísica, **59**, 327–343 (2023)

https://doi.org/10.22201/ia.01851101p.2023.59.02.12

THE 2023 RELEASE OF Cloudy

Marios Chatzikos[1], Stefano Bianchi[2], Francesco Camilloni[3], Priyanka Chakraborty[4], Chamani M. Gunasekera[1], Francisco Guzmán[1,5], Jonathan S. Milby[6], Arnab Sarkar[7], Gargi Shaw[8], Peter A. M. van Hoof[9], and Gary J. Ferland[1]

Received July 27 2023; accepted August 7 2023

ABSTRACT

We describe the 2023 release of the spectral synthesis code Cloudy. Since the previous major release, migrations of our online services motivated us to adopt `git` as our version control system. This change alone led us to adopt an annual release scheme, accompanied by a short release paper, the present being the inaugural. Significant changes to our atomic and molecular data have improved the accuracy of Cloudy predictions: we have upgraded our instance of the Chianti database from version 7 to 10; our H- and He-like collisional rates to improved theoretical values; our molecular data to the most recent LAMDA database, and several chemical reaction rates to their most recent UDfA and KiDA values. Finally, we describe our progress on upgrading Cloudy's capabilities to meet the requirements of the X-ray microcalorimeters aboard the upcoming *XRISM* and *Athena* missions, and outline future developments that will make Cloudy of use to the X-ray community.

RESUMEN

Se describe el lanzamiento de la version 2023 del código de síntesis espectral Cloudy. La migración de nuestros servicios *online* motivó la adopción de `git` como nuevo sistema de control de versiones. Este cambio condujo a un plan de lanzamientos anuales, acompañados de un artículo breve, comenzando por el presente. Cambios significativos en los datos atómicos y moleculares mejoran la exactitud de las predicciones de Cloudy mediante las actualizaciones de la base de datos de Chianti de la versión 7 a la 10, las transiciones colisionales en iones de uno y dos electrones, los datos moleculares a la versión más reciente de la base de datos LAMBDA y varias constantes de reacción moleculares a los valores de UDfA y KiDA más recientes. Finalmente, se describe el proceso de adaptación de Cloudy a los requisitos de los microcalorímetros a bordo de las misiones *XRISM* y *Athena* y el progreso para hacer Cloudy útil para la comunidad de astrofísica de rayos X.

Key Words: atomic data — galaxies: active — globular clusters: general — molecular data — software: development

1. INTRODUCTION

Cloudy is an *ab initio* spectral synthesis code for astrophysical plasmas ranging from far from equilibrium to local thermodynamic equilibrium (LTE) and strict thermodynamic equilibrium (STE). Development started in 1978, and has been ongoing since then, with each new release extending the physical systems the code can model. Previous review papers capture the state of the code at that time, namely, Ferland et al. (1998), Ferland et al. (2013) and Fer-

[1]Physics & Astronomy, University of Kentucky, Lexington, Kentucky, USA.

[2]Dipartimento di Matematica e Fisica, Università degli Studi Roma Tre, via della Vasca Navale 84, 00146 Roma, Italy.

[3]Max-Planck-Institut für extraterrestrische Physik, Giessenbachstraße, 85748 Garching, Germany.

[4]Center for Astrophysics | Harvard & Smithsonian, Cambridge, MA, USA.

[5]Now at Physics & Astronomy, University of North Georgia, Dahlonega, Georgia, USA.

[6]Arts & Sciences Hive, University of Kentucky, Lexington, Kentucky, USA.

[7]Kavli Institute for Astrophysics and Space Research, Massachusetts Institute of Technology, 70 Vassar St, Cambridge, MA, USA.

[8]Department of Astronomy and Astrophysics, Tata Institute of Fundamental Research, Mumbai 400005, India.

[9]Royal Observatory of Belgium, Ringlaan 3, 1180 Brussels, Belgium.

land et al. (2017). Much of the physics is discussed in Osterbrock & Ferland (2006).

In the past, we aimed to release code only following major changes to the source code and our quantum physics data. The underlying principle had been to deliver our users with a product that would have maximal impact on their research. A consequence of this policy had been infrequent releases, with only seven (7) taking place in the period 1998-2017. The 2006-2010 releases (C06, C07, C08, and C10) were not accompanied by a review paper, which may have left some users wondering how significant the changes in each new version were. Subsequent releases were accompanied by a major review article of Cloudy's capabilities, which further delayed each release. In this dilemma, we had contemplated if a better release policy might be pursued.

The changes described in § 2 were the impetus we needed to adopt a new release policy. This has essentially been enabled by transitioning to the `git` version control system, which makes branch updates trivial, and eases the process of bringing them back into the mainline of the code. With this in place, we are now able to implement our previous aspirations: annual code releases, each accompanied by a lightweight *release* paper.

The present describes the 2023 release of Cloudy (C23), a major update to C17 in terms of atomic data, and it is structured as follows. § 2 describes the major changes that the project has undergone these past few years. § 3 and § 4 describe changes to our atomic and molecular data. § 5 outlines recent improvements to our treatment of grains. § 6 presents a summary of improvements to Cloudy's X-ray capabilities. § 7 and § 8 deal with other improvements and new SEDS in Cloudy, respectively. § 9 describes changes to Cloudy infrastructure, including commands. Finally, § 10 discusses current development efforts that should be released in the next few years, as well as our aspirations for future development.

2. ONLINE MIGRATION

Fundamental changes to our infrastructure have occurred in the last few years, most of them happening in Fall of 2019 and Fall of 2020. First, we were forced to move our user forum to a new website. Then, in Fall 2020, our project was forced to vacate the servers that hosted `https://www.nublado.org`, due to policy changes following the acquisition of the host company by a third party. The University of Kentucky has hosted our server since then. The migration to a new server allowed us to migrate to a more modern control system, as well, namely `git`. As described below, one of us (JM) carried out the Fall 2020 migration.

2.1. *Migration of nublado.org*

There were few (if any) viable options for migrating the entire project to a new host without significant manual intervention. That being the case, it was decided that this was an opportunity to migrate Cloudy to more modern and flexible version control and tooling. Trac[10] is rather dated at this point. It has not seen a significant update in many years, and it is built on Python 2.x, which is no longer being developed or supported. Subversion[11] (SVN) is still actively maintained, but many development projects have moved to using Git, which has a larger community of users and developers. After reviewing options for Git project hosting, it was ultimately decided to use GitLab[12] hosted at UK for the Cloudy source code, issue tracker, and wiki. GitLab offers a free, open-source edition and provides free access to their licensed features and support services for open-source research software.

Migrating the existing data to GitLab in its entirety would be a difficult task. The existing SVN repository contained several decades of revision history, and the Trac interface held a large number of wiki articles and issue data. It was decided that the existing code revision history would not be migrated to Git. Instead, there would be an initial commit in the Git repository containing a reference to the Subversion repository for historical purposes. This greatly simplified the migration process. Issue data and wiki pages were migrated to GitLab using TracBoat[13]. This tool provided a very basic semi-automated migration but did not preserve all aspects of the content. In particular, wiki links were removed and had to be re-added manually.

The existing Trac site and Subversion repository were migrated to a new system at UK for historical reference purposes. They were configured as read-only, and the default destination for project links is redirected to the GitLab instance. Static files, including data sets, were also migrated and continue to be available and updated as needed.

2.2. *User Forum Migration*

A forum where Cloudy users can post questions or report problems has been available since

[10] `https://trac.edgewall.org/`
[11] `https://subversion.apache.org/`
[12] `https://about.gitlab.com/`
[13] `https://github.com/tracboat/tracboat`

June 2005. It had been hosted on `yahoo.com` until Fall 2019, when the company decided to withdraw support for groups. A key requirement for choosing a new host was to preserve the history of questions and answers posted on `yahoo.com`. `groups.io` met our needs, and the forum migrated to `https://cloudyastrophysics.groups.io`.

The new platform has allowed for more versatility. Our new setup now features a `Main` group, which preserves and extends our Q&A service. It also carries an `Announcements` group, where important announcements, e.g., about CLOUDY workshops, are made; a `Code` group, where users can share scripts with other users; and finally a `Results` group, where users can share results obtained using CLOUDY with the broader community. Users are encouraged to subscribe to all these groups.

3. ATOMIC PHYSICS

3.1. *Upgrade to Chianti Version 10*

CLOUDY has now adopted Chianti version 10.0.1. Previously, the code had been using version 7.1, released in 2013. The difficulty with upgrading earlier has been due to the changes the database format since v7.1. To remedy this, we developed a script to reprocess the version 10 data into the version 7 format. A detailed discussion of the script and changes to spectral line predictions as a result of the new database is presented in Gunasekera et al. (2022a). The reprocessing script has been made open-source and is available at `https://gitlab.nublado.org/arrack`.

Due to the large number of additional atomic levels in version 10, the full reprocessed Chianti database is >15 times the size of version 7. Since many of these levels are above the ionization limit of the corresponding species, we have omitted all auto-ionizing levels from the default version utilized by CLOUDY. Both the full reprocessed v10 database and the one without the auto-ionizing levels can be downloaded from `http://data.nublado.org/chianti/`.

3.2. *Updates to the Stout Database*

The format of the Stout (Lykins et al. 2015) data files has been updated[14]. The most important change is that the spectroscopic information must now be enclosed in double quotes in the `*.nrg` files. This makes it easier for the code to extract this information, which is now included in the **save line labels** output. Also, the keywords in the `*.coll` files have been updated to make parsing easier. The new format is designated by the magic number "17 09 05".

The Stout database now supports having multiple atomic or molecular datasets for a given species. This is necessary because it is not always possible to unequivocally decide which calculation is the better one. In such a case, one of these datasets will be designated as the default set, but the user has the option to switch to a different set using the new option to the **species** command. For example, in the command **species "Fe+6" dataset="alt"**, `alt` is the nickname for the alternate dataset; CLOUDY will use the data in the `Fe_7_alt.*` for this species.

Fe III collision strengths are updated to Badnell & Ballance (2014). We had previously used data from Zhang (1996). Energies are from NIST with missing levels taken from Badnell & Ballance (2014). Laha et al. (2017) describe how the data were matched to experimental energies. Tests show that the total Fe III cooling increases by nearly 50%.

Certain "baseline" models (i.e., models without accurate collisions, see Ferland et al. 2017) in the Stout database have been updated to use collisional, transition probability, and energy data from the ADAS database. NIST energies are employed for the lowest excited levels, to permit the correct identification of spectral lines of astronomical interest. The species that have been updated include Mg^{+9} (Liang & Badnell 2011), Al^{+2} (Liang et al. 2009), and S^{+4} (Fernández-Menchero et al. 2014).

3.3. *Fe II*

The Fe II ion has a complex structure with 25 electrons, and is a "grand challenge" problem in atomic physics. An accurate set of radiative and collisional atomic data is therefore needed to treat selective excitation, continuum pumping, and fluorescence, which are known to be crucial for the Fe II emission (e.g., Verner et al. 2000; Baldwin et al. 2004; Bruhweiler & Verner 2008; Jin et al. 2012; Wang et al. 2016; Netzer 2020). Uncertainties in the atomic data have been a longstanding limitation in interpreting line intensities.

Until recently, CLOUDY shipped with the Verner et al. (1999) model, which has 371 levels that reach 11.6 eV, has about 68,000 transition probabilities, but uses the "g-bar" approximation for collision strengths. Due to its limitations, Sarkar et al. (2021) explored three other atomic models, that are now available with CLOUDY; their energy levels are compared in Figure 1.

Of relevance to the 2000–3000Å ultraviolet range are the datasets of Tayal & Zatsarinny (2018) and

[14] For a full description of the new format see `https://gitlab.nublado.org/cloudy/cloudy/-/wikis/StoutData`.

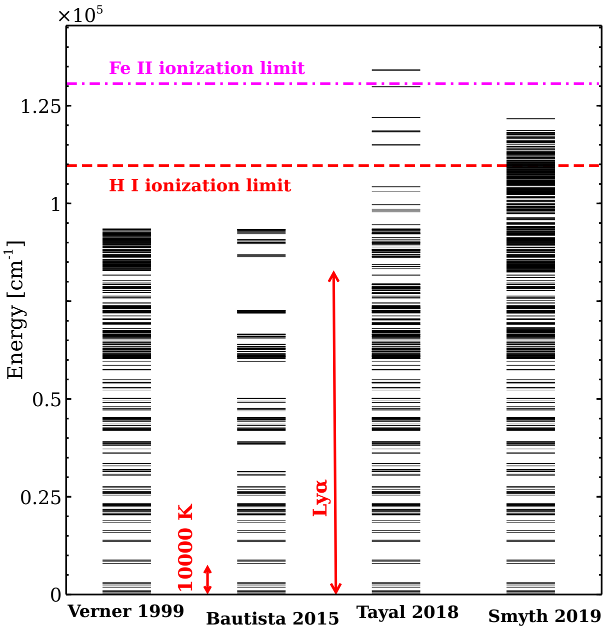

Fig. 1. Energy level structure of the Fe II models available with CLOUDY. From left to right, the atomic datasets are those of Verner et al. (1999), Bautista et al. (2015), Tayal & Zatsarinny (2018), and Smyth et al. (2019). The H I and Fe II ionization limits, the Lyα energy, an important source of photoexcitation for Fe II, and the thermal energy corresponding to 10^4 K are also indicated. Adapted from Sarkar et al. (2021). The color figure can be viewed online.

Smyth et al. (2019). The Tayal & Zatsarinny (2018) model has 340 energy levels with the highest energy of $\approx$ 16.6 eV, that is, it goes above the ionization limit (16.2 eV). However, its density of states in high-lying energy levels is low, as shown in Figure 1. Transitions between these energy levels produce about 58,000 emission lines with uncertainties in transition probabilities of $\lesssim 30\%$ (in the 2200Å–7800Å). On the other hand, the Smyth et al. (2019) model includes 716 levels in the close coupling (scattering model) calculation, with the highest energy level reaching 26.4 eV. These levels produce about 256,000 emission lines. The Smyth et al. (2019) dataset also contains autoionizing levels, but its density of states in the high-lying energy states is larger than the Tayal & Zatsarinny (2018) dataset. Further details on these atomic models can be found in Sarkar et al. (2021). Both models have been incorporated into CLOUDY.

Sarkar et al. (2021) showed that with the Smyth et al. (2019) dataset, CLOUDY produces a spectrum that is in satisfactory agreement with the template spectrum of the I Zw 1 Seyfert galaxy (Vestergaard & Wilkes 2001). Briefly, the better agreement of the

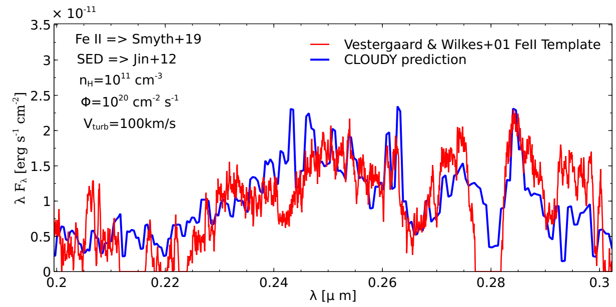

Fig. 2. Comparison between the observed Fe II UV template of Vestergaard & Wilkes (2001) and the CLOUDY predicted Fe II UV spectrum with $V_{\rm turb}$ = 100 km/s. The color figure can be viewed online.

Smyth dataset is due to the higher density of highly excited states, which enhance the effects of continuum fluorescence and lead to brighter emission lines at short wavelengths. Further details are described in the paper. Figure 2 illustrates the quality of that comparison.

3.4. *Kα Energies*

We incorporated precise H-like Kα energies for elements between $6 \leq Z \leq 30$ to match laboratory energies (Chakraborty et al. 2020a). Figure 3 compares the difference in Kα energies between NIST (Kramida et al. 2018) and CLOUDY for the updated CLOUDY energies and the old CLOUDY energies appearing in C17.02. The revised Kα energies are $\approx$ 15-4000 times more precise than those of C17.02. This energy precision is also much superior to the energy accuracy of the current and future X-ray instruments like *Chandra*, *XMM-Newton*, *XRISM*, and *Athena*, as shown in Figure 3. The improved CLOUDY energies will therefore be in excellent agreement with the future microcalorimeter observations.

3.5. *Inner Shell Energies*

We updated the fluorescence Kα energies of Si II-XI and S II-XIII used in CLOUDY with the experimental data reported in Hell et al. (2016). The energies of the lines in the past versions of CLOUDY are mainly taken from Table 3 of Kaastra & Mewe (1993), which contains the fluorescence yields, energies and Auger electron numbers for elements and ions from Be to Zn. Even though these values were in accordance with the theoretical calculations available at the time of the publication, today, this dataset is not accurate enough to model some already available high-resolution spectra (Amato et al. 2021; Camilloni et al. 2021), and certainly for future X-ray spectra having eV resolution.

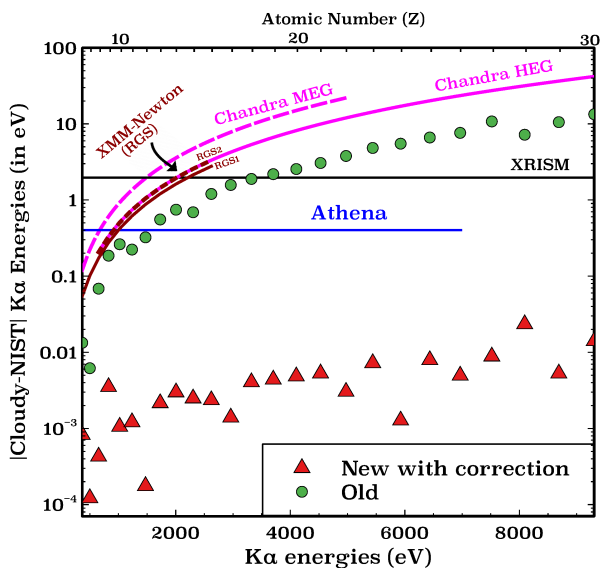

Fig. 3. The absolute value of the difference between NIST and CLOUDY Kα energies versus Kα energies for H-like ions of elements between $6 \leq Z \leq 30$. Red triangles show the difference between energies in the current version (as of C17.03) of CLOUDY and NIST, while green circles show the same difference for previous versions of CLOUDY (from $\approx$2005 to C17.02). The color figure can be viewed online.

For this reason, we updated the energies from O-like to Be-like ions of Si and S (Si VII-XI and S IX-XIII) adopting the centroids for unresolved blends given in Table 3 of Hell et al. (2016). Regarding the low-ionization lines, individual energies are taken from their Table 5, where the values of Si II-IV, Si V-VI, S II-VI and S VII-VIII are listed. Kα_1 and Kα_2 are not experimentally resolved in Hell et al. (2016), and their difference in energy is lower than the expected resolution of future X-ray microcalorimeters, so we assumed the same energy for both. Camilloni et al. (2021) provided a demonstration of the impact that such an update can have on the high-resolution spectra of the high mass X-ray binary Vela X-1 (see Figure 4).

3.6. *ℓ-changing Collisions*

Momentum-changing collisions by protons were deeply revised in C17. An upgrade of the theory of Pengelly & Seaton (1964, hereafter PS64), dubbed PS-M, was published by Guzmán et al. (2017b), correcting the results at high density and low temperature of PS64 and getting a better agreement with the quantum-mechanical *ab initio* results from Vrinceanu & Flannery (2001, hereafter VF01). The theory has been further refined by Badnell et al. (2021), now called PS-M20. PS-M/PS-M20

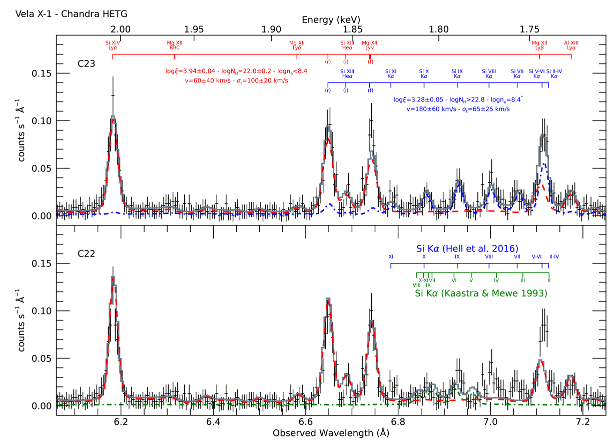

Fig. 4. Visually co-added *Chandra* MEG ± 1 order spectra of the HMXB Vela X-1 at the orbital phase $\phi_{orb} = 0.75$ (see Amato et al. 2021). *Top*: Best fit model with CLOUDY (grey solid line), using the improved energies for the Si fluorescence lines, available in C23. The specific contributions of each gas component are labeled (red dashed line and blue dot-dashed line), together with the best-fit parameters and 90% confidence level uncertainties (see Camilloni et al. 2021, for details). *Bottom*: As above, but with the previous version of CLOUDY, C17. The low ionization component is here labeled in green, together with the adopted Si Kα lines (from Kaastra & Mewe 1993). For ease of comparison, the improved energies from Hell et al. (2016) are in blue, as in the top panel. Adapted from Camilloni et al. (2021). The color figure can be viewed online.

results were in better agreement with the quantal calculations than the semi-classical calculations from Vrinceanu et al. (2012) (hereafter VOS12), which underestimate VF01 by a factor ≈ 6 (Guzmán et al. 2016). Semi-classical rates were corrected by Vrinceanu et al. (2017) to get agreement with VF01 and PS-M. Vrinceanu et al. (2019) report in their Figure 2 a disagreement of PS-M rates with quantum mechanical rates for high n. However, we have confirmed that PS-M rates actually agree with the quantum mechanical ones for the results plotted in their figure. Their reported disagreement can be explained because they calculated the excitation $\ell \rightarrow \ell + 1$ collisions incorrectly using the formula given by Guzmán et al. (2017b), optimized for de-excitation collisions ($\ell \rightarrow \ell - 1$). If micro-reversibility is applied to the results of Vrinceanu et al. (2019) the obtained rates agree with the quantum ones for the entire range of the figure (Badnell et al. 2021).

Guzmán et al. (2017a) compared in their Tables 1 and 2 PS-M effective recombination rates to $n = 2$ levels of hydrogen with the ones quoted in Tables 4.10 and 4.11 of Osterbrock & Ferland (2006), obtained from Pengelly & Seaton (1964). PS-M produces effective recombination coefficients to $2s$ that are bigger in a $\approx 0.6\%$ for Case A and a $\approx 0.1\%$ for Case B, while recombination to $2p$ is smaller by $\approx 1-2\%$. Similarly, they found an agreement up to $\approx 5\%$ for the emissivities of $2s\,^2\mathrm{S} \rightarrow 2p\,^2\mathrm{P}^o_{3/2}$ and up to a $\approx 0.5\%$ for $2s\,^2\mathrm{S} \rightarrow 2p\,^2\mathrm{P}^0_{3/2} \rightarrow 2p\,^2\mathrm{P}^o_{1/2}$. We do not expect this to influence Lyα or the two-photon emission spectrum.

PS-M20 theory has been implemented in the latest versions of Cloudy for H-like and He-like ions. Cloudy selects PS-M20 theory by default if not specified. The command that selects the new PS-M20 results is:

```
database H-like collisions l-mixing
                                    Pengelly PSM20
```

for H-like collisions, and

```
database He-like collisions l-mixing PSM20
```

for He-like systems.

3.6.1. *The Importance of a Correct Number of Resolved Levels: Printing ℓ-changing Critical Densities*

Accurate modeling of recombination lines for H-like and He-like ions requires a good description of the ion energy levels. Cloudy distinguishes between angular momentum *ℓ-resolved* levels and *collapsed* levels, for which ℓ-levels are populated according to their statistical weight (see Ferland et al. 2013, for more details).

Critical densities are defined as the density where collisional rates equal radiative de-excitation, $n_{e,c}\,q_{lu} = \tau_{ul}^{-1}$ (Pengelly & Seaton 1964), where τ_{ul} is the half-life of radiative de-excitation between u and ℓ sub-shells, and q_{lu} is the effective coefficient of collisional excitation between ℓ and u sub-shells. Then averaging over ℓ we can obtain the critical density for the shell n:

$$n_{e,c} = \frac{1}{q_n \tau_n}, \tag{1}$$

for densities above $n_{e,c}$, collisions will be faster than radiative decay and dominate, ultimately bringing the n-shell to be statistically populated in its ℓ-sub-shells.

Cloudy now has a new command,

```
print critical densities
```

that can be used to print ℓ-changing critical densities for H-like and He-like ions in the output file. This

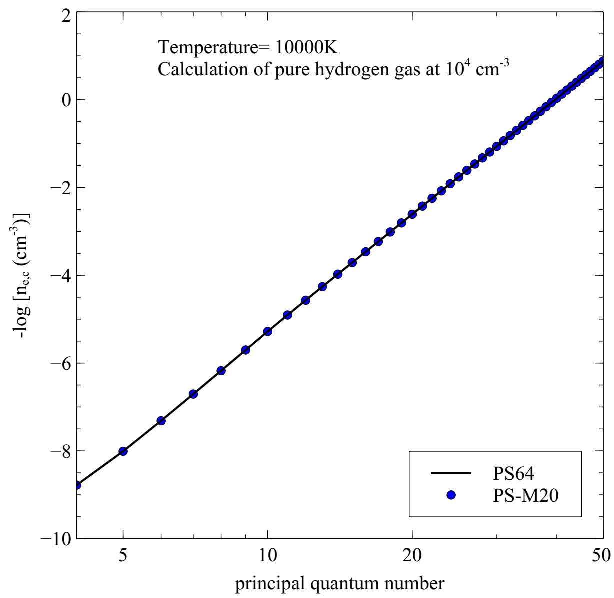

Fig. 5. Comparison of critical densities from equation 1 with ℓ-changing collisions from PS-M20 with the results of Figure 4 of Pengelly & Seaton (1964). We have chosen a pure hydrogen gas at electron temperature $T = 10000$K and electron density $n_e = 10^4\,\mathrm{cm}^{-3}$. The agreement is complete. The color figure can be viewed online.

command aims to help choose a physically-motivated number of resolved levels to employ in a simulation for each ion.

Optionally, `H-like` or `He-like` can be added together with an element name to specifically print the critical densities for an ion. For example, while the command line above prints critical densities for all resolved levels included in the simulations for all H-like and He-like ions, the more specific command,

```
print critical densities H-like
```

prints only critical densities for H-like ions, while

```
print critical densities H-like helium
```

prints only critical densities for the He^+ ion.

In Figure 5 we have plotted the critical densities obtained with Cloudy using PS-M ℓ-changing theory versus the principal quantum number. Critical densities from Figure 4 of Pengelly & Seaton (1964) are also plotted for comparison. Complete agreement is shown in the figure. When densities are higher than the critical densities, collisions dominate and the ℓ quantum numbers redistribution is faster. At much higher densities the population of the ℓ-sub-shells will be statistical. Figure 5 can be used to determine the number of levels that should be treated as resolved in ℓ. As a rule of thumb, it is safe to add ten units to the principal quantum number for which the density is critical to ensure that collisions will statistically populate the levels treated as collapsed. For example, in a simulation of an H II region with density $n_e = 10^4\,\mathrm{cm}^{-3}$, the principal quantum number corresponding to that density would be $n \approx 15$, according to Figure 5 (we can use the `print critical density` command to verify the critical densities for all resolved levels). A safe number of resolved levels to use is all levels $n \leq 25$, that can be included in the simulations with the line (Ferland et al. 2017):

```
database H-like hydrogen levels resolved 25
```

Note that different conditions of electron temperature and densities might cause the critical densities to vary, obeying the temperature dependence of the ℓ-changing cross sections, as well as their dependence on density due to the Debye cut-off of the collision probabilities (Pengelly & Seaton 1964; Guzmán et al. 2016).

3.7. *n-changing Collisions*

Principal quantum number-changing electron collision data were analyzed by Guzmán et al. (2019). C17 and previous versions used semi-empirical data from Vriens & Smeets (1980, hereafter VS80). Guzmán et al. (2019) suggested using the semiclassical straight trajectory Born approximation of Lebedev & Beigman (1998, hereafter LB98). The latter is within a factor of ≈ 2 of VS80 collisions and has the same dependency on the high- and low-energy range. Care must be taken when dealing with highly charged ions as the straight trajectory approximation would fail, especially at low energies, producing an underestimation of the rates. In that case, it would not be safer to use VS80, as this is intended only for atoms. Further theoretical work is needed for a better theory for highly charged ions.

While LB98 is the default theory for both H-like and He-like n-changing collisions, it is possible to choose between different theories in CLOUDY using the command:

```
database H-like collisions Lebedev
```

where `H-like` can be modified to `He-like` and the options are:

- `Lebedev` (default) for semiclassical straight trajectory theory (Lebedev & Beigman 1998).
- `Vriens` for Vriens & Smeets (1980) semi-empirical approximation.
- `Fujimoto` for the semi-empirical formula fit of Fujimoto (1978).
- `van regemorter` for the averaged gaunt factor formula proposed by van Regemorter (1962).

A comparison and analysis of these theories and application to different cases can be found at Guzmán et al. (2019).

3.7.1. *Masing of Hnα Lines*

In contrast to C17, masing of hydrogen lines is now allowed. Guzmán et al. (2019) predict masing of H$n\alpha$ radio recombination lines for low-density clouds ($n_e \leq 10^8\,\mathrm{cm}^{-3}$). These authors also predict masing of the H$n\alpha$ lines, with n ranging between 50 and 190, for a model of the Orion Blister. However, the number of masing lines decreases for data sets other than LB98. In these cases, the higher collisional rates bring the populations of the Rydberg levels closer to LTE, thus suppressing masing.

4. MOLECULAR DATA

4.1. H_2

A large model of molecular hydrogen was introduced by Shaw et al. (2005). The level energies, which we use to derive line wavelengths, have been updated to Komasa et al. (2011). This work incorporates many high-order effects in the H_2 wavefunctions, which result in ≈ 1 wavenumber changes in level energies. We derive line wavelengths from these energies, so small changes in wavelength result. The Komasa et al. (2011) energies are thought to be a significant improvement over previous data sets.

The previous version of CLOUDY included the Lique (2015) H – H_2 collisional data as an option, although they were not used by default. We now use this as our preferred H – H_2 collision data set. Compared with previous calculations, these data extend to higher vibrational manifolds and include ortho-para changing reactive collisions. Tests show that the H_2 2.121 μm line intensity changes by roughly 50%, becoming stronger in some PDR sims.

4.2. *Other Molecules*

Molecular lines are sensitive to underlying physical conditions. Hence, they reveal physical conditions in various astrophysical environments when interpreted correctly. It is always our aim to predict more molecular lines with better precision. We do it in two ways. Firstly, by including more molecules in the CLOUDY molecular network. Secondly, by updating the existing molecular network. Below, we mention such recent efforts.

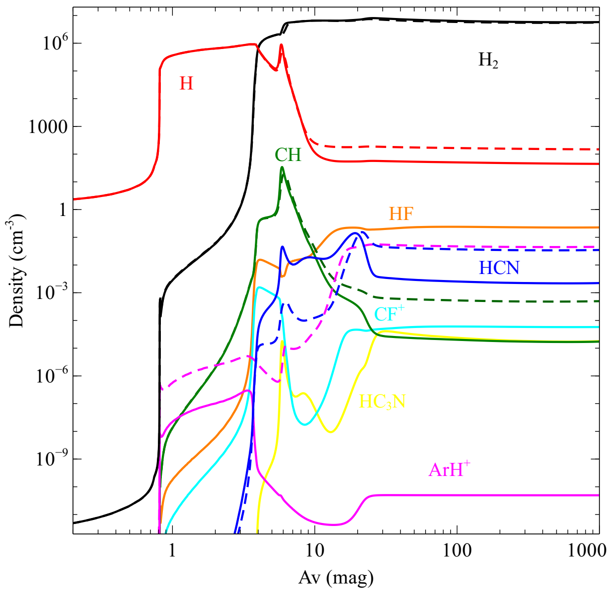

Fig. 6. Variation of densities of a few molecules as a function of A_V for an H II and PDR model ("h2_orion_hii_pdr.in" from the Cloudy download under the directory `tsuite`). The name of each molecule and the line representing its density are depicted in the same color. The solid lines represent simulations using this version, and the dashed lines represent simulations using an earlier version C17. The color figure can be viewed online.

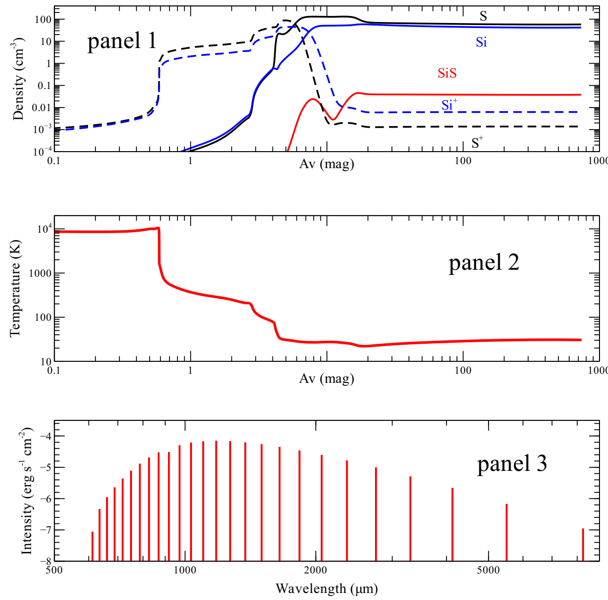

Fig. 7. Panel 1: Variation of SiS density as a function of A_V for an H II and PDR model ("h2_orion_hii_pdr.in" from the Cloudy download under the directory `tsuite`). Panel 2: Variation of temperature across the cloud. Panel 3: Model predicted intensities of various SiS rotational lines. The color figure can be viewed online.

Shaw et al. (2022) have included the gas-phase energy levels, radiative and collisional rates for HF, CF^+, HC_3N, ArH^+, HCl, HCN, CN, CH, and CH_2 into Cloudy's molecular network. The energy levels and collisional rate coefficients were taken from the upgraded LAMDA Database (van der Tak et al. 2020). However, reaction rates stem from the UMIST Database for Astrochemistry (UDfA 2012; RATE12), specifically, Roueff et al. (2014); Schilke et al. (2014); Priestley et al. (2017). As a result, Cloudy now predicts the line intensities and column densities of these molecules in addition to those included in the previous version. Figure 6 (Shaw et al. 2022) shows the variation of densities of a few molecules as a function of A_V. The name of each molecule and the line representing its density are depicted in the same color. The solid lines represent simulations using this version, and the dashed lines represent simulations using the earlier version C17.

Likewise, we have included the gas-phase chemical reactions, energy levels, and radiative and collisional rates of the SiS molecule (Shaw et al. 2023a). The energy levels, Einstein's radiation coefficients and collisional rate coefficients with H_2 molecules were taken from the upgraded LAMDA database. In addition, we have included collisions with H (Anusuri 2019) and He (Vincent et al. 2007; Toboła et al. 2008). The chemical reaction rates were taken from various sources, UDfA, namely Zanchet et al. (2018), Willacy & Cherchneff (1998), Doddipatla et al. (2021); and the Kinetic Database for Astrochemistry,[15] respectively. Figure 7 (Shaw et al. 2023a) demonstrates predicted intensities of various rotational lines of SiS for an H II and PDR model ("h2_orion_hii_pdr.in") from the Cloudy download under the directory `tsuite`.

Shaw et al. (2023a) included only rotational levels of SiS. However, we have now included the vibrotational levels (private communication with Ziwei Zhang).

Any species' predicted column densities and line intensities depend on rate coefficients. We use mostly UDfA rate coefficients. In the UDfA, a two-body gas-phase chemical reaction rate coefficient k ($\mathrm{cm^3\,s^{-1}}$) is given by the usual Arrhenius-type formula,

$$k = \alpha \left(\frac{T}{300}\right)^{\beta} \exp(-\gamma/T), \qquad (2)$$

[15] `https://kida.astrochem-tools.org/`

where T is the gas temperature. Reactions with $\gamma < 0$ will become unphysically large at low temperatures. Röllig (2011) has addressed the divergence of rate coefficients at low temperatures. A similar problem occurs for high temperatures encountered with CLOUDY. We apply a temperature cap T_{cap} for $\beta > 0$ to avoid this. For $T > T_{cap}$, the rate coefficients retain the same values as at T_{cap}. Though ad hoc, we choose $T_{cap} = 2500$K (Shaw et al. 2023b). This affects the warm, 5000K - 10000K, collisionally ionized clouds.

Cosmic-ray ionization rate plays an important role in ISM and is an active field of research. Shaw & Ferland (2021) demonstrated that the abundance of PAHs affects the free electron density, which changes the H_3^+ density and hence the derived cosmic-ray ionization rate of hydrogen. We suggested that for the average Galactic PAH abundance, the cosmic-ray ionization rate of atomic hydrogen be $3.9 \pm 1.9 \times 10^{-16}\,\mathrm{s}^{-1}$. The command

```
cosmic rays background 1.95 linear
```

sets this rate. Furthermore, we showed that the cosmic-ray ionization rate of hydrogen derived using H_3^+ is much higher when PAHs are absent.

Furthermore, Shaw et al. (2020) updated the mean kinetic energy of the secondary electrons (from 20 eV to 36 eV) produced by cosmic rays. This affects the cosmic-ray dissociation of molecular hydrogen and dense cloud chemistry.

5. GRAIN DATA

5.1. *New Refractive Index Files*

New refractive index files have been added for astronomical silicate and graphite using the data described in Draine (2003). These add much more structure to the inner-shell photoionization edges seen in the X-ray regime.

5.2. *Interstellar Grain Absorption*

We have introduced a new option to the `metals deplete` command to use the more self-consistent depletion pattern described in Jenkins (2009). An in-depth discussion on this depletion pattern and how it affects the predicted spectra is presented in Gunasekera et al. (2022b, 2023). This new element-selective depletion option can be enabled with the

```
metals deplete Jenkins 2009
```

command. The depletion parameters A_X, B_X, and z_X, specific for each element X, are read in from an external file called `Jenkins09_ISM_Tab4.dep`, and are used to compute the depletion scale factor D_x using the equation

$$D_x = 10^{B_X + A_X(F_* - z_X)}, \tag{3}$$

where F_* represents the degree of depletion across all elements. This D_x factor then multiplies the reference abundance to produce the post-depletion gas-phase abundances. By default, $F_* = 0.5$. However, its value may be adjusted with the command

```
metals depletion jenkins 2009 fstar <value>
```

where the `<value>` must range between 0 and 1.

An analysis of strong spectral-lines (log([O III] λ5007/Hβ), log([N II] λ6583/Hα), log([S II] $\lambda\lambda$6716,6731/Hα), and log([O I] λ6300/Hα)) from a CLOUDY model of a generalized H II region, based on SDSS-IV MaNGA observations (Bundy et al. 2015; Yan et al. 2016), revealed that varying F_* affects the spectral line intensities and the thermal balance of the ionized cloud (Gunasekera et al. 2023). The user must alter the grain abundance to match the degree of depletion (F_*). To do this, compute the fraction of the total abundance of heavy elements locked in dust grains in the given F_* relative to the total abundance of heavy elements locked in dust grains at $F_* = 0.5$,

$$grains = \frac{\sum_X (X_{dust}/H)_{F_*}}{\sum_X (X_{dust}/H)_{0.5}}. \tag{4}$$

This fraction can then be given in the `grains` command to change the dust abundance self-consistently.

6. X-RAY PREDICTIONS

6.1. *Microcalorimeters*

Historically, CLOUDY made X-ray predictions but was not designed for high-resolution spectral analysis. In preparation for the upcoming microcalorimeter missions *XRISM* and *Athena*, we have extended CLOUDY to make it compatible with high-resolution spectral analysis in the X-ray regime. Chakraborty et al. (2020b) demonstrated the effects of Li-like iron on the Fe XXV Kα line intensities via resonant Auger destruction (RAD; e.g., Ross et al. 1978; Matt et al. 1996; Liedahl 2005). Although initially motivated by the Perseus cluster, this analysis was extended to include a wide range of column densities encountered in astronomy.

We also showed line-broadening effects produced by electron scattering. The command `no scattering escape` was introduced to ignore scattering of photons off of thermal electrons (Chakraborty et al. 2020b). When line photons scatter off high-speed electrons, a fraction of them receive large Doppler shifts from their line center, creating super-broad Gaussian profiles. Such broad line profiles will not be detected in future high-resolution X-ray telescopes. The purpose of the above command is to model the unscattered photons that will be observed by these future X-ray missions. The command `no absorption escape` was introduced to ignore absorption by background opacities.

Comparing the observed spectra by *Hitomi* with Cloudy simulated spectra, Chakraborty et al. (2020c) presented a novel diagnostic for measuring column densities transitioning from optically thin (Case A) to optically thick (Case B) in H- and He-like iron. The effects of metallicity and turbulence on Fe XXV Kα line ratios were also demonstrated using the Perseus cluster as a reference.

We have also updated the collision strengths of the Fe Kα lines using recent calculations by Si et al. (2017), replacing the old collision rates by Zhang & Sampson (1987). The new rates are calculated based on the independent process and isolated resonance approximation using distorted waves (IPIRDW) technique. Updates to the collision rates resulted in significant differences in the estimated Fe Kα line ratios, as described in Chakraborty et al. (2020c).

Chakraborty et al. (2021) extended the classic Case A and Case B (Osterbrock & Ferland 2006) to less familiar regimes Case C and Case D in the X-ray band. Previous works on these limits focused on the optical, ultraviolet, and infrared regimes (Menzel 1937; Baker & Menzel 1938; Chamberlain 1953; Ferland 1999; Peimbert et al. 2017), but X-ray wavelengths were rarely studied. The net X-ray spectrum for all four cases within the energy range 0.1-10 keV was simulated at the resolving power of *XRISM*.

Chakraborty et al. (2022) demonstrated atomic processes modifying soft X-ray spectra. This includes the enhancement in line intensities via continuum pumping in photoionized environments, and suppression in line intensities through photoelectric absorption and electron scattering in collisionally-ionized and photoionized enviromnents. A hybrid of Cloudy simulated collisionally-ionized and photoionized model was used to fit the *Chandra* Medium Energy Grating (MEG) spectrum from V1223 Sgr, an intermediate polar. This was the first application of the new Cloudy interface compatible with high-resolution spectral analysis in the X-ray regime.

We also increased the default number of levels in our default instance of the Fe^{16+} ion. The default limit to the number of its levels suppressed the 15.013 Å line, which is prominent in soft X-ray spectra. Ferland et al. (2017) has an extensive discussion of our choice of a default number of levels, the effects on a calculation, and how to change it.

Finally, we have improved the energy grid resolution of Cloudy's coarse continuum to better suit it for tailoring models to the upcoming *XRISM* mission.

6.2. *Inner Shell Ionization*

The X-ray portion of most SEDs has little effect on the ionization of an ionized cloud, as discussed for AGN in the first appendix of Temple et al. (2023). A more general discussion is presented here.

The photoionization rate for a given shell n is

$$\Gamma_n = \int_{\nu_0}^{\infty} \sigma_\nu \ \phi_\nu \ d\nu \ \ [\mathrm{s}^{-1}], \tag{5}$$

where ν_0, σ_ν are the photoionization threshold of shell n [Ryd] and the cross section [cm^{-2}], respectively, and ϕ_ν is the flux of ionizing photons [cm^{-2} s^{-1} Ryd^{-1}]. The total photoionization rate is the sum over all shells is

$$\Gamma_{total} = \Sigma_n \ \Gamma_n \quad [\mathrm{s}^{-1}]. \tag{6}$$

Consider the case of O^{2+}, a common ion of the 3^{rd} most abundance element which produces the very strong O III lines. Three subshells, $1s^2$, $2s^2$, and $2p^2$, contribute to the total photoionization rate. We use the data fitted by (Verner et al. 1996). The cross sections are shown in Figure 8. The K-shell cross sections are nearly one dex smaller than the valence shell.

The radiation field shape enters in equation 5. Figure 9 shows a power-law continuum, one with $f_\nu \propto \nu^{-1}$. This is an exceptionally hard SED with a large number of K-shell photons compared with L-shell. Even quasars, with their non-thermal continuum, are not this hard. This will overestimate the importance of K-shell photoionization. The upper panel of Figure 9 shows this SED as νf_ν.

The photon flux ϕ_ν enters in the photoionization rate. This is the ratio $\phi_\nu \propto f_\nu / h\nu \propto \nu^{-2}$. This is shown in the lower panel. The flux of K-shell photons is about 150 times smaller than the flux of L shell photons.

Cloudy includes a command to report each shell's photoionization rate Γ_n. We need this to treat Auger electron ejection and fluorescent emission properly. That rate is shown in the following Table 1.

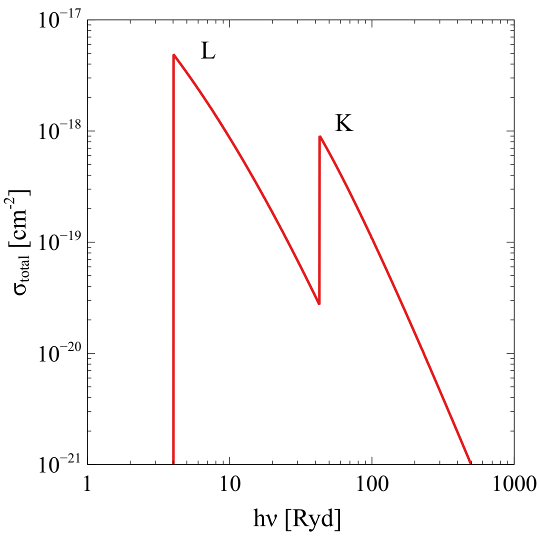

Fig. 8. The total opacity of doubly ionized oxygen is shown. The K and L shell edges are marked. The color figure can be viewed online.

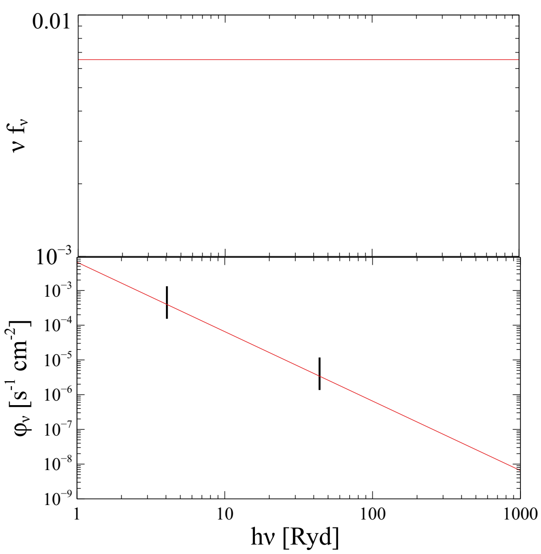

Fig. 9. The upper panel shows the SED for an $f_\nu \propto \nu^{-1}$ SED, an exceptionally hard continuum. The lower panel gives the photon flux, $\phi_\nu \propto f_\nu/h\nu \propto \nu^{-2}$. The hash marks indicate the locations of the K and L shells. The photon flux in the K shell is ≈ 2 dex smaller than the L shell. The color figure can be viewed online.

The L shell rates are about 150 times larger than the K shell rates, due to the different photon fluxes, cross-sections, and energy ranges. The implication is that the K-shell rates are negligible compared with the valence shell rates. One result is that differences in the X-ray portion of a SED will have little impact on UV - IR emission.

TABLE 1

PHOTOIONIZATION RATES PER SUBSHELL

Shell	Γ_n
$1s^2$	8.84×10^{-13}
$2s^2$	4.71×10^{-14}
$2p^2$	1.28×10^{-10}

There were several papers published in the 1970s that discussed inner shell processes at length. This physics is fully included in Cloudy. Many of those papers overstated the importance of inner shell physics on the ionization.

Although the inner shell physics has little effect on the ionization of the gas, it will be important for producing X-ray fluorescent emission lines as well as X-ray transmission spectroscopy. High-resolution X-ray observations of absorbing clouds in front of the X-ray continuum source could measure the features.

7. MISCELLANEOUS IMPROVEMENTS

The photoionization thresholds of most ions have been slightly updated as of C17.02. In this release, the entries for the radiative recombination continua on the line stack have updated wavelengths to make them consistent with the new thresholds.

The ionization potentials employed by Cloudy have been updated. The new values are extracted from NIST and are current as of 2022-11-15. The differences between the datasets for the elements up to zinc are at most 0.5%. In addition, in preparation for future development, our ionization potential data set includes all natural elements and all their ions. That is, our list extends up to plutonium, instead of up to krypton.

The solar abundances of Lodders et al. (2009) have been added to Cloudy as of C17.01.

To fix a bug where many blends were not predicted on the emergent line stack, the requirements for adding lines to a blend have been tightened. Blend components now have to be transmitted lines (i.e. have type 't', as indicated in the **save line labels** output) that are associated to a database transition. As a result, many blend components have been removed, mostly predictions for the recombination contribution to a given line. These predictions were based on ad hoc theories that are invalid over the entire parameter range that Cloudy covers. The components that have been removed are still available as separate entries on the line stack.

Detailed information about the changes can be found on our wiki.[16]

The label for the inward component of continuum bands has been changed to "InwdBnd". Previously that was "Inwd". This led to ambiguities with individual Fe II lines when the big Fe II model was used.

The labels for collisional heating and cooling of the gas by grains have been renamed to "GrCH" and "GrCC", respectively. Previously, they were both called "GrGC".

The code now uses the 2018 CODATA adjustment for the fundamental physical constants.

8. SEDS IN CLOUDY

Support for the Khaire & Srianand (2019) synthesis models of the extragalactic background light has been added since C17.01. These SEDs cover the range from the far infrared to TeV γ-rays, with an emphasis on the extreme ultraviolet background responsible for the observed ionization of the intergalactic medium for redshifts between $0 \leq z \leq 15$.

In addition, four AGN SEDs described by Jin et al. (2012) and Jin et al. (2017) are now included, see Figure 10, as well as the SED for NGC 5548 of Dehghanian et al. (2019).

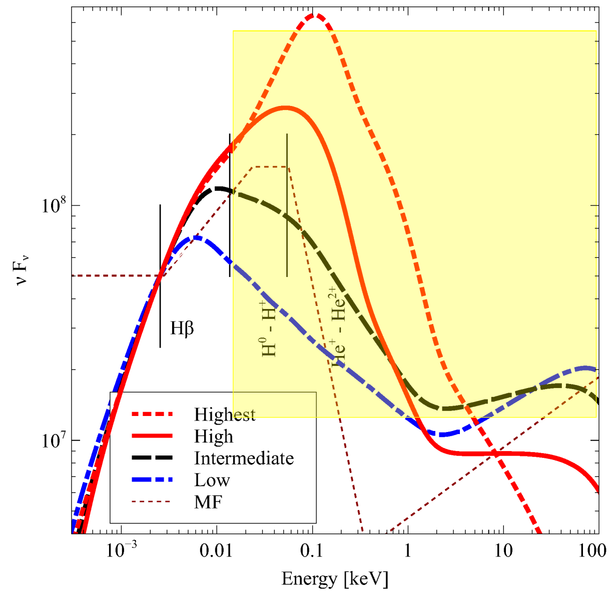

Fig. 10. This figure, from Ferland et al. (2020), compares the SEDs of Jin et al. (2012) and Jin et al. (2017) over a range of Eddington ratio. The curve marked "MF" is taken from Mathews & Ferland (1987) and obtained with the **TABLE AGN** command. The color figure can be viewed online.

9. INFRASTRUCTURE CHANGES

9.1. *Migration to C++11*

The code has been ported to C++11. This version of the C++ standard delivers significant new functionality and fixes many issues with the old C++98 standard we were using until now. Adopting the new standard enables writing more versatile code. Compilers with full support for the C++11 standard have been available since April 2013 (though some vendors only finalized their support later). By now, these compilers should be widely available, and this change should not impact the ability of our users to use CLOUDY. Users now need a compiler with the following minimum requirements. For GNU g++ version 4.8.1 or later, for LLVM clang++ version 3.3 or later, for the Intel compiler version 15.0 or later, and for the Oracle Developer Studio compiler version 12.5 or later.

9.2. *Executing the Code*

CLOUDY now supports the `-e` flag on the command line. After this flag, the user may enter one or more CLOUDY commands separated by a semicolon. This averts the need to create an input file for very simple (test) models. It can also be useful when calling CLOUDY from a shell script.

The executable now accepts the `-s [ seed ]` command line flag. This will set a fixed seed for the random number generator and is intended for debugging and testing purposes. The parameter is a 64-bit seed in hexadecimal form. If the seed is omitted, a default fixed value will be used. It is not recommended to use this flag in normal CLOUDY runs.

The `-a` flag on the command line has been removed. This flag was only used in debugging and had been deprecated for some time.

The code has been enhanced to catch floating point exceptions and segmentation faults on supported platforms (this includes all major compilers on Linux and MacOS). This makes grid runs even more resilient against errors in one of the grid models, allowing the code to finish the grid despite these errors.

If some models in a grid fail, the **save** output for that grid point may be missing. As a workaround, the code now creates a stub file for the missing output by taking the correct output from another grid point and replacing all numbers by zeros.

In previous versions, when CLOUDY aborted (e.g. due to too many convergence failures) it would try to soldier on and produce some (most likely wrong)

[16] `https://gitlab.nublado.org/cloudy/cloudy/-/wikis/NewC22`

output despite the failure. This is no longer done. The code now stops immediately after the abort.

Most compilers will now generate a backtrace of the call stack at the end of the output if an error occurs. This is useful for debugging purposes.

9.3. *Reading and Writing Files*

For several years CLOUDY allowed the user to supply a custom search path for searching data files. The development of this feature has now been finalized. The code now uses a consistent policy for finding files that it needs to read. All commands will look in the local directory first, and then in the data directory (this is the standard search path). The user can alter the search path by defining the environment variable CLOUDY_DATA_PATH before the code is started up. This gives the user more freedom to choose where custom data files are stored. Setting this variable will no longer affect the compilation of the code (as was the case in C17 and before). The code will always write output in the local directory. This is now enforced.

9.4. *Parser Changes*

We have started modifying the parser to check the script's syntax more strictly. The long-term goal is to check everything that is typed. In this release, we will start by fully checking the command name itself. Abbreviating the command is still allowed (as was already the case in previous releases) but all the typed characters will now be checked. We will enforce US spelling where relevant.

The input deck's set of allowed comment characters has been significantly reduced. Since version C17.01, it is no longer allowed to use "c" or "C" to start a comment. In the current version, only comments starting with "#" or "##" are allowed. Comments of the first type will be echoed in the main output, while comments starting with "##" will not be echoed.

The parser now supports line disambiguation. The CLOUDY line stack may contain seemingly duplicate entries with the same label and wavelength but which are actually different lines. This can create problems if you want to use such a line. One example is the H I 4.65247 μm line, which may be either the $7 \rightarrow 5$ or the $35 \rightarrow 7$ line. You can now optionally supply the lower and upper level index, or the energy of the lower level, to indicate which line you want. The **save line labels** output contains the necessary information to do this. This new syntax is supported by all commands that read line identifications. It is also supported by the subroutines *cdLine*, *cdEmis*, and *cdGetLineList*. This type of disambiguation is not possible for all lines on the line stack.

9.5. *Numerical Methods*

The old random number generators have been removed from CLOUDY. These were based on the Mersenne twister algorithm and the Box-Muller method for generating random numbers with a normal (Gaussian) distribution. The new code uses a fully vectorized version of xoshiro256** (Blackman & Vigna 2021)[17], while the random numbers with a normal distribution are now generated using the Ziggurat algorithm (Marsaglia & Tsang 2000). Both methods are much faster than the old ones. An additional advantage is that the new code is fully aware of parallelization in the code, meaning that parallel ranks created with MPI or fork will automatically have a different sequence of random numbers. The code now generates a random seed at the start of execution by default (when available derived from `/dev/urandom`, otherwise using the system time), unless the `-s` command line parameter described above is used.

9.6. *New, Modified, and Deleted Commands*

Since C17.01 the **save xspec** command has a new option **normalize**. In versions prior to C17, the spectra would always have the same normalization as the **save continuum** output. This can be inconvenient for comparing spectra in grids where the normalization of the spectra can be vastly different. When using the **normalize** keyword, all spectra will be normalized to 1 photon $\mathrm{cm^{-2}\,s^{-1}\,keV^{-1}}$ at a photon energy of 1 keV. The user can alter the latter value to a different photon energy.

Since C17.02, the **save transmitted continuum** command also works in luminosity mode, and the keyword **last** is implicitly assumed to avoid useless output. The format of the **save transmitted continuum** file has changed, so files from versions C17.01 and older will no longer be accepted. Spherical dilution will now be implicitly handled when the keyword **scale** is used, and the first and second models both set a radius.

The command **database h-like keep fine structure** has been added. This allows the fine-structure components of the hydrogen-like lines to be reported on the line stack. Previous versions of the code already computed these components but did not report them. This behavior is still the default, but by including this command, the fine-structure lines will be added to the line stack.

[17] `http://xoshiro.di.unimi.it`.

The commands **crash segfault**, **crash abort**, **crash grid**, and **crash bounds array** have been added to emulate additional sources of errors. The **crash bounds heap** command has been removed as CLOUDY no longer uses this method of allocating memory. The **crash undefined** commands have been reorganized and the only option left (without any additional keywords) is to test access to an undefined variable on the stack (this used to be called **crash undefined stack | auto**).

The **set assert abort** command has been removed. Its effect was identical to the `-a` command line flag, which was only used for debugging the code. The **stop nTotalIoniz** command has been removed. This was a debugging tool that was very rarely used. The **drive** family of commands have been removed. These were designed to test certain aspects of the code interactively. They have not been used in a long time and are obsolete. The **state** command has been removed. This was an unfinished experimental feature to save or restore the state of the code. This project has now been abandoned as it was too difficult to do. The **plot** family of commands has been removed (as was already announced in HAZY). This was obsolete code for producing ASCII plots on line printers.

The option to set the seed for the random number generator has been removed from the **database H2 noise** and **database H-like | He-like error generation** commands. Using a random seed is now the default, so the user is no longer needed to set the seed.

The **table SED** command now accepts the **Flambda** keyword in the SED data file. Fluxes in F_ν or νF_ν units were already accepted, now F_λ units can also be used.

The upper limit to the number of lines that can be supplied to the **print line sum** and **save lines emissivity** commands has been removed.

The command **set blend** has been added, allowing the user to define custom line blends. This command allowed us to move most of the blends that used to be hardwired into the code (e.g., Blnd 1909) to a new init file called `blends.ini` that is part of the data directory. This file is parsed automatically when starting up CLOUDY, unless the **no blends** command is included in the script.

The **abundances** command has been modified. It is now mandatory to include an element symbol in front of the abundance, which will determine what element the abundance belongs to. This makes the command much safer. It also allows the user to put the elements in arbitrary order and removes the need to complete the list of abundances. The **elements read** command has been removed as it is no longer needed.

The **database He-like FSM** command has been removed. It was not working correctly, and moreover, Bauman et al. (2005) found that as a result of the principle of spectroscopic stability, it had very little impact on the predictions for the He I spectrum. The situation is different, though, for highly charged ions, e.g. Fe XXV. For such ions, the individual fine-structure components can be spectroscopically resolved and treating fine-structure mixing would be warranted. Implementing this will be postponed to a future release.

9.7. *Storing SED Grids*

The SED grids supported by CLOUDY no longer need to be compiled into binary form. The code now directly reads the ASCII files to obtain the necessary information. Compiling the ASCII files is still supported, but now produces a completely different type of file that contains indices into the ASCII file. This step is optional but is strongly recommended for large grids to speed up the code. With this setup, recompiling stellar atmosphere grids is no longer necessary when the frequency mesh is changed. Compiling SEDs in an external format (such as Starburst99 or the Rauch stellar atmosphere grids) is still mandatory to obtain the ASCII files.

10. FUTURE DIRECTIONS

Work is under way to extend and improve CLOUDY. Some of these features will be available, at least in part, by the time of the next release, while others may require longer to come to fruition. Some of these directions were already discussed by van Hoof et al. (2020).

As explained above, the X-ray capabilities of CLOUDY have been extended substantially. Yet, more work remains to be done. We are currently working on resolving the doublets of Lyman-like emission lines ($np \to 1s$ transitions) in hydrogenic ions (Gunasekera, in preparation). This feature should be available in the next major release. In addition, we plan to extend CLOUDY to include the results of experiments on inner-shell ionization. In the longer run, we should update the charge-exchange data of the code with modern calculations, e.g., with the `Kronos` database[18] (e.g., Mullen et al. 2016; Cumbee et al. 2016, 2018; Lyons et al. 2017).

Over the last one or two decades, astronomy has entered its high-precision era. So must CLOUDY.

[18] `https://www.physast.uga.edu/research/stancil-group/atomic-molecular-databases/kronos`

Given that much of what we know about the chemical composition and kinematics of celestial sources comes from spectroscopy, it is of paramount importance to improve the atomic data the code employs to make quantitative predictions for, and to interpret, observations. A program is underway (PI: Chatzikos) to produce high-quality atomic data that combine laboratory-grade wavelengths (i.e., energies) with accurate transition probabilities and collision strengths. The new models will be added to our Stout database.

Other aspects of CLOUDY that are under active development include time-dependent calculations and the radiative transfer module of the code. We aim to publicly release these updates in the next one or two releases.

MC acknowledges support from NSF (1910687), NASA (19-ATP19-0188, 22-ADAP22-0139), and STScI (HST-AR-14556.001-A). GJF acknowledges support by NSF (1816537, 1910687), NASA (ATP 17-ATP17-0141, 19-ATP19-0188), and STScI (HST-AR- 15018 and HST-GO-16196.003-A). SB acknowledges support from PRIN MUR 2017 "Black hole winds and the baryon life cycle of galaxies: the stone-guest at the galaxy evolution supper" and from the European Union Horizon 2020 Research and Innovation Framework Programme under grant agreement AHEAD2020 n.871158. GS acknowledges WOS-A grant from the Department of Science and Technology (SR/WOS-A/PM-2/2021). GS thanks Ziwei Zhang for providing the vib-rotational data of SiS.

REFERENCES

Amato, R., Grinberg, V., Hell, N., et al. 2021, A&A, 648, 105, https://doi.org/10.1051/0004-6361/202039125

Anusuri, B. 2019, Heliyon, 5, e01647, https://doi.org/10.1016/j.heliyon.2019.e01647

Badnell, N. R. & Ballance, C. P. 2014, ApJ, 785, 99, https://doi.org/10.1088/0004-637X/785/2/99

Badnell, N. R., Guzmán, F., Brodie, S., et al. 2021, MNRAS, 507, 2922, https://doi.org/10.1093/mnras/stab2266

Baker, J. G. & Menzel, D. H. 1938, ApJ, 88, 52, https://doi.org/10.1086/143959

Baldwin, J. A., Ferland, G. J., Korista, K. T., Hamann, F., & LaCluyzé, A. 2004, ApJ, 615, 610, https://doi.org/10.1086/424683

Bauman, R. P., Porter, R. L., Ferland, G. J., & MacAdam, K. B. 2005, ApJ, 628, 541, https://doi.org/10.1086/430665

Bautista, M. A., Fivet, V., Ballance, C., et al. 2015, ApJ, 808, 174, https://doi.org/10.1088/0004-637X/808/2/174

Blackman, D. & Vigna, S. 2021, ACM Trans. Math. Softw., 47, https://doi.org/10.1145/3460772

Bruhweiler, F. & Verner, E. 2008, ApJ, 675, 83, https://doi.org/10.1086/525557

Bundy, K., Bershady, M. A., Law, D. R., et al. 2015, ApJ, 798, 7, https://doi.org/10.1088/0004-637X/798/1/7

Camilloni, F., Bianchi, S., Amato, R., Ferland, G., & Grinberg, V. 2021, RNAAS, 5, 149, https://doi.org/10.3847/2515-5172/ac0cff

Chakraborty, P., Ferland, G. J., Bianchi, S., & Chatzikos, M. 2020a, RNAAS, 4, 184, https://doi.org/10.3847/2515-5172/abc1dd

Chakraborty, P., Ferland, G. J., Chatzikos, M., et al. 2022, ApJ, 935, 70, https://doi.org/10.3847/1538-4357/ac7eb9

Chakraborty, P., Ferland, G. J., Chatzikos, M., Guzmán, F., & Su, Y. 2020b, ApJ, 901, 68, https://doi.org/10.3847/1538-4357/abaaab

———. 2020c, ApJ, 901, 69, https://doi.org/10.3847/1538-4357/abaaac

———. 2021, ApJ, 912, 26, https://doi.org/10.3847/1538-4357/abed4a

Chamberlain, J. W. 1953, ApJ, 117, 399, https://doi.org/10.1086/145705

Cumbee, R. S., Liu, L., Lyons, D., et al. 2016, MNRAS, 458, 3554, https://doi.org/10.1093/mnras/stw527

Cumbee, R. S., Mullen, P. D., Lyons, D., et al. 2018, ApJ, 852, 7, https://doi.org/10.3847/1538-4357/aa99d8

Dehghanian, M., Ferland, G. J., Kriss, G. A., et al. 2019, ApJ, 877, 119, https://doi.org/10.3847/1538-4357/ab1b48

Doddipatla, S., He, C., Goettl, S. J., et al. 2021, SciA, 7, https://doi.org/10.1126/sciadv.abg7003

Draine, B. T. 2003, ApJ, 598, 1026, https://doi.org/10.1086/379123

Ferland, G. J. 1999, PASP, 111, 1524, https://doi.org/10.1086/316466

Ferland, G. J., Chatzikos, M., Guzmán, F., et al. 2017, RMxAA, 53, 385, https://doi.org/10.48550/arXiv.1705.10877

Ferland, G. J., Done, C., Jin, C., Landt, H., & Ward, M. J. 2020, MNRAS, 494, 5917, https://doi.org/10.1093/mnras/staa1207

Ferland, G. J., Korista, K. T., Verner, D. A., et al. 1998, PASP, 110, 761, https://doi.org/10.1086/316190

Ferland, G. J., Porter, R. L., van Hoof, P. A. M., et al. 2013, RMxAA, 49, 137, https://doi.org/10.48550/arXiv.1302.4485

Fernández-Menchero, L., Del Zanna, G., & Badnell, N. R. 2014, A&A, 572, 115, https://doi.org/10.1051/0004-6361/201424849

Fujimoto, T. 1978, Semi-Empirical Cross Section and Rate Coefficients for Excitation and Ionization by

Electron Collision and Photoionization of Helium. Institute of Plasma Physics Report, Japan, IIIP Jam-8, Nagoya University

Gunasekera, C. M., Chatzikos, M., & Ferland, G. J. 2022a, Astro, 1, 255, https://doi.org/10.3390/astronomy1030015

Gunasekera, C. M., Ji, X., Chatzikos, M., Yan, R., & Ferland, G. 2022b, MNRAS, 512, 2310, https://doi.org/10.1093/mnras/stac022

———. 2023, MNRAS, 520, 4345, https://doi.org/10.1093/mnras/stad322/mnras/stad322

Guzmán, F., Badnell, N. R., Chatzikos, M., van Hoof, P. A. M., Williams, R. J. R., & Ferland, G. J. 2017a, MNRAS, 467, 3944, https://doi.org/10.1093/mnras/stx269

Guzmán, F., Badnell, N. R., Williams, R. J. R., van Hoof, P. A. M., Chatzikos, M., & Ferland, G. J. 2016, MNRAS, 459, 3498, https://doi.org/10.1093/mnras/stw893

———. 2017b, MNRAS, 464, 312, https://doi.org/10.1093/mnras/stw2304

Guzmán, F., Chatzikos, M., van Hoof, P. A. M., Balser, D. S., Dehghanian, M., Badnell, N. R., & Ferland , G. J. 2019, MNRAS, 486, 1003, https://doi.org/10.1093/mnras/stz857

Hell, N., Brown, G. V., Wilms, J., et al. 2016, ApJ, 830, 26, https://doi.org/10.3847/0004-6347X/830/1/26

Jenkins, E. B. 2009, ApJ, 700, 1299, https://doi.org/10.1088/0004-637X/700/2/1299

Jin, C., Done, C., Ward, M., & Gardner, E. 2017, MNRAS, 471, 706, https://doi.org/10.1093/mnras/stx1634

Jin, C., Ward, M., & Done, C. 2012, MNRAS, 425, 907, https://doi.org/10.1111/j.1365-2966.2012.21272.x

Kaastra, J. S. & Mewe, R. 1993, A&AS, 97, 443

Khaire, V. & Srianand, R. 2019, MNRAS, 484, 4174, https://doi.org/10.1093/mnras/stz174

Komasa, J., Piszczatowski, K., Łach, G., et al. 2011, Journal of Chemical Theory and Computation, 7, 3105, J. Chem. Theory Comput., 7, 10, https://doi.org/10.1021/ct200438t

Kramida, A., Ralchenko, Y., Nave, G., & Reader, J. 2018, APS Division of Atomic and Molecular Physics Meeting, abstract id.M01.004

Laha, S., Tyndall, N. B., Keenan, F. P., et al. 2017, ApJ, 841, 3, https://doi.org/10.3847/1538-4357/aa7071

Lebedev, V. S. & Beigman, I. L. 1998, Physics of highly excited atoms and ions (Berlin, Heidelberg: Springer)

Liang, G. Y. & Badnell, N. R. 2011, A&A, 528, 69, https://doi.org/10.1051/0004-6361/201016417

Liang, G. Y., Whiteford, A. D., & Badnell, N. R. 2009, A&A, 500, 1263, https://doi.org/10.1051/0004-6361/200911866

Liedahl, D. A. 2005, AIPC 774, X-RAY DIAGNOSTICS OF ASTROPHYSICAL PLASMAS: Theory, Experiment, and Observation, 99, https://doi.org/10.1063/1.1960918

Lique, F. 2015, MNRAS, 453, 810, https://doi.org/10.1093/mnras/stv1683

Lodders, K., Palme, H., & Gail, H.-P. 2009, LanB, 4, 712, (Berlin Heidelberg: Springer), https://doi.org/10.1007/978-3-540-88055-4_34

Lykins, M. L., Ferland, G. J., Kisielius, R., et al. 2015, ApJ, 807, 118, https://doi.org/10.1088/0004-637X/807/2/118

Lyons, D., Cumbee, R. S., & Stancil, P. C. 2017, ApJS, 232, 27, https://doi.org/10.3847/1538-4365/aa8d16

Marsaglia, G. & Tsang, W. W. 2000, Journal of Statistical Software, 5, 1, https://doi.org/10.18637/jss.v005.i08

Mathews, W. G. & Ferland, G. J. 1987, ApJ, 323, 456, https://doi.org/10.1086/165843

Matt, G., Brandt, W. N., & Fabian, A. C. 1996, MNRAS, 280, 823, https://doi.org/10.1093/mnras/280.3.823

Menzel, D. H. 1937, ApJ, 85, 330, https://doi.org/10.1086/143827

Mullen, P. D., Cumbee, R. S., Lyons, D., & Stancil, P. C. 2016, ApJS, 224, 31, https://doi.org/10.3847/0067-0049/224/2/31

Netzer, H. 2020, MNRAS, 494, 1611, https://doi.org/10.1093/mnras/staa767

Osterbrock, D. E. & Ferland, G. J. 2006, Astrophysics of gaseous nebulae and active galactic nuclei, 2nd. ed. D. E. Osterbrock and G. J. Ferland (Sausalito, CA: University Science Books)

Peimbert, M., Peimbert, A., & Delgado-Inglada, G. 2017, PASP, 129, 082001, https://doi.org/10.1088/1538-3873/aa72c3

Pengelly, R. M. & Seaton, M. J. 1964, MNRAS, 127, 165, https://doi.org/10.1093/mnras/127.2.165

Priestley, F. D., Barlow, M. J., & Viti, S. 2017, MNRAS, 472, 4444, https://doi.org/10.1093/mnras/stx2327

Röllig, M. 2011, A&A, 530, 9, https://doi.org/10.1051/0004-6361/201014743

Ross, R. R., Weaver, R., & McCray, R. 1978, ApJ, 219, 292, https://doi.org/10.1086/155776

Roueff, E., Alekseyev, A. B., & Le Bourlot, J. 2014, A&A, 566, 30, https://doi.org/10.1051/0004-6361/201423652

Sarkar, A., Ferland, G. J., Chatzikos, M., et al. 2021, ApJ, 907, 12, https://doi.org/10.3847/1538-4357/abcaa6

Schilke, P., Neufeld, D. A., Müller, H. S. P., et al. 2014, A&A, 566, 29, https://doi.org/10.1051/0004-6361/201423727

Shaw, G., Ferland, G., & Chatzikos, M. 2023a, RNAAS, 7, 45, https://doi.org/10.3847/2515-5172/acc1ea

———. 2023b, RNASS, 7, 153, https://doi.org/10.3847/2515-5172/ace9b5

Shaw, G. & Ferland, G. J. 2021, ApJ, 908, 138, https://doi.org/10.3847/1538-4357/abdab2
Shaw, G., Ferland, G. J., Abel, N. P., Stancil, P. C., & van Hoof, P. A. M. 2005, ApJ, 624, 794, https://doi.org/10.1086/429215
Shaw, G., Ferland, G. J., & Chatzikos, M. 2022, ApJ, 934, 53, https://doi.org/10.3847/1538-4357/ac7789
Shaw, G., Ferland, G. J., & Ploeckinger, S. 2020, RNAAS, 4, 78, https://doi.org/10.3847/2515-5172/ab97ae
Si, R., Li, S., Wang, K., et al. 2017, A&A, 600, 85, https://doi.org/10.1051/0004-6361/201630027
Smyth, R. T., Ramsbottom, C. A., Keenan, F. P., Ferland, G. J., & Ballance, C. P. 2019, MNRAS, 483, 654, https://doi.org/10.1093/mnras/sty3198
Tayal, S. S. & Zatsarinny, O. 2018, PHRvA, 98, 012706, https://doi.org/10.1103/PhysRevA.98.012706
Temple, M. J., Matthews, J. H., Hewett, P. C., et al. 2023, MNRAS, 523, 646, https://doi.org/10.1093/mnras/stad1448
Toboła, R., Lique, F., Kłos, J., & Chałasiński, G. 2008, 2008, JPhB, 41, 155702, https://doi.org/10.1088/0953-4075/41/15/155702
van der Tak, F. F. S., Lique, F., Faure, A., Black, J. H., & van Dishoeck, E. F. 2020, Atoms, 8, 15, https://doi.org/10.3390/atoms8020015
van Hoof, P. A. M., Van de Steene, G. C., Guzmán, F., et al. 2020, CoSka, 50, 32, https://doi.org/10.31577/caosp.2020.50.1.32
van Regemorter, H. 1962, ApJ, 136, 906, https://doi.org/10.1086/147445
Verner, D. A., Ferland, G. J., Korista, K. T., & Yakovlev, D. G. 1996, ApJ, 465, 487, https://doi.org/10.1086/177435
Verner, E. M., Verner, D. A., Baldwin, J. A., Ferland, G. J., & Martin, P. G. 2000, ApJ, 543, 831, https://doi.org/10.1086/317159
Verner, E. M., Verner, D. A., Korista, K. T., Ferguson, J. W., Hamann, F., & Ferland, G. J. 1999, ApJS, 120, 101, https://doi.org/10.1086/313171
Vestergaard, M. & Wilkes, B. J. 2001, ApJS, 134, 1, https://doi.org/10.1086/320357
Vincent, L. F. M., Spielfiedel, A., & Lique, F. 2007, A&A, 472, 1037, https://doi.org/10.1051/0004-6361:20077869
Vriens, L. & Smeets, A. H. M. 1980, Phys. Rev. A, 22, 940, https://doi.org/10.1103/PhysRevA.22.940
Vrinceanu, D. & Flannery, M. R. 2001, Phys. Rev. A, 63, 032701, https://doi.org/10.1103/PhysRevA.63.032701
Vrinceanu, D., Onofrio, R., Oonk, J. B. R., Salas, P., & Sadeghpour, H. R. 2019, ApJ, 879, 115, https://doi.org/10.3847/1538-4357/ab218c
Vrinceanu, D., Onofrio, R., & Sadeghpour, H. R. 2012, ApJ, 747, 56, https://doi.org/10.1088/0004-637X/747/1/56
———. 2017, MNRAS, 471, 3051, https://doi.org/10.1093/mnras/stx1783
Wang, T., Ferland, G. J., Yang, C., Wang, H., & Zhang, S. 2016, ApJ, 824, 106, https://doi.org/10.3847/0004-637X/824/2/106
Willacy, K. & Cherchneff, I. 1998, A&A, 330, 676
Yan, R., Bundy, K., Law, D. R., et al. 2016, AJ, 152, 197, https://doi.org/10.3847/0004-6256/152/6/197
Zanchet, A., Roncero, O., Agúndez, M., & Cernicharo, J. 2018, ApJ, 862, 38, https://doi.org/10.3847/1538-4357/aaccff
Zhang, H. 1996, A&AS, 119, 523
Zhang, H. & Sampson, D. H. 1987, ApJS, 63, 487, https://doi.org/10.1086/191171

S. Bianchi: Dipartimento di Matematica e Fisica, Università degli Studi Roma Tre, via della Vasca Navale 84, 00146 Roma, Italy (stefano.bianchi@uniroma3.it).
F. Camilloni: Max-Planck-Institut für extraterrestrische Physik, Giessenbachstraße, 85748 Garching, Germany (fcam@mpe.mpg.de).
P. Chakraborty: Center for Astrophysics | Harvard & Smithsonian, Cambridge, MA (priyanka.chakraborty@cfa.harvard.edu).
M. Chatzikos: Physics & Astronomy, University of Kentucky, Lexington KY 40506 (mchatzikos@uky.edu).
G. Ferland: Physics & Astronomy, University of Kentucky, Lexington KY 40506 (gary@uky.edu).
C. Gunasekera: Physics & Astronomy, University of Kentucky, Lexington KY 40506 (cmgunasekera@uky.edu).
F. Guzmán: Physics and Astronomy, University of North Georgia, Dahlonega GA 30597 (francisco.guzmanfulgencio@ung.edu).
J. Milby: Arts & Sciences Hive, University of Kentucky, Lexington KY 40506 (jon@uky.edu).
A. Sarkar: Kavli Institute for Astrophysics and Space Research, Massachusetts Institute of Technology, 70 Vassar St, Cambridge, MA 02139, USA (arnabsar@mit.edu)
G. Shaw: Department of Astronomy and Astrophysics, Tata Institute of Fundamental Research, Mumbai 400005, India (gargishaw@gmail.com).
P. A. M. van Hoof: Royal Observatory of Belgium, Ringlaan 3, 1180 Brussels, Belgium (p.vanhoof@oma.be).

Revista Mexicana de Astronomía y Astrofísica, **59**, 345–377 (2023)

https://doi.org/10.22201/ia.01851101p.2023.59.02.13

TRACING THE ASSEMBLY HISTORIES OF GALAXY CLUSTERS IN THE NEARBY UNIVERSE

C. A. Caretta[1], H. Andernach[1,2], M. Chow-Martínez[1,3], R. Coziol[1], J. De Anda-Suárez[4], C. Hernández-Aguayo[5,6], J. M. Islas-Islas[1,7], M. M. Mireles-Vidales[1], M. A. Muñiz-Torres[1], H. Santoyo-Ruiz[8], J. J. Trejo-Alonso[1,9], Y. Venkatapathy[1,10], and J. M. Zúñiga[1]

Received February 14 2023; accepted August 14 2023

ABSTRACT

We have compiled a sample of 67 nearby ($z < 0.15$) clusters of galaxies, for which on average more than 150 spectroscopic members are available and, by applying different methods to detect substructures in their galaxy distribution, we have studied their assembly history. Our analysis confirms that substructures are present in 70% of our sample, having a significant dynamical impact in 57% of them. A classification of the assembly state of the clusters based on the dynamical significance of their substructures is proposed. In 19% of our clusters, the originally identified brightest cluster galaxy is not the central gravitationally dominant galaxy (CDG), but turns out to be either the second-rank, or the dominant galaxy of a substructure (a SDG, in our classification), or even a possible "fossil" galaxy in the periphery of the cluster. Moreover, no correlation was found in general between the projected offset of the CDG from the X-ray peak and its peculiar velocity.

RESUMEN

Recopilamos una muestra de 67 cúmulos cercanos ($z < 0.15$) de galaxias, con un promedio de más de 150 miembros espectroscópicos. Con diferentes métodos para detectar subestructuras en la distribución de sus galaxias, estudiamos la historia de ensamblaje. Confirmamos la presencia de subestructuras en el 70% de nuestros cúmulos, con un impacto dinámico significante en el 57% de ellos. Proponemos una clasificación de los estados de ensamblaje de los cúmulos basada en la significancia dinámica de sus subestructuras. En el 19% de ellos, la galaxia "más brillante" no es la galaxia gravitacionalmente dominante central (CDG), sino la segunda galaxia dominante, o bien la galaxia dominante de una subestructura (una SDG), o incluso una galaxia "fósil" en la periferia del cúmulo. No se encontró correlación entre el desplazamiento proyectado de la CDG respecto al pico de emisión en rayos-X y su velocidad peculiar.

Key Words: galaxies: clusters: general — galaxies: groups: general — large-scale structure of Universe

1. INTRODUCTION

According to the hierarchical structure formation paradigm, gravity brings together smaller mass systems into larger, more massive ones: in a sequential process, galaxies assemble in groups, and groups merge to form clusters which, at the present epoch, have started to congregate over the largest

[1]Departamento de Astronomía (DCNE-CGT), Universidad de Guanajuato, Callejón de Jalisco s/n, C.P. 36023, Guanajuato (Gto.), México.

[2]Thüringer Landessternwarte, Sternwarte 5, D-07778, Tautenburg, Germany.

[3]Instituto de Geología y Geofísica, Universidad Nacional Autónoma de Nicaragua, Managua, Nicaragua.

[4]Tecnológico Nacional de México, ITS Purísma del Rincón, Purísma del Rincón (Gto.), México.

[5]Max-Planck-Institut für Astrophysik, Karl-Schwarzschild-Str. 1, D-85748, Garching, Germany.

[6]Excellence Cluster ORIGINS, Boltzmannstrasse 2, D-85748, Garching, Germany.

[7]Universidad Tecnológica de Tulancingo, Tulancingo (Hgo.), México.

[8]Descubre Museo Interactivo de Ciencia y Tecnología, Aguascalientes (Ags.), México.

[9]Facultad de Ingeniería, Universidad Autónoma de Querétaro, Querétaro (Qro.), México.

[10]Instituto de Radioastronomía y Astrofísica, Universidad Nacional Autónoma de México, Morelia (Mich.), México.

scale appearing as superclusters. At each mass scale, the environment where the object (galaxy, group or cluster) forms influences how it grows and evolves, through complex physical processes that still need to be investigated and further clarified. This makes retracing the assembly histories of such objects/systems a difficult but paramount task.

The effects of the environment on galaxy formation and evolution have been extensively studied (*e.g.*, Dressler 1980; Caldwell et al. 1993; Poggianti et al. 2006), originally in terms of the cluster-field dichotomy. However, the discussion has recently taken a new turn, after realizing that groups and clusters are part of the cosmic web, namely, the large-scale structure (LSS). Within this new paradigm, the global environment of galaxies has a foamy texture, a structure full of voids (*e.g.*, Tempel et al. 2009; Varela et al. 2012; Einasto et al. 2014; Dupuy et al. 2019) that are encircled by a web of filaments (*e.g.*, Porter et al. 2008; Poudel et al. 2017; Santiago-Bautista et al. 2020), where the bulk of the intergalactic gas is found (*e.g.*, Fraser-McKelvie et al. 2011; Planck Collab. 2014; Reiprich et al. 2021), and connected through nodes, where the density of matter is highest. It is along the backbone of the filaments that groups of galaxies form, before migrating and merging within rich clusters of galaxies in the nodes.

Information about the fundamental properties of these structures and their member galaxies has also improved significantly thanks to many surveys: large-scale redshift surveys (*e.g.*, Shectman et al. 1996; Da Costa et al. 1998; Falco et al. 1999; Cole et al. 2005; Jones et al. 2009; Baldry et al. 2010; Huchra et al. 2012; Albareti et al. 2017), optical CCD-based photometric surveys (*e.g.*, Hambly et al. 2001a; Skrutskie et al. 2006; Aihara et al. 2011; Shanks et al. 2015; Dey 2019; Chambers et al. 2019; Abbott et al. 2021), and interferometric radio surveys (*e.g.*, Becker et al. 1995; Condon et al. 1998; Barnes et al. 2001; Lacy et al. 2020). These studies allowed various physical processes for the formation and evolution of galaxies to be identified, with efficiencies varying with the density of the environments of structures on different scales. Fundamentally, this has shown that understanding how galaxies form and evolve requires understanding how the structure and characteristics of their environments affect their intrinsic properties: their mass, morphology, star formation history and even BH formation and AGN activity.

However, this also implies being able to distinguish environmental effects from those related to secular evolution (the question of whether this is due to "nature or nurture"). A panoply of galaxy characteristics are used to achieve this goal, like their colors, their shapes, their orientations and spins, or equivalent parameters extracted from comparing their spectra with synthetic stellar population models. When studying groups and clusters, distinguishing between nature and nurture also necessitates recognizing the dynamical states of these systems, as reflected by the different distributions of galaxies, intergalactic gas (intracluster medium, ICM, or intragroup medium, IGM) and dark matter (the so-called halo-occupation problem). Reconciling all these different aspects is theoretically demanding and observationally expensive, which complicates the task of building a comprehensive model of their formation and evolution.

Usually, studies related to the structure and evolution of galaxy groups and clusters suffer from one or more of the following limitations: (i) only projected positional data are used for substructure analyses (*e.g.*, Lopes et al. 2006; Ramella et al. 2007; Wen & Han 2013); (ii) the use of photometric redshifts (*e.g.*, Wen & Han 2015; Bonjean et al. 2018) –clearly the estimation of redshifts using only photometry has improved a lot during recent years, but photometric redshifts still lack the accuracy to determine cluster membership and dynamical state in the way that is possible with spectroscopic redshifts–; (iii) only a small number of member galaxies with spectroscopic redshifts are available (frequently affecting high-redshift cluster studies); (iv) many spectroscopic redshifts are available but only for a small number of clusters (*e.g.*, Tyler et al. 2014; Song et al. 2017; Liu et al. 2018); (v) cluster samples that are biased in richness and mass, or focused on special aspects, like regularly shaped clusters, dominated by cD galaxies, showing strong X-ray emission or an ICM with strong Sunyaev-Zel'dovich (SZ) signal (*e.g.*, Oegerle & Hill 2001; Rumbaugh et al. 2018; Lopes et al. 2018). To palliate these limitations, we aim to build a database collecting information related to the environments of different structures in the nearby Universe (from groups to superclusters), that is as complete and homogeneous as possible. In this paper, we concentrate more specifically on defining a sample of galaxy clusters that have a large range of richness, to establish their dynamical and evolutionary states in order to trace their assembly histories.

For that, we need to better investigate the importance of substructures and their dynamically dominant galaxies for the cluster evolution as a whole.

We make a clear distinction here between the photometric ranking of member galaxies of a galaxy system (cluster or group), which has lead to the terms BCG (Brightest Cluster Galaxy) and BGG (Brightest Group Galaxy), and a ranking that takes into account their dynamical relevance and evolution. Because today we have enough information to study the assembly and evolution of galaxy clusters, this distinction becomes necessary. Thus, we define, for each cluster or group, a CDG (Central Dominant Galaxy), and one or more SDGs (Substructure/Subcluster/Satellite Dominant Galaxies) for each of the cluster substructures when they are present. The CDG and SDGs of a cluster are usually the brightest galaxies of this cluster, and we will retain the term BCGs to refer colectivelly to them. In other words, BCGs and BGGs are photometrically defined prior to a dynamical analysis, while CDGs and SDGs are a reclassification of the BCGs and BGGs according to their host sub-systems and dynamical importance.

Moreover, assuming that CDGs with a cD (or D) type morphology form by cannibalizing galaxies falling toward the center of the potential wells of the clusters (*e.g.*, Coziol et al. 2009; Zhao et al. 2015), one would naturally expect their masses to show some specific relation with the masses of their parent structures, M_{Cl}–M_{CDG} (*e.g.*, Stott et al. 2010; Lavoie et al. 2016). In particular, we would expect CDGs in dynamically relaxed clusters to lie at the bottom of the potential wells of their systems. However, observations show that, for most of the clusters, the positions of many cDs are offset from the peak in X-ray emission, the latter assumed to settle more rapidly to the bottom of the potential well, or having high peculiar velocities within the cluster compared to the center of the radial velocity distribution (Coziol et al. 2009; Martel et al. 2014; Lauer et al. 2014). This points to most of the clusters being unrelaxed, or maybe to the presence of some undetected projection effects.

Another difficulty lies in the cannibalism mechanism itself. How can mergers happen efficiently in a systems where the velocity dispersion of galaxies increases as they fall into deep potential wells (*e.g.*, Merritt 1985; Tonry 1985; Mihos 2004)? Alternatively, an important part of the formation of galaxies now in clusters could have happened in smaller-mass systems, like groups, where the velocity dispersion (and thus the amount of ICM) is smaller, the groups then merging to form or enrich more massive clusters. This phenomenon is known in literature as pre-processing (*e.g.*, Caldwell et al. 1993; Caretta et al. 2008; Donnari et al. 2021).

Within the cosmic web paradigm, one needs to ponder how the constant feeding of clusters by the merging and accretion of groups forming in filaments tempered these expectations. For instance, assuming mergers take place regularly, substructures in the distribution of galaxies would be expected to be common at low redshifts. This would naturally explain the CDG–X-ray offsets, since the ICM having a higher impact parameter than galaxies would follow a different path towards virialization, reaching equilibrium more rapidly.

Common mergers of groups within a cluster would also be expected to disrupt the cool core (CC) of this system, making the CDG wobble around the distorted potential well, explaining its peculiar velocity (*e.g.*, Harvey et al. 2017). This could also have an important impact on the formation of cD galaxies. In the evolution scenario proposed by Lavoie et al. (2016), for example, it is proposed that a CDG transforms into a cD by cannibalism only when, after a cluster-scale merger event, the most massive galaxies of the merging groups, displaced from their initial potential, migrate towards the potential center of the newly formed cluster; this temporary imbalance increases dynamical friction and thus favors cannibalism. Consequently, one would expect the magnitude gaps to increase between the CDG and its luminous neighbors, but not necessarily between the second and third-rank galaxies, due to their large velocity dispersion.

All these considerations suggest that, assuming that groups in filaments continuously merge to form clusters, several primeval group CDGs might appear among the BCGs of a cluster. Moreover, due to the different time-scales for the relaxation of such complex systems, we might also expect the galaxy distributions and characteristics to reflect some specific aspects of their merger processes. By compiling and studying a well characterized sample of galaxy clusters, therefore, it should be possible to distinguish different states of the merger process, and to better document their assembly histories.

The sample we present in this article is an effort in this direction. It is composed of 67 optically selected Abell galaxy clusters that are nearby ($z < 0.15$), and for which a large number (above 100) of spectroscopically confirmed potential members are available. This sample includes a fair distribution of all Bautz-Morgan (BM) type clusters and various levels of ICM X-ray properties (from luminous to under-luminous, AXU). The article is organized in the following way. In § 2, we present the data used in our study: we introduce the cluster and galaxy samples and describe the information retrieved from the photometric, astrometric and spectroscopic observations. In § 3, we describe the methods we used to characterize the galaxy systems and their structures: center and membership determination, characterization of dynamical parameters (like cluster redshift, velocity dispersion, richness, mass, gravitational binding, and CDG offsets and gaps), and optical substructuring analyses. Our results about the dynamical properties and level of substructuring, for the outer, inner, and core regions of the systems, are discussed in § 4. This is followed by a brief summary and conclusions in § 5. For our analysis, we assume a standard ΛCDM cosmology, with $\Omega_\Lambda = 0.7$, $\Omega_{\rm M} = 0.3$ and $\rm H_0 = 70\ h_{70}$ km s^{-1} Mpc^{-1}.

2. DATA

2.1. *Cluster Sample*

To build our sample of galaxy clusters, we started with the compilation maintained by one of us (Andernach et al. 2005, see also Chow-Martínez et al. 2014), where we included clusters for which at least $N_z = 100$ spectroscopic-redshifts from the literature were available. These are nearby, optically selected Abell-ACO (Abell et al. 1989) galaxy clusters, with richness varying from poor to rich, and located within the redshift range $0.005 < z < 0.150$. In each cluster, a galaxy is identified as a potential member when its apparent position puts it inside a projected Abell radius, $R_{\rm A} = 2.14 h_{70}^{-1}$ Mpc, and its radial velocity has a value within ± 2 500 km s^{-1} of a preliminary estimate for the central velocity of the system. However, its final acceptance as member will depend on a more thorough analysis, which is explained in § 3.

Our cluster sample is presented in Table 1, together with some relevant data taken from the literature. The first seven columns reproduce the original ACO data for the clusters: the cluster ID (Column 1), its equatorial coordinates, RA and Dec, in J2000 (Column 2 and Column 3), its richness ($\mathcal{R}$ in Column 4), distance class ($\mathcal{D}$ in Column 5), BM-type (BM in Column 6; Bautz & Morgan 1970) (we have converted the original scale I, II, III to 1, 3, 5 and intermediate types 2 and 4), and Rood-Sastry type when available (RS in Column 7; Rood & Sastry 1971; Struble & Rood 1982). The X-ray characteristics for each cluster are given in Columns 8 to 14: alternative X-ray name when existent (Column 8), equatorial coordinates of the X-ray emission peak (centroid position; J2000 RA and Dec in Column 9 and Column 10), the X-ray luminosity inside r_{500} (Column 11; this is the radius at which the mean interior overdensity is 500 times the critical density, ρ_c, at the respective redshift), r_{500} itself (Column 12; mostly from Piffaretti et al. 2011), and the X-ray temperature as measured by Migkas et al. (2020) in Column 13, or by others as indicated in Column 14. Note that there are new temperatures for four clusters, based on XMM-Newton and Chandra, presented for the first time in this table (see Appendix A). Finally, we list the membership of a cluster in a supercluster (Column 15), based on the *Master SuperCluster Catalog* (MSCC; Chow-Martínez et al. 2014), followed in Column 16 by an alternate or common name, when available, or the name of the pair when it is the case, and multiplicity, m, of the supercluster in Column 17, the multiplicity being the number of Abell clusters forming the supercluster.

This sample is well balanced in terms of BM types, covering all the possible different dynamical states: containing 17, 17, 9, 9 and 15 clusters, respectively, with BM types 1 to 5. It also follows roughly the distribution of richness of ACO clusters, clearly favoring low richness systems, in accordance with the power-law mass distribution function for clusters: 20 are classified as $\mathcal{R} = 0$ (poorest; 30-49 galaxies), 24 as $\mathcal{R} = 1$ (50-79), 20 as $\mathcal{R} = 2$ (80-129) but only 2 as $\mathcal{R} = 3$ (130-199) and 1 as $\mathcal{R} \geq 4$ (richest; more than 200 galaxies). However, due to the spectroscopic selection criterion, the distribution of Abell distance classes ($\mathcal{D}$ varying from 0 to 7) is not equally represented, favoring nearby clusters. Although we cannot claim completeness, this sample can be considered a fair representation of optically selected Abell clusters at low redshifts.

Most of these clusters (59 or 88%) are detected in X-rays. Fifty-three are included in the compilation of X-ray clusters by Piffaretti et al. (2011). The other six X-ray clusters in our sample, namely A0118, A2040, A2801, A2804, A3556 and A3716, were detected by previous surveys (respectively by Kowalski et al. 1984; Stewart et al. 1984; Obayashi et al. 1998; Sato et al. 2010; Ebeling et al. 1996, the last reference applying to the last two clusters). A3716 was also identified as a SZ source by the Planck satellite (Planck Collab. 2016), with which catalog we have 43 clusters (64%) in common. The range in temperature, $k\rm T_X$, is also quite large, varying from 1 to 12 keV, which is typical of low-mass to relatively massive clusters. Only 8 clusters in our sample, namely A0634, A2870, A3095, A4012, A4049, S0334, S0336 and S0906, have not yet been detected in X-rays. These might be considered as "Abell

TABLE 1

CLUSTER SAMPLE

ACO data							X-ray data							LSS data		
ACO	RA_{ACO} [deg]$_{J2000}$	Dec_{ACO} [deg]$_{J2000}$	$\mathcal{R}$	$\mathcal{D}$	BM[a]	RS	Alt_Name	RA_X [deg]$_{J2000}$	Dec_X [deg]$_{J2000}$	L_{500} [10^{44} erg/s]	r_{500} [Mpc]	kT_X [keV]	Ref.[b]	MSCC[c]	SC_Name	m
(1)	(2)	(3)	(4)	(5)	(6)	(7)	(8)	(9)	(10)	(11)	(12)	(13)	(14)	(15)	(16)	(17)
A2798	9.3916	−28.5417	1	5	2	–	J0037.4-2831	9.3625	−28.5311	0.5455	0.7476	3.39	5	33	Scl(C)	24
A2801	9.6404	−29.0752	1	6	1	–	...	9.6346	−29.0789	...	...	3.20	2	33	Scl(C)	24
A2804	9.9149	−28.9088	1	5	2	–	...	9.9113	−28.8892	...	...	1.00	8	33	Scl(C)	24
A0085	10.4075	−9.3425	1	4	1	cD	J0041.8-0918	10.4587	−9.3019	5.1001	1.2103	7.23	10	39	PisCet-N	11
A2811	10.5386	−28.5426	1	5	2	–	J0042.1-2832	10.5363	−28.5358	2.7341	1.0355	5.89	10	33	Scl(C)	24
A0118	13.9329	−26.4127	1	5	5	I	...	...	...	...	...	...	...	33	Scl(NE)	24
A0119	14.0890	−1.2629	1	3	4	C	J0056.3-0112	14.0762	−1.2167	1.4372	0.9413	5.82	10	45	-	4
A0122	14.3571	−26.2799	1	5	2	B	J0057.4-2616	14.3529	−26.2806	0.8612	0.8165	3.70	11	33	Scl(NE)	24
A0133	15.6610	−21.7982	0	4	1	cD	J0102.7-2152	15.6754	−21.8736	1.4602	0.9379	4.25	10	27	PisCet-C	9
A2870	16.9299	−46.9165	0	3	1	–	...	...	...	...	...	1.07	11	41	Phe	8
A2877	17.4554	−45.9006	0	2	1	C	J0110.0-4555	17.5017	−45.9228	0.1815	0.6249	3.28	10	41	Phe	8
A3027	37.6300	−33.0953	0	4	5	–	J0230.7-3305	37.6812	−33.0986	0.4186	0.7200	3.12	5	iso	-	1
A0400	44.4107	6.0333	1	1	4	I	J0257.6+0600	44.4121	6.0061	0.2211	0.6505	2.25	10	iso	Southern GW	1
A0399	44.4851	13.0164	1	3	2	cD	J0257.8+1302	44.4575	13.0492	3.5929	1.1169	6.69	10	108	+A0401	2
A0401	44.7373	13.5823	2	3	1	cD	J0258.9+1334	44.7396	13.5794	6.0886	1.2421	7.06	10	108	+A0399	2
A3094	47.8608	−26.9289	2	4	2	–	J0311.4-2653	47.8542	−26.8997	0.3343	0.6907	3.15	11	114	-	3
A3095	48.1094	−27.1464	0	4	2	–	...	...	...	...	...	...	...	114	-	3
A3104	48.5788	−45.4150	0	4	1	–	J0314.3-4525	48.5825	−45.4242	1.0275	0.8662	3.56	10	115	HorRet-B	9
S0334	49.0794	−45.1168	0	4	3	–	...	...	...	...	...	...	...	115*	HorRet-B	9
S0336	49.3815	−44.7012	0	4	3	–	...	...	...	...	...	...	...	115*	HorRet-B	9
A3112	49.4845	−44.2349	2	4	1	cD	J0317.9-4414	49.4937	−44.2389	3.8159	1.1288	5.49	10	115	HorRet-B	9
A0426	49.6517	41.5151	2	0	4	L	J0319.7+4130	49.9467	41.5131	6.2174	1.2856	6.42	4	96	PerPis	3
S0373	54.6289	−35.4545	0	0	1	C	J0338.4-3526	54.6163	−35.4483	0.0197	0.4017	1.56	4	iso	Southern SC	1
A3158	55.7526	−53.6426	2	4	2	–	J0342.8-5338	55.7246	−53.6353	2.7649	1.0667	5.42	10	117	HorRet-A	26
A0496	68.4045	−13.2462	1	3	1	cD	J0433.6-1315	68.4100	−13.2592	1.8530	0.9974	4.64	10	iso	-	1
A0539	79.1463	6.4540	1	2	5	F	J0516.6+0626	79.1554	6.4378	0.5377	0.7773	3.04	4	iso	-	1
A3391	96.5644	−53.6812	0	4	1	–	J0626.3-5341	96.5950	−53.6956	1.1601	0.8978	5.89	10	160	-	3
A3395	96.8796	−54.3994	1	4	2	F	J0627.2-5428	96.9000	−54.4463	1.3755	0.9298	5.10	7	160	-	3
A0576	110.3506	55.7389	1	2	5	I	J0721.3+5547	110.3425	55.7864	0.7571	0.8291	4.27	10	iso	-	1
A0634	123.6404	58.0479	0	3	5	F	...	...	...	...	...	...	...	iso	-	1
A0754	137.2086	−9.6366	2	3	2	cD	J0909.1-0939	137.1978	−9.6412	3.8497	1.1439	8.93	9	198	+A0780	2
A1060	159.2137	−27.5265	1	0	5	C	J1036.6-2731	159.1742	−27.5244	0.3114	0.7015	2.79	10	365	HyaCen	10
A1367	176.1231	19.8390	2	1	4	F	J1144.6+1945	176.1521	19.7589	1.1046	0.9032	3.81	10	295	ComLeo	5
A3526	192.2157	−41.3058	0	0	2	F	J1248.7-4118	192.1996	−41.3078	0.6937	0.8260	3.40	10	365	HyaCen	9
A3530	193.9037	−30.3540	0	4	2	–	J1255.5-3019	193.8937	−30.3306	0.6805	0.8043	3.62	10	389	Shapley(W)	24
A1644	194.3115	−17.3535	1	4	3	cD	J1257.1-1724	194.2904	−17.4003	1.8975	0.9944	5.25	10	370	+A1631	2
A3532	194.3299	−30.3702	0	4	4	C	J1257.2-3022	194.3204	−30.3769	1.3233	0.9201	4.63	10	389	Shapley(W)	24
A1650	194.6926	−1.7530	2	5	2	cD	J1258.6-0145	194.6712	−1.7569	3.4706	1.1015	5.72	10	376	SGW	6
A1651	194.8456	−4.1862	1	4	2	cD	J1259.3-0411	194.8396	−4.1947	3.8536	1.1252	7.47	10	376	SGW	6
A1656	194.9530	27.9807	2	1	3	B	J1259.7+2756	194.9296	27.9386	3.4556	1.1378	7.41	10	295	ComLeo	5
A3556	201.0260	−31.6605	0	4	1	–	...	200.9350	−31.8380	...	...	3.08	6	389	Shapley(C)	24
A1736	201.7173	−27.1093	0	2	5	I	J1326.9-2710	201.7250	−27.1833	1.6675	0.9694	3.34	10	389	Shapley(N)	24
A3558	201.9782	−31.4922	4	3	1	–	J1327.9-3130	201.9896	−31.5025	3.1385	1.1010	5.83	10	389	Shapley(C)	24
A3562	203.3825	−31.6729	2	3	1	–	J1333.6-3139	203.4012	−31.6611	1.3458	0.9265	5.10	10	389	Shapley(C)	24
A1795	207.2522	26.5852	2	4	1	cD	J1348.8+2635	207.2208	26.5956	5.4781	1.2236	6.42	10	414	Boo	24
A2029	227.7447	5.7617	2	4	1	cD	J1510.9+0543	227.7292	5.7200	8.7267	1.3344	8.45	10	457	-	6
A2040	228.1884	7.4300	1	4	5	C	...	228.2113	7.4317	...	...	2.41	1	454	-	6
A2052	229.1896	7.0003	0	3	2	cD	J1516.7+0701	229.1833	7.0186	1.4421	0.9465	2.88	10	458	Her-S	4
A2065	230.6776	27.7226	2	3	5	C	J1522.4+2742	230.6104	27.7094	2.6279	1.0480	6.59	10	463	CrB	14
A2063	230.7578	8.6394	1	3	3	cD	J1523.0+0836	230.7725	8.6025	1.1388	0.9020	3.34	10	458	Her-S	4
A2142	239.5672	27.2246	2	4	3	B	J1558.3+2713	239.5858	27.2269	10.6761	1.3803	11.63	10	472	+A2148	2
A2147	240.5716	15.8954	1	1	5	F	J1602.3+1601	240.5779	16.0200	1.3584	0.9351	4.26	10	474	Her-C	5
A2151	241.3125	17.7485	2	1	5	F	J1604.5+1743	241.2863	17.7300	0.5088	0.7652	2.10	10	474	Her-C	5
A2152	241.3435	16.4486	1	1	5	F	J1605.5+1626	241.3842	16.4419	0.1283	0.5783	2.41	6	474	Her-C	1
A2197	247.0436	40.9072	1	1	5	L	J1627.6+4055	246.9175	40.9197	0.0674	0.5093	2.21	3	485	Her-N	4
A2199	247.1540	39.5243	2	1	1	cD	J1628.6+3932	247.1583	39.5486	1.9007	1.0040	4.04	10	485	Her-N	4
A2204	248.1903	5.5785	3	5	3	C	J1632.7+0534	248.1937	5.5706	13.6256	1.3998	10.24	10	out	-	-
A2244	255.6834	34.0468	2	5	2	cD	J1702.7+3403	255.6787	34.0619	4.0452	1.1295	5.99	10	492	-	3
A2256	255.9313	78.7174	2	3	4	B	J1703.8+7838	255.9533	78.6444	3.5435	1.1224	8.23	10	495	-	3
A2255	258.1293	64.0926	2	3	4	C	J1712.7+6403	258.1967	64.0614	2.9491	1.0678	7.01	10	iso	NEP SC	1
A3716	312.8866	−52.7121	1	3	4	F	...	312.9873	−52.6301	...	...	2.19	11	309#	-	3
S0906	313.1034	−51.9613	0	4	3	–	...	...	...	...	...	...	...	309#	-	3
A4012	352.9398	−33.8239	0	6	4	–	...	...	...	...	...	...	...	584	-	3
A2634	354.5766	27.0270	1	1	3	cD	J2338.4+2700	354.6071	27.0125	0.4414	0.7458	3.71	10	592	+A2666	2
A4038	356.9246	−28.1387	2	2	5	B	J2347.7-2808	356.9300	−28.1414	1.0295	0.8863	2.84	10	595	+A4049	2
A4049	357.8971	−28.3718	0	3	5	–	...	...	...	...	...	...	...	595	+A4038	2
A2670	358.5571	−10.4190	3	4	2	cD	J2354.2-1024	358.5560	−10.4130	1.3365	0.9113	4.45	10	iso	-	1

[a]**BM** types I, I-II, II, II-III and III, coded as 1, 2, 3, 4 and 5.

[b][1] Stewart et al. (1984), [2] Obayashi et al. (1998), [3] Finoguenov et al. (2001), [4] Ikebe et al. (2002), [5] Cruddace et al. (2002), [6] Fukazawa et al. (2004), [7] Vikhlinin et al. (2009), [8] Sato et al. (2010), [9] Planck Collab. (2011), [10] Migkas et al. (2020), [11] This work.

[c][iso] Isolated, [out] not in MSCC ($z > 0.15$); S-clusters not in MSCC, but with [*] percolated in SSCC (*Southern Super-Cluster Catalog;* Chow-Martínez et al. 2014) with the respective MSCC supercluster, and clusters with [#] percolated only in SSCC (SSCC number used here).

X-ray Underluminous" Cluster candidates (AXUs, for short, *e.g.*, Trejo-Alonso et al. 2014).

2.2. *Spectroscopic Data for Member Galaxies*

From the information gathered in the compilation described by Andernach et al. (2005), we retrieved, for each galaxy, the celestial coordinates and line-of-sight (LOS) heliocentric radial velocities with their uncertainties. Due to the diversity of the sources, these data are not homogeneous. To assess this problem, we treated the different quality of redshift data by adopting distinct approaches: (1) eliminating data with large ($\geq$ 400 km s^{-1}) estimated uncertainties, (2) eliminating obvious outliers as described further below, (3) using the average of the radial velocities for every single galaxy, (4) taking advantage of the statistics to minimize the stochastic errors (for example, calculating mean velocities and velocity dispersion for the clusters).

For the celestial coordinates, we adopted the strategy of inspecting every close pair of entries with separations larger than $3''$ (they rarely exceed $30''$), tentatively associated to the same galaxy, directly on a DSS2 image (Digitized Sky Survey, STScI) using the Aladin interface (Bonnarel et al. 2000). Multiple redshift entries for the same galaxy are not uncommon and, once the multiple velocities for the same galaxy were judged consistent, we proceeded to average the different measurements, taking great care in excluding outlier values (above 3 sigma, when there are at least three independent velocity measurements). After applying this process to each cluster, we obtained a list of potential member galaxies, all with a single position, average LOS velocity and respective uncertainties (typically $\pm$ 0.5" and $\pm$ 60 km s^{-1}, respectively, per galaxy).

2.3. *Astrometric and Photometric Data of Galaxies*

Although the galaxy coordinates, calculated as in the last paragraph, are precise enough, they are not homogeneous, combining more accurate positions with poorer ones. To calculate mean pairwise separations (see below), for example, we need to improve these positions. To this end, we cross-correlated the position of each galaxy in our lists with the positions in two astrometric and photometric catalogues covering the whole sky, SuperCOSMOS (Hambly et al. 2001a) and Two Micron All Sky Survey (2MASS; Skrutskie et al. 2006).[11] SuperCOSMOS is a relatively deep optical survey, reaching $b_J \approx 19.5$ with acceptable levels for completeness, $> 95\%$, and contamination, $< 5\%$ (Hambly et al. 2001b). Although it has good astrometry, with an uncertainty of order $\pm\ 0.25''$ (Hambly et al. 2001c), the typical uncertainty of the magnitudes is relatively large, $\pm$ 0.3 mag (Hambly et al. 2001b), because it was obtained from the digitization of photographic sky survey plates. 2MASX (the catalogue of 2MASS eXtended sources), on the other hand, is a digital NIR survey reaching $K_s \approx 13.5$, with nominal levels of completeness and contamination respectively of $> 90\%$ and $< 2\%$. Although the uncertainty in astrometry is about the same as in SuperCOSMOS ($0.3''$, for extended sources), the quality of the magnitudes is better, with a typical uncertainty $\pm$ 0.03 (Jarrett et al. 2000). Also, since the NIR is less affected by dust extinction (*e.g.*, Fitzpatrick 1999), the K-correction is minimal (*e.g.*, Fukugita et al. 1995; Chilingarian et al. 2010) compared to the optical. Particular care is devoted to the photometry of the brightest galaxies in 2MASS because the data come mostly from a special catalogue, the Large Galaxy Atlas (Jarrett et al. 2003), which is dedicated to galaxies that are more extended than $1'$.

The only drawback of 2MASS is the depth of the survey: at the magnitude limit $K_s \approx 13.5$ the mean redshift of galaxies is $z \approx 0.08$ (Jarrett 2004). This implies that only a fraction (about 50%) of the galaxies, the brightest in our sample, have an entry in 2MASX. Another disadvantage is the limited capacity of 2MASS to separate galaxies that are very close in projection, which is the case of faint "dumbbell" CDGs/SDGs in our sample (although this does not happen for galaxies in the Large Galaxy Atlas). SuperCOSMOS performs better in "deblending" galaxies, but then fails in accuracy determining their magnitudes once they are separated, their brightness being usually underestimated. Therefore, although we matched our data with the astrometric and photometric data in both catalogues, for the sake of homogeneity we used only 2MASS in the present paper. Absolute magnitudes for the BCGs were calculated after correcting for Galactic extinction, using the recalibration done by Schlafly & Finkbeiner (2011) of the dust maps of Schlegel et al. (1998), and applying a K-correction as determined by Chilingarian et al. (2010).

[11] The most recent CCD-based surveys, like the Sloan Digital Sky Survey (SDSS; Ahn et al. 2012), the Mayall z-band Legacy Survey (MzLS) + Dark Energy Camera Legacy Survey (DECaLS) (Dey 2019), and the Dark Energy Survey (DES; Abbott et al. 2021), were not used because they only cover small regions of the sky; at most about 1/3, and 3/4 in the case of the Panoramic Survey Telescope and Rapid Response System (PanSTARRS; Chambers et al. 2019).

3. METHODS TO CHARACTERIZE THE GALAXY SYSTEMS AND THEIR STRUCTURES

3.1. *Central and Substructure Dominant Galaxies and the Definition of the Cluster Center*

In any cluster, group or substructure of galaxies we classify as SDG/CDG the galaxy that, being among the BCGs, occupies the most central position around the gravitational potential well of its (sub-)system. From a practical observational point of view, a CDG/SDG must be coincident or very close to the local surface density peak in the sky distribution of the member galaxies. This also implies that its position is expected to be located near the X-ray emission peak (c.f. § 4.4) when this emission is detected.

In each substructured cluster, we identify (based on criteria to be explained below) one substructure as the "main" (or gravitationally dominant) substructure and adopt its SDG as the CDG for the whole system. Also, as a general rule, we adopt the position of the CDG/SDG as the location of the dynamical center of the cluster/substructure.

In the literature, the physical characteristics of the BCG are commonly used as a trade mark of its system. However, identifying which galaxy is the BCG obviously depends on which band-pass is used. For example, a very bright spiral galaxy, especially in a starburst phase, in the outskirts of a cluster, could easily be brighter in B or V than a giant and red elliptical near its center (*e.g.*, NGC 1365 in Fornax/S0373). This is why we define our BCGs to be more luminous in K_s, which is a better proxy for the stellar mass of galaxies, and thus consistent with the idea that a CDG/SDG should also be the most massive galaxy of its cluster/substructure.

Adopting these definitions, in 81% of our cluster sample we found the CDG to be coincident with the original BCG, according to prescriptions given by, for example, Abell (or others like Bautz & Morgan 1970; Rood & Sastry 1971; Struble & Rood 1982). However, in the remaining 19% of the clusters the BCG is not the CDG, for one of the following three reasons: (i) the BCG is really a SDG, like in the case of Fornax (NGC 1316), forming 13% of our cluster sample (we classified them as "Fornax-like" clusters); (ii) the BCG is located close to the center of the cluster (as confirmed by X-ray emission or based on other dynamical analyses) but is only slightly brighter than the real CDG, as in Coma (BCG: NGC 4889, CDG: NGC 4874), forming 4% of our sample (they are classified as "Coma-like" clusters); (iii) the BCG is a giant elliptical galaxy located at the periphery of the cluster, forming 2% of our sample (we classify these galaxies as "fossil group candidates", without, at this point, gathering more data to confirm this candidacy).

3.2. *Cluster Membership*

When clusters are separated by less than 6 h_{70}^{-1} Mpc on the sky, the areas subtended by their $R_{\rm A}$ overlap. There are 38 clusters in our sample for which this is the case. To separate the members (or populations) of these clusters, we first merged the lists of their potential member galaxies, eliminating the duplicated entries as assigned by different sources in the literature to the different systems. Then we proceeded to separate the galaxies that are members of each cluster, by applying a method similar to the one described in § 3.4 for identifying substructures.

To double-check our results, we also applied to the superposed clusters a two-body Newtonian criterion for gravitationally bound systems (see Beers et al. 1982, and § 3.5). The results (bound *vs.* unbound) obtained by this process are in good agreement with previous results in the literature (Gregory & Thompson 1984; Krempéc-Krygier et al. 2002; Pearson & Batuski 2013; Yuan et al. 2005). It is worth noting that 4 of the 11 bound complexes in Table 2 are consistent with supercluster "cores" (Zúñiga *et al.*, in preparation); those are: Her-C (MSCC 474), Scl (MSCC 033), HorRet-B (MSCC 115) and Shapley (MSCC 389). Among the other bound systems, three are typical pairs, A0399-A0401, A2052-A2063A and A3530-A3532, and four, A0122-A0118, A2199-A2197, A2877-A2870 and A4038A-A4049, are examples of a massive cluster (main cluster, first of the pair) linked by a filament made of various groups (secondary system; c.f. § 4.2).

After homogenizing the galaxy coordinates by applying the match with photometric data, and after defining the different centers and correcting for superposed clusters, we proceeded to check the membership of the galaxies in their respective clusters using a more robust approach. The principle is simple: considering that, in a gravitationally-bound system, the galaxies must have velocities that do not exceed the escape velocity, their distribution in a projected phase-space (PPS) diagram, formed by the LOS velocity as a function of projected cluster-centric distance, *e.g.*, Figure 1, must be enclosed within a trumpet-shaped curve, usually called "caustic", as defined by the escape velocity (*e.g.*, Regös & Geller 1989; López-Gutiérrez et al. 2022). Details about the method for defining and fitting caustics are presented in Chow-Martínez (2019). In Figure 1, all

TABLE 2

SUPERPOSED CLUSTERS IN OUR SAMPLE

Projected information					Gravitational binding	
Clusters	Sep.† [h_{70}^{-1} Mpc]	N_z	N_g	N_c	Bound	Unbound
A0118–A0122	2.95	190	119	111	A0118-A0122	
A0399–A0401	3.03	245	217	184	A0399-A0401	
A1736A–A1736B#	0.83	464	219	215		A1736A, A1736B
A2052–A2063A	5.53	959	378	369	A2052-A2063A	
A2147–A2151–A2152A	4.94,3.69	2096	936	880	A2147-A2151	A2152A
A2197–A2199	3.05	1684	815	774	A2197-A2199	
A2798B–A2801–A2804–A2811B	4.36,2.40,5.32	424	381	342	A2798B-A2801-A2804	A2811B
A2870–A2877	1.92	428	237	174	A2877-A2870*	
A3094A-A3095	1.52	253	170	154		A3094A, A3095♮
A3104–S0334–S0336–A3112B	2.96,2.23,3.85	563	268	221	S0336♮-A3112B-S0334♮-A3104	
A3391–A3395	3.03	761	343	318		A3391, A3395
A3526A–A3526B#	0.29	1041	336	330		A3526A, A3526B
A3530–A3532	1.69	411	238	213	A3530-A3532	
A3556–A3558–A3562	3.32,4.83	2057	863	800	A3556-A3558-A3562§	
A3716–S0906	1.67	409	219	194		A3716, S0906♮
A4038A–A4049	2.09	816	247	237	A4038A-A4049*	

†Projected separation between nearest clumps.
#Clusters slightly separated in projection and separable in redshift.
*Clusters considered to be substructures.
♮Clusters that are possible satellite groups.
§A fourth non-Abell cluster was clearly identified within this system (AM 1328−313).

the galaxies falling outside the caustic for the cluster A0085 are discarded, leaving only those that are considered as gravitationally bound.

Applying the caustics analysis, we found that on average 10% of the candidate member galaxies in each cluster, at least in relatively isolated systems, must be discarded. For the overlapping clusters above, these galaxies are usually bound to another cluster of the complex. Obviously, no single galaxy is assigned to more than one cluster.

3.3. *Determination of Cluster Dynamical Parameters*

To establish the dynamical properties of each system, we first measure two robust kinematical parameters, known as the biweight central value, $C_{\rm BI}$, and scale, $S_{\rm BI}$ (Beers et al. 1990). Using these parameters, we calculate preliminary values for the systemic radial velocities, $v_{\rm c}$, and velocity dispersions, $\sigma_{\rm c}$, considering the N_c members. Then we proceed by defining, for each cluster, a projected aperture on the sky consistent with the virial radius.

This implies first estimating r_{200}, the radius inside which the mean density of galaxies exceeds $200 \times \rho_c$ at the redshift of the cluster. Following the prescription by Carlberg et al. (1997):

$$r_{200} = \frac{\sqrt{3}\,\sigma_{\rm c}}{10\,H(z)}, \qquad (1)$$

where

$$H(z) = H_0\sqrt{\Omega_r(1+z)^4+\Omega_m(1+z)^3+\Omega_k(1+z)^2+\Omega_\Lambda}\,,$$

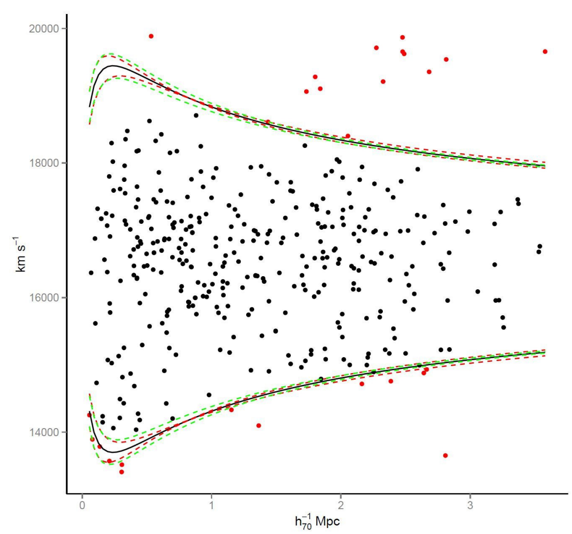

Fig. 1. Example of applying the caustics method to the cluster A0085; the caustics are the black solid lines, while the red dashed lines indicate the rms of the fit and the green dashed lines the bootstrap uncertainty (1 000 simulations). Black points (that is, the ones within the caustics) are taken to be the bound members, while red points are discarded as cluster members. The color figure can be viewed online.

assuming Ω_r (radiation) and Ω_k (curvature) are about zero. Since the virial radius depends on the redshift and cosmology (*e.g.*, Bryan & Norman 1998), a local value of $1.3 \times r_{200}$, corresponding to about r_{100}, is usually adopted (*e.g.*, Kopylova & Kopylov 2018). Once the circular aperture corresponding to the virial radius is determined, we counted the number of galaxies inside it, N_a, and recalculated the systemic radial velocity, $v_{\rm cl}$, and its velocity dispersion, $\sigma_{\rm cl}$, using once again $C_{\rm BI}$ and $S_{\rm BI}$.

These N_a galaxies are also used to calculate the projected radius, $R_{\rm p}$, equal to twice the harmonic mean projected separation, using the relation:

$$R_{\rm p} = N_a(N_a - 1)\left(\sum_{i<j}^{N_a} \frac{1}{|r_{ij}|}\right)^{-1}, \qquad (2)$$

where r_{ij} is the pairwise projected separation between galaxies. Estimation of the virial mass, $M_{\rm vir}$, follows the relation:

$$M_{\rm vir} = \frac{\alpha\pi}{2G}\,\sigma_{\rm cl}^2\,R_{\rm p}, \qquad (3)$$

where the factor α quantifies the isotropy level of the system ($\alpha = 3$ when complete isotropy is assumed), applied to $\sigma_{\rm cl}$, while the factor $\pi/2$ is applied to deproject $R_{\rm p}$ (Limber & Mathews 1960). Finally, the virial radius is obtained using the relation:

$$R_{\rm vir}^3 = \frac{3}{4\pi}\frac{M_{\rm vir}}{\rho_{\rm vir}} = \frac{\alpha\,\sigma_{\rm cl}^2\,R_{\rm p}}{18\pi\,H^2(z)}, \qquad (4)$$

where the virial density is defined as $\rho_{\rm vir} = 18\pi^2(3H^2(z)/8\pi G)$.

3.4. *Substructure Analysis*

Several tests, in different spatial dimensions, have been proposed for the detection of substructures in galaxy clusters based on optical data: in 1D, as applied to the redshifts (*e.g.*, Bird & Beers et al. 1993; Hou et al. 2009), in 2D, as applied to galaxy projected celestial coordinates (*e.g.*, Geller & Beers 1982; Fitchett & Webster 1987; West et al. 1988; Kriessler & Beers 1997; Flin & Krywult 2006), and in 3D, as applied to both redshifts and coordinates (*e.g.*, Dressler & Shectman 1988; Serna & Gerbal 1996; Pisani 1996; Einasto et al. 2010; Yu et al. 2015). However, not all these tests have the same efficiency. Through a study of 31 different tests, Pinkney et al. (1996) found the 3D-test developed by Dressler & Shectman (1988, DS herafter) to be the most sensitive, concluding that, in general, the higher the dimension of a test, the more powerful it is in distinguishing substructures. This was confirmed subsequently by Einasto et al. (2012), who also showed that 3D-tests are more robust than 2D-tests, and 2D-tests more robust than 1D-tests. However, both groups recommended the application of more than one test.

Tests for detecting substructures using X-ray data have also been proposed (*e.g.*, Mohr et al. 1993; Buote & Tsai 1995; Andrade-Santos et al. 2012). However, because the tests are based on X-ray surface brightness, the detection of substructures is usually limited to the densest, most concentrated ($R < r_{500}$) regions of the clusters (*e.g.*, Piffaretti & Valdarnini 2008), which might complicate comparisons with substructures detected in the optical. In the study made by Lopes et al. (2018), for example, only $\approx 60\%$ of the substructures detected in optical were also detected in X-ray, both inside r_{500}. They also found the fraction of substructures to increase with the aperture used, as well as with the mass of the cluster and its redshift (up to $z \approx 1$; see also Jeltema et al. 2005). Although these trends are consistent with various levels of relaxation (for example, clusters being less relaxed in the past than now), establishing a firm connection, as well as a time scale to reconstruct the assembly histories of clusters, is not straightforward and needs independent confirmation.

In principle, this is what a study of the CDG dynamical characteristics can contribute. More specifically, the projected position offset of a CDG relative to the X-ray peak and its peculiar velocity relative to the centroid of the distribution of galaxy members are two parameters expected to be correlated with the level of relaxation of the clusters (*e.g.*, Zhang et al. 2011; Lavoie et al. 2016; Lopes et al. 2018): the smaller the offset and peculiar velocity, the higher the level of relaxation. This assumes that migration through dynamical friction of the CDG towards the center of the cluster is less rapid than that of the hot gas. Comparing these two parameters with the level of substructuring in clusters – the higher the number of substructures the lower the level of relaxation– should consequently complement our view about their assembly histories.

Thus, to reconstruct the assembly histories of the clusters in our sample, we will develop our study of substructures applying different tests, with different dimensions, in the optical, comparing with X-ray substructuring information and radio data from the literature whenever available, and each time comparing the results (as an independent test) with the dynamical characteristics of the CDGs in their respective clusters.

Radial velocity distributions (1D test): We start by directly inspecting the LOS velocity distributions of galaxies within the clusters, comparing them with a Gaussian distribution. The physical motivation of this test is the following: as the system tends toward relaxation, the absolute values of *skewness* and excess *kurtosis* (with respect to the value of 3 for a Gaussian distribution) also tend to decrease. This is a straightforward test that is easy to quantify.

Adopting a level below 0.3 as an upper limit for relaxation, only 25% of the clusters in our sample present LOS velocity histograms consistent with a Gaussian. This indicates that as much as 75% of the clusters in our sample show a possible signal of being substructured, as disclosed, more specifically, by two or more noticeable peaks in the LOS velocity distribution or platykurtic *kurtosis* values.

Projected distribution of galaxies (2D-test): The second test consists in tracing the isodensity contour map of the projected galaxy distribution in each cluster, where any galaxy density peak may be considered as a significant substructure (Geller & Beers 1982) since only spectroscopically confirmed members were considered. The (probability) density maps were obtained using a bivariate adaptive kernel, fitted by the function:

$$G(x,y) = \frac{1}{2\pi\sigma_x\sigma_y\sqrt{1-\rho^2}} \exp\left(-\frac{z}{2(1-\rho^2)}\right), \quad (5)$$

where z (do not confuse with redshift) is equal to:

$$z \equiv \frac{(x-\mu_x)^2}{\sigma_x^2} - \frac{2\rho(y-\mu_y)(y-\mu_y)}{\sigma_x\sigma_y} + \frac{(y-\mu_y)^2}{\sigma_y^2}, \quad (6)$$

and where, when the parameters x, y are not strongly correlated, one can assume $\rho = 0$.

In Figure 2 the surface density map of the member galaxy distribution of the cluster A0085 is shown as example. In this figure, the isodensity contours are codified in colors, with a cross indicating the density peak. Also shown are the positions of the CDG (open square) and peak in X-ray ($\times$ symbol). Note that although the CDG is slightly off-centered from the distribution of the galaxies, its position is almost the same as the peak in X-ray. Despite the substructures, this looks like a relatively well evolved cluster.

As it is difficult to resume the information on substructure in a table we offer the isodentity maps of all of our clusters on an accompanying web site (`www.astro.ugto.mx/recursos/HP_SCls/Top70.html`).

X-ray surface brightness maps (2D- test): X-ray surface brightness maps are constructed and used as supplementary information for identifying

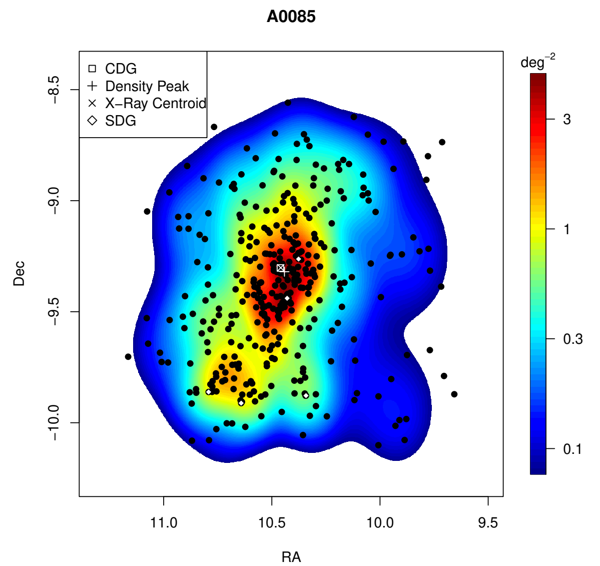

Fig. 2. Example of an isodensity map for the cluster A0085. The isodensity levels are coded by colors, in units of the probability density to find spectroscopic member galaxies/deg^2 (mean probability density equals to 1). The position of the peak in density is indicated, as well as the position of the CDG, SDGs and X-ray centroid. The color figure can be viewed online.

the substructures. Apart from applying an algorithm to independently detect substructures in these data, we checked every substructure detected in the optical for its counterpart in X-rays. This made possible, for example, to find cases of multimodal main structures that would not be identifiable from the optical data alone.

Using the ALADIN interface, we traced the X-ray surface brightness maps for all our clusters, overlaid in red contours on top of the respective DSS2 R-band[12] image. The X-ray data come from ROSAT[13] soft band (surface brightness in the 0.1–2.4 keV). It is worth to note that the all-sky sensitivity of ROSAT is limited to about 10^{-13} erg s^{-1} cm^{-2} (*e.g.*, Vikhlinin et al. 1998; Burenin et al. 2007). This is enough for detecting $kT_X \geq 1$ keV clusters, but not enough for identifying substructures in the cooler ones. All these maps can also be examined in the webpage accompanying this article.

The example shown in Figure 3 is once again for A0085. A smoothing parameter of 4 in *ds9* was used. The lowest contour in X-ray was traced at the 3σ level, followed by contours at levels of 6, 12, 24 and 48 σ. The cyan $\times$ symbol is the X-ray peak emission,

[12] `https://archive.stsci.edu/cgi-bin/dss\_form`

[13] `http://heasarc.gsfc.gov/docs/rosat/rosat3.html`

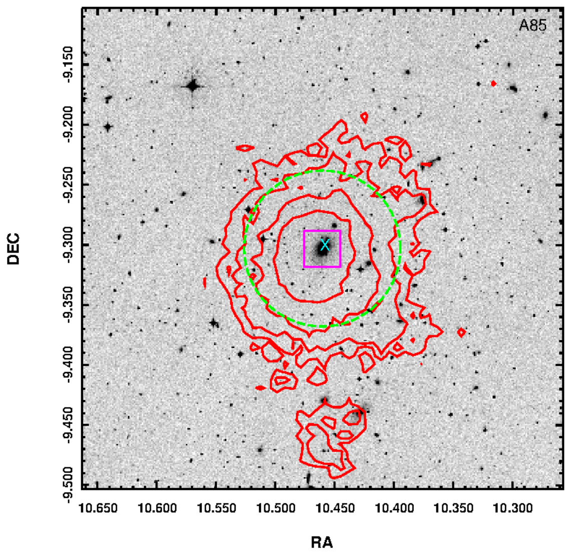

Fig. 3. Example of an X-ray map (red contours over the DSS image), for the cluster A0085. The position of the X-ray peak is indicated (cyan '×' symbol), as well as the position of the CDG (magenta square). The green circle marks a 0.5 h_{70}^{-1} Mpc radius around the CDG. The color figure can be viewed online.

the magenta square locates the CDG and the green circle corresponds to a 0.5 h_{70}^{-1} Mpc radius around it. Usually, an optical image of size $30' \times 30'$ in the plane of the sky is sufficient to show the distribution of the X-ray emission. Comparing with Figure 2, one can see that the detected gas in A0085 covers a smaller area (volume) than the distribution of the galaxies in the cluster, and that the CDG is only slightly displaced from the X-ray peak.

Dressler & Shectman test (3D-test): The DS-test (Dressler & Shectman 1988) is performed in two steps. The first step consists in calculating the δ_i parameter for each member galaxy:

$$\delta_i^2 = \frac{N_{nn}+1}{\sigma_c^2}[(\bar{v}_{local} - v_c)^2 + (\sigma_{local} - \sigma_c)^2], \quad (7)$$

where v_c and σ_c are the cluster global parameters, while $\bar{v}_{local}$ and σ_{local} are local parameters, calculated for the $N_{nn} = 10$ nearest neighbors of each member galaxy (see Bravo-Alfaro et al. 2009, for a discussion of these local parameters and the number of nearest neighbors).

The second step consists in calculating, for each cluster, the parameter $\Delta = \sum \delta_i$ and comparing its value with a set of 1000 Monte Carlo simulations, obtaining the probability p that a value $\Delta > \Delta_{observed}$ would have been obtained by chance. We, thus, calculate $P_{\rm sub} = 100 * (1-p)$, which is the probability that the cluster is substructured. Based on this test, a cluster with $P_{\rm sub} > 90\%$ can be considered to be significantly substructured.

Because Δ tends to equal the number of galaxy members when the cluster is close to relaxation (*e.g.*, Pinkney et al. 1996), we used the ratio Δ/N_c as an iterative parameter for the test. Note that, differing from the traditional way substructures are identified by this test, we do not consider only specific concentrations of galaxies with high δ values in the projected distribution.[14] Specifically, when $\Delta/N_c > 1.2$, we analyse both the 3D distribution of galaxies in RA, Dec and v_{local} and the respective 2D PPS diagram to identify, in the former, the volume separation surfaces between the substructures (*e.g.*, López-Gutiérrez et al. 2022). In this pseudo-3D volume, substructure members are more smoothly distributed, defining a more isolated *locus* (local concentration) than in a RA-Dec-z-volume, while in the PPS they show the typical caustics-shape distribution. Therefore, after separating the substructures from the remaining main structure, we recalculate Δ/N_c to see whether it is below 1.2, and if not, iterate again to isolate new substructures.

Note that in applying this test there are cases for which it is not correct to assume there is only one main structure. This happens when there are two or more substructures that are comparable in mass, as well as being much more massive than all the other substructures in the cluster. These are examples of "bimodal" or "multi-modal" clusters.

The parameters calculated from the dynamical and substructure analyses are reported in Table 3. In Column 1, we give the updated cluster ID. Note that the entries in Table 3 slightly differ from those in Table 1. More specifically, the clusters A2870 and A4049 were determined (see § 3.2) to be part of other massive clusters, respectively A2877 and A4038A. On the other hand, two clusters had their well-known LOS components considered separately, A1736 becoming A1736A and A1736B, and A3526 becoming A3526A and A3526B. Consequently, although the number of entries in both tables are the same, 67 clusters, their identities are somewhat different. In Table 3, the equatorial coordinates of the corresponding CDGs (and by convention, cluster centers) are given in Columns 2 and 3, followed

[14]By considering only high δ values, one may lose bimodal clusters, where the cluster is formed by two equally massive substructures with small δ (see a discussion on the limitations of the DS method in Islas-Islas et al. 2015).

TABLE 3: BASIC DATA ON CLUSTERS OF THE SAMPLE

ID[a] (1)	RA_{CDG} [deg]$_{J2000}$ (2)	Dec_{CDG} [deg]$_{J2000}$ (3)	v_{CDG} [km/s] (4)	N_g (5)	N_c (6)	v_c [km/s] (7)	σ_c [km/s] (8)	r_{200} [Mpc][b] (9)	N_a (10)	v_{cl} [km/s] (11)	σ_{cl} [km/s] (12)	R_p [Mpc][b] (13)	R_{vir} [Mpc][b] (14)	M_{vir} [$M_\odot$][b] (15)	skew (16)	kurt (17)	P_{sub} [%] (18)	N_{sub} m,hs,ls (19)	$\mathcal{A}$ (20)	r_{ox} [kpc][b] (21)	v_{pec} [km/s] (22)
A2798B	9.37734	-28.52947	33338	81	78	33604	697	1.353	60	33544	757	1.148	1.748	6.01	-0.313	-0.502	87.4	1,0,0	U	96.5	-185.3
A2801	9.62876	-29.08160	33660	50	45	33773	652	1.259	35	33640	699	1.553	1.833	6.94	-0.397	-0.024	15.5	1,0,0	U	42.4	18.0
A2804	9.90753	-28.90620	33546	88	80	33378	663	1.292	48	33669	516	1.277	1.403	3.11	-0.346	-0.982	97.6	2,0,0	M	126.3	-110.6
A0085A	10.46051	-9.30304	16613	368	352	16561	1011	2.027	321	16570	1045	2.030	2.668	20.20	-0.444	-0.118	99.9	1,2,3	S	8.2	32.2
A2811B	10.53717	-28.53577	32466	146	139	32354	831	1.625	103	32329	947	1.701	2.316	13.90	0.162	-0.042	94.3	1,0,2	S	5.5	123.7
A0118	13.74348	-26.37515	34068	119	80	34384	681	1.341	59	34287	689	1.206	1.667	5.23	0.349	-0.635	90.4	1,2,0	S	· · ·	-212.7
A0119	14.06709	-1.25549	13323	339	333	13299	810	1.633	294	13301	853	1.430	2.082	9.51	-0.175	0.246	99.9	1,2,1	S	125.2	21.1
A0122	14.34534	-26.28134	33804	111	31	34076	659	1.265	28	34062	677	1.190	1.641	4.98	0.337	-0.266	46.8	1,0,0	U	50.6	-231.7
A0133A	15.67405	-21.88215	17048	137	132	16830	713	1.425	86	16838	778	1.320	1.899	7.30	0.077	-0.393	77.7	1,2,0	S	33.9	198.8
A2877-70	17.48166	-45.93122	7213	237	174	7034	652	1.326	112	7143	679	0.999	1.596	4.20	0.273	-0.398	100.0	1,2,0	S	27.8	68.4
A3027A	37.70600	-33.10375	23541	167	102	23429	668	1.335	82	23494	713	1.618	1.904	7.52	-0.278	-0.814	97.2	1,1,1	S	113.9	43.6
A0400	44.42316	6.02700	6789	115	61	6959	323	0.682	51	6947	343	0.635	0.870	0.68	0.100	-1.007	76.0	1,1,0	S	39.8	-154.4
A0399	44.47119	13.03080	21483	101	69	21138	957	1.894	69	21146	950	1.414	2.209	11.70	-0.225	-0.460	13.3	1,0,0	U	110.1	314.8
A0401	44.74091	13.58287	22297	116	115	22053	1028	2.036	114	22061	1026	1.574	2.407	15.10	0.263	-0.352	40.8	1,0,0	U	18.6	219.8
A3094A	47.85423	-26.93122	20552	126	114	20489	548	1.090	84	20539	637	1.305	1.648	4.83	0.628	0.243	88.3	1,0,0	U	148.3	12.2
A3095	48.11077	-27.14016	19314	44	40	19485	306	0.606	21	19557	327	0.664	0.845	0.65	-0.018	-0.932	10.5	1,0,0	L	· · ·	-228.1
A3104	48.59055	-45.42024	21785	62	53	21777	413	0.823	28	21681	498	0.782	1.178	1.77	0.039	-0.106	39.5	1,2,0	S	34.4	97.0
S0334	49.08556	-45.12110	22401	22	27	22373	518	1.030	26	22363	534	0.811	1.249	2.11	0.449	1.037	27.4	1,0,0	L	· · ·	35.4
A3112B	49.49025	-44.23821	22764	120	97	22631	672	1.337	74	22669	705	1.861	1.982	8.46	0.271	-0.572	99.9	1,1,0	S	13.2	88.3
S0336	49.45997	-44.80069	22849	54	44	23223	506	1.006	32	23186	538	1.140	1.405	3.02	0.178	-0.606	3.2	1,0,0	L	· · ·	-312.8
A0426A	49.95042	41.51167	5231	360	314	5254	1030	2.104	314	5262	1029	1.395	2.359	13.50	0.030	-0.535	97.1	1,0,2	P	4.0	-30.5
S0373	54.62118	-35.45074	1452	272	229	1452	334	0.688	98	1461	390	0.308	0.749	0.430	-0.025	-0.428	100.0	1,2,1	S	1.7	-9.0
A3158	55.72063	-53.63130	17327	258	249	17764	1064	2.138	249	17735	1066	1.341	2.353	13.90	0.260	-0.478	49.6	1,2,2	S	19.1	-385.2
A0496	68.40767	-13.26196	9841	358	351	9892	688	1.395	279	9925	712	1.364	1.822	6.31	0.030	-0.535	99.9	1,1,0	S	8.5	-81.3
A0539	79.15555	6.44092	8257	143	132	8679	571	1.160	92	8631	698	0.882	1.557	3.92	-0.249	0.825	100.0	1,2,0	S	6.5	-363.5
A3391	96.58521	-53.69330	16361	119	100	16831	760	1.519	75	16776	817	1.270	1.936	7.74	0.159	-0.482	9.8	1,0,0	U	24.4	-393.0
A3395	96.90105	-54.44936	14571	224	218	14875	722	1.450	199	14878	746	1.264	1.823	6.42	-0.158	-0.494	100.0	2,2,1	M	10.9	-292.5
A0576	110.37600	55.76158	11435	238	220	11351	810	1.638	191	11350	866	1.633	2.202	11.20	0.031	-0.114	100.0	1,2,0	S	84.3	81.9
A0634	123.93686	58.32109	8029	140	132	8006	318	0.646	70	8037	395	0.792	1.029	1.13	0.057	-0.061	73.4	1,0,0	L	· · ·	-7.8
A0754$\nparallel$	137.13495	-9.62974	16451	468	386	16246	757	1.520	333	16258	820	1.484	2.045	9.10	-0.024	0.373	100.0	2,2,2	M	239.1	183.1
A1060	159.17796	-27.52858	3808	382	380	3709	652	1.335	343	3694	678	0.951	1.574	3.99	0.122	-0.532	100.0	1,0,5	P	4.9	112.6
A1367	176.00905	19.94982	6260	339	286	6451	547	1.115	226	6444	597	1.157	1.539	3.76	-0.026	-0.629	100.0	2,0,2	M	366.0	-180.1
A3526A	192.20392	-41.31166	2948	235	235	3088	491	1.005	126	2993	564	0.836	1.335	2.43	-0.482	-0.191	100.0	1,0,3	P	3.8	-44.6
A3526B	192.51645	-41.38207	4593	101	95	4580	276	0.552	45	4636	317	0.480	0.754	0.44	0.300	-0.359	99.9	1,1,0	S	· · ·	-42.3
A3530	193.90001	-30.34749	16187	126	110	16036	615	1.231	94	16064	631	1.272	1.632	4.63	0.305	-0.567	99.5	1,1,0	S	66.5	116.7
A1644	194.29825	-17.40957	14225	307	301	14085	987	1.989	288	14095	1008	1.507	2.365	14.00	-0.049	0.201	86.6	1,0,2	P	39.6	124.2
A3532	194.34134	-30.36348	16303	112	103	16753	423	0.849	58	16709	443	0.929	1.160	1.66	-0.130	-0.798	93.5	1,2,0	S	87.9	-384.6
A1650	194.67290	-1.76139	25328	220	192	25216	673	1.330	146	25249	723	1.581	1.903	7.55	0.188	0.016	2.1	1,0,0	U	27.3	72.9
A1651	194.84383	-4.19612	25622	221	191	25454	833	1.651	158	25453	876	1.782	2.250	12.50	0.132	-0.569	59.2	1,0,2	P	25.5	155.8
A1656	194.89879	27.95939	7157	969	969	6976	993	2.025	919	6997	995	1.734	2.474	15.70	-0.100	-0.018	100.0	1,1,8	S	57.9	156.4
A3556	201.02789	-31.66996	14406	102	102	14435	505	1.016	90	14436	520	1.048	1.347	2.59	0.354	-0.606	99.0	2,0,0	M	630.5	-28.6
A1736A	201.68378	-27.43940	10506	74	74	10363	417	0.840	36	10499	386	0.955	1.075	1.30	0.102	-0.997	100.0	1,3,0	S	· · ·	6.8
A1736B$\nparallel$	201.86685	-27.32468	13574	145	141	13665	839	1.689	126	13678	844	1.355	2.029	8.82	0.022	-0.500	99.0	1,1,1	S	610.8	-99.5
A3558	201.98701	-31.49547	14073	548	548	14455	950	1.912	469	14476	955	1.893	2.460	15.80	-0.230	-0.478	100.0	1,0,1	P	25.0	-384.4
A3562	203.39474	-31.67227	14693	231	98	14541	564	1.138	82	14561	594	1.221	1.549	3.94	0.037	-0.634	43.6	1,0,0	U	42.6	125.9
A1795	207.21880	26.59301	18968	179	164	18893	764	1.525	154	18889	780	1.278	1.876	7.09	-0.049	0.210	98.3	1,0,0	U	13.8	74.3
A2029	227.73376	5.74491	23353	202	155	23052	934	1.850	155	23051	931	0.989	1.931	7.82	0.096	-0.791	92.8	1,0,0	U	132.8	280.4
A2040B	228.19781	7.43426	13713	153	150	13472	567	1.141	104	13527	627	1.327	1.653	4.77	0.312	0.026	97.8	1,1,0	S	43.3	178.0
A2052	229.18536	7.02167	10332	178	176	10295	581	1.179	120	10416	648	1.115	1.600	4.28	0.356	0.003	100.0	1,1,0	S	9.1	-81.2
A2065	230.62053	27.71228	21828	204	169	21889	1043	2.071	168	21878	1043	1.712	2.504	17.00	0.129	-0.720	99.0	1,0,0	U	47.1	-46.6
A2063A	230.77209	8.60918	10377	200	193	10312	667	1.350	142	10345	762	1.165	1.809	6.18	-0.069	-0.132	99.4	1,0,1	P	16.5	30.9
A2142	239.58345	27.23335	27254	232	191	26975	820	1.618	157	27036	828	1.767	2.157	11.10	-0.087	-0.276	66.7	1,0,1	P	41.0	200.0
A2147	240.57086	15.97451	10595	481	453	10929	918	1.858	397	10889	935	1.966	2.466	15.70	0.215	-0.286	100.0	2,2,0	M	119.9	-283.7
A2151$\nparallel$	241.28754	17.72997	9378	331	311	10906	743	1.502	276	10898	768	1.551	1.999	8.35	-0.064	-0.573	100.0	3,2,2	M	3.1	-1466.6
A2152	241.37175	16.43579	13268	124	116	13283	398	0.799	64	13266	406	1.038	1.139	1.56	0.934	0.724	98.6	2,0,0	M	42.1	1.9
A2197	246.92114	40.92690	9511	294	276	9108	546	1.109	185	9114	573	1.402	1.593	4.21	0.258	-0.797	100.0	3,0,1	M	16.9	385.3
A2199	247.15948	39.55138	9296	521	498	9089	753	1.529	459	9090	779	1.302	1.907	7.21	-0.055	-0.058	100.0	1,0,3	P	6.4	199.9
A2204A	248.19540	5.57583	45528	111	96	45274	760	1.456	38	45497	1101	1.838	2.588	20.30	0.669	0.092	95.5	1,2,0	S	52.1	26.9
A2244	255.67697	34.06010	29543	106	102	29811	1154	2.282	102	29778	1161	1.491	2.546	18.30	0.166	-0.851	63.8	1,0,0	U	15.2	-213.8
A2256	256.11352	78.64056	17778	295	280	17567	1222	2.449	280	17567	1222	1.514	2.683	20.60	0.009	-0.624	99.9	1,2,2	S	129.2	199.3
A2255	258.11981	64.06070	22068	189	181	24100	992	1.973	179	24126	1000	1.802	2.470	16.40	-0.316	-0.518	100.0	1,2,0	S	183.7	-1904.7
A3716	312.98715	-52.62983	14112	157	140	13517	746	1.501	123	13508	783	1.247	1.878	6.99	0.168	-0.915	88.8	2,0,1	M	0.9	578.0
S0906	313.18576	-52.02746	13947	62	54	14481	340	0.680	26	14446	440	0.824	1.113	1.46	0.002	0.014	57.4	1,0,0	L	· · ·	-476.1
A4012A	352.96231	-34.05553	16241	93	85	16219	473	0.947	39	16249	575	1.043	1.436	3.15	-0.126	0.431	73.1	1,0,0	L	· · ·	-7.6
A2634	354.62244	27.03130	9117	192	185	9262	695	1.409	166	9268	717	1.251	1.780	5.87	-0.274	-0.177	94.9	1,1,0	S	51.7	-146.5
A4038A-49	356.93768	-28.14070	8672	247	237	8799	683	1.385	180	8873	753	1.150	1.789	5.95	0.252	-0.017	100.0	1,2,0	S	14.4	-195.2
A2670	358.55713	-10.41900	23157	308	288	22791	909	1.805	251	22799	970	1.153	2.089	9.91	0.066	-0.258	100.0	1,0,0	U	31.7	332.7

[a] A capital letter after the ACO name indicates the line-of-sight component of the cluster (see Chow-Martínez et al. 2014). A $\nparallel$ symbol indicates the cluster center is not at the X-peak substructure. [b] Length and mass parameters are also in units of h_{70}.

in Column 4 by their LOS velocities. Column 5 reports the number of candidate members after splitting up the intersecting neighbors, N_g, and Column 6, the number of galaxies, N_c, considered to be bound (included within the caustics) in each cluster. Other dynamical parameters are reported in Column 7 ($v_{\rm c}$), Column 8 ($\sigma_{\rm c}$), both for the N_c members, Column 9 (r_{200}), Column 10 (N_a), Column 11 ($v_{\rm cl}$), Column 12 ($\sigma_{\rm cl}$), the last three for the members inside the circular aperture, Column 13 ($R_{\rm p}$), Column 14 ($R_{\rm vir}$) and Column 15 ($M_{\rm vir}$). Parameters associated to the substructure analyses are shown in Columns 16 to 18: the *skewness*, the excess *kurtosis*, and $P_{\rm sub} = 100 * (1 - p)$, respectively.

Note that some clusters in our sample do not have their ICM emission centered on the **main** structure of their clusters, but on a substructure (A0754, A1736B and A2151). These are marked with a '$\neq$' in the first column of the Table 3.

3.5. *Gravitational Binding*

For the 16 superposed clusters appearing in Table 2, as well as for the substructures reported in Table 8, we complemented our analysis by applying a test for gravitational binding. Since the evolutionary state of a system like a galaxy cluster is also related to its geometry in redshift space, any density enhancement present in real space will also appear as a density enhancement in redshift space: systems representing small overdensities, where the Hubble flow has not yet been significantly perturbed, appear essentially undistorted, while those that are clearly collapsing, the Hubble flow being slowed down, appear flattened along the LOS. On the other hand, systems that are close to virial equilibrium appear as particularly elongated condensations in redshift space, a phenomenon known in the literature as *Fingers-of-God*. Because of this effect, it is possible to assess what is the global dynamical state of a galaxy system at the scale of a cluster by evaluating its distortions in redshift space.

As explained by Sargent & Turner (1977), this level of distortion can be determined, for a pair of objects (galaxies, groups or clusters), by determining the separation between the members of the pair and the angle χ between the separation vector and the plane of the sky. Such angle is measured as follows: let θ_{12} be the angular separation between the center of the two galaxies, z_1 and z_2 (with $z_2 \geq z_1$) being their respective redshifts, then the physical distance (d_{12}) and projected separation (ℓ_{12}) in the plane of the sky are given, respectively, by:

$$d_{12} = \frac{c}{H_0}\left[z_1^2 + z_2^2 - 2z_1 z_2 \cos\theta_{12}\right]^{1/2}, \qquad (8)$$

and

$$\ell_{12} = \frac{c}{H_0}\,(z_1 + z_2)\tan\frac{\theta_{12}}{2}, \qquad (9)$$

the angle χ between the separation vector being equal to:

$$\chi = \arctan\left[\frac{1}{2}\left(\frac{z_2}{z_1} - 1\right)\cot\frac{\theta_{12}}{2}\right], \qquad (10)$$

where $0 \leq \chi \leq \pi/2$.

For a homogeneous spherical system following the expansion flow, $\langle\chi\rangle$ approaches the isotropic value of 32.7°; $\langle\chi\rangle$ tends to lower values for a collapsing (flattened) system and larger values for a virialized (elongated) one. Note, however, that for a non-spherical system, the geometrical elongation/flattening could dominate $\langle\chi\rangle$, masking their real dynamical state.

Assuming a symmetric geometry, on the other hand, the same angle χ can be used to test the Newtonian criterion for gravitational binding of two systems (Beers et al. 1982). This allows one to determine whether the pairs are either relaxed, collapsing or expanding, or not bound but simply close in space. Within the context of a two-body-problem, the orbits of the two galaxies or systems, with masses M_1 and M_2, are assumed to be linear, with no rotations or discontinuities around the center of mass. The projected separation between their centers would then be $R_p = R\cos\chi\,(= \ell_{12})$ and their relative velocity projected along LOS, $V_r = V\sin\chi$, where R is the physical distance ($= d_{12}$) between them and V is their relative velocity. Considering that the energy criterion for gravitational binding is, $\frac{1}{2}v_{esc}^2 \leq \frac{GM}{R}$, where v_{esc} is the escape velocity, we assume $V = v_{esc}$ and estimate the total mass to be $M = M_1 + M_2$, yielding the condition for the pair to be bound:

$$V_r^2 R_p \leq 2GM\sin^2\chi\cos\chi. \qquad (11)$$

Having evaluated these parameters for the 16 cases of superposed clusters in our sample, we determined, as reported in Table 2, that 5 pairs and 2 clusters are only apparent superpositions.

3.6. *CDG Related Parameters*

CDG–X-ray offset: The offsets for 52 of the 59 clusters detected in X-rays in our sample were calculated based on the coordinates of the peak emission in X-ray compiled by Piffaretti et al. (2011). However, for A2151 we did not use this source because the peak reported by these authors, although the brightest in this cluster, corresponds to the emission of a subcluster. Instead, we used the coordinates of the main structure as reported by Tiwari & Singh

(2021). For 5 of the 6 remaining clusters, the coordinates for the X-ray peaks came from three different studies (Ebeling et al. 1996; Ledlow et al. 2003; Sato et al. 2010). This leaves one cluster, namely A0118, for which information is missing. The offsets, $r_{\rm ox}$, reported in Column 21 of Table 3, correspond to the angular separations transformed into the physical separations in kpc at the redshift of each cluster.

To compare these offsets with those reported in the literature, we also calculated the relative offsets, using the relation:

$$\Delta r_{\rm ox} = r_{\rm ox}/r_{500}. \quad (12)$$

Note that since Piffaretti et al. (2011) is our only source for r_{500}, we only calculated $\Delta r_{\rm ox}$ for the 52 clusters in common with these authors (to be reported further in Table 5).

Consistent with a typical cooling time of 4 Gyr (see Figure 2 in Zhang et al. 2011), a cluster with an offset $r_{\rm ox} < 30\ h_{70}^{-1}$ kpc, equivalent to $\Delta r_{\rm ox} \lesssim 0.03$, can be considered to be relaxed. Compared with the literature, this relaxation threshold is between two previously proposed values: Lavoie et al. (2016) used $\Delta r_{\rm ox} = 0.05$ and Lopes et al. (2018) used $\Delta r_{\rm ox} = 0.01$.

Peculiar velocity: We calculated the peculiar velocity of the CDGs using the formula (*e.g.*, Coziol et al. 2009):

$$v_{\rm pec} = \frac{v_{\rm CDG} - v_{\rm cl}}{1 + z_{\rm cl}}. \quad (13)$$

We also calculated the respective relative peculiar velocity using the definition (*e.g.*, Lauer et al. 2014):

$$\Delta v_{\rm pec} = |v_{\rm pec}|/\sigma_{\rm cl}. \quad (14)$$

We report the values obtained for $v_{\rm pec}$ in Column 22 of Table 3, while $\Delta v_{\rm pec}$ is reported in Table 5. According to this parameter, we consider a system to be relaxed when $|v_{\rm pec}| < 175$ km s^{-1}, which is equivalent to $\Delta v_{\rm pec} \lesssim 0.21$.

CDG luminosities: As described in § 2.3, we used the K_s absolute magnitudes of the CDGs, $M_{\rm Ks}$, as a proxy for their stellar masses. Comparison of these masses with the masses (or number of galaxies) of the substructure hosting the CDGs can yield important information about the assembly histories of the clusters. In particular, one could expect the most massive CDGs to be located in the most massive substructures, and these massive substructures to form the main subclusters of their respective clusters. The absolute magnitudes of the CDGs are reported further in Table 5.

Magnitude gaps: Another important parameter relating the assembly history of the CDG to its cluster is its magnitude gap: assuming a CDG grows in mass by cannibalizing its neighbors, its magnitude gap is expected to increase with time. For our sample, we have calculated two gaps: (i) the difference in magnitude between the CDG and second-rank member, Δm_{12}, and (ii) the difference in magnitude between the second and third-rank members, Δm_{23}.

Note that when a CDG differs from the original BCG of the cluster (which is the case for 19% of the clusters in our sample, see § 3.1), the identification of the second-rank galaxy varies with the type of cluster: for both the Fornax-like clusters and clusters with a fossil candidate in their outskirts, the second-rank galaxy is the second-rank of the main structure, while in Coma-like cluster the second-rank is the initial BCG, brighter than the CDG; this produces a negative Δm_{12}. The various gaps are also reported in Table 5.

4. PROPERTIES AND ASSEMBLY HISTORIES OF CLUSTERS

4.1. *Global Cluster Properties*

Using the optical data related to galaxy membership, we show in Figure 4 the histograms characterizing the "global" properties of the clusters identified in Table 3. In the upper left panel, we show the distribution of r_{200}, which is commonly used as a reference radius. The median of 1.35 h_{70}^{-1} Mpc, corresponding to only 63% of the $R_{\rm A}$, implies the galaxy concentrations in our sample of clusters are relatively high. In the upper right panel, the two distributions for the number of galaxies within the caustic, N_c, and galaxies within virial aperture radius, N_a, confirm this trend, the medians amounting to 150 and 114 galaxies, respectively. In the lower left panel, the distribution of redshifts is found to be positively skewed, since the mode appears before the median at $z = 0.054$. This shows that most of our clusters are nearby, and thus, assuming they formed in the distant past, had had enough time to virialize. Finally, in the lower right panel, the distribution for the velocity dispersion within $1.3 \times r_{200}$ has a median value of 723 km s^{-1}, which is typical for Abell clusters.

Based on the above distributions, we conclude that our sample is composed mostly of nearby, relatively rich clusters, where the concentrations of galaxy and velocity dispersion are remarkably high, justifying the assumption that those are systems that had had sufficient time to evolve internally and should then be expected to be close to virialization.

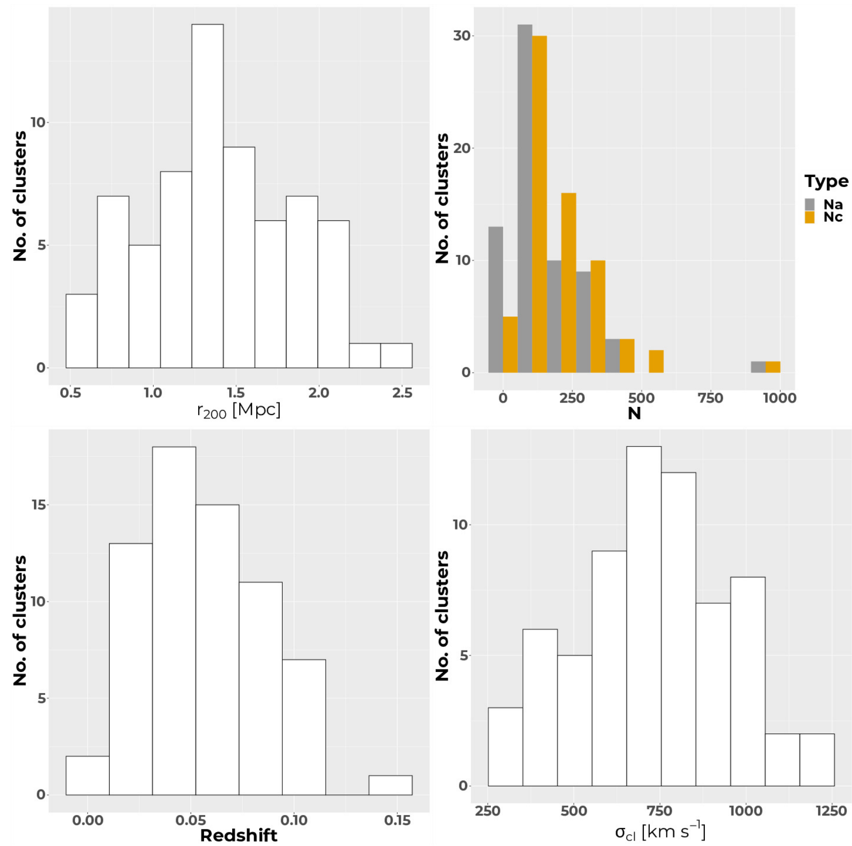

Fig. 4. Global properties of the clusters as defined in Table 3: Upper left, estimated r_{200} radii; upper right, number of galaxies within the caustics (N_c, orange) and within the virial radius (N_a, gray); lower left, redshifts; and lower right, velocity dispersions (σ_{cl}). The color figure can be viewed online.

Consistent with this assumption, the distribution of the virial masses in the right panel of Figure 5 is found to be significantly negatively skewed, with a median 6.4 $\times 10^{14}$ h_{70}^{-1} $M_\odot$. However, the distribution for the virial radii, in the left panel, does not follow this trend, spannig a relatively large range, with a median value of 1.82 h_{70}^{-1} Mpc, corresponding to 0.85 times the R_A. This peculiarity may suggest that the clusters either have different assembly states or even different assembly histories.

Comparing our virial masses with those of the literature was not straightforward, since published estimates of these are rare. One suitable source is the GalWeight cluster catalog (GalWCat19; Abdullah et al. 2020), where the masses of 1 800 clusters were determined within three different projected radii: r_{100}, r_{200} and r_{500}. There are 18 clusters in this catalog that are also in our sample, and we compare, in Figure 6, their three different masses, M_{100}, M_{200} and M_{500} with our M_vir estimate. The three linear fits we obtained are relatively good, with comparable correlation coefficients $R \approx 0.83$, 0.87 and 0.89, respectively. However, since our virial masses were estimated using a proxy for r_{100} (cf. § 3.3), the comparison that counts for us is that with M_{100}. In the lower panel, the fit shows our virial mass estimate to be in good agreement with those of GalWCat19 for r_{100}, the residuals being due probably to the different ways the membership of galaxies in each cluster was determined, and the mean redshifts of galaxies in our data compared to only SDSS redshifts in theirs.

To disentangle the assembly history of these clusters, we discuss in the following sections the implications of various dynamical parameters and classifications obtained for three different internal regions within the clusters. The three regions are the following: (i) the *outer* region, from R_vir down to r_{500}, as traced by the optical data on galaxy membership; (ii) the *inner* region, inside r_{500}, as traced by X-ray emission; (iii) and the innermost *core*, characterized by gas cooling and CDG properties. Typical radii for these regions are $R_\mathrm{vir} \approx 1.8\, h_{70}^{-1}$ Mpc, $r_{500} \approx 0.9\, h_{70}^{-1}$ Mpc and core radius (r_{core}) about 0.3 h_{70}^{-1} Mpc (note that more specific values will

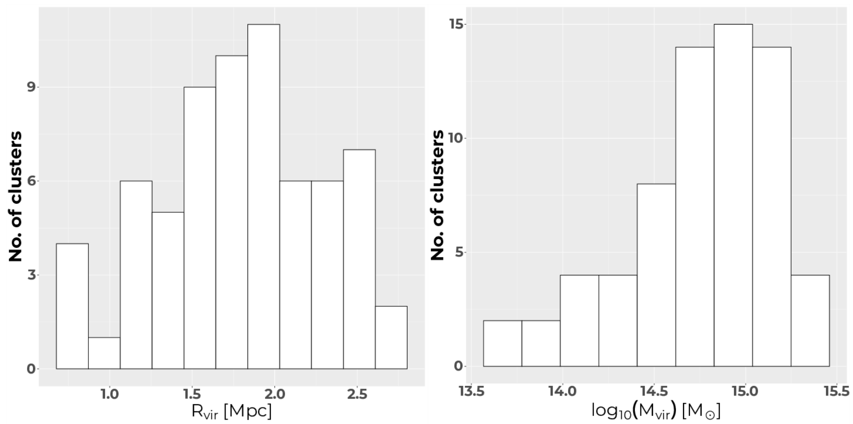

Fig. 5. Distributions of virial radius (left panel) and virial mass (right panel).

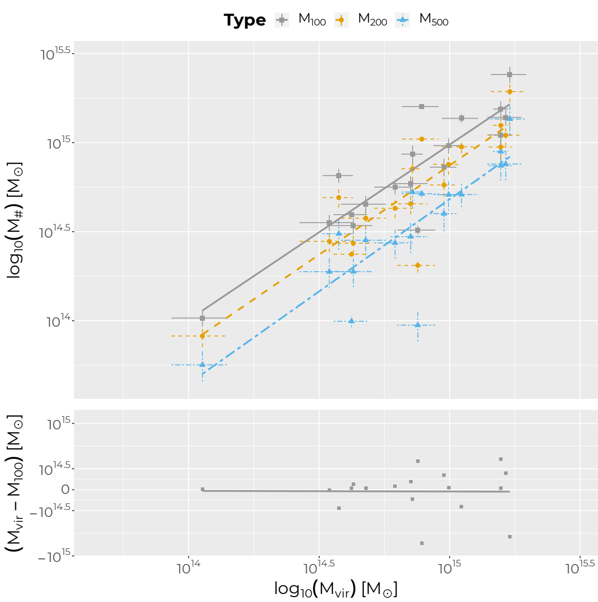

Fig. 6. Comparison of our mass estimates with the virial masses in the GalWeight galaxy cluster catalog. Blue triangles, M_{500}, orange circles, M_{200} and gray squares M_{100}. The three lines are linear fits to points with the same colors. In the lower panel, the residual corresponds to the comparison of our virial mass with M_{100}. The color figure can be viewed online.

be defined for the various radii as our analysis progresses).

4.2. *Outer Region*

The assembly state of the outer region is characterized by the presence or absence of substructures (cf. § 3.4). According to the DS-test, the 43 clusters with $P_{\rm sub} \geq 90\%$ in Column 18 of Table 3 could be considered to have substructures. This represents 64% of our cluster sample. However, considering all the results for the different tests, substructures appear to be secure in only 39 of these clusters and probable, with $P_{\rm sub} \lesssim 90\%$, in 8 further clusters. In total, the number of clusters with substructures in our sample could thus be as high as 70%. Consequently, since either fraction is relatively high, it seems safe to conclude that substructures are extremely common in nearby clusters.

Taken at face value, the presence of numerous clusters with substructures suggests that many of these systems did not yet reach equilibrium, and what we observe, consequently, are different phases of a still ongoing process. To better characterize these different phases, it seems therefore important to first classify all the substructures in terms of their dynamical significance. This implies determining the gravitational impact that a substructure, when present, has on the whole cluster.

As a first approximation, this gravitational impact can be estimated by comparing the relative richness, N_s/N_c, formed by the ratio of the number of galaxies in each substructure, N_s, to the total number of galaxies within the caustics, N_c. Using the numbers in Table 8 of Appendix B, we distinguish three levels of dynamical significance:

Main (*m*): High relative richness, $N_s/N_c \geq 0.50$. This level characterizes the dynamically dominant substructures in any cluster. In the case of multi-modal clusters (for example, A2804), the sum of the membership ratios of the main modes is indeed larger than 0.50. In Table 8, the substructures with this level of significance are identified by appending the suffix **m** to their ID.

Highly significant (*hs*): Intermediate relative richness, $0.05 \leq N_s/N_c < 0.50$. This level characterises substructures that are sufficiently massive to affect the dynamics of their host clusters. In Table 8 the suffixes (**n, s, e, w, c**, or a combination thereof) are added to the ID of the substructures indicating its location relative to the main structure (North, South, East, West or central, respectively).

Low-significance (*ls*): Low relative richness, $N_s/N_c < 0.05$. These are low-mass clumps of galaxies, attached to a more massive host cluster, that do not affect its dynamics. They are not listed in Table 8.

It is worth to note that the m substructure in our sample with the lowest value of N_s/N_c is A1736Am (0.581), while the *hs* substructure with the highest N_s/N_c is A3027Acw (0.235). Thus, the cut in $N_s/N_c = 0.5$ seems to be a good discriminator for this separation. The numbers of substructures with relative richness levels m, *hs* and *ls* are indicated in Column 19 of Table 3 using three numbers (m, *hs*, *ls*). For example, while A2798B and A2801 only have one main structure each, $N_{\text{sub}} = (1, 0, 0)$, A2804, a bimodal cluster, has two, $N_{\text{sub}} = (2, 0, 0)$. A more complex cluster is A0085A, which has one main structure, two *hs* and three *ls* substructures, $N_{\text{sub}} = (1, 2, 3)$. A still more complex cluster is A2151, a trimodal cluster marked as $N_{\text{sub}} = (3, 2, 2)$.

In Column 20 of Table 3 an extra parameter appears, $\mathcal{A}$, which is used to qualify the "assembly state" of a cluster based on its level of substructuring. This classification was inspired by the morphological classifications of ICM X-ray emission proposed in Buote & Tsai (1995) and Jones & Forman (1999). We distinguish five assembly states: high-mass, Unimodal clusters (U); Low-mass unimodal (L); Multi-modal (M); Primary (P) with only *ls* substructures attached to the m mode; and finally Substructured (S), formed by the m mode and at least one *hs* substructure.

The way we distinguish between U and L clusters depends on the mass criterion $3.5 \times 10^{14} M_{\odot}$: U is more massive and L less massive or equal to this mass. In fact, the regular (unimodal) clusters may be either the "beginning" or the "end" of a merging process. They are the beginning if the poor clusters have had time to arrive close to relaxation, while in a relatively isolated environment. As the end, they are the final result of the virialization process of rich clusters. In fact there is no theoretical criterion justifying this distinction, and we chose pragmatically a threshold: the clusters for which we could see relatively relaxed X-ray isophotes were assumed to be close to virialization, while in the abscence of X-ray emission (implying a less dense or colder ICM, undetectable with ROSAT sensitivity, for example), we assumed the other state.

To be classified as M, a cluster must be formed by two or more m modes, with comparable richness. Consequently, in M clusters the CDG of the cluster is ill-defined, since there are different SDGs competing for this position (one for each mode, at least). For practicality, we choose as the CDG the SDG of the most central mode (usually the richest in galaxies and/or brightest in X-ray). This convention allows us to define a central position for the cluster and serves as reference for the magnitude gaps. Of the ten M-type clusters identified in Table 3, three, namely A0754, A2147 and A2152, show multiplicity only in the optical, while four, A1367, A2151, A2197 and A2804, show multiplicity in both optical and X-rays, and three others, A3356, A3395 and A3716, only in X-rays.

Finally, S and P clusters have both only one main structure and some substructures: in an S cluster there are *hs* substructures and in a P cluster they are all *ls*.

Adopting the above definitions, we count 21% U, 13% P, 42% S, 15% M and 9% L clusters. In terms of masses, Table 4 shows that U and P clusters are more massive than S and M clusters, while L clusters are the least massive of all. Thus, poor L clumps could represent the building blocks of future 'massive' clusters. Also, the distribution in radii presented in Table 4 reveals that the "size" of a cluster and, most specifically, its virial radius increases with its mass.

Although 70% of the clusters (M, S and P) show some evidence of substructuring, considering the significance in terms of relative richness and mass, only 57% (M and S) are expected to be dynamically affected by their substructures. This implies that at least 57% of the clusters in our sample have not yet reached virialization. This may be compared to previous numbers reported for local cluster samples, *e.g.* Lopes et al. (2018), who found that substructuring ranges between 37–75%, in 40 SZ-detected clusters, and between 32–65%, in 62 X-ray clusters (both samples taken from Andrade-Santos et al. 2017). As a whole, for 31 clusters in common with these authors, our results agree for 80% of them.

How does this classification of substructures fit the model of cluster formation? According to the hierarchical model, clusters form mainly by the mergers of groups of galaxies. Within this paradigm U-type clusters would be examples of systems that merged in the distant past and their virialization pro-

TABLE 4

TYPICAL PARAMETERS IN DIFFERENT ASSEMBLY CLASS CLUSTERS

Cluster class	N	$M_{\rm vir}$ mean(median) [$10^{14} M_\odot$]	$R_{\rm vir}$ mean(median) [Mpc]	r_{200} mean(median) [Mpc]	r_{500} mean(median) [Mpc]	r_{core} mean(median) [Mpc]
U	14	9.2(7.7)	1.99(1.93)	1.60(1.52)	0.94(1.05)	0.32(0.31)
P	9	9.6(11.1)	2.02(2.16)	1.61(1.62)	1.04(1.00)	0.32(0.34)
S	28	8.1(6.3)	1.81(1.82)	1.38(1.39)	0.79(0.92)	0.29(0.29)
M	10	6.2(6.4)	1.72(1.82)	1.32(1.45)	0.56(0.63)	0.27(0.29)
L	6	1.9(2.1)	1.18(1.25)	0.82(0.95)	- (-)	0.19(0.20)

cess would thus be well advanced. P-type clusters would also have formed in the past and represent cases that, being massive, have recently attracted small groups in their environment without an important change in their relaxation state. This reinforces the idea that the cluster formation process is continuous. Consequently, clusters with significant substructures (M and S) would be examples of relatively more recent mergers (which occurred in the last 1–2 Gyr; Lisker et al. 2018; Benavides et al. 2020; Haggar et al. 2023). Their differences are explained by the importance of the merger: in S-type clusters a massive clump is accreting smaller mass groups (minor mergers), while in M-type clusters the masses of the merging entities are comparable (major mergers). Since average masses of M-type clusters are smaller, they could represent the previous step of the formation of the massive main clumps of S-type clusters. By comparing the sum of the merging masses (main + substructures) with the total mass of the cluster, in S clusters the merging masses are 7% less massive than the cluster mass (median 10%), compared to 23% (median 30%) in M clusters. Obviously, M clusters must be relatively less relaxed than S clusters.

The best examples of poor clusters might be the six L clusters. Indeed, the relatively low masses and small numbers of member galaxies in these systems make them comparable to groups. This might also explain why these poor clusters are not observed in X-ray: simply because they do not have sufficiently deep potential wells for infalling gas to heat up and emit detectable amounts of X-rays. This is the case of candidate AXU clusters like A0634 and A4012, for which confirmation should be obtained using eROSITA (Predehl et al. 2021). The four remaining L clusters also look like they could be either infalling or satellite groups of more massive clusters (see Table 2): these are the cases of S0334 related to A3104, S0336 related to A3112B, and possibly A3095 related to A3094A and S0906 related to A3716 (for which binding could not be established). Other infalling groups, composed by two clumps either and residing well inside the caustics of their **main** cluster are: A2870, related to **A2877**, and A4049, related to **A4038**. These cases would also be excellent candidates to search for evidence, in their galaxies' properties, of pre-processing.

4.3. *Inner Region*

The region inside r_{500} is where the gas accumulates and gets very hot, emitting X-rays. In our sample, only eight clusters are undetected in X-rays (Table 1). However, quantitative information on ICM evolution is scarce and restricted to two parameters: dynamical status of the cluster ICM (71% of X-ray detected clusters) and core cooling status (81%). In Table 5 the values for these parameters in clusters with different $\mathcal{A}$ classes are reported in Columns 2 and 4, respectively. In Column 2, the symbol ✓ indicates a relaxed status while an $*$ indicates a disturbed ICM. The main sources for this information were Parekh et al. (2015) and Laganá et al. (2019). In general, conclusions about the dynamical state of the inner region are confirmed by the different sources, except in four cases, the clusters A2029, A2052, A2063A and A2244, for which evidence of disturbance is still debated. In Column 3 of Table 5 we added information about the detected presence of radio halos and/or radio relics, mostly from Van Weeren et al. (2019), Knowles et al. (2022) and Botteon et al. (2022). For the 4 cases above, these data indicate disturbance for A2029, A2063A and A2244, and no information concerning diffuse radio emission for A2052. In general, the presence of radio halos and/or relics coincides with the disturbed status of the ICM X-ray data (except for two substructured clusters, A0133A and A1656).

Although the cooling state is related to the core of the clusters, we will discuss it here, together with the remaining X-ray information. In Column 4 of Table 5, the core cooling status is codified as follows (see, for example, Käfer et al. 2019): strong-cool-cores (SCC), which have cooling times $t_{cool} < 1$ Gyr and usually show a temperature drop towards the center and small core radii (< 100 kpc; *e.g.*, Ota et al. 2006); non-cool-cores (NCC), with $t_{cool} > 7.7$ Gyr (see also Hudson et al. 2010), with flat central temperature profiles and large core radii; and weak-cool-cores (WCC), with intermediate characteristics (although sometimes also classified as cool-cores). In some clusters the index 's' is also added when "sloshing" (the presence of spiral-shaped central cold fronts) is observed. In terms of assembly state, clusters with SCC or WCC are expected to be closer to relaxation, that is, they had enough time to settle, and radiatively cool. NCC clusters, on the other hand, are likely to be younger, or disturbed due to recent mergers, or even re-heated by AGN feedback. Finally, evidence of sloshing in these cores might suggest more recent accretion.

How do these classifications in X-ray fit our general interpretation based on the assembly classes, U, P, S and M? The best agreement is for the M class: 9 out of 9 clusters in Table 5 are considered disturbed according to the X-ray emission (Column 2), while 5 are NCC and 1 is WCC (Column 4) of a total of 6 with this information. Although the situation is more complex for the S and P clusters, the agreement is also relatively good. For the S-type clusters, 11 out of 17 are considered disturbed based on the X-ray distribution, while 11 are NCC, 4 are WCC and only 7 are SCC. However, considering the evidence of sloshing in five of the SCC, as much as 20 out of 22 S-type clusters could be considered to have a non-relaxed ICM. Note that the diagnostics based on X-ray distribution and core temperature differ in five cases, the ambiguity increasing for the WCC and SCC. This ambiguity appears clearer in the P-type clusters: although 7 out of 7 have non-relaxed ICM, 5 out of 9 are WCC and 4 are SCC with sloshing. Considering their particular assembly state histories –these are old and massive clusters accreting smaller mass systems– some level of ambiguity in the core cooling status might naturally be expected. The U class, however, is definitely the most surprising. Although we expect all of these clusters to be close to relaxation based on the X-ray distribution, only 2 out of 9 seem to be, 5 are suggested to be disturbed and 2 are ambiguous. The core cooling states draw a similar complex picture: 4 are NCC (usually also disturbed), 5 are WCC (one with sloshing), and 2 are SCC (also one with sloshing). This is relatively unexpected, since most of our U-type clusters lying at low redshifts should have had time to reach relaxation through interactions.

However, the fact that very few clusters are classified as U, combined with the "unusual" characteristics of their inner regions compared to their outer region (absence of substructures), suggest that the process of virialization, even in the most evolved systems, does not depend solely on time but also on complex processes involved in their assembly history. Merging can happen anytime in the history of a cluster –possibly taking it out of a previous equilibrium situation. Also, merging of major and minor subclusters has different consequences, and the same applies to different ICM properties. Thus, different regions sampled by optical and X-ray observation may show distinct moments of this assembly history. In fact, this could explain the frequent disagreement between optical and X-ray results concerning the dynamical state of galaxy clusters.

4.4. *Core Region*

In this innermost region, the most relevant feature is the CDG, and possibly other dominant galaxies. Consistent with its definition, the CDG position in a cluster is expected to indicate its dynamical center. This is also the expectation for the X-ray emission peak (or centroid), although the two components, galaxies and gas, may be subject to different levels of disturbance with respect to the global potential well, dominated by dark matter. This is why the dynamical status of the CDG, with respect to the gas distribution and to the radial velocity distribution of galaxies, is an important information to compare with the assembly status discussed above.

In the left panel of Figure 7, the distribution of $\Delta r_{\rm ox}$ for the total sample is shown, with an assumed upper threshold for relaxed CDGs, $\Delta r_{\rm ox} = 0.03$, marked as a yellow vertical line. We see that 55% of the clusters (29 out of 53) are well above the threshold. The median for $\Delta r_{\rm ox}$ is 0.04 or about $r_{\rm ox} = 40 h_{70}^{-1}$ kpc. This suggests that more than half of the clusters in our sample have a non-relaxed CDGs.

In the right panel of Figure 7, we trace the distribution for $\Delta v_{\rm pec}$. By definition of the CDG, in a dynamically relaxed system one would expect $\Delta v_{\rm pec}$ to tend to zero. However, assuming a typical upper threshold $\Delta v_{\rm pec} = 0.21$, the percentage of clusters that have higher values is as high as 46% (31 out of 67). With a median $\Delta v_{\rm pec} = 0.185\ \sigma_{\rm cl}$, corresponding to a median $v_{\rm pec}$ of $\pm$ 147 km s^{-1}, once again it is clear that a large number of clusters cannot be assumed to have relaxed CDGs.

Note that, compared with the literature (*e.g.*, Coziol et al. 2009; Lauer et al. 2014; Lopes et al. 2018), our median value for $\Delta v_{\rm pec}$ is relatively low. This is not due to a difference in sample but rather to a

TABLE 5

ASSEMBLY STATE OF THE CLUSTERS

$\mathrm{ID}_{\mathrm{cl}}$ (1)	Inner (2)	Radio (3)	CC (4)	Δr_{ox} (5)	Δv_{pec} (6)	Offsets (7)	Δm_{12} (8)	Δr_{12} (9)	Δm_{23} (10)	Δr_{13} (11)	Comments (12)
					U						
A0122	–	–	–	0.062	0.342	∗	0.000	0.01	1.618	0.41	b(db)
A0399	∗	R	N	0.099	0.331	∗	0.916	0.37	0.433	0.65	u
A0401	∗	R	N	0.015	0.214	∗	1.056	1.08	0.133	0.74	u
A1650	✓	–	W	0.025	0.100	✓	0.512	1.06	0.082	1.07	u
A1795	✓	mH?	S	0.011	0.095	✓	0.636	0.91	0.015	0.96	u
A2029	✓/∗	mH	S,s	0.100	0.301	∗	1.954	0.22	0.161	0.93	u
A2065	∗	H?	W	0.045	0.044	∗	0.000	0.02	0.054	0.09	m(db),For
A2244	∗/✓	H	W	0.013	0.184	✓	1.025	1.11	0.186	0.92	u
A2670	–	–	W	0.035	0.342	∗	1.131	0.71	0.183	0.93	u
A2798B	–	R	–	0.129	0.244	∗	0.000	0.34	0.172	0.35	m(db)
A2801	–	–	N	···	0.025	∗	1.125	0.39	0.080	0.60	u
A3094A	–	–	–	0.215	0.019	∗	0.855	0.23	0.546	0.88	u
A3391	∗	–	N	0.027	0.481	∗	0.000	0.02	1.502	0.87	b(db)
A3562	∗	H	W,s	0.046	0.211	∗	0.330	1.07	0.795	0.45	u
					P						
A0426A	∗	mH	S,s	0.003	0.029	✓	0.436	0.11	0.407	0.07	b
A1060	–	–	W/S	0.007	0.166	✓	0.230	0.03	0.005	0.46	b,BSp
A1644	∗	–	S,s	0.040	0.123	∗	1.186	0.67	0.295	0.67	u
A1651	∗	–	W	0.023	0.177	✓	1.128	0.58	0.097	0.35	u
A2063A	∗/✓	R	W	0.018	0.040	✓	0.870	1.03	0.014	1.44	u
A2142	∗	mH	W,s	0.030	0.241	∗	0.295	0.17	-0.075	0.61	b
A2199	∗	–	S,s	0.006	0.256	∗	1.271	1.14	0.179	0.55	u
A3526A	–	–	S,s	0.005	0.078	✓	1.223	0.74	0.015	0.82	u
A3558	∗	H	W,s	0.023	0.402	∗	0.801	0.49	0.273	0.15	u
					L						
A0634	–	–	–	···	0.019	✓	0.332	0.29	0.214	0.75	n
A3095	–	–	–	···	0.697	∗	0.405	0.39	0.428	0.37	n
A4012A	–	–	–	···	0.013	✓	1.947	0.93	0.018	0.27	u
S0334	–	–	–	···	0.066	✓	0.359	0.04	0.587	0.10	n,For,BSp
S0336	–	–	–	···	0.581	∗	0.514	0.38	0.352	0.23	n,Sp
S0906	–	–	–	···	1.082	∗	0.732	0.20	0.367	0.47	u,BSp
					S						
A0085A	∗	R	S	0.007	0.031	✓	1.532	0.54	0.059	0.49	u
A0118	–	–	–	···	0.313	∗	-0.228	0.12	0.467	0.49	b,For
A0119	∗	–	N	0.133	0.024	∗	0.532	0.13	0.194	0.75	u
A0133A	✓	R	S,s	0.036	0.255	∗	1.506	0.17	0.036	1.23	u,For
A0400	∗	–	N	0.061	0.450	∗	0.000	0.01	1.175	0.10	b(db)
A0496	∗	–	S,s	0.009	0.114	✓	1.126	0.85	0.087	0.90	u
A0539	–	–	N	0.008	0.520	∗	0.000	0.01	0.404	0.28	m(db)
A0576	∗	–	W	0.102	0.094	∗	0.000	0.02	1.088	0.14	b(db)
A1656	✓	HR	N	0.051	0.157	∗	-0.534	0.20	1.117	0.70	b,BSp
A1736A	–	–	–	···	0.017	✓	0.142	0.73	0.798	1.16	b(far)
A1736B	∗	–	N	0.630	0.117	∗	0.916	0.98	0.369	0.48	u
A2040B	–	–	–	···	0.283	∗	0.727	0.51	0.080	0.40	u,For
A2052	∗/✓	–	S,s	0.010	0.125	✓	0.928	0.92	0.072	0.22	u
A2204A	✓	mH	S,s	0.037	0.024	∗	0.000	0.57	0.646	0.37	m(db)
A2255	∗	HR	N	0.172	1.904	∗	0.122	0.08	0.006	0.60	m
A2256	∗	HR	N	0.115	0.163	∗	0.107	0.18	0.000	0.07	m(db)
A2634	✓	–	W	0.069	0.204	∗	0.102	0.79	0.914	0.55	u
A2811B	–	H	N	0.005	0.130	✓	0.828	1.00	0.049	1.09	u
A2877-70	–	–	W	0.044	0.100	✓	1.231	0.59	0.125	0.37	u
A3027A	–	–	–	0.158	0.061	∗	-0.146	0.57	0.977	0.70	b(far),For
A3104	–	–	–	0.040	0.195	∗	0.927	0.48	0.049	0.28	u
A3112B	✓	–	S	0.012	0.125	✓	1.070	0.91	0.646	0.74	u
A3158	∗	–	N	0.018	0.361	∗	0.268	0.08	0.755	0.18	b

TABLE 5. CONTINUED

ID_{cl} (1)	Inner (2)	Radio (3)	CC (4)	Δr_{ox} (5)	Δv_{pec} (6)	Offsets (7)	Δm_{12} (8)	Δr_{12} (9)	Δm_{23} (10)	Δr_{13} (11)	Comments (12)
					S						
A3526B	–	–	–	···	0.133	✓	0.450	0.73	1.099	0.74	u
A3530	–	–	N	0.083	0.185	∗	1.002	0.06	0.798	0.89	b
A3532	✓	–	N	0.096	0.867	∗	0.000	0.07	0.952	0.49	b(db)
A4038A-49	∗	R	W	0.016	0.259	∗	0.141	0.14	0.443	0.13	b,For
S0373	–	–	S,s	0.004	0.022	✓	0.159	0.43	0.306	0.06	u,For,BSp
					M						
A0754	∗	HR	N	0.209	0.223	∗	0.933	0.42	0.139	0.41	u
A1367	∗	R	N	0.405	0.301	∗	0.511	0.66	0.030	0.86	b(far)
A2147	∗	–	N	0.128	0.303	∗	0.416	0.18	0.238	0.55	b,fos
A2151	∗	–	–	0.005	1.910	∗	-0.252	0.07	0.121	0.37	m,For
A2152A	–	–	–	0.073	0.004	∗	0.408	0.76	0.541	0.80	n
A2197	∗	–	W	0.033	0.672	∗	0.823	1.07	0.409	0.95	u,For
A2804	∗	–	N	···	0.214	∗	0.051	0.50	0.165	0.65	b(far)
A3395	∗	R	N	0.012	0.391	∗	0.228	0.59	0.151	0.51	b(far)
A3556	∗	–	–	···	0.054	∗	0.339	0.75	0.315	0.23	b(far)
A3716	∗	–	–	···	0.738	∗	0.088	0.30	0.019	0.64	m

[a]Codes for X-ray (inner region) and Offsets (core) are: [✓] Relaxed; [∗] Disturbed; [–] No Data. References for ICM dynamical states are: Schuecker et al. (2001); Rines et al. (2001); Parekh et al. (2015); Vikhlinin et al. (2009); Ichinohe et al. (2019); Laganá et al. (2019); Tiwari & Singh (2021).

[b]Codes for diffuse radio emission are: mini Radio-Halo [mH], Radio-Halo [H], Radio-Relic (shock) [R] and both halo and relic [HR].

[c]Codes for cooling status of the core are: Strong cool-core [S], Weak-cool-core [W], Non-cool-core [N]; [s] indicates cold gas sloshing (cold gas front) is detected. References for core cooling status are: White (2001); Finoguenov et al. (2001); Chen et al. (2007); Sato et al. (2010); Lakhchaura & Singh (2014); Lovisari et al. (2015); Käfer et al. (2019).

[d]Codes are: [u] unique CDG (choice of CDG is obvious, $\Delta m_{12} > 0.5$); [b] binary central dominant BCGs (CDG is the most central or brightest), may also be a "Coma-like" system (BCG is brighter than CDG); [db] CDG is dumbell type; [far] binary dominant BCGs, but 2^{nd}-rank is far out of core radius; [m] multiple central dominant BCGs (3 or more BCGs inside 0.5 magnitud range); [n] weakly dominant CDG (giant elliptical); [fos] fossil group candidate BCG; [BSp] there is a bright spiral among the BCGs.

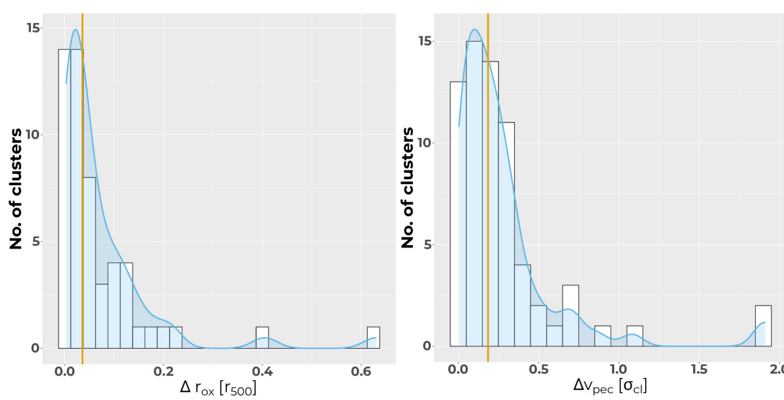

Fig. 7. Left: Distribution of the relative projected positional offset of CDGs with respect to the X-ray peak (Δr_{ox}). Right: distribution of the relative peculiar velocity of CDGs with respect to the cluster systemic velocity (Δv_{pec}). The vertical yellow lines in the two panels are the thresholds separating relaxed form non-relaxed clusters. The color figure can be viewed online.

difference in the identification of the CDG. For example, in the cluster A2197, Lauer et al. (2014) assumed NGC 6173 is the BCG, instead of NGC 6160, which we identified as the real CDG. Since NGC 6173 turned out to be the SDG of a substructure of A2197 (A2197me in Appendix B), its v_{pec} is naturally estimated to be larger than for NGC 6160. This emphasizes that a thorough analysis of the substructures in clusters is necessary to better determine the assembly state of the clusters. However, despite our

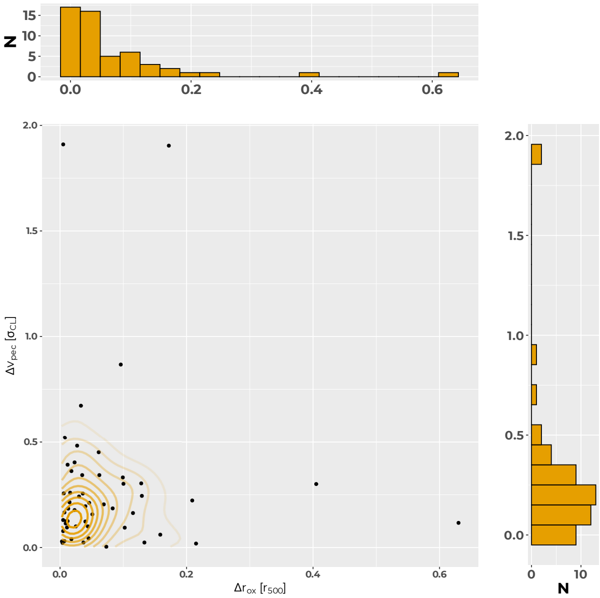

Fig. 8. Distribution of offsets, parameterized. The color figure can be viewed online.

careful analysis, the upgraded cluster peculiar velocities and velocity dispersions, we must still conclude that a significantly large number of nearby clusters do not have a relaxed core.

In fact, considering the clusters individually or in any of the assembly state class, we found no correlation between $\Delta r_{\rm ox}$ and $\Delta v_{\rm pec}$, as can be seen in Figure 8 (compare, also, Column 21 with Column 22 of Table 3), a fact already noted in the literature (*e.g.*, Lauer et al. 2014; De Propris et al. 2021). This advocates against the use of only one of these parameters as the proxy for the shift from the bottom of the cluster potential well, as proposed by, *e.g.*, Lopes et al. (2018). In the present work we consider both together as indicators of the displacement of the CDG with respect to the bottom of the cluster potential well. Thus, we find that 70% of the clusters in our sample present significant disturbances in their mere core. The parameters $\Delta r_{\rm ox}$ and $\Delta v_{\rm pec}$ are reported respectively in Columns 5 and 6 of Table 5. In Column 7, both offsets are used to classify the state of the CDG, adopting the same code as for Column 2, that is, the mark $*$ is assigned when any of them indicates dynamical disturbance.

To obtain a more comprehensive view of the impact of substructures, we show in Figure 9 violin plots for $\Delta r_{\rm ox}$ and $\Delta v_{\rm pec}$, for each class of assembly state. In the upper left panel ($\Delta r_{\rm ox}$), the only trend visible is for the CDGs in the P class to lie below the threshold. This is confirmed for the pairs (U,P) and (P,S), a difference in the distribution being found using a Mann-Withney test at 95% CL, with $P = 0.008$ and $P = 0.025$, respectively. However, a Kruskal-Wallis test performed comparing the whole classes (with Dunn's post-tests) found no statictically significant differences. Similarly, a Kruskal-Wallis test for $\Delta v_{\rm pec}$, in the upper right panel, was also negative, with $P = 0.512$. Thus, we see no evidence for $\Delta r_{\rm ox}$ and $\Delta v_{\rm pec}$ to be related to the classes of assembly state.

In the lower panels of Figure 9, we compare the distribution of $\Delta r_{\rm ox}$ (left) and $\Delta v_{\rm pec}$ (right) separating the clusters based on the core cooling status. Performing a Kruskal-Wallis test for $\Delta r_{\rm ox}$, we find a statistically significant difference between the NCC and SCC (with $P = 0.011$) but not between NCC and WCC or WCC and SCC. However, for $\Delta v_{\rm pec}$ the difference is much more significant ($P \ll 0.0001$) between both NCC and SCC and WCC and SCC (but no difference between NCC and WCC as before). We find a 60% probability for WCC and NCC clusters to be associated with clusters that have both high $\Delta r_{\rm ox}$ and $\Delta v_{\rm pec}$, the trends being more obvious in S and M clusters than in U and P clusters. Considering that the latter two classes represent more massive clusters than the two former ones (cf. Table 4), the U and P clusters, consequently, are possibly slightly more relaxed than the S and M clusters. This is consistent with the complex assembly history of the clusters suggested by the assembly state classes. This correlation has already been pointed out in the literature: Zhang et al. (2011), for instance, found that the CDG–X-ray offset is related to the central cooling time of the clusters, for the HIFLUGCS X-ray flux limited galaxy cluster sample, suggesting that the system must be close to relaxed to have its cooling flow enhanced, or a CC formed.

In general, the fact that the probability of association between the parameters related to the galaxies and gas in the core is not higher than 60% suggests that these two components most probably follow different paths towards equilibrium, the virialization time-scale, most specifically, being much smaller for the gas than for galaxies.

4.5. *Results on the Co-Evolution of CDGs and Clusters*

The remaining columns in Table 5 are dedicated to report the evolutionary parameters for the CDGs: the magnitude gaps Δm_{12} (Column 8) and Δm_{23} (Column 10); the projected separation (clustercentric distance) of the 2^{nd}-rank, Δr_{12}, and 3^{rd}-rank, Δr_{13} (Columns 9 and 11, respectively); and additional comments in Column 12.

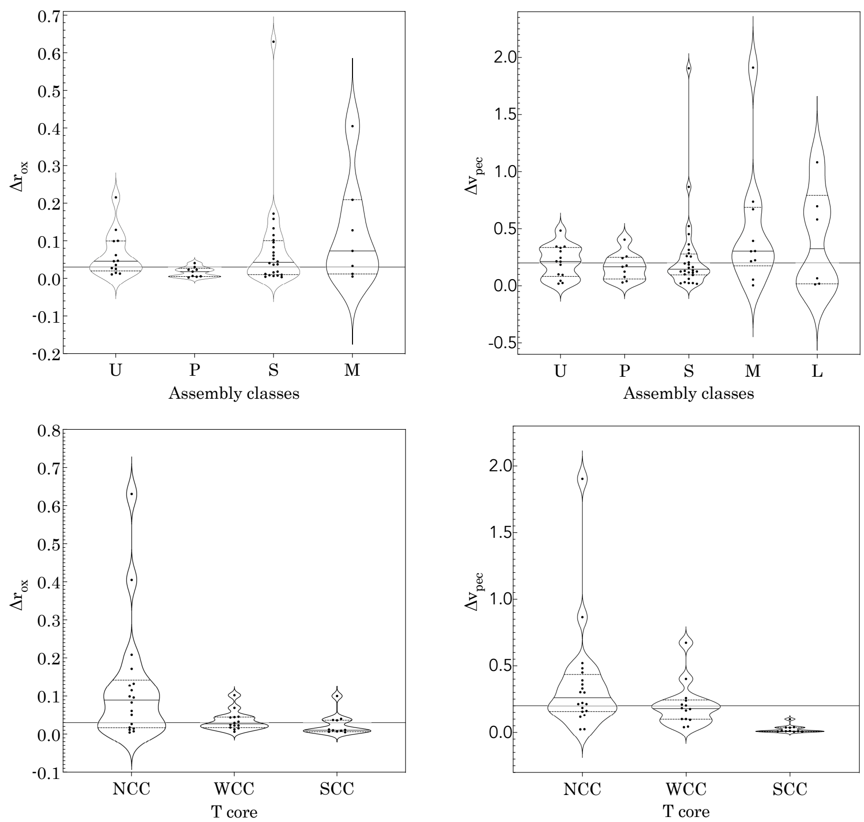

Fig. 9. Distributions of CDG parameters in different assembly classes (upper panel) and different core cooling status (lower panel): Left panels, Δr_{ox}, right panels, Δv_{pec}. In each graphic, the threshold for relaxation associated to the parameter is shown as a horizontal line.

Using M_{Ks} as a proxy for the stellar mass of the CDG (*e.g.*, Schneider, Gunn & Hoessel 1983), we traced in the left panel of Figure 10 its distribution for all the CDGs in our sample. A relatively good Gaussian fit suggests some level of similarity in the evolution of these CDGs. However, the distribution of the magnitude gaps, Δm_{12}, in the right panel of Figure 10, is clearly bimodal, indicating different assembly histories for the CDGs themselves.

This can also be appreciated in Figure 11, which shows the distribution of absolute magnitudes for the CDGs and their respective second-rank galaxies as a function of the magnitude gaps Δm_{12}. As the gap increases, the luminosity of the CDG (its mass) grows almost linearly, while the luminosity of the second-rank galaxy slowly declines. Note that, due to our thorough analysis of substructures and definition of CDGs, it is not surprising that the change in mass we find is much faster than what was seen before (e.g., Smith et al. 2010). Although systems showing large magnitude gaps are consistent with a model where the CDG co-evolve with its cluster, the bimodality clearly suggests more complex assembly histories for the CDGs.

To shed more light on the co-evolution of the CDGs and their clusters, we compare how the two magnitude gaps, Δm_{12} and Δm_{23}, vary in the different assembly classes. This is done in the upper panels of Figure 12. Although there is an apparent trend for U and P clusters to have larger magnitude gaps between the CDG and second-rank galaxy than for the S and M clusters, a Kruskal-Wallis test found no statistically significant difference ($P = 0.190$). Similarly, a Kruskal-Wallis test found no statistically significant difference ($P = 0.125$) for Δm_{23}.

In the lower panels of Figure 12 we compare the two magnitude gaps for the different core cooling states. This time the Kruskal-Wallis test clearly identified a statistically significant difference for Δm_{12}, with $P = 0.002$, between the pairs (NCC, SCC) and (WCC, SCC), but not for Δm_{23}. This is consistent with what we found before for $\Delta r_{\rm ox}$ and $\Delta v_{\rm pec}$. Consequenlty, despite the clear evidence of co-evolution of the clusters and their CDGs, espe-

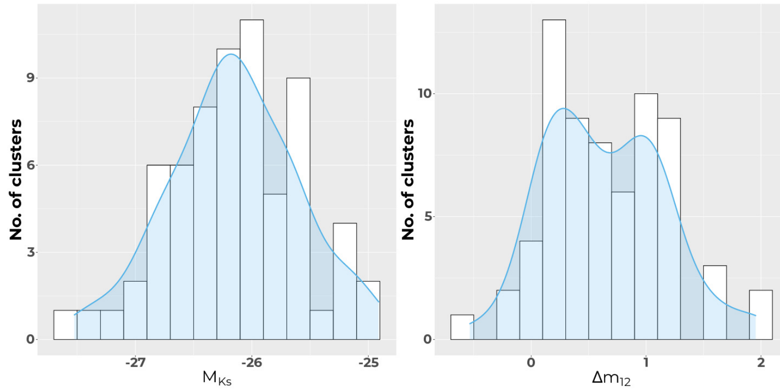

Fig. 10. Distributions of CDGs properties: Left panel, CDG M_{Ks}, right panel, Δm_{12}. The color figure can be viewed online.

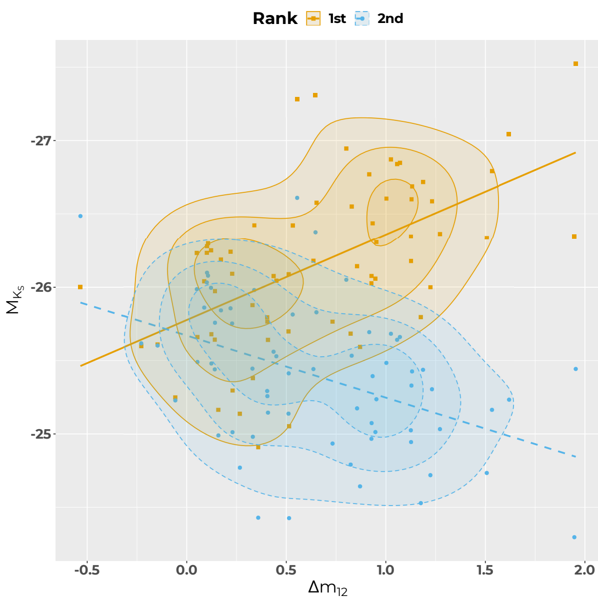

Fig. 11. Distributions of absolute magnitudes for CDGs and 2^{nd}-rank galaxies as function of the magnitude gap. The color figure can be viewed online.

cially in the core, the fact that the assembly state classes contain a mixture of core cooling states seems to confirm the complex assembly history of clusters in general.

5. SUMMARY AND CONCLUSIONS

In this study we traced the assembly histories for a sample of 67 relatively rich (median $N_c = 150$ spectroscopic members) and nearby ($z < 0.15$) galaxy clusters, by classifying their level of substructuring in their outer regions (mostly beyond r_{500}) and estimating the dynamical impact of such subclumps on the host clusters. We also identified and characterized the dynamical properties of the CDGs of the clusters and compared them to the ICM equilibrium state, from X-ray literature data, mapped in the inner part and innermost core regions.

On the accompanying webpage[15], we offer the complete set of figures describing all clusters presented in this article: distribution of galaxies in each complex, system and significant substructure, projected number densities (like in Figure 2), X-ray contour images (like in Figure 3), CDG optical images, together with further information completing the data presented in the various tables included in the present article.

The following is a brief summary of our findings and conclusions:

- In 19% of the cluster in our sample, the classical BCG (directly identified from photometry) is not the CDG (gravitationally dominant galaxy). Among the discrepant cases we distinguish most specifically three different groups: binary central dominant galaxies with the second brightest as the CDG (Coma-like clusters), a BCG that is the SDG of a substructure (Fornax-like clusters), and clusters with a peripheric fossil candidate, where the BCG appears relatively isolated in the outskirt of the cluster.

- Using robust methods to determine cluster membership allowed us to more thoroughly determine the global dynamical parameters of the clusters: radial velocity of the system, velocity dispersion of galaxy members, virial mass and radius.

- Using different algorithms to detect substructures and estimate their gravitational impact on their host clusters, our analysis allowed us

[15] `www.astro.ugto.mx/recursos/HP_SCls/Top70.html`

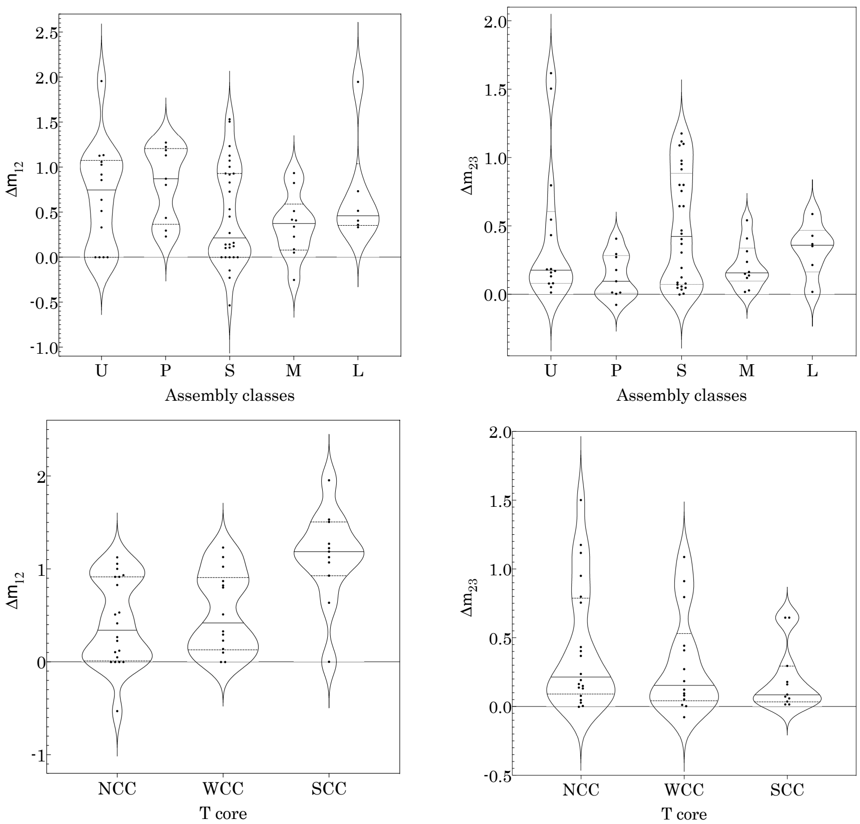

Fig. 12. Comparison of magnitude gaps in different assembly classes (upper panels and cooling states (lower panels).

to determine that, although as many as 70% of nearby clusters show evidence of substructures, those dynamically significant only appear in 57% of the clusters.

- Based on the significance level of the impact of the substructure, we defined five classes of assembly states: high-mass, Unimodal (U); Low-mass unimodal (L); Multi-modal (M); Primary (P), with low-mass substructures attached to a main structure; and, finally, Substructured (S), formed by a main structure and high-mass substructures. We count 21% U, 13% P, 42% S, 15% M and 9% L clusters. In terms of masses, U and P clusters are more massive than S and M clusters, while L clusters are less massive, explaining why they are not detected in X-ray.

Our classification of clusters in terms of substructures seems consistent with a hierarchical model of formation, where clusters form by the mergers of groups of galaxies:

- U clusters are examples of massive systems that merged in the distant past and, consequently, their virialization process is well advanced.
- P clusters also formed in the past and, because they are massive, they still accrete small groups from their environment.
- M and S clusters, which have significant substructures, are examples of relatively more recent mergers: in S clusters massive clumps are accreting smaller mass groups (minor mergers), while in M clusters the masses of the merging entities are comparable (major mergers).
- L clusters are the best examples of poor clusters in our sample: their masses and richness are comparable to those of massive groups, and, like the latter, are usually poor in gas. Their environment suggests that some of them are either infalling or satellites of more massive clusters.

The classes can be interpreted as a "sequence" of different global assembly states possible for the clusters: they begin as a poor cluster (L) or a pile-up of small systems (M), then grow and pass to a state where a main structure starts to dominate (S), then become massive, although still accreting small groups (P), and finally become massive and regular/relaxed (U). Note that this is a snapshot of the assembly state, which can evolve in time: a U cluster can still accrete (becoming a P or S) or merge (becoming a M), for example. However, although there is a dispersion in masses, this dispersion is not that high. This is because the era of cluster evolution is relatively recent, and they did not have time to pass the process of a major merger much more than once or twice. Capturing smaller clumps (minor mergers), on the other hand, may have been frequent, but with a smaller impact on their global masses. Also, the availability of new systems to be captured is decreasing with time because of the accelerated expansion of the Universe.

Our comparison of the properties of CDGs ($\Delta r_{\rm ox}$, $\Delta v_{\rm pec}$, Δm_{12} and Δm_{23}) in the clusters with different assembly state classes and with the characteristics of the ICM in the inner region (different core cooling status) allows us to obtain a more precise view about the assembly process of the clusters.

- Considering the clusters individually or in any of the assembly states, we found no correlation between $\Delta r_{\rm ox}$ (CDG–X-ray offset) and $\Delta v_{\rm pec}$ (CDG peculiar velocity). We suggest the use of both together to characterize the dynamical state of the CDGs.

- We found a 60% probability for WCC and NCC clusters to be associated with clusters that have both high $\Delta r_{\rm ox}$ and $\Delta v_{\rm pec}$, the trends being more obvious in more massive clusters. Considering the difference in masses, this suggests that U and P clusters are more relaxed than S and M clusters.

- Comparing how the two magnitude gaps, Δm_{12} and Δm_{23}, vary in the different assembly states, we found only an apparent trend for U and P cluster to have larger magnitude gaps between the CDG and second-rank galaxy than the S and M clusters, while no trend is visible for Δm_{23}.

- However, we also found a significant difference for Δm_{12}, the gap being smaller in NCC and WCC than in SCC, while no difference is detected for Δm_{23}.

We conclude that, despite of clear evidence of co-evolution of the clusters and their CDGs, especially considering the gas in the core, the fact that the assembly state classes contain a mixture of core cooling states seems to confirm a complex assembly history of clusters. In general, the two baryonic components of clusters, galaxies and gas, probably follow different paths towards equilibrium, the relaxation time-scale, most specifically, being much smaller for the gas than for the galaxies. This difference implies that, even in the most evolved systems, the virialization and evolution of the CDG are complex processes that do not depend solely on time but also on the frequency and impact of mergers, cooling and heating of the ICM by shocks and feedback, cannibalism, pre-processing, among others. How much of this evolution is due to pre-processing in the initial groups, however, is still an open question.

We acknowledge financial support from *Universidad de Guanajuato* (DAIP), *Convocatoria Institucional de Investigación Científica*, projects 087/2010, 219/2013, 205/2019 and 138/2022. Y.V. acknowledges financial support from the postdoctoral-fellowship "*2do. año de estancia posdoctoral en México*" from CONACyT and UNAM-DGAPA-PAPIIT IN111620 grant.

This research has made use of "Aladin sky atlas" developed at CDS, Strasbourg Observatory, France, the NASA/IPAC Extragalactic Database (NED) which is operated by the Jet Propulsion Laboratory, California Institute of Technology, under contract with the National Aeronautics and Space Administration, the SuperCOSMOS Science Archive, prepared and hosted by the Wide Field Astronomy Unit, Institute for Astronomy, University of Edinburgh, which is funded by the UK Science and Technology Facilities Council and the Two Micron All Sky Survey, which is a joint project of the University of Massachusetts, the Infrared Processing and Analysis Center/California Institute of Technology, funded by the National Aeronautics and Space Administration and the National Science Foundation and the Digitized Sky Surveys, produced at the Space Telescope Science Institute under U.S. Government grant NAG W-2166.

APPENDIX

A. NEW TEMPERATURE MEASUREMENTS

We estimated the temperature for seven galaxy clusters of our sample using data from both XMM-Newton[16] and Chandra[17] (Table 6), four of which are previously unreported in the literature. This section briefly discusses the procedure for spectral fitting and computing temperatures.

The data from XMM-Newton were reduced using the *XMM-Newton Science Analysis Software* (SAS), version 14.0.0. The raw data, downloaded in the

[16] `http://nxsa.esac.esa.int/nxsa-web/`
[17] `https://chandra.harvard.edu/`

TABLE 6

X-RAY DATA FOR THE TARGETED GALAXY CLUSTERS

Cluster ID (1)	z_{spec} (2)	X-ray peak $\alpha_{J2000}, \delta_{J2000}$ (3)	Telescope (4)	Observation ID (5)	Date of Observation (6)	Exposure time (ks) (7)
A0122	0.113	00 57 24.7, -26 16 50	XMM	0504160101	2007 Dec 3	56.92
A2811	0.108	00 42 08.7, -28 32 09	XMM	0404520101	2006 Nov 28	25.91
A2870	0.024	01 07 43.2, -46 54 59	XMM	0205470301	2004 May 15	11.91
A0399	0.072	02 57 56.4, 13 00 59	Chandra	3230	2002 Nov 18	49.28
A3094	0.068	03 11 25.0, -26 53 59	Chandra	5799	2005 Nov 28	40.15
A3716	0.046	20 51 16.7, -52 41 43	Chandra	15133, 15583	2012 Dec 24/20	14.77, 16.08
A4038	0.028	23 47 43.2, -28 08 29	Chandra	4992	2004 Jun 28	33.97

[1]X-ray data obtained from XMM-Newton (http://nxsa.esac.esa.int/nxsa-web/) and Chandra (https://chandra.harvard.edu/). Columns: (1) Cluster ID; (2) spectroscopic redshift coming from NED (http://ned.ipac.caltech.edu); (3) Optical RA, Dec (J2000.0); (4) Telescope; (5) Observation ID; (6) Date of Observation; and (7) Exposure Time.

TABLE 7

ESTIMATED X-RAY TEMPERATURES FOR THE TARGETED GALAXY CLUSTERS

Cluster (1)	Projected radius (armin) (2)	Physical radius (Mpc) (3)	$k\mathrm{T_X}$ (keV) (4)
A0122	4.0	0.5	3.70 ± 0.07
A2811	4.2	0.5	5.04 ± 0.05
A2870	8.6	0.25	1.07 ± 0.07
A0399	6.0	0.5	6.49 ± 0.27
A3094	6.4	0.5	3.15 ± 0.48
A3716N	4.6	0.25	2.19 ± 0.26
A3716S	4.6	0.25	3.65 ± 0.27
A4038	7.4	0.25	3.15 ± 0.05

[1]Columns: (1) Cluster ID; (2) radius used to extract spectra, (3) relative physical radius covered in the plan of sky, (4) estimated temperature from Model TBabs*mekal.

form of observation data files (ODF), were processed in the following steps: (i) Generation of calibrated event lists for the EPIC (MOS1, MOS2, and PN) cameras using the latest calibration data; this step was done using the SAS packages `cifbuild`, `odfingest`, `epchain`, and `emchain`. (ii) Creation of the background light curves to identify time intervals with poor quality data, and filtering of the EPIC event lists to exclude periods of high background flaring and bad events. (iii) Creation of a sky image of the filtered data set; these steps were performed using SAS packages `evselect`, `tabgtigen`, and `xmm_select`.

Finally, we extracted the spectra from the source and background using the task `especget` from SAS. This task produced two sets of files called the response matrix files (redistribution matrix file, RMF, and ancillary response file, ARF). Similarly, the Chandra data were obtained from the Chandra Data Archive (CDA)[18] and operated by the Chandra Interactive Analysis of Observations CIAO, version 4.6.1, with calibration database version 4.6.1. In addition, the CIAO tool `chandra_repro` was applied to perform initial processing and obtain a new event file. These files are used for spectral fittings.

A.1. *Spectral Model Fitting:*

We extracted the spectra within a fixed radius of 0.5 h_{70}^{-1} Mpc and excluded the point sources from this region. In some cases, the object was not centered on the observed field, so that we had to reduce the size of the extraction circle (see Table 7). The spectra from both XMM-Newton and Chandra, were fitted using *XSPEC* spectral fitting software, version 12.5.1 (Arnaud 1996). The photon counts of each cluster spectrum were grouped into bins with at least one count per bin. The spectral model was fitted to the data using the Ftools task `grppha`. The Galactic HI column (nH) was derived from the HI map from the Leiden/Argentine/Bonn (LAB) survey (Kalberla et al. 2005). This parameter was fixed while fitting the X-ray spectrum. The redshift of the spectral model was fixed to the cluster spectroscopic redshift coming from the NED database[19]. Finally, we employed a fitting model to multiply a TBABS absorption model (Wilms et al. 2000) and a single-temperature, optically thin, thermal plasma component (the MEKAL code in XSPEC terminology, Mewe et al. 1986) to model the X-ray emission from ICM plasma.

[18] `https://cxc.harvard.edu/cda/`
[19] `http://ned.ipac.caltech.edu`

B. LIST OF M AND HS SUBSTRUCTURES FOR P, S AND M CLUSTERS.

TABLE 8

SUBSTRUCTURES DETECTED IN THE CLUSTERS OF OUR SAMPLE. SDG: SUBSTRUCTURE DOMINANT GALAXY

$\mathrm{ID_{sub}}$ (1)	$\mathrm{RA_{SDG}}$ (2)	$\mathrm{Dec_{SDG}}$ (3)	SDG (4)	N_s (5)	v_s (6)	σ_s (7)	r_{200} (8)	N_a (9)	v_{sub} (10)	σ_{sub} (11)	R_p (12)	R_{vir} (13)	M_{vir} (14)
A2804**m**w	9.907535	−28.906199	6dF J0039377-285422	48	33790	323	0.631	27	33836	404	0.842	1.036	1.256
A2804**m**e	10.008486	−28.902040	GALEX J004002.00-285407.9	32	32688	380	0.743	6	32268	314	0.540	0.757	0.487
A085Acw	10.376354	−9.262768	KAZ 364	22	14352	473	0.954	20	14414	482	0.529	1.019	1.121
A085A**m**	10.460515	−9.303040	MCG -02-02-086	272	16745	799	1.603	218	16738	852	1.813	2.242	12.000
A085Ase	10.792272	−9.861486	GIN 011	25	15083	272	0.547	15	15132	271	0.515	0.687	0.345
A2811B**m**	10.537175	−28.535772	2MASX J00420892-2832087	123	32345	891	1.745	107	32340	947	1.766	2.345	14.500
A0118**m**	13.743478	−26.375153	2MASX J00545843-2622305	51	34586	702	1.369	46	34470	728	1.666	1.925	8.056
A0118c	13.874743	−26.396147	SARS 013.26663-26.66683	14	33958	338	0.660	13	33996	368	0.329	0.712	0.407
A0118e	13.958530	−26.365671	SARS 013.35062-26.63606	15	34171	584	1.139	15	34171	584	0.381	1.017	1.189
A0119**m**	14.067088	−1.255492	UGC 00579	277	13276	876	1.768	266	13281	893	1.302	2.080	9.488
A0119n	14.258582	−0.875172	UGC 00588	25	13402	450	0.909	23	13417	456	0.626	1.040	1.187
A0119ne	14.365250	−0.471357	GIN 021	23	13197	422	0.852	17	13188	461	0.651	1.062	1.263
A0133Anw	15.008555	−21.488472	ESO 541-G007	13	16585	474	0.951	13	16585	474	1.113	1.289	2.283
A0133A**m**	15.674046	−21.882154	ESO 541-G013	109	16762	723	1.453	87	16833	774	1.340	1.901	7.333
A0133Ane	15.999613	−21.372469	ESO 541-G016	10	17550	154	0.308	2	17436	205	0.698	0.630	0.267
A2870w	16.226784	−46.999523	2MASX J01045442-4659582	27	6396	329	0.672	24	6418	336	0.787	0.923	0.812
A2870e	16.927452	−46.907574	IC 1625	23	6919	235	0.480	17	6964	239	0.455	0.611	0.237
A2877**m**	17.481663	−45.931217	IC 1633	124	7231	647	1.318	99	7169	676	0.856	1.511	3.574
A3027Acw	37.482681	−33.177345	GALEX J022955.81-331036.6	24	23769	406	0.806	21	23821	423	1.054	1.164	1.721
A3027A**m**	37.706005	−33.103752	2dFGRS S518Z162	73	23283	697	1.384	63	23318	731	1.363	1.828	6.653
A0400**m**	44.423164	6.026997	NGC 1128	51	7011	336	0.684	42	7027	347	0.561	0.841	0.616
A0400ne	44.587616	6.095203	CGCG 415-046	10	6769	73	0.149	3	6768	94	0.228	0.260	0.018
A3104**m**	48.590549	−45.420238	LCRS B031238.4-453620	38	21784	446	0.887	28	21736	511	0.785	1.201	1.874
A3104e	49.033882	−45.391937	2MFGC 02678	10	21609	271	0.541	9	21589	278	0.698	0.769	0.493
A3104se	49.237873	−45.540817	LCRS B031514.7-454323	5	22160	125	0.248	2	22128	53	0.152	0.152	0.004
A3112Bn	49.472656	−44.041534	2MASX J03175343-4402295	7	23838	303	0.601	7	23838	303	0.718	0.819	0.601
A3112B**m**	49.490250	−44.238213	ESO 248-G006	90	22549	596	1.185	56	22526	595	1.637	1.695	5.283
A0426A**m**	49.950980	41.511680	NGC 1275	297	5289	1023	2.092	296	5295	1024	1.322	2.309	12.700
S0373sw	50.674120	−37.208200	NGC 1316	20	1705	200	0.410	16	1728	230	0.238	0.484	0.115
S0373n	52.081950	−31.068180	NGC 1340	23	1283	249	0.513	16	1248	229	0.624	0.664	0.298
S0373**m**	54.621180	−35.450740	NGC 1399	178	1454	343	0.705	98	1458	390	0.307	0.748	0.427
A3158nw	55.549149	−53.390938	2MASX J03421179-5323273	16	18631	207	0.414	6	18711	104	0.541	0.367	0.053
A3158**m**	55.720634	−53.631302	ESO 156-G008 NED01	190	17373	1077	2.161	190	17373	1077	1.193	2.279	12.600
A3158cs	55.873669	−53.692135	2MASX J03432968-5341316	20	18594	287	0.575	15	18603	334	0.616	0.836	0.628
A0496nw	67.818871	−12.455068	IC 0377	36	9376	452	0.917	33	9384	468	0.943	1.219	1.890
A0496**m**	68.407669	−13.261956	MCG -02-12-039	315	9957	682	1.383	272	9933	715	1.330	1.812	6.210
A0539**m**	79.155548	6.440917	UGC 03274 NED05	110	8649	637	1.295	100	8645	674	0.982	1.576	4.073
A0539se	79.819481	5.757124	2MASX J05191667+0545256	15	8735	200	0.407	9	8777	243	0.646	0.694	0.348
A0539e	80.000107	6.680067	CGCG 421-028	7	8902	118	0.240	2	8809	69	0.428	0.261	0.018
A3395nw	96.518044	−54.029495	LEDA 423636	35	14534	614	1.238	34	14514	613	0.670	1.295	2.299
A3395**m**	96.901047	−54.449364	ESO 161-G008	166	14980	740	1.491	161	14995	746	1.032	1.703	5.241
A3395se	97.606720	−54.762615	ESO 161-IG012 NED01	13	14587	398	0.801	13	14587	398	0.544	0.905	0.786
A0576sw	108.784760	55.419525	CGCG 261-039	16	11328	305	0.618	5	11213	108	1.023	0.471	0.110
A0576**m**	110.375999	55.761581	CGCG 261-056 NED02	191	11359	861	1.743	183	11351	878	1.563	2.189	11.000
A0576ne	110.941490	56.581875	2MFGC 05892	13	11483	421	0.851	9	11474	231	1.051	0.787	0.512
A0754nw	136.941254	−9.392439	2MASX J09074590-0923327	24	16494	303	0.609	15	16487	295	0.615	0.770	0.488
A0754s	137.009079	−9.993835	2MASX J09080217-0959378	30	15827	541	1.088	30	15827	541	0.595	1.144	1.592
A0754**m**w	137.134949	−9.629739	2MASX J09083238-0937470	193	16168	820	1.647	173	16182	880	0.981	1.867	6.931
A0754**m**e	137.330139	−9.699759	2MASX J09091923-0941591	118	16438	776	1.559	116	16450	782	0.881	1.665	4.922
A1060**m**	159.177963	−27.528584	NGC 3311	343	3698	676	1.385	323	3701	694	0.884	1.560	3.886
A1367**m**nw	176.009048	19.949820	NGC 3842	152	6546	512	1.045	122	6532	556	0.818	1.308	2.313
A1367**m**se	176.270782	19.606382	NGC 3862	117	6330	599	1.222	109	6309	608	0.882	1.424	2.979
A3526A**m**	192.203918	−41.311665	NGC 4696	210	3061	510	1.045	124	2991	569	0.817	1.332	2.414
A3526B**m**	192.516449	−41.382072	NGC 4709	90	4563	276	0.566	47	4634	317	0.501	0.764	0.459
A3530**m**	193.900009	−30.347490	ESO 443-G011	101	16087	611	1.227	88	16105	633	1.195	1.601	4.367
A3530s1	193.929596	−30.718328	2MASX J12554310-3043059	9	15480	246	0.495	7	15509	256	0.511	0.660	0.306
A3532s2	193.980011	−30.721376	2MASX J12555520-3043169	7	16945	198	0.398	5	16878	163	0.574	0.506	0.139
A3532n	194.253647	−29.951527	2MASX J12570087-2957054	16	17021	279	0.561	9	17062	342	0.717	0.894	0.765
A3532**m**	194.341339	−30.363482	PKS 1254-30	80	16671	427	0.857	57	16700	443	0.908	1.151	1.628
A1644**m**	194.298248	−17.409575	2MASX J12571157-1724344	288	14077	1011	2.039	283	14088	1018	1.473	2.363	13.900
A1651**m**	194.843826	−4.196117	2MASX J12592251-0411460	177	25463	862	1.707	160	25465	877	1.808	2.262	12.700
A1656sw	194.351242	27.497778	NGC 4839	54	7412	404	0.822	54	7412	404	0.540	0.918	0.803
A1656**m**	194.898788	27.959389	NGC 4874	828	6921	1046	2.132	813	6927	1039	1.611	2.487	15.900
A3526Be	196.608917	−40.414490	ESO 323-G077	5	4615	101	0.208	4	4656	113	0.255	0.308	0.030
A3556**m**	201.027893	−31.669956	ESO 444-G025	102	14424	504	1.016	90	14436	520	1.047	1.346	2.586
A1736Anw	201.544220	−26.826834	6dF J1326106-264937	14	9974	158	0.321	6	9976	148	0.208	0.342	0.042
A1736A**m**	201.683777	−27.439398	ESO 509-G008	43	10500	271	0.549	18	10481	311	0.517	0.759	0.457
A1736Acn	201.898788	−27.042744	ESO 509-G016	8	10977	168	0.340	7	11059	186	0.449	0.512	0.141
A1736Ase	202.062210	−27.976803	MCG -05-32-027	9	9862	140	0.283	2	9850	23	0.172	0.091	0.001
A1736Bcn	201.703033	−27.143835	ESO 509-G009	28	14064	568	1.145	28	14064	568	0.505	1.120	1.488
A1736B**m**	201.866852	−27.324682	IC 4252	107	13600	866	1.748	97	13572	878	1.372	2.092	9.668
A3558**m**	201.987015	−31.495474	ESO 444-G046	525	14408	953	1.920	448	14419	961	1.850	2.452	15.600
A2040Bsw	227.880768	7.251906	CGCG 049-033	14	13399	164	0.331	8	13330	211	0.649	0.631	0.265
A2040B**m**	228.197815	7.434258	UGC 09767	136	13491	600	1.210	97	13584	663	1.309	1.708	5.263
A2052nw	228.094116	7.727029	CGCG 049-041	18	9881	253	0.514	8	9934	309	1.054	0.958	0.918
A2052**m**	229.185364	7.021667	UGC 09799	158	10355	588	1.192	120	10416	648	1.115	1.599	4.276
A2063A**m**	230.772095	8.609181	CGCG 077-097	189	10312	672	1.364	145	10347	758	1.196	1.818	6.284
A2142**m**	239.583450	27.233349	2MASX J15582002+2714000	182	27031	827	1.634	155	27046	830	1.745	2.152	11.000

TABLE 8. CONTINUED

ID_{sub} (1)	RA_{SDG} (2)	Dec_{SDG} (3)	SDG (4)	N_s (5)	v_s (6)	σ_s (7)	r_{200} (8)	N_a (9)	v_{sub} (10)	σ_{sub} (11)	R_p (12)	R_{vir} (13)	M_{vir} (14)
A2147**m**s	240.570862	15.974513	UGC 10143	185	10706	854	1.732	178	10706	867	1.181	1.979	8.111
A2147**m**n	240.582687	16.346182	UGC 10144	210	11039	950	1.925	200	11030	964	1.479	2.288	12.600
A2147s	240.981934	14.902552	IC 1168	27	10564	467	0.946	15	10686	557	0.651	1.208	1.846
A2147se	241.606033	15.685868	UGC 10201	31	11740	489	0.989	31	11740	489	0.755	1.162	1.648
A2151sw	240.883575	17.198523	NGC 6034	32	10351	438	0.889	30	10348	434	0.552	0.968	0.950
A2151**m**w	241.148987	17.721445	NGC 6041	63	11006	871	1.764	63	11006	871	1.083	1.927	7.498
A2151**m**c	241.287537	17.729971	NGC 6047	92	10436	652	1.323	89	10434	663	0.645	1.353	2.589
A2151**m**n	241.566620	18.249800	NGC 6061	77	11186	341	0.691	57	11229	359	0.801	0.965	0.942
A2151e	241.663986	17.761154	IC 1194	22	11632	452	0.915	22	11632	452	0.371	0.870	0.692
A2152**m**nw	241.360168	16.442734	2MASX J16052644+1626338	56	13504	478	0.964	39	13480	466	0.857	1.172	1.698
A2152**m**se	241.371750	16.435793	UGC 10187 NED2	60	13126	255	0.514	19	13203	296	0.586	0.763	0.469
A2197**m**w	246.293030	40.892746	NGC 6146	67	8900	343	0.697	47	8870	331	0.782	0.909	0.782
A2197**m**c	246.921143	40.926899	NGC 6160	111	9575	463	0.939	64	9574	541	0.958	1.348	2.558
A2197**m**e	247.436890	40.811710	NGC 6173	92	8786	395	0.802	68	8774	380	0.709	0.965	0.934
A2199**m**	247.159485	39.551380	NGC 6166	461	9086	785	1.595	441	9083	795	1.244	1.903	7.175
A2204Aw	247.792801	5.530654	2MASX J16311027+0531503	7	45236	371	0.710	7	45236	371	0.571	0.849	0.718
A2204An	248.111099	5.839127	2MASX J16322666+0550208	8	44975	264	0.507	4	45025	237	0.120	0.375	0.062
A2204A**m**	248.195404	5.575833	VLSS J1632.7+0534	77	45378	856	1.639	42	45406	1062	1.985	2.595	20.500
A2256cf	255.294220	78.726463	2MASX J17011061+7843352	27	17181	719	1.444	27	17181	720	0.599	1.384	2.832
A2256cb	255.700409	78.740837	2MASX J17024809+7844270	16	19704	250	0.500	12	19718	209	0.453	0.552	0.182
A2256**m**	256.113525	78.640564	UGC 10726	231	17530	1168	2.341	231	17530	1167	1.427	2.552	17.800
A2255sw	257.713409	63.853771	2MASX J17105121+6351135	12	24487	383	0.760	9	24556	442	0.567	0.974	1.011
A2255**m**	258.119812	64.060699	ZwCl 1710.4+6401A	155	24063	1072	2.128	154	24050	1069	1.564	2.465	16.300
A2255e	258.788116	64.048248	2MASX J17150914+6402536	14	24244	287	0.569	6	24078	206	0.599	0.597	0.232
A3716**m**	312.987152	−52.629829	ESO 187-G026	140	13509	744	1.501	123	13508	783	1.246	1.877	6.986
A2634sw	354.218323	26.509964	UGC 12708	13	9490	272	0.552	11	9434	268	0.646	0.741	0.425
A2634**m**	354.622437	27.031303	NGC 7720	172	9243	716	1.454	160	9235	736	1.217	1.796	6.031
A4038A**m**	356.937683	−28.140705	IC 5358	196	8872	725	1.474	166	8910	773	1.056	1.769	5.765
A4049s	357.903015	−28.365068	IC 5362	23	8307	270	0.549	23	8307	270	0.639	0.742	0.424
A4049n	357.976715	−27.929789	MCG -05-56-025	18	8809	88	0.180	6	8837	67	0.159	0.184	0.007

REFERENCES

Abbot, T. M. C., Adamów, M., Aguena, M. et al. 2021, ApJS, 255, 20, https://doi.org/10.3847/1538-4365/ac00b3

Abdullah, M. H., Wilson, G., Klypin, A., et al. 2020, ApJS, 246, 2, https://doi.org/10.3847/1538-4365/ab536e

Abell, G. O., Corwin, H. G. Jr., and Olowin, R. P. 1989, ApJS, 70, 1, https://doi.org/10.1086/191333

Ahn, C. P., Alexandroff, R., Allende Prieto, C., et al. 2012, ApJS, 203, 21, https://doi.org/10.1088/0067-0049/203/2/21

Aihara, H., Allende Prieto, C., An, D., et al. 2011, ApJS, 193, 29, https://doi.org/10.1088/0067-0049/193/2/29

Albareti, F. D., Allende-Prieto, C., Almeida, A., et al. 2017, ApJS, 233, 25, https://doi.org/10.3847/1538-4365/aa8992

Andernach, H., Tago, E., Einasto, M., Einasto, J., & Jaaniste, J. 2005, ASPC 329, Nearby-Large Scale Structures and the Zone of Avoidance (San Francisco, CA: ASPC), 283, https://doi.org/10.48550/arXiv.astro-ph/0407097

Andrade-Santos, F., Lima Neto, G. B., & Laganá, T. F. 2012, ApJ, 746, 139, https://doi.org/10.1088/0004-637X/746/2/139

Andrade-Santos, F., Jones, C., Forman, W. R., et al. 2017, ApJ, 843, 76, https://doi.org/10.3847/1538-4357/aa7461

Arnaud, K. A. 1996, ASPC 101, Astronomical Data Analysis Software and Systems V, ed. G. H. Jacoby and J. Barnes, 17

Baldry, I. K., Robotham, A. S. G., Hill, D. T., et al. 2010, MNRAS, 404, 86, https://doi.org/10.1111/j.1365-2966.2010.16282.x

Barnes, D. G., Staveley-Smith, L., de Blok, W. J. G., et al. 2001, MNRAS, 322, 486, https://doi.org/10.1046/j.1365-8711.2001.04102.x

Bautz, L. P. & Morgan, W. W. 1970, ApJ, 162, 149, https://doi.org/10.1086/180643

Becker, R. H., White, R. L., & Helfand, D. J. 1995, ApJ, 450, 559, https://doi.org/10.1086/176166

Beers, T. C., Geller, M. J., & Huchra, J. P. 1982, 257, 23, https://doi.org/10.1086/159958

Beers, T. C., Flynn, K., & Gebhardt, K. 1990, AJ, 100, 32, https://doi.org/10.1086/115487

Beers, T. C., Gebhardt, K., Huchra, J. P., et al. 1992, ApJ, 400, 410, https://doi.org/10.1086/172006

Benavides, J. A. Sales, L. V., & Abadi, M. G. 2020, MNRAS, 498, 3852, https://doi.org/10.1093/mnras/staa2636

Bird, C. M. & Beers, T. C. 1993, AJ, 105, 1596, https://doi.org/10.1086/116540

Bonjean, V., Aghanim, N., Salomé, P., Douspis, M., & Beelen, A. 2018, A&A, 609, 49, https://doi.org/10.1051/0004-6361/201731699

Bonnarel, F., Fernique, P., Bienaymé, O., et al. 2000, A&AS, 143, 33, https://doi.org/10.1051/aas:2000331

Botteon, A., Shimwell, T. W., Cassano, R., et al. 2022, A&A, 660, 78, https://doi.org/10.1051/0004-6361/202143020

Bravo-Alfaro, H., Caretta, C. A., Lobo, C., Durret, F., & Scott, T. 2009, A&A, 495, 379, https://doi.org/10.1051/0004-6361:200810731

Bryan, G. L. & Norman, M. L. 1998, ApJ, 495, 80, https://doi.org/10.1086/305262
Buote, D. A. & Tsai, J. C. 1995, ApJ, 452, 522, https://doi.org/10.1086/176326
Burenin, R. A., Vikhlinin, A., Hornstrup, A., Ebeling, H., Quintana, H., and Mescheryakov, A. 2007, ApJS, 172, 561, https://doi.org/10.1086/519457
Caldwell, N., Rose, J. A., Sharples, R. M., Ellis, R. S., & Bower, R. G. 1993, AJ, 106, 473, https://doi.org/10.1086/116656
Caretta, C. A., Islas-Islas, J. M., Torres-Papaqui, J.P., Bravo-Alfaro, H., & Andernach, H. 2008, MmSAI, 79, 1201, https://doi.org/10.48550/arXiv.0902.2293
Carlberg, R. G., Yee, H. K. C., & Ellingson, E. 1997, ApJ, 478, 462, https://doi.org/10.1086/303805
Chambers, K. C., Magnier, E. A., Metcalfe, N., et al. 2016, arXiv: 1612.05560, https://doi.org/10.48550/arXiv.1612.05560
Chen, Y., Reiprich, T. H., Böhringer, H., Ikebe, Y., & Zhang, Y. -Y. 2007, A&A, 466, 805, https://doi.org/10.1051/0004-6361:20066471
Chilingarian, I. V., Melchior, A. -L., & Zolotukhin, I. Y. 2010, MNRAS, 405, 1409, https://doi.org/10.1111/j.1365-2966.2010.16506.x
Chow-Martínez, M., Andernach, H., Caretta, C. A., & Trejo-Alonso, J. J. 2014, MNRAS, 445, 4073, https://doi.org/10.1093/mnras/stu1961
Chow-Martínez, M. 2019, PhD. Thesis, Univ. Guanajuato, México
Cole, S., Percival, W. J., Peacock, J. A., et al. 2005, MNRAS, 362, 505, https://doi.org/10.1111/j.1365-2966.2005.09318.x
Condon, J. J., Cotton, W. D., Greisen, E. W., et al. 1998, AJ, 115, 1693, https://doi.org/10.1086/300337
Coziol, R., Andernach, H., Caretta, C. A., Alamo-Martínez, K. A., & Tago, E. 2009, AJ, 137, 4795, https://doi.org/10.1088/0004-6256/137/6/4795
Cruddace, R., Voges, W., Böhringer, H., et al. 2002, ApJS, 140, 239, https://doi.org/10.1086/324519
da Costa, L., N., Willmer, C. N. A., Pellegrini, P. S., et al. 1998, AJ, 116, 1, https://doi.org/10.1086/300410
De Propris, R., West, M. J., Andrade-Santos, F., et al. 2021, MNRAS, 500, 310, https://doi.org/10.1093/mnras/staa3286
Dey, A., Schlegel, D. J., Lang, D., et al. 2019, AJ, 157, 168, https://doi.org/10.3847/1538-3881/ab089d
Donnari, M., Pillepich, A., Joshi, G. D., et al. 2021, 500, 4004, https://doi.org/10.1093/mnras/staa3006
Dressler, A. 1980, ApJ, 236, 351, https://doi.org/10.1086/157753
Dressler, A. & Shectman, S. A. 1988, AJ, 95, 985, https://doi.org/10.1086/114694
Dupuy, A., Courtois, H. M., Dupont, F., et al. 2019, MNRAS, 489, 1, https://doi.org/10.1093/mnrasl/slz115
Ebeling, H., Voges, W., Böhringer, H., et al. 1996, MNRAS, 281, 799, https://doi.org/10.1093/mnras/281.3.799
Einasto, M., Tago, E., Saar, E., et al. 2010, A&A, 522, 92, https://doi.org/10.1051/0004-6361/201015165
Einasto, M., Vennik, J., Nurmi, P., et al. 2012, A&A, 504, 123, https://doi.org/10.1051/0004-6361/201118697
Einasto, M., Letzen, H., Tempel, E., et al. 2014, A&A, 562, 87, https://doi.org/10.1051/0004-6361/201323111
Falco, E. E., Kurtz, M. J., Geller, M. J., et al. 1999, PASP, 111, 438, https://doi.org/10.1086/316343
Finoguenov, A., Arnaud, M., & David, L. P. 2001, ApJ, 555, 191, https://doi.org/10.1086/321457
Fitchett, M. & Webster, R. 1987, ApJ, 317, 653, https://doi.org/10.1086/165310
Fitzpatrick, E. L. 1999, PASP, 111, 63, https://doi.org/10.1086/316293
Flin, P. & Krywult, J. 2006, A&A, 450, 9, https://doi.org/10.1051/0004-6361:20041635
Fraser-McKelvie, A., Pimbblet, K. A., & Lazendic, J. S. 2011, MNRAS, 415, 1961, https://doi.org/10.1111/j.1365-2966.2011.18847.x
Fukazawa, Y., Makishima, K., & Ohashi, T. 2004, PASJ, 56, 965, https://doi.org/10.1093/pasj/56.6.965
Fukugita, M., Shimasaku, K., & Ichikawa, T. 1995, PASP, 107, 945, https://doi.org/10.1086/133643
Geller, M. J. & Beers, T. C. 1982, PASP, 94, 421, https://doi.org/10.1086/131003
Gregory, S. A. & Thompson, L. A. 1984, 286, 422, https://doi.org/10.1086/162617
Haggar, R., Kuchner, U., Gray, M. E., et al. 2023, MNRAS, 518, 1316, https://doi.org/10.1093/mnras/stac2809
Hambly, N. C., MacGillivray, H. T., & Read, M. A. 2001a, MNRAS, 326, 1279, https://doi.org/10.1111/j.1365-2966.2001.04660.x
Hambly, N. C., Irwin, M. J., & MacGillivray, H. T. 2001b, MNRAS, 326, 1295, https://doi.org/10.1111/j.1365-2966.2001.04661.x
Hambly, N. C., Davenhall, A. C., Irwin, M. J., & MacGillivray, H. T. 2001c, MNRAS, 326, 1315, https://doi.org/10.1111/j.1365-2966.2001.04662.x
Harvey, D., Courbin, F., Kneib, J. P., & McCarthy, I. G. 2017, MNRAS, 472, 1972, https://doi.org/10.1093/mnras/stx2084
Hou, A., Parker, L. C., Harris, W. E., & Wilman, D. J. 2009, ApJ, 702, 1199, https://doi.org/10.1088/0004-637X/702/2/1199
Huchra, J. P., Macri, L. M., & Masters, K. L. 2012, ApJS, 199, 26, https://doi.org/10.1088/0067-0049/199/2/26
Hudson, D. S., Mittal, R., Reiprich, T. H., et al. 2010, A&A, 513, 37, https://doi.org/10.1051/0004-6361/200912377
Ichinohe, Y., Simionescu, A., Werner, N., Fabian, A. C., & Takahashi, T. 2019, MNRAS, 483, 1744, https://doi.org/10.1093/mnras/sty3257
Ikebe, Y., Reiprich, T. H., Böhringer, H., Tanaka, Y., & Kitayama, T. 2002, A&A, 383, 773, https://doi.org/10.1051/0004-6361:20011769

Islas-Islas, J. M. 2015, PhD. Thesis, Univ. Guanajuato, México
Jarrett, T. H., Chester, T., Schneider, S., Skrutskie, M., & Huchra, J. P. 2000, AJ, 119, 2498, https://doi.org/10.1086/301330
Jarrett, T. H., Chester, T., Cutri, R., Schneider, S. E., & Huchra, J. P. 2003, AJ, 125, 525, https://doi.org/10.1086/345794
Jarrett, T. 2004, PASA, 21, 396, https://doi.org/10.1071/AS04050
Jeltema, T. E., Canizares, C. R., Bautz, M. W., & Buote, D. A. 2005, ApJ, 624, 606, https://doi.org/10.1086/428940
Jones, C. & Forman, W. 1999, ApJ, 511, 65, https://doi.org/10.1086/306646
Jones, D. H., Read, M. A., Saunders, W., et al. 2009, MNRAS, 399, 683, https://doi.org/10.1111/j.1365-2966.2009.15338.x
Käfer, F., Finoguenov, A., Eckert, D., Sanders, J. S., & Reiprich, T. H. 2019, A&A, 628, 43, https://doi.org/10.1051/0004-6361/201935124
Kalberla, P. M. W., Burton, W. B., Hartmann, D., et al. 2005, A&A, 440, 775, https://doi.org/10.1051/0004-6361:20041864
Knowles, K., Cotton, W. D., Rudnick, L., et al. 2022, A&A, 657, 56, https://doi.org/10.1051/0004-6361/202141488
Kopylova, F. G. & Kopylov, A. I. 2018, AstBu, 73, 267, https://doi.org/10.1134/S199034131803001X
Kowalski, M. P., Ulmer, M. P., Cruddace, R. G., & Wood, K. S. 1984, ApJS, 56, 403, https://doi.org/10.1086/190991
Krempéc-Krygier, J., Krygier, B., & Krywult, J. 2002, BaltA, 11, 296
Kriessler, J. R. & Beers, T. C. 1997, AJ, 113, 80, https://doi.org/10.1086/118235
Lacy, M., Baum, S. A., Chandler, C. J., et al. 2020, PASP, 132, 5001, https://doi.org/10.1088/1538-3873/ab63eb
Laganá, T. F., Durret, F., & Lopes, P. A. A. 2019, MNRAS, 484, 2807, https://doi.org/10.1093/mnras/stz148
Lakhchaura, K. & Singh, K. P. 2014, AJ, 147, 156, https://doi.org/10.1088/0004-6256/147/6/156
Lauer, T. R., Postman, M., Strauss, M. A., Graves, G. J., & Chisari, N. E. 2104, ApJ, 797, 82, https://doi.org/10.1088/0004-637X/797/2/82
Lavoie, S., Willis, J. P., Démoclès, J., et al. 2016, MNRAS, 462, 4141, https://doi.org/10.1093/mnras/stw1906
Ledlow, M. J., Voges, W., Owen, F. N., & Burns, J. O. 2003, AJ, 126, 2740, https://doi.org/10.1086/379670
Li, Y. -T. & Chen, L. -W. 2019, MNRAS, 482, 4084, https://doi.org/10.1093/mnras/sty2408
Limber, D. N. & Mathews, W. G. 1960, ApJ, 132, 286, https://doi.org/10.1086/146928
Lisker, T., Vijayaraghavan, R., Janz, J., et al. 2018, ApJ, 865, 40, https://doi.org/10.3847/1538-4357/aadae1
Liu, A., Yu, H., Diaferio, A., et al. 2018, ApJ, 863, 102, https://doi.org/10.3847/1538-4357/aad090
Lopes, P. A. A., de Carvalho, R. R., Capelato, H. V., et al. 2006, ApJ, 648, 209, https://doi.org/10.1086/505630
Lopes, P. A. A., Trevsian, M., Laganá, T. F., et al. 2018, MNRAS, 478, 5473, https://doi.org/10.1093/mnras/sty1374
López-Gutiérrez, M. M., Bravo-Alfaro, H., van Gorkom, J. H., et al. 2022, MNRAS, 517, 1218, https://doi.org/10.1093/mnras/stac2526
Lovisari, L., Reiprich, T. H., & Schellenberger, G. 2015, A&A, 573, 118, https://doi.org/10.1051/0004-6361/201423954
Martel, H., Robichaud, F., & Barai, P. 2014, ApJ, 786, 79, https://doi.org/10.1088/0004-637X/786/2/79
Mcnamara, B. R., Wise, M., Sarazin, C. L., Januzzi, B. T., & Elston, R. 1996, ApJ, 466, 9, https://doi.org/10.1086/310162
Merritt, D. 1985, ApJ, 289, 18, https://doi.org/10.1086/162860
Mewe, R., Lemen, J. R., & van den Oord, G. H. J. 1986, A&AS, 65, 511
Migkas, K., Schellenberger, G., Reiprich, T. H., et al. 2020, A&A, 636, 15, https://doi.org/10.1051/0004-6361/201936602
Mihos, J. C. 2004, Clusters of Galaxies: Probes of Cosmological Structure and Galaxy Evolution, Carnegie Observatories Centennial Symposia, ed. J. S. Mulchaey, A. Dressler, and A. Oemler (CUP), 277
Mohr, J. J., Fabricant, D. G., & Geller, M. J. 1993, ApJ, 413, 492, https://doi.org/10.1086/173019
Obayashi, H., Makishima, K., & Tamura, T. 1998, PASJ, 50, 537, https://doi.org/10.1093/pasj/50.5.537
Oegerle, W. R. & Hill, J. M. 2001, AJ, 122, 2858, https://doi.org/10.1086/323536
Ota, N., Kitayama, T., Masai, K., & Mitsuda, K. 2006, ApJ, 640, 673, https://doi.org/10.1086/500294
Parekh, V., van der Heyden, K., Ferrari, C., Angus, G., & Holwerda, B. 2015, A&A, 575, 127, https://doi.org/10.1051/0004-6361/201424123
Perason, D. W. & Batsuki, D. J. 2013, MNRAS, 436, 796, https://doi.org/10.1093/mnras/stt1614
Piffaretti, R. & Valdarnini, R. 2008, A&A, 491, 71, https://doi.org/10.1051/0004-6361:200809739
Piffaretti, R., Arnaud, M., Pratt, G. W., Pointecouteau, E., & Melin, J. -B. 2011, A&A, 534, 109, https://doi.org/10.1051/0004-6361/201015377
Pinkney, J., Roettiger, K., Burns, J. O., & Bird, C. M. 1996, ApJS, 104, 1, https://doi.org/:10.1086/192290
Pisani, A. 1996, MNRAS, 278, 697, https://doi.org/10.1093/mnras/278.3.697
Planck Collaboration, Ade, P. A. R., Aghanim, N., et al. 2011, A&A, 536, 11, https://doi.org/10.1051/0004-6361/201116458

Planck Collaboration, Ade, P. A. R., Aghanim, N., et al. 2014, A&A, 571, 29, https://doi.org/10.1051/0004-6361/201321523

Planck Collaboration, Ade, P. A. R., Aghanim, N., et al. 2016, A&A, 594, 27, https://doi.org/10.1051/0004-6361/201525823

Poggianti, B. M., von der Linden, A., De Lucia, G., et al. 2006, ApJ, 642, 188, https://doi.org/10.1086/500666

Porter, S. C., Raychaudhury, S., Pimbblet, K. A., & Drinkwater, M. J. 2008, MNRAS, 388, 1152, https://doi.org/10.1111/j.1365-2966.2008.13388.x

Poudel, A., Heinämäki, P., Tempel, E., et al. 2017, A&A, 597, 86, https://doi.org/10.1051/0004-6361/201629639

Predhel, P., Andritschke, R., Arefiev, V., et al. 2021, A&A, 647, 1, https://doi.org/10.1051/0004-6361/202039313

Ramella, M., Biviano, A., Pisani, A., et al. 2007, A&A, 470, 39, https://doi.org/10.1051/0004-6361:20077245

Regös. E. & Geller, M. J. 1989, AJ, 98, 755, https://doi.org/10.1086/115177

Reiprich, T. H., Veronica, A., Pacaud, F., et al. 2021, A&A, 647, 2, https://doi.org/10.1051/0004-6361/202039590

Rines, K., Mahdavi, A., Geller, M. J., et al. 2001, ApJ, 555, 558, https://doi.org/10.1086/321513

Rood, H. J. & Sastry, G. N. 1971, 83, 313, https://doi.org/10.1086/129128

Rumbaugh, N., Lemaux, B. C., Tomczak, A. R., et al. 2018, MNRAS, 478, 1403, https://doi.org/10.1093/mnras/sty1181

Santiago-Bautista, I., Caretta, C. A., Bravo-Alfaro, H., Pointecouteau, E., & Andernach, H. 2020, A&A, 637, 31, https://doi.org/10.1051/0004-6361/201936397

Sargent, W. L. W. & Turner, E. L. 1977, ApJ, 212, 3, https://doi.org/10.1086/182362

Sato, K., Kelley, R. L., Takei, Y., et al. 2010, PASJ, 62, 1423, https://doi.org/10.1093/pasj/62.6.1423

Schlafly, E. F. & Finkbeiner, D. P. 2011, ApJ, 737, 103, https://doi.org/10.1088/0004-637X/737/2/103

Schlegel, D. J., Finkbeiner, D. P., & Davis, M. 1998, ApJ, 500, 525, https://doi.org/10.1086/305772

Schneider, D. P., Gunn, J. E., & Hoessel, J. G. 1983, 264, 337, https://doi.org/10.1086/160602

Schuecker, P., Böhringer, H., Reiprich, T. H., & Feretti, L. 2001, A&A, 378, 408, https://doi.org/10.1051/0004-6361:20011215

Serna, A. & Gerbal, D. 1996, A&A, 309, 65, https://doi.org/10.48550/arXiv.astro-ph/9509080

Shanks, T., Metcalfe, N., Chehade, B., et al. 2014, MNRAS, 451, 4238, https://doi.org/10.1093/mnras/stv1130

Shectman, S. A., Landy, S. D., Oemler, A., et al. 1996, ApJ, 470, 172, https://doi.org/10.1086/177858

Skrutskie, M. F., Cutri, R. M., Stiening, R., et al. 2006, AJ, 131, 1163, https://doi.org/10.1086/498708

Smith, G. P., Khosroshahi, H. G., Dariush, A., et al. 2010, MNRAS, 409, 169, https://doi.org/10.1111/j.1365-2966.2010.17311.x

Song, H., Hwang, H. S., Park, C., & Tamira, T. 2017, ApJ, 842, 88, https://doi.org/10.3847/1538-4357/aa72dc

Stewart, G. C., Fabian, A. C., Jones, C., & Forman, W. 1984, ApJ, 285, 1, https://doi.org/10.1086/162470

Stott, J. P., Collins, C. A., Sahlén, M., et al. 2010, ApJ, 718, 23, https://doi.org/10.1088/0004-637X/718/1/23

Struble, M. F. & Rood, H. J. 1982, AJ, 87, 7, https://doi.org/10.1086/113081

Tempel, E., Einasto, J., Einasto, M., Saar, E., & Tage, E. 2009, A&A, 495, 37, https://doi.org/10.1051/0004-6361:200810274

Tiwari, J. & Singh, K. P. 2021, MNRAS, 500, 5524, https://doi.org/10.1093/mnras/staa3619

Tonry, J. L. 1985, AJ, 90, 2431, https://doi.org/10.1086/113948

Trejo-Alonso, J. J., Caretta, C. A., Laganá, T. F., et al. 2014, MNRAS, 441, 776, https://doi.org/10.1093/mnras/stu595

Tyler, K. D., Bai, L., & Rieke, G. H. 2014, ApJ, 794, 31, https://doi.org/10.1088/0004-637X/794/1/31

Van Weeren, R. J., de Gasperin, F., Akamatsu, H., et al. 2019, SSRv, 215, 16, https://doi.org/10.1007/s11214-019-0584-z

Varela, J., Betancourt-Rijo, J., Trujillo, I., & Ricciardelli, E. 2012, ApJ, 744, 82, https://doi.org/10.1088/0004-637X/744/2/82

Vikhlinin, A., McNamara, B. R., Forman, W., Jones, C., & Quintana, H. 1998, ApJ, 502, 558, https://doi.org/10.1086/305951

Vikhlinin, A., Burenin, R. A., Ebeling, H., et al. 2009, ApJ, 692, 1033, https://doi.org/10.1088/0004-637X/692/2/1033

Wen, Z. L. & Han, J. L. 2013, MNRAS, 436, 275, https://doi.org/10.1093/mnras/stt1581

__________. 2015, ApJ, 807, 178, https://doi.org/10.1088/0004-637X/807/2/178

West, M. J., Oemler, A. J., & Dekel, A. 1988, ApJ, 327, 1, https://doi.org/10.1086/166163

White, D. A. 2000, MNRAS, 312, 663, https://doi.org/10.1046/j.1365-8711.2000.03163.x

Wilms, J., Allen, A., & McCray, R. 2000, ApJ, 542, 914, https://doi.org/10.1086/317016

Yu, H., Serra, A. L., Diaferio, A., & Baldi, M. 2015, ApJ, 810, 37, https://doi.org/10.1088/0004-637X/810/1/37

Yuan, Q. -R., Yan, Y. -B., & Zhou, X. 2005, ChJAA, 5, 216, https://doi.org/10.1088/1009-9271/5/2/002

Zhang, Y. -Y., Andernach, H., Caretta, C. A., et al. 2011, A&A, 526, 105, https://doi.org/10.1051/0004-6361/201015830

Zhao, D., Aragón-Salamanca, A., & Conselice, C. J. 2015, MNRAS, 453, 4444, https://doi.org/10.1093/mnras/stv1940

H. Andernach, C. A. Caretta, M. Chow-Martínez, R. Coziol, J. M. Islas-Islas, M. M. Mireles-Vidales, M. A. Muñiz-Torres, J. J. Trejo-Alonso, Y. Venkatapathy, and J. M. Zúñiga: Departamento de Astronomía (DCNE-CGT), Universidad de Guanajuato, Callejón de Jalisco s/n, C.P. 36023, Guanajuato (Gto.), México (c.augusto@ugto.mx).

H. Andernach: Thüringer Landessternwarte, Sternwarte 5, D-07778, Tautenburg, Germany.

M. Chow-Martínez: Instituto de Geología y Geofísica, Universidad Nacional Autónoma de Nicaragua, Managua, Nicaragua.

J. De Anda-Suárez: Tecnológico Nacional de México, ITS Purísma del Rincón, Purísma del Rincón (Gto.), México.

C. Hernández-Aguayo: Max-Planck-Institut für Astrophysik, Karl-Schwarzschild-Str. 1, D-85748, Garching, Germany.

C. Hernández-Aguayo: Excellence Cluster ORIGINS, Boltzmannstrasse 2, D-85748, Garching, Germany.

J. M. Islas-Islas: Universidad Tecnológica de Tulancingo, Tulancingo (Hgo.), México.

H. Santoyo-Ruiz: Descubre Museo Interactivo de Ciencia y Tecnología, Aguascalientes (Ags.), México.

J. J. Trejo-Alonso: Facultad de Ingeniería, Universidad Autónoma de Querétaro, Querétaro (Qro.), México.

Y. Venkatapathy: Instituto de Radioastronomía y Astrofísica, Universidad Nacional Autónoma de México, Morelia (Mich.), México.

Revista Mexicana de Astronomía y Astrofísica, **59**, 379–388 (2023)

https://doi.org/10.22201/ia.01851101p.2023.59.02.14

CALIBRATION OF 122 SENSL MICROFJ-60035 SIPMS AND THE REDUCTION OF OPTICAL CROSS-TALK DUE TO COUPLED LIGHT GUIDES

F. Rehbein[1], T. Bretz[1], A. Biland[2], R. Alfaro[3], J. Audehm[1], G. Do[1], M. M. González[4], Y. F. Pérez Araujo[4], M. Schaufel[5], J. Serna-Franco[3], and I. Torres[6]

Received February 14 2023; accepted August 14 2023

ABSTRACT

Recent silicon photomultipliers (SiPMs) boast excellent production quality, eliminating the need for individual breakdown voltage calibration. We present measurements of cross-talk probability and relative gain for 122 SensL MicroFJ-60035-TSV SiPMs. These semiconductor photosensors have replaced photomultiplier tubes in many applications due to their single-photon resolution, insensitivity to magnetic fields, robustness, and cost-effective photon detection at lower voltages. Light guides expand SiPMs' small photosensitive area, and optical coupling reduces cross-talk probability compared to bare sensors at nominal bias voltage, as demonstrated in this study.

RESUMEN

Los fotomultiplicadores de silicio (SiPMs) de generaciones recientes tienen una alta calidad de producción, lo que elimina la necesidad de calibrar individualmente el voltaje de caída. En este estudio, se midió la probabilidad de interferencia y la ganancia relativa de 122 SiPMs SensL MicroFJ-60035-TSV. Estos dispositivos semiconductores reemplazan a los tubos fotomultiplicadores en diversas aplicaciones debido a su capacidad para detectar un solo fotoelectrón, su insensibilidad a campos magnéticos, su robustez, y su mejora en la eficiencia de detección de fotones con menor voltaje y costos. Para aumentar el área fotosensible de los SiPMs se utilizan guías de luz. Al comparar sensores acoplados ópticamente a guías de luz con sensores aislados a voltaje base, se observa que el acoplamiento óptico reduce significativamente la interferencia en los sensores estudiados.

Key Words: instrumentation: detectors — methods: observational — techniques: image processing — telescopes

1. INTRODUCTION

In many applications, the ability to detect very faint light flashes requires photo sensors with a high photo detection efficiency and a high level of robustness. Silicon Photomultipliers (SiPMs) provide durability, low operation voltage, and robustness against bright light exposure. For instance, in imaging air-Cherenkov astronomy, SiPMs were initially applied in the First G-APD Cherenkov Telescope (FACT) (Anderhub et al. 2013) as a replacement for classical photo multiplier tubes. The telescope has successfully operated now for almost ten years (Dorner et al. 2019). Its ability to operate even under bright background illumination, such as moonlight (Knoetig et al. 2013), provides an increased duty cycle (Dorner et

[1]Physics Institute 3A, RWTH Aachen University, Germany.
[2]ETH Zurich, Switzerland.
[3]Instituto de Física, UNAM, México.
[4]Instituto de Astronomía, UNAM, México.
[5]Physics Institute 3B, RWTH Aachen University, Germany.
[6]INAOE, México.

al. 2019) of almost 30%. The robustness and stability of the sensors allow for consistent unbiased monitoring of astronomical sources enabling unprecedented long-term studies (e. g. Beck et al. (2019)).

Significant improvement of the photo detection efficiency of SiPMs during the recent decades have facilitated the construction of compact telescopes with an aperture diameter of only 50 cm (Bretz et al. 2018). They are also the first imaging air-Cherenkov telescopes utilizing refractive optics based on a Fresnel lens in operation. Based on this design, similar telescopes were constructed to achieve hybrid measurements together with extensive air shower arrays. Hybrid measurements allow resolving the ambiguity on shower age, intrinsic to air shower arrays, and on shower distance, intrinsic to telescopes, enabling for inexpensive low-resolution optics. Measurements are ongoing with the IceAct telescope at the IceCube neutrino observatory at the South Pole, for example, for the improvement of veto capabilities (Rysewyk et al. 2020), and together with the High Altitude-Water Cherenkov Observatory (HAWC) (Springer & HAWC Collaboration 2016) in Mexico for calibration and increased sensitivity (Audehm et al. 2019). Compared with the original design, these telescopes implement further improvements, including solid light guides with an increased collection efficiency and SiPMs with further enhanced photo detection efficiency. This study discusses results obtained with two telescopes at the HAWC site: named the HAWC's Eye telescopes.

The following paragraphs only summarize the properties that are relevant for the context of this paper, and do not aim to present a complete description of the functioning and characteristics of SiPMs. A detailed review of Silicon Photomultipliers is given in Klanner (2019). They combine multiple Geiger-mode Avalanche Photo Diodes (G-APDs) into one sensor, which are also commonly known as Single-Photon Avalanche Diodes (SPAD). In the following, the individual diodes will be referred to as cells. The diodes are operated in Geiger-mode, i. e. the diode is biased with a voltage above its breakdown voltage. Above this threshold, impinging photons generate electron-hole pairs, which may induce a self-sustaining particle cascade. The initiated current causes a voltage drop at the built-in quenching resistor. When the applied voltage falls below the breakdown voltage, the avalanche is stopped. The released charge is independent of the number of initial electron-hole pairs, and depends only on physical properties of the diode and the difference between the applied bias voltage and the breakdown voltage. The charge released by one discharge is commonly referred to as photon equivalent (p.e.). The voltage difference is known as overvoltage. The released charge is also independent of the energy and angle of the incident photon. Random discharges triggered by thermal excitation are known as dark counts.

Secondary discharges induced by trapped charge carriers are called after-pulses. Their probability drops exponentially after the initial breakdown. As the time constant of this exponential decay is typically of the same order as the recharge time of the cell, and the released charge is intrinsically limited by the charge state of the cell, contributions from after-pulses are highly suppressed during the early recharge phase. For more details see Klanner (2019). In the present study, the analysis is based on charge integration over only a small time-window. Therefore, the effect of after-pulses can be neglected. Furthermore, the total after-pulse probability of recent sensors is less than a few percent[7].

The arrangement of hundreds to tens of thousands of cells in one sensor may introduce additional noise features into the measured signal, e. g. optical crosstalk. Optical crosstalk is induced by photons emitted during recombination, triggering secondary breakdowns in neighboring cells. This alters the amplitude of the measured signal. For high multiplicities, it contributes a statistical increase. Usually, a low crosstalk probability can only be achieved by a selection of a device type specifically built to achieve low crosstalk probability. Modern SiPMs comprise thin optical trenches that surround the active area of the cells to reduce direct crosstalk between neighboring cells (Pagano et al. 2012). The crosstalk probability refers to the fraction of signals with at least one secondary breakdown out of all signals. A detailed description of different photon paths relevant to the crosstalk process is given in Rech et al. (2008). This paper targets particularly those photons reflected at the protective window of the sensor. A measurement which spatially resolves crosstalk photons exiting the protective window of a SiPM is presented in Engelmann et al. (2018). A special case is the so-called delayed crosstalk caused by additional photons from Geiger discharges. These photons can then create an electron-hole pair in the non-depleted Si. The resulting charged particles can move into a neighboring pixel's amplification area and trigger a Geiger discharge there (Klanner 2019). Less probable than afterpulses in the same cell, the effect of delayed

[7] $< 5\%$ for SensL MicroFJ-60030-TSV at 5 V overvoltage (ON Semiconductor Data Sheet. 2018)

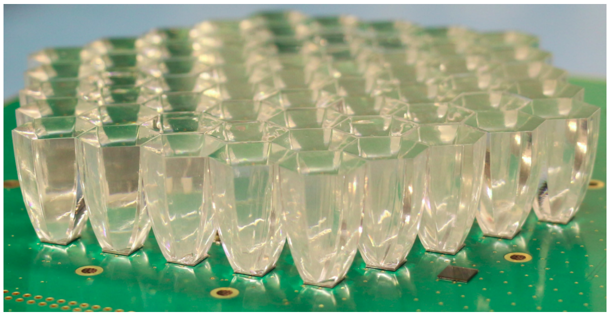

Fig. 1. Picture of the camera of the HAWC's Eye telescope. 61 SiPMs are optically coupled to solid light guides. One of the three textbfbare pixels can be seen on the bottom right of the picture. The color figure can be viewed online.

crosstalk photons on a small integration window can be neglected as well.

Delayed crosstalk that comes early enough to be included in the integration window just contributes to the relevant crosstalk of the signal. Delayed crosstalk that comes with a delay longer than the integration window does not contribute to the signal and can thus be ignored.

The following study demonstrates that a well-designed light guide which is optically coupled to the protective window decreases crosstalk probability. This is achieved by coupling a transparent material with a comparable refractive index to the protective window, suppressing total reflection. Due to the special shape of the coupled light guide, these photons can be directed out of its entrance aperture, thus avoiding triggers in neighboring cells.

2. EXPERIMENTAL SETUP

For the presented measurements, two telescopes of the HAWC's Eye type are utilized. They are located at the HAWC site in Mexico and can be operated remotely. The camera of each telescope features 64 sensors, out of which 61 sensors are optically coupled to solid light guides to increase their light collection area. The remaining three SiPMs ("textbfbare pixels") are used for calibration purposes. Figure 1 shows a picture of the camera of one of the telescopes prior to its assembly. Due to transport damage, one of the two cameras misses one sensor and three light guides. Moreover, one of its light guides remains loosely on the respective SiPM. The utilized data acquisition is identical to the system installed in the FACT telescope. A detailed description of the readout circuit can be found in Anderhub et al. (2013).

TABLE 1

SPECIFICATIONS OF THE SENSL MICROFJ-60035-TSV*

Parameter	Value
Active area	6.07×6.07 mm^2
Number of cells	22292
Fill factor	75%
Breakdown voltage V_{br}	24.45 ± 0.25 V
Temperature coefficient of V_{br}	21.5 mV/°C
Peak sensitivity wavelength λ_p	420 nm
PDE at λ_p	38% (50%)
Recharge time constant	50 ns
Gain	2.9×10^6 (6.3×10^6)
Dark count rate	50 (150) kHz/mm^2
Dark current (typical)	0.9 (7.5) μA
Crosstalk probability	8% (25%)
Afterpulsing probability	0.75% (5.0%)

*Sensors according to the data sheet provided by the manufacturer (ON Semiconductor Data Sheet. 2018). The performance parameters are given for an overvoltage of 2.5 V (6 V) at a temperature of 21°C.

2.1. *Sensors and Bias Power Supply*

The utilized sensors are of type SensL[8] MicroFJ-60035-TSV (ON Semiconductor Data Sheet. 2018) which, for this study, are operated at an overvoltage of 5 V. The relevant specifications of the sensor are summarized in Table 1. Each sensor has an active area of 6.07×6.07 mm^2 and consists of 22 292 cells. They are composed of a thin layer of silicon with a thickness of 0.09 mm and a protective window of 0.37 mm thickness. The protective window is made of a glass substrate with a refractive index of 1.53 at a reference wavelength of 436 nm. According to the specifications provided in ON Semiconductor Data Sheet. (2018), this sensors achieve a peak photo detection efficiency of 50% when operated at a wavelength of 420 nm and with the maximum overvoltage of 6 V above their nominal breakdown voltage of 24.5 V. The data sheet defines the minimum and maximum breakdown voltage as 24.2 V and 24.7 V at a temperature of 21 °C. This range corresponds to a maximum gain variation of $\pm 5\%$ at 5 V overvoltage. It is expected that the typical sensor-to-sensor variation of breakdown voltages is smaller. The bias voltage is supplied from a power supply based on the design discussed in Schaufel et al. (2017). It adjusts the applied voltage of each sensor individually to compensate for a change of breakdown voltage with temperature. The temperature sensors provide an absolute precision of 1 °C without additional calibration. In total, 64 temperature sensors are located on the backside of the printed circuit board opposite

[8] Now OnSemi.

the SiPMs. It is implied that the temperature sensors and the SiPMs are in thermal equilibrium, as the typical dark current of only a few μA corresponds to a negligible heating capacity and no significant temperature gradient has been measured between individual sensors. In total, this system is expected to provide a precision of the temperature measurement better than 2 °C, corresponding to a systematic relative deviation in overvoltage of less than 1% for the given temperature coefficient of 21.5 mV/°C at 5 V overvoltage. After calibration and without load, each channel of the bias power supply provides a voltage with a precision of typically 2 mV, but not higher than 10 mV. Compared to the overvoltage, the precision of the power supply can therefore be neglected. The uncertainty of the gain is therefore limited by the uncertainty of the breakdown voltage and yields a total systematic relative uncertainty of the gain of 5%. When accounting for the applied overvoltage and the sensor temperature of 28 °C (see § 3), the dark count rate is expected to be of the order of 200 kHz/mm^2. As shown in the following, dark count measurements allow for determining sensor properties, such as the crosstalk probability and the gain. This helps to characterize and calibrate the SiPMs.

2.2. *Light Guides*

Light guides are often used in SiPM applications to increase their small photosensitive area. They are particularly common in SiPM cameras to decrease dead space for a limited budget. In the camera of the FACT telescopes, solid light guides are successfully applied since 2011 (Anderhub et al. 2013; Huber et al. 2011). The required acceptance angle of the applied light guides is usually defined by the numerical aperture of the imaging optics and by the requirements on the attenuation of stray light. Their exit aperture is given by the SiPM surface area. These constraints and the acceptance angle of the SiPM inherently limit their maximum concentration factor since, according to Liouville's theorem, the phase-space distribution function is constant along the trajectories of the system. As the refractive index of the material changes the effective path length of the trajectories, the maximum concentration factor is proportional to the refractive index n squared, i. e.

$$\frac{A}{a} \propto n^2, \tag{1}$$

with the entrance aperture A and the exit aperture a. The acceptance angle of the sensor is always limited by the critical angle for total reflection at the silicon surface.

The light guides of the HAWC Eye camera are made of Plexiglas with a refractive index which is comparable to the one of the protective window of the sensors. The refractive index of the Plexiglas at 436 nm is 1.50 (Beadie et al. 2015) and for the sensor 1.53 (ON Semiconductor Data Sheet. 2018). The shape of the light guides was designed to support an opening angle of 33.7° corresponding to the view of an edge pixel at 60 mm distance from the camera center and a numerical aperture $f/D = 502$ mm / 550 mm $= 0.9$ of the optical system (Koschinsky et al. 2017). This leads to a compression factor of 5.5. With their refractive index of $n = 1.5$, they achieve a concentration factor about twice as large when compared to a corresponding hollow light guide; see also a more detailed discussion in Bretz & Ribordy (2013). The shape of the light guides is characterized by a hexagonal entrance window with a radius of 7.4 mm and a square output window. The length of the light guide is 23.5 mm. The hexagonal aperture has been chosen to minimize dead spaces in the camera, the square output window matches the sensor size. Four edges of the hexagon are connected to the four edges of the quadratic base. The two parallel sides form a Winston surface each, i. e. a tilted parabola with its focal point at the opposite side of the square surface (Winston, et al. 2005). The remaining two edges are connected to the center of the two remaining sides of the square and also follow the Winston principle. The four remaining side walls are constructed with straight lines connecting the edges at any height. All light-guides have been manufactured with a CNC milling machine and manually polished. Each light guide is optically coupled to its sensor with a very thin layer of optical glue of similar refractive index. All light guides have been glued manually allotting the glue with a dispensing pipette. The light guides have been placed carefully with the help of a fineplacer. None of the joints show impurities or other flaws. The following study shows comparable results of all those pixels coupled to a light guide and, therefore, no indication of relevant fluctuations of the coupling quality.

If the overall performance of solid and hollow light guides is evaluated for the case of an optimized concentration factor, reflection and absorption also have to be considered: Total reflection outperforms coated or polished surfaces. Internal absorption for Plexiglas is of the order of 1%/cm and can be neglected[9]. If light guides are covered by a protective window which is optically not coupled, an additional

[9]Note that absorption in data sheets usually includes the effect of Fresnel reflection at both surfaces.

Fresnel loss of about 4% has to be taken into account at each window-air interface. This is always the case in the application of hollow light guides.

Optimized light guides are designed such that the maximum acceptance angle of the silicon is fully utilized by incoming cosmic rays. That means that for each outgoing ray, at least one light path exists that leads the photon out of the guide. Consequently, optical coupling to a light guide leads to a reduced probability for these photons to be reflected back into the sensor. On the contrary, in case of the application of non-optimized guides, photons might be internally reflected back to the sensor and trigger random cells instead of direct neighbors. These cells have a higher probability to be fully charged, as direct neighbors might have been discharged by other crosstalk photons already. For the first crosstalk photon, this is not the case, as neighbors are generally charged. Therefore these reflected photons increase the probability for higher multiplicities, which means that non-optimized light guides can even increase the crosstalk probability.

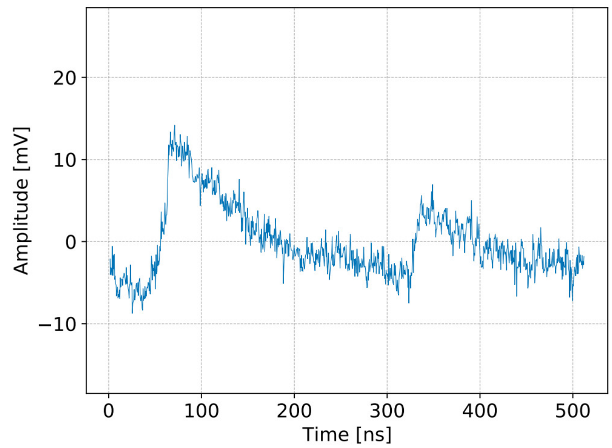

Fig. 2. Example of a signal trace. The sampling rate corresponds to 2 Gsample/s. The displayed example was selected to represent a typical signal trace. The expectation value for the number of dark counts, given the sensor temperature and the measured dark count rate, is 3.5 Hz. The color figure can be viewed online.

3. METHOD

To measure the crosstalk probability, the signal induced by dark counts can be utilized. The excellent single-p.e. resolution of SiPMs allows to distinguish between signals generated by a different number of discharges. To obtain such a dark count spectrum, the integrated charge of random pulses induced by thermal excitation is extracted from the signal traces and filled into a histogram.

Dark counts are recorded triggering random readout events without ambient light to minimize the background of impinging photons. For each telescope, 100 000 events were triggered at a frequency of 80 Hz. The spatial temperature average of the sensors of both focal planes was 28 °C with a typical spread of less than 1 °C. All individual sensors were stable during data taking within 0.2 °C. The channels were read out with the maximum sampling depth of 1024 samples per channel at a sampling rate of 2 Gsample/s. An example of a signal trace is shown in Figure 2.

A similar study on dark count spectra has been published by FACT (Biland et al. 2014), which uses the same data acquisition system and software as described in Anderhub et al. (2013). Therefore, the same algorithm to extract the pulses from the recorded data was adopted. The approach is described here only briefly for completeness.

In the first stage, a baseline is determined and subtracted for each channel individually. As some channels suffer from periodic electronic noise, a sliding average with an adopted length of 10 samples, which corresponds to 5 ns, is applied. The resulting trace is scanned for a threshold crossing of 5 mV between two consecutive samples. Then, a local maximum is searched between 5 and 35 samples after the threshold crossing. The arrival time is defined by the last sample within the 30 samples before the local maximum with an amplitude that does not fall below 50% of the maximum value. Integrating the raw signal for 15 ns (30 samples), starting at the arrival time, yields the integrated charge. In addition to the original algorithm, to account for time dependency of the background, the first turning point before the leading edge, i. e. the first sample with a larger amplitude than the preceding sample, is determined and subtracted as baseline from the raw signal before integration. An artificial dead time comparable to the total pulse length of 100 ns is introduced in the algorithm to skip the falling edge of detected pulses. Since the pulse extraction algorithm is designed to identify SiPM-like pulses, misidentification of electronics noise and the corresponding pedestal-peak in the spectrum are highly suppressed.

Due to the absence of a light guide, the signals from the three textbfbare pixels in each camera, which are utilized for generating an additional calibration output, experienced an 18% attenuation when compared to the remaining 61 pixels.

3.1. *Spectrum Function*

The properties of the sensors are extracted from their dark count spectrum. To properly describe the measured dark count spectrum, one has to account for the probability P_N to measure a multiplicity of N breakdowns induced by the initial breakdown of a single cell, as well as noise that smears out this distribution. In Biland et al. (2014) various distribution functions are compared. It is demonstrated that the best description of the dark count spectra is the modified Erlang distribution. At high multiplicities, it outperforms other distribution functions, in particular the widely used Borel distribution. The coefficients of the modified Erlang distribution are given by

$$\alpha_N = \frac{(Nq)^{N-1}}{[(N-1)!]^{\nu}} \text{ with } q \equiv p \cdot e^{-p}. \tag{2}$$

The fit parameter ν originates from the fact that the number of potential crosstalk triggers by each breakdown is limited by the geometry of the sensor and is usually $\nu \approx 1$. The parameter p describes the probability for a breakdown to trigger an additional breakdown in a neighboring cell and should not be confused with what is generally referred to as crosstalk probability. The crosstalk probability p_{xt} can be derived as

$$p_{xt} = \frac{\sum_{i=2}^{\infty} p_i}{\sum_{j=1}^{\infty} p_j}. \tag{3}$$

Two types of noise sources are considered in this analysis. The charge released in each avalanche undergoes cell-to-cell fluctuations and thus scales with the number of breakdowns. The electronics noise is independent of the multiplicity. Both types of noise are assumed to be Gaussian. Therefore, the measured dark count spectrum can be described by a sum of Gaussian distributions for multiplicity N with a width given by

$$\sigma_N = \sqrt{\sigma_{el}^2 + N\sigma_{pe}^2} \ , \tag{4}$$

where σ_{el} and $\sqrt{N}\sigma_{pe}$ are the Gaussian widths for the electronics noise and the amplitude-dependent charge fluctuations, respectively. Electronics noise in this context means noise of the whole electronics chain, including the thermal noise on capacitors (known as *kTC noise*) of the SiPM itself. The resulting distribution can be written as

$$f(x) = A_1 a_1 \cdot \sum_{i=1}^{\infty} \alpha_i \frac{e^{-\frac{1}{2}\left(\frac{x-x_i}{\sigma_i}\right)^2}}{a_i}. \tag{5}$$

The parameter A_1 denotes the amplitude of the single-p.e. peak. Introducing the gain g and a baseline shift x_0, the position of the mean of each Gaussian and their normalization are defined as

$$x_i = x_0 + i \cdot g \text{ and } a_i = \sigma_i \sqrt{2\pi}. \tag{6}$$

Integration of $f(x)$ over the whole range of extracted signals results in the total number of dark counts, and can be used to calculate the dark count rate if the extraction efficiency is known.

The SiPM's integrated signals are recorded and organized into a histogram. During the analysis, five of the total 122 SiPMs (61 in each camera) were excluded because they exhibited unexpected patterns attributed to periodic noise in their traces. Among these sensors, two pairs are positioned at the same locations within their respective cameras. The third sensor in one camera coincides with the missing sensor in the other camera. Since the affected sensors share identical positions in both cameras, the issue is likely associated with the electronics and cannot be resolved remotely.

The individual spectra fitted parameters are estimated with the maximum log-likelihood method for the distribution described in Equation 5. Since the fit result does not strongly depend on the exact value of the exponent ν (see Equation 2), and in a fit with that parameter free all fits yield results consistent with one, the exponent has been fixed to one in all fits. As expected, the obtained baseline offset x_0 is negligible compared to the gain, as the baseline has been subtracted during signal extraction.

An example of a fit to the spectrum of two single SiPMs is shown in Figure 3. It compares the dark count spectrum of a SiPM optically coupled to a light guide to a textbfbare pixel without a light guide. The fit is used to determine properties of each pixel individually, including the relative gain and the crosstalk probability. Figure 4 shows the dark count spectrum of two randomly chosen SiPMs with a light guide. It illustrates that typical sensor-to-sensor fluctuations are considerably smaller than the difference between sensors with optically coupled light guides and textbfbare sensors.

To compile all spectra into a single histogram, the baseline offset x_0 and the gain g are used to normalize the individual signals to their multiplicity N. The resulting histogram is displayed in Figure 5. To demonstrate proper normalization, in the displayed fit the baseline offset has been fixed to zero and the gain to one.

Indicating a measure of the fit quality is generally omitted, as the purpose of the fit is not to verify

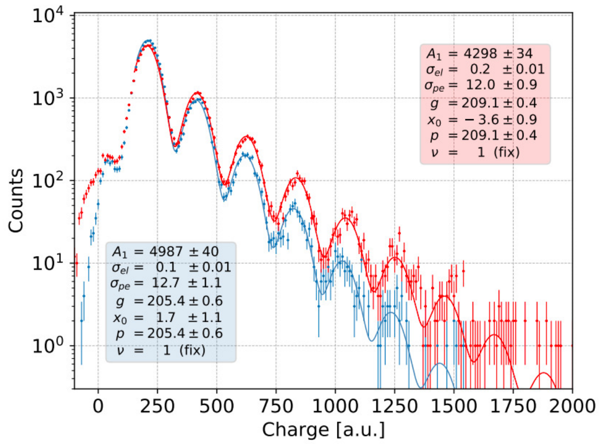

Fig. 3. Dark count spectrum extracted from a single SiPM optically coupled to a light guide (blue) and a textbfbare pixel without a light guide (red). The lines show the fit to the distribution as introduced in Equation 5 with the exponent ν fixed to the value extracted from the compiled spectrum shown in Figure 5. All fit parameters are displayed in the colored boxes. The color figure can be viewed online.

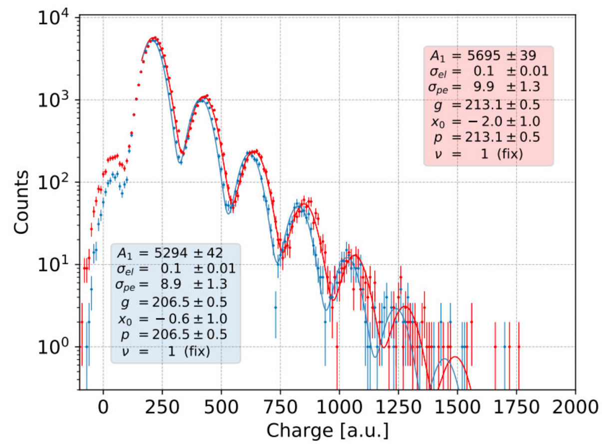

Fig. 4. Dark count spectra extracted from a two randomly chosen SiPMs coupled to a light guide. The lines show the fit to the distribution as introduced in Equation 5 with the fit parameters displayed in the colored boxes. The color figure can be viewed online.

the model but to extract reasonable parameters from the measured spectra, which is obviously achieved. All fits have been scanned manually and checked to represent the measured spectra reasonably well.

4. RESULTS

All results follow from measurements at a temperature of 28 °C and an overvoltage of 5 V.

Gain Distribution. In the obtained spectrum, the distance between two consecutive peaks represents a measurement for the charge released in a single breakdown, i.e. the gain (Biland et al. 2014). Figure 6 shows the distribution of the gain normalized to the average gain of all 122 pixels included in the analysis. The distribution has a spread of roughly 3%. All values are within a range from 92% to 107%. The breakdown voltage has not been calibrated for each sensor individually. Thus, the applied bias voltage is set according to the data sheet values for the breakdown voltage and an intended overvoltage of 5 V. The width of the distribution is well consistent with systematic deviations coming from the provided operation range of the manufacturer (±5%) and the precision of the temperature feedback system (±1%).

Dark Count Rate. In general, the total number of extracted pulses allows determining the dark count rate of the sensors. However, this requires a precise knowledge of the efficiency of the method.

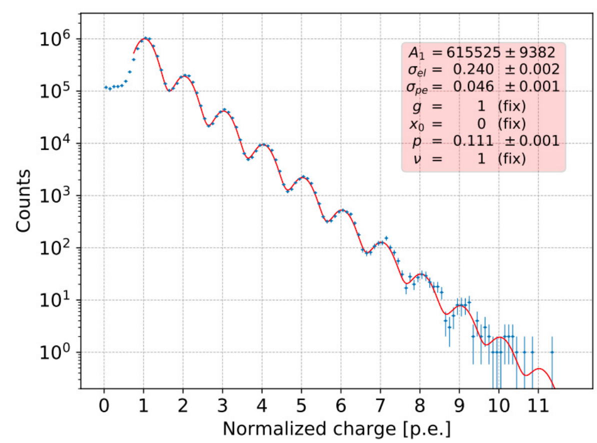

Fig. 5. Normalized dark count spectrum compiled from the majority of all SiPMs that are expected to have identical properties, i. e. which are optically coupled to a light guide and do not suffer a reduced gain. The red line shows the fit as introduced in Equation 3.4 with fixed values for the exponent ($\nu = 1$) and the gain ($g = 1$). The color figure can be viewed online.

For an overvoltage of 5 V and a temperature of 28 °C a dark count rate around 200 kHz/mm^2 is expected, derived from the data sheet values. This corresponds to a total rate of over 7 MHz for each sensor (considering its effective area shown in Table 1). In contrast to the study in Biland et al. (2014), the longer tails of the pulses produce significant pile-up, reducing the efficiency of the described pulse extraction algorithm considerably. Without a detailed simulation,

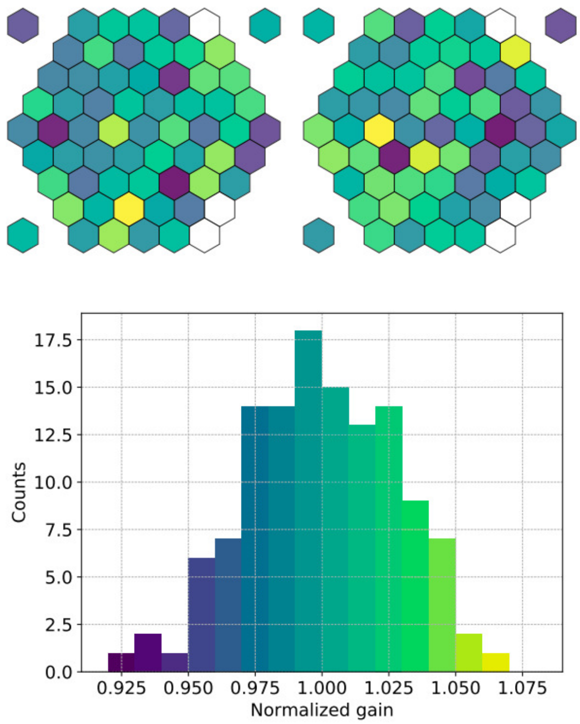

Fig. 6. Distribution of the resulting gain from a fit to the dark count spectrum of each of the 122 SiPMs normalized to the average gain. The gain of the six pixels with a lower electronics gain has been scaled accordingly. The arrangement in the two cameras shows a homogeneous distribution. The colors of the histogram bars match the colors of the camera display. The color scale ranges from purple (low) to yellow (high). Data were taken at a temperature of 28 °C and an overvoltage of 5 V. The color figure can be viewed online.

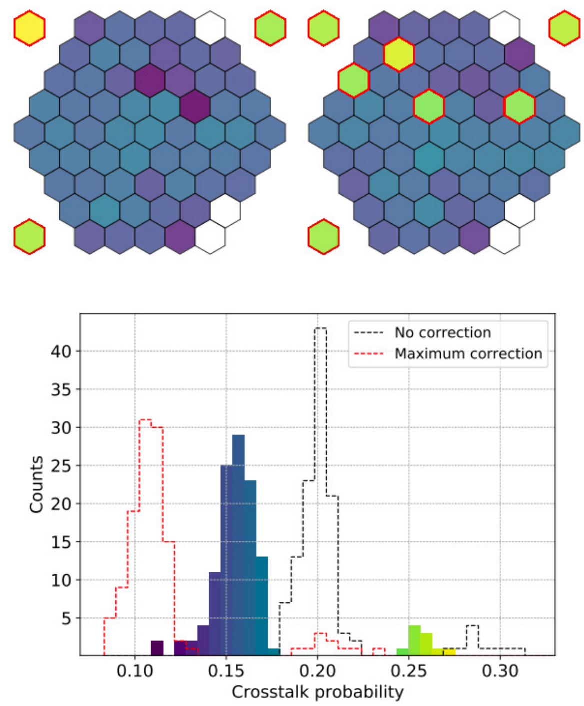

Fig. 7. Distribution of the resulting crosstalk probability from a fit to the dark count spectrum of 122 SiPMs accounting for coincident Poisson events. Two separated distributions are visible with a mean of 0.154 ± 0.011 and 0.257 ± 0.012, respectively. The locations of the corresponding pixels in the two cameras coincide exactly with the pixels with and without an optically coupled light guide. Pixels without coupling are marked in red. The colors of the histogram bars match the colors of the camera display. The color scale ranges from purple (low) to yellow (high). The dashed lines represent the same distribution without correction (black) and the maximum correction taking the dark count rate from the data sheet (red). Data were taken at a temperature of 28 °C and an overvoltage of 5 V. The color figure can be viewed online.

a precise estimate of the efficiency is not possible. Taking only the artificial dead time into account, the extracted pulse rate is around 100 kHz/mm^2. However, statistically about half of the pulses are expected on the falling edge (i. e. within 100 ns) of a preceding pulse and the pulse extraction is intentionally only sensitive to pulses starting close to the baseline. This extends the average dead time after a successfully detected pulse, i. e. the time of significantly reduced pulse extraction efficiency due to the tail of the pulse, by another 50% to typically at least 150 ns. Thus the measured number of pulses corresponds to at least 150 kHz/mm^2, which is reasonably close to the expectation. Additionally, the dark count rate of sensors of the same type can differ significantly for different wafers (Aharonian et al. 2021). Since all applied sensors come from the same wafer, one cannot rule out a below-average dark count rate due to a slightly better production quality.

Optical Crosstalk. The distribution of the crosstalk probability p_{xt}, as evaluated by fitting the modified Erlang distribution to the measured dark count spectra, is depicted in Figure 7. To account for coincident random breakdowns inside the integration window, the crosstalk probability is corrected as described in Futlik et al. (2011). Using the measured dark count rate for each pixel, the crosstalk probability is corrected using formula (2) of the above paper. For completeness, the figure also shows the distribution without this correction as well as the correction using the data sheet value of 200 kHz/mm^2. Two clearly distinct distributions are visible, corresponding to the SiPMs with and without an optically coupled light guide. As expected, the ten SiPMs without optically coupled light guides show a significantly larger crosstalk probability. The distribution of the coupled SiPMs has a mean of 0.154 ± 0.011, compared to the textbfbare sensors with a mean crosstalk probability of 0.257 ± 0.012, corresponding to a relative reduction of $(40 \pm 5)\%$. The absolute crosstalk probability, which is 0.20 for an overvoltage of 5 V, is larger than the value derived from the data sheet values. This value can be estimated by interpolating the data sheet values, 2.5 V and 6 V overvoltage, assuming a linear dependence within this voltage range. Although such a linear dependence has been shown for other sensors (Sun & Maricic 2016), this linear interpolation has to be seen as an approximation, and induces an uncertainty on the data sheet value of the crosstalk probability of the order of 0.01 to 0.02. Taking into account the uncertainties on the dark count rate, the data sheet value, and the width of the measured distribution, the measured crosstalk probability for the sensors without optical coupling is consistent with the expectation. Many standard methods utilize rate measurements with fixed thresholds (e.g. at 0.5 p.e. and 1.5 p.e.) to determine a crosstalk probability. In this approach, identical pulses originating from different multiplicities remain indistinguishable, while the integration of the individual Gaussians in the distribution function correctly assigns them proportionally. The systematic difference has been checked by integrating the whole distribution function starting at 0.5 p.e. and 1.5 p.e. respectively, yielding a value higher by +0.02.

5. SUMMARY AND CONCLUSIONS

In this study, the characteristics of 122 SiPM sensors of type SensL MicroFJ-60030-TSV have been evaluated. This has been done using the cameras of two HAWC's Eye telescopes, applying readout electronics originally produced for the FACT telescope. Out of these 122 sensors, 112 sensors are properly coupled to solid optical light guides. The bias power has been provided by a power supply achieving a precision of $\gg 1\%$ that was neglected in this study. The temperature-based overvoltage stabilization works with a precision corresponding to 1% of the sensors' overvoltage, including systematic effects from uncalibrated temperature sensors. For temperature-based voltage compensation, the temperature coefficient from the data sheet was applied. The maximum range of allowed breakdown voltages given by the manufacturer corresponds to $\pm 5\%$ for an overvoltage of 5 V. Therefore, the systematic contributions are dominated by the knowledge of the breakdown voltage.

The measurement of the relative gain of 122 sensors showed a maximum deviation from the mean value of $\pm 7.5\%$ with a variance of only 3%. This is well consistent with the data sheet of the manufacturer. While in a similar study of the FACT camera, the breakdown voltage for each sensor had still to be calibrated to achieve a variance of 2.4%, this study intentionally has omitted all calibrations related to the SiPMs themselves and applied a temperature-based voltage compensation circuit without additional absolute calibration of the temperature sensors.

In addition, the crosstalk probability of 112 sensors with, and nine without, optical coupling to light guides has been investigated. Since with optically coupled light guides crosstalk photons that are reflected on the protective window can leave the SiPM, the probability for optical crosstalk has decreased. A reduction by 40% from an average probability of 26% for the textbfbare sensors to an average probability of 15% has been confirmed for sensors with an optically coupled light guide. An additional single light guide shows an unclear status of optical coupling. As its crosstalk value falls exactly into the distribution of the nine pixels without light guide, it can be concluded that no proper coupling exists for this sensor as well.

The absolute values of the measured crosstalk probability and its reduction due to optical coupling to solid light guides cannot be transferred to other SiPM types, as the amount of crosstalk photons that are reflected at the entrance window highly depends on the physical properties of the sensor, but it provides a good indication of the order of the effect.

Reduction of crosstalk probability was also investigated in a laboratory setup for the solid light guides used in the FACT telescope while they were coupled to SiPMs of type Hamamatsu S14520-3050 VN. A relative decrease of the optical crosstalk probability by about 29% (Tajima 2020) was observed. This result confirms the significant reduction demonstrated in this paper. As a different sensor type and light guides of different geometrical properties were applied, the measured values cannot be compared directly.

The analysis of the performance of the photo sensors installed in the two HAWC's Eye telescopes confirms the high precision of recent SiPMs. It demonstrates that even for high precision requirements, the application of data sheet values is sufficient. Apart from a reasonable precise power supply, no additional calibration is necessary. This study also confirms that coupling the sensors to well-designed light guides reduces optical crosstalk between neighboring cells significantly.

We thank Johannes Schumacher for his excellent design of the bias power supply, and the electronics and mechanics workshop of the Physics Institute 3A and 3B of RWTH Aachen University for their support. We also acknowledge Kazuhiro Furuta, Akira Okumura, and Hiroyasu Tajima for their measurement cited in the conclusions. This work was partially funded by the Excellence Initiative of the German federal and state governments and the German Academic Exchange Service, the DGAPA PAPIIT (project number IG101320) and the CONACYT-DAAD (project 279446).

REFERENCES

Aharonian, F., An, Q., Axikegu, B. L., et al. 2021, EPJC, 81, 657, https://doi.org/10.1140/epjc/s10052-021-09414-z

Anderhub, H., Backes, M., Biland, A., et al. 2013, JInst, 8, 6008, https://doi.org/10.1088/1748-0221/8/06/P06008

Audehm, J., Serna, J., Alfaro, R., et al. 2019, ICRC 36, 636, https://doi.org/10.22323/1.358.0636

Beadie, G., Brindza, M., Flynn, R. A., Rosenberg, A., & Shirk, J. S. 2015, ApOpt, 54, 139, https://doi.org/10.1364/AO.54.00F139

Beck, M., Arbet-Engels, A., Baack, D., et al. 2019, ICR, 36, 630, https://doi.org/10.22323/1.358.0630

Biland, A., Bretz, T., Buß, J., et al. 2014, JInst, 9, 0012, https://doi.org/10.1088/1748-0221/9/10/P10012

Bretz, T., Hebbeker, T., Kemp, J., et al. 2018, JInst, 13, 7024, https://doi.org/10.1088/1748-0221/13/07/P07024

Bretz, T. & Ribordy, M. 2013, Aph, 45, 44, https://doi.org/10.1016/j.astropartphys.2013.03.004

Dorner, D., Arbet-Engels, A., Baack, D., et al. 2019, ICRC, 36, 665, https://doi.org/10.22323/1.358.0665

Engelmann, E., Popova, E., & Vinogradov, S. 2018, EPJC, 78, 971, https://doi.org/10.1140/epjc/s10052-018-6454-0

Futlik, L. L., Levin, E. V., Vinogradov, S. L., et al. 2011, BLPI, 38, 302, https://doi.org/10.3103/S1068335611100058

Huber, B., Braun, I., Anderhub, H., et al. 2011, ICRC, 9, 2, https://doi.org/10.7529/ICRC2011/V09/0136

Klanner, R. 2019, NIMPA, 926, 36, https://doi.org/10.1016/j.nima.2018.11.083

Knoetig, M. L., Biland, A., Bretz, T., et al. 2013, arXiv:1307.6116, https://doi.org/10.48550/arXiv.1307.6116

Koschinsky, J. P., Audehm, J., Auffenberg, J., et al. 2017, Verhandlungen der Deutschen Physikalischen Gesellschaft, (Muester2017issue), 1

ON Semiconductor, Data sheet J-Series SiPM Sensors, Datasheet Rev. 6, 2018, Accessed: 2020-02-10

Pagano, R., Corso, D., Lombardo, S., et al. 2012, IEEE Transactions on electron devices, 59, 2410, https://doi.org/10.1109/TED.2012.2205689

Rech, I., Ingargiola, A., Spinelli, R., et al. 2008, OExpr, 16, 8381, https://doi.org/10.1364/OE.16.008381

Rysewyk, D., Lennarz, D., DeYoung, T., et al. 2020, APh, 117, 102417, https://doi.org/10.1016/j.astropartphys.2019.102417

Schaufel, M., Bretz, T., Schumacher, J., et al. 2017, ICRC, 35, 786, https://doi.org/10.22323/1.301.0786

Springer, R. W. & HAWC Collaboration. 2016, NPPP 279, 87, https://doi.org/10.1016/j.nuclphysbps.2016.10.013

Sun, Y. & Maricic, J. 2016, JInst, 11, 1087, https://doi.org/10.1088/1748-0221/11/01/C01078

Tajima, H. Private Communication, 2020

Winston, R., Minano, J. C., & Benitez, P. G. 2005, Nonimaging Optics, Academic Press

F. Rehbein, T. Bretz, J. Audehm, & G. Do: Physics Institute 3A, RWTH Aachen University, Sommerfeldstraße 16, 52074 Aachen, Germany. (florian.rehbein@rwth-aachen.de)

A. Biland: ETH Zurich, Inst. for Particle Physics and Astrophysics, Otto-Stern-Weg 5, 8093 Zurich, Switzerland.

R. Alfaro & J. Serna-Franco: Instituto de Física, Universidad Nacional Autónoma de México, 04510 CDMX, México.

M. M. González & Y.F. Pérez Araujo: Instituto de Astronomía, Universidad Nacional Autónoma de México, 04510 CDMX, México.

M. Schaufel: Physics Institute 3B, RWTH Aachen University, Sommerfeldstraße 16, 52074 Aachen, Germany.

I. Torres: Instituto Nacional de Astrofísica, Óptica y Electrónica, 72840 San Andrés Cholula, Puebla, México.

Revista Mexicana de Astronomía y Astrofísica, **59**, 389–399 (2023)

https://doi.org/10.22201/ia.01851101p.2023.59.02.15

LATE ACCELERATED EXPANSION OF THE UNIVERSE IN DIFFUSIVE SCENARIOS

Eduard Fernando Piratova Moreno[1] and Luz Ángela García[2]

Received January 16 2023; accepted August 21 2023

ABSTRACT

We present a diffusion model in a cosmological framework to describe the accelerated expansion of the Universe at late times. We first introduce a scalar field in Einstein's field equations to account for the effect of diffusion as the driver of today's expansion. We also study a second option for the diffusion source: a perfect fluid with a barotropic equation of state. We establish the equations that relate the fluid evolution with the cosmic budget and find analytical solutions of the field equations with different diffusion coefficients: constant, redshift-dependent, and σ proportional to the Hubble parameter. Our main finding is that diffusive processes in the Universe are viable scenarios to effectively describe the expansion dynamics once the model's free parameters are gauged. The choice of the diffusion coefficient and the equation of state of the cosmic fluid determines the solutions of the density fractions and the transition to an accelerated expansion of the Universe at present.

RESUMEN

Presentamos un modelo de difusión en un marco cosmológico para describir la expansión acelerada del Universo en la época actual. Primero exploramos un campo escalar en las ecuaciones de campo para explicar el efecto de la difusión como el generador de la expansión actual. Además, estudiamos el efecto de un fluido perfecto con una ecuación de estado barotrópica, y encontramos las soluciones de las ecuaciones de campo para coeficientes de difusión: constante, dependiente del *redshift* y σ proporcional al parámetro de Hubble. Nuestro principal hallazgo es que procesos de difusión en el Universo son escenarios viables para describir la dinámica de la expansión una vez que los parámetros libres del modelo son calibrados. La elección del coeficiente de difusión con corrimiento al rojo y la ecuación de estado del fluido cósmico determinan la forma de las soluciones de las fracciones de densidad y la transición a una expansión acelerada del Universo en la actualidad.

Key Words: cosmology: theory — dark energy — diffusion

1. INTRODUCTION

Observations of the luminosity distances of supernovae Ia at the end of the last century allow us to establish that the Universe is experiencing an acceleration in its expansion (Riess et al. 1998; Perlmutter et al. 1999), meaning that galaxies are receding from each other faster and faster. Suppose that our theory of gravity is correct and gravitational interaction is always attractive. In that case, the only way to explain the expansion speeding up is by introducing a negative pressure that overcomes the effect of gravity at large scales.

When astronomers confirmed today's accelerated expansion of space-time, it was proposed that the standard cosmological model was missing an element: the so-called dark energy, a dilute component of the matter-energy budget, not yet detected by our instruments. But its very nature was unknown; thus, the first proposal was that dark energy was the manifestation of the quantum fluctuations of the vacuum, and it was linked to the cosmological constant Λ, an old idea that Einstein introduced in the twenties (Krauss & Turner 1995; Carroll 2001; Peebles & Ratra 2003).

With the introduction of the idea of dark energy, our current standard model ΛCDM accounts

[1]Fundación Universitaria Los Libertadores.
[2]Universidad ECCI.

for three main components: 5% of ordinary matter (matter formed by baryons; in other words, all the elements of the Periodic Table); ≈25% of cold dark matter (CDM): matter that does not interact with electromagnetic radiation, therefore, invisible to our telescopes (Planck Collaboration et al. 2020). If dark matter is cold, then the particles that formed it decoupled from the cosmic fluid at a very early stage of the Universe, and it only interacts with ordinary matter through gravity; ≈70% of dark energy, manifested in the cosmological constant Λ.

Nonetheless, there is no explanation for the connection between Λ and the fluctuations around the ground state of the vacuum (Padmanabhan 2003). Also, a discrepancy of no less than 120 orders of magnitude between the prediction of the energy density calculated with cosmological methods and the same quantity from high-energy physics is still unsettled. Thus, it seems appropriate to consider other forms of dark energy, apart from the cosmological constant, or to contemplate modified gravity models instead (Joyce et al. 2016; Nojiri et al. 2017; Lonappan et al. 2018; Böhmer & Jensko 2021). The latter approach is outside the scope of this work, but it is an extensive and prolific field.

To date, there are countless candidates for dark energy: quintessence scalar fields (Ratra & Peebles 1988; Caldwell et al. 1998; Carroll 1998), tachyons and phantom fields (Bagla et al. 2003; Cai et al. 2010), topological defects and branes (Chowdhury et al. 2023), etc. Further attempts to describe this dark component of the cosmic budget include extra degrees of freedom in the Hubble parameter through sterile neutrinos (García et al. 2011), evolving early dark energy models as presented in García et al. (2021) -with an effective parameterization of the equation of state- or Benaoum et al. (2023) -as a modified version of the Chaplygin gas-.

Our lack of knowledge of what is causing today's increased expansion is not the only open question in modern cosmology. The so-called Hubble tension is a critical issue in the era of precision astronomy (Riess et al. 2022; Kamionkowski & Riess 2022). The tension arises because of the discrepancy between the Hubble constant H_o estimated from the early Universe (with proxies such as the cosmic microwave background or the baryon acoustic oscillations) and local measurements based on the distance ladder (as luminosity distances of SN1a, variable Cepheid stars, among others). The difference between the early and late Universe estimates has reached 5σ. One candidate to resolve this tension that has gained momentum in the community is the inclusion of early forms of dark energy. For instance, García & Castañeda (2022) use different statistical methods to calculate the best value for today's expansion rate, H_o.

In this document, we propose an alternative to a generic dark energy model paradigm: what if the expansion rate increases in time due to diffusion that transfers energy from a cosmic solvent to galaxies? In physics, diffusion is an effective and macroscopic process that explains many phenomena, ranging from heat conduction, Brownian motion, fluid mixing, viscosity, etc. At the microscopic level, diffusion results from collisions among molecules due to thermal motions. The collisions scatter the molecules, and this movement occurs in the direction where concentration decreases. However, this behavior must be interpreted by its macroscopic effects, because local variations of the medium may generate flows reversing in short dynamical times (Callaghan 2010; Katopodes 2018).

The diffusion coefficient σ is of special interest in this investigation. The quantity σ is a scalar that depends on both the solvent and the solute properties. It provides insights into the speed at which the solute disperses within the solvent at each point at a given instant. The diffusion coefficient could often depend on the space-time coordinates, thus showing anisotropies or time evolution of the solvent-solute system. But σ could also depend on the solute, solvent, (or both) concentration.

Despite the great scope of this phenomenological description, there is still no consistent theory of diffusion in general relativity. Numerous efforts have been made in recent years in search of this formulation (Bonifacio 2012; Faccio et al. 2013). However, there are a few works in the literature regarding diffusion processes that could explain cosmic expansion at late times. Calogero (2011, 2012) explored introducing a scalar field ϕ in Einstein's field equations to describe the evolution of the diffusion coefficient, the scale factor, and the entropy of the system. The authors set constraints on the dynamics of the matter field where galaxies are immersed. In Calogero et al. (2013), they extended their study by performing a perturbative analysis to understand the structure formation in a Universe with diffusion as the driver of the cosmic accelerated expansion. Moreover, Velten et al. (2014) defined some invariants and used them as parameters to study the behavior of the Hubble parameter and the matter density fraction over time. Finally, Alho et al. (2015) presented a complete dynamical system, based on the equations of motion discussed in Calogero (2011, 2012) and provided attractor solutions for this dynamical system.

More recently, Perez et al. (2021) and Linares Cedeño et al. (2021) presented different cosmological diffusion models to alleviate the current Hubble tension through different models to recreate the instantaneous diffusion process and unimodular gravity, respectively.

This paper is presented as follows: Section 2 introduces the main assumptions, the metric, and the energy-momentum tensor we use to treat diffusion in the Universe. In § 3, we modify the canonical field equations to account for a scalar field ϕ as the diffusion source. We solve the differential equations in this system. Also, we derive the conditions for the solvent and solute density fractions in terms of the diffusion coefficient and the effective equation of state of the cosmic fluid. § 4 is devoted to studying a diffusive perfect fluid introduced in the energy-momentum tensor. Once again, we solve the differential equations to recover the evolution of the density fractions and consider three different functional forms for the diffusion coefficient σ. Finally, we summarize the main findings of this work in § 5. We compare our results with similar works in this research topic and present the caveats and limitations of our model. Unless stated differently, we assume the Planck Collaboration et al. (2020) cosmological parameters and set $c = 1$.

2. DIFFUSION IN THE FRIEDMANN-LEMAITRE-ROBERTSON-WALKER UNIVERSE

In this investigation, we explore the possibility that the ongoing accelerated expansion of the Universe is due to diffusion in space-time. Along this work, we consider galaxies as particles of a matter solute that are receding apart under the influence of a dilute solvent, uniformly distributed and delivering its energy to generate the speed-up of such expansion.

Our theoretical model obeys the cosmological principle, i.e., the Universe is homogeneous and isotropic at large scales, as observed by recent wide galaxy surveys and large-scale structure probes.

A Universe under the latter assumptions is described by the line element of the Friedmann-Lemaitre-Robertson-Walker (FLRW) with a flat spatial curvature ($K = 0$); the geometry favored by CMB results from Planck Collaboration et al. (2020):

$$\begin{aligned} ds^2 =& dx^\mu dx^\nu g_{\mu\nu} \\ =& -dt^2 + a^2(t)\left[dr^2 + r^2\left(d\theta^2 + \sin^2\theta d\phi^2\right)\right], \end{aligned} \tag{1}$$

with $a(t)$ the scale factor that only depends on the temporal component because of the space-time homogeneity. This metric is the solution of Einstein's field equations in the cosmological case:

$$G_{\mu\nu} = R_{\mu\nu} - \frac{1}{2} g_{\mu\nu} R = 8\pi G T_{\mu\nu}. \tag{2}$$

Following the original interpretation of (2), the geometry of the space-time is completely defined by the distribution of matter-energy in the momentum–energy tensor $T_{\mu\nu}$, on the right-hand side of the equation:

$$T_{\mu\nu} = (\rho + p) u_\mu u_\nu + p g_{\mu\nu}, \tag{3}$$

where the four-velocity u_μ defines the direction of the fluid's flow. The terms ρ and p are the energy density and pressure of each constituent in the cosmological plasma.

Unlike the standard cosmological model, where diffusion is nonexistent, we allow the inclusion of diffusion in our treatment to explain the accelerated cosmic expansion. Thus, the covariant derivative of the energy-momentum tensor is related to the diffusive coefficient σ and the number density of the fluid n, such that:

$$\nabla_\mu T^{\mu\nu} = \sigma n u^\nu. \tag{4}$$

The Bianchi identity $\nabla^\mu G_{\mu\nu} = 0$ implies that the covariant derivative of the energy-momentum tensor $\nabla^\mu T_{\mu\nu}$ must be exactly zero in the canonical cosmic scenario, which contradicts (4). Hence, an additional term needs to be plugged into the Einstein equations (2) to account for the presence of diffusion.

3. DIFFUSION DUE TO A SCALAR FIELD ϕ

The first attempt to induce diffusion in Einstein's field equations is by introducing a scalar field, a mathematical prescription extensively explored by Calogero (2012); Calogero et al. (2013); Velten et al. (2014); Alho et al. (2015). With a scalar field ϕ, the field equations change as follows:

$$G_{\mu\nu} + \phi g_{\mu\nu} = 8\pi G T_{\mu\nu}. \tag{5}$$

Equation (5), along with (4) , lead to a homogeneous wave equation $\nabla^\mu \nabla_\mu \phi = 0$ and:

$$\partial_t \phi = -\sigma n. \tag{6}$$

On the other hand, the conservation of the fluid number density condition $\nabla_\mu (n u^\nu) = 0$ implies that

$$n(t) \cdot a(t) = \text{constant} \qquad \therefore \qquad n(t) = \frac{n_o a_o^3}{a^3(t)}. \tag{7}$$

The FLRW metric (1) in combination with the modified field equations presented in (5), lead us to the following conditions:

$$3H^2 - \phi = 8\pi G\rho_m, \tag{8a}$$

$$-2\frac{\ddot{a}}{a} - H^2 + \phi = 8\pi G p_m. \tag{8b}$$

where $H = \frac{da}{dt}\frac{1}{a}$ is the Hubble parameter, ϕ is the scalar field, and ρ_m and p_m are the energy density and pressure of the matter field (galaxies of the Universe). Plugging the Hubble parameter H in eqs. (8) gives

$$H^2 = \frac{8\pi G}{3}\rho_m + \frac{\phi}{3}, \tag{9a}$$

$$\frac{\ddot{a}}{a} = -\frac{4\pi G}{3}(\rho_m + p_m) + \frac{\phi}{3}. \tag{9b}$$

We define the density fractions for matter and the scalar field, Ω_m and Ω_ϕ, such as:

$$\Omega_m = \frac{8\pi G}{3H_o^2}\rho_m \quad \text{and} \quad \Omega_\phi = \frac{\phi}{3H_o^2}. \tag{10}$$

Rearranging eqs. (9a) and (9b) in terms of the density fractions Ω and using the relations $1+z = \frac{a_o}{a} = \frac{1}{a}$ and conditions (6) and (7), we obtain a set of differential equations:

$$\dot{\Omega}_m - 3(1+\omega)\frac{\Omega_m}{1+z} = -\dot{\Omega}_\phi, \tag{11}$$

$$\dot{\Omega}_\phi = \left(\frac{8\pi G n_o}{3H_o^3}\right)\sigma\frac{(1+z)^2}{\sqrt{\Omega_m + \Omega_\phi}}. \tag{12}$$

Here, the symbol $\cdot$ denotes a derivative with respect to the redshift z, n_o is the number density of particles today, and ω, the equation of state of the background fluid.

3.1. *Solution in the ϕCDM Model with a Constant Diffusion Coefficient σ*

Under the assumption of a constant diffusion coefficient σ, the solution of the system of differential equations defined in (11) and (12) is given by:

$$\Omega_m(z) = \Omega_{m,o}(1+z)^2, \tag{13}$$

$$\Omega_\phi(z) = \Omega_{\phi,o}(1+z)^2 \tag{14}$$

where $\Omega_{m,o}$ and $\Omega_{\phi,o}$ are today's density fractions. This solution agrees with the derivation presented in Calogero et al. (2013). It exhibits a quadratic evolution with redshift of the energy fractions of the matter and the scalar field component, Ω_m and Ω_ϕ, respectively.

The parameter of the equation of state follows the constraint:

$$\omega = \frac{2}{3}\frac{\Omega_{m,o} + \Omega_{\phi,o}}{\Omega_{m,o}} - 1.$$

If we assume known values for $\Omega_{m,o}$ and $\Omega_{\phi,o}$, the diffusion coefficient σ in this scenario is given by:

$$\sigma = \frac{3\Omega_{\phi,o}H_o^3}{4\pi G n_o}.$$

3.2. *Solution in the ϕCDM Model with a Variable σ Term*

Let us consider a solution for the system of equations (11)-(12) that allows us to keep the quadratic form of the solutions found in the previous subsection and avoid any restriction on ω. In such a case, σ is a function of z, and the density fractions are given by:

$$\Omega_m(z) = \Omega_{m,o}(1+z)^{3\Omega_{m,o}(1+\omega)}, \tag{15}$$

$$\Omega_\phi(z) = \Omega_{\phi,o}(1+z)^{3\Omega_{m,o}(1+\omega)}. \tag{16}$$

The diffusion coefficient has the following behavior:

$$\sigma(z) = \left(\frac{9H_o^3 \cdot \Omega_{m,o} \cdot \Omega_{\phi,o}}{8\pi G n_o}\right)\frac{(1+\omega)}{(1+z)^{3-(9/2\cdot\Omega_{m,o}(1+\omega))}}, \tag{17}$$

$$= \sigma_o\frac{(1+\omega)}{(1+z)^{3-(9/2\cdot\Omega_{m,o}(1+\omega))}}. \tag{18}$$

Figure 1 showcases the deceleration parameter $q(z)$ and the density fractions $\Omega/E^2(z)$ of both matter and scalar field ϕ as a function of redshift. Following results from the latest surveys, the x-axis is displayed up to $z \approx 9$ since very few galaxies had been formed before that redshift. An additional assumption has been made here: that the cosmic fluid always has an equation of state that follows the condition $\omega > -1/3$ to satisfy the weak energy condition. We study cases such as the pure-radiation fluid in navy blue ($\omega = 1/3$), matter-only in pink ($\omega = 0$), or the adiabatic limit ($\omega = -1/3$) for which the weak energy condition holds.

The top panel of Figure 1 reveals interesting insights into the dynamics of the Universe under the presence of the scalar field: only values of ω larger than 1/2 have a transition from matter to the De-Sitter-dominated Universe (accelerated expansion of the Universe). Smaller values of the effective equation of state either have a very early turnover from

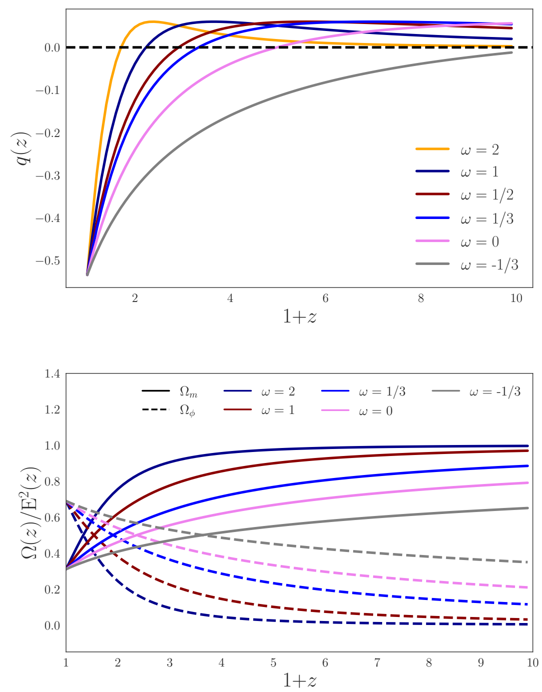

Fig. 1. Deceleration parameter and density fractions vs. redshift, (respectively, on the top and bottom panels), in the presence of a scalar field ϕ. The top panel shows the trend followed by the deceleration parameter $q(z)$ with different effective equations of state ω associated with the cosmic fluid. The horizontal dashed line represents $q(z) = 0$; below that, the Universe experiences an accelerated expansion. On the bottom panel, we display the density fractions for matter Ω_m (solid lines) and the scalar field Ω_ϕ (dashed lines) for different equations of state of the effective cosmic fluid. Today's energy fractions, $\Omega_{m,o}$ and $\Omega_{\phi,o}$, have been set to Planck Collaboration et al. (2020) cosmology. The color figure can be viewed online.

one domination era to the other, or the Universe is always subjected to a cosmic accelerated expansion under the influence of this field.

On the other hand, the bottom panel of Figure 1 displays the evolution of the normalized energy density fractions for matter (solid lines) and the scalar field (dashed lines) as a function of the cosmic fluid equation of state ω. All cases confirm that energy is being released from the field to matter through diffusion. Values of ω smaller than $-1/3$ (grey line) do not present diffusion from the scalar field to the cosmic fluid, so we leave them aside from this analysis.

Finally, it is worth noting that neither of these plots directly depends on the value of σ_o. Instead, the strong dependence lies on ω, which also determines the evolution of the diffusion coefficient σ, according to equation (17).

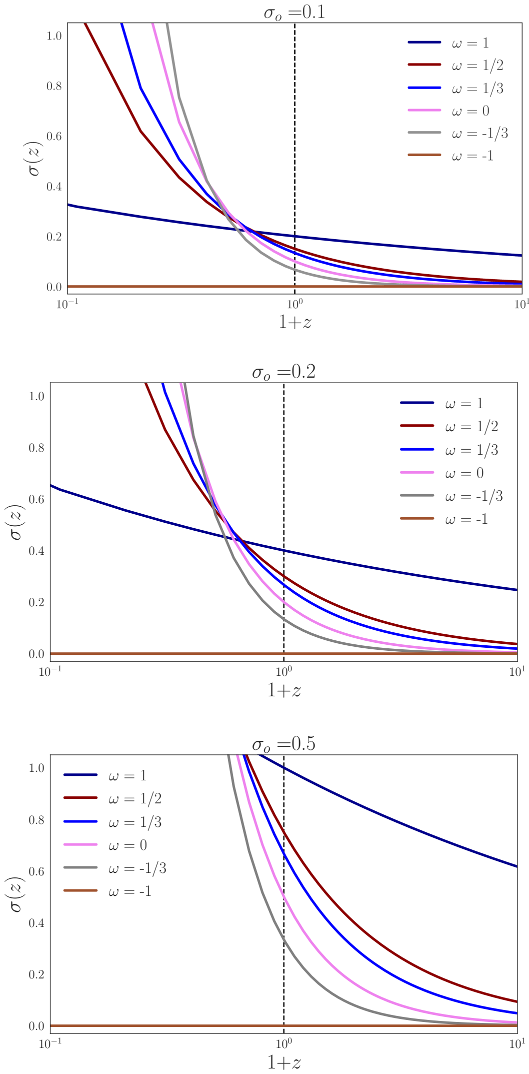

Fig. 2. Diffusion coefficient σ as a function of the redshift, when a scalar field ϕ is imposed in Einstein's field equations to be the source of the diffusion. We include a brown line representing the ΛCDM model in which diffusion does not occur at any point during cosmic history ($\sigma = 0$). The black dashed line indicates the present (i.e., $z = 0$). Cases with $\sigma_o = 0.1$, 0.2, and 0.5 are displayed in the upper, center, and lower panels, respectively. The color figure can be viewed online.

Figure 2 shows different trends for the diffusion coefficient $\sigma(z)$ with redshift, with an increasing value of $\sigma_o = \frac{9H_o^3 \cdot \Omega_{m,o} \cdot \Omega_{\phi,o}}{8\pi G n_o}$ from top to bottom.

As expected, Figure 2 shows that large values of σ_o lead to a prompter energy release from the scalar field through diffusion. We emphasize that the physical mechanism by which the energy is exchanged between the field and galaxy flow is outside this paper's scope. Nonetheless, the trends in Figure 2 indicate that diffusion in this model occurs continuously and not as a sudden (instantaneous) event.

To conclude this section, we perform a sanity check. Given an equation of state that is exactly -1, no diffusion occurs. The accelerated expansion is due to the dynamics of the field -and a possible link to Λ- rather than a diffusive process driven by ϕ itself.

4. DIFFUSIVE PROCESSES DRIVEN BY A PERFECT FLUID

In this section, we study a different type of solution of the Einstein equations that consider a term $\phi g_{\mu\nu}$ on the left-hand side of the equation (2). Instead, we introduce a perfect fluid with a barotropic equation of state $p_D = \omega_D \rho_D$ (we use the subscript D to identify this fluid, which is driving the diffusion).

In this case, the energy-momentum tensor is given by:

$$T'_{\mu\nu} = (\rho_m + \rho_D + p_m + p_D) u_\mu u_\nu + (p_m + p_D) g_{\mu\nu}. \quad (19)$$

With this choice of $T'_{\mu\nu}$, the solutions of the Einstein equations are:

$$3H^2 = 8\pi G(\rho_m + \rho_D), \quad (20a)$$

$$-2\frac{\ddot{a}}{a} - H^2 = 8\pi G(p_m + p_D). \quad (20b)$$

The latter equations lead to the relations:

$$H^2 = \frac{8\pi G}{3}(\rho_m + \rho_D),$$

$$\frac{\ddot{a}}{a} = -\frac{4\pi G}{3}(\rho_m + \rho_D + p_m + p_D).$$

In addition to the Friedmann equations above, we present a modified version of the continuity equation that comes from eq. (4):

$$\partial_t \rho_i + 3H(\rho_i + p_i) = \sigma n_m. \quad (22)$$

The right term of equation (22) is positive (negative) for matter (diffusive) fluid. As before, we define the density fraction of the diffusive fluid Ω_D as:

$$\Omega_D = \frac{8\pi G \rho_D}{3H_o^2}. \quad (23)$$

Re-writing the derivatives in terms of the redshift z in eq. (22) and setting the system of first-order differential equations from (23) and (22) with the density fractions Ω_m and Ω_D, we obtain:

$$(1+z)\dot{\Omega}_m - 3(1+\omega_m)\Omega_m = -\left(\frac{8\pi G n_o}{3H_o^3}\right)\sigma \frac{(1+z)^3}{\sqrt{\Omega_m + \Omega_D}}, \quad (24a)$$

$$(1+z)\dot{\Omega}_D - 3(1+\omega_D)\Omega_D = \left(\frac{8\pi G n_o}{3H_o^3}\right)\sigma \frac{(1+z)^3}{\sqrt{\Omega_m + \Omega_D}}. \quad (24b)$$

We stress that the system of differential equations in (24) satisfies the Bianchi identity and introduces an additional perfect fluid in the momentum-energy tensor in eq. (4). As discussed by Calogero (2011), one can add an extra term in the stress tensor $T_{\mu\nu}$ on the right-hand side of Einstein's field equations and re-interpret the inclusion of the scalar field in the geometry side (see § 3).

4.1. *Solution with a Constant Diffusion Coefficient* σ

The solution of the system of equations (24) with constant diffusion coefficient σ is given by:

$$\Omega_m(z) = \Omega_{m,o}(1+z)^2, \quad (25)$$

$$\Omega_D(z) = \Omega_{D,o}(1+z)^2. \quad (26)$$

The solutions above must satisfy the following conditions:

$$\omega_D = -\frac{\Omega_{m,o} + \Omega_{D,o}}{3\Omega_{D,o}}, \quad (27)$$

$$\sigma = \frac{3H_o^3 \Omega_{m,o}}{8\pi G n_o}. \quad (28)$$

Given these solutions, both σ and ω_D have fixed values in cosmic history.

4.2. *Solutions with a Variable Diffusion Coefficient* σ

Now, if we allow σ to have evolution with redshift, the solution of the set of differential equations (24) is given by:

$$\Omega_m(z) = \Omega_{m,o}(1+z)^{3+3\omega_D\Omega_{D,o}}, \quad (29a)$$

$$\Omega_D(z) = \Omega_{D,o}(1+z)^{3+3\omega_D\Omega_{D,o}}. \quad (29b)$$

On the other hand, the diffusion coefficient is described by the following relation:

$$\sigma(z) = \omega_D\left(-\frac{9H_o^3 \cdot \Omega_{m,o} \cdot \Omega_{D,o}}{8\pi G n_o}\right)(1+z)^{(3/2+9/2\omega_D\Omega_{D,o})}, \quad (30)$$

$$= \sigma_o(1+z)^{(3/2+9/2\omega_D\Omega_{D,o})}. \quad (31)$$

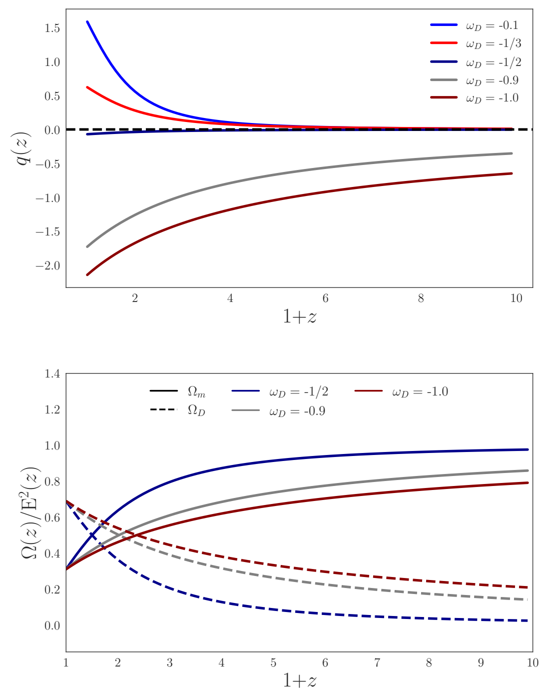

Fig. 3. Deceleration parameter and density fractions vs. redshift, respectively, on the top and bottom panels, in the presence of a perfect fluid with a barotropic equation of state $p = \omega_D \rho$. On the top, we show the deceleration parameter $q(z)$ with different values for equations of state ω_D, such that $\omega_D < 0$, therefore σ is strictly positive. The horizontal dashed line represents $q(z) = 0$; below that, the Universe experiences an accelerated expansion. On the bottom panel, we display the density fractions for matter Ω_m (solid lines) and the perfect fluid Ω_D (dashed lines) for different equations of state that lead to a negative deceleration parameter. As before, we assume Planck Collaboration et al. (2020) cosmological parameters for the density fractions at $z = 0$. The color figure can be viewed online.

with:

$$\sigma_o = -\omega_D \left(\frac{9H_o^3 \cdot \Omega_{m,o} \cdot \Omega_{D,o}}{8\pi G n_o} \right). \tag{32}$$

Equation (32) reveals that ω_D must be strictly negative such that $\sigma > 0$, and diffusion is a feasible process. Figure 3 shows the resulting evolution of the Universe with the solutions of the density fractions presented in eq. (29) and the condition found for ω_D.

One can notice from Figure 3 that not every negative value of ω_D would lead to an accelerated expansion of the Universe. Values of ω_D greater than $-1/2$ conduct to a positive deceleration parameter; hence, introducing a diffusive fluid does not cause the effect we are looking for. We rule out these solutions in the rest of the analysis.

However, we also highlight that solutions with $\omega_D < -1/2$ lead to an accelerated expansion in all the redshift range considered. The latter is a consequence of the solutions of eq. (29) not depending explicitly on the diffusion coefficient but on the equation of state of the diffusive fluid.

The bottom panel of Figure 3 shows the evolution of the density fraction only for the values of ω_D that lead to an accelerated expansion of the Universe, i.e., equations of state that are smaller than $-1/2$.

Figure 4 presents the behavior of the diffusion coefficient as a function of redshift for different values of σ_o.

It is worth noting that a particular value of ω_D leads to a $\sigma(z) = \sigma_o$, as seen in the blue lines in Figure 4. This specific value is determined by eq. (27), i.e., a diffusive perfect fluid with a constant coefficient.

4.3. *Solution for Diffusive Processes with* $\sigma = \tilde{\sigma}_o E(z)$

This subsection assumes that the diffusion coefficient is proportional to the function $E(z)$. We remind the reader that $H(z) = H_o E(z)$, and H_o is the Hubble constant that can be measured with different cosmological proxies.

When diffusion occurs in physical scenarios, it is customary to assume that the diffusion coefficient is proportional to the density of the solute. However, the cosmological case is much more complex; thus, it is perfectly natural to explore a case where σ depends on the density fraction of both the solute Ω_m and the solvent Ω_D. A function that relates both densities is $E(z)$. With this choice for $\sigma(z)$, the set of differential equations (24) are decoupled and its solution is given by:

$$\begin{aligned}
\Omega_m(z) =& \Omega_{m,o}(1+z)^3 - \frac{8\pi G n_o \tilde{\sigma}_o}{3H_o^3}(1+z)^3 \ln(1+z), \\
\Omega_D(z) =& \left(\Omega_{D,o} + \frac{8\pi G n_o \tilde{\sigma}_o}{9H_o^3 \omega_D} \right)(1+z)^{3(1+\omega_D)} - \\
& \frac{8\pi G n_o \tilde{\sigma}_o}{9H_o^3 \omega_D}(1+z)^3.
\end{aligned}$$

Rearranging the terms, it is easy to see that our solutions could be interpreted as a perturbative term on σ_o to the background solutions in a generic dark

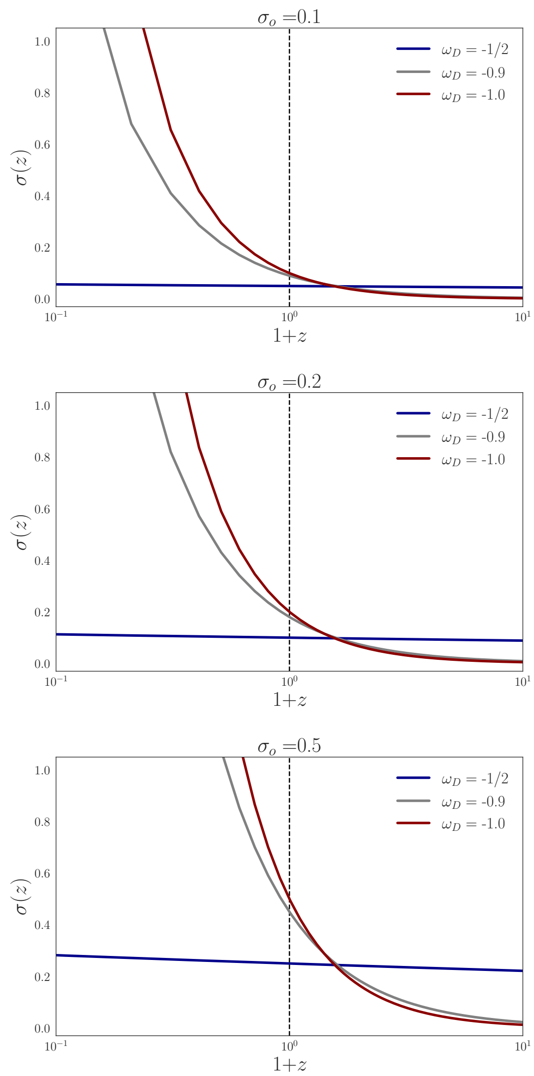

Fig. 4. Diffusion coefficient σ as a function of the redshift, in the presence of a diffusive perfect fluid. The black dashed line indicates the present (i.e., $z = 0$). Cases with $\sigma_o = 0.1$, 0.2, and 0.5 are shown from top to bottom. Regardless of the value of σ_o, $\omega_D \approx -1/2$ leads to a constant diffusion coefficient, exactly the prediction made in equation (27). The color figure can be viewed online.

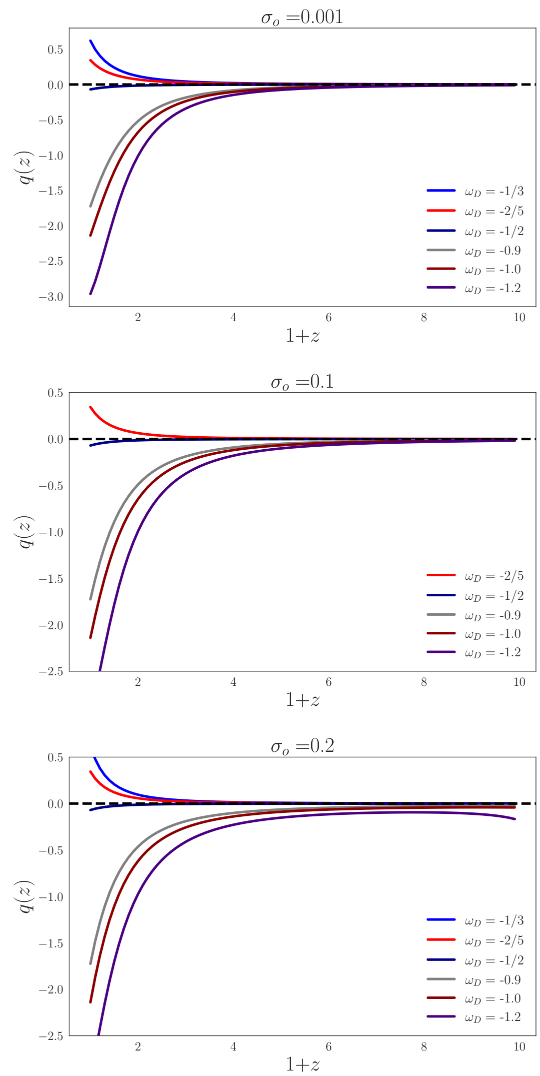

Fig. 5. Deceleration parameter as a function of redshift, when a diffusive fluid is imposed on the energy-momentum tensor. The horizontal dashed line represents $q(z) = 0$; below that, the Universe experiences an accelerated expansion. Although there are no mathematical restrictions on the values for ω_D, values greater than $-1/2$ lead to a positive deceleration parameter, independent of the value of σ_o. We assume Planck Collaboration et al. (2020) cosmological parameters for the density fractions at $z = 0$. The color figure can be viewed online.

energy model ωCDM.

$$\Omega_m(z) = \Omega_{m,o}(1+z)^3 - \sigma_o(1+z)^3 \ln(1+z), \quad (33)$$

$$\Omega_D(z) = \Omega_{D,o}(1+z)^{3(1+\omega_D)} + \frac{\sigma_o}{\omega_D}\left((1+z)^{3(1+\omega_D)} - (1+z)^3\right). \quad (34)$$

Notice that if $\sigma_o \to 0$, we recover the density fractions for non-interactive fluids: $\Omega_i \propto (1+z)^{3(1+\omega_i)}$. Another striking point of this set of solutions is that they do not impose any constraint on the parameters ω_D and σ_o.

Figure 5 shows the deceleration parameter as a function of redshift for different values of ω_D and σ_o (from top to bottom).

Due to the nature of these solutions and the explicit dependence of the density fractions (therefore, the deceleration parameter) on σ, there is an unexpected outcome that needs further investigation: values of $\sigma(z)$ larger than 0.25 exhibit a very sharp (discontinuous) transition from a negative to a positive deceleration parameter $q(z)$. This trend can be anticipated with the inflection of the indigo line at high redshift ($\omega_D = -1/2$) in the lower panel of Figure 5.

Finally, we show the density fractions of both matter and diffusive fluids as a function of redshift in Figure 6.

The perturbative nature of these solutions is exhibited in Figure 6. When σ_o is small (0.001; upper panel), the density fractions look alike to the cosmic scenario with non-interactive fluids. This is also true in the middle panel when σ_o increases by one order of magnitude over the previous σ, but it is still smaller than $\Omega_{m,o}$ by a factor of $\approx 1/30$. Nevertheless, if σ_o and $\Omega_{m,o}$ are of the same order of magnitude (lower panel), the energy transfer from the diffusive fluid to the matter component is much more complex, and the process does not follow the order of the domination eras as known: first the matter domination-epoch, and subsequently, when the diffusive fluid overcomes the matter density fraction, a stage of accelerated expansion of the Universe occurs.

5. DISCUSSION AND CONCLUSIONS

In this work, different scenarios for diffusion have been explored, one driven by a scalar field $\phi(t)$, but also with a perfect fluid with a barotropic equation of state, with ω_D. The former case has been extensively covered by Calogero (2011, 2012); Calogero et al. (2013); Velten et al. (2014); Alho et al. (2015), and their results were used as our primary comparison of the solutions presented in § 3.

As opposed to Calogero et al. (2013), we establish exact expressions for the density fractions of the cosmic fluid and the scalar field as a function of redshift, and the effective equation of state ω of the background fluid. We also present two proposals for the evolution of the diffusion coefficient that mostly depend on today's density fractions and the equation of state ω: constant or redshift-dependent. In the latter case, ω is a free parameter of our theoretical model. Still, effective values of $\omega \gtrsim 1$ reproduce a smooth transition from a positive to a negative deceleration parameter at $z \approx 1$ (the most likely scenario according to a large set of observations).

The second part of the document is devoted to a diffusive perfect fluid that is included in the energy-momentum tensor. This fluid is not only stress-free (perfect fluid condition), but also there is a

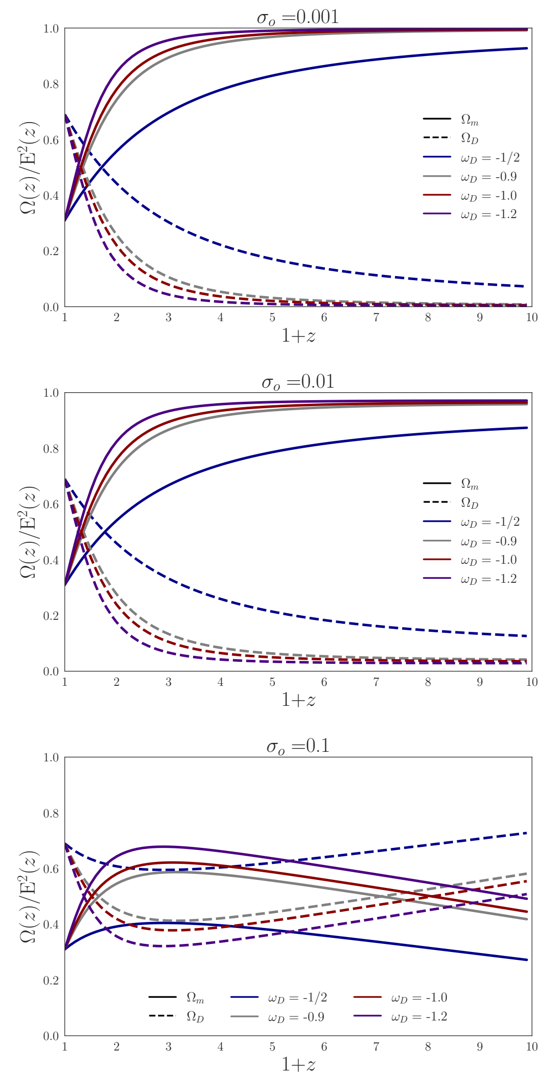

Fig. 6. Density fractions vs. redshift when a perfect fluid with a barotropic equation of state $p = \omega_D \rho$ is introduced as a diffusion source. The matter and diffusive fluid density fractions are presented in solid and dashed lines. Notably, the diffusion coefficient can be used as a perturbative parameter in this set of solutions. Therefore, we display the evolution of the density fractions with increasing values of σ in descending panels. We have assumed Planck Collaboration et al. (2020) cosmological parameters for today's density fractions. The color figure can be viewed online.

barotropic equation of state $p = \omega_D \rho$ that defines its evolution. This is a completely original treatment for diffusion that could explain the Universe's accelerated expansion at late times.

Three cases are considered for the diffusion coefficient: a constant value, redshift dependent, or proportional to the normalized Hubble parameter $E(z)$.

With this assumption for σ, we find the solutions for the density fractions Ω_m (matter) and Ω_D (diffusive fluid), as well as the restrictions for ω_D.

Our main findings are summarized as follows:

- Constant σ: the solutions of the differential equations are quadratic in redshift and exhibit trends similar to the scalar field density fraction. However, as expected, the expressions found for σ_o and ω_D differ from the results presented in § 3.

- $\sigma = \sigma(z)$: the evolution of the density fractions is less restricted compared to that with a constant diffusive term. In order to have a positive σ_o, the equation of state of the fluid ω_D is strictly negative. In addition, $\omega_D < -\frac{\Omega_{m,o}+\Omega_{D,o}}{3\Omega_{D,o}}$ to have a negative deceleration parameter (in other words, an accelerated expansion of the Universe at this time). With the inferred cosmological parameters from Planck Collaboration et al. (2020), the threshold for $\omega_D \approx -1/2$.

- $\sigma(z) \propto E(z)$: this proposal is physically motivated by the fact that the diffusion coefficient can be described as proportional to the solvent's density. Nonetheless, in the cosmological case, the energy fraction of matter is intrinsically linked to the other fluids' density fraction; thus, we can recover all of this dependence as a function of $E(z)$. Interestingly, this theoretical model offers a solution for the energy fractions that explicitly depends on the diffusion coefficient. Even more importantly, diffusion is a perturbation to the cosmological solutions to non-interactive fluids in a ωCDM cosmology.

This work offers a new perspective to explain the Universe's accelerated expansion at late times through diffusion, either caused by a scalar field ϕ or by a perfect barotropic fluid. But as any novel model it is not free of open questions and caveats that need to be addressed in future investigations.

One limitation of our model is that it does not consider the internal structure of galaxies, and all collapsed systems are assumed to have the same mass as in a classical statistical distribution. Also, we adopt a description of galaxies as particles in the solute and neglect any feedback with the intergalactic medium. All of the above could be correct at large cosmological scales but could not hold at the galaxy groups level.

In line with the previous caveat, we highlight that we only consider the Hubble flow, and peculiar velocities are not examined. If perturbations to the FLRW metric are calculated, transverse velocities should change the diffusion scheme presented here.

Our solutions are also restricted to the Planck Collaboration et al. (2020) cosmological parameters. However, there is no reason to assume the values of the energy fractions of the fields today have to match the ones in Planck cosmology. The next step for this work will be to calculate the free parameters of our model with the large set of cosmological proxies that are publicly available and provide an estimate for the Hubble constant H_o. Thus, we will be able to comment on the Hubble tension, and also set constraints on the diffusion coefficient σ.

The most pressing matter is that diffusive processes are still incompletely formulated in curved space-time. This theoretical diffusion scheme is a macroscopic effective description built on our limited knowledge of the energy transfer processes from the solvent to the solute. Needless to say, this is an extremely challenging problem at a microscopic level in general relativity.

On the other hand, if one could propose an experiment to quantify the value of σ, then it would be possible to rule out from the scenario the existence of the scalar field ϕ, or the perfect fluid with the equation of state ω_D. Even if we set upper limits for the value of σ, we could formulate experiments to estimate the effects of this solvent at a perturbative level.

Assuming that the solvent is a scalar field ϕ, introduced in the field equations in the same way as the cosmological constant Λ, does this mean that the field has finite energy to deliver to the matter field? If so, what will eventually occur when the diffusion mechanism suddenly stops?

This phenomenological model is based on the assumption that a diffusive solvent exists, but what is the nature and origin of such an agent? Is there another fundamental interaction experienced by the solvent (scalar field or perfect fluid) one can use to study its physical properties?

The authors thank Universidad ECCI and Fundación Universitaria Los Libertadores for granting them resources to develop this project.

REFERENCES

Alho, A., Calogero, S., Machado Ramos, M. P., & Soares, A. J. 2015, AnPhy, 354, 475, https://doi.org/10.1016/j.aop.2015.01.010

Bagla, J. S., Jassal, H. K., & Padamanabhan, T. 2003, PhRvd, 67, 063504, https://doi.org/10.1103/PhysRevD.67.063504

Benaoum, H. B., García, L. Á., & Castañeda, L. 2023, arXiv:2307.05917, https://doi.org/10.48550/arXiv.2307.05917

Böhmer, C. G. & Jensko, E. 2021, PRD, 104, 024010, https://doi.org/10.1103/PhysRevD.104.024010

Bonifacio, J. 2012, Brownian Motion in Curved Spacetimes, MAPH480 Project (New Zealand, University of Canterbury)

Cai, R.-G., Su, Q., & Zhang, H.-B. 2010, JCAP, 2010, 12, https://doi.org/10.1088/1475-7516/2010/04/012

Caldwell, R. R., Dave, R., & Steinhardt, P. J. 1998, Ap&SS, 261, 303, https://doi.org/10.1023/A:1002028230277

Callaghan, P. T. 2010, in Diffusion MRI: Theory, Methods, and Applications, ed. D. K. Jones, OUP, 45, https://doi.org/10.1093/med/9780195369779.003.0004

Calogero, S. 2011, JCAP, 2011, 016, https://doi.org/10.1088/1475-7516/2011/11/016

__________. 2012, JGP, 62, 2208, https://doi.org/10.1016/j.geomphys.2012.06.004

Calogero, S. & Velten, H. 2013, JCAP, 11, 025, https://doi.org/10.1088/1475-7516/2013/11/025

Carroll, S. M. 1998, PhRvL, 81, 3067, https://doi.org/10.1103/PhysRevLett.81.3067

__________. 2001, LRR, 4, 1, https://doi.org/10.12942/lrr-2001-1

Chowdhury, D., Tasinato, G., & Zavala, I. 2023, arXiv:2307.01188, https://doi.org/10.48550/arXiv.2307.01188

Faccio, D., Belgiorno, F., Cacciatori, S., et al. 2013, LNP, 870, https://doi.org/10.1007/978-3-319-00266-8

García, L. Á., Tejeiro, J. M., & Castañeda, L. 2011, Primordial nucleosynthesis in the presence of sterile neutrinos, Proceedings of the International School of Physics "Enrico Fermi", 178, 309, https://doi.org/10.3254/978-1-60750-974-5-309

García, L. Á., Castañeda, L., & Tejeiro, J. M. 2021, NewA, 84, 101503, https://doi.org/10.1016/j.newast.2020.101503

García, L. Á. & Castañeda, L. 2022, Ciencia en Desarrollo, 1, 2E, https://doi.org/10.19053/01217488.v1.n2E.2022.15216

Joyce, A., Lombriser, L., & Schmidt, F. 2016, ARNPS, 66, 95, https://doi.org/10.1146/annurev-nucl-102115-044553

Kamionkowski, M. & Riess, A. G. 2022, arXiv:2211.04492, https://doi.org/10.48550/arXiv.2211.04492

Katopodes, N. D. 2018, Free-Surface Flow: Environmental Fluid Mechanics, Butterworth-Heinamenn

Krauss, L. M. & Turner, M. S. 1995, GReGr, 27, 1137, https://doi.org/10.1007/BF02108229

Linares Cedeño, F. X. & Nucamendi, U. 2021, PDU, 32, 100807, https://doi.org/10.1016/j.dark.2021.100807

Lonappan, A. I., Kumar, S., Ruchika, Dinda, B. R. & Sen, A. A. 2018, PhRvD, 97, 043524, https://doi.org/10.1103/PhysRevD.97.043524

Nojiri, S., Odintsov, S. D., & Oikonomou, V. K. 2017, PhR, 692, 1, https://doi.org/10.1016/j.physrep.2017.06.001

Padmanabhan, T. 2003, PhR, 380, 235, https://doi.org/10.1016/S0370-1573(03)00120-0

Peebles, P. J. & Ratra, B. 2003, RvMP, 75, 559, https://doi.org/10.1103/RevModPhys.75.559

Perez, A., Sudarsky, D., & Wilson-Ewing, E. 2021, GReGr, 53, 7, https://doi.org/10.1007/s10714-020-02781-0

Perlmutter, S., Aldering, G., Goldhaber, G., et al. 1999, ApJ, 517, 565, https://doi.org/10.1086/307221

Planck Collaboration, Aghanim, N., Akrami, Y., et al. 2020, A&A, 641, 6, https://doi.org/10.1051/0004-6361/201833910

Ratra, B. & Peebles, P. J. E. 1988, PhRvD, 37, 3406, https://doi.org/10.1103/PhysRevD.37.3406

Riess, A. G., Filippenko, A. V., Challis, P., et al. 1998, AJ, 116, 1009, https://doi.org/10.1086/300499

Riess, A. G., Yuan, W., Macri, L. M., et al. 2022, ApJ, 934, 7, https://doi.org/10.3847/2041-8213/ac5c5b

Velten, H., & Calogero, S. 2014, arXiv:1407.4306, https://doi.org/10.48550/arXiv.1407.4306

Luz Ángela García: Cra. 19 No. 49-20, Bogotá, Colombia, Código Postal 111311. (lgarciap@ecci.edu.co).

Eduard Fernando Piratova Moreno: Cra. 16 No. 63A-68, Bogotá, Colombia, Código Postal 111221. (efpiratovam@libertadores.edu.co).

Revista Mexicana de Astronomía y Astrofísica, **59**, 401–402 (2023)

https://doi.org/10.22201/ia.01851101p.2023.59.02.16

ERRATUM: A VINDICATION OF THE RR LYRAE FOURIER LIGHT CURVE DECOMPOSITION FOR THE CALCULATION OF METALLICITY AND DISTANCE IN GLOBULAR CLUSTERS. (RMxAA, 2022, 58, 257)

A. Arellano Ferro

Instituto de Astronomía, Universidad Nacional Autónoma de México, Ciudad Universitaria, México.

Received May 11 2023; accepted May 15 2023

Table 1 was unfortunately mistaken for an older version that carried some inaccurate entries. Table 1, as included in this note, is the correct one, supersedes the one originally published, and should be preferred by interested readers.

TABLE 1

MEAN VALUES OF [Fe/H], GIVEN IN THREE DIFFERENT SCALES, AND M_V FROM A HOMOGENEOUS FOURIER DECOMPOSITION OF THE LIGHT CURVES OF RRL CLUSTER MEMBERS.[1]

GC	Oo	$[Fe/H]_{ZW}$	$[Fe/H]_{UV}$	$[Fe/H]_N$	M_V	N	$[Fe/H]_{ZW}$	$[Fe/H]_{UV}$	$[Fe/H]_N$	M_V	N	Ref.	$E(B-V)$	$\mathcal{L}$
NGC (M)				RRab					RRc					
1261	I	-1.48±0.05	-1.38	-1.27	0.59±0.04	6	-1.51±0.13	-1.38	-1.41	0.55±0.02	4	25	0.01	−0.71
1851	I	-1.44±0.10	-1.33	-1.18	0.54±0.03	10	-1.40±0.13	-1.28	-1.28	0.59±0.02	5	23	0.02	−0.36
3201	I	-1.49±0.10	-1.39	-1.29	0.60±0.04	19	-1.47±0.08	-1.37	-1.36	0.58±0.01	2	3	diff.	+0.08
4147	I	–	–	–	–	–	-1.72±0.26	-1.68	-1.66	0.57±0.05	6	4	0.01	+0.55
5272 (M3)	I	-1.56±0.16	-1.46	-1.46	0.59±0.05	59	-1.65±0.14	-1.57	-1.56	0.56±0.06	23	24	0.01	+0.08
5904 (M5)	I	-1.44±0.09	-1.33	-1.19	0.57±0.08	35	-1.49±0.11	-1.39	-1.38	0.58±0.03	22	19	0.03	+0.31
6171 (M107)	I	-1.33±0.12	-1.22	-0.98	0.62±0.04	6	-1.02±0.18	-0.90	-0.88	0.59±0.03	4	22	0.33	−0.73
6229	I	-1.42±0.07	-1.32	-1.13	0.61±0.06	12	-1.45±0.19	-1.32	-1.58	0.53±0.10	8	20	0.01	+0.24
6266[6] (M62)	I	-1.31±0.11	-1.64	–	0.63±0.03	12	-1.45±0.19	-1.32	-1.58	0.51±0.03	8	3	0.47	+0.55
6362	I	-1.25±0.06	-1.13	-0.83	0.62±0.01	2	-1.21±0.15	-1.09	-1.10	0.59±0.05	6	27	0.06	−0.58
6366	I	-0.84	-0.77	-0.31	0.71	1	–	–	–	–		11[2]	0.80	−0.97
6401	I	-1.36±0.09	-1.24	-1.04	0.60±0.07	19	-1.27±0.23	-1.09	-1.16	0.58±0.03	9	21	diff	+0.13
6712	I	-1.25±0.06	-1.13	-0.82	0.55±0.03	6	-1.10±0.04	-0.95	-0.96	0.57±0.18	3	30	0.35	−0.62
6934	I	-1.56±0.14	-1.48	-1.49	0.58±0.05	15	-1.53±0.12	-1.41	-1.50	0.59±0.03	5	26	0.10	+0.25
6981 (M72)	I	-1.48±0.11	-1.37	-1.28	0.63±0.02	12	-1.66±0.08	-1.60	-1.55	0.57±0.04	4	14	0.06	+0.14
7006	I	-1.51±0.13	-1.40	-1.36	0.61±0.03	31	-1.53	-1.44	-1.43	0.55	1	33	0.08	−0.28
Pal13	I	-1.64±0.15	-1.56	-1.67	0.65±0.05	4	–	–	–	–	–	28	0.10	−0.30
288	II	-1.64	-1.58	-1.42	0.38	1	-1.59	-1.52	-1.54	0.58	1	1	0.03	+0.98
1904 (M79)	II	-1.63±0.14	-1.55	-1.47	0.41±0.05	5	-1.71	-1.66	-1.69	0.58	1	2	diff	+0.74
4590 (M68)	II	-2.07±0.09[3]	-2.21	-2.01	0.49±0.07	5	-2.09±0.03	-2.24	-2.23	0.53±0.01	15	5	0.05	+0.17
5024 (M53)	II	-1.94±0.06[3]	–2.00	-1.68	0.45±0.05	18	-1.84±0.13	-1.85	-1.85	0.52±0.06	3	6	0.02	+0.81
5053	II	-2.05±0.14[3]	-2.18	-2.07	0.46±0.08	3	-2.00±0.18	-2.05	-2.06	0.55±0.05	4	7	0.18	+0.50
5286[6]	II	-1.68±0.15	-1.64	–	0.52±0.04	59	-1.71±0.23	-1.68	–	0.57±0.04	23	3	0.24	+0.80
5466	II	-2.04±0.14[3]	-2.16	-2.01	0.44±0.09	8	-1.90±0.21	-1.89	-1.96	0.53±0.06	5	8	0.00	+0.58
6205 (M13)	II	-1.60	-1.54	-1.00	0.38	1	-1.70±0.20	-1.63	-1.71	0.59±0.05	3	29	0.02	+0.97
6254 (M10)	II?	–	–	–	–	–	-1.59	-1.52	-1.52	0.52	1	32	0.25	+1.00
6333 (M9)	II	-1.91±0.13[3]	-1.96	-1.72	0.47±0.04	7	-1.71±0.23	-1.66	-1.66	0.55±0.04	6	9	diff	+0.87
6341 (M92)	II	-2.12±0.18[3]	-2.16[5]	-2.26	0.45±0.03	9	-2.01±0.11	-2.11	-2.17	0.53±0.06	3	10	0.02	+0.91
6809[6]	II	-1.61±0.20	-1.55	–	0.53±0.09	59	–	–	–	–	–	3	0.08	+0.87
7078 (M15)	II	-2.22±0.19[3]	-2.46	-2.65	0.51±0.04	9	-2.10±0.07	-2.24	-2.27	0.52±0.03	8	15	0.08	+0.67
7089 (M2)	II	-1.60±0.18	-1.51	-1.25	0.53±0.13	10	-1.76±0.16	-1.73	-1.76	0.51±0.08	2	16	0.06	+0.38[4]
7099 (M30)	II	-2.07±0.05[3]	-2.21	-1.88	0.40±0.04	3	-2.03	-2.14	-2.07	0.54	1	17	0.03	+0.89
7492	II	-1.68	-1.63	-0.83	0.37	1	–	–	–	–	–	18[5]	0.00	+0.76

TABLE 1. CONTINUED

GC	Oo	$[Fe/H]_{ZW}$	$[Fe/H]_{UV}$	$[Fe/H]_N$	M_V	N	$[Fe/H]_{ZW}$	$[Fe/H]_{UV}$	$[Fe/H]_N$	M_V	N	Ref.	$E(B-V)$	$\mathcal{L}$
NGC (M)				RRab					RRc					
6402 (M14)	Int	-1.44±0.17	-1.32	-1.17	0.53±0.07	24	-1.23±0.21	-1.12	-1.12	0.58±0.05	36	32	0.57	+0.65
6779 (M56)	Int	-1.97[3]	-2.05	-1.74	0.53	1	-1.96	-2.03	-2.05	0.51	1	34	0.26	+0.98
6388	III	-1.35±0.05	-1.23	-1.00	0.53±0.04	2	-0.67±0.24	-0.64	-0.56	0.61±0.07	6	12	0.40	–1.00
6441	III	-1.35±0.17	-1.23	-0.80	0.43±0.08	7	-1.02±0.34	-0.82	-1.00	0.55±0.08	8	13	0.51	–0.73

Notes: [1] Quoted uncertainties are 1-σ errors calculated from the scatter in the data for each cluster. The number of stars considered in the calculations is given by N. [2]. The only RRL V1 is probably not a cluster member. [3] This value has a -0.21 dex added, see § 1 for a discussion. [4]. Our calculation. [5] Based on one light curve not fully covered. [6] Metallicity and M_V taken from the compilation of Contreras et al. (2010). References are the source of the Fourier coefficients: 1. Arellano Ferro et al. (2013b); 2. Kains et al. (2012); 3. Arellano Ferro et al. (2014); 4. Arellano Ferro et al. (2018b); 5. Kains et al. (2015), 6. Arellano Ferro et al. (2011); 7. Arellano Ferro et al. (2010); 8. Arellano Ferro et al. (2008b); 9. Arellano Ferro et al. (2013a); 10. Yepez et al. (2020); 11. Arellano Ferro et al. (2008a); 12. Pritzl et al. (2002) ; 13. Pritzl et al. (2001); 14. Bramich et al. (2011); 15. Arellano Ferro et al. (2006); 16. Lázaro et al. (2006); 17. Kains et al. (2013) ; 18. Figuera Jaimes et al. (2013); 19. Arellano Ferro et al. (2016); 20. Arellano Ferro et al. (2015b); 21. Tsapras et al. (2017); 22. Deras et al. (2018); 23. Walker (1998); 24. Cacciari et al. (2005); 25. Arellano Ferro et al. (2019); 26. Yepez et al. (2018); 27. Arellano Ferro et al. (2018a); 28. Yepez et al. (2019); 29. Deras et al. (2019); 30. Deras et al. (2020); 31. Arellano Ferro et al. (2020); 32. Yepez et al. (2022); 33. Rojas Galindo et al. (2021); 34. Deras et al. (2022).

Revista Mexicana de Astronomía y Astrofísica, **59**, 403–404 (2023)

OBITUARY

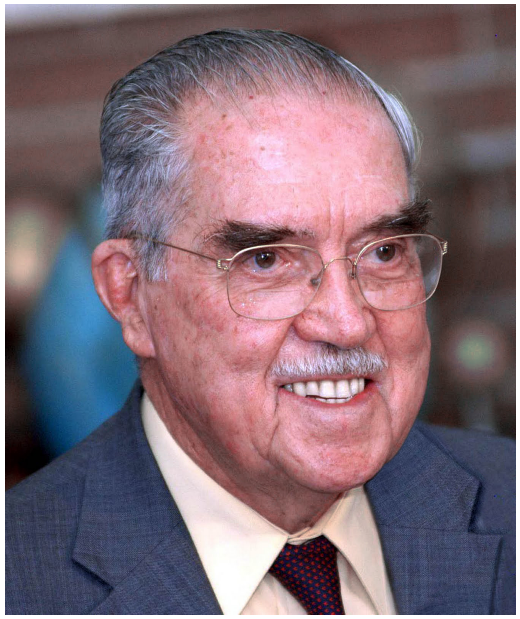

José Antonio Ruiz de la Herrán Villagómez
1925–2022

On September 5, 2022, Engineer José de la Herrán passed away at the age of 96. He was a multifaceted character who stood out as an engineer, popularizer, collector, athlete, politician and musician. We astronomers met de la Herrán in his capacity as designer and coordinator of the construction of the telescope with a 2.1-meter-diameter mirror that was installed at the UNAM National Astronomical Observatory in San Pedro Mártir, Baja California. In 1980 we went with de la Herrán and a group of technicians and astronomers, including myself, to start using that telescope. When we arrived at the telescope, de la Herrán, as if nothing was happening, climbed over its structure, reaching the upper part. I was very surprised at his ability, but later I learned that among his many hobbies, de la Herrán liked to climb trees and had a surprising nimbleness for a man over fifty years of age. In the following decades, the 2.1-meter telescope became the workhorse of Mexican astronomy.

That same year he told me that he believed his work on the 2.1-meter telescope was finished, and that he would like to focus on outreach. At his request, he was transferred from the Institute of Astronomy to the University Center for Science Communication, both departments of UNAM. At the Center he would play an important role in the design and construction of many of the exhibits in the "Universum" Science Museum. Since 2007, the planetarium of this museum bears his name.

His work as a popularizer was remarkable. He was an advisor to the "El Túnel de la Ciencia" project that we can still visit in the La Raza Metro station in Mexico City. He gave hundreds of lectures. In 1979, together with Christine Allen and Arcadio Poveda, he founded the "Discovering the Universe" section in the Science and Development magazine, published by CONACyT. Additionally, he published several books that reached a wide audience. His latest book, "I am a technologist", is autobiographical and based on interviews by Juan Tonda, who also provided an informative prologue.

The life of Engineer José de la Herrán was full of interesting events and incidents, propitiated by his adventurous spirit. His father was also an engineer and worked for radio station XEW, The Voice of Latin America from Mexico. He frequently accompanied his father to the XEW facilities and, while he was doing his work, José sniffed around the studios and facilities. One day he saw Agustín Lara playing a piece on the piano in his very special way. Whenever he could, a fascinated José would spy on Lara and gradually learned to play the piano in his style.

But at the same time he maintained his interest in the technical aspects of communications. He was linked to the construction of XEQ-FM (the first FM radio station in Mexico) and the studios of XEW Television Channel 2. He was also linked to the planning of the cable television system in Mexico City.

On many occasions, his curiosity allowed him to be in the right place at the right time. In 1969, he learned that the Apollo 11 mission was going to attempt to land humans on the Moon. Somehow he managed to make it to Cape Kennedy a few hours before the launch, and the event organizers placed him in a temporary grandstand built for journalists from around the world. From that vantage point he watched the pillar of fire and heard the roar of the mighty Saturn V rocket that would successfully carry Armstrong and Aldrin to the lunar surface.

Many of the things I mention here are illustrated with film material in an interesting UNAM documentary that you can find on YouTube under the title "José de la Herrán, Technologist.

He was a member of the Consultative Council of Sciences of the Presidency of the Republic, and of the Astronomical Society of Mexico, among many institutions. Likewise, he received many awards, including the National Award for Sciences and Arts in the area of Technology and Design in 1983, and the National University Award in the area of Artistic Creation and Extension of Culture in 2005.

He enjoyed life very much. I remember once traveling to a small town in Michoacán where there was a highly recommended restaurant. Upon entering the restaurant I found José sitting at a table with his sister Esther, already enjoying the culinary specialties of the place.

José had transformed his house into a mixture of workshop, museum, laboratory and library. In his travels throughout Mexico he had collected devices such as telescopes, clocks, radios, motors and film cameras that he repaired and used in his demonstrations. He donated several of these artifacts to the "Universum" Science Museum.

He also thought that we scientists and technologists really liked to criticize politicians, but that we would not accept a political position. So, from 1991 to 1994, he became a candidate and was elected as a Representative for the I Federal Electoral District of Mexico City. From that position he promoted science, technology and outreach.

We learned with sadness of his passing. A few months before, Dr. Arcadio Poveda, promoter and collaborator of de la Herrán in the San Pedro Mártir 2.1-meter telescope project, had passed away.

Mexico needs many Josés de la Herrán and Arcadios Poveda.

Luis Felipe Rodríguez

Revista Mexicana de Astronomía y Astrofísica, **59**, 405–406 (2023)

OBITUARY

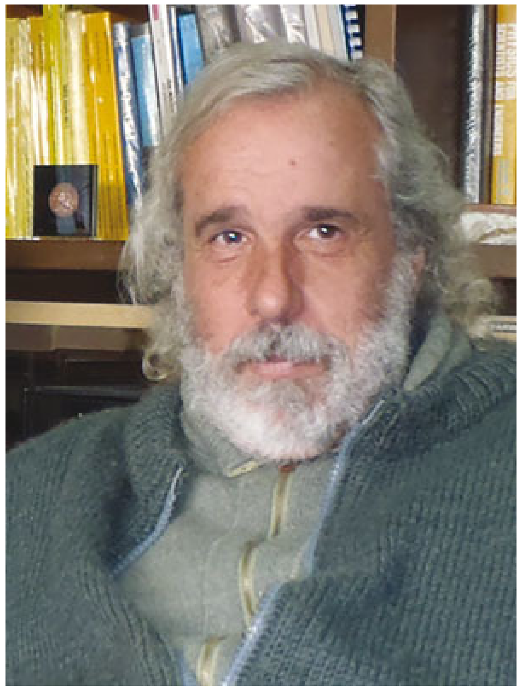

Alejandro Cristian Raga Rassmussen
1957–2023

On July past we learned of the untimely and sudden death of Dr. Alejandro Cristian Raga Rassmussen. Alex, as he was known to everyone, was an extraordinary person, characterized by his joy of living and by the great quality and versatility of his research.

He was born in 1957 in Buenos Aires, Argentina and obtained his Bachelors Degree in physics in 1982 at the University of Buenos Aires, and his Masters and PhD in astronomy at the University of Washington, Seattle, where he was located from 1982 to 1985. His PhD thesis advisor was Karl-Heinz Bhm, an expert on the physical foundations of stellar and interstellar astrophysics. Alex and Karl-Heinz went on to publish a score of important papers together. From 1986 to 1995 Alex held postdoctoral and, later, research fellow positions in Canada and the United Kingdom.

In spite of his having tenure in his last position in the United Kingdom, he chose to move to Mexico in 1995, in good part to work with Jorge Cantó, a distinguished researcher at the Institute of Astronomy of the National Autonomous University of Mexico (UNAM) in Mexico City. They integrated a formidable duo, with Jorge mastering the analytic approach to theoretical problems and Alex extending their results to a diversity of situations using a numerical approach. The informative Astrophysics Data System tells us that they collaborated in 127 refereed publications that have received over 3,000 citations. In total, Alex accumulated more than 10,000 citations. He published with around 300 coauthors. The enclosed Figure 1 shows his co-authorship network restricted to colleagues with whom he published two or more papers.

He made important contributions in several fields of astronomy. In particular, his work has been crucial to fully understand the so-called Herbig-Haro objects (co-discovered by the Mexican Guillermo Haro) and the

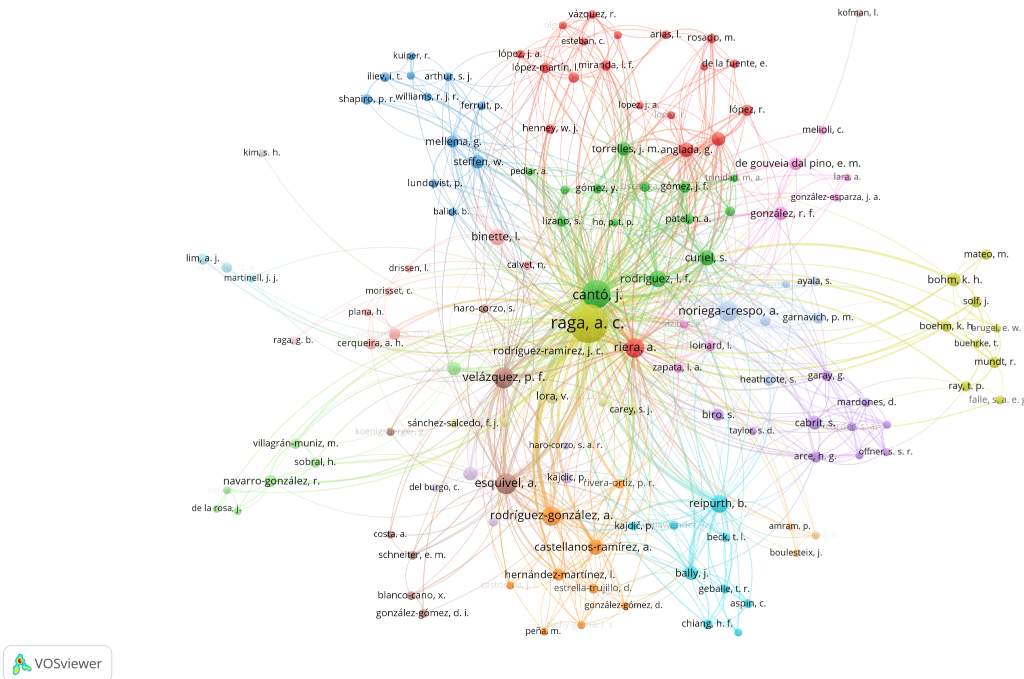

Fig. 1. Co-authorship network restricted to colleagues with whom he published two or more papers.

present paradigm of these objects owes much to his ideas. Alex was the person to go to when you had data of a new astronomical phenomenon. I remember that strong X-ray emission was found in a cluster of massive stars near the galactic center. He and a group of collaborators accurately and promptly explained the emission in terms of shocks between the powerful winds of the stars in the cluster.

He ventured successfully into topics outside of the astronomy of the interstellar medium. These included modeling the explosions of the Popocatepetl volcano, revisiting the Viking results on Mars, analyzing shock waves produced in the laboratory, and even discussing the sociology of astronomy as applied to Herbig-Haro objects 1 and 2. He was also a frequent collaborator of this journal. Among many abilities, he played the piano for his friends. His bonhomie and thunderous laughter generally characterized him. But this bonhomie could transform into indignation when he perceived an injustice. I remember that at one meeting he publicly faced an eminent astronomer that had been unfairly treating other speakers.

Over the years, he directed some 20 theses. Many of his students are part of the group he formed at the Institute of Nuclear Research of UNAM, to where he moved in 2001 from the Institute of Astronomy. Alex received many distinctions and awards: the Guggenheim Fellowship, the Award of the Mexican Academy of Sciences, the TWAS Prize, and the UNAM Award, just to name some of them.

Alex was in love with the sea. I remember that his family and mine together rented a house in the Mayan Riviera. Alex brought his windsurfing gear and was at sea for hours. Later, he bought a sailboat and, much to the concern of his friends, he undertook long solo cruises in the Caribbean. He also had a cabin next to the beach in Guatemala; that was where he became ill of thrombosis complications and passed away.

He is survived by his daughter Micaela and by his companion Magda. We will remember him every time we consult one of his many contributions to astronomy or drink a good cup of coffee, another of his hobbies.

I thank Pablo F. Velázquez and Vicente Rodríguez-Gómez for their help in preparing this obituary. I also acknowledge the use of VOSviewer for providing the tools to visualize Alex's coauthorship network. The photo was contributed by Primoz Kajdic.

Luis Felipe Rodríguez

AUTHOR INDEX

La *Revista Mexicana de Astronomía y Astrofísica*, fundada en 1974, publica trabajos originales de investigación en todas las ramas de la astronomía, astrofísica y temas vinculados a éstas. Se editan dos números por año y su distribución es gratuita a todas las instituciones relacionadas con los campos cubiertos por esta revista.

La política editorial de la *RMxAA* consiste en enviar a arbitrar los artículos recibidos a especialistas en el campo. Los interesados en publicar en nuestra revista deberán enviar por correo electrónico, a la dirección rmaa@astro.unam.mx, la versión completa de su artículo en formato PostScript o PDF y el archivo LaTeX. Estos archivos deberán ir acompañados de una carta de presentación. Todos los trabajos deben ser preparados en inglés usando la versión más reciente del macro en LaTeX de la *RMxAA* "rmaa.cls" (disponible en https://www.irya.unam.mx/rmaa/). Se requiere un "Abstract" no mayor que 12 líneas, y un "Resumen" en español (este último podrá ser provisto por los editores de ser necesario); también se incluirán de 1 a 6 palabras clave ("Keywords") de la lista de las revistas astronómicas internacionales. Se requiere que cada tabla incluida en el texto esté numerada y con título; las figuras deberán estar en formato PostScript (.ps) o PostScript encapsulado (.eps), estar numeradas y con leyenda explicativa. Se requiere que cada tabla y figura estén mencionadas en el texto. El estilo de las referencias sigue las normas astronómicas internacionales recientes. Para mayor información sobre el estilo de la *RMxAA* se puede consultar el archivo de ejemplo que viene incluido en los macros. La publicación es gratuita para los autores.

En 1995 se inició la Serie de Conferencias de la *Revista Mexicana de Astronomía y Astrofísica*, dedicada a la publicación de las memorias de reuniones astrónomicas efectuadas en México y en otros países del continente. Hasta 1994 las memorias de reuniones astronómicas de la región se publicaron como volúmenes especiales de la *RMxAA*.

Las condiciones de publicación de cada volumen de las memorias de conferencias serán el resultado de un convenio establecido entre la *RMxAC* y los organizadores de cada evento. Los detalles de la publicación, que incluyen fechas y extensión de los textos, serán anunciados por los editores de cada conferencia. Las contribuciones extensas estarán en inglés con un resumen en español (o portugués en caso de las Reuniones regionales). Los resúmenes de las reuniones que no son temáticas tendrán una extensión máxima de 300 palabras incluyendo título, autores y afiliación; serán exclusivamente en inglés. Los macros LaTeX para las memorias se encuentran en http://www.astroscu.unam.mx/~rmaa. Todas las contribuciones y resúmenes deberán estar en estos formatos.

Se concede permiso a los autores de artículos y libros científi-cos para citar trabajos publicados en la *RMxAA* y en la *RMxAC* siempre y cuando se dé la referencia completa. También se permite la reproducción de figuras y tablas bajo las mismas condiciones.

La *RMxAA* aparece indexada en Current Contents, Science Citation Index, Astronomy and Astrophysics Abstracts, Physics Briefs, Publicaciones Científicas en América Latina, Astronomy and Astrophysics Monthly Index, PERIODICA, RedALyC, Latindex y SciELO.

The *Revista Mexicana de Astronomía y Astrofísica*, founded in 1974, publishes original research papers in all branches of astronomy, astrophysics and closely related fields. Two numbers per year are issued and are distributed free of charge to all institutions engaged in the fields covered by the *RMxAA*.

All papers received by the *RMxAA* are sent to a specialist in the field for refereeing. Authors interested in publishing in the *RMxAA* should send their papers to the e-mail address rmaa@astro.unam.mx, in PostScript or PDF format, along with the LaTeX file. A submission letter should also be sent. Papers should be prepared in English, using the most recent version of the *RMxAA* LaTeX document class "rmaa.cls" (available from https://www.irya.unam.mx/rmaa/). An "Abstract" of at most 12 lines is required, as well as a "Resumen" in Spanish. The latter can be provided by the Editors, if necessary. A total of six or fewer "Keywords", taken from the lists of international astronomical journals should be included. Tables should be numbered and include a title. Figures should be submitted in PostScript (.ps) or Encapsulated PostScript (.eps) format, should be numbered, and should include a caption. Both tables and figures should be mentioned in the text. The style of the references follows recent international astronomical usage. For more information about the style norms of *RMxAA* please consult the example included in the LaTeX package. Publication in *RMxAA* is free of charge to authors.

The Conference Series of *Revista Mexicana de Astronomía y Astrofísica* was founded in 1995 to publish the proceedings of astronomical meetings held in Mexico and other countries throughout the continent. Until 1994 such proceedings had been published as special issues of *Revista Mexicana de Astronomía y Astrofísica*.

Conditions of publication of proceedings of each conference will be the result of a mutual agreement between the *RMxAC* and the organizing committee. Details of publication, including length of papers, will be announced by the editors of each event. The extensive contributions should be in English, and should include an abstract in Spanish (or Portuguese for regional meetings). The abstracts of non-thematic meetings should not exceed 300 words including title, authors, and affiliation; they should be exclusively in English. The LaTeX templates specially prepared for proceedings can be obtained at http://www.astroscu.unam.mx/~rmaa; all papers should be submitted in this format.

Authors of scientific papers and books may quote articles published both in *RMxAA* and *RMxAC* provided that a complete reference to the source is given. Reproduction of figures and tables is also permitted on the same basis.

The *RMxAA* is indexed in Current Contents, Science Citation Index, Astronomy and Astrophysics Abstracts, Physics Briefs, Publicaciones Científicas en América Latina, Astronomy and Astrophysics Monthly Index, PERIODICA, RedALyC, Latindex, and SciELO.